UNIVERSIDAD NACIONAL DEL LITORAL

DOCTORADO EN INGENIERÍA

Contribuciones al modelado computacional de fractura frágil: nuevas estrategias y métodos híbridos.

Javier Alexander Zambrano Carrillo

FICH

FACULTAD DE INGENIERÍA

Y CIENCIAS HÍDRICAS

INTEC

INSTITUTO DE DESARROLLO TECNOLÓGICO

PARA LA INDUSTRIA QUÍMICA

CIMEC

CENTRO DE INVESTIGACIÓN

DE MÉTODOS COMPUTACIONALES

sinc(*i*)

INSTITUTO DE INVESTIGACIÓN EN SEÑALES,

SISTEMAS E INTELIGENCIA COMPUTACIONAL

Tesis de Doctorado **2025**

Doctorado en Ingeniería

Mención mecánica computacional

Título de la obra:

Contribuciones al modelado computacional de fractura frágil: nuevas estrategias y métodos híbridos

Autor: Javier Alexander Zambrano Carrillo

Lugar: Santa Fe, Argentina

Palabras Claves:

Mecánica computacional, mecánica de fractura,
modelo de campo de fase, fractura frágil, propagación de grietas,
mecanismos de interacción grieta-interface, tenacidad y resistencia a la fractura,
materiales compuestos, diseños bioinspirados,
metodología escalonada, estrategia de control de longitud de arco,
método de elemento finito, método de Galerkin libre de elementos mejorado,
métodos híbridos.

UNIVERSIDAD NACIONAL DEL LITORAL

Facultad de Ingeniería y Ciencias Hídricas

Instituto de Desarrollo Tecnológico para la Industria Química

Centro de Investigación de Métodos Computacionales

Instituto de Investigación en Señales, Sistemas e Inteligencia Computacional

Contribuciones al modelado computacional de fractura frágil: nuevas estrategias y métodos híbridos

Javier Alexander Zambrano Carrillo

Tesis remitida al Comité Académico del Doctorado
como parte de los requisitos para la obtención
del grado de
DOCTOR EN INGENIERÍA
Mención Mecánica Computacional
de la
UNIVERSIDAD NACIONAL DEL LITORAL

2025

Secretaría de Posgrado, Facultad de Ingeniería y Ciencias Hídricas, Ciudad Universitaria,
Paraje “El Pozo”, S3000, Santa Fe, Argentina.

UNIVERSIDAD NACIONAL DEL LITORAL

Facultad de Ingeniería y Ciencias Hídricas

Instituto de Desarrollo Tecnológico para la Industria Química

Centro de Investigación de Métodos Computacionales

Instituto de Investigación en Señales, Sistemas e Inteligencia Computacional

Contribuciones al modelado computacional de fractura frágil: nuevas estrategias y métodos híbridos

Javier Alexander Zambrano Carrillo

Lugar de trabajo:
CIMEC
Centro de Investigación de Métodos Computacionales
Facultad de Ingeniería y Ciencias Hídricas
Universidad Nacional del Litoral

Director:
Alfredo Edmundo Huespe CIMEC (CONICET-UNL) / FICH - UNL

Co-director:
Santiago Serebrinsky YTEC-CONICET / YPF TECNOLOGÍA

Jurado Evaluador:
Dr. Adrián Lew School of Mechanical Engineering / Stanford University, USA
Dr. Ignacio Iturrioz UFRGS / Universidade Federal do Rio Grande do Sul, Brasil
Dr. Juan Elías Pérez Ipiña CONICET / Consejo Nacional de Investigaciones Científicas y Técnicas

2025

2025 – 40° Aniversario de la Creación del Consejo Interuniversitario Nacional

ACTA DE EVALUACIÓN DE TESIS DE DOCTORADO

En la sede de la Facultad de Ingeniería y Ciencias Hídricas de la Universidad Nacional del Litoral, a los siete días del mes de julio del año dos mil veinticinco, se reúnen en forma online sincrónica los miembros del Jurado designado para la evaluación de la Tesis de Doctorado en Ingeniería, Mención "Mecánica Computacional", titulada ***"Contribuciones al modelado computacional de fractura frágil: nuevas estrategias y métodos híbridos."***, desarrollada por el Ing. Javier Alexander ZAMBRANO CARRILLO, PAS N° 145154440, bajo la dirección del Dr. Alfredo Huespe y la codirección del Dr. Santiago Serebrinsky. Ellos son: Dr. Adrián Lew, el Dr. Ignacio Iturrioz y el Dr. Juan Elías Pérez Ipiña.----------

La Presentación oral y la defensa de la Tesis se efectúan bajo la modalidad online sincrónica según lo establecido por Resolución CS N° 382/21.

Luego de escuchar la Defensa Pública y de evaluar la Tesis, el Jurado considera:

Que el documento escrito deja en evidencia las contribuciones realizadas por el tesista, así como las publicaciones presentadas en revistas internacionales.

La presentación ha sido clara y las respuestas a las preguntas del Jurado fueron solventes y precisas.

Por lo tanto, el Jurado resuelve aprobar la tesis con calificación 10 (Diez) Sobresaliente.

Sin más, se da por finalizado el Acto Académico con la firma de los miembros del Jurado al pie de la presente. ----------

----------	----------	----------
Dr. Adrián Lew	Dr. Ignacio Iturrioz	Dr. Juan Elías Pérez Ipiña

FACULTAD DE INGENIERÍA Y CIENCIAS HÍDRICAS – SANTA FE
DR. JOSE LUIS MACON
SECRETARIO DE POSGRADO
Facultad de Ingeniería y Cs. Hídricas

Universidad Nacional del Litoral
Facultad de Ingeniería y Ciencias Hídricas

Secretaría de Posgrado

Ciudad Universitaria
C.C. 217
Ruta Nacional Nº 168 – Km. 472,4
(3000) Santa Fe
Tel: (54) (0342) 4575 229
Fax: (54) (0342) 4575 224
E-mail: posgrado@fich.unl.edu.ar

Declaración legal del autor

Esta Tesis ha sido remitida como parte de los requisitos para la obtención del grado de Doctor ante la Universidad Nacional del Litoral y ha sido depositada en la Biblioteca de la Facultad de Ingeniería y Ciencias Hídricas para que esté disponible a sus lectores bajo las condiciones estipuladas por el Reglamento de la mencionada Biblioteca.

Citaciones breves de esta disertación son permitidas sin la necesidad de un permiso especial, en la suposición de que la fuente sea correctamente citada. Solicitudes de permiso para una citación extendida o para la reproducción de este manuscrito en un todo o en parte serán exigidas por el portador legal del derecho de propiedad intelectual de la misma.

Javier Alexander Zambrano Carrillo

Dedicado a mis Padres.

Simplemente gracias infinitas.

Agradecimientos

Primeramente, agradezco a la República Argentina por abrirme sus puertas y bridarme la valiosa oportunidad de realizar un doctorado. También expreso mi gratitud a las instituciones que respaldaron el desarrollo de esta tesis: el Consejo Nacional de Investigaciones Científicas y Técnicas (CONICET), la Facultad de Ingeniería y Ciencias Hídricas de la Universidad Nacional del Litoral (FICH-UNL), que además me brindo la oportunidad de desempeñarme como docente, y el Centro de Investigación de Métodos Computacionales (CIMEC), un excelente espacio de trabajo y un referente en el ámbito de la Mecánica Computacional.

Quiero expresar un agradecimiento especial al Dr. Alfredo Huespe, mi director de doctorado, por haberme recibido y apoyado siempre con total disposición a lo largo de mi estancia doctoral. En el ámbito académico, ha sido un gran maestro y excelente profesional, siempre a la vanguardia en la investigación científica. En el ámbito personal, ha sido un amigo con gran generosidad.

Extiendo mi gratitud al Dr. Juan Carlos Álvarez Hostos, quien fue el responsable de motivarme a postularme para este doctorado. Su apoyo tanto académico como personal ha sido invaluable, y le agradezco profundamente por su amistad y orientación durante toda mi estadia doctoral.

Agradezco también a todos aquellos con los que tuve el gusto de colaborar y aprender durante este proceso. En particular, al equipo de investigación con el que trabajé, integrado por el: Dr. Sebastian Toro, Dr. Carlos Mendez, Dr. Pablo Sanchez y el Dr. Santiago Serebrinsky, mi co-director de tesis y un excelente profesional. Asimismo, expreso mi gratitud a mis compañeros del CIMEC por su apoyo y los momentos compartidos que enriquecieron mi experiencia doctoral.

Mi más profundo agradecimiento es para mis padres, Maria Carrillo y José Zambrano, por siempre apoyarme de forma incondicional en lo que me propongo a pesar de las adversidades de la vida. Son ellos los responsables de lo que hoy soy como profesional y siempre ocuparán la primera plana de todos mis éxitos.

Finalmente agradezco a mi segunda madre, la Sra. Irlanda Carrero y mi hermana de vida, Anair Salazar, por estar siempre pendiente de mí y brindarme una mano amiga en todo momento.

Resumen

La siguiente tesis comprende la aplicación de un conjunto de estrategias numéricas para el modelado de fractura frágil, a través de la implementación del modelo de campo de fase y métodos de solución híbridos. El modelo de campo de fase es un enfoque que describe la fractura mediante un campo escalar que varía en un intervalo de $[0, 1]$, donde 0 representa material intacto y 1 indica material completamente dañado. Mientras que los valores intermedios en dicho intervalo corresponden a estados de daño parcial. Una de las principales ventajas de este modelo es su capacidad para simular la evolución de grietas sin necesidad de re-mallado, ni modificaciones geométricas, permitiendo así representar trayectorias de fractura complejas, incluidas bifurcaciones y ramificaciones.

Por consiguiente, en esta tesis se implementan diversas herramientas numéricas que integran tanto modelos constitutivos acoplados como técnicas avanzadas de resolución numérica, con diversos propósitos relacionados primeramente con el análisis de los mecanismos de interacción entre una grieta propagante que incide con una interface, a través de la implementación de un modelo de campo de fase acoplado con un modelo de superficie cohesiva. Donde el primer modelo permite estudiar la propagación de una grieta en un determinado medio y el segundo modelo se emplea para analizar la degradación de una interface presente en un cuerpo. Según lo reportado en la literatura, la ocurrencia de cada mecanismo depende exclusivamente de las propiedades de fractura del material, que caracterizan tanto la interface como el medio en el que se propaga la grieta. Los resultados obtenidos con este enfoque indican que estos modos de interacción están gobernados por un criterio mixto que involucra las relaciones de tenacidad y resistencia del medio y la interface.

Por otra parte, con el objetivo de optimizar el análisis de la propagación de grietas en diferentes geometrías mediante el modelo de campo de fase, se implementan técnicas de resolución numéricas mejoradas, por medio de la aplicación de una técnica de control de longitud de arco, utilizando un esquema escalonado, lo que permite generar algoritmos computacionales eficientes, capaces de trazar curvas de equilibrio completas en problemas de fractura frágil. Este enfoque permite ampliar las capacidades del modelo de campo de fase, para abordar una mayor variedad de problemas. Seguidamente, la implementación de un método numérico acoplado entre el método de elemento finito (MEF) y el método de Galerkin libre de elementos mejorado (MGLEM) superpuesto introduce una herramienta novedosa para la resolución de diversos problemas, que abarcan desde la transferencia de calor y la elasticidad lineal, hasta la mecánica de fractura basada en el modelo de campo de fase. Esto produce una mejora sustancial en el costo computacional que implica resolver problemas de este tipo, preservando una descripción detallada de los campos que circundan la punta de la grieta propagante, sin necesidad de apelar a una malla refinada en toda la región intersectada por la grieta.

Seis trabajos surgen como resultado de los estudios realizados en esta tesis, de los cuales cuatro son publicaciones en revistas internacionales, un resumen publicado en un congreso internacional y un trabajo completo publicado en un congreso nacional.

Abstract

This thesis encompasses the application of a set of numerical strategies for modeling brittle fracture through the implementation of the phase-field model and hybrid solution methods. The phase-field model is an approach that describes fracture using a scalar field varying in the range of $[0, 1]$, where 0 represents intact material and 1 indicates fully damaged material. Intermediate values in this range correspond to states of partial damage. One of the main advantages of this model is its ability to simulate crack evolution without requiring re-meshing or geometric modifications, enabling the representation of complex fracture trajectories, including bifurcations and branching.

Consequently, this thesis implements various numerical tools that integrate both coupled constitutive models and advanced numerical solution techniques. These tools are used primarily to analyze the mechanisms of interaction between a propagating crack and an interface. This is achieved through the implementation of a phase-field model coupled with a cohesive surface model. The phase-field model enables the study of crack propagation in a given medium, while the cohesive surface model is employed to analyze the degradation of an interface present in a body. As reported in the literature, the occurrence of each mechanism depends exclusively on the fracture properties of the material, which characterize both the interface and the medium where the crack propagates. The results obtained with this approach indicate that these interaction modes are governed by a mixed criterion involving the toughness and strength ratios of the medium and the interface.

Furthermore, with the aim of optimizing the analysis of crack propagation in different geometries using the phase-field model, improved numerical resolution techniques are implemented. These include an arc-length control technique using a staggered scheme, which allows the development of efficient computational algorithms capable of tracing complete equilibrium paths in brittle fracture problems. This approach enhances the capabilities of the phase-field model to address a broader variety of problems. Additionally, the implementation of a coupled numerical method combining the finite element method (FEM) and the Overset Improved Meshfree Galerkin Method (IEFG) introduces an innovative tool for solving various problems. These range from heat transfer and linear elasticity to fracture mechanics based on the phase-field model. This coupling substantially improves the computational cost of solving such problems while preserving a detailed description of the fields surrounding the crack tip without requiring a refined mesh throughout the entire region intersected by the crack.

Six works have resulted from the studies conducted in this thesis, including four publications in international journals, one abstract published in an international conference, and one full paper published in a national conference.

Índice general

Índice de figuras

Índice de tablas

Parte I

Introducción

Capítulo 1

Introducción

1.1. De qué trata esta tesis

La mecánica de fractura es una disciplina esencial en la ingeniería de materiales, cuyo propósito es comprender y predecir el comportamiento de los materiales cuando se ven sometidos a cargas que inducen la propagación de grietas. Los desafíos para modelar y simular fenómenos de fractura siguen siendo significativos, por ende, a medida que los materiales se vuelven más sofisticados y los problemas de ingeniería más complejos, se requieren métodos de análisis más precisos y robustos.

Esta tesis aborda algunos de estos desafíos utilizando enfoques avanzados de modelado, con énfasis en la aplicación de métodos acoplados que combinan tanto modelos constitutivos como técnicas numéricas mejoradas para resolver una variedad de problemas de la mecánica de fractura. Se conoce que las propiedades de resistencia y tenacidad, desempeñan un papel fundamental en la determinación del mecanismo de interacción que surge entre una grieta propagante en un medio sólido que impacta en una interface adhesiva, donde dichas interfaces pueden caracterizarse por tensiones críticas y tenacidad.

Este es un problema importante en la mecánica de fractura, debido a que existe una fuerte interacción entre las propiedades mecánicas de los materiales relacionados con la resistencia y tenacidad de los mismos, que determinan las condiciones bajo las cuales una grieta se nucleará y propagará en un sólido como bien se encuentra discutido en la literatura a través de la clara vision aportada tanto por Leguillon [2] como por Ritchie [3].

El mecanismo resultante de esta interacción posee consecuencias relevantes en variados problemas a nivel tecnológico, como por ejemplo la influencia que tiene en la tenacidad extrínseca de los compuestos laminados (Noselli et al. [4]), los problemas de fractura hidráulica con aplicación en yacimientos de petróleo no convencionales (Chuprakov et al. [5], Garagash [6], Giovanardi et al. [7], Gutiérrez [8]) y la evaluación del mecanismo de transición entre fractura intergranular y transgranular en microestructuras heterogéneas, (Foulk III et al. [9], Chen et al. [10]). Otro ejemplo clave donde estas propiedades juegan un papel prominente se encuentra en los diseños bioinspirados, los cuales tratan de imitar la exquisita estructura de los biomateriales con el propósito de desarrollar materiales artificiales bioinspirados con características mecánicas avanzadas.

Las propiedades mecánicas superiores de estos diseños bioinspirados se deben a la mezcla ingeniosa de sus materiales constitutivos que poseen propiedades de fractura contrastadas. Ji y Gao [11] reportaron que las grandes relaciones de aspecto y una alineación escalonada de las plaquetas minerales (fase rígida del material) son los factores clave que contribuyen a la gran rigidez y resistencia de los nanocompuestos biológicos.

Los diferentes mecanismos que producen un aumento de la tenacidad estructural tanto en diferentes materiales compuestos, como en los diseños bioinspirados se encuentran plenamente relacionados con un criterio mixto en el cual intervienen las relaciones entre la tenacidad y la resistencia de los materiales que componen al medio y las interfaces presentes en los modelos y esto se puede ver evidenciado en

trabajos pasados donde se estudia ampliamente el problema de una grieta propagante incidiendo en una interface implementando diferentes enfoques tanto analíticos como numéricos.

Por otra parte, un problema adicional al modelar problemas de fractura cuasi-frágil, es la existencia de puntos límite y retrocesos en la trayectoria de equilibrio estructural. Este ingrediente requiere el uso de estrategias de control de carga para manejar numéricamente los problemas de crecimiento inestable de grietas. En el área que comprende los problemas de fractura cuasi-frágil, un procedimiento automático dirigido a resolver este problema es la estrategia de control basada en limitar la disipación de energía (Gutiérrez [12]) o la tasa de liberación de energía (Verhoosel et al. [13]) en cada paso de carga. Alternativamente, otra técnica innovadora se muestra en el estudio realizado por Zambrano et al. [14].

En el contexto del costo computacional asociado a la resolución de problemas de fractura frágil mediante el modelo de campo de fase, es importante considerar que las mallas utilizadas deben cumplir una condición vinculada con la longitud característica del material. En particular, la zona de propagación de la grieta debe estar discretizada con elementos cuyo tamaño sea igual o inferior a un tercio o un quinto de dicha longitud, con el objetivo de capturar de manera eficiente el campo de fase. Como consecuencia, este requisito impone severas restricciones en la carga computacional del modelo numérico.

Algunas herramientas alternativas se han postulado en la literatura para manejar dicha problemática, entre las cuales se tiene el uso de métodos híbridos utilizando tanto el método de elemento finito (MEF) como el método de Galerkin libre de elementos mejorado (MGLEM). Se conoce que la mayoría de los procedimientos híbridos MEF-MGLE requieren de elementos de interface que utilizan funciones de rampa para una transición suave entre las regiones MEF y MGLE, por lo que la implementación de estos enfoques en escenarios que involucran geometrías de topología compleja puede ser muy desafiante. Sin embargo, algunos autores (Álvarez Hostos et al. [15], Zambrano-Carrillo et al. [16]) han logrado recientemente realizar tal acoplamiento sin la necesidad de elementos de transición.

De acuerdo con las ideas expuestas anteriormente, esta tesis se encuentra enmarcada en tres temáticas clave, las cuales motivan al desarrollo de la misma y representan la continuación de los variados aportes realizados por el grupo de investigación en mecánica de fractura del Centro de Investigación de Métodos Computacionales (CIMEC), a través de las diversas publicaciones en revistas y trabajos de tesis realizados. Por consiguiente, estas líneas temáticas se enfoncan primeramente en el estudio de los mecanismos de interacción entre una grieta propagante que incide en una interface, continuando con el análisis de los diseños bioinspirados para el incremento de tenacidad en materiales compuestos, seguidamente el desarrollo de algoritmos computacionales para el trazado eficiente de curvas de equilibrio completas y finalmente en la implementación de métodos numéricos acoplados para la resolución de problemas de fractura frágil.

En base a las temáticas mencionadas previamente, el capítulo II de esta tesis presenta los fundamentos necesarios para comprender el contenido de los capítulos posteriores. Este capítulo aborda el modelo de campo de fase utilizado en nuestros estudios, se describen las metodologías numéricas para el modelado de propagación de grietas que impactan con una interface. Seguidamente, se expresan las nociones fundamentales de los materiales bioinspirados. Luego, se hace referencia a las técnicas de control de avance de grieta y los esquemas de resolución en problemas de fractura frágil y finalmente se realizan comentarios sobre los métodos numéricos acoplados que combinan el MEF y MGLE. Posteriormente en el capítulo III se realiza un análisis de los diferentes mecanismos de interacción entre una grieta que propaga a través de un medio e incide con una interface, lo cual esta vinculado con el Apéndice A y B.

Luego, el capítulo IV se centra en los diseños bioinspirados destinados a mejorar la tenacidad en materiales compuestos, lo cual esta relacionado con el trabajo anexado en el Apéndice C. En el capítulo V se exponen las estrategias de control y resolución para llevar a cabo la solución de problemas de fractura frágil, vinculado con el Apéndice D. Por consiguiente, el capítulo VI analiza un método híbrido acoplado para la solución de diversos tipos de problemas. Finalmente, el capítulo VII reúne las conclusiones principales de esta tesis.

Por lo tanto, esta tesis se enfoca en contribuir al desarrollo de estrategias numéricas destinadas a

optimizar la simulación de la fractura frágil. Particularmente, implementando el modelo de campo de fase en combinación con técnicas avanzadas para la resolución de las ecuaciones derivadas de dicho modelo, acompañado de métodos híbridos que contribuyen a mejorar el factor costo computacional que son inherente a la solución de este tipo de problemas. En este contexto, se estudian problemas que van desde el analisis de la propagación de grietas en materiales compuestos, el diseño de algoritmos computacionales para el trazado eficiente de curvas de equilibrio, hasta la implementación alternativa de métodos numéricos superpuestos, todos enmarcados dentro de la mecánica de fractura frágil.

1.2. Objetivos

1.2.1. Objetivo general

Desarrollar estrategias numéricas avanzadas que optimicen la simulación de fractura frágil, integrando el modelo de campo de fase con técnicas de resolución eficientes y métodos híbridos, para abordar de manera robusta y precisa problemas complejos de propagación de grietas en materiales y estructuras homogéneas y heterogéneas.

1.2.2. Objetivos específicos

- Implementar el modelo de campo de fase para simular de manera precisa la nucleación y propagación de grietas en materiales frágiles, junto con el modelo de superficie cohesiva, considerando las relaciones entre resistencia y tenacidad, aunque fundamentalmente el papel que juegan ambas propiedades, en medios tanto homogéneos como heterogéneos y en presencia de interfaces.
- Diseñar y aplicar algoritmos computacionales innovadores para el trazado eficiente de curvas de equilibrio completas en problemas de fractura frágil, mediante el uso de una técnica de control de avance de grietas y un esquema escalonado de resolución numérica optimizada, con el propósito de mejorar la robustez y la eficiencia en los cálculos asociados.
- Implementar métodos híbridos como el modelo numérico acoplado tipo Overset MEF-MGLEM, para abordar problemas con geometrías complejas y reducir el costo computacional en simulaciones de fractura frágil.
- Validar y comparar las estrategias numéricas propuestas mediante experimentos numéricos y análisis de resultados obtenidos en problemas clásicos de la mecánica de fractura, evaluando su precisión, robustez y ventajas frente a métodos tradicionales.

1.3. Estructura de la tesis

Esta tesis se desarrolla bajo el formato de tesis por compilación, cuyo propósito principal es integrar de manera coherente los trabajos publicados. Por ende, la estructura de la tesis está diseñada para proporcionar al lector una visión clara de la secuencia de aprendizajes adquiridos y contribuciones realizadas durante el desarrollo del doctorado, destacando tanto las dificultades encontradas en el proceso de investigación como las razones detrás de las soluciones adoptadas. Esta estructura tiene como finalidad facilitar la lectura de las publicaciones incluidas, las cuales contienen los aportes concretos alcanzados y se reproducen en los Apéndices.

Para evitar redundancias, se ha procurado minimizar la repetición de información o la presentación de resultados ya expuestos en los artículos publicados. No obstante, algunos capítulos incluyen contenido no publicado con el propósito de reforzar los conceptos principales. Particularmente esto sucede en el último capítulo, donde se exponen los aportes más destacados de la tesis, incluyendo trabajos en continuo desarrollo.

Por lo tanto, la estructura general de la tesis se encuentra constituida por cinco partes: (I) Introducción, (II) Preliminares, (III) Aportes al desarrollo de estrategias numéricas para optimizar la simulación de fractura frágil, (IV) Conclusiones, y (V) Apéndices, las cuales se explican a continuación:

- La “Parte I: Introducción” aborda el contexto general de lo que trata esta tesis y establece los objetivos propuestos. Esta sección consta de un único capítulo.
- La ”Parte II: Preliminares”se incluye en la tesis con el fin de garantizar que sea razonablemente completa, manteniendo al mismo tiempo el enfoque de tesis por compilación. Su único capítulo tiene como objetivo presentar una recopilación de conceptos establecidos en la literatura, que no constituyen aportes originales de esta tesis, pero que son fundamentales para sustentar la teoría presentada. Estos conceptos, generalmente no incluidos en las publicaciones debido a su naturaleza de conocimiento general, abarcan una variedad de temas estudiados durante el doctorado. Entre ellos se encuentran: la descripción del modelo de campo de fase para fractura frágil, las técnicas numéricas para modelado de propagación de grietas incidiendo con una interface, las nociones fundamentales de los diseños bioinspirados, la técnica de control de longitud de arco y esquemas de resolución numérica para problemas de fractura frágil y finalmente comentarios sobre métodos numéricos acoplados que combinan el MEF y MGLE. Aunque se hace referencia a este material a lo largo de la tesis, los lectores familiarizados con estos conceptos pueden omitir este capítulo sin inconvenientes.
- La “Parte III: Aportes al desarrollo de estrategias numéricas para la simulación de fractura frágil” se compone de los cuatro capítulos que abordan las principales contribuciones de esta tesis. Los capítulos 3 y 4 se centran en el análisis de los mecanismos de interacción que surgen entre una grieta propagante y una interface, tanto en geometrías clásicas de la mecánica de fractura como en diseños bio-inspirados. Por otro lado, los capítulos 5 y 6 se enfocan en la discusión de técnicas de control y esquemas de resolución para problemas de fractura frágil, utilizando tanto el modelo de campo de fase como la combinación de métodos numéricos híbridos.
- La “Parte IV: Conclusiones” está compuesta por un capítulo conciso que expone las principales contribuciones de este trabajo.
- La “Parte V: Apéndices” contiene los seis trabajos publicados que constituyen esta tesis, cuatro de ellos son publicaciones en revistas internacionales, un resumen publicado en un congreso internacional y un trabajo completo publicado en un congreso nacional.

Finalmente, en la Figura 1.1 se propone una secuencia de lectura recomendada, organizada según el contenido de los capítulos y su relación con las publicaciones.

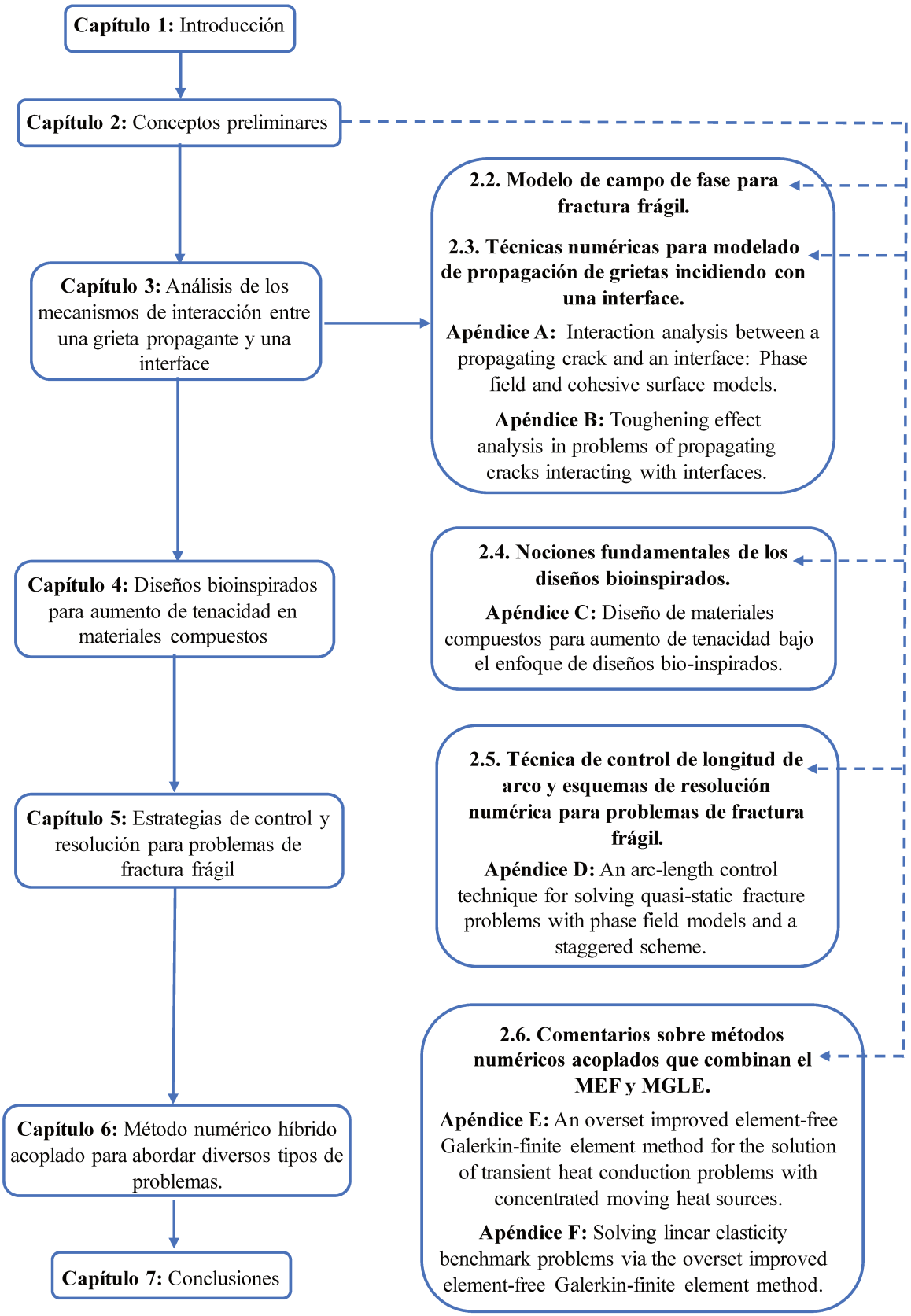

Figura 1.1: Estructura de la tesis, con secuencia de lectura recomendada.

Parte II

Preliminares

Capítulo 2

Conceptos preliminares

2.1. Introducción

Este capítulo tiene como objetivo presentar de manera concisa las principales temáticas empleadas en el desarrollo de esta tesis, las cuales son esenciales para su comprensión en los próximos capítulos. Los temas abordados en este capítulo se exponen en el siguiente orden: la sección 2.2 se encuentra dedicada al modelo de campo de fase, donde se analizan sus nociones fundamentales, formulación, y las ventajas e inconvenientes del mismo. Seguidamente, la sección 2.3 proporciona una breve descripción de los enfoques numéricos empleados para modelar la interacción de una grieta propagante que impacta en una interface. La sección 2.4 expone las nociones fundamentales correspondientes a los diseños bioinspirados. Posteriormente, la sección 2.5 aborda lo referente a la técnica de longitud de arco y los diferentes esquemas utilizados en la solución numérica de problemas de fractura frágil, presentando las ventajas y dificultades de su implementación. Finalmente, en la sección 2.6 se presentan diversos comentarios relacionados con el empleo de métodos numéricos acoplados que combinan el método de elemento finito (MEF) y el método de Galerkin libre de elementos (MGLE) para la resolución de problemas en un contexto general.

2.2. Modelo de campo de fase para fractura frágil

Las dificultades asociadas al modelado de grietas discontinuas (discretas), motivaron otras técnicas computacionales en las que las trayectorias de las grietas se determinan automáticamente como parte de la solución. Dentro de estas técnicas numéricas, actualmente se tiene una muy popular denominada el modelo de campo de fase (PFM por sus siglas en inglés), dicho modelo básicamente parte de la formulación para fractura frágil originalmente contribuida por Francfort y Marigo [17], la cual esta basada únicamente en la idea de Griffith de la competencia entre la energía almacenada del cuerpo y la energía de fractura.

Este modelo de fractura es capaz de tratar cuestiones como la trayectoria de la grieta y la nucleación de la misma. En la versión original de Francfort y Marigo, más en sintonía con la Mecánica de Fractura Lineal Elástica (LEFM, por sus siglas en inglés), el concepto de nucleación no existía. En versiones posteriores, y con una reinterpretración de los parámetros del modelo, el concepto de nucleación se puede abordar con esta técnica.

Sin embargo, como se señaló en dicho trabajo, su modelo hereda una limitación fundamental de la Mecánica de Fractura Lineal Elástica, la cual se relaciona con la inexistencia de una tensión máxima admisible y por ende, un criterio de resistencia del material. Entre los muchos métodos numéricos originalmente concebidos para la implementación numérica del modelo Francfort-Marigo (Bourdin y Chambolle [18], Negri y Paolini [19] Fraternali [20], Schmidt et al. [21]), las regularizaciones de Ambrosio-Tortorelli (Ambrosio y Tortorelli [22], Ambrosio [23]), originalmente introducidas en Bourdin [24], se

han convertido en una herramienta muy habitual.

Por otra parte, es necesario clarificar que el modelo de campo de fase implementado en nuestros estudios, no corresponde conceptualmente al modelo presentado por Francfort-Marigo, que requiere minimizar una energía, mientras que la aproximación empleada en nuestros análisis se asume como punto de partida el principio de trabajos virtuales, del cual se derivan directamente todas las ecuaciones de balance respectivas. Esta metodología pertenece a una línea en la mecánica de sólidos argumentada por Gurtin y Podio-Guidugli [25], [26].

Siguiendo esta metodología de Gurtin se tiene el trabajo de Fried et al. [27], el cual establece una aproximación donde la variable de campo de fase no se ve como una variable interna del modelo constitutivo, sino más bien es un descriptor cinemático microestructural embebido dentro de la teoría de los materiales micromórficos (Capriz [28]). Por ende, estas y otras aplicaciones que implican variables microestructurales, microfuerzas y microbalances se utilizan en nuestro enfoque (Capriz [28]).

El modelo de campo de fase se ha aplicado a una amplia variedad de problemas de fractura, incluyendo la fractura de materiales ferromagnéticos y piezoeléctricos (Abdollahi y Arias [29], Wilson et al. [30]), grietas térmicas (Maurini et al. [31], Bourdin et al. [32]), fractura hidráulica (Bourdin et al. [33], [34] Chukwudozie [35], Wilson y Landis [36]). Se ha empleado para tener en cuenta los efectos dinámicos (Larsen et al. [37], Bourdin et al. [38], Hofacker y Miehe [39]), el comportamiento dúctil (Alessi et al. [40], Ambati et al. [41], Miehe et al. [42]), efectos cohesivos (Conti et al. [43], Crismale y Lazzaroni [44], Freddi y Iurlano [45]), y grandes deformaciones (Ambati et al. [46], Borden et al. [47], Miehe et al. [42]).

Aunque los modelos de campo de fase se concibieron originalmente como aproximaciones al enfoque variacional de la fractura de Francfort y Marigo, en el límite decreciente de su parámetro de regularización, estos modelos también tienen sus vínculos con los modelos de daño por gradiente (Frémond y Nedjar [48], Lorentz y Andrieux [49]). En este contexto, el parámetro de regularización se mantiene fijo y se interpreta como la longitud interna del material.

En particular, Pham y Marigo [50], [51] propusieron un principio de evolución para una energía similar a la del trabajo de Ambrosio-Tortorelli, basado en la irreversibilidad, la estabilidad y el equilibrio energético. Este enfoque, al que se hace referencia como modelos variacionales de campo de fase, introduce una tensión crítica proporcional a $\sqrt{G/\ell}$.

Como se observa en Pham et al. [52], Bourdin et al. [32], y Nguyen et al. [53], este método puede potencialmente reconciliar los criterios de tensión y tenacidad para la nucleación de grietas, recuperar el efecto de tamaño pertinente a escalas de longitud pequeñas y grandes, y proporcionar un enfoque robusto y relativamente simple para modelar la propagación de grietas en entornos complejos tanto bidimensionales como tridimensionales.

2.2.1. Formulación del modelo de campo de fase para fractura frágil

Se formula una teoría de campo de fase para fracturas en sólidos bajo condiciones de pequeñas deformaciones y temperatura constante. Se descartan las fuerzas inerciales y cualquier fenómeno físico dependiente del tiempo, por lo que la variable de pseudo-tiempo "t", utilizada a continuación, solo tiene en cuenta una secuencia ordenada de eventos mecánicos mediante un parámetro que aumenta monotonamente. Se considera un cuerpo $\mathcal{B}$, los puntos materiales del cuerpo denotados por $\boldsymbol{X}$, con un borde definido $\partial\mathcal{B}$ (Figura 2.1) y su vector normal unitario es $\boldsymbol{n}$.

Para describir la deformación y la fractura en $\mathcal{B}$, se introduce como descriptores cinemáticos el campo de vectores de desplazamiento, $\boldsymbol{u}(\boldsymbol{X}, t)$, y la variable de campo de fase, $\varphi(\boldsymbol{X}, t)$, en el tiempo t en $\mathcal{B}$. El campo de fase toma valores en el intervalo $[0, 1]$. Si $\varphi = 0$ en un punto, entonces no está fracturado. En cambio si $\varphi = 1$ en un punto, el mismo se encuentra fracturado. Los valores de φ entre cero y uno corresponden a material parcialmente fracturado. Los puntos que satisfacen $\varphi = 1$ identifican grietas, es decir, una frontera libre de tracción incrustada en el material volumétrico. Sin embargo, argumentos

termodinámicos que abogan por la irreversibilidad de los procesos de fractura imponen una restricción para la evolución del campo de fase tomando: $\dot{\varphi} \geq 0$.

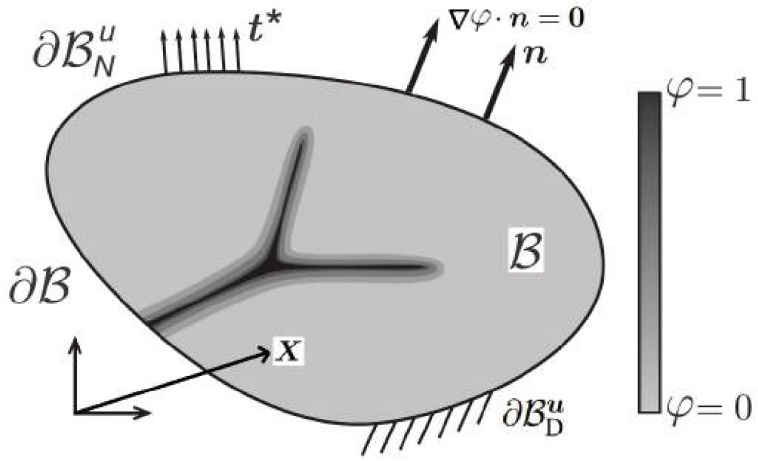

Figura 2.1: Cuerpo $\mathcal{B}$ con borde $\partial\mathcal{B}$.

Ambos descriptores primales independientes, $\boldsymbol{u}$ y φ, caracterizan el estado mecánico de $\mathcal{B}$ en el pseudo-tiempo t. Estos se agrupan en el vector $\boldsymbol{U} = \{\boldsymbol{u}, \varphi\}$. Las condiciones de admisibilidad para $\boldsymbol{U}$ se establecen en la forma $\boldsymbol{U} \in \mathcal{K}$, donde el conjunto $\mathcal{K}$ considera la regularidad adecuada y las condiciones de frontera tipo Dirichlet para cada descriptor. En particular, se consideran desplazamientos $\boldsymbol{u}^*$ fijados en una parte de la frontera de Dirichlet $\partial\mathcal{B}_{\mathrm{D}}^{\boldsymbol{u}}$ de $\mathcal{B}$. Las variaciones virtuales de $\boldsymbol{U}$ se denotan como $\delta\boldsymbol{U} = \{\delta\boldsymbol{u}, \delta\varphi\}$, y sus condiciones de admisibilidad se definen a través de $\delta\boldsymbol{U} \in \mathcal{V}$, donde el espacio vectorial $\mathcal{V}$ contempla los requisitos de regularidad apropiados y las restricciones especificadas en $\boldsymbol{U} \in \mathcal{K}$.

Por consiguiente, se asume que los procesos de deformación y fractura para un cuerpo $\mathcal{B}$ deben ser consistentes con el Principio Variacional del Trabajo Virtual, del cual se derivan las ecuaciones de balance de fuerzas, donde se tiene el campo de fuerzas externas por unidad de volumen en $\mathcal{B}$, $\boldsymbol{b}$, y las tracciones externas por unidad de área en $\partial\mathcal{B}_N^{\boldsymbol{u}}$, $\boldsymbol{t}^*$, que son variales duales de $\boldsymbol{u}$, donde $\partial\mathcal{B}_N^{\boldsymbol{u}}$ es la frontera de Neumann asociada a $\boldsymbol{u}$ (Figura 2.1). El tensor de tensiones de Cauchy $\boldsymbol{\sigma}$, definido en $\mathcal{B}$, y la deformación $\boldsymbol{\varepsilon}$ forman un par conjugado.

2.2.2. Principio variacional del trabajo virtual

Los trabajos virtuales internos y externos, $\delta\mathcal{W}^{\mathrm{int}}$ y $\delta\mathcal{W}^{\mathrm{ext}}$ respectivamente, para cualquier parte $\mathcal{P}$ del cuerpo $\mathcal{B}$ se definen de la siguiente manera:

$$\delta\mathcal{W}^{\mathrm{int}}(\mathcal{P}; \delta\mathbf{U}) = \int_{\mathcal{P}} \left(\boldsymbol{\sigma} \cdot \delta\boldsymbol{\varepsilon} + \boldsymbol{\xi} \cdot \nabla\delta\varphi + \pi\, \delta\varphi\right) \mathrm{d}\mathcal{P}, \quad \forall \delta\mathbf{U} \in \mathcal{V}\,, \tag{2.1}$$

$$\delta\mathcal{W}^{\mathrm{ext}}(\mathcal{P}; \delta\mathbf{U}) = \int_{\mathcal{P}} \left(\mathbf{b} \cdot \delta\mathbf{u}\right) \mathrm{d}\mathcal{P} + \int_{\partial\mathcal{P}} (\mathbf{t}^* \cdot \delta\mathbf{u})\, \mathrm{d}(\partial\mathcal{P}), \quad \forall \delta\mathbf{U} \in \mathcal{V}\,, \tag{2.2}$$

donde se tiene el tensor de tensiones de Cauchy ($\boldsymbol{\sigma}$), la variación de la deformación ($\delta\boldsymbol{\varepsilon}$), el campo de microtensiones ($\boldsymbol{\xi}$), la variación del gradiente del campo de fase ($\nabla\delta\varphi$), el campo de microfuerzas internas (π), la variación del campo de fase ($\delta\varphi$), el campo de fuerzas externas ($\boldsymbol{b}$), la variación del campo de desplazamiento ($\delta\boldsymbol{u}$) y las tracciones externas ($\boldsymbol{t}^*$)

A partir de las ecuaciones 2.1-2.2, se expresa una versión extendida del Principio Variacional del Trabajo Virtual tomando en cuenta detalles específicos de la presente formulación, para cualquier pseudo-tiempo "t", encontrar $\mathbf{U} \in \mathcal{K}$ tal que:

$$\int_{\mathcal{P}} \left(\boldsymbol{\sigma} \cdot \delta\boldsymbol{\varepsilon} + \boldsymbol{\xi} \cdot \nabla\delta\varphi + \pi\, \delta\varphi\right) \mathrm{d}\mathcal{P} - \int_{\mathcal{P}} \left(\boldsymbol{b} \cdot \delta\boldsymbol{u}\right) \mathrm{d}\mathcal{P} - \int_{\partial\mathcal{P}} (\boldsymbol{t}^* \cdot \delta\boldsymbol{u})\, \mathrm{d}(\partial\mathcal{P}) + \int_{\mathcal{P}} \pi_r\, \delta\varphi \, \mathrm{d}\mathcal{P} = 0\,, \quad \forall \delta\boldsymbol{U} \in \mathcal{V}, \;\; \text{con} \;\; \pi_r\, \dot{\varphi} = 0, \;\; \pi_r \leq 0, \;\; \dot{\varphi} \geq 0\,. \tag{2.3}$$

La primera línea de 2.3 representa la diferencia entre los trabajos virtuales internos y externos. El último término de 2.3 incorpora en el modelo la restricción inspirada en la termodinámica $\dot{\varphi} \geq 0$ (irreversibilidad del daño). El campo π_r es el Multiplicador de Lagrange asociado (reactivo), y las restricciones $\pi_r \dot{\varphi} = 0$, $\pi_r \leq 0$, son las condiciones de complementariedad relacionadas con dicha restricción de desigualdad.

Admitiendo variaciones independientes para los descriptores primarios de desplazamiento en 2.3, se derivan las ecuaciones de balance integral, las cuales pueden ser localizadas utilizando un procedimiento convencional. La forma local resultante de equilibrio para el cuerpo $\mathcal{B}$ se da mediante las siguientes ecuaciones:

$$\mathrm{Div}\, \boldsymbol{\sigma} + \boldsymbol{b} = \boldsymbol{0}\,, \quad \forall \mathbf{X} \in \mathcal{B}\,, \tag{2.4}$$

$$\boldsymbol{\sigma}\, \boldsymbol{n} = \boldsymbol{t}^*\,, \quad \forall \mathbf{X} \in \partial\mathcal{B}^{\mathbf{u}}_{\mathrm{N}}\,. \tag{2.5}$$

Por ende, al asumir variaciones para los descriptores primarios del campo de fase en 2.3 y después de aplicar un procedimiento de localización estándar, se obtiene:

$$\mathrm{Div}\, \boldsymbol{\xi} - (\pi_a + \pi_r) = 0\,, \quad \forall \mathbf{X} \in \mathcal{B}\,, \tag{2.6}$$

$$\boldsymbol{\xi} \cdot \boldsymbol{n} = \boldsymbol{0};, \quad \forall \mathbf{X} \in \partial\mathcal{B}^{\varphi}_{\mathrm{N}}\,, \tag{2.7}$$

donde se reemplaza la microfuerza interna π por sus componentes activa y reactiva, π_a y π_r, respectivamente. La componente reactiva, junto con las condiciones de complementariedad: $\pi_r \dot{\varphi} = 0$, $\pi_r \leq 0$, y $\dot{\varphi} \geq 0$, se introduce en el modelo para garantizar la restricción termodinámica: $\dot{\varphi} \geq 0$.

Por lo tanto, se tienen las ecuaciones de balance de fuerza que presentan el tensor de tensiones de Cauchy $\boldsymbol{\sigma}$, definido en $\mathcal{B}$, el campo de fuerzas externas por unidad de volumen en $\mathcal{B}$, $\boldsymbol{b}$, y las tracciones externas por unidad de área en $\partial\mathcal{B}^{u}_{N}$, $\boldsymbol{t}^*$. Por otro lado, se tienen las ecuaciones de balance de microfuerzas, donde el descriptor del campo de fase φ, tiene asociadas tres variables duales: el campo de microfuerzas internas π por unidad de volumen, el campo de microfuerzas externas γ por unidad de volumen y la microtracción externa ς^* por unidad de área en $\partial\mathcal{B}^{\varphi}_{\mathrm{N}}$, donde $\partial\mathcal{B}^{\varphi}_{\mathrm{N}}$ es la frontera de Neumann relacionada con φ. Sin embargo, en concordancia con Duda et al. [54] que representa el trabajo principal en el cual se basa nuestro modelo de campo de fase, asumimos además que el sistema de cargas externas conjugadas a φ es nulo. Por lo tanto, ni γ, ni ς^* se consideran en la formulación. Además, un campo vectorial de microtensiones $\boldsymbol{\xi}$ es la variable conjugada del gradiente del campo de fase $\nabla\varphi$.

2.2.3. Consistencia termodinámica

Además de los balances de fuerza estándar y microfuerza descritos en la subsección previa, la primera y segunda ley de la termodinámica se imponen a través de un postulado de desequilibrio energético. Tal desigualdad requiere que la potencia mecánica consumida por las agentes circundantes en $\mathcal{P}$, aquí denotado como $\dot{\mathcal{W}}^{\mathrm{ext}}$, exceda o sea igual a la tasa de cambio de la energía libre en $\mathcal{P}$. Introduciendo la noción de densidad de energía libre ψ del material, el desequilibrio energético se expresa:

$$\frac{d}{dt}\left(\int_{\mathcal{P}} \psi \, \mathrm{d}\mathcal{P}\right) \leq \dot{\mathcal{W}}^{\text{ext}}(\mathcal{P}; \dot{\mathbf{U}}) \, , \tag{2.8}$$

con $\dot{\mathcal{W}}^{\text{ext}}$ definido de manera similar a como se describe en 2.2 y $\dot{\mathbf{U}}$ almacenando las velocidades de los descriptores primarios. Las variaciones virtuales admisibles $\delta\mathbf{U}$ y velocidades realizables $\dot{\mathbf{U}}$ pertenecen al mismo espacio funcional $\mathcal{V}$, por lo tanto, existe una correspondencia entre los conceptos relacionados con los trabajos virtuales y las potencias realizables.

Insertando 2.2 en 2.8, y después de localizar la desigualdad integral, se obtiene:

$$\dot{\psi} - \boldsymbol{\sigma} \cdot \dot{\boldsymbol{\varepsilon}} - \boldsymbol{\xi} \cdot \nabla\dot{\varphi} - \pi_a \, \dot{\varphi} \leq 0 \, , \quad \forall \mathbf{X} \in \mathcal{B} \text{ y } \forall \dot{\mathbf{U}} \in \mathcal{V} \, , \tag{2.9}$$

Esto representa la forma puntual de desequilibrio energético para el material constituyente del medio continuo (bulk), respectivamente. Se puede observar que el Multiplicador de Lagrange reactivo π_r no participa en 2.9. El mismo no induce potencia realizable, siendo ortogonal a las restricciones de sus variables primarias correspondientes.

2.2.4. Relación constitutiva

La estructura matemática de la desigualdad 2.9 dicta algunas opciones naturales para seleccionar los argumentos independientes en la definición de la densidad de energía libre del material del medio continuo (ψ). Dado que la presente formulación se ocupa de materiales independientes de la tasa, se permite posibles dependencias funcionales en la siguiente lista de variables $\{\boldsymbol{\varepsilon}, \varphi, \nabla\varphi\}$, por lo tanto se tiene:

$$\psi = \hat{\psi}(\boldsymbol{\varepsilon}, \varphi, \nabla\varphi) \, . \tag{2.10}$$

Tomando como base las ideas empleadas por Coleman y Noll [55], se asume que las respuestas constitutivas $\boldsymbol{\sigma}$, $\boldsymbol{\xi}$, π_a se obtienen como la derivada parcial de la densidad de energía libre con respecto a sus variables duales correspondientes:

$$\boldsymbol{\sigma} = \frac{\partial\psi(\boldsymbol{\varepsilon}, \varphi, \nabla\varphi)}{\partial\boldsymbol{\varepsilon}} \quad , \quad \boldsymbol{\xi} = \frac{\partial\psi(\boldsymbol{\varepsilon}, \varphi, \nabla\varphi)}{\partial\nabla\varphi} \quad , \quad \pi_a = \frac{\partial\psi(\boldsymbol{\varepsilon}, \varphi, \nabla\varphi)}{\partial\varphi} \, . \tag{2.11}$$

Por consiguiente, las funciones de respuesta constitutiva introducidas en 2.10 ahora se especializan para obtener una instancia particular que caracteriza la implementación actual del modelo de campo de fase. La respuesta de la energía libre ψ se divide en dos términos:

$$\psi(\boldsymbol{\varepsilon}, \varphi, \nabla\varphi) = \hat{\psi}_e(\boldsymbol{\varepsilon}, \varphi) + \hat{\psi}_f(\varphi, \nabla\varphi) \, , \tag{2.12}$$

con

$$\begin{aligned}
&\hat{\psi}_e(\boldsymbol{\varepsilon}, \varphi) = \left((1-\varphi)^2\right) \hat{\psi}_e^{pos}(\boldsymbol{\varepsilon}) + \hat{\psi}_e^{neg}(\boldsymbol{\varepsilon}) \, , \\
&\hat{\psi}_e^{pos}(\boldsymbol{\varepsilon}) = \frac{1}{2}\left(\lambda \langle \mathrm{tr}\, \boldsymbol{\varepsilon} \rangle^2 + 2\mu\boldsymbol{\varepsilon}^{pos} : \boldsymbol{\varepsilon}^{pos}\right) \, , \\
&\hat{\psi}_e^{neg}(\boldsymbol{\varepsilon}) = \frac{1}{2}\left(\lambda \langle -\mathrm{tr}\, \boldsymbol{\varepsilon} \rangle^2 + 2\mu\boldsymbol{\varepsilon}^{neg} : \boldsymbol{\varepsilon}^{neg}\right) \, , \\
&\boldsymbol{\varepsilon}^{pos} = \sum_{k=1}^{3} \langle \varepsilon_k \rangle \, \mathbf{e_k} \otimes \mathbf{e_k} \, , \qquad \boldsymbol{\varepsilon}^{\mathbf{neg}} = \sum_{\mathbf{k=1}}^{\mathbf{3}} - \langle -\varepsilon_{\mathbf{k}} \rangle \, \mathbf{e_k} \otimes \mathbf{e_k} \, ,
\end{aligned} \tag{2.13}$$

donde este término $(1-\varphi)^2$ es la función de degradación de la energía elástica, que tiende a cero cuando $\varphi \to 1$. Luego λ y μ son los parámetros de Lamé, ε_k y $\mathbf{e_k}$ son el k-ésimo autovalor y autovector de

ε, respectivamente. El operador de corchetes angulares, $\langle\cdot\rangle$, [56] es la parte positiva del argumento. La partición de $\hat{\psi}_e$ definida en la ecuación 2.13 se toma de Miehe et al. [57]. El segundo término en la ecuación 2.12 resulta:

$$\hat{\psi}_f(\varphi, \nabla\varphi) = G_{_{PF}} \left(\frac{\varphi^2}{2\ell_{_{PF}}} + \frac{\ell_{_{PF}}}{2} |\nabla\varphi|^2 \right) , \tag{2.14}$$

donde la energía de fractura se denota como $G_{_{PF}}$ y $\ell_{_{PF}}$ es una longitud característica que gobierna la distribución espacial del campo de fase en la región vecina a la grieta. En vista de 2.11, el tensor de tensiones de Cauchy se especifica de la siguiente forma:

$$\boldsymbol{\sigma} = \left((1-\varphi)^2\right) \left(\lambda \langle \operatorname{tr} \boldsymbol{\varepsilon} \rangle \mathbf{I} + \mathbf{2}\mu\boldsymbol{\varepsilon}^{\mathbf{pos}}\right) + \left(-\lambda \langle -\operatorname{tr} \boldsymbol{\varepsilon} \rangle \mathbf{I} + \mathbf{2}\mu\boldsymbol{\varepsilon}^{\mathbf{neg}}\right) , \tag{2.15}$$

y considerando de nuevo 2.11, la micro-tensión y la micro-fuerza resultan:

$$\boldsymbol{\xi} = G_{_{PF}} \, \ell_{_{PF}} \, \nabla\varphi \, , \tag{2.16}$$

$$\pi_a = \frac{G_{_{PF}}}{\ell_{_{PF}}} \varphi - 2(1-\varphi)\hat{\psi}_e^{pos}(\boldsymbol{\varepsilon}) \, , \tag{2.17}$$

respectivamente.

Si se considera 2.16 y 2.17, se puede reescribir 2.6 como:

$$G_{PF}\ell_{PF}\triangle\varphi - \frac{G_{_{PF}}}{\ell_{_{PF}}} \varphi + 2(1-\varphi)\hat{\psi}_e^{pos}(\boldsymbol{\varepsilon}) - \pi_r = 0 \, , \tag{2.18}$$

teniendo en cuenta que π_r es la reacción necesaria para garantizar la restricción de irreversibilidad $\dot{\varphi} \geq 0$ y, como tal, debe cumplir las condiciones $\pi_r \leq 0$ and $\pi_r \dot{\varphi} = 0$. Se debe expresar que al igual que en el trabajo de Duda et al. [54], se sigue la estrategia propuesta por Miehe et al. [57] que lleva a la reformulación de 2.18. De acuerdo con dicha estrategia, π_r se define como:

$$\pi_r = -2(1-\varphi)\big(\overbrace{\mathcal{H}(t) - \hat{\psi}_e^{pos}(\boldsymbol{\varepsilon}, t)}^{\Delta\hat{\psi}_e^{pos}} \big) \, , \tag{2.19}$$

donde la función de campo del historial compacto $\mathcal{H}(t)$ resulta:

$$\mathcal{H}(t) = \max_s h(s), \quad s \in [0, t] \, , \tag{2.20}$$

con

$$h(t) := \hat{\psi}_e^{pos}(\boldsymbol{\varepsilon}, t) \, . \tag{2.21}$$

Dado que $\Delta\hat{\psi}_e^{pos} \geq 0$, la desigualdad $\pi_r \leq 0$ se satisface automáticamente.

2.2.5. Fortalezas y desventajas de los modelos de campo de fase

En base a la revisión de la literatura, se puede inferir que algunas de las principales fortalezas que presentan los modelos de campo de fase (PFMs) son las siguientes:

- Lo que hace particularmente atractivo al modelo de campo de fase es su capacidad para simular de manera elegante procesos de fractura complejos, incluyendo la iniciación, propagación, coalescencia y ramificación de grietas, tanto en situaciones generales como en geometrías tridimensionales, sin necesidad de criterios adicionales. La evolución del campo de la grieta suavizado en una malla fija, permite el seguimiento automático de las grietas en propagación.

- Bajo la premisa de la idea anterior, esto también representa una ventaja significativa sobre la descripción discreta de fracturas, cuya implementación numérica requiere un tratamiento explícito (en el caso clásico del método de elementos finitos) o implícito (en el contexto de los métodos de elementos finitos extendidos) de las discontinuidades. La posibilidad de evitar el laborioso seguimiento de superficies de grieta complejas en 3D simplifica considerablemente la implementación.

- La estructura variacional de estos modelos permite abordar problemas de fractura con múltiples físicas.

- Una característica particular de los modelos de campo de fase es que requieren un conjunto mínimo de parámetros, como el módulo de Young, la relación de Poisson, la energía de fractura (todos medibles experimentalmente) y la longitud característica (que puede determinarse en función de la resistencia a tracción del material considerado) para materiales frágiles. En otras palabras, los modelos de campo de fase no dependen de parámetros definidos arbitrariamente por el usuario.

- Los modelos de campo de fase poseen una gran popularidad, ya que esta clase de modelos han sido un concepto ampliamente aceptado en ciencia de materiales (para modelar transiciones o transformaciones de fase mediante una regularización de la interface) durante décadas, aunque con diferentes enfoques.

En cuanto a los inconvenientes, se tiene que la principal limitación de los modelos de campo de fase es su alto costo computacional, debido al uso de mallas extremadamente finas, ya que el tamaño de los elementos finitos debe ser lo suficientemente pequeño para resolver adecuadamente el parámetro de longitud característica del modelo. Los avances en hardware y tecnologías computacionales (adaptatividad de mallas, métodos globales/locales, métodos multiescala, métodos de reducción de orden del modelo) incrementarán la eficiencia de las simulaciones con modelos de campo de fase. En los siguientes capítulos de esta tesis proponemos una técnica para sortear este inconveniente.

2.3. Técnicas numéricas para modelado de propagación de grietas incidiendo con una interface

La deflexión de grietas y la delaminación en interfaces desempeñan un papel fundamental en el rendimiento de muchos sistemas compuestos. Los materiales frágiles (cerámicas, concretos o epoxis) pueden reforzarse mediante la adición de fibras relativamente frágiles, siempre que ocurra la deflexión de una grieta en las interfaces entre las fibras y la matriz. Si no se produce la deflexión de la grieta, una grieta que se propaga a través de la matriz continuará sin obstáculos al encontrarse con la fibra. Esto resulta en un refuerzo mínimo o nulo, ya que se disipa poca energía por la fractura de una fibra frágil.

Por el contrario, si ocurre la deflexión de la grieta, esta se ve efectivamente atenuada. Además, si la grieta rodea las fibras y continúa propagándose sin penetrarlas, las fibras intactas que quedan en la estela de la grieta puentean las superficies de la misma. En ese caso, se pueden lograr contribuciones significativas al refuerzo mediante la energía disipada por fricción en las interfaces desadheridas entre la fibra y la matriz (Campbell et al. [58], Evans y Marshall [59], Aveston [60], Aveston y Kelly [61]). Más detalles sobre el comportamiento de estos mecanismos entre una grieta que propaga e incide con una interface se discuten en el capitulo III de esta tesis.

La optimización de compuestos que exhiben deflexión de grietas y delaminación de interfaces requiere comprender cómo las propiedades de la interface y del material base afectan la mecánica del problema. Por ende, para estos análisis se pueden emplear dos criterios de fractura diferentes: un criterio basado en tensiones y otro basado en energía.

Estos conducen a dos tipos diferentes de parámetros materiales que forman la base para el diseño de interfaces. Un criterio de fractura basado en tensiones expresa el criterio de deflexión-penetración en

términos de las resistencias relativas de la interface y el sustrato. Por otro lado, un criterio de fractura basado en energía expresa el criterio de deflexión-penetración en función de las tenacidades relativas de la interface y el sustrato. También existe el escenario donde este análisis se realiza integrando ambos criterios, como se demostró en el trabajo de Parmigiani y Thouless [62]

La visión de zona cohesiva proporciona un marco analítico coherente para la fractura, que incorpora de forma natural tanto criterios de resistencia como de energía. El modelado de zonas cohesivas tiene sus orígenes en los primeros modelos de Dugdale [63] y Barenblatt [64], que consideraron los efectos de tensiones finitas en la punta de una grieta. Un modelo de zona cohesiva incorpora una región de material delante de la grieta (la zona cohesiva) que presenta una ley característica de tracción-separación que describe el proceso de fractura. En una ley típica de tracción-separación, las tracciones a través del plano de la grieta aumentan con el desplazamiento hasta alcanzar una resistencia cohesiva máxima y luego decaen a cero en un desplazamiento crítico de apertura. Cuando se alcanza el desplazamiento crítico, se asume que el material en la zona cohesiva ha fallado y la grieta avanza.

Este enfoque para modelar la fractura se volvió particularmente útil con el desarrollo de técnicas computacionales avanzadas, ya que permitió predecir la propagación de grietas en diferentes geometrías (Hillerborg et al. [65], Needleman [66], [67], Tvergaard y Hutchinson [68], Ungsuwarungsri y Knauss [69]). El comportamiento de fractura tiende a estar dominado por dos cantidades características de la ley de tracción-separación: una tenacidad característica (el área bajo la curva), G, y una resistencia característica (estrechamente relacionada con la resistencia cohesiva $\hat{\sigma}$ en muchas leyes de tracción-separación). Los modelos de zona cohesiva proporcionan un enfoque particularmente poderoso para analizar la fractura, ya que sus predicciones son bastante insensibles a los detalles específicos de la ley de tracción-separación, dependiendo únicamente de estos dos parámetros característicos.

Sin embargo, en la actualidad, la mayoría de las investigaciones dentro del contexto del enfoque de campo de fase para la fractura se han centrado en el análisis de cuerpos continuos, homogéneos y compuestos reforzados. Un intento de modelar la fractura cohesiva en el material base utilizando el enfoque de campo de fase fue propuesto en Verhoosel y de Borst [70] mediante una modificación adecuada de la formulación variacional para tener en cuenta los saltos de desplazamiento. En ese marco, se encontró que el modelado de las discontinuidades de desplazamiento representa una complicación significativa que requiere imponer una restricción adicional basada en un campo auxiliar que representa el salto en el desplazamiento a través de la grieta, el cual debe ser constante en la dirección ortogonal a la grieta.

Recientemente se ha propuesto un esquema de modelado dentro del contexto de la formulación de campo de fase, que tiene en cuenta tanto la fractura frágil del material base como el daño de la interface (Nguyen et al. [71], [72]). Este enfoque alternativo se basa en la definición de una nueva formulación energética que combina la energía de daño del material base y la energía superficial cohesiva de la interface, la cual se activa mediante el método de level set. Esta metodología de Nguyen et al. [71], [72], aunque prometedora para interfaces rígidas, no permite la consideración de discontinuidades preexistentes, lo cual es el caso de las capas adhesivas.

Por consiguiente, en el trabajo de Paggi y Reinoso [73] se desarrolla un marco de modelado que combina el modelo de campo de fase para la fractura frágil en el material base y el modelo de zona cohesiva para una interface preexistente como se ilustra esquemáticamente en la figura 2.2. De manera similar a Nguyen et al. [71], [72], esta estrategia de modelado se basa en la definición de un solo funcional, que tiene en cuenta la disipación de energía de los dos modelos de fractura mencionados anteriormente. Sin embargo, en lugar de usar el método de level set para trazar la discontinuidad de salto en las caras de la grieta, se propone un nuevo elemento finito de interface totalmente compatible con el enfoque de campo de fase. Dentro de esta formulación, las tracciones cohesivas se calculan en función de los desplazamientos relativos en la interface, como en los elementos de interface clásicos (Paggi y Wriggers [74], [75], [76]).

En este sentido, se postula un posible acoplamiento entre la energía de fractura de la interface G_i y el daño no local en el material base circundante a través de una dependencia de la rigidez de la interface

en la variable media del campo de fase evaluada en los flancos de la interface. Esta formulación permite distinguir de manera unívoca entre las formas de disipación en la interface y en el material base, y también puede tratar situaciones complejas donde la cantidad de daño en el material base afecta la respuesta de la interface, por ejemplo, mediante una degradación de la resistencia de la misma. En el trabajo anexado en el Apéndice A se presenta una metodología de modelado semejante a la expuesta en el trabajo de Paggi y Reinoso [73], pero con ciertas diferencias que serán argumentadas en el capítulo III de esta tesis.

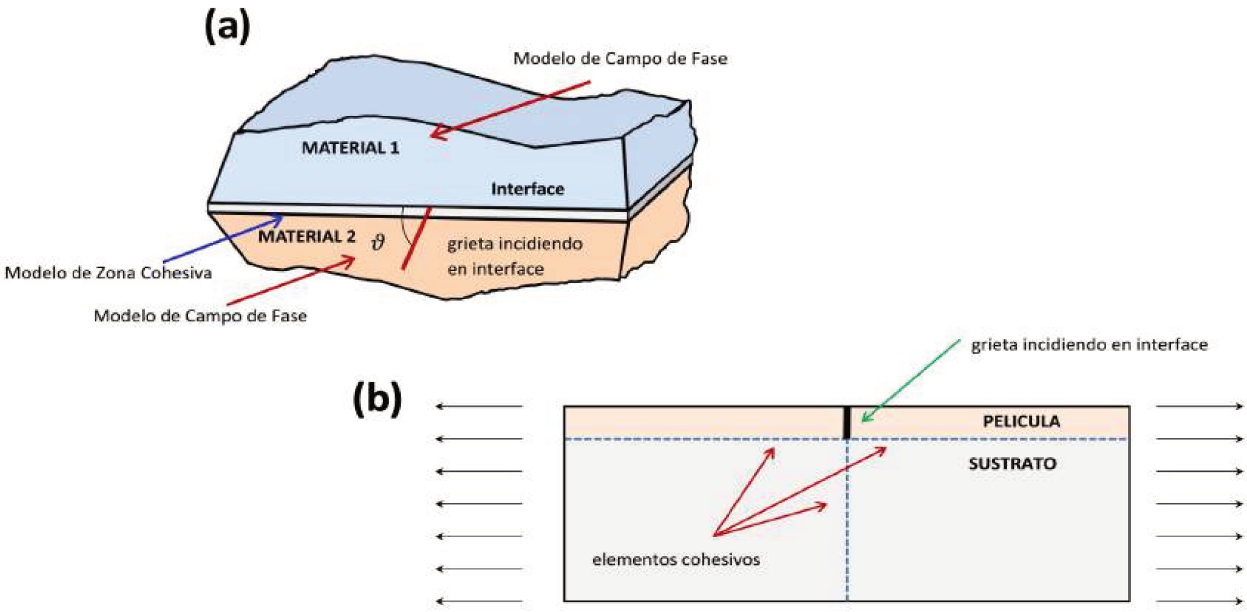

Figura 2.2: Problemas de deflexión-penetración en sólidos con interfaces: (a) Grieta en una interface bi-material, (b) Grieta en un sistema película-sustrato.

Bajo este mismo contexto de implementación de una metodología numérica que combina el modelo de campo de fase con un modelo de zona cohesiva, para analizar la competencia de los mecanismos que interactuan entre una grieta propagante que impacta con una interface se destaca el trabajo de Aranda et al. [77], en el cual se aborda el problema de la competencia entre la penetración y la deflexión de una grieta que incide en una interface débil de tipo curvo. En este estudio se analiza cómo las propiedades mecánicas y geométricas de la probeta afectan a dicha competencia entre estos dos principales mecanismos (penetración y deflexión).

Con el propósito de validar las ventajas del uso de interfaces débiles curvadas como arrestadores de grietas, Aranda et al. [77] establece que, para lograr este efecto es fundamental que estas interfaces sean capaces de desviar la grieta. Para ello, se definen los parámetros de la interface que promueven esta desviación. Mediante un análisis dimensional del problema, básicamente se estudia el efecto de parámetros adimensionales clave como la relación de la tenacidad a la fractura de la interface con el medio $\left(G_c^i \,/\, G_c^m\right)$ y la relación de resistencia a la tracción de la interface con el medio $\left(\sigma_c^i \,/\, \sigma_c^m\right)$.

Para llevar a cabo este análisis se emplearon varios enfoques como la Mecánica de Fractura Elástica Lineal (LEFM, por sus siglas en inglés) y un modélo numérico combinado entre el campo de fase y el modelo de zona cohesiva (PF + CZM, por sus siglás en inglés). En relación a la discusión de la influencia de cada uno de los parámetros adimensionales mencionados anteriormente, en el comportamiento competitivo entre los mecanismos de penetración y deflexión, se tiene que el efecto de $\left(G_c^i \,/\, G_c^m\right)$, se identificó como el parámetro principal que gobierna dicha competencia penetración/deflexión según la Mécanica de Fractura Lineal Elástica. Cuando el parámetro $\left(G_c^i \,/\, G_c^m\right)$ aumenta la grieta tiende a penetrar en lugar de desviarse, por ende, este parámetro regula si la penetración o la desviación es más

favorable exclusivamente desde un punto de vista energético.

En cuanto al modelo de campo de fase combinado con el modelo cohesivo, el comportamiento es cualitativamente similar a la metodología anterior en lo que respecta a $\left(G_c^i \ / \ G_c^m\right)$, pero está mucho más influenciado por otros parámetros, como la relación de resistencia a la tracción de la interface con el medio $\left(\sigma_c^i \ / \ \sigma_c^m\right)$.

Las predicciones correspondientes al efecto de $\left(\sigma_c^i \ / \ \sigma_c^m\right)$ varían significativamente entre los enfoques que fueron considerados. En primer lugar, los análisis basados en LEFM son independientes de esta relación, ya que la resistencia no juega un papel en la Mecánica de Fractura Elástica Lineal. En contraste, el enfoque numérico PF+CZM predice un marcado efecto de la relación de resistencias en la competencia entre penetración y deflexión. Esto se debe al papel determinante de la resistencia en el modelo de zona cohesiva y, en cierta medida, en el campo de fase. Este efecto es especialmente relevante para grietas de corta propagación, siendo de esperarse que para grietas con mayor propagación la energía de fractura desempeñe un papel predominante. No obstante, como se describió en Parmigiani y Thouless [62] para modelos CZM+CZM, y en Zambrano et al. [78] para modelos PF+CZM, la grieta deflectada en la mayoría de los casos es lo suficientemente corta como para evitar la influencia de la tenacidad. Por lo tanto, según el modelo PF+CZM, la propagación de la grieta puede preferir la deflexión o la penetración, aunque esta preferencia no siempre se alinea con la solución más favorable desde el punto de vista energético.

2.4. Nociones fundamentales de los diseños bioinspirados

Los materiales naturales como el hueso, el diente y el nácar son nano-compuestos de proteínas y minerales que exhiben una combinación excepcional de rigidez y tenacidad. Los resultados experimentales indican que, aunque la rigidez de los biocompuestos es similar a la de su componente mineral, su resistencia a la fractura y su tenacidad son significativamente superiores a las del mineral.

Este rendimiento excepcional de los biocompuestos se debe a sus complejas estructuras jerárquicas en diferentes escalas de longitud (Weiner y Wagner [79]). Por ejemplo, las conchas marinas presentan de 2 a 3 órdenes de estructura laminar (Currey [80], Menig et al. [81]), mientras que el hueso posee hasta 7 órdenes de jerarquía (Weiner y Wagner [79], Currey [82]). La figura 2.3 muestra la nanoestructura de algunos biocompuestos típicos.

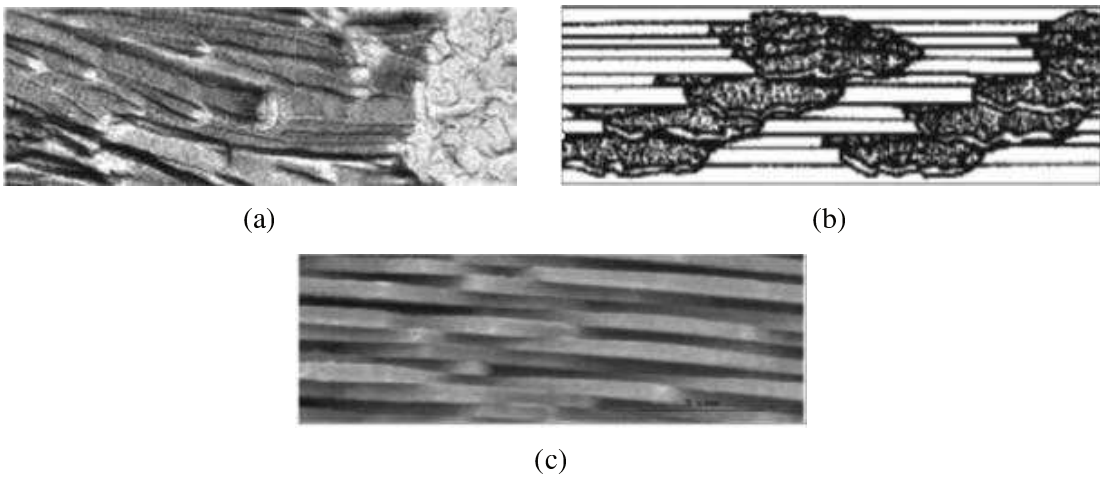

Figura 2.3: Nanoestructura de algunos tejidos biológicos duros típicos: (a) diente, (b) hueso y (c) concha.

Si bien la estructura jerárquica completa de los biomateriales, como el hueso, es extremadamente compleja y variable, resulta especialmente interesante observar que sus unidades estructurales básicas, las

fibrillas de colágeno mineralizadas, son bastante universales. Estas están diseñadas a escala nanométrica, con inclusiones minerales duras de tamaño nanométrico incrustadas en una matriz de proteína blanda (Gao et al. [83]).

Por ejemplo, en el nivel más bajo de la jerarquía, la nanoestructura del hueso (fibrillas mineralizadas) está compuesta por plaquetas minerales con un espesor de unos pocos nanómetros, dispuestas en un patrón escalonado dentro de una matriz de colágeno (Weiner y Wagner [79]).

La dentina es un tejido calcificado similar al hueso, donde la matriz rica en colágeno está reforzada por cristales de fosfato de calcio (Weiner et al. [84], Tesch et al. [85]). De manera similar, las paredes celulares de la madera están formadas por fibrillas de celulosa incrustadas en una matriz blanda de hemicelulosa-lignina.

Dado que las fibrillas mineralizadas son la unidad elemental de muchos biocompuestos complejos, es fundamental comprender cómo sus propiedades mecánicas dependen tanto de las propiedades de sus constituyentes como del estilo de disposición de los diferentes materiales a nivel de las fibrillas individuales. Los componentes de las fibrillas minerales presentan propiedades mecánicas extremadamente distintas: el mineral es rígido y frágil, mientras que la proteína (en estado húmedo) es mucho más blanda, pero también considerablemente más tenaz que el mineral.

Aumentar la cantidad de partículas minerales incrementa siempre la rigidez, pero también la fragilidad del tejido óseo. Entonces, podríamos preguntarnos cómo lograr que el biocompuesto sea lo suficientemente rígido sin sacrificar su tenacidad. La naturaleza resuelve este problema de manera elegante mediante un diseño del tamaño, la forma y la distribución del material en las nanoestructuras de los biocompuestos.

Estudios previos (Gao et al. [83], Ji y Gao [86]) reportaron que las altas relaciones de aspecto y el patrón de alineación escalonada de las plaquetas minerales son factores clave que contribuyen a la gran rigidez de los biomateriales. Por otro lado, las proteínas situadas entre las plaquetas minerales escalonadas desempeñan un papel esencial en la absorción y disipación de una cantidad significativa de energía de fractura. Además, como lo muestran Gao et al. [83], a escala nanométrica el mineral frágil se vuelve insensible a defectos, lo que le permite soportar grandes tensiones sin fracturarse de manera frágil y, en consecuencia, mejorar la tenacidad de los biomateriales.

Es evidente que tanto los componentes orgánicos y minerales como su disposición contribuyen de manera equitativa a la resistencia de los biomateriales. El biocompuesto combina las propiedades óptimas de ambos componentes: la rigidez y la tenacidad. Esta combinación poco común de propiedades materiales proporciona simultáneamente rigidez y resistencia a la fractura. Desde la perspectiva de la ciencia de materiales, una mejor comprensión de los principios de construcción subyacentes podría contribuir al diseño de materiales compuestos mejorados.

Los materiales naturales han sido perfeccionados por la evolución a lo largo de millones de años. La idea esencial del diseño de materiales bioinspirados es analizar cómo, en ciertos casos, las formas de estos materiales (bien diseñados) en la naturaleza pueden explicarse mediante leyes físicas y matemáticas. Una vez que se abstraen los principios y mecanismos de diseño eficiente de la naturaleza, es posible utilizarlos para desarrollar materiales sintéticos avanzados.

Por ende, uno de los objetivos clave en el estudio de los biomateriales es imitar su estructura excepcional para desarrollar materiales artificiales bioinspirados con propiedades mecánicas avanzadas. Por ejemplo, se han explorado diversas técnicas para fabricar nácar artificial. Métodos como la técnica de ensamblaje capa por capa, la estrategia de reticulación y la técnica de grabado láser se han utilizado para producir compuestos similares al nácar, conformados por tabletas rígidas e intercapas blandas (Cheng et al. [87], Tang et al. [88], Valashani y Barthelat [89]).

2.5. Técnica de control de longitud de arco y esquemas de resolución numérica para problemas de fractura frágil

En la evolución cuasi-estática de fracturas frágiles en un sólido elástico, donde las fracturas son impulsadas por el incremento gradual de las condiciones de carga, se pueden encontrar comportamientos de ablandamiento y retrocesos abruptos. Tales situaciones requieren el control por longitud de arco para seguir adecuadamente el camino de equilibrio completo. Las técnicas de longitud de arco han sido una herramienta indispensable en la mecánica de sólidos no lineales, desde los trabajos pioneros de Riks [90], Crisfield [91] y Ramm [92].

Mientras que estas técnicas de longitud de arco fueron desarrolladas en el contexto del comportamiento de retroceso abrupto, causado por no linealidades geométricas, a lo largo de las últimas décadas se han propuesto diversos avances a los procedimientos originales de longitud de arco, con el fin de incrementar su versatilidad y eficiencia computacional.

Una aplicación particularmente interesante de las técnicas de longitud de arco es su uso para seguir el comportamiento de retroceso abrupto, como resultado de no linealidades materiales, especialmente en fenómenos de falla localizada. En estas situaciones, los procedimientos originales de longitud de arco han mostrado carecer de robustez debido a que no consideran la naturaleza localizada de la fuente de no linealidad. Se han propuesto diversas técnicas modificadas para tener en cuenta este comportamiento localizado, entre las cuales se encuentran una serie de procedimientos semi-automáticos para seleccionar los grados de libertad que contribuyen al comportamiento no lineal del sistema (Geers [93], [94]).

Algunos trabajos se basan en la idea de que una técnica apropiada de longitud de arco puede obtenerse seleccionando una ecuación de restricción motivada físicamente. En este sentido, las ecuaciones de control de desplazamiento de apertura de boca de grieta (CMOD por sus siglas en inglés) y de deslizamiento de boca de grieta (CMSD por sus siglas en inglés) propuestas por De Borst [95], pueden considerarse trabajos pioneros. En el contexto de estas ecuaciones de control, se desarrolló un control de tasa de liberación de energía para el seguimiento de trayectoria, en la simulación de fenómenos de falla localizada, incluidos el agrietamiento discreto, el daño difuso y la plasticidad con ablandamiento (Gutiérrez [12], Verhoosel et al. [13]).

La versatilidad del control de tasa de liberación de energía ha sido demostrada en una variedad de aplicaciones, incluyendo casos en los que coexisten no linealidades geométricas y materiales. Cuando se aplica en el contexto de simulaciones de fractura discreta, la técnica de longitud de arco basada en la tasa de liberación de energía tiene la capacidad de controlar indirectamente la tasa a la que una fractura se propaga mediante la selección adecuada del incremento de disipación de energía. En Vignollet et al. [96] se ha demostrado que el control de la tasa de liberación de energía puede aplicarse con éxito en simulaciones de campo de fase, donde el incremento de disipación está relacionado con el incremento del área de la superficie de fractura a través de la tasa crítica de liberación de energía.

En el caso de las simulaciones de campo de fase, la relación entre la restricción de longitud de arco y el incremento del área de la superficie de fractura puede expresarse de manera explícita. Es decir, el área de la superficie de fractura puede expresarse como una función de la solución del campo de fase. Esto permite una prescripción directa de los incrementos del área de la superficie. Esta dependencia explícita permite la selección del incremento del parámetro de longitud de arco, basado en un criterio que relaciona el crecimiento de la superficie de la grieta con el tamaño de la malla empleada, lo que proporciona una forma natural de controlar la precisión del esquema de longitud de arco.

Por otro lado, otro aspecto destacado en esta temática se centra en las ventajas comparativas entre las dos alternativas principales para resolver las ecuaciones acopladas derivadas de la formulación matemática para el problema de fractura frágil: el esquema monolítico (monolithic scheme) y el esquema escalonado (staggered scheme).

Por consiguiente, si el campo de desplazamientos y el campo de fase se calculan de manera simultánea se utilizan los esquemas monolíticos, los cuales suelen presentar mayores tasas de convergen-

cia, ya que ambas soluciones (desplazamientos y campo de fase) se resuelven simultáneamente dentro de un único bucle de Newton–Raphson. Sin embargo, este enfoque enfrenta dificultades conocidas relacionadas con la propagación discontinua de grietas en simulaciones cuasi-estáticas. La pérdida de convexidad del problema dificulta la convergencia de las soluciones, por lo que generalmente se requieren tratamientos numéricos adicionales para mejorar su robustez (Wick [97]).

Por otro lado, los esquemas escalonados son más robustos y fáciles en su implementación. Estos se basan en un algoritmo de separación de operadores, en el cual el problema mecánico y el problema de campo de fase se resuelven de forma alternada. Se pueden considerar tanto estrategias explícitas como implícitas. Los enfoques explícitos (Miehe et al. [98], Nguyen et al. [71]) asumen que el campo de fase permanece constante durante un paso incremental de tiempo al calcular el campo de desplazamientos.

El campo de fase se actualiza en el siguiente paso de tiempo una vez que el problema mecánico ha convergido. Este enfoque ha demostrado ser extremadamente robusto, incluso en casos de propagación discontinua de grietas. No obstante, este tipo de estrategias generalmente requiere pasos de tiempo muy pequeños, lo cual no es viable para muchas aplicaciones de ingeniería.

Los enfoques implícitos pueden mitigar esta dependencia del tamaño del paso de tiempo (Amor et al. [99], Helfer et al. [100]). El método implícito propuesto por Amor et al. [99], Ambati et al. [41], conocido comúnmente como esquema de minimización alternada, resuelve de forma independiente dos problemas de minimización para los campos de desplazamiento y campo de fase, fijando uno de estos campos en cada iteración. De manera similar a los enfoques explícitos, este método calcula el campo de desplazamientos manteniendo constante el campo de fase, pero actualiza a dicho campo de fase en el paso de tiempo actual y luego vuelve a calcular un nuevo desplazamiento.

Por lo tanto, a diferencia de los enfoques explícitos, en el procedimiento de minimización alternada se garantiza la convergencia del campo de fase en cada paso de tiempo. Este método es muy estable, aunque usualmente converge de forma extremadamente lenta, pero se pueden emplear métodos de relajación para acelerar el proceso (Farrell y Maurini [101]). La experiencia de Helfer et al. [100] muestra que los enfoques implícitos funcionan con pasos de tiempo relativamente grandes, pero suelen requerir numerosas iteraciones para encontrar soluciones convergentes, especialmente en presencia de propagación discontinua de grietas. No obstante, este tipo de estrategias resulta atractivo para muchos problemas de ingeniería sometidos a cargas a largo plazo (por ejemplo, simulaciones de combustible nuclear, Helfer et al. [100]), en los cuales no son aceptables pasos de tiempo pequeños.

Dentro de la perspectiva del argumento anterior y con el propósito de desarrollar un esquema de solución que permita emplear pasos de tiempo grandes, manteniendo al mismo tiempo una buena eficiencia y robustez en casos de propagación discontinua de grietas, se tiene el trabajo de Lu et al. [102], en el cual se presenta un esquema escalonado, denominado enfoque semi-implícito, para simulaciones cuasi-estáticas de fractura frágil. Donde el primer componente clave de este método se basa en un enfoque implícito de un solo bucle modificado, en el cual se propone integrar la actualización del campo de fase, dentro del bucle de Newton del problema mecánico para mejorar la tasa de convergencia de dicha variable. Dado que el campo de fase se actualiza después de calcular cada estimación incremental del desplazamiento, la convergencia del problema mecánico puede verse fuertemente perturbada, pero se puede esperar una convergencia más rápida del campo de fase en comparación con el esquema de minimización alternada (Amor et al. [99]; Ambati et al. [41]).

De hecho, como se muestra en los ejemplos simulados en dicho trabajo (Lu et al. [102]), el campo de fase puede converger relativamente más rápido que el campo de desplazamientos, y pequeñas variaciones en el campo de fase pueden afectar significativamente el equilibrio mecánico. En particular, durante los pasos de propagación discontinua, un campo de fase globalmente estable no garantiza inmediatamente el equilibrio mecánico. Por ende, se observa que este problema genera un número considerable de iteraciones únicamente necesarias para lograr esa convergencia mecánica, incluso después de que el campo de fase haya convergido.

Una forma sencilla de superar este problema podría ser adoptar un criterio de convergencia menos

estricto para el problema mecánico. Sin embargo, esto no fue considerado en dicho trabajo. En su lugar, a nivel del esquema de solución, se propuso aplicar una resolución tipo explícita para la convergencia mecánica fijando la variable de campo de fase, una vez que se haya alcanzado la convergencia de esta variable mediante el procedimiento implícito propuesto. Por lo tanto, este esquema semi-implícito, que combina enfoques implícitos y explícitos, presenta una doble ventaja: permite pasos de tiempo grandes y es robusto ante propagaciones discontinuas de grietas.

2.6. Comentarios sobre métodos numéricos acoplados que combinan el MEF y MGLE

Es ampliamente reconocido en la literatura que los métodos sin malla ofrecen una perspectiva prometedora para la resolución de diversos problemas en el contexto de la mecánica computacional. Esta perspectiva ha ganado relevancia con el tiempo, convirtiéndose en una técnica ampliamente utilizada en numerosas aplicaciones de ingeniería, como por ejemplo: el modelado de grandes deformaciones, daño material, fronteras móviles, materiales disímiles o estratificados, y la iniciación, nucleación y crecimiento de grietas.

Entre estos métodos, uno de los más conocidos y aplicados es el método de Galerkin libre de elementos (MGLE), el cual posee un gran potencial para resolver problemas de la mecánica de sólidos, tanto lineales como no lineales, de manera eficiente y con alta precisión. No obstante, también se sabe que el MGLE tiende a ser computacionalmente más costoso que el MEF para una tarea específica.

Este inconveniente del MGLE se mantiene a pesar de las analogías con el MEF, más allá de las diferencias relativas a la construcción de las funciones de forma y el ensamblaje de los sistemas de ecuaciones algebraicas. Esta limitación específica ha llevado al desarrollo de técnicas híbridas MGLE-FEM destinadas a mejorar la eficiencia computacional, ya que estos enfoques se conciben principalmente para acotar la implementación del MGLE a regiones específicas que requieren aproximaciones de orden superior para proporcionar una buena precisión.

La primera técnica acoplada MGLE-FEM fue introducida por Belytschko et al. [103], utilizando elementos de interface en la región de acoplamiento con funciones de forma compuestas por una interpolación lineal a través del procedimiento de mínimos cuadrados móviles del MGLE y la interpolación estándar de FEM. Se demostró que este procedimiento cumple con la consistencia en el marco de problemas de elastostática, elastodinámica y fractura dinámica.

Existen también otros trabajos en los que el MGLE-FEM acoplado se utiliza para permitir la imposición directa de condiciones de contorno de tipo Dirichlet en las posiciones nodales, lo que se realiza utilizando una tira de elementos finitos para la discretización a lo largo de las fronteras correspondientes (Krongauz y Belytschko [104], Huerta et al. [105]).

Por otro lado, la mayoría de los procedimientos de acoplamiento MGLE-FEM reportados en la literatura reciente involucran regiones previamente bien especificadas para ser discretizadas mediante el MEF y el MGLE, con una relación topológica prescrita para ser acopladas adecuadamente. Por consiguiente, Rohit et al. [106] presentaron una revisión sobre la implementación en las últimas décadas de los procedimientos acoplados entre métodos sin malla y MEF que han aparecido como una nueva alternativa en los métodos computacionales con importantes logros.

Además, se analizaron los notables avances en la resolución de las principales deficiencias de los métodos convencionales y de los métodos sin malla en fases prematuras. Dicho trabajo también incluyó una revisión exhaustiva de las distintas técnicas de acoplamiento utilizadas para los elementos de interface de los métodos sin malla y el MEF. La formulación de funciones de forma tanto en el MEF como en el MGLE se discutió en general, mostrando la contribución clave de las técnicas de acoplamiento MGLE-FEM en la solución numérica de problemas de mecánica de sólidos y estructural.

En particular, se ha comprobado que las técnicas híbridas MGLE-FEM son útiles en la mecánica de fractura elástica lineal (Pathak et al. [107]) y en la modelización del crecimiento de grietas en materiales

tanto dúctiles (Kumar et al. [108]) como frágiles (Thongraksa et al. [109]).

En el contexto de implementar mejoras en estos métodos acoplados Ullah et al. [110] han desarrollado un novedoso procedimiento de acoplamiento adaptativo automático basado en errores de MGLE-FEM para problemas de mecánica de sólidos lineales, no lineales y también dependientes de la trayectoria. Las funciones de forma para las aproximaciones del MGLE se construyeron a través de la formulación de máxima entropía, permitiendo un cumplimiento débil de la propiedad delta de Kronecker. Esta característica particular no sólo ha permitido la imposición de condiciones de contorno Dirichlet en forma de valores nodales prescritos, sino que también ha eliminado la necesidad de elementos de interface en el acoplamiento entre las regiones MGLE y MEF.

A pesar de las ventajas que presentan las soluciones numéricas híbridas basadas en MGLE-FEM, estos métodos de acoplamiento siguen requiriendo límites de transición bien definidos en las zonas donde MGLE y MEF comparten nodos comunes. Por ende, con el propósito de abordar este tipo de necesidades de relación topológica en los procedimientos basados en el acoplamiento de dominios, recientemente se han empezado ha desarrollar métodos de superposición de dominios, en el contexto de métodos tanto sin malla como con malla, como el trabajo presentado por Álvarez Hostos et al. [15], en el cual desarrollaron el método Ov-IEFG-FEM (del inglés overset improved element-free Galerkin-finite element method).

Esta técnica híbrida sin malla/con malla ha sido desarrollada e implementada inicialmente en el contexto de problemas de conducción de calor transitoria con fuentes de calor en movimiento, utilizando una distribución fina de nodos que se mueven con la fuente de calor y se superponen con una malla gruesa que discretiza la geometría del dominio completo. Para más detalles dirigirse al Apéndice E.

En base al potencial del Ov-IEFG-FEM para resolver problemas con gradientes marcados en pequeñas regiones móviles, el mismo fue extrapolado de forma adecuada para resolver diversos problemas de la elasticidad lineal, tomando en cuenta bajo ese mismo contexto, un ejemplo clásico de la mecánica de fractura lineal elástica, lo cual se puede visualizar en detalle en el Apéndice F. En consecuencia, los aportes logrados mediante la implementación de este tipo de enfoque híbrido se presentan y discuten en el capítulo VI de esta tesis.

Parte III

Aportes al desarrollo de estrategias numéricas para la simulación de fractura frágil

Capítulo 3

Análisis de los mecanismos de interacción entre una grieta propagante y una interface

3.1. Introducción

Este capítulo tiene como objetivo proporcionar una lectura complementaria a los dos primeros trabajos que constituyen el apéndice de esta tesis. El primero corresponde a un artículo publicado por Zambrano et al. [78], mientras que el segundo es un resumen presentado como extensión del primer estudio, y publicado por Zambrano et al. [111] en un congreso internacional. Ambos documentos están incluidos en los Apéndices A y B. El propósito de estos trabajos es proponer una nueva metodología de análisis en problemas que implican primordialmente la interacción de una grieta con una interface, tomando en cuenta que este fenómeno se encuentra compuesto por una serie de mecanismos, cuyo comportamiento se estudian en este capítulo.

Por consiguiente, a través de un modelo de campo de fase, como el descrito en el Capítulo II, es posible analizar el comportamiento del campo de tensiones en la punta de una grieta. Esto se realiza teniendo en cuenta la relación entre el parámetro de regularización del modelo de campo de fase y la tensión máxima alcanzada delante de la grieta, lo cual constituye un propósito estándar dentro de la mecánica de fractura.

Luego, al implementar una metodología numérica basada en la combinación del modelo de campo de fase con un modelo de zona cohesiva, dicho modelo cohesivo será descrito en las secciones siguientes de este capítulo, se analizan los diversos mecanismos de interacción entre una grieta que propaga a través de un medio e incide con una interface, proporcionando información clave sobre las condiciones mecánicas bajo las cuales se presentan estos mecanismos para distintas configuraciones geométricas. Consecuentemente, la idea anterior también da cabida para el estudio de los efectos asociados con el incremento de tenacidad en una determinada muestra.

Este capítulo está estructurado de la siguiente manera: en la sección 3.2 se expone el comportamiento del estado de tensiones en la punta de una grieta haciendo uso del modelo de campo de fase y la relación del parámetro de regularización de dicho modelo con la tensiòn máxima alcanzada delante de la grieta. En la sección 3.3 se describe el comportamiento de los mecanismos de interacción entre una grieta propagante que impacta en una interface, haciendo uso de la metodología numérica combinada entre el modelo de campo de fase y el modelo de zona cohesiva, particularmente, dicho modelo cohesivo será descrito en esta sección. Posteriormente, en la sección 3.4 se exponen las causas y los mecanismos implicados en el incremento de tenacidad de una muestra. Finalmente, la sección 3.5 presenta las conclusiones correspondientes a este capítulo.

3.2. El campo de tensiones en la punta de una grieta evaluados con el modelo de campo de fase

La descripción del crecimiento de grietas y fracturas mediante el modelo de campo de fase es una alternativa atractiva a los métodos numéricos basados en representaciones discretas de grietas, ya que la metodología de campo de fase evita el desafío numérico asociado al monitoreo de las discontinuidades introducidas por la grieta, debido a que dicho modelo realiza una representación difusa de la geometría de la fractura. Sin embargo, una predicción precisa de la iniciación del crecimiento de la grieta es imprescindible para garantizar una simulación confiable de las trayectorias de las mismas.

Bajo esta premisa, se llevó a cabo un análisis de los campos de tensiones en las proximidades de la punta de una grieta, evaluados numéricamente mediante el modelo de campo de fase. El objetivo primordial fue analizar el vínculo entre el parámetro de regularización del modelo de campo de fase (ℓ_{PF}), que se interpreta como una longitud característica del material y la tensión máxima alcanzada delante de la grieta.

Desde el punto de vista numérico la evaluación de las tensiones se llevó a cabo considerando la propagación de la grieta a una corta distancia desde la raíz de la muesca original de la muestra, tras la aplicación de la carga, utilizando diferentes longitudes caracteristicas del material. Dicha evaluación con el modelo numérico se comparó con la estimación de la tensión crítica delante de la punta de la grieta, calculada por medio de la siguiente expresión (Duda et al. [54]) que relaciona la longitud característica del material (ℓ_{PF}), con el valor máximo de tensión delante la punta de la grieta ($\hat{\sigma}_0^c$):

$$\hat{\sigma}_0^c = \frac{3\sqrt{3}}{16}\sqrt{\frac{\bar{E}\, G}{\ell_{PF}}}\,, \tag{3.1}$$

donde $\bar{E}$ representa el módulo de Young para un estado de deformación plana del material, G la energía de fractura del mismo y como se mencionó previamente (ℓ_{PF}) debe interpretarse como un parámetro de regularización en su límite tendiendo a cero. Sin embargo, para $\ell_{PF} > 0$, se introduce una resistencia finita del material y, por lo tanto, ℓ_{PF} se convierte en una propiedad material que controla la resistencia del mismo.

En consecuencia, se entiende que el modelo de campo de fase no posee un parámetro explícito que defina directamente la tensión crítica del material. Sin embargo, esta puede estimarse utilizando los parámetros mencionados anteriormente. Cabe destacar que dicha expresión se deriva de la solución analítica unidimensional de un problema de campo de fase elástico homogéneo uniaxial.

Debido a la homogeneidad asumida, todos los gradientes se anulan, por ende, el resultado del problema de campo de fase elástico homogéneo uniaxial (Borden et al. [112]), proporciona las respectivas respuestas tensión-deformación, las cuales pueden observarse en Duda et al. [54]. Donde los valores máximos de tensión de dichas respuestas fueron obtenidos a través de la expresión 3.1. Asimismo, se destaca la sensibilidad de la respuesta tensión-deformación con los parámetros G y ℓ_{PF} del material.

Por otro lado, se debe mencionar que la expresión 3.1 también representa la tensión crítica de falla alcanzada por un modelo de campo de fase tipo AT2, como se detalla en Tanné et al. [113]. Este modelo AT2 es una formulación ampliamente utilizada en la mecánica de fractura basada en el método de campo de fase, derivada de los trabajos originales de Ambrosio y Tortorelli [22].

Dicho modelo busca aproximar la energía de fractura de Griffith mediante una regularización continua. En el contexto de la mecánica de medios continuos, el modelo AT2 se ha convertido en una herramienta efectiva para simular el proceso de iniciación y propagación de grietas. El modelo AT2 utiliza una función de daño $\varphi(x)$, que varía de 0 (material intacto) a 1 (material completamente fracturado), permitiendo suavizar la transición entre las regiones dañadas e intactas del material.

En este contexto, cuando $\ell_{PF} \to 0$ la resistencia del material tiende a infinito; y esto es consistente

con la mecánica de fractura elástica lineal.

Por consiguiente, como se puede observar en el Apéndice A, tanto los resultados para los picos de tensión ortogonal al plano de la grieta obtenidos con el modelo numérico del campo de fase, como las tensiones críticas calculadas con la expresión 3.1 muestran una concordancia satisfactoria, para diferentes valores de longitud característica del material.

Por otro lado, también se realizó la comparación con las distribuciones de tensiones en la punta de una grieta utilizando la Mecánica de Fractura Lineal Elástica (LEFM por sus siglas en inglés). Tal como se muestra en el Apéndice A, se observa una concorcondancia aceptable entre el comportamiento teórico de la LEFM y los resultados del modelo numérico de campo de fase. Por ende, todas estas evaluaciones descritas anteriormente, permiten inferir una validación satisfactoria del modelo numérico del campo de fase empleado en nuestros estudios del Apéndice A. Dicha validación es importante, ya que las distribuciones de tensiones en la punta de una grieta juegan un papel significativo en la predicción de los modos de interacción entre una grieta en propagación y su incidencia con una interface.

3.3. Comportamiento de los mecanismos de interacción entre una grieta propagante y una interface

En esta sección se analizan diferentes contribuciones derivadas del Apéndice A, en relación con los modos de interación entre una grieta que propaga por un determinado medio y choca contra una interface. Estas evaluaciones se realizaron mediante la aplicación de una metodología numérica combinada. Para ello, se emplea un modelo de campo de fase, como el presentado en el Capítulo II, con el cual se modela la propagación de la grieta en el medio, junto con un modelo de superficie cohesiva, a través del cual se simula el proceso de degradación de la interface.

Nuestro modelo de superficie cohesiva se presenta comúnmente en la literatura como una ley cohesiva que relaciona el salto de desplazamiento ($[\![\boldsymbol{u}]\!]$) con el vector de tracción ($\boldsymbol{t}$). Dicho modelo puede interpretarse como una proyección del modelo constitutivo de daño continuo isotropico hacia una ley cohesiva en la interface de falla (Huespe et al. [114]). Por lo tanto, hereda algunas propiedades del modelo de daño continuo original. Un esquema representativo de este modelo cohesivo se ilustra en la figura 3.1.

El modelo cohesivo se deriva proponiendo una función de energía libre por unidad de área de la interface $\mathcal{S}$, $\hat{\psi}_{\mathcal{S}}$ (densidad de energía superficial), la cual esta definida en términos del salto de desplazamiento $[\![\boldsymbol{u}]\!]$ y la variable interna escalar $\bar{\alpha} \in [0, \infty]$, de la siguiente forma:

$$\hat{\psi}_{\mathcal{S}}([\![\boldsymbol{u}]\!], \bar{\alpha}) = \frac{1}{2}\frac{q(\bar{\alpha})}{\bar{\alpha}}([\![\boldsymbol{u}]\!] \cdot \boldsymbol{Q}[\![\boldsymbol{u}]\!]) \ , \tag{3.2}$$

donde $\boldsymbol{Q}$ es un tensor de segundo orden llamado tensor acústico elástico, el cual se define en términos del modulo de Young de la interface E_i, de la siguiente manera:

$$\boldsymbol{Q} = \begin{bmatrix} E_i & 0 \\ 0 & E_i/2 \end{bmatrix} \ , \tag{3.3}$$

y q , $\bar{\alpha}$, representan las variables internas de tipo tensión y deformación. La energía libre $\hat{\psi}_{\mathcal{S}}$ se utiliza como un potencial para determinar el vector de tracción $\boldsymbol{t}$:

$$\boldsymbol{t} = \frac{\partial \hat{\psi}_{\mathcal{S}}([\![\boldsymbol{u}]\!], \bar{\alpha})}{\partial [\![\boldsymbol{u}]\!]} = \frac{q(\bar{\alpha})}{\bar{\alpha}}(\boldsymbol{Q}[\![\boldsymbol{u}]\!]) \ . \tag{3.4}$$

Las ecuaciones cinéticas que definen la evolución de las variables internas se describen mediante:

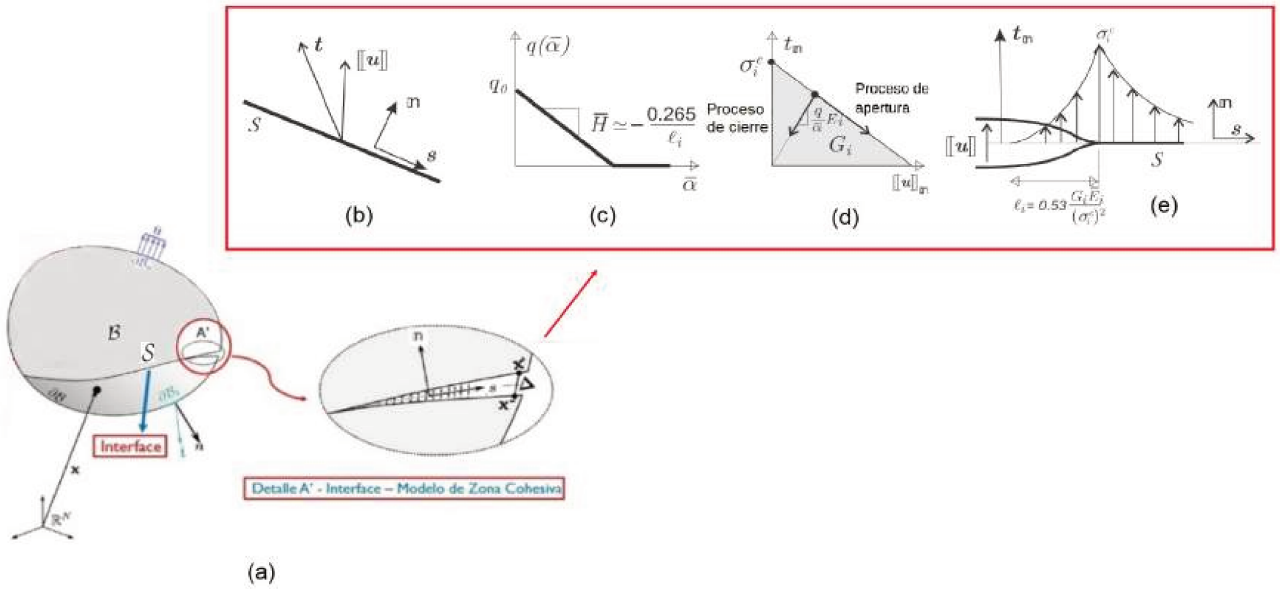

Figura 3.1: (a) Esquema de un cuerpo con una interface cohesiva. (b) Vectores de tracción t y separación $[\![\boldsymbol{u}]\!]$ en la interface. (c) Ley de ablandamiento, $q(\bar{\alpha})$ que gobierna la degradación tracción-sepración. (d) Ley tracción-separación para la apertura de una interface en el modo I. El área bajo la curva es igual a la energía de fractura G_i y la componente de máxima tensión es σ_i^c. (e) Estimación de la longitud característica cohesiva ℓ_i

$$\dot{q} = \bar{H}\dot{\bar{\alpha}} \qquad , \qquad q_0 = q(\bar{\alpha} = 0) = \frac{\sigma_i^c}{\sqrt{E_i}} \, , \tag{3.5}$$

donde σ_i^c representa la tensión cohesiva crítica de la interface y $\bar{H}$ es el módulo de ablandamiento regularizado, el cual define la pendiente de la curva $q = q(\bar{\alpha})$ representada en la figura 3.1c. Dicho módulo de ablandamiento regularizado es caracterizado en téminos de la energía de fractura de la interface G_i de la siguiente forma:

$$\bar{H} = -\frac{1}{2}\frac{(\sigma_i^c)^2}{G_i E_i} \, . \tag{3.6}$$

Las condiciones de carga-descarga se definen a continuación:

$$f_t \leq 0 \qquad , \qquad \dot{\bar{\alpha}} \geq 0 \qquad , \qquad f_t \dot{\bar{\alpha}} = 0 \, , \tag{3.7}$$

en las ecuaciones anteriores se puede observar que α es una función monótonamente creciente y se tiene una disminución de q a lo largo de un pseudo-tiempo t. Ahora, f_t es interpretado como un criterio de daño definido en el espacio de las fuerzas generalizadas $(\boldsymbol{t} \ , \ q)$, y se define de la siguiente forma:

$$f_t = \sqrt{\boldsymbol{t}^{pos} \cdot \boldsymbol{Q}^{-1}\boldsymbol{t}} \ - q \, , \tag{3.8}$$

donde $\boldsymbol{t}^{pos}$ es la contraparte positiva del vector tracción ($\boldsymbol{t}^{pos} = (\langle t_{\boldsymbol{n}} \rangle \, , \langle t_s \rangle)$). Particularmente las interfaces que abren en modo I comienzan a degradarse cuando $t_{\boldsymbol{n}} = \sigma_i^c$.

Estas condiciones de carga-descarga también pueden ubicarse en el espacio de desplazamientos generalizados redefiniendo f_t en términos de las variables $([\![\boldsymbol{u}]\!] \ , \ \bar{\alpha})$, de la siguiente manera:

$$f_\delta \leq 0 \qquad , \qquad \dot{\bar{\alpha}} \geq 0 \qquad , \qquad f_\delta \dot{\bar{\alpha}} = 0 \, . \tag{3.9}$$

donde f_δ se define como:

$$f_\delta = \sqrt{[\![\boldsymbol{u}]\!]^{pos} \cdot \boldsymbol{Q}[\![\boldsymbol{u}]\!]} - \bar{\alpha} \ , \tag{3.10}$$

donde $[\![\boldsymbol{u}]\!]^{pos}$ es el vector de salto de desplazamientos con componentes postivas ($[\![\boldsymbol{u}]\!]^{pos} = (\langle [\![u]\!]_{\boldsymbol{n}} \rangle \, , \langle [\![u]\!]_s \rangle)$).

El proceso de degradación de la interface esta caracterizado por la condición $\dot{\bar{\alpha}} > 0$. También a partir de la ecuación 3.10 y la condición mencionada $\dot{\bar{\alpha}} > 0$, α puede interpretarse como la apertura máxima efectiva de la grieta a lo largo del historial del proceso de carga. Para mayores detalles de este modelo cohesivo, consúltese el Apéndice A.

Por otra parte, de este modelo cohesivo se puede obtener una longitud característica de la interface, la cual se define de la siguiente manera:

$$\ell_i = 0.53 \frac{E_i G_i}{(\sigma_i^c)^2} \ , \tag{3.11}$$

donde E_i es el modulo de Young de la interface, G_i es la energía de fractura de la interface y $(\sigma_i^c)^2$ representa la tensión crítica alcanzada en la interface. El coeficiente 0.53 se ha determinado mediante una experimentación numérica exhaustiva. Esta longitud característica de la interface representa de manera aproximada la distancia entre el punto de la interface, donde la cohesión se libera por completo y aquel con la máxima tracción delante de la punta de la grieta (Figura 3.1e).

Por otro lado, un enfoque numérico estrechamente vinculado a la metodología empleada en nuestro trabajo es la contibución de Paggi y Reinoso [73], estos autores integran una técnica de campo de fase para la fractura frágil junto con un modelo de zona cohesiva, semejante al descrito por Needleman [115], con el cual se modela el proceso de degradación de la interface. No obstante, una diferencia clave del trabajo de Paggi et al. en comparación con el nuestro radica en el modelo de descohesión de la interface.

Ya que en la metodología numérica adoptada en nuestro estudio, el modelo cohesivo de la interface no se ve afectado por la degradación del medio vecino caracterizado por la variable de campo de fase. Por ende, no se necesita extender el campo de fase a la interface, y en consecuencia, puede ser completamente independiente en ambos lados de la interface. Además este enfoque sugiere escenarios de modelado alternativos donde las discontinuidades del campo de fase, a través de la interface pueden utilizarse para mejorar la caracterización de los mecanismos de interacción.

En este sentido, la idea previamente expuesta representa una contribución significativa de nuestro trabajo, ya que propone un enfoque numérico alternativo, no implementado en la literatura para aquel momento, que facilita el análisis de la interacción de una grieta propagante que incide con una interface en diversos tipos de problemas. Asimismo, es importante mencionar que considerando las diferencias entre nuestra metodología y la de Paggi et al., las conclusiones más relevantes con respecto a los modos de interacción obtenidas con nuestro enfoque, pueden diferir de aquellas derivadas del enfoque de Paggi et al.

3.3.1. Análisis de los resultados obtenidos del estudio realizado

Es importante mencionar que los modos de interacción comprenden un conjunto de mecanismos que se ilustran en la figura 3.2. Donde en una muestra genérica compuesta por dos medios y una interface sometida a una tensión remota (Figura 3.2a), se manifiesta el mecanismo de penetración, el cual ocurre cuando la grieta impacta con la interface y la cruza (Figura 3.2b), luego se tiene el mecanismo de deflexión donde una vez que la grieta choca con la interface, se desvía y se propaga a traves de ella (Figura 3.2c). Un tercer mecanismo ocurre cuando la grieta esta propagando a través de la interface y se desvía fuera de la misma, penetrando en el medio 2 (Figura 3.2d)

Por consiguiente, el propósito fundamental de este análisis se basa en la captura de los distintos mecanismos de interacción previamente descritos, en un problema de una interface ortogonal a la dirección de propagación de la grieta, donde se evaluaron propiedades elásticas y de fractura (módulo de Young

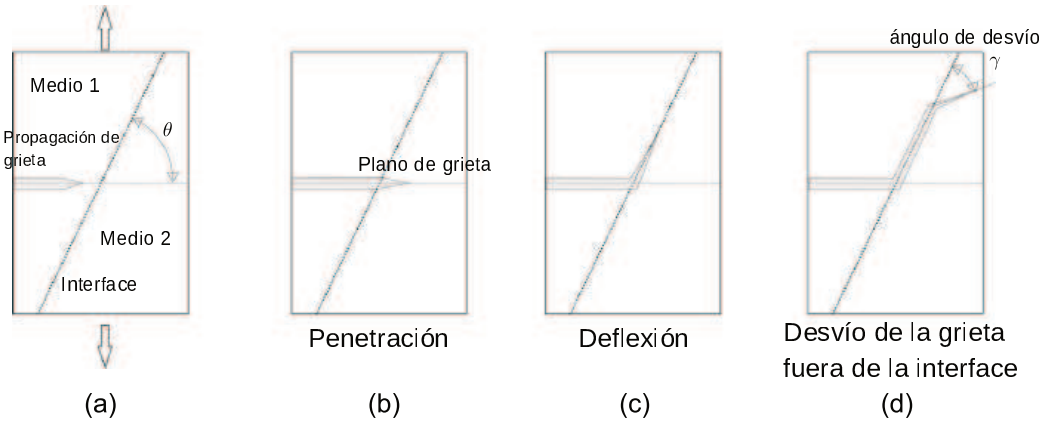

Figura 3.2: Modos de interacción entre una grieta en propagación que impacta sobre una interface con un ángulo θ. (a) Esquema del problema. (b) Penetración. (c) Deflexión. (d) Desvío de la grieta fuera de la interface.

E, coeficiente de poisson ν, energía de fractura G y longitud característica ℓ) idénticas tanto en la fibra como en el sustrato de una muestra determinada. Además, este mismo problema se analizó manteniendo constantes los parámetros de fractura $(G\ ,\ \ell)$ en la fibra y el sustrato de la muestra, pero variando la rigidez de ambos materiales.

Seguidamente, se estudió el problema de una interface inclinada con un ángulo de $\theta = 30°$ respecto a la dirección de propagación de la grieta. Finalmente, se evaluó el caso del desvío de una grieta que propaga a través de una interface inclinada y su posterior salida de la misma. Para detalles con respecto a la geometría de las muestras y propiedades mecánicas utilizadas, en cada uno de los casos simulados consultar el Apéndice A.

Se debe destacar que nuestro análisis se basó en el trabajo de Parmigiani y Thouless [62], el mismo fue llevado a cabo solamente utilizando un modelo de zona cohesiva en todo el dominio, lo cual radica en una diferencia con respecto a la metodología numérica combinada implementada en nuestro estudio. En este trabajo la conclusión más significativa radica en el hecho de que los modos de interacción resultantes, no se encuentran solamente gobernados por la razón G_s/G_i (energías de fractura de la interface y del medio 2 (sustrato)), como se podría esperar desde un punto de vista puramente energético, sino que tambien la razón σ_s^c/σ_i^c (tensiones críticas de la interface y del medio 2), toma protagonismo.

Por ende, se infiere que un criterio mixto de tenacidad-resistencia determina la condición bajo la cual ocurre el modo de interacción. En nuestro estudio se alcanzó una conclusión similar a la reportada por Parmigiani y Thouless [62], utilizando el enfoque numérico combinado de campo de fase y superficie cohesiva, evidenciándose ciertas diferencias con respecto a dicho trabajo.

En un contexto general, para los diferentes casos de estudios que fueron testeados el comportamiento de los modos de interacción, se puede representar de forma esquemática como se ilustra en el gráfico de la figura 3.3, donde se define un espacio conformado por G_s/G_i y σ_s^c/σ_i^c, y se observan dos curvas.

La curva roja representa el límite de la región que describe un mecanismo de deflexión, mientras que la curva azul marca el límite de la región asociada al mecanismo de penetración. Por lo tanto, todos los puntos en el gráfico situados a la izquierda de esta curva límite azul corresponden al mecanismos de penetración, y todos los puntos ubicados a la derecha de la curva límite roja representan el mecanismo de deflexión.

Básicamente, para la construcción de dichas curvas se establecen condiciones en el modelo de interface, donde se determina y se fija tanto la longitud característica de la interface como su tensión crítica. Luego, a partir de las propiedades del sustrato correspondientes a su modulo de Young E_s, su energía de fractura G_s y su longitud característica perteneciente al modelo de campo de fase ℓ_{PF}, se determina la tensión crítica del sustrato. Con esta información, junto con la tensión crítica de la interface previamente

fijada, y las energías de fractura de ambos materiales, se obtiene el punto de partida en el espacio de coordenadas (G_s/G_i , σ_s^c/σ_i^c), las cuales se van modificando de manera sistemática para caracterizar los distintos modos de interacción (deflexión-penetración).

El comportamiento de estas curvas sugiere que existe una zona disjunta o de transición donde ambos mecanismos (deflexión y penetración) compiten por prevalecer y se encuentra representada en el gráfico esquemático (Figura 3.3) por la curva segmentada negra entre ambas curvas de deflexión y penetración.

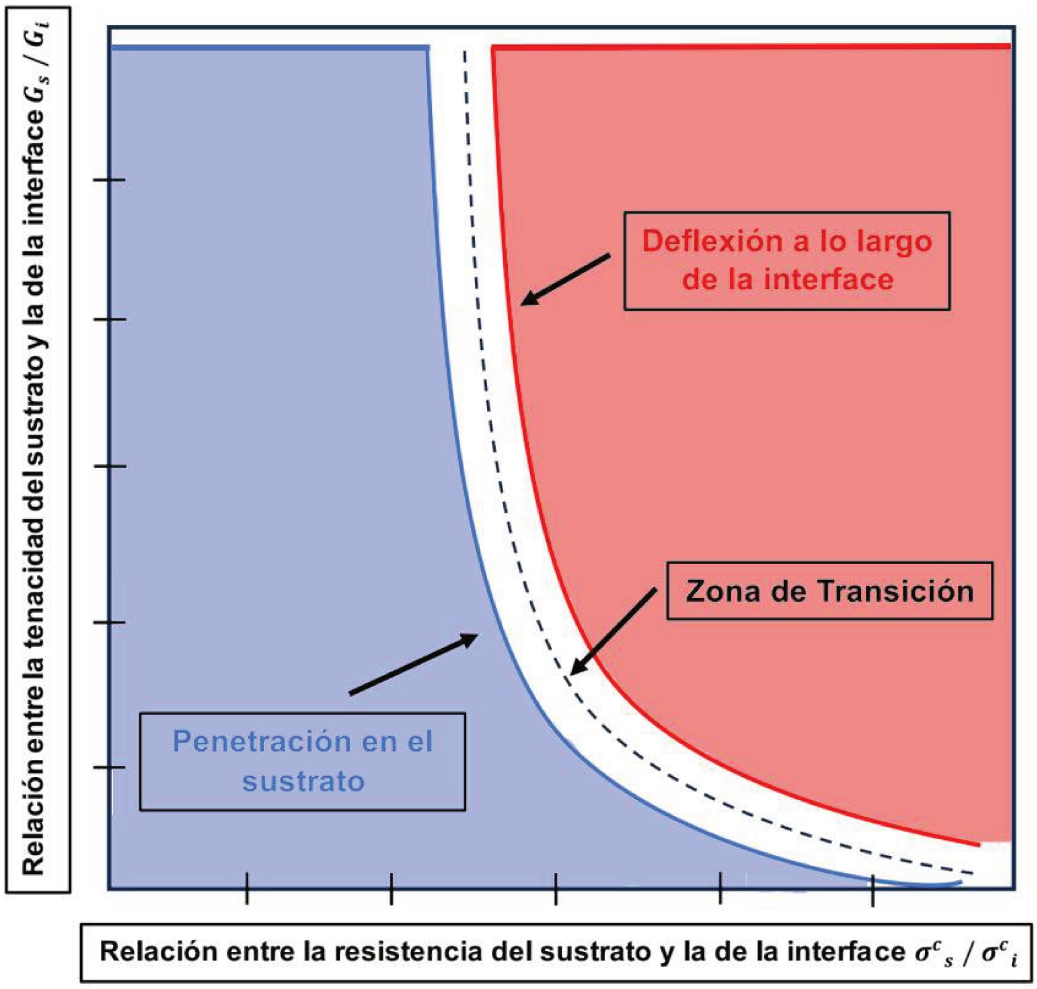

Figura 3.3: Comportamiento esquemático de mecanismos de penetración y deflexión de una grieta propagante que incide en una interface que forma $\theta = 90^\circ$ con respecto a la dirección de propagación de la grieta.

Por consiguiente, se puede visualizar tanto en el esquema representativo (Figura 3.3), como en los resultados del Apéndice A, para todos los casos que fueron testeados, que la parte superior derecha del gráfico representa el escenario en el que la grieta probablemente se desvía hacia la interface. Mientras que la parte inferior izquierda del gráfico representa la situación donde la grieta probablemente penetra en el sustrato.

En otras palabras, se tiene que a bajas relaciones G_s/G_i y σ_s^c/σ_i^c se promueve el mecanismo de penetración. Por el contrario, los valores altos de estas relaciones promueven el mecanismo de deflexión. También se observa que a medida que la relación σ_s^c/σ_i^c disminuye, la curva segmentada negra tiende a tener un comportamiento asintótico vertical.

Por otro lado, analizando escenarios particulares se tiene que con altas relaciones G_s/G_i, el cambio del modo de interacción, solo depende de la relación σ_s^c/σ_i^c y no de la relación G_s/G_i. En consecuencia,

en esta región del espacio paramétrico (G_s/G_i , σ_s^c/σ_i^c), el modo de interacción penetración/deflexión depende estrictamente de un criterio de resistencia. Por el contrario, para bajas relaciones G_s/G_i, la curva segmentada negra parece mostrar una tendencia hacia un comportamiento asintótico horizontal.

No obstante, no queda claro que exista un valor asintótico. Cuando esta curva se aproxima a valores muy bajos de G_s/G_i, el parámetro σ_s^c/σ_i^c no juega un papel prominente en la determinación del cambio del mecanismo de interacción. Por lo tanto, en esta región del espacio, el modo de interacción penetración/deflexión probablemente depende de un criterio de tenacidad. Entre ambos escenarios límite, la predicción del modo de interacción según el enfoque utilizado depende de ambas relaciones y, por ende, se infiere que un criterio mixto de resistencia/tenacidad gobierna el modo de interacción.

En un contexto general, este comportamiento se cumplió plenamente para cada uno de los casos que fueron testeados. Por otra parte, los argumentos expresados previamente coinciden totalmente con los reportados por Parmigiani et al., lo cual también se le atribuye al efectivo funcionamiento de la metodología numérica que fue planteada en nuestro trabajo, representando así otra contribución relevante, ya que se validan cada una de las conclusiones obtenidas en dicho trabajo de Parmigiani et al.

Particularmente, se debe mencionar que para la captura del tercer modo de interacción mostrado en la figura 3.2d, el cual tiene que ver con una grieta que se propaga por una interface y luego sale de la misma penetrando al sustrato, es importante señalar que este modo de interacción resulta de dos mecanismos en competencia los cuales son: el proceso de decohesión de la interface y la grieta que abandona dicha interface y se propaga en una dirección diferente. Por ende, para inducir este modo de interacción en la geometría específica que hemos estudiado (placa bajo tracción con interface a $\theta = 30°$ de la figura 3.2d), se manipularon los parámetros de fractura de la interface aumentando los valores de G_i y (σ_i^c) a lo largo de la misma para desencadenar la desviación. Mayores detalles de este proceso se pueden observar en el Apéndice A.

En el mismo contexto de la idea anterior, se puede plantear un escenario alternativo para poder capturar este tercer modo de interacción, dicho escenario se encuentra relacionado con el juego de la orientación de la interface con respecto a la direccion de propagación de la grieta, implementando interfaces de baja y alta resistencia, para explorar el comportamiento de transición entre penetración y deflexión de la grieta.

Esta alternativa está desarrollada desde el punto de vista experimental en el trabajo de Alam et al. [116], en el cual se utilizaron interfaces de baja resistencia y se concluyó que la transición penetración-deflexión de la grieta, se encontraba en un rango para el ángulo incidente entre $80°$ y $85°$. Mientras que para el caso de interfaces de alta resistencia, el valor del ángulo incidente de transición penetración-deflexión de la grieta se situaba entre $75°$ y $80°$. Por consiguiente, se debe mencionar que para nuestro estudio se utilizó la alternativa expresada previamente, sin obtener éxito en la captura de este tercer mecanismo de interacción, dichos problemas pudieran solventarse realizando alguna re-calibración de nuestro modelo, para este caso particular, lo cual representaría un trabajo futuro dentro de esta misma área de investigación.

3.4. Conclusiones relevantes del estudio sobre el incremento de la tenacidad estructural de una muestra

En la literatura se establece que el mecanismo de deflexión es uno de los principales responsables en el incremento de la tenacidad estructural de una determinada muestra. Por lo cual se realizaron los testeos respectivos para validar dicho fenómeno con nuestra metodología numérica, particularmente tomando el caso de una grieta que se desvía por una interface inclinada y se propaga a través de ella. Se pudo apreciar que una vez que la grieta impacta en la interface y se propaga a través de la misma, el proceso de deflexión de la grieta requiere un incremento adicional de carga.

En consecuencia, este resultado implica un apreciable incremento de la tenacidad estructural de la muestra testeada. Dicho comportamiento se puede apreciar en el gráfico de la figura 3.4, con el modelo

de interface original que fue implementado en nuestro análisis.

Por consiguiente, para comprender este efecto evaluado por el modelo numérico, realizamos un análisis adicional, el cual se basaba en comparar las cargas máximas resultantes de dos pruebas adicionales. La primera probando una interface más fuerte y la segunda posicionando la raíz de la muesca inicial de la muestra junto a la interface. En dichas pruebas no se observó un incremento de la tenacidad estructural de la muestra, lo cual se visualiza en las curvas roja y azul de la figura 3.4.

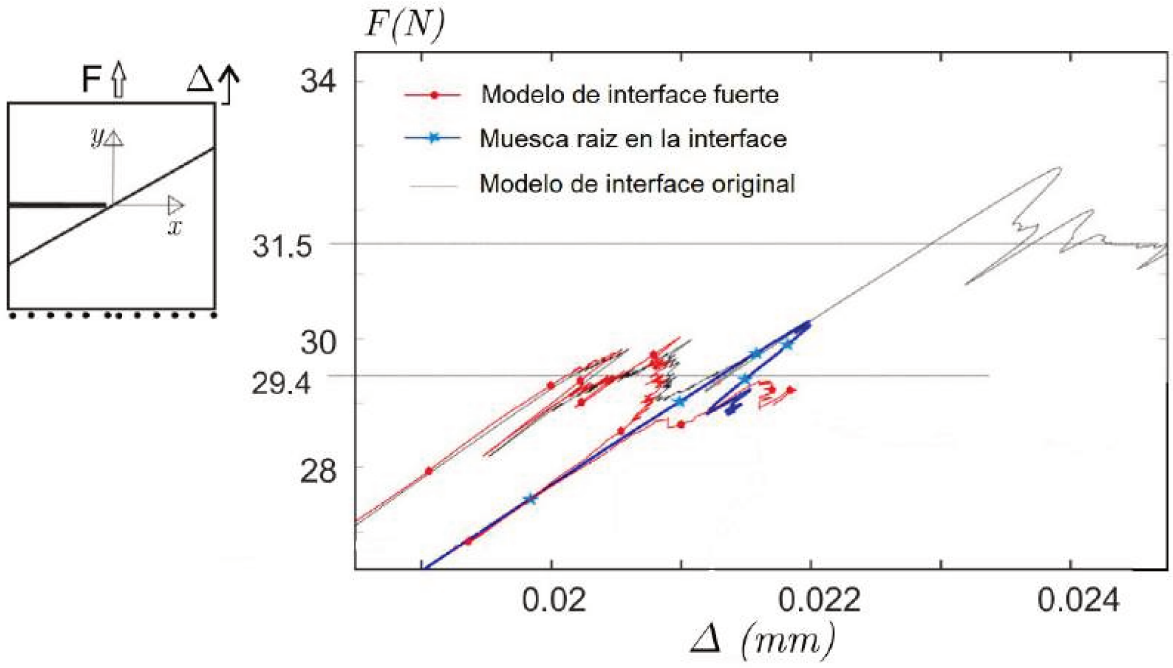

Figura 3.4: Comparación de pruebas para el análisis del incremento de tenacidad de una muestra.

Por lo tanto, se puede inferir que este comportamiento se debe a un efecto tipo escudo (shield), producido por la degradación de la interface, lo cual ocurre antes de que la grieta choque contra ella. Dicho efecto se le atribuye al proceso de avance de la grieta, lo cual induce a la apertura de la interface antes de que choque contra la misma, ya que si se observa el campo de tensión delante de la punta de la grieta justo cuando la misma comienza a propagarse, dichos valores de tensión son similares a la resistencia de la interface que se encuentran a una distancia determinada por delante de la punta de la grieta.

Por ende, tal degradación de la interface produce una caída de tensión en el sustrato de la parte derecha de la interface, lo cual prescribe la evolución del daño en esa misma zona y es la razón por la cual la grieta no penetra en la interface, sino que se desvía hacia ella, requiriendo cargas externas aún mayores.

Por otro lado, existen numerosos problemas de fractura en el contexto de la propagación de grietas con interfaces, en los cuales se presenta este efecto tipo escudo (shield), originando un incremento de la tenacidad estructural del material. Como ejemplos de dichos problemas se tienen: la propagación de microfisuras en materiales compuestos laminados, la fractura intergranular/transgranular en metales policristalinos, el puenteo de grietas en cerámicas estructurales, los mecanismos de fractura en materiales biomiméticos, entre otros.

Estos problemas que evidencian incremento de la tenacidad pueden ser estudiados tanto con la metodología numérica combinada que fue presentada en este capítulo, como también empleando solamente un modelo de zona cohesiva, originando así una comparación en un contexto evaluativo de los resultados obtenidos por ambas técnicas, como se hace mención en el Apéndice B.

3.5. Conclusiones

En este capítulo se demuestra que a través de un modelo numérico acoplado de campo de fase y superficie cohesiva se captura algunos aspectos relevantes de las respuestas complejas de problemas de interacción de grietas con interfaces, que resulta en una predicción cuantitativa similar a las metodologías basadas solo utilizando un modelo de zona cohesiva, para modelar fracturas tanto en el medio como en la interface de una muestra.

Por otra parte, se establece el rol fundamental que juega el parámetro de regularización del campo de fase, como una longitud característica del material, lo cual permite capturar de manera efectiva tanto las distribuciones de tensiones en la punta de una grieta como los diferentes mecanismos de interacción entre una grieta propagante y una interface.

Por medio del testeo de diversos casos de estudio se infiere que dichos mecanismos de interacción resultan como consecuencia de un criterio mixto que involucra tanto la resistencia como la tenacidad de los materiales, que constituyen el sustrato y la interface de una determinada muestra.

Finalmente se analizan las causas y mecanismos que originan un aumento de la tenacidad estructural de una muestra, debido a la interacción grieta-interface para una configuración determinada, demostrando la importancia del efecto tipo escudo (shield), debido a la degradación de la interface.

Capítulo 4

Diseños bioinspirados para aumento de tenacidad en materiales compuestos

4.1. Introducción

Este capítulo tiene como propósito presentar el trabajo publicado por Zambrano et al. [117] en un congreso nacional, incluido en el Apéndice C. El trabajo se desarrolló bajo el enfoque de los diseños bioinspirados, explorando las caracteristicas que contribuyen al incremento de tenacidad estructural en estos sistemas. Muchos materiales naturales son compuestos y dependen de la deflexión de grietas para alcanzar niveles excepcionales de tenacidad (Nardone y Prewo [118], Folsom et al. [119], He et al. [120], Tu et al. [121]). El nacár es un ejemplo sobresaliente de este tipo de materiales con tenacidad excepcional, lograda mediante la combinación de un mineral inorgánico duro y frágil con una proteína flexible. Esta proteína se encuentra en las interfaces entre los componentes minerales y actúa como un agente de unión que puede delaminarse y disipar energía cuando se intenta fracturar el compuesto.

En este contexto, resulta esencial analizar las diferentes estructuras geométricas asociadas al nácar, que es ampliamente reconocido por sus destacadas propiedades mecánicas, como se mencionó en el capítulo II, las cuales lo distinguen frente a otros tipos de materiales. De este modo, mediante la aplicación de la metodología numérica combinada presentada en el Capítulo III, es posible capturar el comportamiento mecánico global de los diseños bioinspirados, lo que facilita el estudio de los mecanismos clave que favorecen la mejora de su tenacidad estructural.

El presente capítulo se organiza de la siguiente manera: la sección 4.2 se describen, en primer lugar, los mecanismos de aumento de tenacidad estructural desde una perspectiva general de materiales compuestos y, luego, en el contexto específico de los biocompuestos. A continuación, la sección 4.3 se enfoca en los aspectos relacionados con la respuesta mecánica global de los diseños bioinspirados, correspondientes a las configuraciones geométricas simuladas en nuestro trabajo. Luego, en la sección 4.4 se exponen las características del modelado numérico aplicado a tres tipos de configuraciones geométricas que imitan la estructura del nácar. Seguidamente, en la sección 4.5 se analiza el comportamiento de los mecanismos de deflexión y penetración, junto con otras ideas complementarias. Finalmente, en la sección 4.6 se presentan las conclusiones de este capítulo.

4.2. Mecanismos de aumento de tenacidad estructural en materiales compuestos

Los sólidos laminados se emplean comúnmente como materiales de ingeniería, con aplicaciones que van desde componentes estructurales ligeros hasta recubrimientos de alta resistencia. Generalmente, los compuestos de alta resistencia son frágiles, por lo que es necesario mejorar su tenacidad macroscópica

mediante un ajuste adecuado de la topología y las propiedades interfaciales. Existen diversas estrategias de refuerzo disponibles, las cuales se derivan en algunos tipos de mecanismos de aumento de tenacidad (Noselli et al. [4]), como la multiplicación de grietas, la desviación de grietas y también se hace enfasis en el incremento de tenacidad presente en los biomateriales. Por consiguiente, se analizan cada uno de ellos a continuación.

4.2.1. Aumento de tenacidad mediante la multiplicación de grietas

Las cerámicas monolíticas pueden contener una zona de protección en la punta de la grieta mediante microfisuración. Este mecanismo genera un pequeño aumento en la tenacidad macroscópica, como lo han discutido Kreher y Pompe [122], Evans y Faber [123], Rose [124], Hutchinson [125] y Shum y Hutchinson [126]. Para que este mecanismo funcione, es esencial que las microfisuras se detengan en los límites de grano o en las interfaces de partículas y que sean altamente estables en su estado de detención.

La zona de microfisuración reduce el factor de intensidad de tensiones en la punta de la grieta, K_{punta}, mediante dos mecanismos: (i) la zona de microfisuración es más flexible que el material remoto, y (ii) las microfisuras liberan tensiones residuales locales al formarse, lo que genera una deformación dilatacional en dicha zona. Sin embargo, el grado de protección en la punta de la grieta debido a la zona de microfisuración es solo moderado. Hutchinson [125] demostró que la reducción en K_{punta} está entre el 30 % y el 40 % para zonas fuertemente microfisuradas en materiales cerámicos, como las observadas por Ruehle et al. [127].

Si se considera, como ejemplo, el aumento de tenacidad macroscópico que surge de un arreglo paralelo de n grietas semi-infinitas bajo un campo de intensidad de tensiones en modo I remoto, como se muestra en la figura 4.1a. La magnitud del factor de intensidad de tensiones en la punta de la grieta, así como la combinación de modos, variará de una grieta a otra.

4.2.2. Desviación de la grieta

La desviación en la punta de una grieta ofrece la posibilidad de incrementar la tenacidad tanto en materiales compuestos laminados como los conformados por partículas. El caso de un sólido laminado con una grieta preexistente ortogonal a las interfaces se ilustra en la figura 4.1b. La presencia de interfaces débiles o frágiles entre las capas permite la posibilidad de desviación de la punta de la grieta, lo que lleva a la propagación de la grieta a lo largo de la interface.

4.2.3. Incremento de tenacidad en la naturaleza: el papel de la jerarquía estructural

Los compuestos de polímero-cerámica se encuentran ampliamente distribuidos en la naturaleza, como se observa en estructuras como conchas, huesos y cuernos (Currey [80], Lin y Meyers [128], Bertoldi et al. [129]). El nácar, también conocido como la madre perla, es un ejemplo típico de un compuesto estructural natural. Está compuesto por plaquetas frágiles de aragonita (95 % en volumen) y delgadas capas de biopolímeros (5 % en volumen), organizadas en una microestructura tipo “bloque y capa adhesiva” (brick-and-mortar).

Además de la estructura básica tipo “bloque y capa adhesiva”, se han identificado estructuras más complejas que contribuyen significativamente a la tenacidad del nácar. Por ejemplo, en las capas de matriz orgánica se encuentran puentes minerales (Song et al. [130]), mientras que en las superficies superior e inferior de las tabletas se identifican islas minerales a escala nanométrica (Wang et al. [131]). También en algunas especies de nácar se observa ondulación de las tabletas e interbloqueo entre ellas.

Asimismo, en las plaquetas de aragonita del nácar, consideradas frágiles, se han identificado arquitecturas únicas de nanopartículas y biopolímeros, las cuales permiten una propagación de grietas ajustable dentro de las mismas, mejorando significativamente su tenacidad y resistencia (Huang y Li [132], Li et al. [133]). Tanto la estructura básica de “bloque y capa adhesiva” como las detalladas estructuras sub-

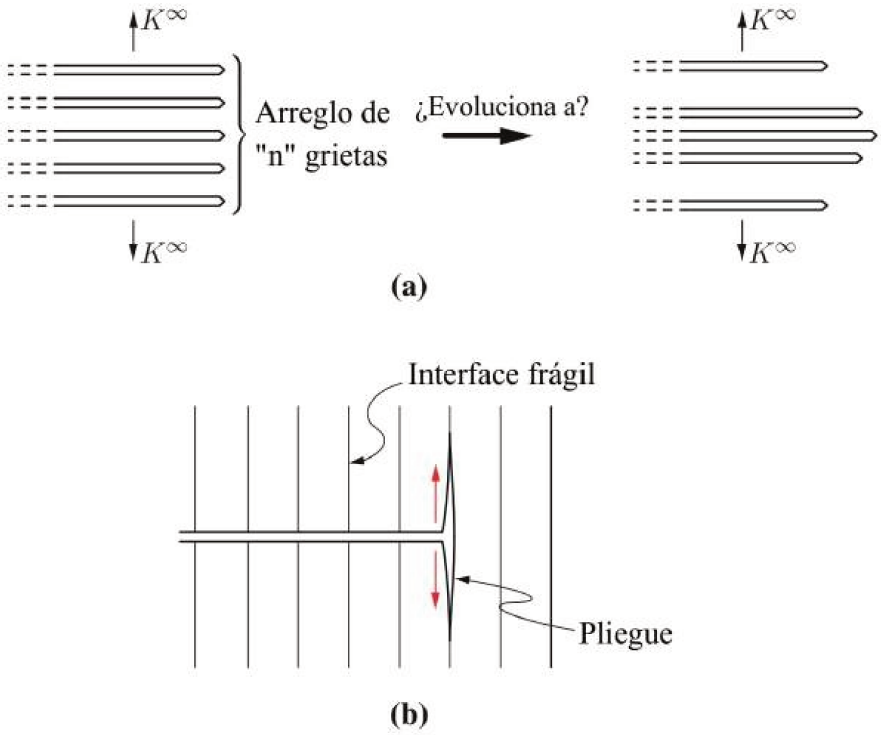

Figura 4.1: Representación esquemática de los posibles mecanismos de aumento de tenacidad: a) Multiplicación de grietas; b) Desviación de grietas en sólidos laminados a lo largo de una interface frágil.

yacentes mencionadas anteriormente, influyen en las interacciones entre los materiales duros y blandos, que son la clave para las excelentes propiedades mecánicas del nácar.

A pesar de las propiedades mecánicas relativamente limitadas de sus constituyentes, estos biomateriales estructurales exhiben un notable nivel de tenacidad macroscópica, como se expresó anteriormente y se han propuesto posibles explicaciones para ello.

Se han identificado varios mecanismos de incremento de tenacidad, como el puenteo de grietas, el redondeo de grietas, la disminución de la concentración de tensiones en la punta de grieta mediante la nucleación de microcavidades, el papel de las propiedades mecánicas de la proteína en la disipación de la energía de fractura (Smith et al. [134]), la rugosidad en la interface proteína-mineral (Wang et al. [131]), el extremo desajuste del módulo elástico, lo cual origina una gran disparidad en la rigidez entre los componentes (Murali et al. [135]) y la deflexión de grietas a lo largo de interfaces viscoplásticas (Jackson et al. [136], [137], Gao et al. [83], Espinosa et al. [138]).

4.3. Comportamiento mecánico de los diseños bioinspirados

La respuesta mecánica de los diseños bioinspirados se fundamenta en un proceso dividido en etapas (Liu et al. [139]), donde las interfaces horizontales y verticales juegan un papel esencial, ya que el momento de activación de dichas interfaces define en gran medida, las distintas etapas de la respuesta mecánica de las diversas configuraciones tipo nácar.

Es fundamental destacar que las plateletas que conforman la fase rígida en los diseños bioinspirados también pueden romperse debido a la propagación de grietas, lo cual es altamente relevante con vista al modelo numérico. Esto se debe a que nuestra metodología numérica captura este mecanismo mediante la implementación del modelo de campo de fase en las plateletas.

Por lo tanto, se establece un escenario donde existe el juego entre la rotura de las plateletas de la

fase rígida del material, lo cual sería equivalente a un mecanismo de penetración como se mencionó en el capítulo III contra el desvío de la grieta a lo largo de las interfaces de la fase blanda del material, análogo a un mecanismo de deflexión. Ambos mecanismos desempeñan también un papel fundamental en el comportamiento de los diseños bioinspirados.

Esta respuesta teórica se ilustra en la figura 4.2, donde en la etapa I del proceso de deformación, se activan las interfaces horizontales, lo que corresponde al punto A en la curva teórica tensión-deformación. Este punto representa el primer pico de la curva global asociada a una tensión σ_I, la cual define la resistencia de las interfaces horizontales y marca el inicio de la evolución del daño en las mismas.

Posteriormente, se tiene la etapa II, en la cual se activan las interfaces verticales y aquellas con cierto grado de inclinación dentro de la configuración respectiva, lo que genera un segundo pico en la curva teórica tensión-deformación, identificado con el punto B. En este punto, la tensión σ_{II} refleja la resistencia de las interfaces verticales y casi verticales. Asismismo, en esta etapa se visualiza en la interface un modo de apertura de fractura tipo deslizamiento.

Finalmente, el proceso global concluye con la falla total de la muestra, representada por el punto C en la curva teórica tensión-deformación. Cabe destacar que en las tres configuraciones geométricas (Flat Table, Interlocking y Non-Interlocking) simuladas se logró reproducir satisfactoriamente el comportamiento previamente descrito.

Esto demuestra la precisión, efectividad y utilidad de la metodología numérica combinada de campo de fase y superficie cohesiva para capturar la respuesta mecánica de estos diseños bioinspirados. Además, esta metodología numérica abre nuevas oportunidades para optimizar su diseño, especialmente en el contexto de su fabricación mediante tecnologías avanzadas como la manufactura aditiva.

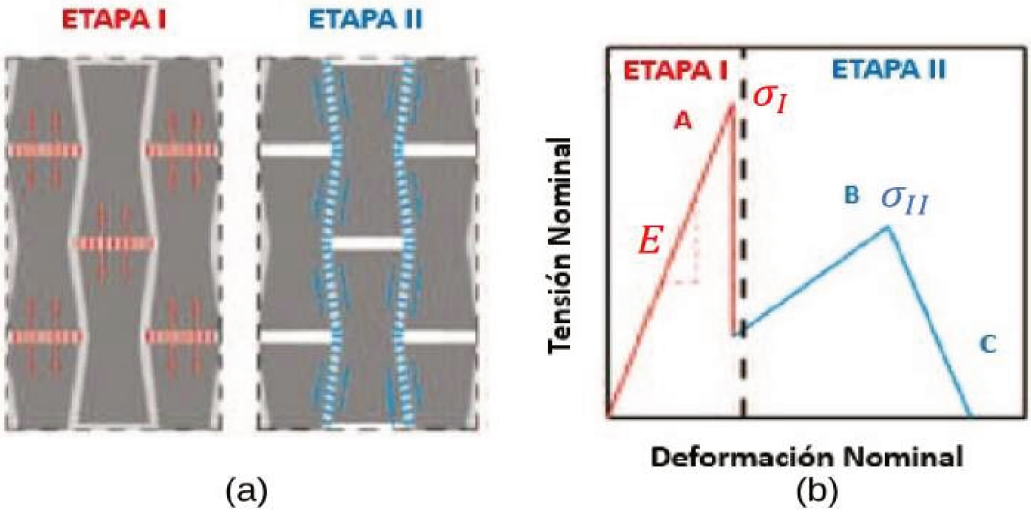

Figura 4.2: (a) Deformación teórica por etapas de las interfaces, (b) Curva teórica tensión-deformación dividida por etapas de deformación

En consecuencia, la respuesta numérica obtenida mediante nuestra metodología combinada se muestra en la figura 4.3, donde se presentan las curvas Fuerza vs Desplazamiento, para cada una de las configuraciones evaluadas. En estas curvas se evidencia claramente el comportamiento mecánico previamente descrito, en concordancia con la curva tensión-deformación teórica planteada en la literatura (Liu et al. [139]).

En la respuesta numérica obtenida, es importante mencionar que dentro de nuestra metodología implementada, el modelo cohesivo por el cual se simuló las interfaces tanto horizontales como verticales y casi verticales de las diferentes configuraciones geométricas testeadas, no degrada bajo estados de compresión debido a diversas razones. Primeramente el modelo cohesivo esta diseñado para degradar la rígidez del material cuando hay separación (apertura de grietas), que es característica de los estados de

tracción.

Por otro lado, bajo el contexto del efecto de cierre de grietas, si existe una grieta previa que estaba abierta, al aplicar compresión las caras de la grieta tienden a cerrarse. El modelo cohesivo generalmente considera que al cerrarse la grieta, no hay más degradación de la resistencia del material. Otro motivo es debido a que nuestro modelo incorpora la división de tracción-compresión para asegurar que solo se degrade bajo tracción y no bajo compresión, evitando así patrones de propagación de grietas no físicos en estados de carga compresiva.

Con respecto al escenario de corte, nuestro modelo descompone las tracciones en sus componentes normales y tangenciales, estableciendo tensiones críticas tanto en las interfaces horizontales como las verticales y casi verticales en las diversas configuraciones geométricas simuladas. Por ende, la componente de la tracción normal maneja la apertura en modo I de las interfaces horizontales, mientras que la componente tangencial regula el deslizamiento a lo largo de las interfaces verticales y casi verticales. Esto permite simular grietas que se deslizan sin abrirse por completo, lo que es común en materiales bajo tensiones cortantes.

Por lo tanto, la configuración entrelazada (Interlocking), representada por la curva verde en el gráfico de la figura 4.3, es la que exhibe la mayor rigidez y resistencia en las interfaces horizontales en comparación con las demás configuraciones. Esta respuesta se atribuye al aumento en la longitud de las interfaces casi verticales y su conexión con las horizontales, lo que genera un efecto de entrelazamiento cuando el ángulo es menor a $0°$.

Este efecto inhibe la propagación de la grieta alrededor de dichas interconexiones, cuando las plaquetas minerales se deslizan entre sí. Por lo tanto, esta configuración entrelazada disipa una mayor cantidad de energía en comparación con las otras dos configuraciones evaluadas, lo que se traduce en un incremento significativo de la tenacidad estructural de este diseño.

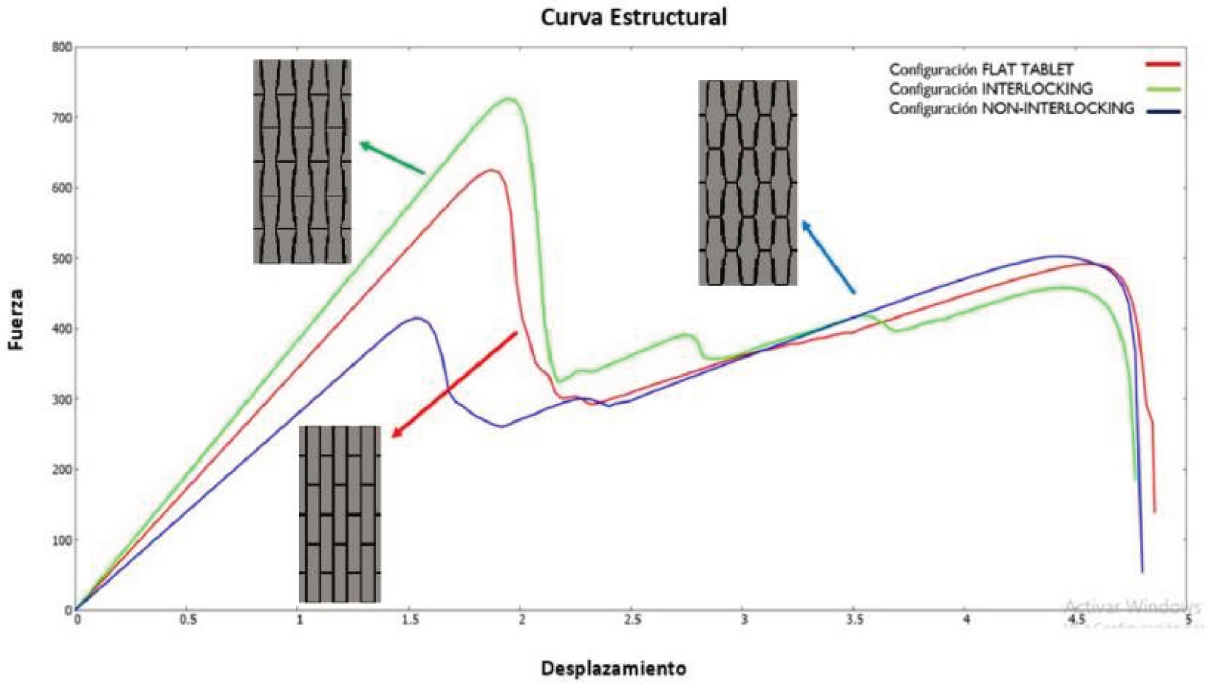

Figura 4.3: Respuesta numérica de las configuraciones Tableta Plana (Flat Table), Entrelazada (Interlocking) y No Entrelazada (Non-Interlocking)

4.4. Modelado numérico de los diseños bioinspirados mediante el enfoque combinado de campo de fase y superficie cohesiva

Las ideas fundamentales del trabajo anexado en el Apéndice C, se centran en capturar tanto el comportamiento mecánico de diversas configuraciones geométricas inspiradas en la estructura tipo “bloque y capa adhesiva” (brick-and-mortar) del nácar, como los mecanismos responsables del incremento de la tenacidad en dichas configuraciones. Bajo esta premisa, se llevó a cabo un modelado numérico para los diseños bioinspirados, utilizando el enfoque numérico combinado presentado en el Capítulo III.

Dado que en la literatura existen pocos trabajos que utilicen una metodología numérica de este tipo para analizar la respuesta mecánica de los diseños bioinspirados. Se considera que este estudio introduce una contribución a esta área de investigación.

Dicha metodología numérica combinada, que integra el modelo de campo de fase y el modelo de superficie cohesiva, se aplicó a tres tipos de configuraciones geométricas que imitan a la estructura del nácar, las cuales se denominan: Tableta Plana (“Flat Table”), Entrelazada (“Interlocking”) y No Entrelazada (“Non-Interlocking”).

Estas configuraciones están compuestas por dos fases materiales, una fase rígida, representada por las plaquetas minerales, la cual fue simulada mediante el modelo de campo de fase y una fase blanda correspondiente a las interfaces horizontales, verticales y casi verticales compuestas de proteínas, modeladas bajo el enfoque de superficie cohesiva. Una representación del biocompuesto (nácar), y su esquema geométrico se ilustran en la figura 4.4

Cabe destacar que las tres configuraciones mencionadas anteriormente, se construyen a partir de una celda unitaria, en la cual se consideran diversos parámetros clave para la respuesta mecánica de los diseños bioinspirados, incidiendo en el desempeño de la fractura con una combinación inusual de resistencia y tenacidad. Estos parámetros son denominados: la fracción de volumen de la fase rígida, la relación de aspecto de la tableta mineral y el ángulo de ondulación de dicha tableta, el cual produce el efecto de entrelazamiento característico de estas celdas unitarias, las cuales se esquematizan en el figura 4.5.

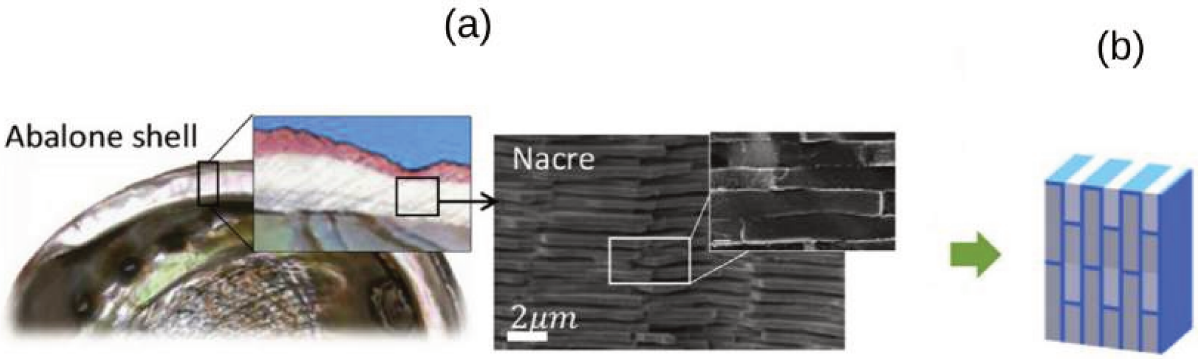

Figura 4.4: Estructura del nácar. (a) Microestructura tipo “bloque y capa adhesiva” (brick-and-mortar) en la capa nacarada de una concha de abalón, (b) Diseño de la microestructura biomimética del nácar.

Por consiguiente, la primera estructura compuesta de la figura 4.5 similar al nácar con tabletas planas, posee un ángulo de ondulación de $0°$, es decir, las fases blandas del material representadas por las interfaces horizontales son perpendiculares a la distribución de las interfaces verticales. Las otras dos estructuras (Fig. 4.5 b,c), muestran ángulos de ondulación de tabletas negativos y positivos respectivamente, lo cual hace que sean denominadas como compuestos entrelazados y no entrelazados.

Dicho efecto de entrelazamiento influye directamente en el aumento de la tenacidad estructural de estos diseños bioinspirados. Para más detalles con respecto a las propiedades mecánicas empleadas y la metodología de mallado de la geométria, remitirse al Apéndice C.

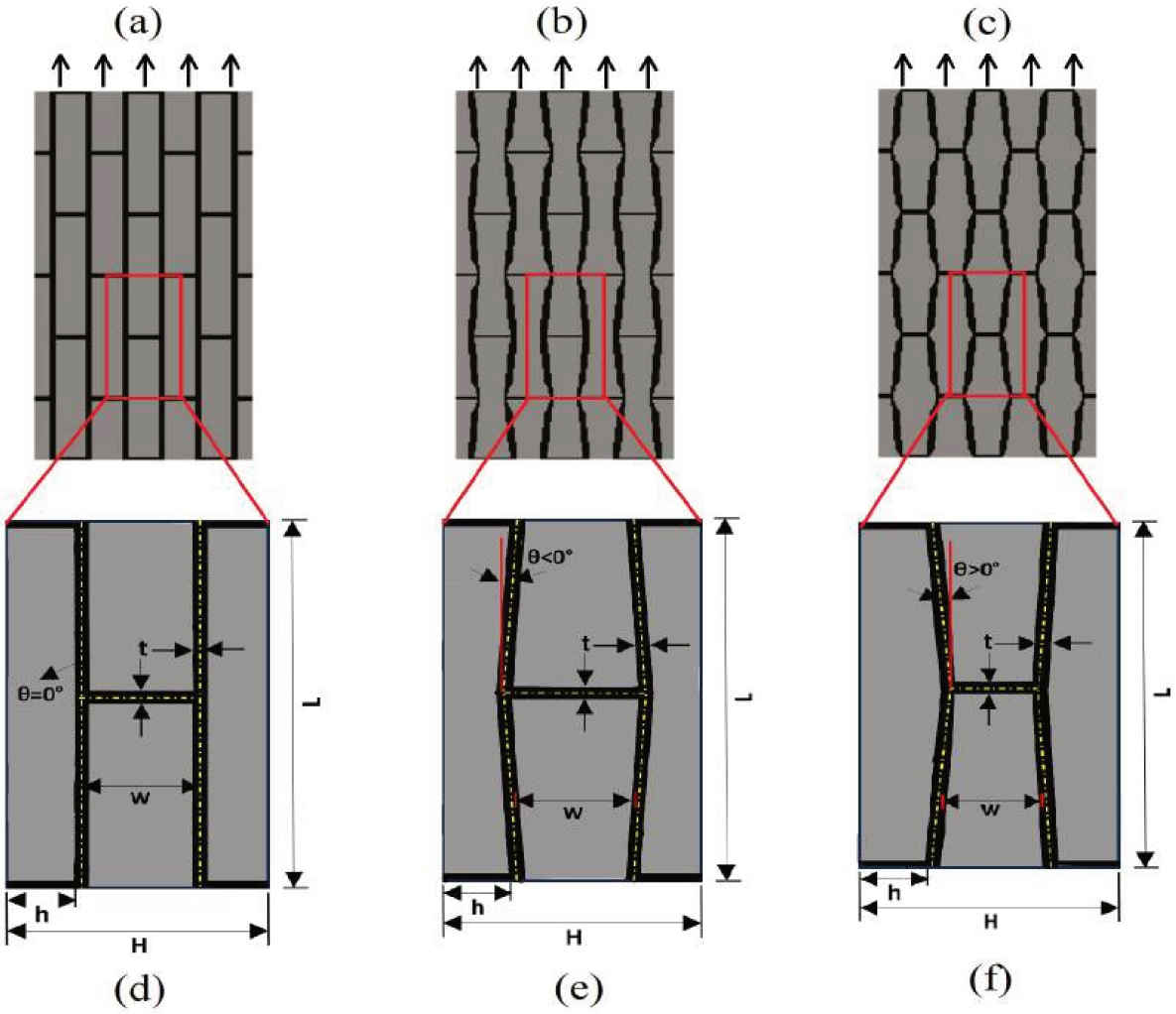

Figura 4.5: (a) Configuración geométrica Tableta Plana (Flat Table), (b) Configuración geométrica Entrelazada (Interlocking), (c) Configuración geométrica No Entrelazada (Non-Interlocking), (d-f) Parámetros geométricos (H, h, L, w, t en mm y θ en grados) de celdas unitarias para las configuraciones Tableta plana, Entrelazada y No Entrelazada para la estructura tipo nácar.

4.5. El rol de la deflexión y penetración de grietas en los diseños bioinspirados

Particularmente, se conoce que un mecanismo que resulta ser destacable para el aumento de la tenacidad se refiere a la deflexión de las grietas, siguiendo las interfaces de las placas minerales, evitando que la grieta penetre las mismas. Una serie de estudios se han desarrollado para la mejor comprensión de este mecanismo, He y Hutchinson [140] utilizaron métodos de ecuaciones integrales y asumiendo materiales linealmente elásticos e isotrópicos en ambos lados de la interface, estimaron el rango de tenacidad de la interface, G_i, en relación con la tenacidad del material del medio en el lado sin grietas del sustrato, G_s, lo que probablemente resulta en la desviación de las grietas hacia la interface en lugar de penetrarla.

El análisis de He y Hutchinson [140] se basa en un criterio puramente energético e incluye casos de materiales frágiles disímiles en ambos lados de la interface, así como diferentes ángulos de incidencia entre la grieta en propagación e interface. Una técnica analítica similar fue utilizada por Martinez y Gupta [141] para investigar el problema de desviación de grietas hacia una interface que une dos materiales elásticos ortotrópicos. Martinez y Gupta [141] señalan que, a diferencia de los criterios basados en resistencia, el criterio de tasa de liberación de energía adoptado para predecir interacciones es muy sensible a

los valores de los parámetros del material.

Por otra parte, es importante mencionar el trabajo de Ji y Gao [86] en el cual se sugiere una relación de aspecto óptima de la plaqueta mineral. Suponiendo que la resistencia del mineral obedece al criterio de Griffith, se obtuvo la siguiente estimación para la relación de aspecto óptima ρ^*:

$$\rho^* = \frac{\sigma_m^f}{\tau_p^f} = \frac{1}{\tau_p^f}\sqrt{\frac{\alpha^2 \gamma E_m}{h}}\,, \tag{4.1}$$

donde σ_m^f es la resistencia a fractura de la plaqueta mineral, τ_p^f es la resistencia a fractura en corte de la proteína, γ es la energía superficial, E_m es el modulo de Young de la plaqueta mineral, α es un parámetro que depende de la geometría de la grieta y h es el espesor de la plaqueta mineral.

La ecuación 4.1 muestra que la relación de aspecto óptima de las plaquetas minerales es inversamente proporcional a la raíz cuadrada del espesor del mineral. Por ende, cuanto más pequeñas son las plaquetas, mayor es la relación de aspecto óptima. Los cristales minerales en el hueso tienen un espesor del orden de unos pocos nanómetros y una relación de aspecto de 30–40, mientras que los del nácar tienen un espesor del orden de unos cientos de nanómetros y una relación de aspecto alrededor de 10, lo que corresponde aproximadamente con la ley de escalamiento predicha por la ecuación 4.1.

Esto explicaría, desde una perspectiva diferente, por qué es importante que el tamaño de las plaquetas minerales se elija a escala nanométrica: los cristales minerales con alta resistencia y tolerancia a defectos son fundamentales para mantener una tensión efectiva significativa en la proteína, la cual, junto con la gran deformación por corte dentro de la proteína y a lo largo de la interface proteína-mineral, proporciona una alta energía de fractura.

En base a las ideas previamente expuestas, llevamos a cabo una evaluación exhaustiva de los mecanismos de deflexión y penetración, centrándonos específicamente en la configuración Tableta Plana (Flat Table). Este análisis se realizó en un espacio definido por la relación entre las energías de fractura de la fase rígida y la fase blanda de material (G_{fr}/G_{fb}), en función de la relación entre las tensiones críticas de ambas fases materiales $(\sigma_{fr}^c/\sigma_{fb}^c)$. Como resultado, se obtuvieron curvas de deflexión y penetración siguiendo el mismo esquema presentado en el capitulo III, (ver resultados en el Apéndice C).

En estas curvas se identifica una zona de transición en la que ambos mecanismos (deflexión-penetración) compiten por prevalecer. En consecuencia, se evidencia que las configuraciones basadas en estructuras tipo nácar, también satisfacen un criterio mixto que integra tanto la resistencia como la tenacidad de las distintas fases materiales presentes en dichas configuraciones.

Por otro lado, como se valida en el gráfico de la figura 4.3, el mecanismo de deflexión de grietas es uno de los principales responsables del incremento de la tenacidad estructural en los diseños bioinspirados, ya que cuando las grietas se desvian por las interfaces (fase blanda del material), el proceso de delaminación que ocurre durante la fractura de la muestra genera una mayor disipación de energía.

Por otra parte, como idea complementaria es relevante destacar que el estudio detallado de los efectos de la variación de las propiedades de las interfaces, tanto horizontales como verticales, en las estructuras escalonadas del nácar resulta muy interesante (Singh et al. [142]), con vista al desarrollo de trabajos futuros en esta misma línea de investigación.

Los efectos relacionados con la resistencia al desprendimiento de la interface, el comportamiento de la energía de fractura y la relación de aspecto de las interfaces, pueden influir de manera significativa en el comportamiento mecánico global de las estructuras bioinspiradas. En particular, la evaluación de interfaces, ya sean débiles, fuertes o intermedias, revela diferencias distintivas en su respuesta tensión-deformación.

Por ejemplo, las interfaces débiles pueden mostrar un comportamiento de endurecimiento por deformación, sin un desprendimiento distribuido de la interface vertical en las etapas iniciales de carga. Sin embargo, el desprendimiento localizado de la interface vertical, seguido por el desprendimiento de la

interface horizontal, conduce a la falla final.

Por otro lado, las interfaces fuertes exhiben una combinación de comportamientos de ablandamiento y endurecimiento por deformación. En este caso, los mecanismos principales de falla serían la fractura de las plaquetas minerales y la fractura distribuida en la matriz de proteína en las interfaces verticales, seguida de una deslocalización del daño.

Finalmente las interfaces intermedias presentan un comportamiento de ablandamiento por deformación con un régimen extendido de endurecimiento. La falla final se originaría a través de la fractura de las plaquetas minerales y de la matriz de proteínas, acompañada de una deslocalización significativa del daño debido al desprendimiento disperso de las interfaces verticales.

4.6. Conclusiones

En este capítulo se demuestra que una metodología numérica combinada conformada por el modelo de campo de fase y el modelo de superficie cohesiva, es capaz de reproducir de manera eficiente el comportamiento mecánico de los diseños bioinspirados basados en la estructura del nácar. Este enfoque constituye una contribución significativa al establecer una alternativa numérica con diferencias clave en su implementación en comparación con las técnicas utilizadas en la literatura reciente.

Esta herramienta resulta especialmente útil para estudiar los diferentes mecanismos que contribuyen al incremento de la tenacidad estructural de los diseños bioinspirados. Se demuestra que, mediante la modificación de los parámetros geométricos, en particular el ángulo de ondulación entre las interfaces horizontales y verticales en la configuración entrelazada (Interlocking), desempeña un papel importante en el aumento de la tenacidad estructural, como se observa en su respuesta mecánica.

Por otro lado, se demuestra que los diseños bioinspirados cumplen de manera satisfactoria con un criterio mixto que combina la resistencia y tenacidad de los materiales que los componen, validando el comportamiento discutido en el capítulo III respecto a las curvas de deflexión y penetración. Algunos posibles estudios futuros que podrían resultar de interés, en esta misma línea de investigación y que no fueron abarcados en esta tesis incluyen:

- Realizar un estudio parámetrico con todos los indicadores geométricos asociados a la celda unitaria, que conforman las diferentes configuraciones de los diseños bioinspirados, con el propósito de identificar la combinación óptima que maximice la tenacidad estructural de estos diseños.

- Implementar la optimización topológica basada en un modelo de campo de fase para mejorar la resistencia a la fractura de los diseños bioinspirados.

- Analizar el rol que juega el desajuste del módulo elástico en el aumento de la tenacidad estructural de los compuestos bioinspirados, ya que la variación espacial de dicho módulo es un mecanismo relevante para mejorar la tenacidad de los biocompuestos, desempeñando un papel clave tanto en la detención como en el desvío de grietas.

- Estudiar la composición, estructura y propiedades mecánicas de un conjunto de interfaces biológicas representativas en el nácar, con el propósito de comprender las características mecánicas inusuales que poseen estas interfaces, que pueden fomentar al desarrollo de compuestos bioinspirados avanzados que exhiban una significativa disipación de energía en comparación con los compuestos convencionales.

- Estudiar los modelos mecánicos de interfaces en compuestos biológicos naturales (modelo de Gurtin-Murdoch y modelo de cadena tensión-corte), para investigar los mecanismos de influencia que ejercen diversos parámetros mecánicos sobre las propiedades de amortiguamiento en la arquitectura escalonada del nácar.

- Implementar un modelo numérico viscoelástico para la interface de material blando (Proteína), presente en los compuestos bioinspirados con estructuras escalonadas, tomando en cuenta todas las propiedades mecánicas y de amortiguación que juegan un papel fundamental en dicho modelo.

Capítulo 5

Estrategias de control y resolución para problemas de fractura frágil

5.1. Introducción

El propósito de este capítulo es motivar el trabajo realizado y anexado en el Apéndice D, el cual se orienta a la implementación de una técnica de control de longitud de arco para resolver problemas de fractura frágil, utilizando el modelo de campo de fase y un esquema escalonado. Básicamente, el objetivo principal a través de esta técnica es el trazo eficiente de curvas de equilibrio completas. Dicho objetivo se lleva a cabo aplicando una ecuación de control a los grados de libertad de desplazamiento en la etapa mecánica de resolución del problema, lo cual ofrece una mejora sobre estrategias de longitud de arco presentes en la literatura, que se centran en controlar los grados de libertad de daño en la etapa de solución del problema de campo de fase. Los resultados logrados a partir de lo que aquí se expone fueron publicados por Zambrano et al. [14]

Para ello se inicia este capítulo exponiendo en la sección 5.2 diversos enfoques de longitud de arco que se han utilizado en la literatura, para controlar el avance de grietas bajo ciertas restricciones, incluyendo una descripción del funcionamiento de nuestra estrategia propuesta. Luego, en la sección 5.3 presenta los principales aportes de nuestra estrategia alternativa en comparación con otros enfoques similares. Seguidamente, la sección 5.4 se evalúa el rendimiento tanto numérico como computacional de la estrategia de longitud de arco propuesta. Finalmente, en la sección 5.5 se establecen las conclusiones correspondientes a este capítulo.

5.2. Una metodología alternativa de control de longitud de arco para trazar curvas de equilibrio completas

Una dificultad importante en el modelado de problemas de fractura cuasi-frágil es la aparición de puntos límite y retrocesos en la trayectoria de la curva de equilibrio estructural. Este comportamiento exige desarrollar e implementar estrategias de control de avance de grietas que permitan abordar eficientemente los problemas asociados al crecimiento inestable de las mismas.

Se debe mencionar que el método de minimización alternada (AM, por sus siglas en inglés), es un procedimiento robusto de solución escalonada, reportado por Bourdin et al. [143] y seguido por Miehe et al. [57], en el cual en su primera etapa se resuelve la ecuación estándar de balance de fuerzas con la variable de campo de fase fija. Posteriormente, en su segunda etapa se resuelve la ecuación de balance de microfuerzas con los desplazamientos fijos. Por ende, este esquema escalonado básicamente resuelve dos sub-problemas convexos secuenciales, posee buenas propiedades de convergencia y es muy utilizado para la resolución de problemas de fractura frágil empleando el modelo de campo de fase.

Por consiguiente, se han implementado diferentes técnicas de control en el contexto de este problema, que se encuentran basadas en procedimientos para controlar los incrementos de desplazamientos. Por ejemplo, en el trabajo de Duda et al. [54] se reportó un enfoque de este estilo, en la etapa mecánica, es decir en la solución de la ecuación estándar de balance de fuerzas utilizando un método de minimización alternada (AM), en un problema de fractura frágil empleando el modelo de campo de fase. Donde la magnitud controlada es el incremento relativo de desplazamiento entre los dos nodos opuestos a la punta de la grieta. Así, a medida que la grieta se propaga los nodos de control se redefinen para seguir la punta de la grieta.

Por otro lado, Wu [144] propuso una estrategia de longitud de arco empleando también una metodología AM, la cual esta basada en regular los desplazamientos convencionales de apertura de la boca de la grieta (CMOD, por sus siglas en inglés) y los desplazamientos deslizantes de la boca de la grieta (CMSD, por sus siglas en inglés) en muestras pre-agrietadas que experimentan fractura.

No obstante, en un contexto general de problemas de propagación de grietas ambas metodologías mencionadas previamente son inadecuadas. Ya que en el primer caso (Duda et al. [54]), no es posible conocer de antemano la trayectoria de propagación de la grieta y por lo tanto, los nodos a controlar son desconocidos del problema. Para el segundo caso (Wu [144]), las magnitudes CMOD y CMSD no son necesariamente variables monótonamente crecientes durante el proceso de carga, por ende, se convierten en variables poco practicas para ser controladas mediante una estrategia de longitud de arco.

Por tal motivo, en nuestro trabajo anexado en el Apéndice D, se propone una metodología alternativa de control de carga, para la solución de la ecuación estándar de balance de fuerzas empleando una metodología AM o procedimiento de tipo escalonado, tomado del trabajo de Bourdin et al. [143]. En la etapa mecánica del esquema escalonado se resuelve dicha ecuación de balance de fuerzas, la cual se expresa a continuación:

$$\boldsymbol{g}\big(\boldsymbol{u}(s_{n+1}), \boldsymbol{\varphi}_n, \lambda(s_{n+1})\big) = \boldsymbol{0} \ , \tag{5.1}$$

donde $\boldsymbol{u}(s_{n+1})$ son los desplazamientos en el paso $n+1$, $\boldsymbol{\varphi}_n$ es la campo de fase en el paso n, el cual se mantiene fijo y $\lambda(s_{n+1})$ es la magnitud de carga externa en el paso $n+1$, donde $\boldsymbol{u}$ y λ dependen del parámetro de longitud de arco s_{n+1} en el paso $n+1$. En esta misma etapa mecánica se tiene la ecuación de control r, la cual se expresa de la siguiente forma:

$$r\big(\boldsymbol{u}(s_{n+1}), \lambda(s_{n+1}), s_{n+1}\big) = 0 \ , \tag{5.2}$$

la cual depende de los desplazamientos, la magnitud de carga externa y del parámetro de longitud de arco s_{n+1} en el paso $n+1$, que es equivalente al cálculo de la fuerza impulsora de avance de la grieta.

Luego, en la etapa de daño se tiene la ecuación de balance de microfuerzas del campo de fase, la cual se expresa a continuación:

$$\boldsymbol{\jmath}\big(\boldsymbol{u}_n, \boldsymbol{\varphi}(s_{n+1}), \lambda(s_{n+1})\big) = \boldsymbol{0} \quad ; \quad (1 \geq \varphi_j(s_{n+1}) \geq \varphi_j(s_n) \ , \ \forall j) \ , \tag{5.3}$$

la misma se resuelve con los desplazamientos $\boldsymbol{u}(s_{n+1})$ de la etapa mecánica y se obtiene el campo de fase actualizado $\boldsymbol{\varphi}_{n+1}$

Nuestra estrategia de control gobierna los incrementos de desplazamientos en la resolución del problema mecánico, manteniendo la variable de daño fija. Por ende, esta estrategia de control no puede basarse en manejar la magnitud de la disipación de energía del paso, porque la misma es nula mientras se resuelve el problema mecánico.

En su lugar, nuestra estrategia controla el incremento de la fuerza impulsora que aparece en la ecua-

ción de balance de microfuerzas del campo de fase. Esto representa una diferencia clave con respecto a otras técnicas de control de longitud de arco planteadas, como por ejemplo la reportada en el trabajo de Singh et al. [145].

El modelo de campo de fase empleado en esta estrategia alternativa de longitud de arco es el mismo que fue presentado en el capítulo II y como se mencionó previamente la resolución del sistema de ecuaciones discreto, se llevo a cabo utilizando un procedimiento escalonado para este caso de foma explícita. Se puede observar un representación esquematica de la estrategia propuesta en la figura 5.1, para más detalles correspondientes a la misma se pueden visualizar en el Apéndice D.

5.3. Aportes de la estrategia propuesta de longitud de arco con respecto a otras técnicas implementadas

Un conjunto de trabajos previos (Bharali et al. [146], Börjesson et al. [147], Singh et al. [145]), han empleado un procedimiento de longitud de arco, utilizando una ecuación de control que limita los incrementos de la variable de campo de fase. Particularmente, en el trabajo de Singh et al. [145] al igual que en nuestro estudio se implementó una técnica de longitud de arco empleando un esquema escalonado, con ciertas diferencias con respecto a nuestra estrategia, la cual presenta ciertas ventajas que serán expuestas a continuación.

Si partimos de dos estrategias las cuales emplean un procedimiento de longitud de arco combinado con un esquema escalonado, en las cuales se tiene una ecuación de control escalar descrita como $r = 0$, donde r representa la función de control, que se define de la siguiente forma:

$$r\big(\boldsymbol{u}(s_{n+1}), \lambda(s_{n+1}), s_{n+1}\big) = 0 \ , \tag{5.4}$$

el argumento de dicha función depende del desplazamiento $\boldsymbol{u}(s_{n+1})$, del factor de carga $\lambda(s_{n+1})$, que estan reinterpretados como funciones implícitas del parámetro de longitud de arco s_{n+1}.

Se tiene que en la estrategia de Singh et al. [145], se realiza un procedimiento de control de carga que está basado en prescribir el incremento del área de la superficie de fractura, a través de la ecuación $r_{dam} = 0$ y para este caso se resuelve el siguiente sistema en la etapa de campo de fase:

$$\boldsymbol{\jmath}\big(\boldsymbol{u}_n, \boldsymbol{\varphi}(s_{n+1}), \lambda(s_{n+1})\big) = \boldsymbol{0} \quad ; \quad (1 \geq \varphi_j(s_{n+1}) \geq \varphi_j(s_n) \ , \ \forall j) \ , \tag{5.5}$$

$$r_{dam}\big(\boldsymbol{\varphi}(s_{n+1}), \lambda(s_{n+1}), s_{n+1}\big) = 0 \ , \tag{5.6}$$

donde la ecuación 5.5 es el balance de microfuerzas que depende de las variables de desplazamiento $\boldsymbol{u}_n$ la cual se mantiene fija, el campo de fase $\boldsymbol{\varphi}(s_{n+1})$, y el factor de carga $\lambda(s_{n+1})$, donde las últimas dos variables son funciones implícitas del parámetro de longitud de arco s_{n+1}. Dicho balance de microfuerzas viene acompañado con las respectivas condiciones de complementariedad para el campo de fase. Luego la ecuacion 5.6 representa la función de control, la cual depende del campo de fase $\boldsymbol{\varphi}(s_{n+1})$, y el factor de carga $\lambda(s_{n+1})$, que a su vez son funciones implícitas del parámetro de longitud de arco s_{n+1}.

Para este caso el esquema escalonado sigue resolviendo la ecuación discreta del balance de fuerza para encontrar $\boldsymbol{u}_{n+1}$. Por lo tanto, según esta estrategia se infiere que no existe una relación explícita entre $\boldsymbol{u}_{n+1}$ y s_{n+1} en cada paso. Sin embargo, en nuestra estrategia alternativa se realiza un procedimiento de control de carga, prescribiendo el incremento de la variable histórica mediante la ecuación de control $r_{mech} = 0$, por lo tanto las ecuaciones que se resuelven en la etapa mecánica son las siguientes:

$$\boldsymbol{g}\big(\boldsymbol{u}(s_{n+1}), \boldsymbol{\varphi}_n, \lambda(s_{n+1})\big) = \boldsymbol{0} \ , \tag{5.7}$$

$$r_{mech}\big(\boldsymbol{u}(s_{n+1}), \lambda(s_{n+1}), s_{n+1}\big) = 0 \ , \tag{5.8}$$

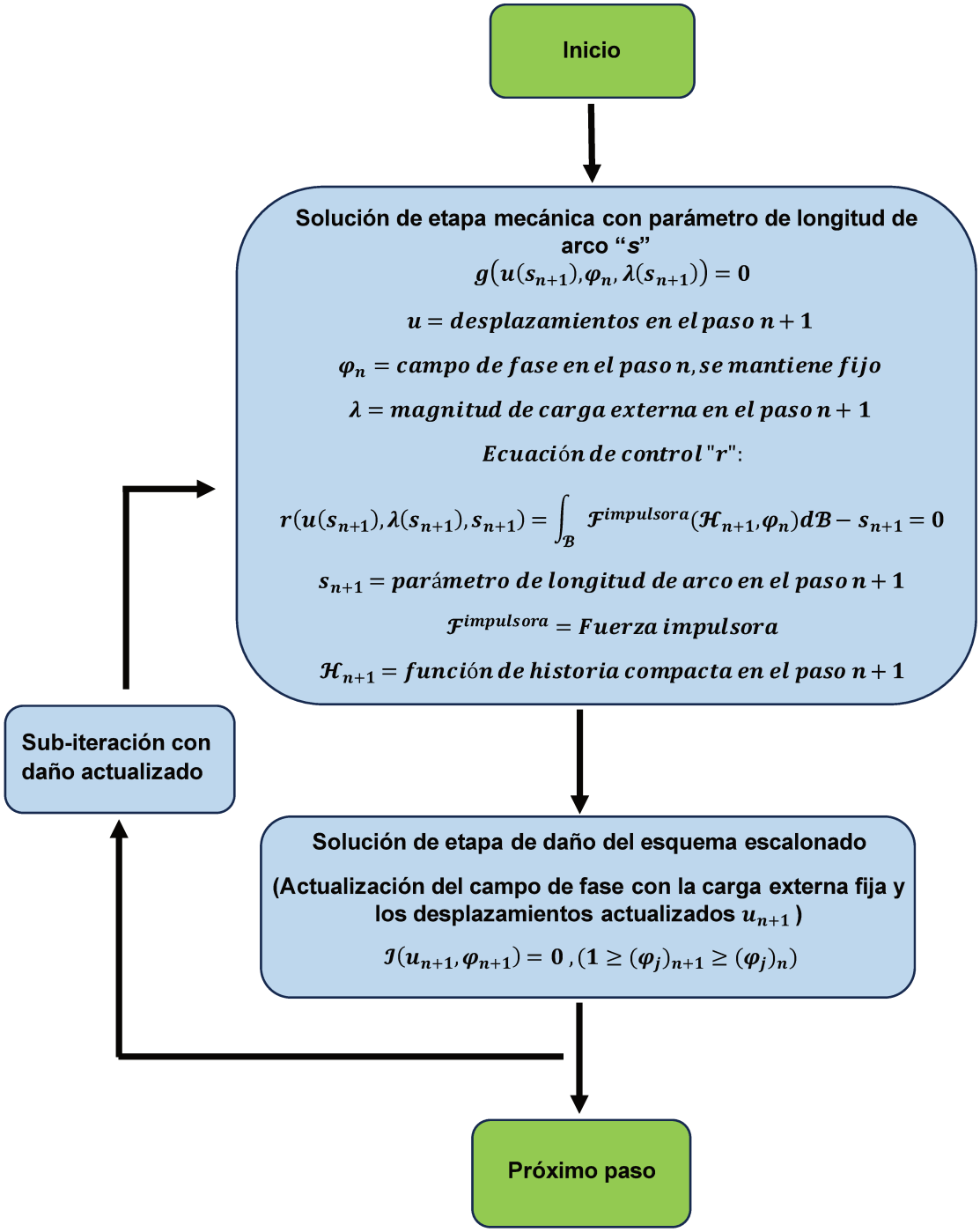

Figura 5.1: Representación esquemática de la estrategia de longitud de arco propuesta con un esquema escalonado explícito.

donde la ecuación 5.7 representa el balance de fuerzas el cual depende del desplazamiento $\boldsymbol{u}(s_{n+1})$, el campo de fase $\boldsymbol{\varphi}_n$ que en este caso se mantiene fijo y el factor de carga $\lambda(s_{n+1})$. Donde tanto el desplazamiento como el factor de carga son funciones implícitas del parámetro de longitud de arco s_{n+1}. Seguidamente, la ecuación 5.8 es la función de control para la etapa mecánica, la cual depende del desplazamiento $\boldsymbol{u}(s_{n+1})$, el factor de carga $\lambda(s_{n+1})$, donde estas últimas son funciones implícitas del del parámetro de longitud de arco s_{n+1}

Por lo tanto, según lo expuesto anteriormente se observa una diferencia fundamental entre ambas estrategias, ya que el procedimiento de control ha sido aplicado en diferentes etapas del esquema escalonado, en el trabajo de Singh et al. [145] se realiza en la etapa de daño o campo de fase y en nuestra técnica se emplea en la etapa mecánica.

También ambas estrategias poseen importantes repercusiones en el contexto algoritmico al resolver ciertos tipos de problemas de campo de fase. Por ejemplo, las metodologías de campo de fase que resuelven la ecuación de balance de microfuerza empleando un problema de optimización con restricciones, pueden integrarse en nuestra estrategia alternativa de longitud de arco utilizando una ecuación de control como 5.4. Por otro lado, las metodologías de campo de fase que imponen restricciones de desigualdad en la ecuación de balance de microfuerza, empleando técnicas de penalización o multiplicadores de Lagrange tambien pueden integrarse de manera similar en nuestra técnica.

Esta integración se puede realizar porque en todas estas metodologías, la característica común aprovechada por nuestro procedimiento es que el incremento del término de fuerza motriz, $(\dot{\mathcal{F}}^{\text{driv}})$, que gobierna el incremento del daño, aunque sea diferente en cada metodología, puede controlarse estrechamente con la misma ecuación de control 5.4.

Por otra parte, cuando la estrategia de longitud de arco limita los incrementos del campo de fase en la ecuación de balance de microfuerzas, el problema de optimización con restricciones debe resolverse de forma monolítica en el espacio extendido de variables (φ, λ) combinado con la ecuación de control $r_{dam} = 0$. En este caso, el problema a resolver ya no puede verse como la condición de optimalidad de un problema de minimización en el espacio aumentado de variables. Por lo tanto, los algoritmos de optimización restringida convencionales son inaplicables.

Otra repercusión algorítmica está relacionada con problemas donde el mecanismo de daño, representado por medio de la variable de campo de fase, coexiste con otros mecanismos disipativos que producen inestabilidad y están vinculados con el desplazamiento $\boldsymbol{u}$, como por ejemplo, sucede en la plasticidad, interfaces cohesivas, etc. Para este escenario, la estrategia de longitud de arco debe gestionar el proceso de carga independientemente del mecanismo que induce la inestabilidad.

Es este contexto, se encuentra otro valor agregado de nuestra estrategia, ya que la misma permite controlar la competencia entre varios mecanismos que originan inestabilidad, a través de la extensión en la definición de la función de control, r_{mech}. No obstante, con la estrategia de longitud de arco reportada por Singh et al. [145] existen dificultades para incluir el control de los grados de libertad (DOFs, por sus siglas en inglés) que experimentan inestabilidad, al llevar a cabo la extensión de la definición de la función de control r_{dam}.

5.4. Evaluación del rendimiento numérico y computacional de la estrategia propuesta de longitud de arco con esquema escalonado

Nuestra estrategia de longitud de arco fue aplicada a 7 pruebas dentro del estudio realizado, las cuales se pueden observar a detalle en el Apéndice D. Bajo un contexto general, se tiene que utilizando un esquema escalonado con un enfoque explícito, en el cual primero se resuelve el problema mecánico (etapa mecánica), seguido del problema de campo de fase (etapa de daño). Se observó que la etapa mecánica de dicho esquema converge de manera satisfactoria a la tolerancia requerida en todos los pasos de solución, independientemente del parámetro $\Delta\hat{\varphi}^{opt}$ que fue testeado.

Donde este parámetro $\Delta\hat{\varphi}^{opt}$ es el incremento óptimo de daño deseado que se impone en las simula-

ciones, ya que nuestra estrategia ajusta el parámetro de longitud de arco s, para obtener incrementos de daño $(\Delta\varphi)$, lo más cercano posible a dicho parámetro $\Delta\hat{\varphi}^{opt}$.

El cumplimiento de esta condición significa que el error de integración se mantiene acotado. Y esta característica del algortimo se pudo visualizar en todos los casos que fueron estudiados, con un alto grado de precisión.

Por otro lado, nuestra estrategia de longitud de arco logra capturar de manera satisfactoria los diferentes retrocesos (snap-back) que ocurren en las curvas de equilibrio que fueron trazadas para cada uno de los casos analizados. También al comparar el comportamiento de la trayectoria de grietas obtenidas en el final del análisis de algunos casos testeados, se puede observar la similitud que poseen con resultados tanto experimentales como numéricos de otros trabajos de referencia.

La efectividad de la estrategia de control de longitud de arco propuesta, también fue evaluada adicionalmente resolviendo la etapa de daño del esquema escalonado mediante la metodología del Problema de Optimización con Restricciones de Frontera (BCOP, por sus siglas en inglés), la cual al ser comparada con nuestra metodologia para resolver el problema de campo de fase, que es un procedimiento estándar basado en la función de historia compacta, ambas soluciones para una cierta tolerancia $\Delta\hat{\varphi}^{opt}$ son practicamente indistinguibles puntualmente para el caso de una placa con muesca de doble borde (DENT, por sus siglas en inglés).

Por otra parte, bajo el mismo contexto de efectividad se tiene que nuestra estrategia de longitud de arco posee un buen desempeño en la gestión de problemas de fractura que experimentan distintos mecanismos de degradación, como la decohesión de la interface y la propagación de grietas fuera de la misma. Ambos mecanismos pueden desencadenar inestabilidades en el proceso de carga, los cuales fueron manejados satisfactoriamente con nuestro procedimiento de longitud de arco.

Por ende, bajo las ideas expresadas previamente se infiere que el rendimiento numérico de nuestra estrategia de longitud de arco es muy satisfactoria. En cuanto al rendimiento computacional se tiene que a través del testeo de algunos ejemplos representativos de la literatura como: una placa con un agujero excéntrico a tracción (EH, por sus siglas en inglés), una placa con muesca y agujero (NPWH, por sus sigles en inglés) y una prueba de una muestra sometida al corte con muesca en un solo borde (SENST, por sus siglas en inglés), los cuales se realizaron analizando tanto el incremento de campo de fase en cada paso del esquema escalonado, como también en el numero de iteraciones requeridas para la solución de la etapa mecánica en cada paso del esquema escalonado, ambos análisis se pueden apreciar a detalle en el Apéndice D.

Donde específicamente considerando la prueba tipo SENST, el cual es un ejemplo de referencia ampliamente utilizado para evaluar el rendimiento de variados algoritmos de campo de fase, se comparó el desempeño de nuestro enfoque con varios trabajos de la literatura, enfatizandose en aspectos como: el tipo de esquema utilizado para la resolución del problema, el numero de elementos o nodos en la malla, el numero de pasos empleados en el esquema de resolución del problema, el numéro de iteraciones promedio en la técnica de Newton-Raphson requeridas para resolver la etapa mecánica, la captura de los retrocesos en el trazo de la curva de equilibrio y finalmente los tiempo de CPU consumidos.

Por lo tanto, en base a todos los aspectos que fueron evaluados en el contexto del rendimiento computacional, se concluye que nuestra metodología implica un costo computacional moderado y proporciona soluciones precisas que exhiben satisfactoriamente comportamientos de retrocesos en el trazo de las curvas de equilibrio, incluso utilizando una tolerancia del daño significativa.

5.5. Conclusiones

En este capítulo se demuestra el buen desempeño de un procedimiento de longitud de arco alternativo a los enfoques tradicionales, en el cual bajo un esquema escalonado explicíto, se hace uso de una ecuación de control que rige el incremento de desplazamientos en la etapa mecánica del problema general. Dicha ecuación de control determina mediante un parámetro de longitud de arco s, el incremento de la fuerza

impulsora que define el aumento del campo de fase en la ecuación de equilibrio de microfuerzas. Por ende, este procedimiento representa una contribución significativa de nuestro estudio.

Esta estrategia de longitud de arco propuesta permite resolver una amplia gama de problemas, los cuales utilizando procedimientos tradicionales originan dificultades en la solución de los mismos. Incluso tomando en cuenta tanto metodologías de optimización con restricciones de desigualdad como múltiples mecanismos que producen inestabilidades.

Por medio de todas las evaluaciónes numéricas realizadas en nuestro estudio se demostró la robutez, precisión y la capacidad de la estrategia de longitud de arco propuesta para trazar curvas de equilibrio completas, capturando los diferentes retrocesos que se presentan en las mismas.

Por otra parte, se contribuye con un nuevo procedimiento para el control del avance de grietas, que es un aspecto esencial en el modelado de problemas de fractura frágil a través del modelo de campo de fase. Lo cual bajo técnicas estándar de control de desplazamiento o de fuerza resulta inestables.

Bajo la inferencia anterior, se demuestra que nuestro procedimiento controla de manera estricta el avance de la grieta en cada paso del análisis, mediante el ajuste del parámetro de longitud de arco para proporcionar un incremento de daño aproximado y que es preestablecido por medio del parámetro de daño óptimo $\left(\Delta\hat{\varphi}^{opt}\right)$. Lo cual origina que el aumento del daño en cada paso del esquema escalonado se mantenga controlado.

Capítulo 6

Método numérico híbrido acoplado para abordar diversos tipos de problemas

6.1. Introducción

El propósito de este capítulo es presentar el enfoque de un método numérico híbrido de tipo superpuesto (Ov-IEFG-FEM, por sus siglas en inglés), el cual es un procedimiento alternativo a los métodos convencionales presentes en la literatura, compuesto por la combinación del método de elementos finitos (FEM, por sus siglas en inglés) y el método de Galerkin libre de elementos mejorado (IEFG, por sus siglas en inglés). Donde bajo el contexto de una discretización superpuesta, es decir empleando una malla de fondo de FEM y sobre ésta una distribución fina de nodos de IEFG. Se evalúan diversos tipos de problemas que van desde la transferencia de calor, donde se inició a testear dicho método alternativo, hasta su implementación en diferentes problemas de referencia de la elasticidad lineal. Los aportes en este capítulo se encuentran sustentados por los trabajos publicados en los Apéndices E y F de esta tesis.

Este capítulo se estructura de la siguiente manera: en la sección 6.2 se expone la metodología numérica del método Ov-IEFG-FEM propuesto, describiendo la secuencia de operaciones que conforman esta técnica. A continuación, en la sección 6.3 se evalúa el desempeño del método Ov-IEFG-FEM en diversas áreas de estudio. Posteriormente, en la sección 6.4 se hace enfasis en el rendimiento computacional del método Ov-IEFG-FEM, destacando las características que lo determinan. Finalmente, la sección 6.5 presenta las conclusiones pertenecientes a este capítulo.

6.2. Metodología del método numérico híbrido de tipo Ov-IEFG-FEM

El método Ov-IEFG-FEM, es una técnica númerica alternativa que trabaja con dominios discretizadsos superpuestos como se representa esquemáticamente en la figura 6.1 para un dominio arbitrario Ω con frontera Γ.

Básicamente la idea es discretizar todo el dominio de un determinado cuerpo con una malla de fondo gruesa, en la cual se llevaran a cabo los cálculos correspondientes a FEM, mientras simultánemente un dominio superpuesto representado por una distribución fina de nodos (puntos rojos en Fig. 6.1) se emplea para enriquecer la solución numérica en un área específica del cuerpo a través del método IEFG con el fin de lograr aproximaciones de orden superior.

Por consiguiente, si se describe esta metodología numérica bajo el contexto de la elasticidad lineal, se considera que el dominio Ω representado en la figura 6.1 está ocupado por un sólido elástico lineal isótropo. Este sólido está sujeto a un conjunto de condiciones tipo Dirichlet y Neumann aplicadas en las fronteras no superpuestas $\Gamma_{\mathbf{u}}$ y $\Gamma_{\mathbf{t}}$, cumpliendo la relación $\Gamma_{\mathbf{u}} \cup \Gamma_{\mathbf{t}} = \Gamma$.

La deformación del sólido está gobernada por la forma cuasi-estática de la ecuación de equilibrio de

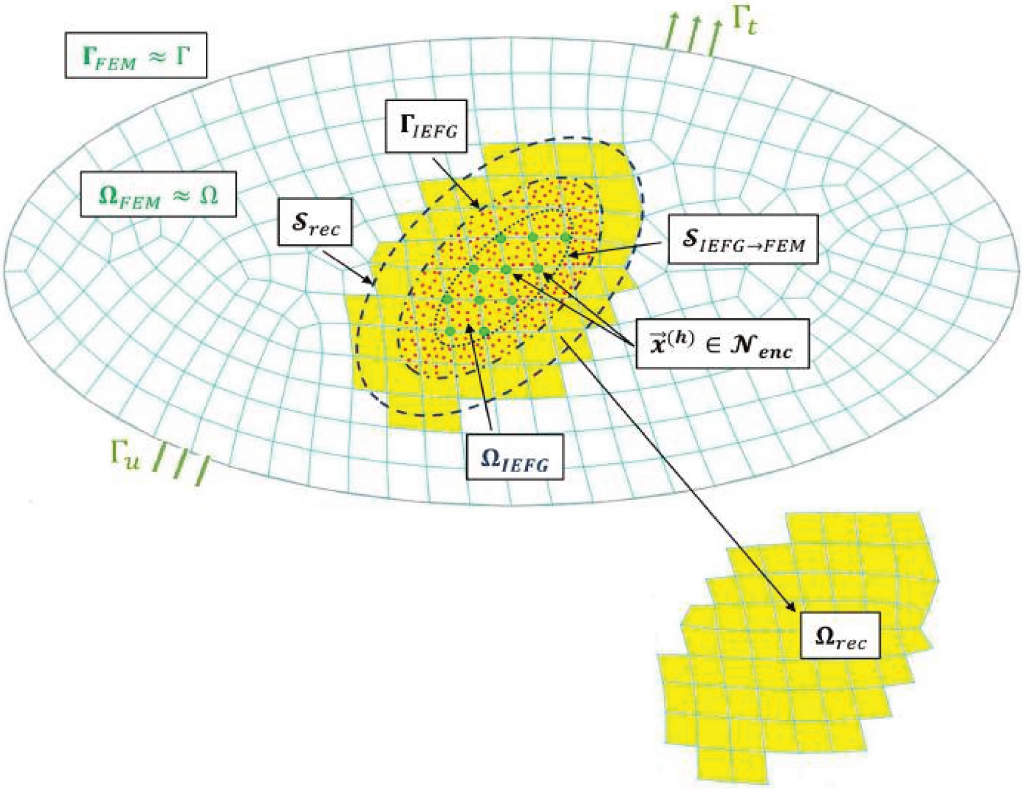

Figura 6.1: Representación del dominio del problema para una solución numérica empleando el método Ov-IEFG-FEM.

fuerzas:

$$\text{Div}\,\boldsymbol{\sigma} + \boldsymbol{b} = \mathbf{0} \qquad \forall \mathbf{x} \in \boldsymbol{\Omega}, \tag{6.1}$$

donde $\boldsymbol{b}$ es la densidad de fuerza del cuerpo y $\boldsymbol{\sigma}$ es el tensor de tensiones de Cauchy. Dicha ecuación, presentada en el artículo anexado en el Apéndice F, se expresa con una notación diferente. En este caso, se adopta la presente notación para mantener la coherencia con la formulación desarrollada previamente en la tesis. La solución de 6.1 está sujeta a las siguientes condiciones de frontera:

$$\begin{aligned} \mathbf{u} &= \mathbf{u}_D \quad \text{en} \quad \Gamma_{\mathbf{u}}, \quad \text{y} \\ \boldsymbol{\sigma} \cdot \hat{\mathbf{n}} &= \mathbf{t} \quad \text{en} \quad \Gamma_{\mathbf{t}}, \end{aligned} \tag{6.2}$$

donde $\mathbf{u}_D$ es el desplazamiento que se va a imponer en $\Gamma_{\mathbf{u}}$, y $\mathbf{t}$ es el vector de tracción superficial en $\Gamma_{\mathbf{t}}$.

El método Ov-IEFG-FEM está diseñado para resolver las ecuaciones gobernantes del problema de elasticidad lineal descritas previamente, obteniendo una solución enriquecida mediante un acoplamiento eficiente de los dominios superpuestos Ω_{FEM} y Ω_{IEFG}, como se ilustra en la figura 6.1.

Los resultados de la solución basada en FEM, obtenidos en la malla de fondo que discretiza Ω_{FEM}, se conservan en las regiones externas al dominio Ω_{IEFG}. Este último está representado por una distribución fina de nodos que enriquecen la solución mediante la técnica IEFG. Además, la frontera Γ_{IEFG} y la superficie cerrada $\mathcal{S}_{\text{IEFG}\to\text{FEM}}$ cumplen un papel clave en la transferencia recíproca de información entre los dominios superpuestos Ω_{FEM} y Ω_{IEFG}.

La frontera Γ_{IEFG} y la superficie cerrada $\mathcal{S}_{\text{IEFG}\to\text{FEM}}$ se representan mediante líneas negras discontinuas y punteadas, respectivamente. La solución basada en FEM se emplea para determinar los despla-

zamientos que serán impuestos en Γ_{IEFG} a través del método de penalización. Por lo tanto, la solución realizada en Ω_{IEFG} mediante el método IEFG está directamente influenciada por los resultados de la malla de fondo.

De manera inversa, la solución obtenida mediante la técnica IEFG en el dominio Ω_{IEFG} se emplea para determinar los desplazamientos que deben imponerse en el conjunto de nodos $\mathcal{N}_{\text{enc}}$ (representados en color verde en la Fig.6.1) de la malla de fondo encerrada por la superficie $\mathcal{S}_{\text{IEFG}\rightarrow\text{FEM}}$.

Cabe resaltar que los desplazamientos a imponer en Γ_{IEFG} se determinan mediante una reconstrucción local de alto orden de la solución basada en FEM. Esta recontrucción se lleva a cabo en el dominio $\Omega_{\text{rec}} \subset \Omega_{\text{FEM}}$, el cual está conformado con aquellos elementos finitos cuyos centros están encerrados por $\mathcal{S}_{\text{rec}}$.

Estos elementos están representados en color amarillo en la figura 6.1, mientras que $\mathcal{S}_{\text{rec}}$ está ilustrado por una línea negra discontinua en la misma figura. El acoplamiento entre las soluciones obtenidas en los dominios superpuestos Ω_{FEM} y Ω_{IEFG} consiste en la imposición segregada/recursiva de las siguientes restricciones cinemáticas:

$$\begin{aligned} \mathbf{u} = \bar{\mathbf{u}}_{\text{IEFG}} \quad \text{en} \quad \mathbf{x}^{(h)}, \quad h \in \mathcal{N}_{\text{enc}}, \quad \text{y} \\ \mathbf{u} = \bar{\mathbf{u}}_{\text{FEM}} \quad \text{en} \quad \Gamma_{\text{IEFG}}, \end{aligned} \tag{6.3}$$

donde $\bar{\mathbf{u}}_{\text{IEFG}}$ corresponde a los desplazamientos calculados en los nodos $h \in \mathcal{N}_{\text{enc}}$ utilizando la solución obtenida en Ω_{IEFG} mediante la técnica IEFG, mientras que $\bar{\mathbf{u}}_{\text{FEM}}$ son los desplazamientos calculados en Γ_{IEFG} empleando las aproximaciones IMLS (del inglés *improved moving least squares*) obtenidas a partir de la reconstrucción local realizada en el conjunto $\mathcal{N}_{\text{enc}}$ de nodos pertenecientes a los elementos incluidos en Ω_{rec}.

Este procedimiento establece una dependencia recíproca entre las soluciones obtenidas tanto en la malla de fondo Ω_{FEM} como en la distribución fina de nodos que representa el dominio Ω_{IEFG}.

Los desplazamientos $\bar{\mathbf{u}}_{\text{IEFG}}$ a imponer en los nodos $h \in \mathcal{N}_{\text{enc}}$ se calculan mediante las aproximaciones IMLS basadas en la solución obtenida a través de la técnica IEFG en la distribución fina de nodos que representa el dominio superpuesto Ω_{IEFG}. Por otro lado, los desplazamientos $\bar{\mathbf{u}}_{\text{FEM}}$ a imponer en Γ_{IEFG} se calculan a partir de la reconstrucción local, también basada en IMLS, del problema mecánico resuelto en la malla de fondo Ω_{FEM} mediante FEM. Para más detalles en base al contexto metodológico del método propuesto consultar el Apéndice F.

Por otra parte, para garantizar una transición continua de desplazamientos a lo largo de la frontera Γ_{IEFG}, es necesario implementar un criterio de distancia entre Γ_{IEFG} y $\mathcal{S}_{\text{IEFG}\rightarrow\text{FEM}}$. Dicho criterio consiste en establecer la distancia $\Gamma_{\text{IEFG}} - \mathcal{S}_{\text{IEFG}\rightarrow\text{FEM}}$ en un rango de 1.5 a 3 veces el tamaño promedio de los elementos de la malla de fondo.

Este criterio de distancia se basa en el trabajo de Storti et al. [148] en el contexto de técnicas tipo quimera basadas en FEM, y fue implementado con éxito por Álvarez-Hostos et al. en la formulación tanto de la técnica sin malla Ov-IEFG [149], como en el enfoque híbrido sin malla/con malla Ov-IEFG-FEM en el marco de problemas de transferencia de calor con fuentes de calor en movimiento, perteneciente a nuestro estudio anexado en el Apéndice E.

Además, este criterio establece que la distancia de separación entre $\mathcal{S}_{\text{rec}}$ y Γ_{IEFG} debe ser al menos igual al tamaño de un elemento de la malla de fondo, lo que resulta suficiente para lograr una reconstrucción precisa y suave mediante el procedimiento IMLS, utilizando los nodos $\mathcal{N}_{\text{rec}}$ de aquellos elementos incluidos en Ω_{rec}.

6.3. Evaluación de diversos tipos de problemas a través del método Ov-IEFG-FEM

6.3.1. Análisis en el contexto de la trasferencia de calor

El método Ov-IEFG-FEM en un principio fue testeado en el área de transferencia de calor para la solución de problemas transitorios de conducción de calor con fuente de calor móvil. Donde dicha fuente de calor recorre desde trayectorias simples como una recta horizontal como trayectorias más complejas en forma sinusoidal y en S.

Seguidamente, este método alternativo también fue evaluado en un problema 3D no lineal con propiedades dependientes de la temperatura y efectos de cambio de fase. Para mayores detalles con respecto a las dimensiones geométricas y propiedades para el modelado de dichos problemas consultar el Apéndice E.

En un contexto general el desempeño del método Ov-IEFG-FEM es satisfactorio en el modelado de este tipo de problemas mencionados previamente, ya que como se puede observar en los diversos resultados mostrados en el Apéndice E, en cuanto a las distribuciones de temperatura que fueron obtenidas en todas las pruebas, el acoplamiento entre los dominios Ω_{FEM} y Ω_{IEFG} posee un comportamiento suave y continuo, lo cual destaca la idoneidad y el potencial del Ov-IEFG-FEM propuesto en escenarios donde se requiere seguir la trayectoria de la fuente de calor móvil, con la distribución fina de nodos.

Además, los perfiles de temperatura obtenidos en las diversas pruebas muestran una excelente concondancia entre el enfoque Ov-IEFG-FEM y una solución estándar basada en FEM, lo cual confirma la precisión de la técnica propuesta.

Por ende, en el contexto de resolución de problemas transitorios de conducción de calor con fuentes de calor móviles, el método Ov-IEFG-FEM demuestra su efectividad para resolver con precisión este tipo de problemas, ya que este enfoque novedoso combina las aproximaciones de alto orden del método IEFG en la región de interés, en este caso específicamente cerca de la fuente de calor, con cálculos basados en FEM, que son menos costosos computacionalmente, usando una malla gruesa fuera de la región de interés con el fin de mejorar la eficiencia computacional.

El Ov-IEFG-FEM permite capturar con éxito altas temperaturas y gradientes térmicos significativos cerca de la fuente de calor móvil, empleando menos incógnitas nodales en comparación con las soluciones basadas en FEM, en todos los casos que fueron testeados, en cuanto al seguimiento de las distintas formas de trayectorias (recto, sinusoidal, tipo S), por parte de la fuente de calor móvil. Esto también se evidencia por los significativos refinamientos de mallas que se emplean en FEM para lograr niveles de estabilidad y precisión comparables al Ov-IEFG-FEM.

El método Ov-IEFG-FEM supera tanto a las soluciones basadas en IEFG como a las soluciones tradicionales basadas en FEM en términos de características de convergencia. El Ov-IEFG-FEM alcanza tasas de convergencia comparables a las soluciones puramente basadas en IEFG y ofrece una mayor precisión en comparación con soluciones basadas en FEM e IEFG. Esto puede atribuirse al hecho de que los errores en la solución numérica de estos problemas están principalmente gobernados por los altos gradientes térmicos desarrollados en la región afectada por la fuente de calor móvil.

Por otro lado, el enfoque Ov-IEFG-FEM a través del método IEFG ofrece más flexibilidad en el refinamiento de nodos dentro de una region específica. Como resultado, el Ov-IEFG-FEM presenta tasas de convergencia similares a las de las soluciones basadas únicamente en IEFG, incluso cuando el problema térmico a lo largo de la mayoría del dominio computacional se resuelve mediante FEM.

El acoplamiento suave y continuo a lo largo de la frontera Γ_{IEFG} siempre se mantiene cuando se utiliza el enfoque Ov-IEFG-FEM, para seguir la fuente de calor móvil con la distribución fina de nodos pertenecientes al dominio superpuesto Ω_{IEFG}, lo que resulta en una excelente precisión numérica y eficiencia computacional.

6.3.2. Análisis en el contexto de la elasticidad lineal

En este contexto el enfoque Ov-IEFG-FEM se implementó para la resolución de diversos problemas muy conocidos en la literatura, los cuales estan relacionados con el análisis de la barra en voladizo de Timoshenko, la placa infinita con un agujero centrado y una probeta con muesca en un borde (SENT, por sus siglas en inglés), la cual es una prueba convencional dentro de la Mecánica de Fractura Elástica Lineal. Para mayores detalles con respecto a dimensionamientos, propiedades y discretizaciones de las distintas pruebas referirse al Apéndice F.

En los análisis exhaustivo de la convergencia y precisiòn desarrollados en las diferentes pruebas, el desempeño del método Ov-IEFG-FEM fue satisfactorio, ya que en un contexto general este enfoque ha mantenido un comportamiento consistente en cuanto al acoplamiento suave y continuo logrado entre las regiones FEM e IEFG a lo largo de la frontera de transición Γ_{IEFG}. Por ende, este comportamiento no solo se ha mostrado en las distribuciones de desplazamientos, sino también en las distribuciones de tensiones de las distintas pruebas realizadas.

Por otro lado, se puede evidenciar el potencial del Ov-IEFG-FEM para obtener soluciones precisas de manera eficiente, mediante cálculos IEFG correctamente distribuidos en el dominio superpuesto Ω_{IEFG}, en las zonas de interés donde se concentran los mayores errores para cada uno de los problemas modelados. Y dicho potencial también queda validado en las diferentes comparaciones realizadas con respecto a las soluciones analíticas de los problemas.

Por consiguiente, en nuestro estudio también se puede visualizar la versatilidad del Ov-IEFG-FEM para resolver adecuadamente problemas en diferentes geometrías sin necesidad de una relación topológica predefinida entre los dominios superpuestos Ω_{FEM} y Ω_{IEFG}. Lo cual es una ventaja de nuestro enfoque Ov-IEFG-FEM en comparación con la mayoría de los procedimientos de acoplamiento EFG-FEM reportados en la literatura que involucran regiones previamente bien especificadas para ser discretizadas mediante FEM y EFG, con una relación topológica prescrita para ser adecuadamente acopladas.

Otra ventaja que presenta nuestro enfoque Ov-IEFG-FEM, derivada de la premisa anterior radica que no requiere elementos de interface, los cuales implementan funciones de rampa para realizar una transición suave entre las fronteras FEM y EFG. Por ende, los procedimientons híbridos convencionales EFG-FEM, que trabajan bajo este enfoque de elementos de interface o transición pueden tener complicaciones con geometrías de topología complejas.

Aunque el acoplamiento entre las regiones FEM e IEFG se lleva a cabo en términos de desplazamientos, las soluciones obtenidas mediante Ov-IEFG-FEM han mostrado un acoplamiento sin discontinuidades en la distribución de tensiones, los cuales están vinculados a las derivadas espaciales de los desplazamientos. Dado que las derivadas espaciales de los cálculos basados en FEM son inherentemente discontinuas, la obtención de distribuciones de tensiones suaves y continuas en todo el dominio del problema ha sido posible en todos los problemas de referencia analizados.

En cuanto al análisis de convergencia del método Ov-IEFG-FEM propuesto, se tiene que el mismo ha superado la correspondiente a las soluciones obtenidas mediante FEM estándar. Además, dichas tasas de convergencia han mostrado una clara tendencia a aproximarse a las obtenidas con soluciones basadas completamente en la técnica IEFG, como se puede observar en los problemas de referencia de la viga en voladizo de Timoshenko y la placa infinita con un agujero centrado.

Se debe destacar que la implementación del Ov-IEFG-FEM es ventajosa en problemas con regiones de gradientes de tensión particularmente pronunciados o elevados, como por ejemplo el problema de la placa infinita con un agujero centrado, donde el error está gobernado principalmente por los marcados gradientes de tensión cerca del agujero, mostrando una clara tendencia hacia una distribución de tensiones prácticamente uniforme lejos de la región del agujero.

Este escenario le permite alcanzar una tasa de convergencia al enfoque Ov-IEFG-FEM que no solo supera claramente a la solución basada puramente en FEM, sino que también se acerca virtualmente a la obtenida mediante cálculos completamente realizados con la técnica IEFG. Por lo tanto, este comportamiento resalta que las características específicas de este problema permiten que el Ov-IEFG-FEM

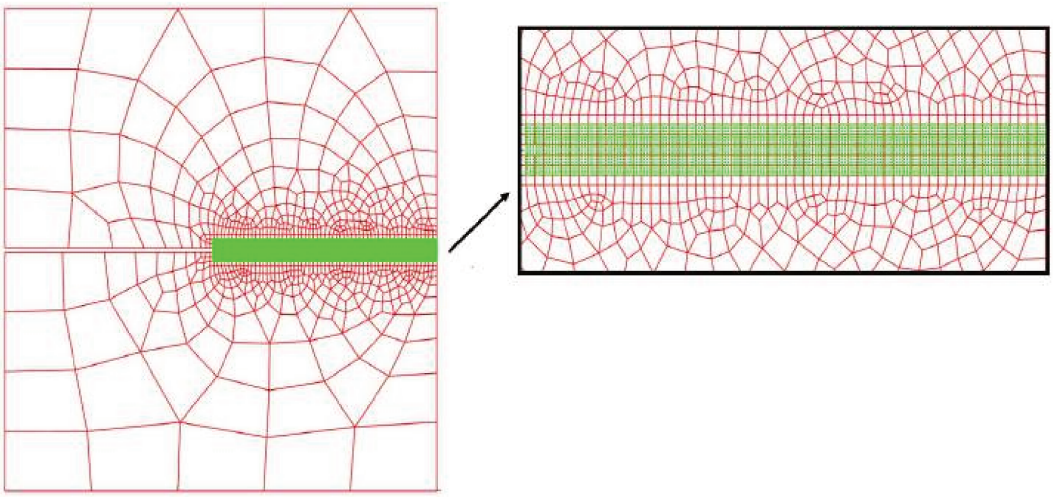

Figura 6.2: Discretización para aplicación del método Ov-IEFG-FEM empleando el modelo de campo de fase. Los cálculos mediante FEM se llevan a cabo en la malla gruesa de color rojo, mientras que los cálculos del IEFG se hacen a través de la distribución fina de nodos representados por los puntos de color verde.

aproveche de manera efectiva la flexibilidad en el refinamiento de nodos y las aproximaciones de alto orden de la técnica IEFG únicamente dentro de la región de interés Ω_{IEFG}.

Siguiendo en sintonia con la premisa anterior, se tiene que otro escenario que hace ideal la implementación del Ov-IEFG-FEM son las características del problema SENT, debido a la singularidad de tensiones en la punta de la grieta lo cual genera gradientes marcados en su entorno, mientras que el campo de tensiones es prácticamente uniforme en el resto del dominio del problema.

Por ende, la distribución fina de nodos correspondientes al dominio superpuesto Ω_{IEFG}, se ubica estratégicamente en una pequeña región que abarca la punta de la grieta, ya que esta zona domina casi por completo el error inherente en la solución numérica de este problema.

6.3.3. Análisis en el contexto de la mecánica de fractura empleando el modelo de campo de fase

En este contexto, se implementó el método Ov-IEFG-FEM en conjunto con el modelo de campo de fase para resolver un problema de fractura frágil bajo un esquema escalonado explícito. Es importante señalar que, hasta el momento, no se ha realizado ninguna publicación sobre este contexto por parte de nuestro grupo de trabajo, lo que indica que se encuentra en una etapa inicial de desarrollo. Por ende, se presentarán resultados preliminares correspondientes al problema seleccionado para la implementación del método.

Para ello se utilizó una muestra tipo SENT, comúnmente empleada como referencia en la literatura. Esta muestra consiste en una placa con una pre-grieta ubicada en el centro de la altura de su borde izquierdo, con el borde inferior completamente restringido y un desplazamiento uniforme impuesto en el borde superior.

La placa se discretizó utilizando una malla de fondo FEM gruesa y estructurada en la zona de propagación de la grieta, mientras que fuera de esta región se empleó una malla no estructurada. Adicionalmente, se superpuso una distribución fina de nodos en forma rectangular, alineada con la dirección de propagación de la grieta, dicha discretización se puede visualizar en la figura 6.2.

En una primera etapa de pruebas, nuestro enfoque Ov-IEFG-FEM, uno de los primeros en su estilo aplicado con modelos de campo de fase según lo evidenciado en la literatura, presentó un buen desempeño en cuanto a la presición de los resultados obtenidos.

Al realizar un estudio basado en el trabajo de referencia de Miehe et al. [98] para el problema tipo

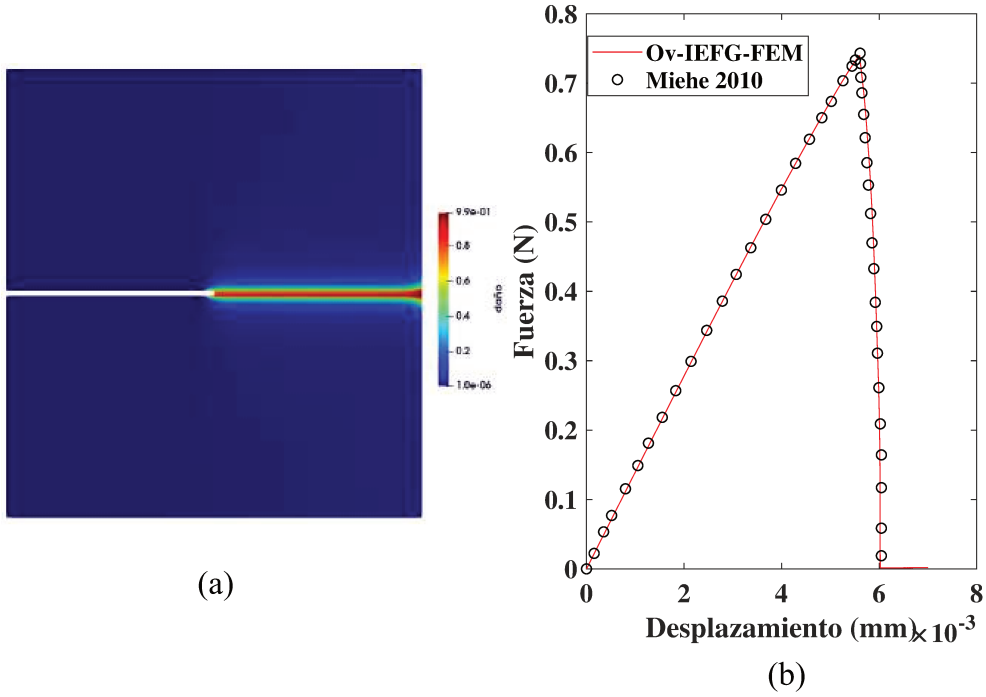

Figura 6.3: (a) Evolución del campo de fase en muestra tipo SENT. (b) Curva Fuerza vs Desplazamiento para muestra tipo SENT.

SENT, utilizando las mismas dimensiones y propiedades elásticas y de fractura reportadas en dicho trabajo, nuestra metodología Ov-IEFG-FEM en combinación con el modelo de campo de fase logró capturar de manera satisfactoria la respuesta mecánica estructural de la muestra, como se aprecia en la figura 6.3b.

También se observa en la figura 6.3a, un comportamiento satisfactorio de la evolución del campo de fase a lo largo de toda la extensión de propagación de la grieta, lo cual es un aspecto fundamental en este tipo de problemas. Además, la implementación Ov-IEFG-FEM con el modelo de campo de fase ofrece la ventaja de emplear mallas FEM menos refinadas en la zona de propagación de la grieta, en contraste con las mallas altamente refinadas en dicha zona utilizadas en las soluciones convencionales de FEM. Esto es posible ya que la precisión en la evolución del campo de fase se logra en el dominio superpuesto mediante la distrbución fina de nodos utilizada para los cálculos de IEFG.

Por lo tanto, la resolución del problema se realiza con un menor número de incógnitas nodales en comparación con las soluciones convencionales mediante FEM. Esta resolución podría optimizarse aún más al emplear una distribución fina de nodos en el dominio superpuesto de IEFG que se desplace siguiendo la punta de la grieta, en lugar de utilizar un dominio superpuesto fijo de forma rectangular, como se implementó en nuestro estudio.

En cuanto al costo computacional en esta etapa inicial de implementación y pruebas, nuestro enfoque Ov-IEFG-FEM presenta un costo similar al de los métodos estándar como FEM. Sin embargo, este rendimiento computacional tiene potencial de mejora, que es precisamente el objetivo clave de implementar este tipo de enfoque y que deja un campo abierto para futuros trabajos en esta línea de investigación.

6.4. Rendimiento computacional del método Ov-IEFG-FEM

Nuestro enfoque alternativo Ov-IEFG-FEM en una perspectiva general presenta un desempeño positivo, en cuanto al rendimiento computacional de los problemas que fueron testeados en el contexto de

la transferencia de calor y la elasticidad lineal, mientras que en el contexto de la mecánica de fractura empleando el modelo de campo de fase todavia necesita mejorar, ya que es una temática que se encuentra en su etapa inicial de desarrollo.

Pero la razón del desempeño satisfactorio en los primeros dos contextos se debe a que el enfoque Ov-IEFG-FEM propuesto permite reducir de manera significativa los tiempos de cálculo en comparación con las soluciones basadas completamente en la técnica IEFG, la cual es una técnica muy conocida en la literatura por su alto costo computacional.

Incluso se debe resaltar que este comportamiento ocurre a pesar de implementar un número total de nodos similar a los utilizados en las técnicas de FEM e IEFG, para realizar los cálculos numéricos. Esto se debe a que el enfoque Ov-IEFG-FEM emplea un número considerablemente menor de nodos para los cálculos IEFG dentro de Ω_{IEFG}, en comparación con las soluciones estándar basadas exclusivamente en IEFG en todo el dominio del problema.

Los tiempos de cómputo de la técnica Ov-IEFG-FEM están predominantemente influenciados por los cálculos IEFG en Ω_{IEFG}, dado que esta técnica sin malla incurre en tiempos computacionales significativamente mayores en comparación con FEM.

Por otra parte, otro aspecto importante es que este buen desempeño del Ov-IEFG-FEM con respecto a la técnica IEFG estándar se ha logrado a pesar de la solución iterativa de sistemas de ecuaciones lineales requerida para el acoplamiento $\Omega_{\text{FEM}} - \Omega_{\text{IEFG}}$, lo cual es consistente con el hecho ampliamente conocido de que la determinación de los nodos del dominio de soporte y el cálculo de las funciones de forma en las técnicas EFG es significativamente más costoso en términos de tiempo computacional que la resolución del sistema de ecuaciones resultante.

Como representación destacable del desempeño satisfactorio de la técnica Ov-IEFG-FEM, en cuanto a rendimiento computacional se refiere, se tiene la prueba tipo SENT dentro del contexto de la elasticidad lineal, realizada en nuestro estudio del Apéndice F, en la cual se simuló dicho problema tanto con las metodologías numéricas estándar FEM e IEFG, como con nuestro enfoque Ov-IEFG-FEM propuesto.

Se evidencia que a pesar de que los tiempos computacionales de FEM son significativamente menores en comparación con los del Ov-IEFG-FEM, incluso tomando en cuenta la reducción sustancial en los tiempos de cálculo lograda por esta técnica en comparación con las soluciones enteramente basadas en IEFG, es importante destacar que, para un número similar de nodos, la precisión alcanzada por FEM no se equipara con la obtenida mediante Ov-IEFG-FEM o IEFG.

Por consiguiente, al llevar a cabo soluciones de FEM altamente refinadas los tiempos de cómputo comienzan a acercarse a los del Ov-IEFG-FEM, lo que indica una disminución en la ventaja de FEM en términos de eficiencia computacional cuando se busca alcanzar niveles similares de precisión, que en nuestro estudio se reflejó con el cálculo del factor de intensidad de tensiones de la muestra (K_I)

Asimismo, es importante enfatizar que las mejoras introducidas por el enfoque Ov-IEFG-FEM se logran sin necesidad de prescribir relaciones topológicas complejas entre la malla de fondo que discretiza Ω_{FEM} y la distribución fina de nodos que representa Ω_{IEFG}. Esta característica permite su fácil implementación en problemas que involucran gradientes marcados en movimiento, lo cual se consigue simplemente posicionando adecuadamente el dominio superpuesto IEFG en función de los cambios en la configuración del dominio del problema.

Se conoce que las técnicas EFG son muy eficientes para el modelado de problemas de mecánica de fractura al igual que FEM, pero estas técnicas EFG poseen la problemática particular de su elevado costo computacional, los cuales a menudo superan significativamente a los de los enfoques tradicionales basados en mallas cuando se emplea un número similar de nodos. Por ende, el enfoque Ov-IEFG-FEM se convierte en una estrategia alternativa para solucionar dicha problemática. Ya que el Ov-IEFG-FEM representa una solución para hacer un uso más eficiente de la alta precisión proporcionada por los cálculos EFG, eliminando la necesidad de procedimientos engorrosos de reconfiguración adaptativa de nodos para capturar eficazmente gradientes marcados.

6.5. Conclusiones

En este capítulo se presenta un enfoque numérico híbrido alternativo (Ov-IEFG-FEM) conformado por el método de elemetos finitos (FEM) y el método de Galerkin libre de elementos mejorado superpuesto (IEFG), el cual se implementa para resolver de manera eficiente y precisa diversos tipos de problemas relacionados con la transferencia de calor, la elasticidad lineal y la mecánica de fractura haciendo uso del modelo de campo de fase.

La técnica Ov-IEFG-FEM aprovecha particularmente la capacidad del método IEFG para capturar gradientes pronunciados tanto de temperaturas como de tensiones, de forma sencilla, mientras reduce significativamente el costo computacional derivado de aplicar el método IEFG en todo el dominio del problema.

Se infiere que al ubicar estratégicamente la distribución fina de nodos correspondiente al dominio superpuesto IEFG, en zonas con elevados gradientes, se mejora la precisión de las soluciones numéricas, sin necesidad de realizar reconfiguraciones extensivas de nodos o adaptaciones de mallas complejas.

Se demuestra que el método Ov-IEFG-FEM puede alcanzar tasas de convergencia comparables a las soluciones basadas exclusivamente en IEFG, mientras que reduce significativamente los tiempos de cómputo en el contexto de problemas de transferencia de calor y elasticidad lineal. Sin embargo, en el contexto de la mecánica de fractura empleando el modelo de campo de fase, aún no es posible establecer una conclusión definitiva sobre este aspecto, ya que dicha temática se encuentra en una etapa preliminar de desarrollo.

Se infiere que una de las ventajas destacada de este enfoque es la reducción significativa de incógnitas nodales, lo que conlleva a una disminución en los tiempos de cómputo, en comparación con las técnicas numéricas estándar que emplean mallas o nodos fijos.

Se demuestra que el enfoque Ov-IEFG-FEM mantiene la eficiencia computacional y además, la implementación sencilla del método, que permite la adaptación de la distribución de nodos del dominio superpuesto mediante simples traslaciones rígidas, resalta su practicidad para manejar eficazmente geometrías en evolución y gradientes en movimiento. Esto resulta particularmente ventajoso en problemas de mecánica de fractura, donde la adaptabilidad y la precisión son fundamentales.

La técnica Ov-IEFG-FEM, en combinación con el modelo de campo de fase, se implementó para resolver un problema de fractura frágil. En una primera fase de pruebas, esta técnica demostró un buen desempeño al capturar de manera satisfactoria la respuesta mecánica estructural de este tipo de problemas.

Se recomienda profundizar en la implementación del enfoque Ov-IEFG-FEM, para el modelado de problemas de fractura frágil mediante el uso del modelo de campo fase, con énfasis en la optimización de la discretización y el rendimiento computacional. Esto permitiría analizar diversos fenómenos y materiales compuestos como los expuestos en los capítulos III y IV de esta tesis, abriendo así nuevas oportunidades para futuros estudios en esta área

Parte IV

Conclusiones

Capítulo 7

Conclusiones

Este capítulo recopila las principales contribuciones alcanzadas a lo largo del desarrollo de esta tesis y proporciona un listado de las publicaciones en revistas indexadas y los trabajos presentados en congresos.

7.1. Contribuciones

En esta tesis se presentan diversas metodologías y técnicas destinadas a realizar de forma eficiente el modelado computacional de problemas de fractura frágil. En este contexto, dichas metodologías se enfocaron en el análisis de diversas áreas de estudio. Por consiguiente, para validar su efectividad, se llevaron a cabo una serie de pruebas cuyos resultados se incluyen en los Apéndices de esta tesis. En síntesis, y en concordancia con los objetivos específicos establecidos en la Sección 1.2.2, se destacan las contribuciones en las siguientes temáticas.

7.1.1. Contribuciones al estudio de los mecánismos de interacción entre una grieta propagante que incide en una interface

Se establece una metodología numérica alternativa que combina el modelo de campo de fase para modelar la propagación de grietas en un determinado medio, y el modelo de superficie cohesiva para simular el proceso de degradación de las interfaces. Donde a diferencia de enfoques similares presentados en la literatura, nuestra metodología presenta un modelo cohesivo, el cual no esta influenciado por la degradación del material circundante, representada mediante la variable de campo de fase.

Por lo tanto, no es necesario extender el campo de fase a la interface como se implementa en diversos modelos de referencia en la literatura, permitiendo que esta sea completamente independiente en ambos lados. En consecuencia, nuestra metodología abre la posibilidad de explorar escenarios de modelado alternativos, donde las discontinuidades del campo de fase a través de la interface, pueden emplearse para mejorar el análisis de los mecanismos de interación.

Bajo la premisa anterior, nuestra metodología numérica ofrece un camino distinto para caracterizar satisfactoriamente la interacción entre una grieta que propaga por un medio e impacta con una interface, sin tener que utilizar solamente uno de los dos modelos constitutivos por separado, para modelar el dominio completo de un determinado cuerpo.

Por otra parte, se valida nuestro enfoque del modelo de campo de fase, el cual parte del principio de las potencias virtuales y junto con el papel fundamental que posee el parámetro de la longitud característica en dicho modelo, lo hace una herramienta útil y eficiente para caracterizar tanto el estado de tensiones en la punta de una grieta como los diversos mecánismos que se producen cuando dicha grieta va propagando y choca con una interface.

Con la captura de los mecanismos de deflexión y penetración a travès de nuestro modelo y repre-

sentados en un espacio definido por las relaciones entre la tenacidad y la resistencia tanto del sustrato como de la interface se demuestra que dichos mecanismos de interacción dependen de un criterio mixto de tenacidad-resistencia, el cual determina la condición bajo la cual sucede cada modo de interacción.

Se establece la relevancia de analizar el efecto tipo escudo (shield) que ocurre durante el proceso de degradación de la interface, el cual trae como respuesta un incremento de la tenacidad estructural de una determinada muestra, donde el principal responsable de dicha respuesta es el mecanismos de deflexión. Bajo este contexto, se abren oportunidades para estudiar por medio de la implementación de nuestra metodología numérica combinada una serie de problemas en los cuales se presentan este tipo de efecto, y por ende, un aumento de la tenacidad del sistema. Dentro de estos problemas se pueden destacar los relacionados con la propagación de microfisuras en materiales compuestos laminados y los mecanismos de fractura en materiales biomiméticos.

7.1.2. Contribuciones al análisis de los diseños bioinspirados

Se establece un enfoque alternativo para la captura satisfactoria del comportamiento mecánico de los diseños bioinspirados, basados en geometrías que imitan la estructura del nácar, reproduciendo eficientemente cada una de las etapas que conforman la respuesta mecánica de estos diseños.

Este enfoque permite analizar detalladamente los diversos mecanismos que juegan un rol clave en el incremento de la tenacidad estructural de los diseños bioinspirados. Lo que permite profundizar en el análisis de los diferentes parámetros geométricos que conforman dichos diseños, donde a través de la modificación de los mismos, se obtiene una mejora sustancial en la respuesta mecánica maximizando la tenacidad estructural, en este caso para las configuraciones basadas en la estructura del nácar.

Bajo el contexto de la premisa anterior, nuestro estudio aporta mejoras para la creación de prototipos basados en los diseños bioinspirados orientados a la fabricación empleando tecnología de impresión 3D, la cual en comparación con las técnicas de fabricación tradicionales ofrece crear materiales bioinspirados con un alto nivel de precisión y exactitud en los detalles estructurales de los mismos.

Se establece que los modos de interacción que toman lugar en el comportamiento mecánico de los diseños bioinspirados, dependen netamente de un criterio mixto que se fundamenta en la combinación tanto de la resistencia como la tenacidad de las fases materiales (rígida y blanda) que coforman los diseños bioinspirados.

Nuestro estudio ofrece la oportunidad de extender la metodología numérica implementada, para analizar fenómenos más complejos direccionados hacia el comportamiento de la interface que conforman la fase blanda de los diseños bioinspirados en estructuras basadas en el nácar, ya que al profundizar en dicho comportamiento se pueden desarrollar diseños bioinspirados más eficientes que exhiban una mayor disipación de energía con respecto a los diseños estándar.

7.1.3. Contribuciones al desarrollo de algoritmos computacionales para el trazado eficiente de curvas de equilibrio completas

Se desarrolla una herramienta útil y eficiente bajo un enfoque de longitud de arco, utilizando un esquema escalonado explícito, donde se hace uso de una ecuación de control que regula el incremento de los desplazamientos dentro de la etapa mecánica de la resolución del problema. Esta ecuación de control posee una importancia fundamental porque permite llevar a cabo un buen manejo del avance de una grieta en un determinado medio, lo cual es un requisito primordial en el modelado de problemas de fractura frágil.

Se demuestra que nuestro enfoque alternativo de longitud de arco, es una metodología muy versátil y robusta, ya que abre el abanico para modelar una gran variedad de problemas, que con métodos convencionales producirian dificultades para llevar a cabo su resolución, como por ejemplo manejar diversos mecanismos que originan inestabilidades en el proceso de fractura de una determinada muestra. Por ende, este enfoque permite el anàlisis de dichas inestabilidades de forma satisfactoria junto con metodologías

constitutivas combinadas.

La técnica propuesta permite capturar de forma eficiente los distintos retrocesos que surgen en la traza de la curva de equilibrio de una muestra determinada, proporcionando una estimación precisa de la energía disipada de dicha muestra. Esto resulta difícil de lograr con esquemas escalonados, tanto explícitos como implícitos, que no incorporan el procedimiento de longitud de arco, ya que tienden a sobrestimar significativamente la energía disipada.

7.1.4. Contribuciones para la resolución de diversos tipos de problemas implementando métodos híbridos acoplados

Se desarrolla un enfoque híbrido alternativo Ov-IEFG-FEM eficiente y preciso compuesto por el método de elementos finitos (FEM) y el método de Galerkin libre de elementos mejorado (IEFG). Básicamente la idea es combinar las ventajas de ambos métodos aplicando una discretización mixta a través de una malla gruesa FEM de fondo y una distribución fina de nodos superpuesta correspondiente al método IEFG.

La técnica Ov-IEFG-FEM aplicada a diversos tipos de problemas posee un desempeño satisfactorio en la obtención de resultados precisos en diferentes áreas de estudio. Estos resultados se presentan con un acoplamiento continuo y suave entre las fronteras FEM y IEFG, sin necesidad de utilizar una relación topológica prescrita para lograr un acoplamiento adecuado entre ambas fronteras, como se estipula en los métodos híbridos EFG-FEM convencionales.

Bajo la premisa anterior, se tiene que nuestro enfoque Ov-IEFG-FEM no requiere el uso de elementos de interface utilizados en procedimientos híbridos EFG-FEM convencionales, los cuales se emplean para garantizar una transición suave entre las zonas FEM y IEFG. Como resultado, estos métodos híbridos convencionales enfrentan desafíos significativos al aplicarse a geometrías con topologías complejas, lo cual con el método Ov-IEFG-FEM propuesto se obtiene una solucion alternativa a dicha situación.

El enfoque Ov-IEFG-FEM contribuye con un bajo costo computacional, manteniendo su eficiencia como se refleja en los diferentes testeos realizados en nuestros estudios correspondientes a las áreas de transferencia de calor y elasticidad lineal. A pesar que el método IEFG involucra altos costos computacionales como bien se conoce, el rendimiento global de la técnica Ov-IEFG-FEM no se ve afectado por esta situación ya que sigue manteniendo una reducción significativa de los tiempos de cómputo.

La contribución previamente descrita también se basa en la ubicación estrategica de la distribución fina de nodos perteneciente al dominio IEFG, la cual se coloca en una zona de interés donde generalmente se presentan los mayores errores inherente a la solución numérica, lo que también permite capturar gradientes marcados de las variables de estudio respectivas.

Se implementó el enfoque Ov-IEFG-FEM en combinación con el modelo de campo de fase para la resolución de problemas de fractura frágil, obteniendo un desempeño satisfactorio en las etapas iniciales de pruebas. Este enfoque es pionero en su tipo al aplicarse junto con el modelo de campo de fase para la solución de este tipo de problemas. En línea con la premisa anterior, esta implementación abre oportunidades para mejorar el redimiento computacional en la solución de problemas de fractura frágil, mediante la optimización del enfoque propuesto. De este modo, dicha técnica junto con el modelo de campo de fase ofrece una alternativa a los procedimientos existentes relacionados con la adaptatividad de mallas, métodos globales/locales, y métodos multiescala.

7.2. Publicaciones científicas

7.2.1. Publicaciones en revistas

- **Zambrano-Carrillo, Javier A.**, Álvarez-Hostos, Juan C., Serebrinsky, Santiago and Huespe, Alfredo E (2024). “Solving linear elasticity benchmark problems via the overset improved element-

free Galerkin-finite element method". *Finite Elements in Analysis and Design*, https://doi.org/10.1016/j.finel.2024.104247.

- Álvarez-Hostos, Juan C., Ullah, Zahur, Storti, Bruno A., Tourn, Benjamín A. and **Zambrano-Carrillo, Javier A.** (2024). "An overset improved element-free Galerkin-finite element method for the solution of transient heat conduction problems with concentrated moving heat sources". *Computer Methods in Applied Mechanics and Engineering*, https://doi.org/10.1016/j.cma.2023.116574.

- **Zambrano, J.**, Toro, S., Sánchez, P.J., Duda, F.P., Méndez, C.G., and Huespe, A.E (2023). "An arc-length control technique for solving quasi-static fracture problems with phase field models and a staggered scheme". *Computational Mechanics*, https://doi.org/10.1007/s00466-023-02388-7.

- **Zambrano, J.**, Toro, S., Sánchez, P.J., Duda, F.P., Méndez, C.G., and Huespe, A.E (2022). "Interaction analysis between a propagating crack and an interface: Phase field and cohesive surface models". *International Journal of Plasticity*, https://doi.org/10.1016/j.ijplas.2022.103341.

7.2.2. Publicaciones y presentaciones en congresos

- **Javier A. Zambrano**, Juan C. Álvarez Hostos, Santiago Serebrinsky and Alfredo E. Huespe (2024). "Aplicación del método de elemento finito y Galerkin libre de elementos mejorado superpuesto a la elasticidad lineal". *MECOM 2024 - XL Congreso Argentino de Mecánica Computacional*. Sesión: Mecánica de Solidos. Rosario, Argentina.

- **Javier A. Zambrano**, Alfredo E. Huespe, Santiago Serebrinsky, Sebastian Toro and Pablo J. Sánchez (2023). "Diseño de materiales compuestos para aumento de tenacidad bajo el enfoque de diseños bioinspirados". *MECOM 2023 - XXXIX Congreso Argentino de Mecánica Computacional - I Congreso Argentino Uruguayo de Mecánica Computacional*. Sesión: Mecánica de Solidos. Concordia, Argentina - Salto, Uruguay.

- **J. Zambrano**, J. Gutierrez, S. Toro, P.J. Sánchez, F.P. Duda, S. Serebrinsky and A.E. Huespe (2023). "Toughening effect analysis in problems of propagating cracks interacting with interfaces". *The Seventh International Conference on Computational Modeling of Fracture and Failure of Materials and Structures*. Sesión: Multi-scale analysis of damage and fracture. Praga, República Checa.

- **J. Zambrano**, S. Toro, P.J. Sánchez, C. Méndez, F. Duda, and A.E. Huespe (2023). "Toughening effect analysis in problems of propagating cracks interacting with interfaces". *Workshop: Critical Structural Integrity Challenges for the Energy Sector: Stress Corrosion Cracking and Hydrogen Embrittlement*. Rio de Janeiro, Brazil.

- **Javier A. Zambrano**, Sebastian Toro, Pablo J. Sánchez, Fernando P. Duda, Carlos G. Méndez, and Alfredo E. Huespe (2022). "Interaction analysis between a propagating crack and an interface: phase field and cohesive surface models". *MECOM 2022 - XXXVIII Congreso Argentino de Mecánica Computacional*. Sesión: Mecánica de Solidos. Bahía Blanca, Argentina.

Parte V

Apéndices

Apéndice A

Interaction analysis between a propagating crack and an interface: Phase field and cohesive surface models

J. Zambrano, S. Toro, P.J. Sánchez, F.P. Duda, C.G. Méndez, A.E. Huespe (2022). "Interaction analysis between a propagating crack and an interface: Phase field and cohesive surface models". *International Journal of Plasticity*, 156, 103341.

Interaction analysis between a propagating crack and an interface: Phase field and cohesive surface models

J. Zambrano[1], S. Toro[1], P.J. Sánchez[1,2], F.P. Duda[3], C.G. Méndez[1], A.E. Huespe[1,1]

[1]CIMEC-UNL-CONICET, Güeme 3450, CP 3000 Santa Fe, Argentina
[2]GIMNI-UTN-FRSF, Lavaise 610, CP 3000 Santa Fe, Argentina
[3]Programa de Engenharia Mecânica - COPPE, Universidade Federal do Rio de Janeiro, Cidade Universitária, Rio de Janeiro, CEP 21941-972, RJ, Brazil

Keywords: Crack-interface interaction mechanisms; Phase-field models; cohesive zone models; toughness and strength based criterion for fracture.

Abstract. The interaction phenomenon between a propagating crack impinging an interface is studied with a phase-field approach in combination with a cohesive surface model. The phase-field technique simulates the crack propagation across the medium, and the cohesive surface model simulates the degradation process of the adhesive interface.

The main assessed mechanisms of this interaction are deflection of the crack into the interface, crack penetration, and kink of the crack out an interface. For a specified load system, the occurrence of each mechanism depends on the material fracture properties characterizing the interface and the medium. According to the results obtained using the present approach, we conclude that these interaction modes are ruled by a mixed criterion involving the ratios of toughness and strengths of the medium and the interface. A lower bound for the ratio between the medium and interface strengths exists below which penetration will likely happen independently of the toughness. This conclusion confirms previous studies of interaction reported elsewhere in the literature performed with a different numerical methodology.

The apparent increase of the structural toughness due to the crack interface interaction and the mechanisms leading to this outcome are also analyzed in one specific case.

An additional contribution of the paper points to describe a variationally consistent mechanical formulation coupling phase-field and cohesive zone models along with its corresponding numerical algorithm. This formulation provides general jump conditions across the interface of the primal descriptors, in particular, the phase-field continuity conditions across the interface. Specific emphasis is given to analyze the effect that the phase-field continuity conditions induce in the kinking of cracks outs of interfaces. Consequently, and considering that the present phase-field approach is not affected by numerical artifacts coming from the finite element mesh discretization, we assess its potential to capture the crack deviation mechanism out of the interface.

A.1. Introduction

The interplay existing between the mechanical properties of materials, strength and toughness, determining the conditions under which a crack will nucleate and propagate in a solid has been extensively discussed in the literature. An enlightened vision of this matter is particularly addressed by Leguillon [2] and additional discussion in Ritchie [3].

Both properties also play a prominent role in determining the interaction mechanism arising between propagating cracks in a solid medium impinging on adhesive interfaces. These interfaces can be characterized by critical stresses and toughness. The mechanism resulting from this interaction has relevant consequences in several technological problems. For example, the interaction mode has a direct influence on the extrinsic toughness of laminate composites (Noselli et al. [4]), when a crack propagating across a

[1]Corresponding author. E-mail address: ahuespe@cimec.unl.edu.ar (A.E. Huespe).

matrix with relatively high toughness either deflects into the interface (matrix/fiber debonding) or penetrates the relative brittle reinforcement component (fiber breakage). This effect, combined with adequate topological designs of architected weak porous interfaces, can be exploited to increase the apparent fracture toughness of composites, such as reported by Conway et al. [150]. Another typical case where this phenomenon has technological consequences is in hydraulic fracture problems with application to non-conventional oil reservoirs. Whether hydraulic fractures impinging on natural interfaces activate or cross them is a relevant effect on the reservoir effective permeability and productivity ([5–7]). A third problem where such interactions play an outstanding role refers to the assessment of the transition mechanism between intergranular and transgranular fracture, in heterogeneous microstructures, see Foulk III et al. [9] and Chen et al. [10].

Due to the impact of these interaction scenarios, the problem of a crack impinging on an interface has been extensively studied in the past using different approaches, either analytical or numerical. He y Hutchinson [140], using integral equation methods and assuming linear elastic isotropic materials at both sides of the interface, estimate the range of interface toughness, G_i, relative to the medium material toughness on the substrate uncracked side, G_s, which likely results in deflection of the cracks into the interface instead of penetrating it. The analysis of He et. al. is based on a purely energetic criterion and includes cases of dissimilar brittle materials at both sides of the interface, as well as different incidence angles between the propagating crack and interface. A similar analytical technique is used by Martinez y Gupta [141] to investigate the crack deflection problem into an interface which bonds two orthotropic elastic materials. Martinez et al. note that, unlike strength-based criteria, the energy release rate criterion adopted to predict interactions is very sensitive to the values of material parameters. This observation is relevant to the solutions obtained in this paper.

Alternatively, several numerical techniques can be used to assess the interaction mechanisms between propagating cracks impinging on interfaces. Parmigiani y Thouless [62] study this problem using cohesive zone models to represent both the cracks in the medium as well as the interface degradation until its final decohesion. They conclude that the resulting interaction mechanism typically depends on a mixed strength-toughness criterion, see also Strom y Parmigiani [151]. This crucial issue is further analyzed in the present work to conclude that a similarly mixed criterion emanates from a phase-field model combined with a cohesive interface approach. The systematic method of analysis followed by Parmigiani et al. to understand the role played by the relevant mechanical properties of the problem is closely adopted in the present paper.

The phase field approach has been widely used for the simulation of propagating fractures in solids in a wide range of problems ([17]). Typically, it has been employed for modeling ductile fracture ([42]), brittle geomaterial ([152]), dynamic fracture ([153]), environmentally assisted cracking ([154] and [155]), between others problems. Particularly, brittle fracture problems, where the effect of strength or toughness takes different roles, have been analyzed with phase-field techniques by Tanné et al. [113]. These authors show that a phase-field model can predict crack nucleation provided that the phase-field regularization parameter (denoted ℓ_{PF} in sub-Section A.2.5) be identified with a material characteristic length. By adopting this premise, the regularization parameter jointly with the fracture toughness automatically introduces a limited peak stress, or material strength, in the phase-field model. Alternative phase-field models proposed by Kumar et al. [156] and Wu y Nguyen [157] consider the material strength independently of ℓ_{PF}. The strength is taken into account by introducing either additional driving force terms in the phase-field equation ((A.34) below) or specific strain energy degradation functions (equation (A.28) below). The remarkable point in all of these approaches is that the critical stress is a key ingredient to predict nucleation of cracks in media without pre-existing fractures as well as in the present analyzed problem entailing cracks interacting with interfaces. In a different context, but considering a phase-field technique that couples brittle fracture and plasticity, Duda et al. [54] have reported a similar conclusion. These authors observe that the critical stress emanating from a phase-field model with a non-null regularization parameter must be comparable with the medium yield stress to induce a combined mechanism

entailing plasticity and crack propagation.

A phase-field technique for modeling the combined effects of cracks in the medium and the decohesion process of adhesive interfaces has been reported by Hansen-Dörr et al. [158]. These authors describe the interface degradation process through a diffuse damage representation by appealing to the spatial distribution of the phase-field variable. Different characteristic lengths determine the fracture process, either in the medium or interface. Using a similar concept to approach the sharp crack with a smeared domain, Nguyen et al. [159] assume a non-null-thickness interface in where exists a phase-field representation capturing the bond strength degradation at the interface. According to the authors, this technique avoids the specific meshing of interfaces. Another similar strategy is proposed in the paper by Chen et al. [10], where cohesive interfaces are also modeled in a phase-field framework. In the last work, two-set of order parameters, one for the medium and other for the interface, are included in the model.

Closer to the numerical methodology here adopted is the contribution of Paggi y Reinoso [73]. These authors combine a phase-field approach for brittle fracture together with a cohesive zone model, similar to the one described by Needleman [160], which simulates the interface degradation process. However, a key difference of Paggi et al.'s work compared to the present one relies on the interface decohesion model. In our methodology, the interface cohesive model is not affected by the degradation of the neighbor medium characterized by the phase field variable. Thus, we do not need to extend the phase-field to the interface, and therefore, it can be fully independent on both sides of the interface. This approach suggests alternative modeling scenarios where phase-field discontinuities across the interface can be used to improve the characterization of interaction mechanisms. Considering such discrepancy between our model and that of Paggi et al., the main conclusions about the interaction modes obtained with the present approach may be considerably different from those obtained using the Paggi et al.'s approach.

Specifically in this work, the assumption of a non-null regularization parameter of the phase-field technique opens the possibility to combine it with a cohesive surface model characterized by a critical strength, σ_i^c, and toughness, G_i. In this context, the continuity condition of every field across the interface has to be carefully considered (general continuity conditions across interfaces involving phase-fields can be seen in Levitas [161] and Duda et al. [162]). We derive the jump conditions from a variationally consistent formulation. Then, and after the specialization of the model constitutive equations and the interface continuity constraints, we show that the resulting methodology is adequate to study fracture problems where the interplay between strength and toughness of the medium plays a prominent role. It can predict quantitatively crack interaction problems in a wide range of material parameters. Further emphasis is given to assess the phase-field continuity conditions and their effects on the interaction problems.

A summary of the paper is the following. The variational basis of the model is presented in Section A.2. The fundamental mechanical ingredients assuming discontinuities in displacements and phase-field across interfaces are defined. Thus, the mechanical consequences for the assumed jumps conditions of these variables are derived from the variational principle assumed in this Section.

Next, in Section A.3, the stress field near the crack tip is studied using the phase-field approach. It is compared with the Linear Elastic Fracture Mechanics (LEFM) solution attained from the corresponding stress intensity factor K_I. The role played by the phase-field characteristic length ℓ_{PF} and the sizes at which the LEFM solution dominates the stress field distribution is particularly analyzed. The conclusions assessed in Section A.3 are crucial to characterize the results presented in Section A.4.

In Section A.4, the interaction phenomena between propagating cracks and interfaces are studied and discussed under different situations. In the last Section A.5 of the paper, the conclusions are exposed.

A very brief summary of the finite element model implementation is presented in Appendix I. The readers can find additional details about the specific implementation of the phase-field model (without interfaces), as well as rigorous numerical validation tests, in a separated contribution of the authors, see Duda et al. [54].

A.2. Preliminaries

We formulate a phase-field theory for fracture in solids under small-strains and isothermal conditions. Inertial forces and any time dependent physical phenomena are neglected, thus the pseudo-time variable "t", used below, only takes into account an ordered sequence of mechanical events via a monotonically increasing parameter.

Let us consider a body $\mathcal{B}$ constituted by two complementary sub-parts $\mathcal{B}^+$ and $\mathcal{B}^-$ connected through a pre-defined cohesive-type sharp interface $\mathcal{S}$, see sketch in Figure A.1. Super-scripts $(\cdot)^+$ and $(\cdot)^-$ are used to denote mechanical entities related to $\mathcal{B}^+$ and $\mathcal{B}^-$, respectively. The boundary of $\mathcal{B}$ is $\partial\mathcal{B}$ and its unit normal vector is $\boldsymbol{m}$. The unit normal vector to $\mathcal{S}$ is denoted $\ltimes$, and it points toward $\mathcal{B}^+$.

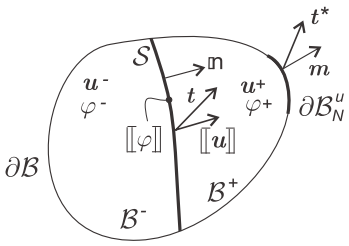

Figura A.1: Solid $\mathcal{B}$ with a cohesive interface $\mathcal{S}$.

To describe deformation and fracture in $\mathcal{B}$, we introduce the displacement vector field, $\boldsymbol{u}(\boldsymbol{X},t)$, and phase-field variable, $\varphi(\boldsymbol{X},t)$, at time t in $\mathcal{B}\setminus\mathcal{S}$. The phase-field takes values on the interval $[0,1]$. If $\varphi=0$ at a point, then it is unfractured. If $\varphi=1$ at a point, it is fractured. Values of φ between zero and one correspond to partially fractured material. Points satisfying $\varphi=1$ identifies cracks, i.e. a traction-free boundary embedded into the bulk material. Thermodynamic arguments advocating irreversibility of fracture processes impose an additional restriction for the phase-filed evolution taking the form: $\dot{\varphi}\geq 0$.

The fields $\boldsymbol{u}$ and φ are smooth away from and up to the interface $\mathcal{S}$; $\boldsymbol{u}^+$ and φ^+ are defined on $\mathcal{B}^+$ and $\boldsymbol{u}^-$ and φ^- are defined on $\mathcal{B}^-$. Considering this assumption, jumps on $\mathcal{S}$ are denoted:

$$[\![\boldsymbol{u}]\!]=\boldsymbol{u}|_{\mathcal{S}}^{+}-\boldsymbol{u}|_{\mathcal{S}}^{-}\quad,\quad\forall\boldsymbol{X}\in\mathcal{S}\,, \tag{A.1}$$

$$[\![\varphi]\!]=\varphi|_{\mathcal{S}}^{+}-\varphi|_{\mathcal{S}}^{-}\quad,\quad\forall\boldsymbol{X}\in\mathcal{S}\,, \tag{A.2}$$

where the symbol $(\cdot)|_{\mathcal{S}}^{-}$ represents the value of $(\cdot)$ on the $\mathcal{S}$ boundary of $\mathcal{B}^-$. Identical meaning for $(\cdot)|_{\mathcal{S}}^{+}$, but evaluated on $\mathcal{B}^+$. Such discontinuities may arise as an outcome of the degradation and decohesion processes at the interface $\mathcal{S}$.

The existence of phase-field discontinuities, $[\![\varphi]\!]$, across interfaces is a further ingredient which is introduced in the present work. The proposed theory assumes a pointwise constraint equation along the interface which is generically denoted as:

$$\mathcal{R}([\![\varphi]\!](\mathcal{S},t))=0\,. \tag{A.3}$$

Even when the approach of handling phase-field jumps across interfaces via a constitutive model is not explored in this work, it is worthy of being assessed in future work. In this case, the following variational formulation could properly manage such a generalization.

With the aim to keep the presentation as simple as possible, we only consider rigorously the inequality constraint: $\dot{\varphi}\geq 0$, relaxing the formalism for $\varphi\geq 0$ and $\varphi\leq 1$. In any case, the same procedure here presented to include the condition $\dot{\varphi}\geq 0$ could be applied to cover all the inequality constrains on φ and $[\![\varphi]\!]$.

A.2.1. Primal descriptors

Four independent primal descriptors are postulated to characterize the mechanical state of $\mathcal{B}$, at pseudo-time "t". They are gathered in the vector $\boldsymbol{U} = \{\boldsymbol{u}^+, \boldsymbol{u}^-, \varphi^+, \varphi^-\}$. Admissibility conditions for $\boldsymbol{U}$ are established in the form $\boldsymbol{U} \in \mathcal{K}$, where the set $\mathcal{K}$ accounts for proper regularity and Dirichlet-type boundary conditions of every descriptor. Virtual variations of $\boldsymbol{U}$ are denoted $\delta\boldsymbol{U} = \{\delta\boldsymbol{u}^+, \delta\boldsymbol{u}^-, \delta\varphi^+, \delta\varphi^-\}$, and their admissibility conditions are defined through $\delta\boldsymbol{U} \in \mathcal{V}$, where the vectorial space $\mathcal{V}$ accounts for appropriate regularity demands and the specified restrictions on $\boldsymbol{U} \in \mathcal{K}$.

The strain tensor $\boldsymbol{E}$ and its corresponding virtual variation $\delta\boldsymbol{E}$, are:

$$\boldsymbol{E} = \frac{\nabla\boldsymbol{u} + (\nabla\boldsymbol{u})^T}{2} \quad , \quad \delta\boldsymbol{E} = \frac{\nabla\delta\boldsymbol{u} + (\nabla\delta\boldsymbol{u})^T}{2} \, , \tag{A.4}$$

respectively, and $\nabla(\cdot)$ denotes the material gradient operator.

A.2.1.1. Derived work-conjugated descriptors

The external force field per unit volume in $\mathcal{B}\backslash\mathcal{S}$, $\boldsymbol{b}$, and the external tractions per unit area in $\partial\mathcal{B}^u_N$, $\boldsymbol{t}^*$, are considered the dual actions conjugate to $\boldsymbol{u}$, where $\partial\mathcal{B}^u_{\mathrm{N}}$ is the Neumann-boundary related to $\boldsymbol{u}$. The Cauchy stress tensor $\boldsymbol{S}$, defined in $\mathcal{B}\backslash\mathcal{S}$ conforms the duality pair of $\boldsymbol{E}$. A constitutive functional dependence is introduced for $\boldsymbol{S}$ in Section A.2.4.

Following to Duda et al. [54], the continuous part of the phase-field descriptor, φ, has associated three work-conjugated actions, namely: the (active) internal micro-force field π_a per unit volume, the external micro-force γ per unit volume and the external micro-traction ς per unit area in $\partial\mathcal{B}^\varphi_{\mathrm{N}}$, where $\partial\mathcal{B}^\varphi_{\mathrm{N}}$ is the Neumann-boundary related to φ. A constitutive law is provided for the active counterpart π_a in Section A.2.4. A micro-stress vector field $\boldsymbol{\xi}$ is the work-conjugate action of the phase-field gradient $\nabla\varphi$. A constitutive relation is provided for $\boldsymbol{\xi}$ in terms of $\nabla\varphi$, see Section A.2.4.

Paired with the displacement discontinuity $[\![\boldsymbol{u}]\!]$ an internal force field per unit area, called $\boldsymbol{t}$, is considered along the interface $\mathcal{S}$. A cohesive-type constitutive law is provided to define $\boldsymbol{t}$ in Section A.2.4.

A.2.2. Basic laws

We stipulate that deformation and fracture processes in $\mathcal{B}$ must be consistent with the Variational Principle of Virtual Work, from which the local-form force balance equation and the phase-field micro-force balance equation are derived. Together with the free-energy imbalance (see sub-Section A.2.3), these two statements comprise the kinetic foundation of the present theory.

A.2.2.1. Virtual Work Variational Principle

The internal and external virtual works, $\delta\mathcal{W}^{\mathrm{int}}$ and $\delta\mathcal{W}^{\mathrm{ext}}$ respectively, for any part $\mathcal{P}$ of the body $\mathcal{B}$ and the part $\mathcal{S}_\mathcal{P}$ of $\mathcal{S}$ intersecting $\mathcal{P}$ are defined as follows:

$$\delta\mathcal{W}^{\mathrm{int}}(\mathcal{P};\delta\boldsymbol{U}) = \int_{\mathcal{P}\backslash\mathcal{S}_\mathcal{P}} \left(\boldsymbol{S}\cdot\delta\boldsymbol{E} + \boldsymbol{\xi}\cdot\nabla\delta\varphi + \pi_a\,\delta\varphi\right)\mathrm{d}\mathcal{P} + \int_{\mathcal{S}_\mathcal{P}} \boldsymbol{t}\cdot\delta[\![\boldsymbol{u}]\!]\,\mathrm{d}\mathcal{S}_\mathcal{P}, \quad \forall\delta\boldsymbol{U}\in\mathcal{V}\,, \tag{A.5}$$

$$\delta\mathcal{W}^{\mathrm{ext}}(\mathcal{P}\backslash\mathcal{S}_\mathcal{P};\delta\boldsymbol{U}) = \int_{\mathcal{P}\backslash\mathcal{S}_\mathcal{P}} \left(\boldsymbol{b}\cdot\delta\boldsymbol{u} + \gamma\,\delta\varphi\right)\mathrm{d}\mathcal{P} + \int_{\partial\mathcal{P}} \boldsymbol{t}_{\partial\mathcal{P}}\cdot\delta\boldsymbol{u}\,\mathrm{d}(\partial\mathcal{P}) + \int_{\partial\mathcal{P}} \varsigma_{\partial\mathcal{P}}\,\delta\varphi\,\mathrm{d}(\partial\mathcal{P}), \quad \forall\delta\boldsymbol{U}\in\mathcal{V}\,, \tag{A.6}$$

where $\boldsymbol{t}_{\partial\mathcal{P}}$ and $\varsigma_{\partial\mathcal{P}}$ are now defined as the actions on the boundary $\partial\mathcal{P}$ of $\mathcal{P}$.

From (A.5)-(A.6), an extended version of the Variational Principle of Virtual Work is postulated attending specific details of the present formulation: for any pseudo-time "t", find $\boldsymbol{U} \in \mathcal{K}$ such that

$$\begin{aligned}
&\int_{\mathcal{P}\setminus\mathcal{S}_{\mathcal{P}}} \left(\boldsymbol{S}\cdot\delta\boldsymbol{E} + \boldsymbol{\xi}\cdot\nabla\delta\varphi + \pi_a\,\delta\varphi\right)\mathrm{d}\mathcal{P} + \int_{\mathcal{S}_{\mathcal{P}}} \boldsymbol{t}\cdot\delta[\![\boldsymbol{u}]\!]\,\mathrm{d}\mathcal{S}_{\mathcal{P}} - \\
&- \int_{\mathcal{P}\setminus\mathcal{S}_{\mathcal{P}}} \left(\boldsymbol{b}\cdot\delta\boldsymbol{u} + \gamma\,\delta\varphi\right)\mathrm{d}\mathcal{P} - \int_{\partial\mathcal{P}} \boldsymbol{t}_{\partial\mathcal{P}}\cdot\delta\boldsymbol{u}\,\mathrm{d}(\partial\mathcal{P}) - \int_{\partial\mathcal{P}} \varsigma_{\partial\mathcal{P}}\,\delta\varphi\,\mathrm{d}(\partial\mathcal{P}) + \\
&+ \int_{\mathcal{S}_{\mathcal{P}}} \Big[\lambda_r\,\mathcal{R}(\delta[\![\varphi]\!]) + \delta\lambda_r\,\mathcal{R}([\![\varphi]\!])\Big]\,\mathrm{d}\mathcal{S}_{\mathcal{P}} + \\
&+ \int_{\mathcal{P}\setminus\mathcal{S}_{\mathcal{P}}} \pi_r\,\delta\varphi\,\mathrm{d}\mathcal{P} = 0\,, \\
&\forall\delta\boldsymbol{U}\in\mathcal{V},\quad \forall\delta\lambda_r\in\mathbb{R},\quad \text{with}\quad \pi_r\,\dot{\varphi} = 0,\quad \pi_r \le 0,\quad \dot{\varphi}\ge 0\,.
\end{aligned} \tag{A.7}$$

The first and second lines of (A.7) is the difference between the internal and external virtual works, respectively. The third line in expression (A.7) accounts for the variational version of constraint in equation (A.3). The (reactive) Lagrange Multiplier associated to constraint (A.3) is λ_r and its admissible virtual variation is $\delta\lambda_r$.

The fourth line of (A.7) incorporates into the model the thermodynamically-inspired restriction $\dot{\varphi} \ge 0$ (irreversibility of damage). The field π_r is the associated (reactive) Lagrange Multiplier, and the restrictions $\pi_r\dot{\varphi} = 0$, $\pi_r \le 0$, and $\dot{\varphi} \ge 0$ are the classical Karush–Kuhn–Tucker optimality conditions related to such inequality constraint.

Admitting independent variations for the displacement primal descriptors in (A.7), we derive integral balance equations, which can be localized using a conventional procedure. The resulting local form of equilibrium for the body $\mathcal{B}$ with cohesive interface $\mathcal{S}$ are given by the following equations:

$$\mathrm{Div}\,\boldsymbol{S} + \boldsymbol{b} = \boldsymbol{0}\,, \quad \forall\boldsymbol{X}\in\mathcal{B}\setminus\mathcal{S}\,, \tag{A.8}$$

$$\boldsymbol{S}\,\boldsymbol{m} = \boldsymbol{t}^*\,, \quad \forall\boldsymbol{X}\in\partial\mathcal{B}^{\boldsymbol{u}}_{\mathrm{N}}\,, \tag{A.9}$$

$$\boldsymbol{S}|^{-}_{\mathcal{S}} \ltimes = \boldsymbol{t}\,, \quad \forall\boldsymbol{X}\in\mathcal{S}\,, \tag{A.10}$$

$$[\![\boldsymbol{S}\ltimes]\!] = \boldsymbol{0}\,, \quad \forall\boldsymbol{X}\in\mathcal{S}\,. \tag{A.11}$$

Also, assuming variations for the phase-field primal descriptors in (A.7) and after applying a standard localization procedure, we obtain:

$$\mathrm{Div}\,\boldsymbol{\xi} + \gamma - (\pi_a + \pi_r) = 0\,, \quad \forall\boldsymbol{X}\in\mathcal{B}\setminus\mathcal{S}\,, \tag{A.12}$$

$$\boldsymbol{\xi}\cdot\boldsymbol{m} = \varsigma\,, \quad \forall\boldsymbol{X}\in\partial\mathcal{B}^{\varphi}_{\mathrm{N}}\,, \tag{A.13}$$

$$\boldsymbol{\xi}|^{-}_{\mathcal{S}}\cdot\ltimes = \mathcal{R}^{\mathrm{adj}}(\lambda_r)\,, \quad \forall\boldsymbol{X}\in\mathcal{S}\,, \tag{A.14}$$

$$[\![\boldsymbol{\xi}\cdot\ltimes]\!] = 0\,, \quad \forall\boldsymbol{X}\in\mathcal{S}\,, \tag{A.15}$$

with $\pi_r\dot{\varphi} = 0$, $\pi_r \le 0$, and $\dot{\varphi} \ge 0$. The operator $\mathcal{R}^{\mathrm{adj}}(\cdot)$ denotes the adjoin of $\mathcal{R}(\cdot)$. The set of equations (D.5)-(A.15) are complemented with the local version of the constraint, which naturally emerge for arbitrary variations $\delta\lambda_r$ in (A.7):

$$\mathcal{R}([\![\varphi]\!]) = 0, \quad \forall\boldsymbol{X}\in\mathcal{S}\,. \tag{A.16}$$

A.2.3. Thermodynamical consistency

In addition to the standard and micro-force balances described in previous sub-Sections, the first and second law of thermodynamics is imposed through an energy imbalance postulate. Such an inequality requires that the mechanical power expended by surrouding agencies to $\mathcal{P}\backslash\mathcal{S}_\mathcal{P}$, here denoted as $\dot{\mathcal{W}}^{\text{ext}}$, exceed or equal the rate of change of the free energy in $\mathcal{P}$. Introducing the notion of free energy densities ψ and $\psi_\mathcal{S}$ of the bulk (per unit volume) and interface (per unit area), respectively, the energy imbalance reads:

$$\frac{\mathrm{d}}{\mathrm{d}t}\left(\int_{\mathcal{P}\backslash\mathcal{S}_\mathcal{P}} \psi \,\mathrm{d}\mathcal{P} + \int_{\mathcal{S}_\mathcal{P}} \psi_\mathcal{S} \,\mathrm{d}\mathcal{S}_\mathcal{P}\right) \leq \dot{\mathcal{W}}^{\text{ext}}(\mathcal{P}\backslash\mathcal{S}_\mathcal{P}; \dot{\boldsymbol{U}}) \,, \tag{A.17}$$

with $\dot{\mathcal{W}}^{\text{ext}}$ defined in similar way as in (A.6) and $\dot{\boldsymbol{U}}$ collecting the primal descriptor velocities. Admissible virtual variations $\delta\boldsymbol{U}$ and realizable velocities $\dot{\boldsymbol{U}}$ belong to the same functional space $\mathcal{V}$, thus there is a correspondence between concepts related to virtual works, see expressions (A.6)-(A.7), and realizable powers.

Inserting (A.6) into (A.17), and after localizing the integral inequality, we obtain:

$$\dot{\psi} - \boldsymbol{S}\cdot\dot{\boldsymbol{E}} - \boldsymbol{\xi}\cdot\nabla\dot{\varphi} - \pi_a\,\dot{\varphi} \leq 0 \,, \quad \forall \boldsymbol{X} \in \mathcal{B}\backslash\mathcal{S} \text{ and } \forall \dot{\boldsymbol{U}} \in \mathcal{V} \,, \tag{A.18}$$

$$\dot{\psi}_\mathcal{S} - \boldsymbol{t}\cdot[\![\dot{\boldsymbol{u}}]\!] \leq 0 \,, \quad \forall \boldsymbol{X} \in \mathcal{S} \text{ and } \forall \dot{\boldsymbol{U}} \in \mathcal{V} \,, \tag{A.19}$$

which represent the point-wise forms of energy imbalances for the bulk material and cohesive surface domain, respectively. Note that the reactive Lagrange Multipliers π_r and λ_r do not participate in (A.18)-(A.19). They do not induce realizable power, being orthogonal to their corresponding primal variable constraints.

On the other hand, in case $[\![\varphi]\!]$ is unconstrained, that is, (A.16) ceases to hold, a constitutive relation has to rule its evolution. Then, an additional contribution involving $[\![\dot{\varphi}]\!]$ would appear in (A.19), opening the way to the formulation of more general phase-field interface conditions. An analogous situation is found in the formulation of phase-field boundary conditions as recently explored by Duda et al. [162].

A.2.4. Constitutive theory

The mathematical structure of inequalities (A.18)-(A.19) dictate some natural choices to select the independent arguments in the definition of bulk and surface free energy densities (ψ and $\psi_\mathcal{S}$ respectively). Since the present formulation concerns with rate-independent materials, we allow for possible functional dependences on the following list of variables $\{\boldsymbol{E}, \varphi, \nabla\varphi, [\![\boldsymbol{u}]\!]\}$, thus we take:

$$\psi = \hat{\psi}(\boldsymbol{E}, \varphi, \nabla\varphi) \,, \tag{A.20}$$

$$\psi_\mathcal{S} = \hat{\psi}_\mathcal{S}([\![\boldsymbol{u}]\!], \bar{\alpha}) \,, \tag{A.21}$$

where $\bar{\alpha}$ is an internal variable for the interface cohesive model. Inspired in the ideas employed by Coleman y Noll [55], it is assumed that the constitutive responses $\boldsymbol{S}$, $\boldsymbol{\xi}$, π_a, $\boldsymbol{t}$ are obtained as the partial derivative of the free energy densities with respect to their corresponding dual variables:

$$\boldsymbol{S} = \frac{\partial\psi(\boldsymbol{E}, \varphi, \nabla\varphi)}{\partial\boldsymbol{E}} \,, \tag{A.22}$$

$$\boldsymbol{\xi} = \frac{\partial\psi(\boldsymbol{E}, \varphi, \nabla\varphi)}{\partial\nabla\varphi} \,, \tag{A.23}$$

$$\pi_a = \frac{\partial \psi(\boldsymbol{E}, \varphi, \nabla\varphi)}{\partial \varphi} \,, \tag{A.24}$$

$$\boldsymbol{t} = \frac{\partial \psi_{\mathcal{S}}(\llbracket \boldsymbol{u} \rrbracket, \bar{\alpha})}{\partial \llbracket \boldsymbol{u} \rrbracket} \,, \tag{A.25}$$

which, jointly with the requirement that:

$$\frac{\partial \psi_{\mathcal{S}}(\llbracket \boldsymbol{u} \rrbracket, \bar{\alpha})}{\partial \bar{\alpha}} \dot{\bar{\alpha}} \leq 0 \,, \tag{A.26}$$

satisfy (A.18) and (A.19).

A.2.5. Constitutive theory specialization

The constitutive response functions introduced in (A.20) and (A.21) are now specialized to obtain a particular instance characterizing the current implementation for phase-field model coupled with cohesive interfaces.

A.2.5.1. Phase-field constitutive model

The present phase-field model follows the one presented by the authors in a previous contribution, see Duda et al. [54] from where, additional details can be obtained. Following this work, we despise the external loading system related with phase-field descriptor. In this sense, neither the external micro-forces per unit volume γ in $\mathcal{B}\backslash\mathcal{S}$ nor external micro-tractions ς are accounted for. Thus, $\gamma = 0$ and $\varsigma = 0$ in the local balance forms (A.12) and (A.13).

The free energy response ψ is partitioned in two terms:

$$\psi(\boldsymbol{E}, \varphi, \nabla\varphi) = \hat{\psi}_e(\boldsymbol{E}, \varphi) + \hat{\psi}_f(\varphi, \nabla\varphi), \tag{A.27}$$

with

$$\begin{aligned}
\hat{\psi}_e(\boldsymbol{E}, \varphi) &= \left((1-\varphi)^2\right) \hat{\psi}_e^{pos}(\boldsymbol{E}) + \hat{\psi}_e^{neg}(\boldsymbol{E}) \,, \\
\hat{\psi}_e^{pos}(\boldsymbol{E}) &= \frac{1}{2}\left(\lambda \langle \operatorname{tr} \boldsymbol{E} \rangle^2 + 2\mu \boldsymbol{E}^{pos} : \boldsymbol{E}^{pos}\right) \,, \\
\hat{\psi}_e^{neg}(\boldsymbol{E}) &= \frac{1}{2}\left(\lambda \langle -\operatorname{tr} \boldsymbol{E} \rangle^2 + 2\mu \boldsymbol{E}^{neg} : \boldsymbol{E}^{neg}\right) \,, \\
\boldsymbol{E}^{pos} &= \sum_{k=1}^{3} \langle \varepsilon_k \rangle \, \boldsymbol{e}_k \otimes \boldsymbol{e}_k \,, \qquad \boldsymbol{E}^{neg} = \sum_{k=1}^{3} - \langle -\varepsilon_k \rangle \, \boldsymbol{e}_k \otimes \boldsymbol{e}_k \,,
\end{aligned} \tag{A.28}$$

where λ and μ are the Lamé parameters, ε_k and $\boldsymbol{e}_k$ are the k-th eigenvalue and eigenvector of $\boldsymbol{E}$, respectively. The angle bracket operator, $\langle \cdot \rangle$, is the positive part of the argument. The partition of $\hat{\psi}_e$ defined in equation (A.28) is taken from Miehe et al. [57]. The second term in equation (A.27) results:

$$\hat{\psi}_f(\varphi, \nabla\varphi) = G_{_{PF}} \left(\frac{\varphi^2}{2\ell_{_{PF}}} + \frac{\ell_{_{PF}}}{2} |\nabla\varphi|^2 \right) . \tag{A.29}$$

where the fracture energy is denoted $G_{_{PF}}$ and $\ell_{_{PF}}$ is the phase-field order parameter with dimension of length.

In view of (A.22), the Cauchy stress tensor is specified as follow:

$$\boldsymbol{S} = \left((1-\varphi)^2\right)\left(\lambda\left\langle \operatorname{tr}\boldsymbol{E}\right\rangle \boldsymbol{I} + 2\mu\boldsymbol{E}^{pos}\right) + \left(-\lambda\left\langle -\operatorname{tr}\boldsymbol{E}\right\rangle \boldsymbol{I} + 2\mu\boldsymbol{E}^{neg}\right) , \tag{A.30}$$

and considering (A.23) and (A.24), the micro-stress and micro-force result:

$$\boldsymbol{\xi} = G_{_{PF}}\, \ell_{_{PF}}\, \nabla\varphi , \tag{A.31}$$

$$\pi_a = \frac{G_{_{PF}}}{\ell_{_{PF}}}\,\varphi - 2(1-\varphi)\hat{\psi}_e^{pos}(\boldsymbol{E}) , \tag{A.32}$$

respectively.

In view of (A.31) and (A.32), we rewrite (A.12) as

$$G_{PF}\ell_{PF}\triangle\varphi - \frac{G_{_{PF}}}{\ell_{_{PF}}}\,\varphi + 2(1-\varphi)\hat{\psi}_e^{pos}(\boldsymbol{E}) - \pi_r = 0 \tag{A.33}$$

recalling that π_r is the reaction necessary to guarantee the irreversibility constraint $\dot{\varphi} \geq 0$ and as such must satisfy the conditions $\pi_r \leq 0$ and $\pi_r\dot{\varphi} = 0$. We anticipate that, as in Duda et al. [54], we follow the strategy due to Miehe et al. [57] leading to the reformulation of (A.33). According with such strategy, π_r is defined as:

$$\pi_r = -2(1-\varphi)\big(\overbrace{\mathcal{H}(t) - \hat{\psi}_e^{pos}(\boldsymbol{E},t)}^{\Delta\hat{\psi}_e^{pos}}\big), \tag{A.34}$$

where the compact history field function $\mathcal{H}(t)$ results:

$$\mathcal{H}(t) = \max_{s} h(s), \quad s \in [0,t], \tag{A.35}$$

with:

$$h(t) := \hat{\psi}_e^{pos}(\boldsymbol{E},t). \tag{A.36}$$

Since $\Delta\hat{\psi}_e^{pos} \geq 0$, the inequality $\pi_r \leq 0$ is automatically satisfied. See Appendix I for details. It is worth noticing that different strategies have been proposed to impose the constraint $\dot{\varphi}$ from the numerical point of view. See, for instance, De Lorenzis y Gerasimov [163] and references therein.

A.2.5.2. Interface constitutive model

The interface free energy $\hat{\psi}_{\mathcal{S}}(\llbracket\boldsymbol{u}\rrbracket,\bar{\alpha})$, in terms of the displacement jump $\llbracket\boldsymbol{u}\rrbracket$ and the scalar internal variable $\bar{\alpha} \in [0,\infty]$, is defined as follows:

$$\hat{\psi}_{\mathcal{S}}(\llbracket\boldsymbol{u}\rrbracket,\bar{\alpha}) = \frac{1}{2}\frac{q(\bar{\alpha})}{\bar{\alpha}}(\llbracket\boldsymbol{u}\rrbracket\cdot\boldsymbol{Q}\llbracket\boldsymbol{u}\rrbracket) \qquad , \qquad \boldsymbol{Q} = \begin{bmatrix} E_i & 0 \\ 0 & E_i/2 \end{bmatrix} , \tag{A.37}$$

$\boldsymbol{Q}$ being a stiffness tensor given in terms of a stiffness modulus E_i and the function $q(\bar{\alpha}) \in [0, q_0]$. In the above expression, the tensor $\boldsymbol{Q}$ is described in the orthogonal coordinate system with the basis defined by the vectors $\boldsymbol{n}$ and $\boldsymbol{s}$, with $\boldsymbol{s}$ parallel to the interface direction, see Figure A.2-a. According with this coordinate system, the components of the jump vector are $\llbracket\boldsymbol{u}\rrbracket = (\llbracket u\rrbracket_{\boldsymbol{n}}, \llbracket u\rrbracket_s)$.

From expression (A.25), the traction vector $\boldsymbol{t}$ (see Figure A.2-a) results:

$$\boldsymbol{t} = \frac{\partial\hat{\psi}_{\mathcal{S}}(\llbracket\boldsymbol{u}\rrbracket,\bar{\alpha})}{\partial\llbracket\boldsymbol{u}\rrbracket} = \frac{q(\bar{\alpha})}{\bar{\alpha}}(\boldsymbol{Q}\llbracket\boldsymbol{u}\rrbracket) . \tag{A.38}$$

The initial conditions for $q(\bar{\alpha})$ is given in terms of a critical cohesive stress σ_i^c as follows:

$$q_0 = q(\bar{\alpha} = 0) = \frac{\sigma_i^c}{\sqrt{E_i}} \,, \tag{A.39}$$

and its evolution law is:

$$\dot{q} = \bar{H}\dot{\bar{\alpha}} \,, \tag{A.40}$$

where the regularized softening modulus, $\bar{H}$, is characterized in terms of the fracture energy parameter, G_i:

$$\bar{H} = -\frac{1}{2}\frac{(\sigma_i^c)^2}{G_i E_i} \,. \tag{A.41}$$

The physical interpretation of the parameters, σ_i^c, G_i, and E_i are sketched in Figure A.2-c.

The starting degradation condition is defined with the criterion $f_t = 0$, where f_t:

$$f_t = \sqrt{\boldsymbol{t}^{pos} \cdot \boldsymbol{Q}^{-1}\boldsymbol{t}} \; - q \,, \tag{A.42}$$

is written in terms of $\boldsymbol{t}$ and its positive counterpart $\boldsymbol{t}^{pos} = (\langle t_{\boldsymbol{n}} \rangle \,, \langle t_s \rangle)$. Thus, in particular, interfaces opening in mode I start to degrade when $t_{\boldsymbol{n}} = \sigma_i^c$. Additionally, the degradation criterion of the cohesive law is defined through the degradation function:

$$f_\delta = \sqrt{[\![\boldsymbol{u}]\!]^{pos} \cdot \boldsymbol{Q}[\![\boldsymbol{u}]\!]} - \bar{\alpha} \,, \tag{A.43}$$

where $[\![\boldsymbol{u}]\!]^{pos}$ is the displacement jump vector with positive components: $[\![\boldsymbol{u}]\!]^{pos} = (\langle [\![u]\!]_{\boldsymbol{n}} \rangle \,, \langle [\![u]\!]_s \rangle)$. Furthermore, the following complementarity (loading-unloading) conditions are satisfied:

$$f_\delta \leq 0 \quad , \quad \dot{\bar{\alpha}} \geq 0 \quad , \quad f_\delta \dot{\bar{\alpha}} = 0 \,. \tag{A.44}$$

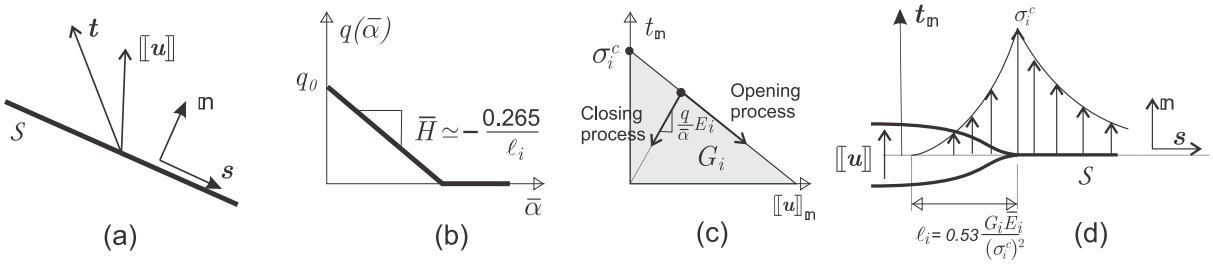

Figura A.2: Interface cohesive model. a) traction $\boldsymbol{t}$ and separation $[\![\boldsymbol{u}]\!]$ vectors at the interface. b) Softening law, $q(\bar{\alpha})$, governing the traction-separation degradation. c) Traction-separation law of an interface opening in mode I. The area below the curve is equal to the fracture energy G_i and the peak stress component is σ_i^c. d) Estimation of the cohesive characteristic length ℓ_i.

The interface degradation process is characterized by the condition $\dot{\bar{\alpha}} > 0$. Note that both conditions, $f_t = 0$ and $f_\delta = 0$, represents the same thermodynamical state for $[\![\boldsymbol{u}]\!] \neq \boldsymbol{0}$, i.e., they are equivalent criteria.

This model predicts a traction-separation law with an initial rigid response, i.e., when the condition $f_t < 0$ and $\bar{\alpha} = 0$ are satisfied. It is easy to prove that (A.26) is satisfied ($[\partial_{\bar{\alpha}}\psi_{\mathcal{S}}]\dot{\bar{\alpha}} = -(q_0\dot{\bar{\alpha}})/2 \leq 0$), as well as , that the integral of the model mechanical dissipation in (A.19) along a process leading to complete interface decohesion gives G_i. Interface unloading (closing) processes are elastic and defined by a degraded stiffness. Figure A.2-c shows a one-dimensional representation of this model.

An interface characteristic length, ℓ_i, can be defined as follows:

$$\ell_i = 0.53\frac{E_i G_i}{(\sigma_i^c)^2} \,, \tag{A.45}$$

that represents very approximately the distance between the interface point where the cohesion is fully released and the one with maximum traction ahead of the crack tip, such as depicted in Figure A.2-d. The coefficient 0.53 has been determined through exhaustive numerical experimentation. Replacing (A.45) into (A.41), the hardening modulus can be written in term of the interface characteristic length, resulting: $\bar{H} \approx -0.265/\ell_i$, such as sketched in Figure A.2-b.

The present cohesive model has been discussed in detail in Huespe et al. [114]. Here, it is implemented with a regularized continuum damage model (Huespe y Oliver [164]) jointly with slender non-null thickness finite elements. Details of the implementation are presented in Appendix I. Even when the stiffness parameter E_i does not play a significant role in the decohesion properties of the interface, it enters into the expression assessing the characteristic length of the interface in equation (A.45). By considering this aspect of the model, it is reasonable to assume that E_i, in equation (A.45), coincides with the Young modulus of the medium in where the interface is embedded. This choice is implicit in the numerical implementation here adopted.

This interface cohesive model can be considered a particular type of the one reported in Ortiz y Pandolfi [165].

A.2.6. Phase-field jump conditions across $\mathcal{S}$

The specific constraint equation (A.3) adopted in this work is $[\![\varphi]\!] = 0$ for every point in $\mathcal{S}$ and pseudo-time t:

$$\mathcal{R}([\![\varphi]\!](\mathcal{S},t)) = [\![\varphi]\!] = 0\ . \tag{A.46}$$

Thus, $\mathcal{R}^{adj}(\cdot)$ in (A.14) results the identity operator.

A.3. Stress field analysis at the crack tip

The analysis of the stress fields, close to the crack tip, assessed with the numerical phase-field model is presented. These fields are compared with the ones resulting from assuming a Linear Elastic Fracture Mechanics (LEFM) approach. Then, a dominance region of the LEFM solution, in terms of the phase-field regularization parameter, is determined.

The main objective of this Section is to evaluate the connection between the phase-field model regularization parameter and the peak stress attained ahead of the crack.

A.3.1. Comparison with LEFM solutions

The Single-Edge Notched plate in Tension (SENT) shown in Figure A.3-a is numerically simulated. The specimen size are given in terms of a reference length value h=0.05 mm. A notch of size $4h/5$ is originally defined and plane strain conditions are assumed. The panel is stretched with uniform vertical displacements, Δ, on the top. Additional mechanical properties of the test are: Young modulus: $E_{_{PF}} = 148.GPa$, Poisson's ratio: $\nu_{_{PF}} = 0.$, plane Young modulus: $\bar{E}_{_{PF}} = E_{_{PF}}/(1-\nu_{_{PF}}^2)$, and fracture energy, $G_{_{PF}}$, satisfying $G_{_{PF}}/(\bar{E}_{_{PF}}h) = 6.93 \times 10^{-6}$. Three different phase-field regularization parameters: $\ell_{_{PF}} = 0.012h$, $\ell_{_{PF}} = 0.006h$, and $\ell_{_{PF}} = 0.003h$ are tested to assess the outcomes.

We perform the stress analysis once the crack has propagated a small distance from the original notch root after loading. This makes the following results independent of the initial phase-field boundary condition imposed to the notch root nodes.

A.3.1.1. Discussion of results

The components σ_{xx} and σ_{yy} of the stress tensor ahead of the crack tip, assessed with the phase-field model, are plotted in Figures A.3-b, c, and d for the three parameters $\ell_{_{PF}}$. We recall that with such small

internal length scales ($\ell_{PF}/h \ll 1$), the fracture conditions assessed with the numerical simulations are consistent with the LEFM model (Tanné et al. [113]), and the dissipated energy tends to be accurately captured (see Figure 4 in Miehe et al. [57]). This is also in consonance with the matched asymptotic analysis presented by da Silva Jr et al. [166] which, when applied to the present study, identifies ℓ_{PF}/h as a perturbation parameter and shows that the LEFM model emerges as the leading approximation of the phase-field model. See additional discussion in sub-Section A.4.1.1 below.

Two outcomes are next analyzed.

1) Role of the phase-field regularization parameter to estimate the representative peak stress ahead of the crack tip.

   1.a) The peak value of the stress component orthogonal to the crack plane, in terms of ℓ_{PF}, is estimated with the following expression reported in the literature, see Duda et al. [54]

$$\hat{\sigma}_0^c = \frac{3\sqrt{3}}{16}\sqrt{\frac{\bar{E}_{PF}\, G_{PF}}{\ell_{PF}}} \,. \tag{A.47}$$

   In Table A.1, the critical stresses computed with the expression (A.47) are compared with the peak stresses attained with the numerical phase-field model. The numerically assessed peak values correspond to the stress component, σ_{yy}^c, orthogonal to the crack plane. These comparisons are presented for the three parameters ℓ_{PF}. The numerical peak stresses are reported with a small error band due to inherent inaccuracies in the data gathering procedure.

   Implicit in expression (A.47) lies the concept that the model demands a non-null regularization parameter, ℓ_{PF}, to display a bounded critical stress in the material. In this context, ℓ_{PF} should be understood as a characteristic length of the material. Further discussion on this point can be found in Tanné et al. [113].

Tabla A.1: Peak stress analysis vs. regularization parameter of the phase-field model, ℓ_{PF}. Peak stress evaluated with the numerical solution, σ_{yy}^c. Estimated critical stress from expression (A.47), $\hat{\sigma}_0^c$.

$\ell_{PF}\ (mm)$	$\sigma_{yy}^c\ (MPa)$	$\hat{\sigma}_0^c\ (MPa)$
$0.003h$	$2290. \pm 15$	$2310.$
$0.006h$	$1585. \pm 15$	$1633.$
$0.012h$	$1120. \pm 5$	$1155.$

   1.b) In cases where the Poisson's ratio of the medium is different from zero, we estimate the peak stress as follows:

$$\sigma_0^c(\nu_{PF}) = \alpha(\nu_{PF})\hat{\sigma}_0^c \quad , \quad \alpha(\nu_{PF}) = \frac{1}{(1-\nu_{PF}^2)^n} \quad , \quad n = 2 \,, \tag{A.48}$$

   where the expression of the coefficient $\alpha(\nu_{PF})$ is pre-assumed, and the exponent $n = 2$ is determined by adjusting the estimated stress $\sigma_0^c(\nu_{PF})$ with numerical experiments, see Figure A.3-e.

   In the following Sections, expressions (A.47) and (A.48) are taken to estimate the peak stress values computed with the phase-field model in terms of the three parameters ℓ_{PF}, $\bar{E}_{PF}$ and G_{PF}.

2) Matching of stress fields near the crack tip between phase-field and LEFM solutions.

   The stress fields ahead of the crack tip on the crack plane assessed with the numerical phase-field model are compared with the solutions given by the LEFM model. The stress components

of the phase-field solutions, σ_{xx} and σ_{yy}, and the component σ_{yy}^{LEFM} of the LEFM solutions are plotted and compared in Figure A.3-b, c, and d. The stress component σ_{yy}^{LEFM} is computed with the expression:

$$\sigma_{yy}^{LEFM}(x) = \frac{K_I}{\sqrt{2\pi(x - r_0)}} \,, \tag{A.49}$$

where K_I is the stress intensity factor in mode I for the SENT specimen. K_I is determined with the usual formula taken from Anderson [167] and using the numerical average stresses on the specimen top, where displacements are imposed. The coordinate r_0 is calculated through a least square procedure to fit (A.49), in the interval $2\ell_{PF} < x < 0.14h$, to the curve $(\sigma_{yy}(x)+\sigma_{xx}(x))/2$ of the phase-field solution.

On the crack plane, along the x-axis, the analytical LEFM solution predicts an stress state satisfying $\sigma_{yy}^{LEFM}(x) = \sigma_{xx}^{LEFM}(x)$. In consequence, we use the relative difference, δ, between the stress components assessed with the phase-field numerical model, σ_{yy} and σ_{xx}, as a criterion to quantify the matching between both stress fields. The normalized difference δ is defined as $\delta = 2(\sigma_{yy} - \sigma_{xx})/(\sigma_{yy} + \sigma_{xx}))$ and is evaluated at a distance $x - r_0 = 0.04h$ of the estimated crack tip. Figure A.3-f plots δ in terms of ℓ_{PF} for the three analysed cases.

A further criterion to assess the matching between both stress fields is based on analyzing the slope of the curve $\log \sigma_{yy}(x)$ vs. $\log(x)$. This plot is shown in Figure A.3-g for the solution corresponding to $\ell_{PF} = 0.003h$ (see also Figure A.3-d). It is noted that the slope is close to $-1/2$, coinciding with the LEFM solution, only for $(x - r_0) > 4\ell_{PF}$. Such criterion defines the dominance zone of the LEFM solution predicted by the phase-field solution. Alternatively, for distances $(x - r_0) < 4\ell_{PF}$, the non-linear response induced by the phase-field variable dominates the solution. The mechanical behavior in the notch root neighborhood is not governed by the inverse square root singularity characteristic of the LEFM solution.

Consequently, different stress field distributions assessed either by a LEFM approach or by a phase-field model entail a significant influence on the prediction of the interaction mode between a propagating crack and an interface. It is also the reason why the interaction mode analysis may differ substantially in both cases if the distance of interaction is less than $4\ell_{PF}$. This feature is analyzed in detail in the following sections.

The results discussed above corroborate the treatment of da Silva Jr et al. [166] in the sense that within a phase-field description: i) a cracked body can be treated as been divided into three regions, namely an outer region (bulk), an inner region (crack), and an intermediate region; ii) all relevant fields admit outer and inner asymptotic expansions in power of ℓ_{PF}/h which match in the intermediate region.

A.4. Interaction analysis between a propagating crack with an interface. The role played by the phase-field model characteristic length

Interaction problems involving propagating cracks in solids impinging on interfaces under plane strain condition are studied in this Section. A sketch of the problems is shown in Figure A.4-a. The mechanical conditions promoting different interaction modes between cracks and interfaces are specifically analyzed. These modes may result in crack penetration, i.e., when the impinging crack penetrates the interface (Figure A.4-b), or in crack deflection with the posterior propagation toward the interface (Figure A.4-c). In the last case, the adhesive interface is decohesioned displaying likely different opening modes. Further, a third interaction mode can likely happen in where the interface crack kinks out of the interface (Figure A.4-d).

The first problem studied in sub-Section A.4.1 corresponds to an interface orthogonal to the propagating crack direction. In the second problem studied in sub-Section A.4.2, the interface form an angle

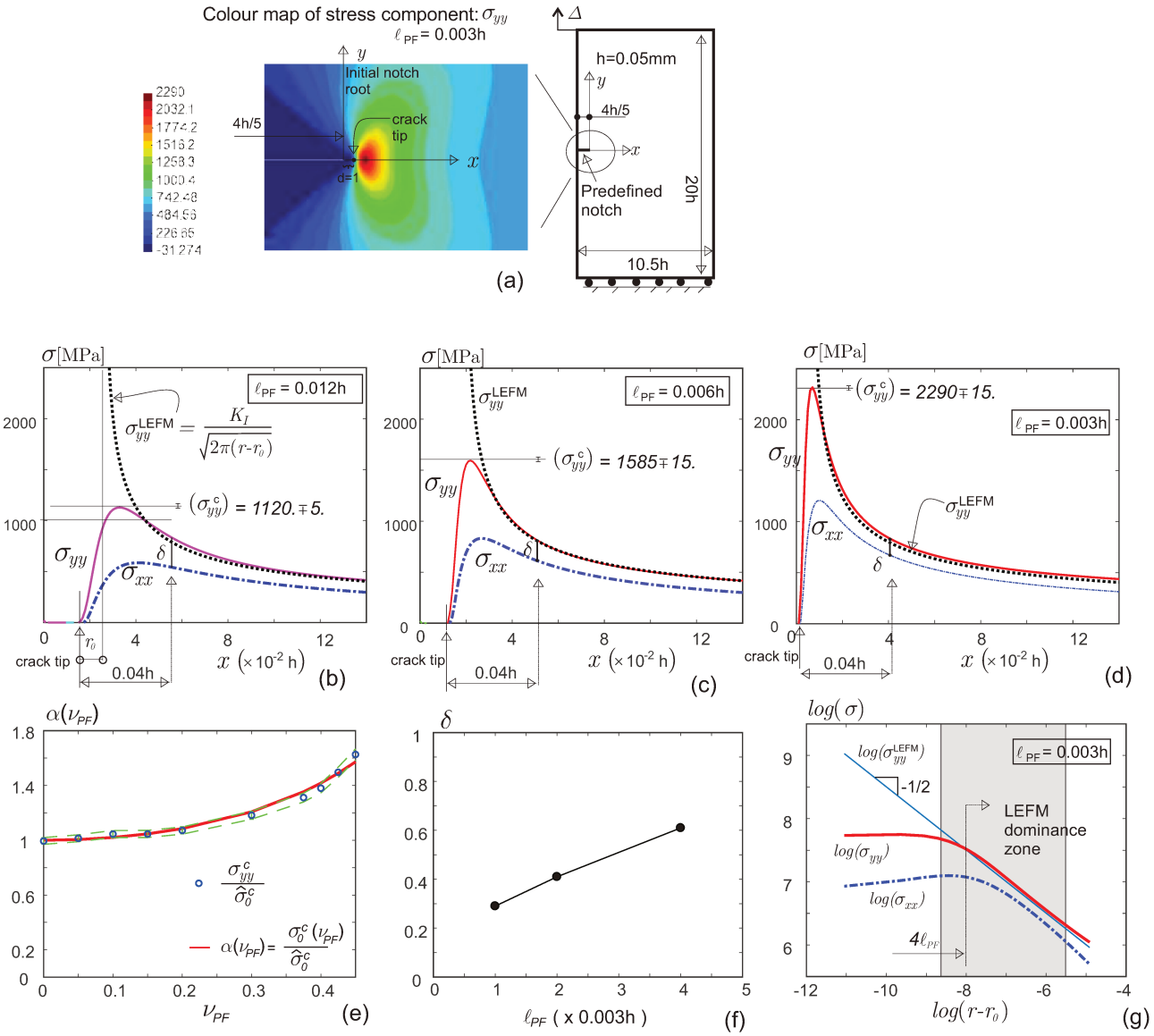

Figura A.3: Single Edge Notch Tension (SENT) specimen. Stress analysis near the crack-tip. a) specimen geometry and loading conditions. Stresses σ_{xx}, σ_{yy} and σ_{yy}^{LEFM} in the crack plane, along the x-axis: b) $\ell_{PF} = 0.012h$, c) $\ell_{PF} = 0.006h$, and d) $\ell_{PF} = 0.003h$. e) Peak stress coefficient, $\alpha(\nu_{PF})$, as a function of the Poisson's ratio. f) Relative difference between stress components σ_{yy} and σ_{xx}, $\delta = 2(\sigma_{yy}(x) - \sigma_{xx}(x))/(\sigma_{yy}(x) + \sigma_{xx}(x))$, evaluated at a distance $x - r_0 = 0.04h$ of the estimated crack tip. g) Plot log-log of stresses σ_{xx}, σ_{yy} and σ_{yy}^{LEFM} in the crack plane, along the x-axis with $\ell_{PF} = 0.003h$.

of $\theta = 30^\circ$ with the propagating crack direction.

In a third sub-Section, we assess the kink of a crack out of the interface, as depicted in Figure A.4-d. In this case, the interfacial decohesion mechanism competes with a crack leaving the interface.

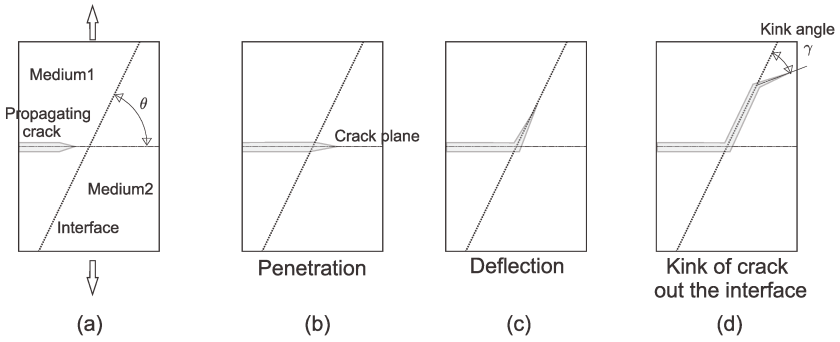

Figura A.4: Interaction modes between a propagating crack impinging on an interface at an angle θ. a) Sketch of the problem. b) Penetration. c) Deflection. d) Kink of the crack out the interface, the crack leaving the interface form an angle γ.

Several parameters govern the interaction modes in this problem. To understand the role played by them, we follow a similar analysis to that adopted by Parmigiani y Thouless [62]. In the paper of Parmigiani et al., the prediction of penetration versus deflection is described in terms of the ratios G_s/G_i and σ_s^c/σ_i^c, where G_i and G_s are the fracture energies of interface and medium 2 in Figure A.4-a, respectively, and σ_i^c and σ_s^c are the critical stresses of the interface and medium 2, respectively. Further parameters of the problem are the Young modulus E_s of medium 1 and 2, Poisson's ratio ν_s, and the interface stiffness modulus E_i. Young moduli are adjusted to define dimensionless number groups similar to those defined in the work of Parmigiani et al.

A relevant conclusion of Parmigiani et al. is that the resulting interaction mode is not only governed by the ratio G_s/G_i, which is expected from a purely energetic point of view, but also on the ratio σ_s^c/σ_i^c. Thus, a mixed toughness–strength criterion determines the condition under which the interaction mode occurs. Using the present phase-field model, we attain a similar conclusion to that reported by Parmigiani et al. However, and due to the stress fields in the medium surrounding the crack tip predicted by the cohesive zone model technique used by Parmigiani et al. are different from those predicted by the phase-field model, the analysis reported by Parmigiani et al. is revisited in the present study and specific conclusions for the particular methodology here reported are drawn.

To carry out a similar analysis to that performed by Parmigiani et al. but using the phase-field model, the characteristic length ℓ_{PF} of the medium has to be connected with a representative critical stress. This objective is achieved by following the conclusions extracted from Section A.3, and particularly, making use of expressions (A.47) and (A.48).

Finite element meshes

We adopt finite element meshes of bilinear quadrilateral elements whose sizes, h^e, satisfy both conditions: i) $h^e \leq \ell_{PF}/3$ and ii) $h^e \leq \ell_i/3$, where ℓ_{PF} is the characteristic length of the material phase-field model where the crack is propagating, and ℓ_i is the characteristic length of the cohesive interface defined in equation (A.45).

In general, this requirement imposes the use of very fine meshes. In the most demanding cases, the finite element sizes have to be of the order $10^{-6}h$ resulting in severe computational burden restrictions on the numerical model.

We simulate the full specimens in all cases, i.e., no symmetry conditions are assumed. Interfaces are modeled with the technique described in Appendix I, thus, slender quadrilateral bilinear finite elements of thickness k are used. The band thickness k is irrelevant in the model if the condition $k \ll \ell_i$ is satisfied.

The coupled mechanical problems involving displacements and phase-field are solved with a stagge-

red time integration scheme, similar to the one described in Table 2 of [54].

Step control methodology

A very rigorous step control methodology is used in the numerical tests. It is based on controlling the relative incremental displacement between two nodes which are separated by the propagating crack, such as depicted in Figure A.5. A set of pair of nodes is defined beforehand. Every pair is defined by a superior node and an inferior node, respect to the crack plane: $[(s_1, i_1), (s_2, i_2), ..., (s_p, i_p)]$. Then, the relative vertical displacement of each pair of nodes is tested in every step of the numerical algorithm. The pair showing the maximum value is taken to control the relative displacement in the next step. A second set of nodes $[(l_1, r_1), (l_2, r_2), ..., (l_q, r_q)]$ is also added to the control scheme which test the horizontal relative displacement of every pair of nodes.

In each step, the displacement increment magnitude is determined by the maximum increment of the phase-field value in the domain. Thus, the maximum increment of the phase-field model per step in the full domain, $\Delta\varphi^{max}_{step}$, has been fixed in the interval $\Delta\varphi^{max}_{step} \in [0.01; 0.03]$ in different situations.

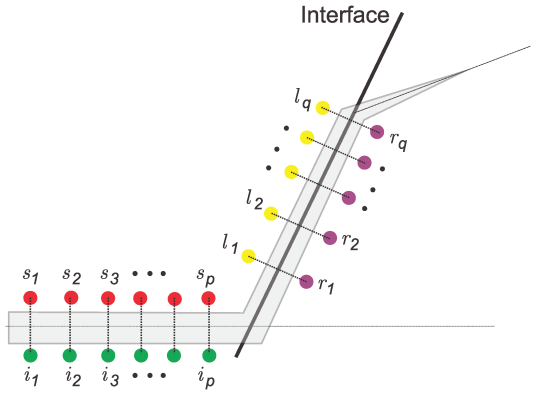

Figura A.5: Step control methodology.

Such control methodology does not apply to simulate general fracture problems. Even though, its use is adequate for the problem simulations addressed in the present work. And most importantly, it allows for a strictly controlled advance of the crack tip, in particular, when the crack intersects the interface, which is an essential requisite for rigorous evaluations of interaction modes.

A.4.1. Interaction mode analysis between a propagating crack and an orthogonal interface

A laminated specimen with a pre-established crack is used to study the interaction mode between a propagating crack and an interface. The geometrical configuration is a single edge-notched specimen displayed in Figure A.6-a.

The specimen is constituted by a fiber, of thickness h, bonded to a substrate of thickness $10h$. The specimen height is $20h$. An initial predefined crack of size $4h/5$ exists in the fiber at the middle of the specimen height. A uniform vertical displacement is imposed on the specimen top. In the initial loading stage, the crack propagates across the fiber the distance of $h/5$ till intersecting the interface. Considering that peak stresses play an important role in the interaction model, as well as the results that are shown in Figure A.3b-d, this first crack propagation stage allows for the full development of the peak stresses in front of the crack tip before its interaction with the interfaces.

A phase-field model simulates the crack propagation in the fiber and substrate. The fiber properties are: Young modulus, E_f, Poisson's ratio, ν_f, fracture energy, G_f, and phase-field model regularization parameter, ℓ_f. The plane strain elastic modulus is $\bar{E}_f = E_f/(1-\nu_f^2)$. Similarly, the substrate properties

are E_s, ν_s, G_s, ℓ_s, with a plane strain elastic modulus $\bar{E}_s = E_s/(1-\nu_s^2)$. The fiber-substrate boundary is modelled as a cohesive interface characterized by a critical stress σ_i and a fracture energy G_i. The interface characteristic length, ℓ_i, is estimated with the expression (A.45).

It has been reported in the literature that the relative fiber-substrate stiffness plays a role in determining the interaction mode in this problem. Following to Dundurs [168], the effect of considering relative stiffness on the stress state is taken into account through only two parameters defined as follows:

$$\alpha = \frac{\bar{E}_f - \bar{E}_s}{\bar{E}_f + \bar{E}_s} \quad ; \quad \beta = \frac{(\lambda_f/\nu_f) - (\lambda_s/\nu_s)}{(\lambda_f/\nu_f) + (\lambda_s/\nu_s)} \,, \tag{A.50}$$

where λ_f, λ_s are the Lamè coefficients ($\lambda = E\nu/((1-2\nu)(1+\nu))$) of fiber and substrate, respectively. We call α and β the first and second Dundur's parameters.

A.4.1.1. Analysis with identical fiber and substrate properties

Two series of simulations are performed with identical fiber and substrate elastic and fracture properties: $\bar{E} = \bar{E}_f = \bar{E}_s$, and $\nu = \nu_f = \nu_s = 0$ $G_s = G_f$, $\ell_f = \ell_s$. Thus, in all these cases, the first and second Dundur's parameters are $\alpha = \beta = 0$.

We adopt similar dimensionless groups to those reported in Parmigiani y Thouless [62] to assess the problems. They are:

- **Series a:** The first series of simulations are performed with the following interface properties: $G_i\bar{E}/((\sigma_i^c)^2 h) = 0.1$ and $G_i/(\bar{E}h) = 10^{-6}$.
- **Series b:** The second series of simulations are performed with the following interface properties: $G_i\bar{E}/((\sigma_i^c)^2 h) = 1.$ and $G_i/(\bar{E}h) = 10^{-6}$.

With these established conditions on the interface model, the pair of substrate fracture properties, G_s and σ_s^c, which are defined relative to the interface fracture properties, $(G_s/G_i, \sigma_s^c/\sigma_i^c)$, are used to systematically characterize the interaction modes between the propagating crack and the interface. Thus, we summarize the full sets of numerical tests in the space $(G_s/G_i, \sigma_s^c/\sigma_i^c)$, and describe regions where different modes of interaction are observed. We recall that the parameter σ_s^c of the substrate phase-field model is handled trough the characteristic length ℓ_s connected by equations (A.47) and (A.48).

The interaction modes for both series of results are summarized in Figure A.6-b. For each series of tests, two curves in red and blue lines with their corresponding symbols are shown. Points in red squares represent numerical solutions displaying a propagating crack deflecting into the interface. Points in blue circles identify numerical solutions displaying a propagating crack that penetrates the substrate. These results suggest that there exist limit curves, which are plotted in black dotted lines in the Figure, separating two disjoint zones. The right-upper part of the plot represents those problems in where the crack likely deflects toward the interface. Contrarily, the left lower part of the plot represents those problems in where the crack likely penetrates the substrate. Tests of Series a and b show a similar trend.

Discussion of results: similarly to the work of Parmigiani et al., we conclude that low ratios G_s/G_i and σ_s^c/σ_i^c promotes the penetration mechanism. Contrarily, high values of these ratios promotes the deflection mechanism.

Furthermore, as the ratio σ_s^c/σ_i^c decreases, the curve in black dotted lines approaches to a vertical asymptote of value $\sigma_s^c/\sigma_i^c \approx 2.5$ for the tests denoted *"Series a"* , and $\sigma_s^c/\sigma_i^c \approx 3$ for the tests denoted *"Series b"*. Similar trends have also been reported by Parmiggian et al., though, for analogous material parameters, these authors find asymptotic values of σ_s^c/σ_i^c which are marginally larger than the ones here reported.

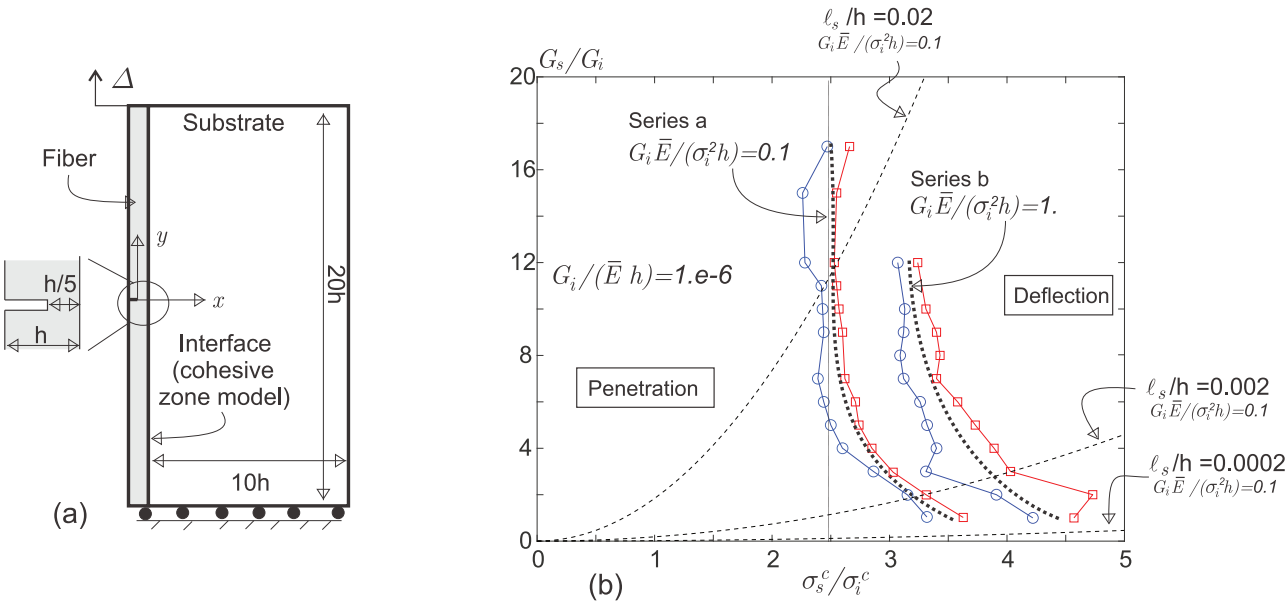

Figura A.6: Interaction analysis among a crack impinging an orthogonal interface with similar fiber-substrate stiffness. a) Geometrical configuration of the laminated edge-cracked panel. b) Analysis with identical fiber and substrate properties (Dundurs's parameters are $\alpha = \beta = 0$). Series a and b of tests are shown. Points in red squares represent solutions displaying a propagating crack deflecting into the interface. Points in blue circles represent solutions displaying a propagating crack penetrating the substrate.

Simulations with high ratios G_s/G_i reveal that the change of the interaction mode only depends on the ratio σ_s^c/σ_i^c but not on the ratio G_s/G_i. Thus, in this region of the parametric space $(G_s/G_i, \sigma_s^c/\sigma_i^c)$, the interaction mode penetration/deflection strictly depends on a strength criterion.

Contrarily, for low ratios G_s/G_i, the limit curve in black dotted lines seems to show a tendency toward an asymptotic horizontal value. Though, it is not clear that an asymptotic value exists. When this curve approaches very low values of G_s/G_i, the parameter σ_s^c/σ_i^c would not play a prominent role for determining the change of the interaction mechanism. Thus, in this region of the space, the interaction mode penetration/deflection likely depends on a toughness criterion.

Between both limit scenarios, the prediction of the interaction mode according with the present approach depends on both ratios, and therefore, a mixed strength/toughness criterion governs the interaction mode. This conclusion completely agrees with that reported by Parmigiani et al.

An analysis of a similar interaction problem has been performed by He y Hutchinson [140] using a LEFM approach, see also Lee et al. [169]. According to He et al., when $G_s/G_i < 4$, the propagating crack likely penetrates the substrate. Contrarily, if $G_s/G_i > 4$, the propagating crack likely deflects into the interface. Such as expected from a LEFM analysis, it is a toughness criterion. Parmigiani et al. have studied the reasons why the interaction analysis determined with the cohesive zone model approach does not agree with the result of He et al. A similar argument used by Parmigiani et al is also valid for explaining the conclusions obtained with the phase-field model.

The numerical simulations of problems corresponding to the lower right part of the plot in Figure A.6-b entail a challenge for the present approach. These problems request extremely small characteristic lengths of the substrate. By a simple manipulation of equation (A.47), we can plot the iso-level curves of ℓ_s/h in the parametric space $G_s/G_i, \sigma_s^c/\sigma_i^c$. These curves are shown for two small values of characteristic lengths: $\ell_s/h = 0.002$ and $\ell_s/h = 0.0002$ related to the *"Series a"* problems. Thus, to simulate a test in the region where these curves intersect the limit black dotted line, we need to define very low values of ℓ_s compared with h. This aspect of the problem demands finite element meshes with prohibitively small elements, even in 2-D problems. A similar adverse situation happens when the cohesive zone model is

used in bulk material and interface to evaluate points in the same region of the space $(G_s/G_i, \sigma_s^c/\sigma_i^c)$, such as mentioned in Parmigiani y Thouless [62].

Furthermore, recalling the analysis performed by Miehe et al. [57], the accuracy of the phase-field technique for capturing the fracture energy of the model depends mainly on the size of the regularization parameter. This size is assessed relative to some characteristic structural length, the initial crack length in this case. The conclusion drawn from Miehe et al. is that the accuracy to capture the fracture energy of the model decreases with the increase of the parameter ℓ_s/h. This issue determines a further restriction on the FE model that has to be contemplated in the present interaction analysis. Thus, an empirical criterion is adopted by which the points of the plane $(G_s/G_i, \sigma_s^c/\sigma_i^c)$ above the iso-level curve $\ell_s/h = 0.02$ involve inaccuracies which may yield wrong conclusions about the interaction mechanism. This iso-level curve is plotted in the Figure A.6-b for the Series b problems. Further analysis about the influence that the regularization parameter size has on crack propagation problems modeled with a phase-field approach has been reported in Tanné et al. [113].

It is noted that we have not attained any result displaying a single deflected crack branch on the interface, such as reported by He y Hutchinson [140], even introducing small perturbations to induce the activation of this propagation mode. The reason why we do not obtain such solutions may be due to the relatively large characteristic lengths adopted in the numerical simulations that preclude this phenomenon. Such as mentioned above, the simulation of problems with even lower values of ℓ_s and ℓ_i than those adopted to plot the points in Figure A.6-b involves very high computational burden.

A.4.1.2. Analysis with dissimilar fiber and substrate properties

Next, we analyse interaction problems using the same edge-cracked specimen of Figure A.6-a and identical fiber-substrate fracture parameters $G_s = G_f$ and $\ell_s = \ell_f$, but with dissimilar stiffness.

The fiber-substrate stiffness satisfy two sets of Dundurs' parameters:

- **Case a)**: $\alpha = -0.5$, $\beta = 0$.
- **Case b)**: $\alpha = +0.5$, $\beta = 0$.

These parameters correspond to a compliant fiber and stiff substrate for **case a**, and a stiff fiber and compliant substrate for **case b**. Additionally, the dimensionless number group relating the interface properties are similar to those defined in the "Series a" problems above. They are: $G_i E_i/((\sigma_i^c)^2 h) = 0.1$ and $G_i/(E_i h) = 1. \times 10^{-6}$. In each case, a) or b), the interface stiffness parameter, E_i, is equal to the Young modulus of the softer material between fiber or substrate.

Figure A.7-a and b display the results for both cases in the space $(G_s/G_i, \sigma_s^c/\sigma_i^c)$. A similar general trend to that observed in the previous analysis, with identical fiber-substrate elastic properties, are replicated. The right-upper part of the plots corresponds to problems displaying crack deflection along the interface, and the left-lower part of the plot identifies problems displaying penetration in the substrate. The difference observed between both set of tests and the estimated limit curve in black dotted lines, with $\alpha = -0.5$ and $\alpha + 0.5$, is marginal.

According to the results reported by Parmigiani y Thouless [62] for similar problems but using a cohesive zone model to simulate the crack propagation across the substrate, the limit curves separating penetration from deflection are notably different for cases a and b. Figure A.8-a,b depict the deformed configurations of the specimens when a crack deflection into the interface happens. These configurations correspond to $\alpha = -0.5$ and $\alpha = 0.5$, respectively. It is noted a feature related to the interface opening mode, and which is mentioned by Parmigiani et al. When the fiber is compliant ($\alpha = -0.5$), the dominant opening mode of the crack on the interface tends to be mode I. Contrarily, when the fiber is stiff ($\alpha = 0.5$), the opening mode of the interface crack tends to be a slip mode. The interface decohesion model used in this work does not distinguish dissimilar fracture energies between modes I and II of crack opening.

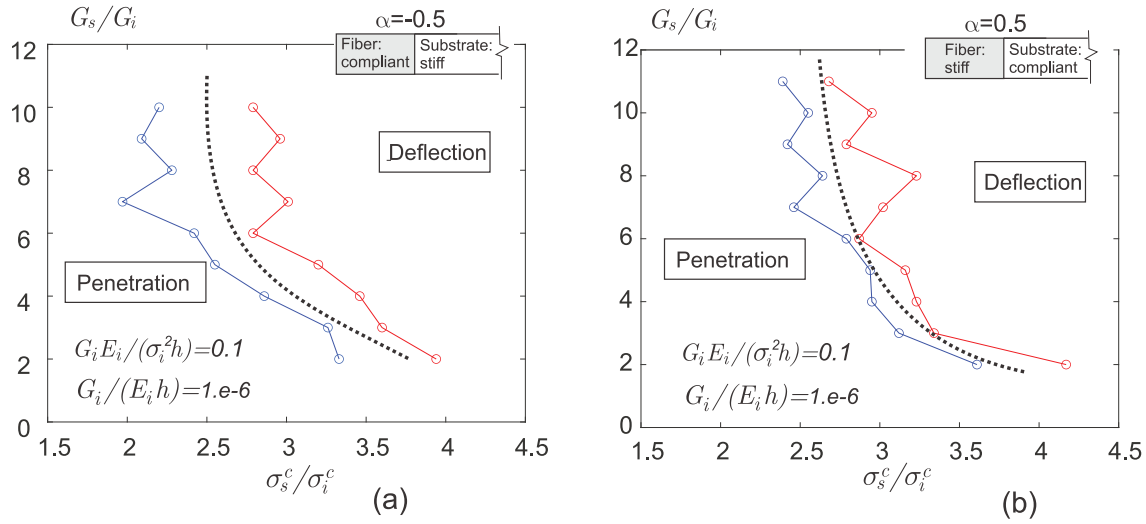

Figura A.7: Interaction analysis among a crack impinging an orthogonal interface with dissimile fiber-substrate stiffness. a) Dundurs's parameters $\alpha = -0.5$ and $\beta = 0$ (compliant fiber and stiff substrate). b) Dundurs's parameters $\alpha = 0.5$ and $\beta = 0$ (stiff fiber and compliant substrate). Points in red squares identify solutions displaying a propagating crack deflecting into the interface. Points in blue circles identify solutions displaying a propagating crack penetrating the substrate. E_i is the Young modulus of the softer material.

This model feature may be the reason for inducing a low sensitivity of the present technique to capture dissimilar responses in the cases a and b.

Figure A.8-c shows the phase-field iso-curves at the instant when the propagating crack in the fiber is close to impinge the interface. It is remarked the continuity of the iso-curves across the interface attained with the present model. In this specific case, the slope continuity across the interface of the iso-curves is also preserved due to the identical fracture parameters of fiber and substrate (recall the balance equation (A.15) across the interface together with the constitutive definition for $\boldsymbol{\xi}$ in (A.31)).

A.4.2. Interaction between a propagating crack impinging an interface with an inclined angle

The interaction analysis of a propagating crack impinging an inclined interface is presented. The geometrical configuration of the problem is depicted in Figure A.9-a. It is a square specimen with $h = 1mm$ and a pre-established crack of $0.47mm$ along the x-axis. The specimen is stretched by imposing a uniform vertical displacement, Δ, on the top. The interface is at a distance 0.03mm from the pre-established notch root and forms an angle of $30°$ with the horizontal direction. After loading, the crack propagates almost horizontally impinging the interface.

Similar to the analysis in the sub-Section above, we assess the medium and interface material fracture parameters promoting either the crack penetration or deflection toward the interface.

The stiffness and fracture properties of the medium are the following: the Young modulus is $E_s = 2080.MPa$, the Poisson's ratio is $\nu_s = 0.375$, the fracture energy, G_s, satisfies $G_s/(\bar{E}_s h) = 1.9 \times 10^{-4}$ and $\ell_s = 0.003h$ (with the plane strain Young modulus $\bar{E}_s = E_s/(1-\nu_s^2) = 2420.MPa$). Identical properties are defined for the medium at both sides of the interface. These properties are kept fixed for the full set of tests.

The interface properties G_i and σ_i^c are modified in each test. They are adopted to assess the limit curve in the space $(G_s/G_i, \sigma_s^c/\sigma_i^c)$ separating different interaction modes between the crack and interface. The results are plotted in Figure A.9-b. The red squares in the plot correspond to solutions in where the propagating crack deflects toward the interface. Alternatively, the blue circles are solutions displaying crack penetration. Thus, the black dotted line results an estimation of the limit curve separating both

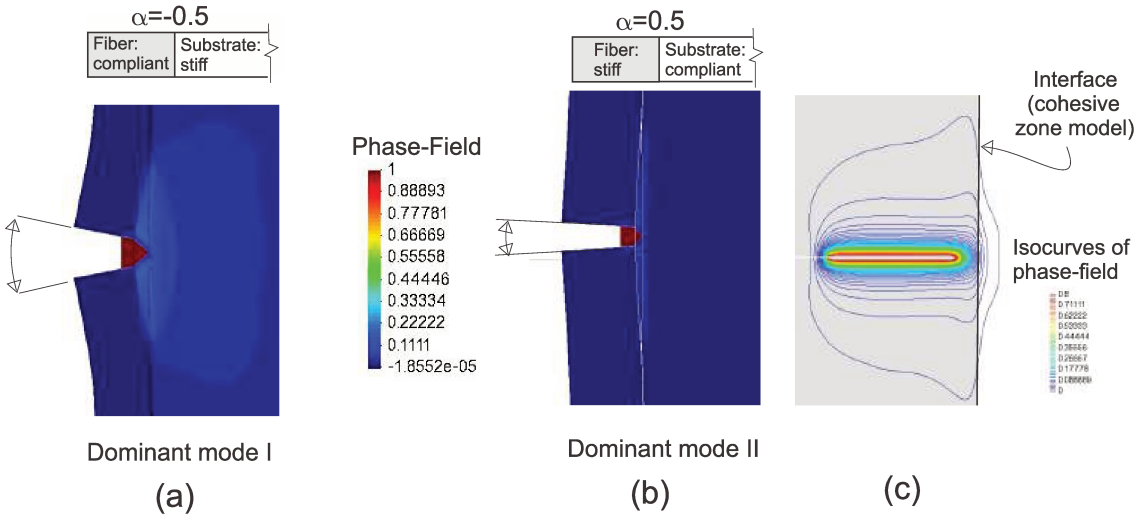

Figura A.8: Interaction analysis between a crack impinging an orthogonal interface with dissimilar fiber-substrate stiffness. a) Deformation mode of crack deviating into the interface: $\alpha = -0.5$. The interface opening displays a dominant mode I. b) Deformation mode of crack deviating into the interface: $\alpha = 0.5$. The interface opening displays a dominant mode II. c) Iso-curves of phase-field when the crack in the fiber is close to impinge the interface.

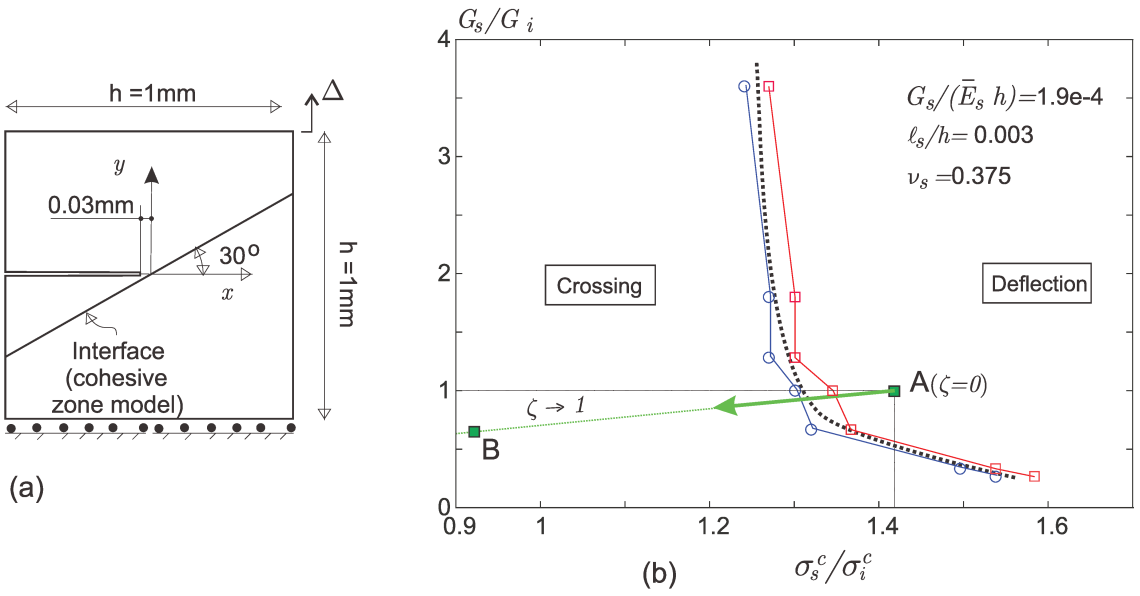

Figura A.9: Interaction between a propagating crack impinging an inclined interface. a) Specimen geometrical configuration. b) The limit curve in black dotted line separates the regions where deflection, or crossing, are observed. Points in red square represent solutions displaying a propagating crack deflecting into the inclined interface. Points in blue circles represent cracks crossing the interface.

interaction modes.

Similarly to the problems studied above, we note that deflection of the crack into the interface is promoted with relatively low interface toughness and strength (G_i and σ_i^c). Contrarily, relatively high interface toughness and stiffness promotes the crack crossing.

A.4.3. Analysis of a crack kinking out of an interface

The kink of a crack out an interface, phenomenon schematized in Figure A.4-d, has been widely analyzed in the literature by assuming that a putative pre-existing crack intersecting the interface induces the crack deviation into the medium, see He y Hutchinson [170] and Martinez y Gupta [141]. For a general setting of cracks kinking in solids without interfaces and with anisotropic elastic properties, see Tankasala et al. [171]. Alternative numerical analysis have also been used. For example, Pro et al. [172] study this phenomenon by modelling interface and bulk material with a cohesive zone approach. Experimental results displaying kink off configurations for cracks incident to interfaces between 90° and 75° are shown in Alam et al. [116].

Kinking of a crack out of an interface results from two competing mechanisms, namely, the interface decohesion process and the crack leaving the interface and propagating in a different direction. In such competition, the kink angle γ between the crack penetrating the medium and the interface is part of the problem solution and plays a significant role in determining which of both mechanisms is the predominant one. Considering this picture, we next analyze a problem where a crack kinks out of an interface. Two outcomes of the problem are specifically studied, the spatial position where the crack abandons the interface and the kink angle γ. We assess their insensitivity to the finite element discretization by comparing two solutions obtained with different finite element meshes.

The simulated problem corresponds to the same specimen shown in Figure A.9-a. The fracture and stiffness properties of the medium are identical to those described in the analysis of the sub-Section A.4.2, i.e., $E_s = 2080.MPa$, $\nu_s = 0.375$, $G_s = 0.46$ and $\ell_s = 0.003h$. Identical properties are defined for the medium at both sides of the interface. These properties are kept fixed for the full set of tests.

The specimen is modeled with two finite element meshes that are structured only in the region where the crack leaves the interface, see details in Figure A.10d-e. In this region, the finite element sizes are $h^e = 3.25 \times 10^{-4} mm$ and $h^e = 7.5 \times 10^{-4} mm$, respectively. Additionally, the directions of the structured meshes are markedly different in both cases, as noted in the detail of Figure A.10d.

Such as mentioned above, the upper-right region of the plot in Figure A.9-b represents the interface properties, relative to the medium properties, of problems in where cracks propagating in the medium deflects toward the interface. By exploring numerically this region, we have not found any case resulting in a crack kinking out of the interface. It means that, at least for the tested set of parameters, problems displaying cracks deflecting into the interface do not find the necessary mechanical conditions for the posterior kinking out of the interface.

Thus, to induce the conditions promoting the initial deflection of the crack toward the interface and the posterior kink of the crack out the interface, we manipulate the interface fracture parameters by increasing the values of G_i^A and $(\sigma_i^c)^A$ along the interface to trigger the kink off, see Pro et al. [172]. We define a set of interface fracture parameters G_i^A and $(\sigma_i^c)^A$ which are in correspondence with the point A in the plot of Figure A.9-b. The interface parameters are increased proportionally to the square of the relative distance, ζ, to the origin of coordinates:

$$G_i(\zeta) = (1+\zeta)^2 G_i^A \qquad , \qquad \sigma_i^c(\zeta) = \frac{(1+\zeta)^2}{1.417} (\sigma_i^c)^A \ , \tag{A.51}$$

The origin of coordinates is approximately the intersection point between the propagating crack and the interface, see the sketch in Figure A.10-b displaying ζ. Note that $\zeta = 1$ identifies the intersection point between the interface and the specimen boundary. Also, note that as ζ increases, the ratio $G_s/G_i, \sigma_s^c/\sigma_i^c$

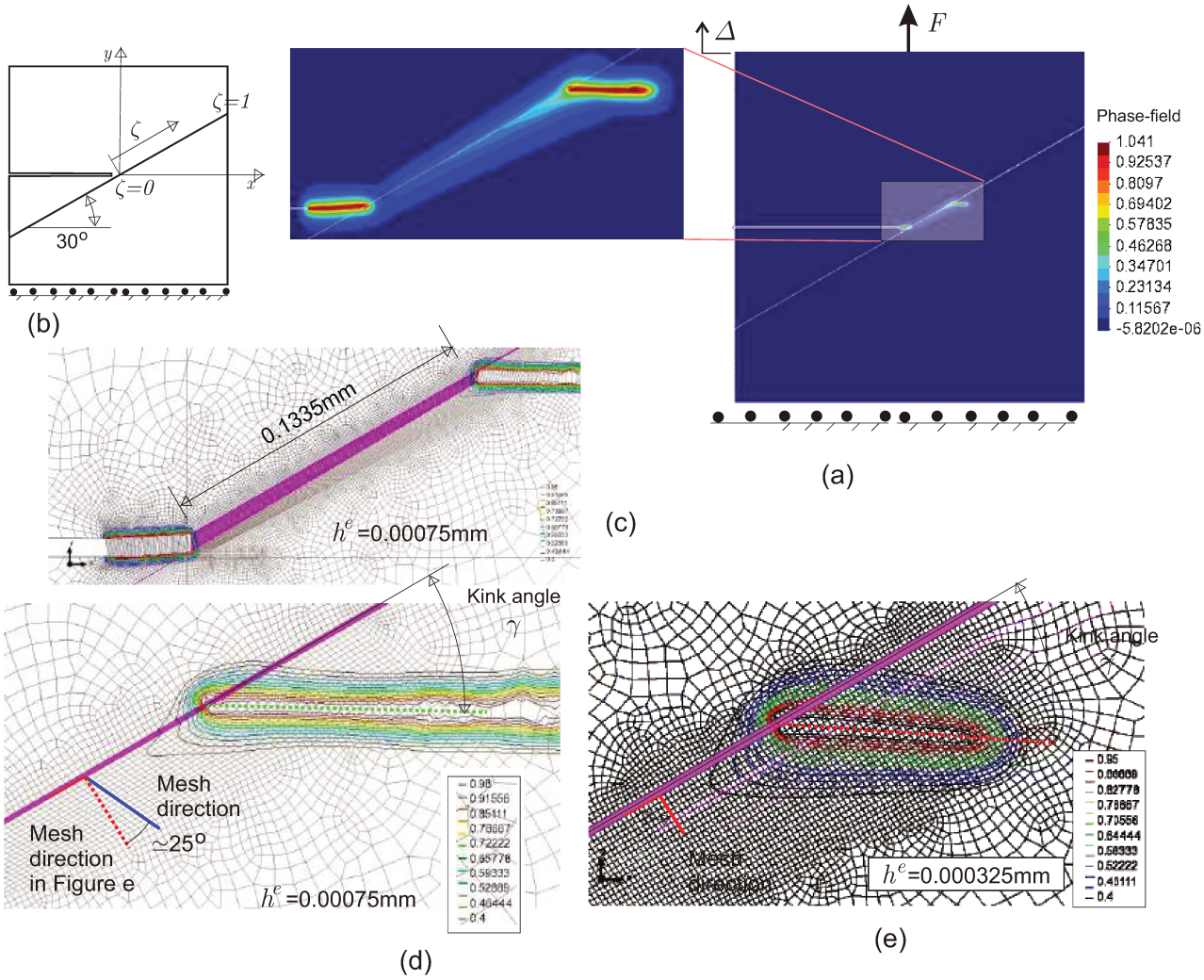

Figura A.10: Analysis of a crack kinking out of an interface. a) Iso-maps of phase-field at the end of analysis. b) The interface parameters changes with the coordinates ζ. c-d) Deformed mesh and phase-field iso-curves, mesh with $h^e = 7.5 \times 10^{-4} mm$. e) Phase-field iso-curves, mesh with $h^e = 3.25 \times 10^{-4} mm$.

decreases. Thus, the variations of the interface fracture properties are represented in the plot of Figure A.9-b with the green segment. Point A corresponds to the interface properties at $\zeta = 0$. Also, note that ℓ_i is proportional to $(1+\zeta)^{-2}$, thus, the interface characteristic length decreases with ζ favouring the kinking off.

With the so-defined interface properties, the crack initiating on the notch root is compelled to deflect toward the interface and posteriorly to abandon the interface.

Figure A.10-a displays the iso-map of phase-field after the crack kinks out of the interface and propagates across the medium. The crack abandons the interface at a distance $\zeta = 0.1335mm$, determined with the coarse mesh (see Figure A.10-c), and $\zeta = 0.1358mm$, determined with the fine mesh. This result means that the conditions where the kink of the crack happens are: $G_s/G_i = 0.65$ and $\sigma_s^c/\sigma_i^c = 0.92$ and are plotted as the point B in Figure A.9-b. The kink angles γ determined with both finite element meshes differ in $2.5°$.

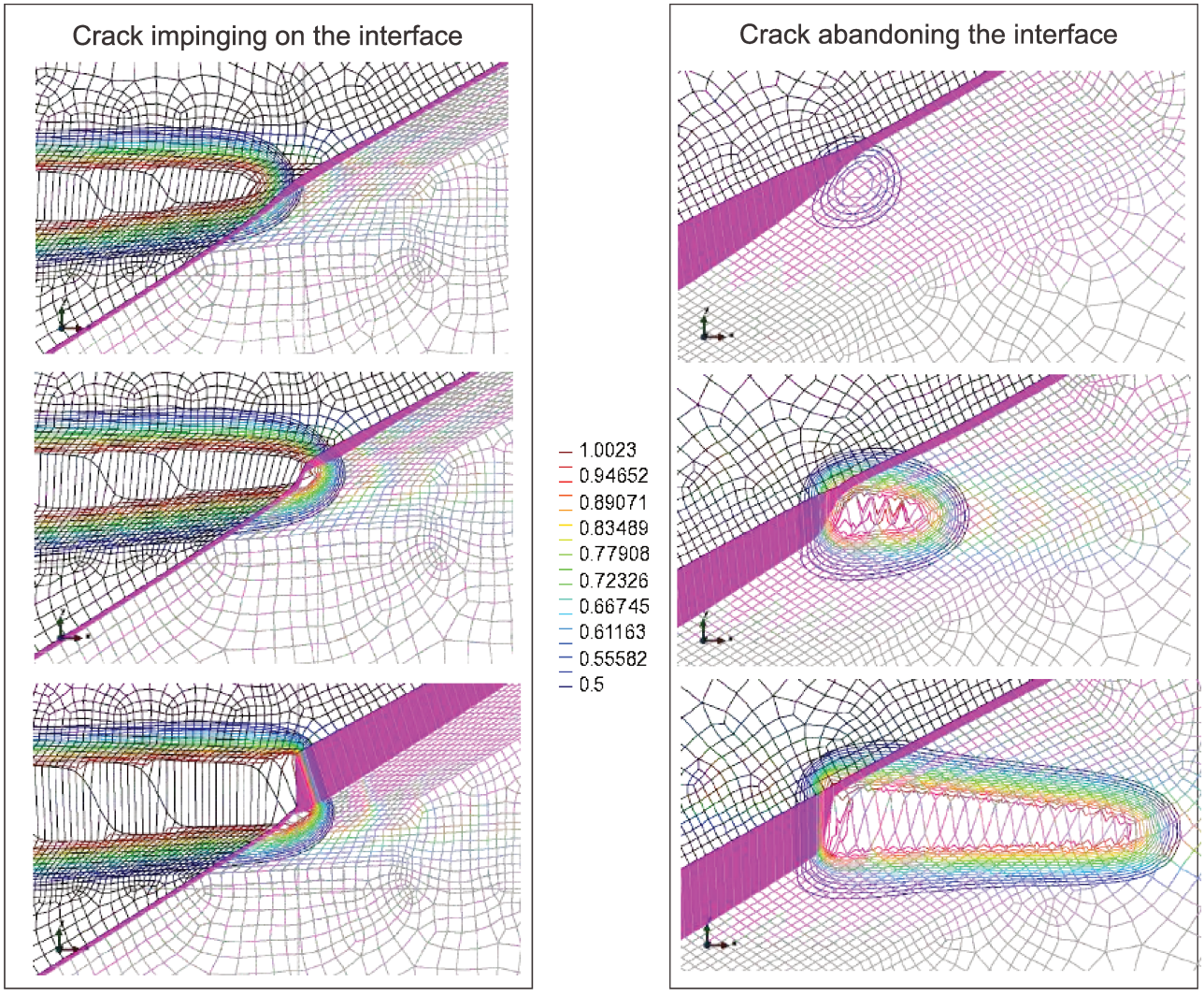

Figura A.11: Analysis of a crack kinking out of an interface. Sequence of deformed meshes and phase-field iso-curves, at different stages of the loading process. Mesh with $h^e = 7.5 \times 10^{-4} mm$. Left column: the crack impinges on the interface. Right column: the crack abandons the interface.

Figure A.11 displays the deformed mesh and the phase-field iso-lines when the crack impinges on the interface (pictures on the left column) and when the crack abandons the interface (pictures on the right column). Only simulations with the coarse mesh are depicted. Observe that the interface is open in

the portion between both cracks propagating in the medium. The pictures on the right column show that the direction of the structured finite element mesh is not coinciding with the crack propagation direction. In the same figure, it can be observed that the intersection angle among the phase-field iso-lines and the interface are non-orthogonal in both analyzed regions. This effect is a direct consequence of the imposed phase-field continuity conditions across the interface and evidences the ability of the methodology to capture the kink angle γ independently of the mesh directionality.

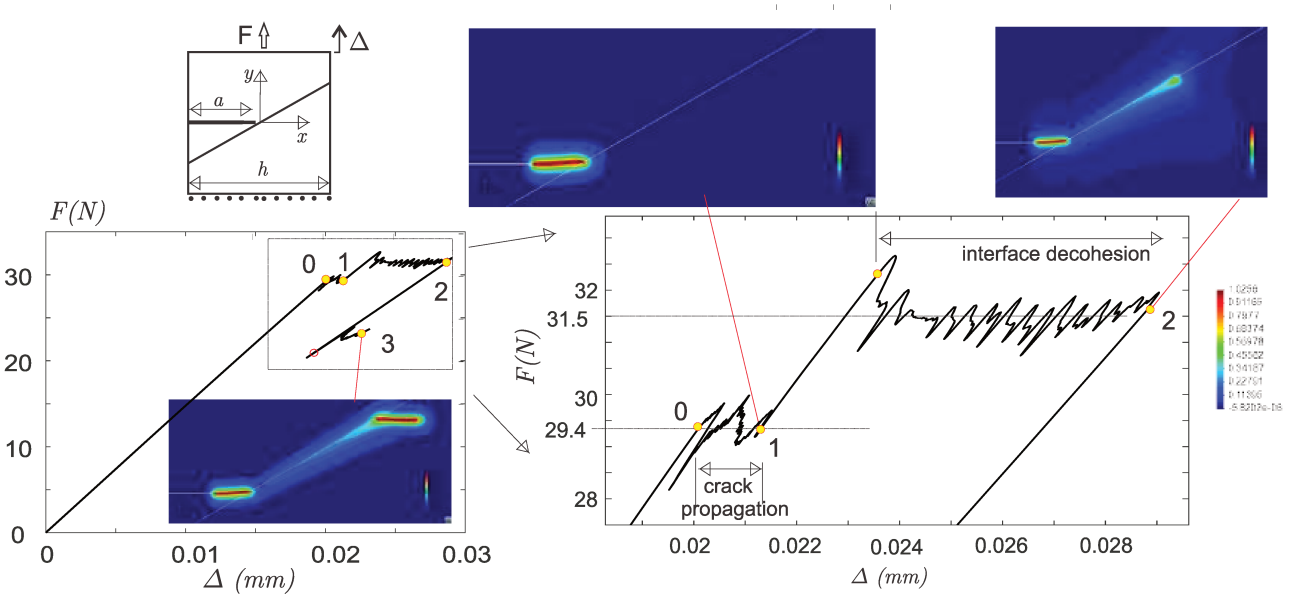

Figura A.12: Analysis of a crack kinking out of an interface. Structural load F versus displacement Δ curve (left plot) and detail of the peak loads (right plot). Mesh with $h^e = 7.5 \times 10^{-4} mm$. Point 0 identifies the initiation of crack propagation; Point 1 identifies the crack impinging on the interface; Point 2 identifies the crack abandoning the interface; Point 3 corresponds to the end of analysis.

A.4.3.1. Apparent toughness increment of the specimen

Figure A.12 plots the structural load, F, versus the vertical displacement of the specimen top, Δ. This curve is smoothed by using a weighted averaged technique involving 5 neighbour steps. The loading control strategy allows for attaining such unstable response. It can be observed the total load at different stages during the loading process. Point 0 shown in the inset of the Figure corresponds to the crack initiation instant. Point 1 indentifies the instant when the crack impinges on the interface, and Point 2 corresponds to the kink of the crack out the interface. Between Points 0 and 1, the crack propagates from the notch root to the interface. This process is carried out at an almost constant load $F \approx 29.4N$. Using the formula reported in Shah et al. [173], the stress intensity factor, according with this load, at which the crack is propagating is:

$$K_I = 0.9841 \frac{F}{h} \sqrt{\pi a} = 36.3 N mm^{-3/2} \text{ ; (specimen with unit thickness).} \tag{A.52}$$

Thus, considering the material toughness:

$$K_{IC} = \sqrt{\bar{E}_s G_s} = 33. N mm^{-3/2} , \tag{A.53}$$

the numerical estimation (A.52) attained with the phase-field model is $10\,\%$ higher than K_{IC}. This figure is within the range of variations estimated for stress intensity factors by different authors and numerical techniques, see Shah et al. [173], as well as, the computed values of K_I using phase-field models in

Tanné et al. [113].

Considering the peak loads in the detail of Figure A.12 (right plot), it is noted that the crack deflection process toward the interface demands a notable increment of load, F, to approximately $31.5N$. This outcome implies an appreciable increment of the specimen apparent toughness. To understand this effect assessed by the model, we perform additional analysis. First, in Figure A.13, we compare the peak loads F resulting from two additional tests:

i) **Specimen with a strong interface:** in this analysis, we assume an interface having a high strength, σ_c^i, which results in an interface remaining fully cohesioned during the loading process. The red curve of Figure A.13 displays the F vs. Δ response of this test. We note that the crack propagation process across the right part of the specimen, after penetrating the interface, demands a load F approximately equal to $29.4N$ displayed between Points 0 and 1 in Figure A.12.

ii) **Specimen with a notch intersecting the interface:** in this test, the materials properties are the original ones specified in sub-Section A.4.3, and the specimen notch is enlarged, along the x-axis, to intersect the interface. The resulting F vs. Δ response is plotted with the blue curve in Figure A.13. Also in this case, the crack propagation load is approximately $29.4N$.

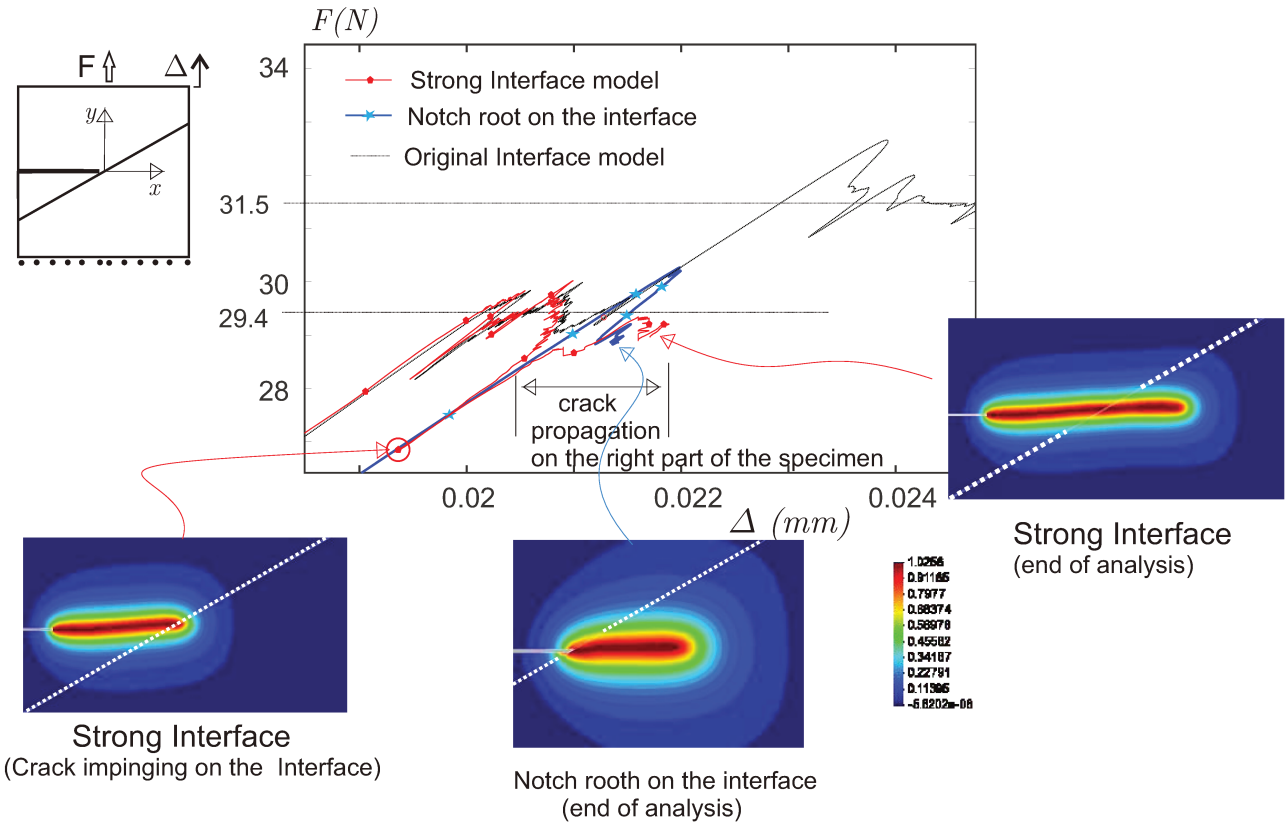

Figura A.13: Curves F vs. Δ of three tests. a) Strong interface (red curve). b) Notch root intersecting the interface (blue curve). c) Original test taken from Figure A.12 (black curve).

According with both results, it is not observed the apparent toughness increment of the specimen depicted in Figure A.12. Therefore, we conjecture that the outcome in Figure A.12 is due to a shield effect produced by the interface degradation which happens before the crack impinges on it. This effect is analyzed in Figure A.14. Let us consider the problem where the material parameters of the substrate are: $E_s = 2080MPa$; $\nu_s = 0.375$; $G_s = 0.45N/mm$, $\ell_s = 0.003mm$, and interface parameters are: $G_i = 0.45N/mm$, and $\sigma_i^c = 190MPa$.

Figure A.14-a displays the stress field $\sigma_{yy}(x)$ ahead of the crack tip, along the x-axis, just after the crack starts to propagate. The peak stress is approximately $250MPa$. The stress values which are similar to the interface strength are observed at a distance of $3.2\ell_s$ ahead of the crack tip. Considering the positive tensile stress state in this region, we can predict that the advancing crack will induce the opening of the interface before it impinges on the interface. Figure A.14-b shows this effect. Such interface degradation yields a stress drop in the medium, on the right part of the interface, such as shown in Figure A.14-c. This Figure plots the principal stresses along the coordinate ζ for points on the right and left of the interface. These plots correspond at a time before the crack impinges on the interface. The maximum principal stresses on the right part of the specimen are lower than that observed for the neighbor points on the left part of the specimen. The lower stress level prescribes the specimen damage evolution on the right of the interface and is the reason why the crack does not penetrate the interface but deflects toward the interface demanding even higher external loads.

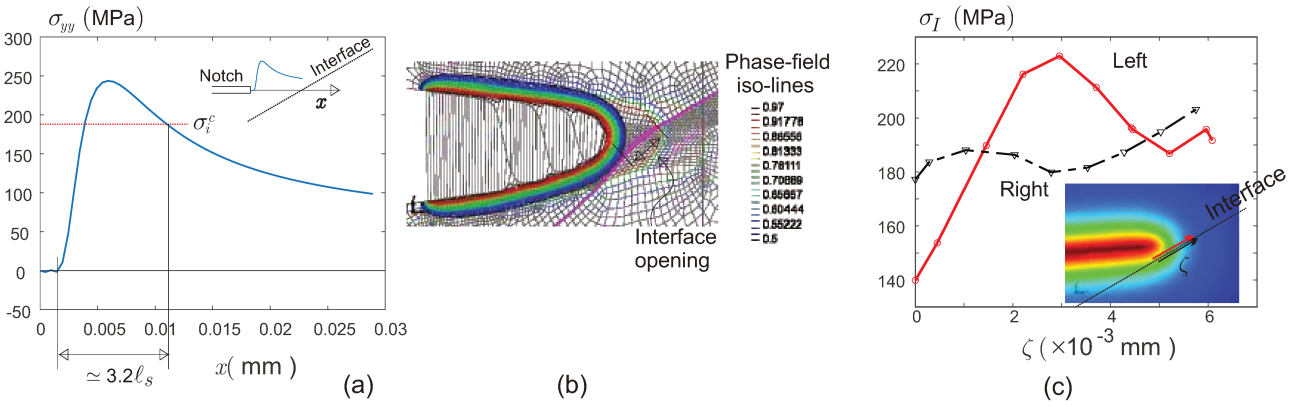

Figura A.14: Shield effect induced by the interface degradation. a) Stress field $\sigma_{yy}(x)$ ahead of the crack tip, along the x-axis. b) Deformed mesh displaying the interface opening before the crack impinges on the interface. c) Principal stress, σ_I, along lines parallel to the interface, on the left and right points of the substrate.

A.5. Conclusions

The numerical technique reported in this work is conceptually very simple. It is a mixture of two well-known models. A phase-field approach formulated in a very general context including jump conditions in the phase field descriptor and a traditional cohesive surface model. Once specialized the general formulation of the phase-field approach results in a very conventional methodology which follows closely the one introduced by Miehe et al. [57].

The specific particularity in the present model results from considering the phase-field regularization parameter as a material characteristic length in conjunction with cohesive surfaces, which are also characterized by its own characteristic length. We prove that this rather simple model captures complex responses of crack interactions problems, that it provides similar quantitative prediction to methodologies based only on cohesive surface model to simulate fractures in the medium and interface, and that it has the additional potentiality to reproduce kinking off phenomena without displaying an excessive dependence with the finite element mesh.

The further conclusion drawn from the specific analysis of a crack impinging on an interface is that different interaction mechanisms result as a consequence of a mixed criterion involving strength and toughness of bulk materials and interface. Most importantly, these model properties influence the interaction mechanisms in a similar mode to that determined using cohesive surface approaches both, the medium and interface. In this sense, the present results confirm the ones reported by Parmigiani y Thouless [62].

We have also analyzed the causes and mechanisms leading to the increase of the apparent structural

toughness due to the crack-interface interaction for a particular configuration. From this analysis, we conclude that the mechanical state on the interface due to the propagating crack, and before it impinges on the interface, plays a role in determining this effect. The relative characteristic lengths of the medium and interface are variables controlling this mechanism. Thus, a mechanical model that includes this stage of the fracture process could respond differently to alternative predictions attained by neglecting the analysis of this stage.

The variational thermodynamic framework followed in this contribution includes jumps in the phase-field descriptor. Thus, this formulation can be adopted for developing models accounting for more general jump conditions, such as the ones including interface constitutive models regulating the phase-field jumps.

Appendix I: Brief description of the model numerical implementation

Traction-separation law resulting from the projection of a continuum damage model onto $\mathcal{S}$

The interface cohesive model of sub-Section A.2.5.2 is implemented with quadrilateral or triangular conventional finite elements, band elements, with a slender geometry which are placed along the interface. This implementation is based on a traction-separation law resulting from a projection of a continuum damage model onto $\mathcal{S}$ which has been originally described in Huespe et al. [114]. Posteriorly, a numerical procedure based on such projection has been proposed by Manzoli et al. [174]. A sketch of the technique using bilinear quadrilateral finite elements is depicted in Figure A.15-a. The constitutive law assigned to the band element is a regularized 3-D continuum damage model such as the one reported in Huespe y Oliver [164] (page 107, Table 1 and Table 3). The regularization of the damage model is introduced to make consistent the finite element kinematics, when $k \to 0$, and displacement jumps $[\![\boldsymbol{u}]\!] \neq 0$, with the constitutive model. Notice that, in such circumstances, the finite element strain results an unbounded value:

$$\lim_{k\to 0} \boldsymbol{E} = \lim_{k\to 0} \frac{[\![\boldsymbol{u}]\!] \otimes^s \ltimes}{k} \approx \infty \ . \tag{A.54}$$

Let us consider the conventional 3-D continuum damage model described in Huespe y Oliver [164]. By multiplying the softening modulus H of this model by k to gives:

$$\bar{H} = kH \ , \tag{A.55}$$

then, the stress $\boldsymbol{S}_S$ assessed with the regularized strain softening is a bounded term. The corresponding traction vector, $\boldsymbol{t} = \boldsymbol{S}_S \ltimes$, as a function of $[\![\boldsymbol{u}]\!]$, exhibits a similar mechanical response to the traction separation law described in Section A.2.5.2. This law can be considered as a projection of the 3-D continuum damage model onto $\mathcal{S}$, see Huespe et al. [114].

A characteristic feature of this traction-separation law is that its stiffness coefficient, E_i, is that of the continuum media in where the interface is embedded.

Implementation of the phase-field equations

Considering equations (A.33)-(A.36), the local balance of the phase-field problem is assessed in every body parts $\mathcal{P}$ as follows:

$$2(1-\varphi(t))\mathcal{H}(t) - \frac{G_{PF}}{\ell_{PF}}\Big[\varphi(t) - {\ell_{PF}}^2 \triangle\varphi(t)\Big] = 0 \ , \tag{A.56}$$

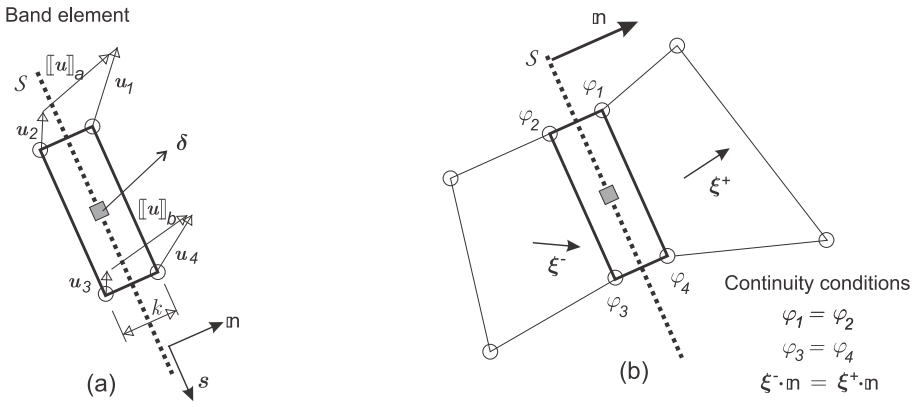

Figura A.15: Sketch of the technique used to implement jump conditions on the interface $\mathcal{S}$. a) The band element is a slender finite element (quadrilateral in this case) on $\mathcal{S}$ featured with a regularized 3-D continuum damage model. b) Phase-field continuity conditions across the band element.

where the compact history field function $\mathcal{H}(t)$ are defined in expressions (A.35) and (A.36). Additionally, the phase-field continuity conditions satisfy on $\mathcal{S}$:

$$[\![\varphi]\!] = 0 \qquad , \qquad [\![\boldsymbol{\xi}]\!] \cdot \ltimes = 0 \ , \tag{A.57}$$

Equation (A.56) is implemented in a finite element code by imposing the jump conditions (A.57) through a Lagrange multiplier technique. Thus, the discrete system of equation derived from this problem can be written as follows:

$$\begin{bmatrix} \mathbb{K}_\varphi + \mathbb{M}_\varphi & \mathbb{B}_\varphi^T \\ \mathbb{B}_\varphi & \mathbf{0} \end{bmatrix} \begin{bmatrix} \hat{\boldsymbol{\varphi}} \\ \hat{\boldsymbol{\lambda}} \end{bmatrix} = \begin{bmatrix} \mathbb{F}_\varphi^{\text{ext}} \ , \\ \mathbf{0} \end{bmatrix} \tag{A.58}$$

where $\hat{\boldsymbol{\varphi}}$ is the vector of nodal parameters of the phase-field interpolation and $\hat{\boldsymbol{\lambda}}$ is the Lagrange multiplier vector related to the constraints (A.57). The matrix $\mathbb{B}_\varphi$ gathers the coefficients of the discrete phase-field continuity equations. The matrices and vectors introduced in (A.58) are defined as follow:

$$\begin{aligned}
&\mathbb{K}_\varphi = \overset{n_{elem}}{\underset{\mathfrak{e}=1}{\Lambda}} \mathbb{K}_\varphi^{\mathfrak{e}} \ , \qquad [\mathbb{K}_\varphi^{\mathfrak{e}}]_{i,j} = \int_{\mathcal{B}^{\mathfrak{e}}} \ell_{PF} G_{PF} \left[(\nabla N_i^{\mathfrak{e}})^T \cdot \nabla N_j^{\mathfrak{e}} \right] \, d\mathcal{B}^{\mathfrak{e}}; \qquad [\nabla N_i^{\mathfrak{e}}] = \begin{bmatrix} N_{i,x}^{\mathfrak{e}} \\ N_{i,y}^{\mathfrak{e}} \end{bmatrix} \ , \\
&\mathbb{M}_\varphi = \overset{n_{elem}}{\underset{\mathfrak{e}=1}{\Lambda}} \mathbb{M}_\varphi^{\mathfrak{e}} \ , \qquad [\mathbb{M}_\varphi^{\mathfrak{e}}]_{i,j} = \int_{\mathcal{B}^{\mathfrak{e}}} \left[2\mathcal{H}(\mathbf{E}) + \frac{G_{PF}}{\ell_{PF}} \right] \left[(N_i^{\mathfrak{e}})^T \cdot N_j^{\mathfrak{e}} \right] \, d\mathcal{B}^{\mathfrak{e}} \ , \\
&\mathbb{F}_\varphi^{\text{ext}} = \overset{n_{elem}}{\underset{\mathfrak{e}=1}{\Lambda}} (\mathbb{F}_\varphi^{\mathfrak{e}})^{\text{ext}} \ , \qquad [(\mathbb{F}_\varphi^{\mathfrak{e}})^{\text{ext}}]_i = \int_{\mathcal{B}^{\mathfrak{e}}} N_i \left[2\mathcal{H}(\mathbf{E}) \right] \, d\mathcal{B}^{\mathfrak{e}} \ ,
\end{aligned} \tag{A.59}$$

where $\overset{n_{elem}}{\underset{\mathfrak{e}=1}{\Lambda}}$ is the assembling operator of the finite element matrices, $\mathbb{K}_\varphi^{\mathfrak{e}}$, $\mathbb{M}_\varphi^{\mathfrak{e}}$, and vector $(\mathbb{F}_\varphi^{\mathfrak{e}})^{\text{ext}}$, respectively. The $i-$th finite element shape functions is denoted N_i. Considering that one scalar continuity condition $[\![\varphi]\!] = 0$ is established for every one of the p pairs of nodes on the right and left boundaries of the band elements, see FigureA.15-b, then, there are p rows of the matrix $\mathbb{B}_\varphi$ imposing every one of these constraints. On the other hand, considering that there are q band elements, one scalar continuity condition $(\boldsymbol{\xi}^+ - \boldsymbol{\xi}^-) \cdot \ltimes = 0$ is established for every one of them. Both terms $\boldsymbol{\xi}^\pm = G_{PF}^\pm \ell_{PF}^\pm (\sum_{i=1}^4 \nabla N_i^\pm \hat{\varphi}_i)$ are evaluated in the centre of elements "+" and "−", respectively, at each side of the corresponding band element, such as shown in Figure A.15-b. These conditions are implemented in the remaining q rows

of the matrix $\mathbb{B}_\varphi$. Therefore, the Lagrange multiplier vector $\hat{\boldsymbol{\lambda}} \in \mathbb{R}^{p+q}$. Note that the phase-field is not interpolated within the band element representing the interface.

Acknowledgments

This research has been supported with grants provided by CONICET, the National University of Litoral, and the fund from ANPCyT: PICT-2020-SERIEA-02793, Argentina.

F.P. Duda gratefully acknowledges the support provided by the Brazilian agency CNPq (309370/2019-1).

Apéndice B

Toughening effect analysis in problems of propagating cracks interacting with interfaces

J. Zambrano, J. Gutierrez, S. Toro, P.J. Sánchez, F.P. Duda, S. Serebrinsky, A.E. Huespe (2023). "Toughening effect analysis in problems of propagating cracks interacting with interfaces". *Proceedings of CFRAC 2023*, Prague.

Toughening effect analysis in problems of propagating cracks interacting with interfaces

J. Zambrano[1], J. Gutierrez[2], S. Toro[1], P.J. Sánchez[1,3], F.P. Duda[4], S. Serebrinsky[2], A.E. Huespe[1,1]

[1]CIMEC-UNL-CONICET, Güeme 3450, CP 3000 Santa Fe, Argentina
[2]YPF Tecnología S.A. (Y-TEC - CONICET), Av. del Petróleo s/n, e/129 y 143 (1923), Berisso, Argentina
[3]GIMNI-UTN-FRSF, Lavaise 610, CP 3000 Santa Fe, Argentina
[4]Programa de Engenharia Mecânica - COPPE, Universidade Federal do Rio de Janeiro, Cidade Universitária, Rio de Janeiro, CEP 21941-972, RJ, Brazil

Abstract. Numerous fracture problems display, at the meso or microscale, phenomena involving the propagation of cracks interacting with interfaces. Examples where this mechanism plays a prominent role are: microcracks propagating in laminated composites, intergranular/transgranular fracture in polycrystalline metals, adhesive joints sandwiched between elastic substrates, crack bridging in structural ceramics, fracture mechanisms in biomimetics materials, among others. A notable result of such interactions refers to the possible effective structural toughening due to shielding effects induced by the interface on the propagating crack. Considering the high interest shown by this issue, the study of propagating cracks approaching interfaces has been the topic of intense research in the last few years.

In this work, following Foulk III et al. [9], we analyze the toughening mechanisms due to a propagating crack interacting with an interface at prescribed angles. The problem consists of a pre-cracked thin film bonded to a substrate, as adopted by Strom y Parmigiani [151]. The initial crack propagates toward the interface penetrating the substrate or deflecting toward the interface. In the last case, the film/substrate interface undergoes debonding. This effect inhibits the substrate crack penetration and may induce an effective structural toughness increase. Special attention is paid here to the unstable conditions arising from the shielding effect introduced by the interface.

The penetration/deflection mechanisms which are competing have usually been modeled using either stress-based criteria or energy-based criteria. However, it has been found that both criteria cooperate in the phenomenon. In the present analysis, we use a numerical methodology appealing to two different techniques. We compare the results obtained with: i) a phase field model characterizing the crack propagation across the film and substrate combined with a Cohesive Zone Model (CZM) characterizing the response of the interface (see Zambrano et al. [78]); and ii) a CZM for describing the crack propagation along the substrate and interface domains (see Gutierrez et al. [175]).

The analysis is performed in the space of parameters defined by the ratio between the substrate and interface toughnesses, Γ_s/Γ_i, and the effective normalized load. The remaining parameters governing the problem, i.e. the characteristic lengths of the interface and phase field model, are also varied accordingly to assess their role in affecting the structural toughness increase.

Conclusions on the capacity of both numerical techniques to assess the apparent toughness and instability response are presented.

[1]Corresponding author. E-mail address: ahuespe@cimec.unl.edu.ar (A.E. Huespe).

Apéndice C

Diseño de materiales compuestos para aumento de tenacidad bajo el enfoque de diseños bio-inspirados

Javier A. Zambrano, Alfredo E. Huespe, Santiago Serebrinsky, Sebastian Toro, Pablo J. Sánchez (2023). "Diseño de materiales compuestos para aumento de tenacidad bajo el enfoque de diseños bio-inspirados". *AMCA* XL 787-796.

Diseño de materiales compuestos para aumento de tenacidad bajo el enfoque de diseños bio-inspirados

Javier A. Zambrano[1], Alfredo E. Huespe[1], Santiago Serebrinsky[2], Sebastian Toro[1], Pablo J. Sánchez[1,3]

[1]CIMEC-UNL-CONICET, Güemes 3450, CP 3000 Santa Fe, Argentina,
zambranoj88@cimec.unl.edu.ar, ahuespe@cimec.unl.edu.ar, storo@cimec.unl.edu.ar,
psanchez@cimec.unl.edu.ar, https://cimec.conicet.gov.ar/
[2]YTEC-YPF-Tecnología, santiago.serebrinsky@ypftecnologia.com, https://y-tec.com.ar/
[3]GIMNI-UTN-FRSF, Lavaise 610, CP 3000 Santa Fe, Argentina, gimni@frsf.utn.edu.ar,
https://www.frsf.utn.edu.ar

Palabras clave: materiales compuestos tipo nácar, resistencia a la fractura, propagación de fisuras, modelo de campo de fase, modelo de zona cohesiva.

Resumen. La gran mayoría de los compuestos biológicos, incluyendo los huesos, dientes y nácares, son interesantes de estudiar ya que poseen propiedades de resistencia a la fractura superiores a la de sus componentes. La compleja mezcla de sus constituyentes tanto rígidos como blandos contribuye a mejorar el comportamiento a la fractura. Este estudio se realiza con el propósito de comprender la resistencia a la fractura de los diseños bio-inspirados, a través de la implementación acoplada del modelo de campo fase y el modelo de interface de superficie cohesiva (Zambrano et al. [78]). Se analiza el proceso de fractura, desde la iniciación del daño, la propagación de múltiples grietas hasta el fallo del material. Las simulaciones numéricas muestran que se puede obtener una mejora de la tenacidad a la fractura.

Keywords: nacre-like composites, fracture resistance, crack propagation, phase-field model, cohesive zone model.

Abstract. The great majority of biological composites, including bones, teeth and nacre, are interesting to study as they exhibit fracture toughness properties superior to those of their constituents. The complex mixture of both stiff and soft constituents contributes to improved fracture behavior. This study is performed with the purpose of understanding the fracture toughness of bio-inspired designs through the coupled implementation of the phase-field model and the cohesive surface interface model (Zambrano et al. [78]). The fracture process, from damage initiation, multiple crack propagation to material failure, is analyzed. Numerical simulations show that an improvement in fracture toughness can be obtained.

C.1. Introducción

Un propósito importante del estudio de los biomateriales es imitar su exquisita estructura para desarrollar materiales artificiales bioinspirados con unas características mecánicas avanzadas. El nácar es conocido por su atractiva combinación de rigidez, resistencia y dureza. Las impresionantes propiedades mecánicas del nácar pueden atribuirse a su estructura básica tipo 'brick-and-mortar'. Dicha estructura se compone de aproximadamente un 95 % de Aragonita ('tableta' de fase rígida con un módulo de Young entre 50-100 GPa) y un pequeño porcentaje de macromoléculas orgánicas ('interface' de fase blanda con un módulo de Young entre 50-100 MPa) (Ji y Gao [11]). Este tipo de morfología se repite y se observa en diferentes escalas de longitud, como si fuese una microestructura replicada jerárquicamente en distintos niveles de observación, que contribuyen a la tenacidad y dureza del nácar.

En algunas especies de nácar se observan puentes minerales en las capas de la matriz orgánica (Song et al. [130]), islotes minerales a nanoescala tanto en la superficie superior e inferior de las tabletas (Wang

et al. [131]), ondulaciones de las tabletas y entrecruzamientos de las mismas. Por otra parte, se observan arquitecturas únicas de nanopartículas y biopolímeros en las placas de Aragonita del nácar, que hasta ahora se consideraban frágiles, lo que permite la propagación de grietas en el interior de dichas placas y mejora enormemente la dureza y la resistencia (Huang y Li [132], Li et al. [133]). La estructura básica de tipo 'brick-and-mortar' y las estructuras detalladas de subnivel mencionadas afectan a las interacciones de los materiales duros y blandos, que son la clave de las excepcionales propiedades mecánicas del nácar (Barthelat et al. [176], Katti et al. [177]). Las propiedades mecánicas superiores de estas estructuras tipo nácar se deben a la mezcla ingeniosa de sus materiales constitutivos que poseen propiedades de fractura contrastadas. Ji y Gao [11] descubrieron que las grandes relaciones de aspecto y una alineación escalonada de las plaquetas minerales son los factores clave que contribuyen a la gran rigidez y resistencia de los nanocompuestos biológicos. En presencia de pregrietas, los materiales heterogéneos mixtos tienen mecanismos de fractura específicos a diferentes escalas de longitud para evitar el fallo catastrófico por alta concentración de tensiones alrededor de la punta de la grieta. Los resultados experimentales de Dimas y Buehler [178] dilucidaron el papel de las variaciones de la relación de rigidez de los constituyentes del material compuesto como una característica importante en la determinación de las propiedades globales del material.

Investigaciones previas han intentado abordar los mecanismos de la alta tenacidad de los biocompuestos desde varios puntos de vista, incluyendo sus estructuras jerárquicas (Menig et al. [81], Kamat et al. [179]), las propiedades mecánicas de la proteína (fase blanda) en la disipación de la energía de fractura (Smith et al. [134]), la rugosidad de la interfaz proteína-mineral (Wang et al. [131]) y la reducción de la concentración de tensiones en una grieta (Okumura y de Gennes [180]). Por ende, los diferentes mecanismos analizados los cuales producen un aumento de la tenacidad estructural tanto en diferentes materiales compuestos, como en los diseños bioinspirados se encuentran plenamente relacionados con un criterio mixto en el cual intervienen las relaciones entre la tenacidad y la resistencia de los materiales que componen al medio y las interfaces presentes en los modelos y esto se puede ver evidenciado en trabajos pasados donde se estudia ampliamente el problema de una grieta incidiendo en una interfaz implementando diferentes enfoques tanto analíticos como numéricos. Un mecanismo que resulta ser remarcable para aumentar la tenacidad se refiere al desvio de las fisuras, siguiendo las interfaces de las placas cerámicas, evitando que la fisura penetre las mismas. Una serie de estudios se han desarrollado para la mejor comprensión de este mecanismo, He y Hutchinson [140] utilizaron métodos de ecuaciones integrales, suponiendo materiales isótropos elásticos lineales a ambos lados de la interfaz, estimaron el rango de tenacidad de la interfaz "Gi", relativo a la tenacidad media del material en el lado no agrietado del sustrato "Gs", que probablemente provoca la desviación de las grietas hacia la interfaz, en lugar de penetrar en ella. El análisis de He y Hutchinson [140] se basa en un criterio puramente energético e incluye casos de materiales frágiles disímiles a ambos lados de la interfaz, así como diferentes ángulos de incidencia entre la grieta que se propaga y la interfaz. Martinez y Gupta [141] utilizaron una técnica analítica semejante para investigar el problema de la desviación de la grieta en una interfaz que une dos materiales elásticos ortotrópicos y observaron que, a diferencia de los criterios basados en la resistencia, el criterio de la tasa de liberación de energía adoptado para predecir las interacciones es muy sensible a los valores de los parámetros del material, dicha observación es importante para las soluciones obtenidas en este trabajo.

Por otra parte, pueden utilizarse varias técnicas numéricas para evaluar los mecanismos de interacción entre grietas que propagan e inciden en una interfaz Parmigiani y Thouless [62] estudiaron este problema implementando modelos de zonas cohesiva para representar tanto la propagación de grietas en el medio, como para simular la degradación de la interfaz hasta su decohesión final. Concluyeron que el mecanismo de interacción resultante depende típicamente de un criterio mixto de resistencia-tenacidad; véase también Strom y Parmigiani [151]. Este hecho es sumamente relevante y se analiza con más detalle en este trabajo concluyendo la presencia de un criterio mixto similar al presentado por Parmigiani y Thouless [62] obtenido de la implementación numérica de un modelo de campo de fase acoplado con

un modelo de superficie cohesiva. Zambrano et al. [78] analizaron el fenómeno de interacción entre una grieta que propaga en un medio y que incide en una interfaz implementado un modelo de campo de fase acoplado con un modelo de superficie cohesiva, donde a través del modelo de campo de fase se simuló la propagación de la grieta en el medio y por medio del modelo de superficie cohesiva se simuló el proceso de degradación de la interface adhesiva, llegando a reproducir de manera satisfactoria la presencia de un criterio mixto de resistencia-tenacidad similar al presentado por Parmigiani y Thouless [62]. Esta temática es sumamente relevante porque dicho criterio mixto se puede ver evidenciado en los diferentes diseños bioinspirados basados en la estructura tipo nácar, como será detallado en este estudio. Por lo tanto, en este trabajo se realiza la aplicación de una implementación numérica acoplada que comprende a los modelos de campo de fase y de superficie cohesiva con el objetivo de evidenciar el aumento de tenacidad en diferentes diseños bioinspirados utilizando la configuración de la estructura tipo nácar, llegando al modelo el cual disipa mayor cantidad de energía y consecuentemente lograr reproducir de manera satisfactoria el cumplimiento de un criterio mixto de resistencia-tenacidad como los obtenidos en los trabajos de Parmigiani y Thouless [62] y Zambrano et al. [78].

C.2. Metodología y Resultados

Este trabajo está basado en los estudios realizados en Parmigiani y Thouless [62] y Zambrano et al. [78], donde se realiza la implementación de una herramienta numérica, en este caso compuesta por los modelos acoplados de campo de fase y de superficie cohesiva, la cual es aplicada en el análisis de diferentes geometrías correspondientes a los diseños bioinspirados, los mismos están compuestos de una fase rígida (componente mineral) y una fase blanda (componente de proteína), donde con el modelo de campo de fase se estudia el comportamiento de la fase rígida del material y con el modelo de superficie cohesiva se analiza el comportamiento de la fase blanda que se compone de interfaces tanto horizontales como verticales. Esquemáticamente el modelado mecánico aplicado en la herramienta numérica se representa en la Fig. C.1.

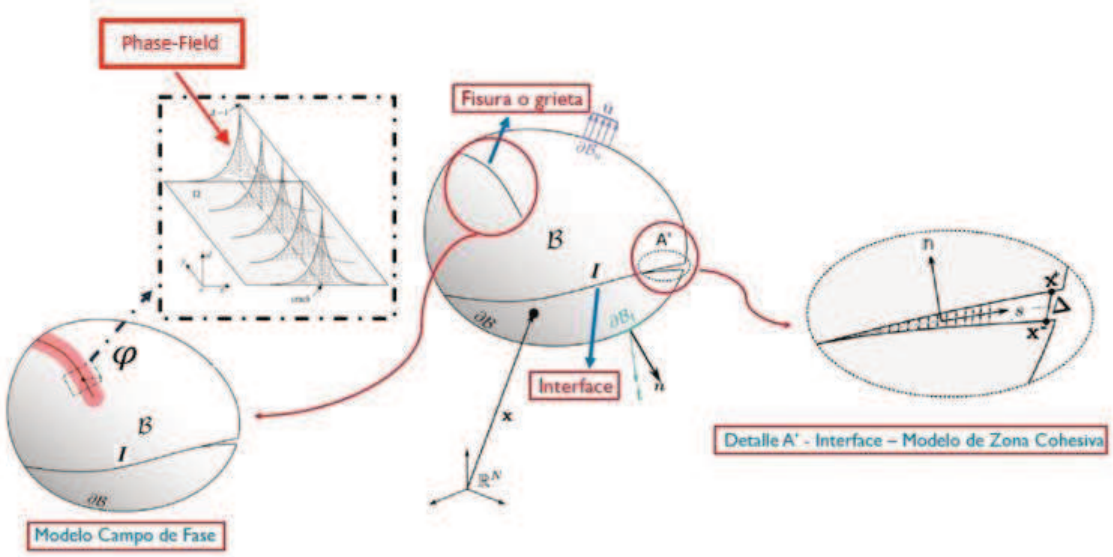

Figura C.1: Esquema de modelado mecánico aplicado en la implementación numérica.

Por ende, la herramienta numérica fue trabajada bajo un enfoque de tipo staggered (por etapas), donde primero es resuelto el problema mecánico para posteriormente resolver el problema de campo de fase, teniendo en cuenta la resolución de cada una de las ecuaciones gobernantes que constituyen a

cada problema y que se muestran en la Fig. C.2. Donde (1) es la ecuación convencional de Cauchy en forma local, (2) es la ecuación de equilibrio de tracciones en el borde del cuerpo, (3) y (4) representan las condiciones de tracción y salto de desplazamiento en la interface del cuerpo, (5) es el balance de fuerzas microscópicas local, (6) representa el equilibrio de micro-tracciones generalizadas en el contorno del cuerpo, finalmente (7) y (8) son las condiciones de micro-tracciones y salto de desplazamiento en la interface del cuerpo.

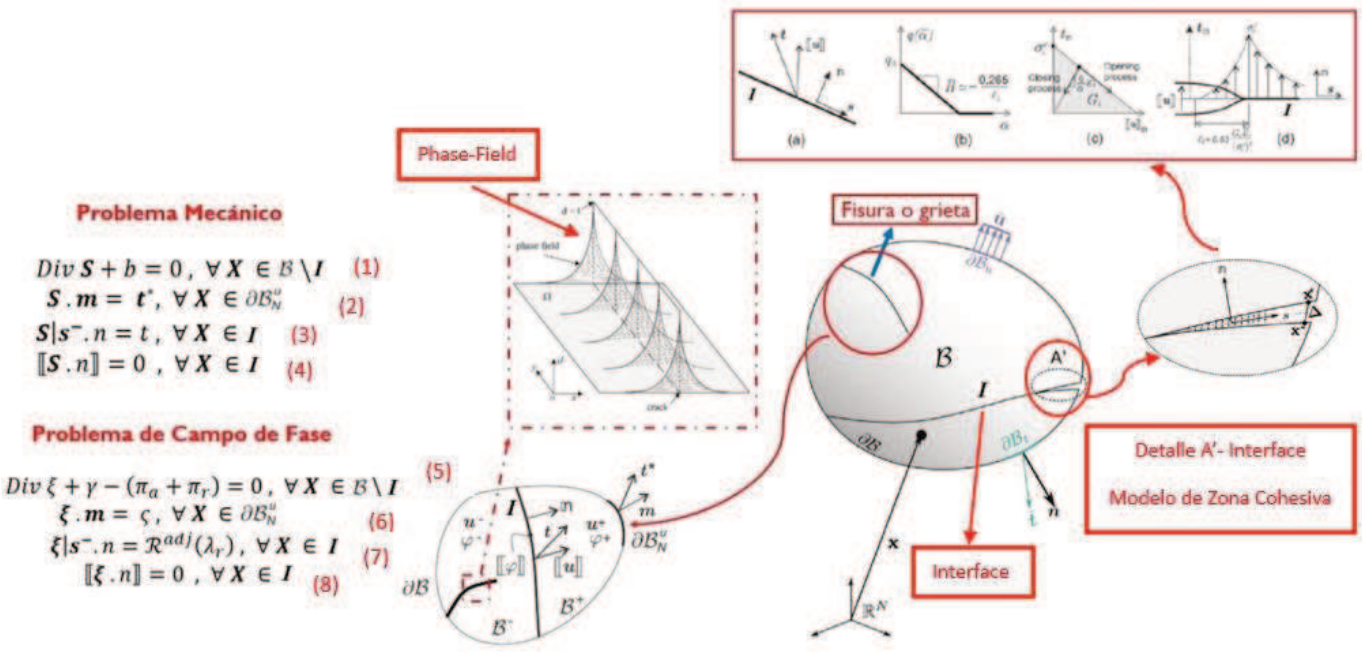

Figura C.2: Ecuaciones gobernantes para los problemas mecánico y de campo de fase aplicadas en la fase rígida del material de los diseños bioinspirados y descripción esquemática del modelo de interface de superficie cohesiva aplicado a la fase blanda del material.

Por consiguiente, también en la Fig. C.2 se visualiza el modelo de superficie cohesiva con el cual se simuló el proceso de degradación de las interfaces tanto horizontales como verticales pertenecientes a la fase blanda que componen a los modelos geométricos de los diseños bioinspirados. El estudio se focaliza en la evaluación de la estructura tipo 'brick-and-mortar' del nácar, tomando en cuenta diferentes parámetros geométricos como lo son: la fracción de volumen de la fase rígida, la relación de aspecto de la tableta y el ángulo de ondulación de la tableta, el cual define el efecto de entrelazamiento en las celdas unitarias que conforman los modelos geométricos. Por lo tanto, en este trabajo utilizamos tres tipos de configuraciones de la estructura tipo nácar, denominadas como: 'Flat Table', 'Interlocking' y 'Non-Interlocking'. A continuación, en la Fig. C.3 se muestran los modelos geométricos que fueron analizados, con sus correspondientes dimensiones y condiciones de borde impuestas. En cuanto a los parámetros geométricos que fueron utilizados para definir la construcción de las celdas unitarias que conforman cada una de las configuraciones mostradas en la Fig. C.3, tomando en cuenta el ángulo de ondulación que forman las interfaces pertenecientes a la fase blanda, que en este trabajo se definieron con el valor numérico de 10° y -10°, en la Fig. C.4, se representa a detalle la construcción de las celdas unitarias.

Para llevar a cabo las respectivas simulaciones se elaboraron mallas que estaban compuestas de elementos cuadriláteros lineales asumiendo deformación plana donde, en la fase rígida se implementó un tipo de mallado no estructurado y por su parte en la fase blanda (Interfaces horizontales y verticales) se utilizó un mallado de tipo estructurado acompañado de una capa de elementos elásticos mallado de la

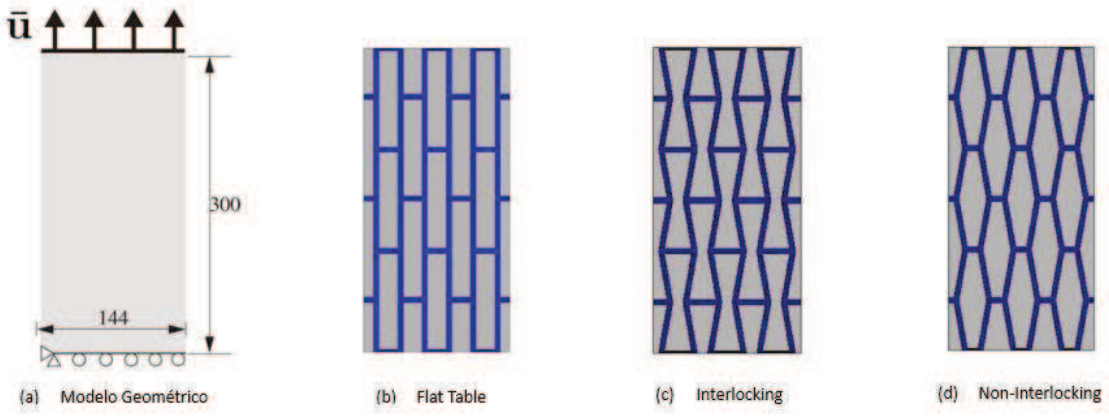

Figura C.3: Estructuras compuestas tipo nácar: (a) Dimensiones de la geometría y condiciones de borde aplicadas, (b) Configuración Flat Table, (c) Configuración Interlocking, (d) Configuración Non-Interlocking.

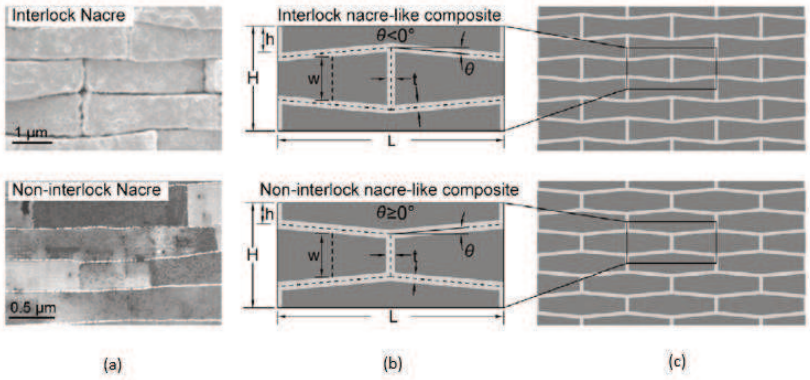

Figura C.4: (a) Imagen de Hyriopsis Cumingii con configuración entrelazada (Interlocking), (b) Parámetros geométricos (H,h,L,w,t en mm y θ en grados) de celdas unitarias, (c) Configuraciones Interlocking y Non-Interlocking para estructura tipo nácar.

misma forma. El número de elementos totales utilizados en la malla de la configuración tipo Flat Table fue de 15067 elementos, en la configuración tipo Interlocking se utilizaron 17564 elementos y finalmente en la configuración Non-Interlocking se utilizaron 14789 elementos. Detallando las condiciones de borde impuestas se tiene que se fijaron los grados de libertad verticales del borde inferior de todas las configuraciones analizadas, así como también se restringió en todas las direcciones el nodo inferior izquierdo para evitar movimientos de cuerpo rígido y se aplico una carga tipo desplazamiento (Δu) en el borde superior de todas las estructuras que fueron estudiadas. En cuanto a las propiedades mecánicas utilizadas en el modelado mecánico, las mismas para el caso del modelo de campo de fase se utilizó una longitud característica (Lc) de 1.06E-1 mm, con una energía de fractura (Gf) de 0.8 N/mm, el Módulo de Young (E) de la fase rígida fue 1930 Mpa y un coeficiente de poisson de 0.33. La capa elástica estuvo configurada con un Módulo de Young (E) de 30 Mpa y un coeficiente de poisson de 0.4. Finalmente, el modelo de interface de superficie cohesiva estuvo configurado para las interfaces verticales con un Módulo de Young (E) de 30 Mpa, un coeficiente de poisson de 0 y una tensión ultima de 2.5 Mpa, por su parte para las interfaces horizontales el Módulo de Young (E) fue de 120 Mpa, con un coeficiente de poisson de 0 y una tensión ultima de 4 Mpa. En la Fig. C.5 se muestran las mallas que fueron utilizadas por tipo de configuración en las diferentes simulaciones.

Las soluciones obtenidas en cuanto a la deformación de las distintas configuraciones que fueron estudiadas, poseen como protagonista principal a las interfaces tanto horizontales como verticales com-

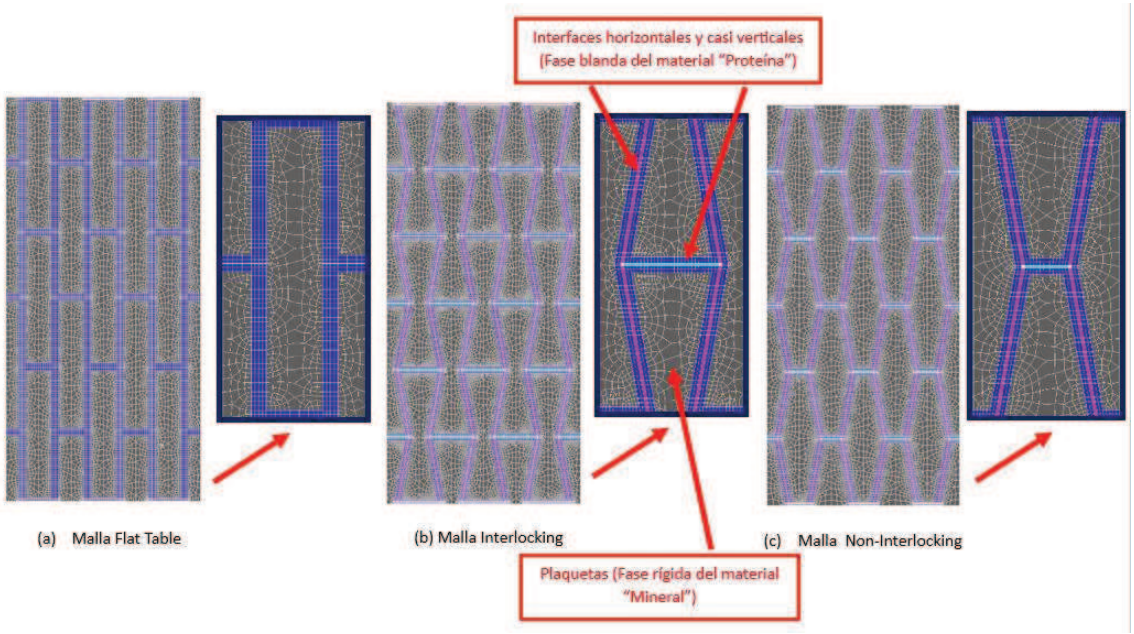

Figura C.5: (a) Malla y celda unitaria para la configuración Flat Table, (b) Malla y celda unitaria para la configuración Interlocking y (c) Malla y celda unitaria para la configuración Non-Interlocking.

puestas de material blando, ya que dicha deformada cumple con un proceso, el cual está dividido en dos etapas, que corresponden al momento de la activación de las interfaces presentes en los respectivos modelos geométricos, estas etapas de deformación se pueden observar en la Fig. C.6. Por consiguiente, se evidencia el proceso completo de la deformación a nivel global en todos los tipos de configuraciones geométricas (Flat Table, Interlocking, Non-Interlocking) que fueron simuladas, donde se puede visualizar que en la ETAPA I del proceso se activan las interfaces horizontales y esto correspondería con el punto A, el cual es el primer pico de la curva tensión-deformación mostrada en la Fig. C.6, y representaría el inicio de la evolución del daño en las interfaces horizontales, posteriormente se alcanza un segundo pico en la curva tensión-deformación denominado el punto B que corresponde a la ETAPA II, en el cual se activan las interfaces verticales y casi verticales, evidenciándose un modo de apertura de fractura de tipo deslizamiento para finalmente llegar al final de la curva tensión-deformación representada por el punto C en el cual las muestras fallan completamente. Se observó que este mecanismo de falla es igual para todas las configuraciones geométricas que fueron analizadas y consecuentemente lo que genera la división de la curva tensión-deformación en dos etapas donde el σ_I perteneciente al primer pico de la curva representaría la resistencia de las interfaces horizontales y a su vez el valor de tensión dominante de la estructura del material compuesto, que define la resistencia global del mismo, y el σ_{II} ubicado en el segundo pico de la curva representaría la resistencia de las interfaces verticales y casi verticales.

En cuanto a los resultados relacionados con el comportamiento de las curvas estructurales (Fuerza vs Desplazamiento) para cada tipo de configuración geométrica, las mismas se muestran en la Fig C.7. En dichas curvas se puede verificar la respuesta a la tracción dividida en dos etapas, como se describió anteriormente. Por ende, se puede observar que la configuración Interlocking (curva verde) presenta tanto mayor rigidez como mayor resistencia global en comparación con las configuraciones Non-Interlocking y Flat Table, ya que su primer pico en su curva estructural que correspondería al punto A de la curva teórica tensión-deformación de la Fig. C.6c y a su vez correspondería al valor σ_I, supera grandemente a las otras dos curvas estructurales pertenecientes a la configuración Flat Table y Non-Interlocking, la razón de esta situación se puede atribuir al aumento de la longitud de las interfaces casi verticales en su interconexión en forma de punta con las interfaces horizontales, respetando el efecto de entrelazamiento cuando

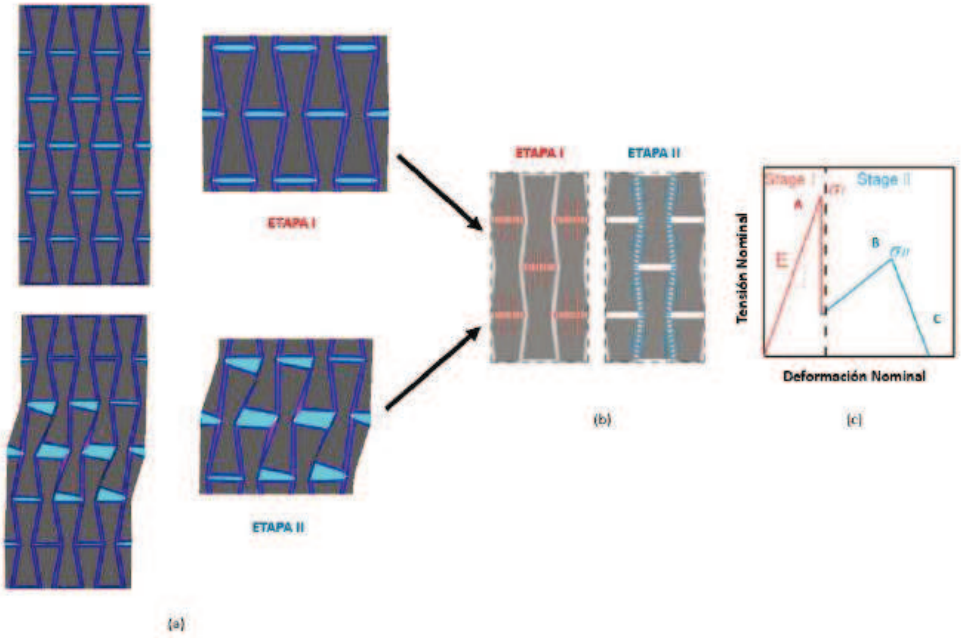

Figura C.6: Proceso de deformación para la configuración Interlocking: (a) Mecanismo de falla de las interfaces obtenida de la simulación numérica, (b) Deformación teórica por etapas de las interfaces, (c) Curva teórica de tensión-deformación clasificada por etapas de deformación.

el ángulo de ondulación en la tableta es menor que 0º, ya que el entrelazamiento suprime la propagación de la grieta alrededor de la interconexión en punta entre las interfaces horizontales y verticales cuando las tabletas se deslizan una con respecto a la otra, consecuentemente esta configuración Interlocking es la estructura que presenta mayor energía disipada, ya que el área bajo su curva estructural es mayor en comparación al área de las curvas de las demás configuraciones. Por otro lado, en la segunda etapa de las curvas estructurales hay un dominio perteneciente a la configuración Non-Interlocking (curva azul) sobre las demás configuraciones, ya que presenta el mayor valor de tensión σ_{II}, correspondiente al punto B de la curva teórica tensión-deformación de la Fig. C.6c. y en este caso la configuración Interlocking posee el valor de tensión σ_{II}, más bajo de las tres curvas estructurales.

Por consiguiente, las distribuciones de tensiones σ_{yy} y la evolución del daño (Phase-Field) presentes en la fase rígida del material, se pueden observar en la Fig. C.8. Donde se visualiza que en la configuración Interlocking existe un mayor valor de tensión cuya distribución es más amplia alrededor de todas las zonas de entrelazado entre las interfaces, lo que contribuye a aumentar la resistencia general de la estructura Interlocking en comparación con las demás configuraciones (Flat Table, Non-Interlocking), donde se evidencia un menor valor de tensión, pero la distribución de la misma se ubica de igual forma que la configuración Interlocking en la interconexión entre las interfaces .

Un análisis con respecto a los mecanismos de deflexión y penetración en términos de las propiedades de resistencia y tenacidad del material que fue utilizado se describe a continuación en la Fig. C.9, la cual fue obtenida trabajando con la configuración geométrica Flat Table. Se visualiza en dicha gráfica un espacio que se define por las siguientes variables en sus ejes: en el eje vertical se tiene la relación entre la energía de fractura de la fase rígida del material (G_{fr}) y la energía de fractura de la fase blanda del material (G_{fb}), con respecto al eje horizontal se tiene la relación entre la tensión crítica de la fase rígida del material (σ^c_{fr}) y la tensión crítica de la fase blanda del material (σ^c_{fb}). Se observa el comportamiento del mecanismo de deflexión perteneciente a los puntos en forma de cuadrado que se sitúan sobre la curva

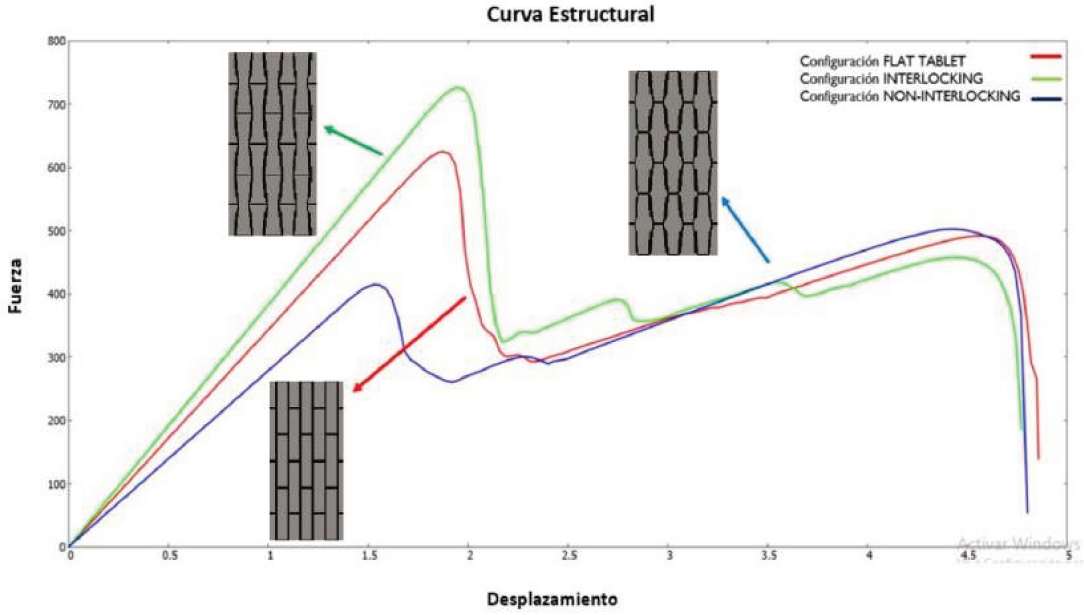

Figura C.7: Curvas estructurales para las configuraciones: Flat Table, Interlocking y Non-Interlocking.

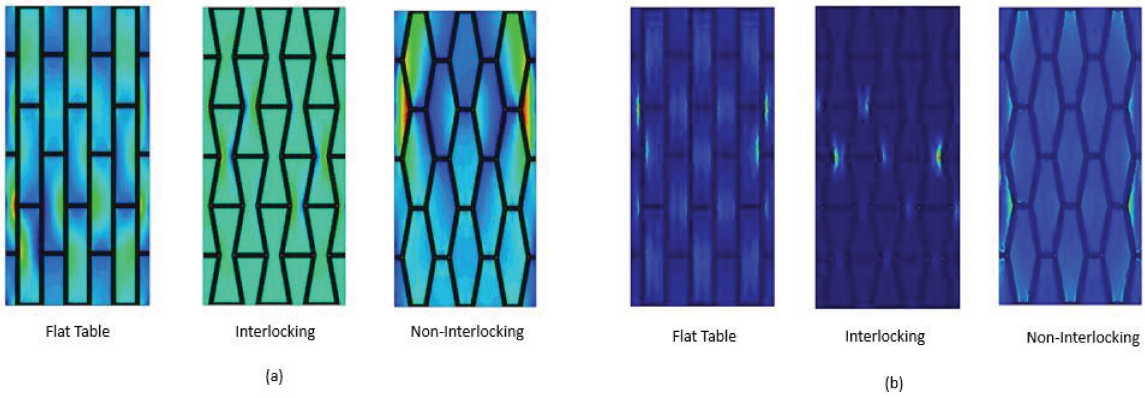

Figura C.8: (a) Distribución de tensiones σ_{yy} en las configuraciones Flat Table, Interlocking, Non-Interlocking, (b) Evolución del daño (Phase-Field) en las configuraciones Flat Table, Interlocking, Non-Interlocking

roja, cada uno de estos puntos es el resultado de una simulación que muestra físicamente como una grieta se desvía por las interfaces verticales de la estructura Flat Table y el mecanismo de penetración que comprende los puntos circulares sobre la curva azul, en la cual cada punto es el resultado de una simulación donde fisicamente una grieta propaga a través de las tabletas ceramicas del material. Por otro lado, se puede observar que existe una zona disjunta entre ambas curvas lo cual significa que ambos mecanismos compiten para ver cual de los dos prevalece y a esto se le denomina zona de transición. Se tiene que la parte superior derecha del gráfico representa el caso en que es muy probable que la grieta se desvié hacia las interfaces verticales de la estructura produciendose la deflexión, mientras que la parte inferior izquierda del mismo representa el caso en que es muy probable que la grieta penetré hacia la tableta ceramica del material dando lugar a la penetración. Se puede inferir que a bajos valores de las relaciones G_{fr}/G_{fb} y $\sigma^c_{fr}/\sigma^c_{fb}$ se favorece la presencia del mecanismo de penetración, por el contrario, valores elevados de estas relaciones favorecen al mecanismo de deflexión, finalmente se nota que a medida que disminuye la relación de resistencia $\sigma^c_{fr}/\sigma^c_{fb}$ se origina un comportamiento asintótico vertical aproximadamente situado en un valor para $\sigma^c_{fr}/\sigma^c_{fb} = 3.8$ donde por debajo de este valor siempre

predominara el mecanismo de penetración. Por lo tanto, se puede afirmar que se captura de manera satisfactoria el mismo comportamiento de las curvas de deflexión y penetración que se encuentran en los trabajos de Parmigiani y Thouless [62] y Zambrano et al. [78].

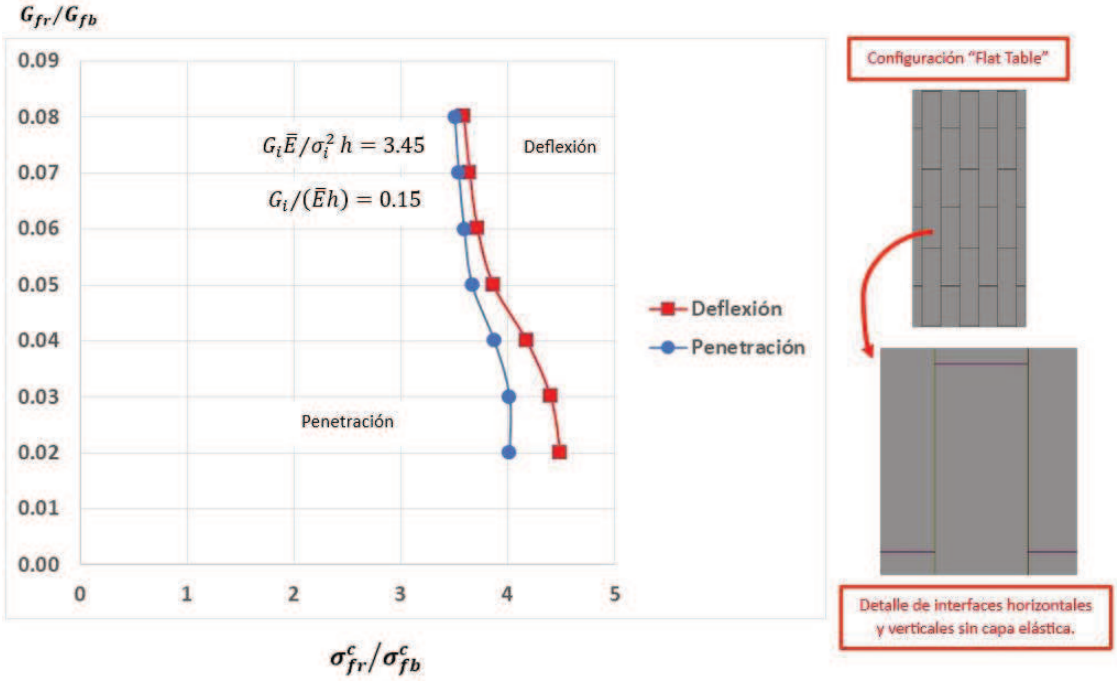

Figura C.9: Curvas de mecanismos de deflexión y penetración para configuración Flat Table.

C.3. Conclusiones

En este estudio, se evalúa el diseño de estructuras compuestas resistentes a la fractura mediante la implementación acoplada del modelo de campo de fase y el modelo de superficie cohesiva. Estas estructuras que conllevan a los diseños bioinspirados se componen de materiales que poseen una fase rígida (mineral) y una fase blanda (proteína) y que presentan una respuesta a la fractura muy interesante. Por ende, se puede inferir lo siguiente:

-La implementación numérica utilizada en el estudio el cual comprende el acoplamiento del modelo de campo de fase y el modelo de superficie cohesiva captura de manera satisfactoria las respuestas complejas en cuanto a los mecanismos que producen un aumento de tenacidad en los diseños bioinspirados.

-Se demostró que la estructura Interlocking de tipo nácar mejora tanto la tenacidad como la resistencia en comparación con las configuraciones Flat Table y Non-Interlocking, por consiguiente, en la estructura Interlocking el campo de tensión es mucho mayor en comparación a las demás estructuras debido al efecto de entrelazado de la fase blanda.

-Se demuestra que el parámetro geométrico relacionado con el ángulo de ondulación de la tableta juega un rol fundamental en el aumento de la tenacidad de las estructuras entrelazadas, pero sin descartar que los otros dos parámetros geométricos como lo son la relación de aspecto de la tableta y la fracción de volumen de la fase rígida también pueden contribuir a dicho aumento de tenacidad manejando la combinación de los tres parámetros.

-Se valida que en los diseños bioinspirados de tipo nácar la presencia de los mecanismos de deflexión y penetración se produce como consecuencia de un criterio mixto en el que juegan un papel fundamental tanto la resistencia como la tenacidad de las fases materiales (rígida y blanda) que intervienen en las estructuras geométricas.

Apéndice D

An arc-length control technique for solving quasi-static fracture problems with phase field models and a staggered scheme

J. Zambrano, S. Toro, P.J. Sánchez, F.P. Duda, C.G. Méndez, A.E. Huespe (2024). "An arc-length control technique for solving quasi-static fracture problems with phase field models and a staggered scheme". *Computational Mechanics* 73 751-772.

An arc-length control technique for solving quasi-static fracture problems with phase field models and a staggered scheme

J. Zambrano[1], S. Toro[1], P.J. Sánchez[1,2], F.P. Duda[3], C.G. Méndez[1], A.E. Huespe[1,1]

[1]CIMEC-UNL-CONICET, Predio Conicet Dr. Alberto Cassano, Santa Fe, CP 3000, Argentina
[2]GIMNI-UTN-FRSF, Lavaise 610, CP 3000 Santa Fe, Argentina
[3]Programa de Engenharia Mecânica - COPPE, Universidade Federal do Rio de Janeiro, Cidade Universitária, Rio de Janeiro, CEP 21941-972, RJ, Brazil

Keywords: arc-length control strategy, phase field models, staggered methodology, path-following algorithm, quasi-static brittle fracture, unstable crack growth.

Abstract. This paper describes a new arc-length control procedure for tracing the equilibrium curve of brittle fracture problems modeled with a phase field approach. The balance equations of this model are solved with a staggered strategy. The control equation of the arc-length procedure determines the displacement increments during the mechanical stage. The arc-length parameter is interpreted as imposing a given increment of the driving force appearing into the micro-force balance equation.

The innovative technique consisting of applying the control equation to the displacement degrees of freedoms (DOFs) of the mechanical stage offers an enhancement over earlier arc-length strategies that focused on controlling the damage DOFs in the micro-force balance equation stage. This advancement enables the phase field approach to handle and simulate a broader range of problems, as demonstrated in this paper.

The arc-length parameter is stepwise adjusted to yield a pre-established maximum damage increment in each staggered scheme step. As a consequence, the crack tip advance can be strictly controlled in every step holding bounded the pseudo-time integration error, even using an explicit staggered strategy. This procedure entails moderate computational costs for tracing the complete equilibrium curve, including unstable responses, limit points, snap-backs, etc., with the subsidiary advantage that lack of convergence has never been detected in the tests presented in this paper. Additionally, line search techniques have not been necessary.

The proposed arc-length procedure is easily implemented in standard finite element codes, and according to our numerical experiments, it does not significantly increase the computational burden of the original explicit staggered strategy.

D.1. Introduction

In recent years, a vast literature aiming at the numerical simulation of quasi-static evolution of brittle fracture problems through phase field models has been reported. One topic of interest discussed in these works refers to the advantages of using one of the two alternatives, monolithic versus staggered, schemes to solve the coupled equations resulting from the mathematical formulation of the problem.

It is mentioned that the non-convex character of the energy in the space defined by the displacements and phase field variables admits many local minimizers. As pointed out in Bourdin et al. [143] and Farrell y Maurini [101], this feature is the reason why serious convergence issues arise when using monolithic strategies. A notable consequence is that the Newton-Raphson scheme does not necessarily provide descent directions of the related optimization problem. However, according to some authors, a monolithic Newton-Raphson scheme can be used combined with line searches admitting negative step directions, as proposed in Gerasimov y De Lorenzis [181]. Monolithic Quasi-Newton (BFGS) strategies, such as the

[1]Corresponding author. E-mail address: ahuespe@intec.unl.edu.ar (A.E. Huespe).

ones advocated by Kristensen y Martínez-Pañeda [182], have also been reported as a successful technique. It is also significant to mention that numerous variants of monolithic Newton-Raphson schemes have been reported. In this line, we cite the works of Wick [97], Heister et al. [183], Lampron et al. [184], Kopaničáková et al. [185], among others.

Alternatively, a robust staggered solution procedure, reported by Bourdin et al. [143] and followed by Miehe et al. [57], the so-called alternate minimization (AM) method can be used. Nice convergence properties of this methodology have been proven by Bourdin [186], Burke et al. [187] and Brun et al. [188]. In the first stage of an AM methodology, the standard force balance equation[2] is solved with fixed phase field (damage) variables. Subsequently, the micro-force balance equation is solved with fixed displacements. Thus, this staggered scheme relies on solving two sequential convex sub-problems, it is very robust, and the partitioning of the total degrees of freddoms (DOFs) in mechanical and phase field for each sub-problem gives additional computational advantages with respect to the monolithic ones. However, one of the principal deficiencies relies on the fact that its convergence rate is slow.

An additional issue, which is of ubiquitous nature when modeling quasi-brittle fracture problems, is the existence of limit points and snap-backs along the structural equilibrium path. This ingredient requests the use of load control strategies for numerically handling unstable crack growth problems. In the area comprising quasi-brittle fracture problems, an automatic procedure addressed to solve this issue is the control strategy based on limiting the energy dissipation (Gutiérrez [12]), or energy release rate (Verhoosel et al. [13]) in every load step. The adaptation of this control strategy for modeling brittle fracture through the phase field methodology with a staggered scheme has been addressed by Singh et al. [145]. Following the original strategy of Gutierrez et al., Singh et al. controls in each staggered step the damage variable increment. Therefore, the original AM methodology of Bourdin et al. is modified, the first stage solves a controlled micro-force balance equation with the proposed arc-length technique, and the second stage solves the standard force balance equation.

Also, Bharali et al. [146] employed a monolithic methodology solved through a Newton-Raphson under-relaxed scheme and controlled with an arc-length technique that limits the increment of the damage DOFs. A close monolithic approach to that described by Bharali et al. with an arc-length technique is shown in Börjesson et al. [147]. To the best of our knowledge, no similar approach has been reported that uses a quasi-Newton scheme controlled by an arc-length technique. Brust y Marcia [190] have presented a procedure for solving large-scale optimization problems with linear equality constraints using quasi-Newton methods. However, the application of this procedure to the area of interest of the present paper is not yet studied.

A procedure for controlling the increments of displacements in the first mechanical sub-problem, i.e., the standard force balance equation, using the AM of Bourdin et al. has been reported previously by the authors, see Duda et al. [54]. In that work, the controlled magnitude is the relative displacement increment between the two nodes opposite the crack tip. Thus, as the crack propagates, the controlling nodes are redefined to follow the crack tip [3]. Also, Wu [144] reported an arc-length strategy addressed to the original AM methodology. Wu proposes a control strategy based on regulating the conventional crack mouth opening displacements (CMOD), crack mouth sliding displacement (CMSD), or a similar magnitude in pre-cracked specimens undergoing fracture. However, in generic crack propagation problems, both control schemes, that of Duda et al. and Wu, are unsuitable. In the first case, it is not possible to know beforehand the crack propagation path, and therefore the nodes to be controlled are unknowns of the problem. In the second case, the CMOD or CMSD magnitudes are not necessarily monotonous

[2] The Euler-Lagrange equations of the variational model derived from the energy minimization of a regularized problem, established in Bourdin et al. [143], references cited therein, and Miehe et al. [57], are the standard force and micro-force balance equations that can be solved with a staggered strategy. However, a general approach to phase field fracture problems that yields similar force and micro-force balance equations without appealing to the existence of a minimum energy law can be followed. This approach has been reported elsewhere. See for, instance, Duda et al. [189], da Silva Jr et al. [166], Duda et al. [54], and references cited therein. Here, this last approach is adopted.

[3] Close to this approach is the strategy reported by Martínez-Pañeda et al. [191] and references cited therein.

increasing variables during the loading process, as shown in the plot of Figure D.3-c below. For these specific problems, this feature makes the CMOD an impractical variable to be controlled through an arc-length strategy.

In the present work, we describe an alternative load control procedure for solving the standard force balance equations adapted to the original AM method of Bourdin et al. The control strategy governs the increments of displacements in the first mechanical sub-problem when the damage variables are held fixed. Thus, by construction, this control strategy cannot be based on handling the energy dissipation magnitude of the step because it is null while solving the mechanical sub-problem. Instead, we control the increment of the driving force that appears in the micro-force balance equation. Compared with the arc-length control technique reported by Singh et al. [145], our strategy can be extended to handle loading processes of more general phase field problems including those whose micro-force balance equation and complementarity conditions are solved via optimization techniques with inequality constraints, or problems with several unstable dissipative mechanisms, not only phase field. Section D.3.2.2 provides additional details on the novelty and advantages of the present methodology, while Sections D.4.2 and D.4.5 describe significant tests that prove these features.

The proposed staggered strategy with the arc-length control procedure is described, implemented, and tested for a specific brittle fracture phase field model, denoted AT2 in Tanné et al. [113] combined with the complementarity conditions satisfied either through the energy history field notion, see Miehe et al. [98], and from now on called the compact history function procedure, or through a Bound-Constrained Optimization Problem (BCOP), as reported in Amor et al. [99].

A summary of the paper is the following. Section D.2 presents a brief description of the phase field model for brittle fracture. Section D.3 describes the control strategy and the staggered scheme for solving the two balance equations of the problem. Also, in this Section, the novelty of this strategy is discussed. In Section D.4, the proposed control strategy is assessed via numerous tests. Our objective is to show the robustness, accuracy, and ability of the precedure to trace equilibrium curves characterized by abrupt snap-backs. Finally, in Section D.5, attention is addressed to assess the computational burden demanded by the methodology.

D.2. Phase field model for brittle fracture

The variational formulation of the phase field model for fracture in solids is briefly described in this Section. We closely follow the mathematical approach discussed by da Silva Jr et al. [166] and Duda et al. [54].

Let us consider a body $\mathcal{B}$ undergoing quasi-static deformations satisfying the small-strain assumption. The boundary of $\mathcal{B}$ is $\partial\mathcal{B}$ with unit normal vector $\boldsymbol{n}$. Deformation and fracture in $\mathcal{B}$ are described by introducing the displacement vector field, $\boldsymbol{u}(\boldsymbol{x},t)$, and phase field variable, $\varphi(\boldsymbol{x},t)$, at time t and $\boldsymbol{x} \in \mathcal{B}$. The phase field takes values on the interval $[0,1]$. If $\varphi = 0$ at a point, then it is unfractured. If $\varphi = 1$ at a point, it is fractured. Values of φ between zero and one correspond to partially fractured material. Points satisfying $\varphi = 1$ identify cracks, i.e. a traction-free boundary embedded into the bulk material. Thermodynamic arguments impose the restriction: $\dot{\varphi} \geq 0$. The fields $\boldsymbol{u}$ and φ are assumed smooth on $\mathcal{B}$.

Both independent primal descriptors, $\boldsymbol{u}$ and φ, characterize the mechanical state of $\mathcal{B}$ at pseudo-time "t". They are gathered in the vector $\boldsymbol{U} = \{\boldsymbol{u}, \varphi\}$. Admissibility conditions for $\boldsymbol{U}$ are established in the form $\boldsymbol{U} \in \mathcal{K}$, where the set $\mathcal{K}$ accounts for proper regularity and Dirichlet-type boundary conditions of every descriptor. In particular, we consider displacements, $\boldsymbol{u}^*$, fixed on a part of the Dirichlet-boundary $\partial\mathcal{B}^{\boldsymbol{u}}_{\mathrm{D}}$ of $\mathcal{B}$. Virtual variations of $\boldsymbol{U}$ are denoted $\delta\boldsymbol{U} = \{\delta\boldsymbol{u}, \delta\varphi\}$, and their admissibility conditions are defined through $\delta\boldsymbol{U} \in \mathcal{V}$, where the vectorial space $\mathcal{V}$ accounts for appropriate regularity requirements and the specified restrictions on $\boldsymbol{U} \in \mathcal{K}$.

The strain tensor, $\boldsymbol{\varepsilon}$, and its virtual variation, $\delta\boldsymbol{\varepsilon}$, are:

$$\boldsymbol{\varepsilon} = \frac{\nabla \boldsymbol{u} + (\nabla \boldsymbol{u})^T}{2} \quad , \quad \delta\boldsymbol{\varepsilon} = \frac{\nabla \delta\boldsymbol{u} + (\nabla \delta\boldsymbol{u})^T}{2} \, , \tag{D.1}$$

respectively, $\nabla(\cdot)$ being the gradient operator.

D.2.1. Conjugate variables

The external force field per unit volume in $\mathcal{B}$, $\boldsymbol{b}$, and the external tractions per unit area in $\partial\mathcal{B}^{u}_{N}$, $\boldsymbol{t}^*$, are dual variables to $\boldsymbol{u}$, where $\partial\mathcal{B}^{\boldsymbol{u}}_{\mathrm{N}}$ is the Neumann-boundary associated to $\boldsymbol{u}$. The Cauchy stress tensor $\boldsymbol{\sigma}$, defined in $\mathcal{B}$, and $\boldsymbol{\varepsilon}$ forms a conjugate pair.

The phase field descriptor, φ, has associated three dual variables: the internal micro-force field π per unit volume, the external micro-force γ per unit volume, and the external micro-traction ς^* per unit area in $\partial\mathcal{B}^{\varphi}_{\mathrm{N}}$, where $\partial\mathcal{B}^{\varphi}_{\mathrm{N}}$ is the Neumann-boundary related to φ. However, in concordance with Duda et al., we further assume that the external loading system conjugated to φ is null. Thus, neither γ nor ς^* is accounted for in the following. Furthermore, a micro-stress vector field $\boldsymbol{\xi}$ is the conjugate variable of the phase field gradient $\nabla\varphi$.

In Section D.2.3, the constitutive relations for $\boldsymbol{\sigma}$, $\boldsymbol{\xi}$, and for the active counterpart, π_a, of π are introduced.

D.2.2. Basic laws

We stipulate that deformation and fracture processes in $\mathcal{B}$ must be consistent with the Variational Principle of Virtual Work. The force balance equation in local form and the phase field micro-force balance equation are derived from this Principle, which, together with the free-energy imbalance comprise the kinetic foundation of the theory in da Silva Jr et al. [166] and Duda et al. [54].

D.2.2.1. Virtual Power Principle

The internal and external virtual powers, $\delta\mathcal{W}^{\text{int}}$ and $\delta\mathcal{W}^{\text{ext}}$, for any part $\mathcal{P}$ of the body $\mathcal{B}$ are defined as follows:

$$\delta\mathcal{W}^{\text{int}} = \int_{\mathcal{P}} \left(\boldsymbol{\sigma} \cdot \delta\boldsymbol{\varepsilon} + \boldsymbol{\xi} \cdot \nabla\delta\varphi + \pi\, \delta\varphi \right) \mathrm{d}\mathcal{P}, \tag{D.2}$$

$$\delta\mathcal{W}^{\text{ext}} = \int_{\mathcal{P}} \left(\boldsymbol{b} \cdot \delta\boldsymbol{u} \right) \mathrm{d}\mathcal{P} + \int_{\partial\mathcal{P}} (\boldsymbol{t}^* \cdot \delta\boldsymbol{u}) \, \mathrm{d}(\partial\mathcal{P}), \tag{D.3}$$

where $\boldsymbol{t}^*$ is the traction vector on the boundary $\partial\mathcal{P}$ of $\mathcal{P}$.

The Virtual Power Principle stipulates that: $\delta\mathcal{W}^{\text{int}} = \delta\mathcal{W}^{\text{ext}} \quad \forall\ \delta\boldsymbol{U} \in \mathcal{V}$. Admitting independent variations of displacements, we derive integral balance equations, which can be localized using a standard procedure. The resulting local form of the force balance equation for the body $\mathcal{B}$ is given by:

$$\begin{aligned} \operatorname{Div}\boldsymbol{\sigma} + \boldsymbol{b} = \boldsymbol{0} \, , \quad & \forall \boldsymbol{x} \in \mathcal{B} \, , \\ \boldsymbol{\sigma}\, \boldsymbol{n} = \boldsymbol{t}^* \, , \quad & \forall \boldsymbol{x} \in \partial\mathcal{B}^{\boldsymbol{u}}_{\mathrm{N}} \ . \end{aligned} \tag{D.4}$$

with $\boldsymbol{n}$ being the unit normal vector to $\partial\mathcal{B}$. Also, assuming variations for the phase field primal descriptors, and after applying a standard localization procedure, we obtain the micro-force balance equation:

$$\begin{aligned} \operatorname{Div}\boldsymbol{\xi} - (\pi_a + \pi_r) = 0 \ , \quad \forall \boldsymbol{x} \in \mathcal{B} \ , \\ \boldsymbol{\xi} \cdot \boldsymbol{n} = \mathbf{0} \ , \quad \forall \boldsymbol{x} \in \partial\mathcal{B}^{\varphi}_{\mathrm{N}} \ , \end{aligned} \tag{D.5}$$

where we have replaced the internal micro-force π by active and reactive components, π_a and π_r, respectively. The reactive component, in combination with the complementarity conditions: $\pi_r \dot{\varphi} = 0$, $\pi_r \leq 0$, and $\dot{\varphi} \geq 0$, is introduced in the model to guarantee the energy imbalance thermodynamic restriction: $\dot{\varphi} \geq 0$, see details in Duda et al. [54].

D.2.3. Constitutive theory

The free energy, ψ, is assumed to be defined in terms of the set of variables $\{\boldsymbol{\varepsilon}, \varphi, \nabla\varphi\}$:

$$\psi = \hat{\psi}(\boldsymbol{\varepsilon}, \varphi, \nabla\varphi) \ , \tag{D.6}$$

and is partitioned into two parts:

$$\psi(\boldsymbol{\varepsilon}, \varphi, \nabla\varphi) = \hat{\psi}_e(\boldsymbol{\varepsilon}, \varphi) + \hat{\psi}_f(\varphi, \nabla\varphi) \ , \tag{D.7}$$

with

$$\begin{aligned} &\hat{\psi}_e(\boldsymbol{\varepsilon}, \varphi) = \left((1-\varphi)^2\right) \hat{\psi}_e^{pos}(\boldsymbol{\varepsilon}) + \hat{\psi}_e^{neg}(\boldsymbol{\varepsilon}) \ , \\ &\hat{\psi}_e^{pos}(\boldsymbol{\varepsilon}) = \frac{1}{2}\left(\lambda \left\langle \operatorname{tr}\boldsymbol{\varepsilon} \right\rangle^2 + 2\mu\boldsymbol{\varepsilon}^{pos} : \boldsymbol{\varepsilon}^{pos}\right) \ , \\ &\hat{\psi}_e^{neg}(\boldsymbol{\varepsilon}) = \frac{1}{2}\left(\lambda \left\langle -\operatorname{tr}\boldsymbol{\varepsilon} \right\rangle^2 + 2\mu\boldsymbol{\varepsilon}^{neg} : \boldsymbol{\varepsilon}^{neg}\right) \ , \\ &\boldsymbol{\varepsilon}^{pos} = \sum_{k=1}^{3} \left\langle \varepsilon_k \right\rangle \boldsymbol{e}_k \otimes \boldsymbol{e}_k \ , \qquad \boldsymbol{\varepsilon}^{neg} = \sum_{k=1}^{3} - \left\langle -\varepsilon_k \right\rangle \boldsymbol{e}_k \otimes \boldsymbol{e}_k \ , \end{aligned} \tag{D.8}$$

where λ and μ are the Lamé parameters, ε_k and $\boldsymbol{e}_k$ are the k-th eigenvalue and eigenvector of $\boldsymbol{\varepsilon}$, respectively. The angle bracket operator, $\langle\cdot\rangle$, is the positive part of the argument. The partition of $\hat{\psi}_e$ defined in equation (D.8) is taken from Miehe et al. [57].

The second term in equation (D.7) results:

$$\hat{\psi}_f(\varphi, \nabla\varphi) = G_c \left(\frac{\varphi^2}{2\ell} + \frac{\ell}{2}|\nabla\varphi|^2\right) \ , \tag{D.9}$$

with G_c and ℓ denoting the fracture energy and the phase field order parameter, respectively.

Thus, the conjugate variables $\boldsymbol{\sigma}$, $\boldsymbol{\xi}$, π_a, are determined through the partial derivative of the free energy densities with respect to their corresponding dual variables:

$$\boldsymbol{\sigma} = \frac{\partial\psi}{\partial\boldsymbol{\varepsilon}} = \left((1-\varphi)^2\right)\left(\lambda \left\langle \operatorname{tr}\boldsymbol{\varepsilon} \right\rangle \boldsymbol{I} + 2\mu\boldsymbol{\varepsilon}^{pos}\right) + \left(-\lambda \left\langle -\operatorname{tr}\boldsymbol{\varepsilon} \right\rangle \boldsymbol{I} + 2\mu\boldsymbol{\varepsilon}^{neg}\right) \ , \tag{D.10}$$

$$\boldsymbol{\xi} = \frac{\partial\psi}{\partial\nabla\varphi} = G_c \, \ell \, \nabla\varphi \ , \tag{D.11}$$

$$\pi_a = \frac{\partial\psi}{\partial\varphi} = \frac{G_c}{\ell}\,\varphi - 2(1-\varphi)\hat{\psi}_e^{pos}(\boldsymbol{\varepsilon}) \ , \tag{D.12}$$

respectively. In equation (D.10), $\boldsymbol{I}$ is the second order identity tensor.

In view of (D.11) and (D.12), we rewrite (D.5) as:

$$\begin{array}{c} G_c\,\ell\,\nabla^2\varphi - \frac{G_c}{\ell}\,\varphi + 2(1-\varphi)\hat{\psi}_e^{pos}(\boldsymbol{\varepsilon}) - \pi_r = 0\ , \\ \text{subjected to:} \quad \pi_r \leq 0 \quad , \quad \dot{\varphi} \geq 0 \quad , \quad \dot{\varphi}\pi_r = 0 \end{array} \tag{D.13}$$

being $\nabla^2(\cdot)$ the Laplacian operator. Considering the staggered scheme that we propose in sub-Section D.3.1, this complementarity problem can be solved using the following strategies:

i) Reformulating the equation (D.13) by introducing the compact history function, $\mathcal{H}(t)$, such as proposed by Miehe et al. [98]. According with such strategy, π_r is defined as:

$$\pi_r = -2(1-\varphi)\big(\mathcal{H}(t) - \hat{\psi}_e^{pos}(\boldsymbol{\varepsilon}, t)\big)\ , \tag{D.14}$$

where $\mathcal{H}(t)$ results:

$$\mathcal{H}(t) = \max_{s} h(s), \quad s \in [0, t]\ , \tag{D.15}$$

with:

$$h(t) := \hat{\psi}_e^{pos}(\boldsymbol{\varepsilon}, t)\ . \tag{D.16}$$

By construction, the last term within the parenthesis in (D.14) is greater than or equal to zero. Therefore, the inequality $\pi_r \leq 0$ is automatically satisfied.

ii) Solving the following inequality-constrained optimization problem with $\boldsymbol{\varepsilon}$ fixed, as proposed by Amor et al. [99]:

$$\min_{1\geq\varphi\geq 0\ ;\ \dot{\varphi}\geq 0} \int_{\mathcal{B}} \psi\left(\boldsymbol{\varepsilon}, \varphi, \nabla(\varphi)\right) d\mathcal{B}\ . \tag{D.17}$$

The functional ψ is given by expressions (D.7)–(D.9). Considering the increments of pseudo-time Δt, the pseudo-times $(t - \Delta t)$ and t and defining $\varphi(t) = \varphi(t - \Delta t) + \Delta\varphi$, we rewrite this problem as follows

$$\min_{\Delta\varphi\geq 0\ ;\ 1\geq\varphi(t)} \int_{\mathcal{B}} \hat{\psi}\Big(\Delta\varphi, \nabla(\Delta\varphi)\Big) d\mathcal{B}\ , \tag{D.18}$$

where $\hat{\psi} = \psi\Big(\boldsymbol{\varepsilon}(t), \varphi(t), \nabla(\varphi(t))\Big)$.

iii) Imposing the inequality constraints via penalization or Lagrangian Multiplier techniques, as studied by Gerasimov y De Lorenzis [192] and references cited therein.

D.3. Discrete equation system of the phase field model

After reformulating the force and micro-force balance equations (D.4)–(D.5) into variational weak forms, replacing the constitutive expressions (D.10)-(D.12) into these weak forms and finally implementing a finite element approach for both balance equations, a rather standard procedure whose details have been described in Duda et al. [54], we finally express the resulting discrete equation system at pseudo-time t as follows:

1) Discrete force balance equations:

$$\boldsymbol{g}\big(\boldsymbol{u}(t), \boldsymbol{\varphi}(t), \boldsymbol{f}^{ext}(t)\big) = \boldsymbol{0}\ ; \tag{D.19}$$

2) Discrete micro-force balance equations:

$$\boldsymbol{\jmath}(\boldsymbol{u}(t), \boldsymbol{\varphi}(t)) = \boldsymbol{0} \quad , \quad (\dot{\varphi}_j \geq 0\ ,\ \forall j)\ ; \tag{D.20}$$

where the variables $\boldsymbol{u}(t), \boldsymbol{\varphi}(t)$ are now reinterpreted as the vectors gathering the displacement and phase field nodal values in the finite element mesh. In the equation (D.19), $\boldsymbol{f}^{ext}(\boldsymbol{u}^*, \boldsymbol{t}^*)$ denotes the vector of external actions that includes the tractions (Neumann boundary conditions) as well as the non-homogeneous displacements (Dirichlet boundary conditions) imposed on the boundary. Complementarity conditions for every component j-th of the vector $\boldsymbol{\varphi}$ are implicit in (D.20).

Next, we assume that the loading condition can be represented through a time-dependent scalar parameter, $\lambda(t)$, that determines the magnitude of the external action imposed on the body at time t, $\boldsymbol{f}^{ext}(\boldsymbol{u}^*, \boldsymbol{t}^*) = \lambda \hat{\boldsymbol{f}}^{ext}$, where $\hat{\boldsymbol{f}}^{ext}$ denotes a unit vector. Thus, $\lambda(t)$ identifies the external load magnitude at pseudo-time t.

D.3.1. Staggered Scheme

The staggered scheme to integrate the phase field problem equations at step $(n+1)$ uses a sequential solution of both balance equations as follows:

- First, given λ_{n+1} at step $n+1$, solve the standard discrete force balance equation with fixed damage variables whose values are those at the step n:

$$\boldsymbol{g}(\boldsymbol{u}_{n+1}, \boldsymbol{\varphi}_n, \lambda_{n+1}) = \boldsymbol{0} \ . \tag{D.21}$$

- Second, the phase field micro-force balance equation (D.20) is solved with fixed external loads, and the displacements are those obtained in the previous stage:

$$\boldsymbol{g}(\boldsymbol{u}_{n+1}, \boldsymbol{\varphi}_{n+1}) = \boldsymbol{0} \qquad , \qquad (1 \geq (\varphi_j)_{n+1} \geq (\varphi_j)_n) \ . \tag{D.22}$$

This process can be iterated by solving (D.21) with the value of the variable $\boldsymbol{\varphi}$ obtained as solution of (D.22). Following the denomination given by Lu et al. [102], we call it an explicit staggered scheme when no iteration is prescribed. This procedure is an alternative to an implicit staggered strategy where iterations of both stages, i.e., the sequential solutions of (D.21) and (D.22), is repeated in a given loading step until reaching the error convergence in a given norm. Explicit and implicit procedures could yield an uncontrolled advance of the crack in a one load step.

In the following, we show that an explicit staggered scheme with controlled error via an arc-length procedure could be a convenient technique for solving phase field brittle fracture problems.

D.3.2. Arc-length procedure with step length adaptation

A procedure for controlling the load increment along the equilibrium path in phase field models can be derived from energy-based control techniques reported in the literature, see [12], [13], [145], and [193].

The strategy consists of introducing a monotonously increasing arc-length parameter, s, governing the evolution of the load factor and displacements in the problem (D.21) jointly with an additional scalar control equation defining the magnitude of the increment of s. We recall that problem (D.21) is characterized by holding fixed the damage variables, and therefore, the dissipation is null in this stage.

The reformulated problem consists of solving:

$$\boldsymbol{g}\big(\boldsymbol{u}(s_{n+1}), \boldsymbol{\varphi}_n, \lambda(s_{n+1})\big) = \boldsymbol{0} \ , \tag{D.23}$$

$$r\big(\boldsymbol{u}(s_{n+1}), \lambda(s_{n+1}), s_{n+1}\big) = 0 \ , \tag{D.24}$$

where $\boldsymbol{u}_{n+1}$ and λ_{n+1} are now reinterpreted as implicit functions of s_{n+1} related through the control

equation (D.24) and defined in the following. Let us consider the term:

$$\mathcal{F}^{\text{driv}}(\boldsymbol{u}(t),\varphi_n) = 2(1-\varphi_n)\mathcal{H}(\boldsymbol{u}(t)) \;, \tag{D.25}$$

such that: $\dot{\mathcal{F}}^{\text{driv}} = 2(1-\varphi_n)\dot{\mathcal{H}}$ and $\mathcal{H}(\boldsymbol{u},t)$ satisfies the conditions (D.15)-(D.16) at pseudotimes t and $t+dt$. Then, rewriting equations (D.13) and (D.14) in rates[4] and operating, they result in:

$$-G_c\,\ell\,\nabla^2\dot{\varphi} + \left(\frac{G_c}{\ell} + 2\mathcal{H}\right)\dot{\varphi} = \underbrace{2(1-\varphi)\dot{\mathcal{H}}}_{\dot{\mathcal{F}}^{\text{driv}}} \;, \tag{D.26}$$

where, we interpret $\dot{\mathcal{F}}^{\text{driv}}$ as being the rate of a driving force governing the evolution of φ. Inspired by the role played by this term, we propose a driving force control-based strategy, reminiscent from May et al. [193], in where (D.24) is defined as follows:

$$\begin{aligned} r\big(\boldsymbol{u}(s_{n+1}),\lambda(s_{n+1}),s_{n+1}\big) &= \int_{\mathcal{B}} \mathcal{F}^{\text{driv}}(\mathcal{H}_{n+1},\varphi_n)\,d\mathcal{B} - s_{n+1} = \\ &= \int_{\mathcal{B}} 2(1-\varphi_n)\mathcal{H}_{n+1}\,d\mathcal{B} - s_{n+1} = 0 \;. \end{aligned} \tag{D.27}$$

Based on these expressions, we use a Newton-Raphson strategy for solving (D.23) and (D.27) at step $n+1$ as follows:

$$\boldsymbol{K}\,\Delta\boldsymbol{u} + \partial_\lambda \boldsymbol{g}\,\Delta\lambda = -res_{\boldsymbol{u}} \;, \tag{D.28}$$

$$\int_{\mathcal{B}} 2(1-\varphi_n)\Delta\mathcal{H}\,d\mathcal{B} - \Delta s = -res_s \;, \tag{D.29}$$

where $\boldsymbol{K}$ is the stiffness matrix, i.e. $\boldsymbol{K} = \partial_{\boldsymbol{u}}\boldsymbol{g}$, the residue of equations (D.23) and (D.27) are denoted $res_{\boldsymbol{u}}$ and res_s, respectively, and $\Delta(\cdot) = (\cdot)_{n+1} - (\cdot)_n$. At every load step, the increment Δs is adjusted according to $\Delta\varphi$, as explained in next sub-Section.

Recalling expressions (D.15) and (D.16), the term $\mathcal{H}_{n+1}$ at step $n+1$ is identified as:

$$\mathcal{H}_{n+1} = \begin{cases} \hat{\psi}_e^{pos}(\boldsymbol{\varepsilon}_{n+1}) = \frac{1}{2}(\boldsymbol{\varepsilon}_{n+1}\cdot\boldsymbol{\sigma}_{n+1}^{pos}) & \text{if} \quad \hat{\psi}_e^{pos}(\boldsymbol{\varepsilon}_{n+1}) > \hat{\psi}_e^{pos}(\boldsymbol{\varepsilon}_n) \\ \mathcal{H}_n & \text{if} \quad \hat{\psi}_e^{pos}(\boldsymbol{\varepsilon}_{n+1}) \le \hat{\psi}_e^{pos}(\boldsymbol{\varepsilon}_n) \end{cases} \;, \tag{D.30}$$

where we define

$$\boldsymbol{\sigma}_{n+1}^{pos} = \begin{cases} (\lambda\,\langle \text{tr}\,\boldsymbol{\varepsilon}_{n+1}\rangle\,\boldsymbol{I} + 2\mu\boldsymbol{\varepsilon}_{n+1}^{pos}) & \text{if} \quad \hat{\psi}_e^{pos}(\boldsymbol{\varepsilon}_{n+1}) > \hat{\psi}_e^{pos}(\boldsymbol{\varepsilon}_n) \\ 0 & \text{if} \quad \hat{\psi}_e^{pos}(\boldsymbol{\varepsilon}_{n+1}) \le \hat{\psi}_e^{pos}(\boldsymbol{\varepsilon}_n) \end{cases} \;, \tag{D.31}$$

as well as the first order approximation of $\dot{\mathcal{H}}$: $\Delta\mathcal{H} = \mathcal{H}(\boldsymbol{\varepsilon}_{n+1}) - \mathcal{H}(\boldsymbol{\varepsilon}_n)$, it results:

$$\Delta\mathcal{H} = \begin{cases} \frac{1}{2}(\Delta\boldsymbol{\varepsilon}\cdot\boldsymbol{\sigma}_n^{pos} + \boldsymbol{\varepsilon}_n\cdot\Delta\boldsymbol{\sigma}^{pos}) & \text{if} \quad \hat{\psi}_e^{pos}(\boldsymbol{\varepsilon}_{n+1}) > \hat{\psi}_e^{pos}(\boldsymbol{\varepsilon}_n) \\ 0 & \text{if} \quad \hat{\psi}_e^{pos}(\boldsymbol{\varepsilon}_{n+1}) \le \hat{\psi}_e^{pos}(\boldsymbol{\varepsilon}_n) \end{cases} \;. \tag{D.32}$$

Also, from the identity $\dot{\mathcal{H}} = \dot{\boldsymbol{\varepsilon}}\cdot\boldsymbol{\sigma}^{pos}$, we consider the following approximate expression: $\Delta\mathcal{H} \approx \Delta\boldsymbol{\varepsilon}\cdot\boldsymbol{\sigma}_{n+1}^{pos}$. Under such conditions, the first term on the left hand side of equation (D.29) is approximated by:

$$\int_{\mathcal{B}} 2(1-\varphi_n)\Delta\mathcal{H}\,d\mathcal{B} \approx \int_{\mathcal{B}} 2(1-\varphi_n)\Delta\boldsymbol{\varepsilon}\cdot\boldsymbol{\sigma}_{n+1}^{pos}\,d\mathcal{B} = \Delta\boldsymbol{u}\cdot\boldsymbol{F}_{int}^{pos} \;, \tag{D.33}$$

[4] The finite element approach of this equation is described in Duda et al. [54].

where we have defined the positive internal force vector:

$$\boldsymbol{F}_{int}^{pos} = \int_{\mathcal{B}} 2(1-\varphi_n)\boldsymbol{B}^T \boldsymbol{\sigma}_{n+1}^{pos}\, d\mathcal{B} \,. \tag{D.34}$$

with $\boldsymbol{B}$ being the conventional strain-displacement matrix.

Finally, taking into account (D.33), equations (D.28) and (D.29) can be solved to obtain:

$$\Delta \boldsymbol{u} = \Delta \boldsymbol{u}_I + \Delta\lambda \Delta \boldsymbol{u}_{II} \;, \tag{D.35}$$

where

$$\Delta \boldsymbol{u}_I = -\boldsymbol{K}^{-1}\, res_{\boldsymbol{u}} \quad , \quad \Delta \boldsymbol{u}_{II} = -\boldsymbol{K}^{-1}\, \partial_\lambda g \;, \tag{D.36}$$

$$\Delta\lambda = \frac{(\Delta s - res_s) - \Delta \boldsymbol{u}_I \cdot \boldsymbol{F}_{int}^{pos}}{\Delta \boldsymbol{u}_{II} \cdot \boldsymbol{F}_{int}^{pos}} \,. \tag{D.37}$$

The vector $\boldsymbol{F}_{int}^{pos}$ is evaluated at each Newton-Raphson iteration of the step $n+1$.

When expression (D.33) is equal to zero, the arc-length strategy switches to an alternative control procedure, as discussed in May et al. [193]. However, this situation has never occurred in the tests assessed in Section D.4.

D.3.2.1. Adjust of the arc-length parameter in terms of $\Delta\varphi$

The arc-length parameter, Δs, at step $n+1$ is adjusted in terms of the phase field variable increment at step n as follows:

$$\Delta s_{n+1} = \Delta s_n \left(\frac{\Delta \hat{\varphi}^{opt}}{\|(\boldsymbol{\varphi}_n - \boldsymbol{\varphi}_{n-1})\|_\infty} \right)^{1/2} \leq \Delta s^{max} \;, \tag{D.38}$$

where $\Delta\hat{\varphi}^{opt}$ and Δs^{max} are two parameters of the algorithm representing the maximum desired phase field increment per staggered scheme step and the maximum allowed size of the arc-length, respectively. This expression is adopted by following the same idea reported by Crisfield [194], formula (9.41), pp. 287, to adjust the arc-length control parameter but written in terms of $\Delta\hat{\varphi}^{opt}$ and $\Delta\varphi = (\|\boldsymbol{\varphi}_n - \boldsymbol{\varphi}_{n-1})\|_\infty$ instead of using, as proposed by Crisfield, the desired number of iterations required by the iterative solver and the number of iterations demanded by the last converged step, respectively.

The proposed methodology follows the strategy of adjusting Δs with expression (D.38), combined with an explicit staggered scheme, i.e., we evaluate only one mechanical and one damage stage per step in the staggered scheme. Furthermore, we calculate the mechanical stage solutions with a tight error tolerance (less than 1×10^{-7}).

The algorithmic performance attained with this strategy is specifically assessed in Section D.5.

D.3.2.2. Novelty of the proposed arc-length control strategy

Previous works, such as Bharali et al. [146],Börjesson et al. [147], and Singh et al. [145] have utilized an arc-length procedure with a control equation that limits the increments of the phase field variable. In particular, Singh et al. describe an arc-length procedure combined with a staggered scheme. Our strategy offers an alternative approach whose advantages are discussed in the following.

Two arc-length strategies combined with staggered schemes

Let us reconsider the staggered scheme described with the equations (D.21) and (D.22) and the control equation indicated through: $r = 0$, where r is the control function whose argument *depends on different variables, according to each arc-length strategies.*

- In the first strategy, such as reported by Singh et al. [145], a loading control procedure based on prescribing the increment of the fracture surface area through equation: $r_{dam} = 0$ is proposed. Then, the micro-force balance equation is solved in combination with the control equation:

$$\boldsymbol{\jmath}\big(\boldsymbol{u}_n, \boldsymbol{\varphi}(s_{n+1}), \lambda(s_{n+1})\big) = \mathbf{0} \quad ; \quad (1 \geq \varphi_j(s_{n+1}) \geq \varphi_j(s_n)\ ,\ \forall j)\ , \tag{D.39}$$

$$r_{dam}\big(\boldsymbol{\varphi}(s_{n+1}), \lambda(s_{n+1}), s_{n+1}\big) = 0\ , \tag{D.40}$$

  with $\boldsymbol{u}_n$ hold fixed. The staggered scheme follows by solving the discrete force balance equations to find $\boldsymbol{u}_{n+1}$. Thus, according to this strategy, there is not an explicit relationship between $\boldsymbol{u}_{n+1}$ and s_{n+1} in each step.

- The present strategy, as shown above, proposes a control load procedure prescribing the increment of the history variable through equation $r_{mech} = 0$. Thus, the equations solved in the mechanical stage are:

$$\boldsymbol{g}\big(\boldsymbol{u}(s_{n+1}), \boldsymbol{\varphi}_n, \lambda(s_{n+1})\big) = \mathbf{0}\ , \tag{D.41}$$

$$r_{mech}\big(\boldsymbol{u}(s_{n+1}), \lambda(s_{n+1}), s_{n+1}\big) = 0\ , \tag{D.42}$$

  with $\boldsymbol{\varphi}_n$ hold fixed. The staggered scheme follows by solving the discrete micro-force balance equations to find $\boldsymbol{\varphi}_{n+1}$. By construction, notice that dissipation due to phase field evolution is null in equations (D.41) and (D.42).

The two control strategies, applied at different stages of the staggered scheme, have significant algorithmic implications when solving certain types of phase field problems, for example:

i) Phase field methodologies that solve the micro-force balance equation using a bound-constrained optimization problem, as formulated in (D.18), can be easily integrated into our arc-length strategy using the control equation (D.27). A numerical test that demonstrates the feasibility and effectiveness of the procedure in this situation is presented in Section D.4.2. Other methodologies that impose inequality constraints on the micro-force balance equation via penalization or Lagrangian Multiplier techniques can also be similarly integrated into our approach. In all these methodologies, the common feature leveraged by our procedure is that the increment of the driving force term, $\dot{\mathcal{F}}^{\text{driv}}$, governing the damage increment, though different in every methodology, can be closely controlled with the same equation (D.27).

   On the other hand, when the arc-length strategy limits the phase field increments in the micro-force balance equation, the problem (D.18) have to be solved monolithically in the extended space of variables (φ, λ) combined with the control equation $r_{dam} = 0$. In this case, the problem to be solved can no longer be viewed as the optimality condition of a minimization problem in the increased space of variables. Thus, conventional constrained optimization algorithms are inapplicable.

ii) Secondly, in problems where the damage mechanism, modeled through the phase field variable, coexists with other dissipative mechanisms that induce instability and are related to $\boldsymbol{u}$, such as happens in plasticity, cohesive interfaces, etc., the arc-length strategy has to manage the loading process whichever the mechanism inducing instability is.

   As discussed earlier, our strategy allows for controlling the competition between several unstable mechanisms by extending the definition of the control function r_{mech}, as demonstrated in the numerical assessment of Section D.4.5. However, with the alternative arc-length strategy, it is

challenging to include the control of displacement DOFs that experience instability by extending the definition of the control function r_{dam}.

D.4. Numerical assessments

With the numerical assessments in this Section, we achieve two objectives. Firstly, we evaluate the performance of the previously outlined arc-length control strategy. The seven tests display unstable crack propagation under displacement or force control demostrating the necessity of using an arc-length procedure for controlling the crack tip advance and the numerical integration error. Secondly, we show the range of problems that can be assessed with the present arc-length technique combined with a staggered strategy. Thus, the Double-Edged Notched Test (DENT), in Section D.4.2, is solved by appealing to the compact history function technique as well as to the Bound-Constrained Optimization Problem (BCOP). Furthermore, the last test in sub-Section D.4.5 displays multiple instability mechanisms, not only those caused by the phase field evolution. This test highlights the capacity of the arc-length procedure for controlling multiple instabilities, including those produced by the phase field evolution.

The computational performance of the algorithm implemented to solve these tests are further analysed in the following Section D.5.

As general comments describing the following seven tests, we mention that the pre-existent cracks in the DENT specimen and the Notched Plate with Hole Test (NPHT) of subsection D.4.3 are modeled with a finite element mesh of unconnected elements. We also consider two different initial conditions for the phase field variable. In general, we assume that $\varphi(\boldsymbol{x}) = 0 \ \forall \boldsymbol{x} \in \mathcal{B}$. However, we also report alternative solutions with a no-null initial condition of $\boldsymbol{\varphi}$, the initial nodal values of $\boldsymbol{\varphi}$ are constrained to 1 in the nodes on the notch root, a procedure used in Singh et al. [145] and here denoted as Phase Field Tip-Enrichment (PFTE). Plane strain conditions are also assumed in all tests, and the bar problem in sub-Section D.4.1 is simulated with a Poisson's ratio $\nu = 0$.

D.4.1. Instability analysis of a uniform tensile bar

We analyze the unstable response of a uniform bar under tensile load. A semi-analytical solution of the problem, similar to the one reported by Pham y Marigo [195], is briefly described. Afterward, we compare the numerical solutions obtained with the present control strategy using a small perturbation of the bar section triggering the non-homogeneous solution. The arc-length control strategy plays a role in transitioning smoothly through the instability region.

D.4.1.1. Semi-analytical solution of an infinite bar under tensile stress

Let us consider a 1D bar of infinite length placed along the $x-$axis undergoing a tensile load. The tensile stress is σ. The balance equation (D.4) particularized for this problem, neglecting body forces, results in $\sigma_{,x} = 0$. The sub-index identifies the derivative with respect to the variable x. Similarly, the first three terms on the left-hand side of the micro-force balance equation (D.13) results:

$$\pi_r(\varphi, \sigma) = G_c \, \ell \, \varphi_{,xx} - \frac{G_c}{\ell} \, \varphi + \frac{\sigma^2}{E(1-\varphi)^3} \leq 0 \qquad , \qquad \dot{\varphi} \geq 0 \qquad , \qquad \dot{\varphi} \pi_r = 0 \, , \tag{D.43}$$

where we have used the identity: $\hat{\psi}_e^{pos}(\boldsymbol{\varepsilon}) = \sigma^2/(2E(1-\varphi)^4)$, with E the Young modulus of the bar. One homogeneous solution, φ^h , satisfying $\varphi^h_{,x} = 0$ is determined from the condition $\pi_r = 0$ and results in:

$$\sigma^h = \sqrt{\frac{G_c E}{\ell} \varphi^h (1-\varphi^h)^3} \, . \tag{D.44}$$

The strain is determined from the constitutive equation (D.10) particularized for the 1D problem:

$$\varepsilon^h = \sqrt{\frac{G_c}{E\ell}\frac{\varphi^h}{(1-\varphi^h)}} \ . \tag{D.45}$$

The solution $\sigma^h(\varepsilon^h)$ with $\varphi^h \in [0,1]$ becomes unstable at the point of maximum stress σ^{hcrit} obtained for $\varphi^{crit} = 0.25$, independently of the material properties. We also consider the non-homogeneous solution of equation $\pi_r(\varphi,\sigma) = 0$, which is reformulated as follows:

$$\left(-(\varphi_{,x})^2 + \frac{\varphi^2}{\ell^2} - \frac{\sigma^2}{G_c E\ell(1-\varphi)^2}\right)_{,x} = 0 \ , \tag{D.46}$$

whose solution is:

$$-(\varphi_{,x})^2 + \frac{\varphi^2}{\ell^2} - \frac{\sigma^2}{G_c E\ell(1-\varphi)^2} - k_\sigma = 0 \ , \tag{D.47}$$

being k_σ a constant term determined from the boundary condition at $x \to \infty$, where $\varphi_{,x} \to 0$, $\sigma = \sigma_\infty$ and $\varphi(x \to \infty) = \varphi_\infty$. Thus, k_σ results in:

$$k_\sigma = \frac{\varphi_\infty^2}{\ell^2} - \frac{\sigma_\infty^2}{G_c E\ell(1-\varphi_\infty)^2} \ . \tag{D.48}$$

With these values of k_σ and σ_∞, there is a phase field solution, $\varphi(x)$, with $\varphi(0) = \varphi_0 \geq \varphi_\infty$ and $\varphi_{,x}(0) = 0$, satisfying (D.47). Thus, equation (D.47) can be integrated as follows:

$$x(\varphi^*) = \int_{\varphi_0}^{\varphi^*} \left(\frac{\varphi^2}{\ell^2} - \frac{\sigma_\infty^2}{G_c E\ell(1-\varphi)^2} - k_\sigma\right)^{-1/2} d\varphi \ , \tag{D.49}$$

where $\varphi^* \geq \varphi_\infty$, and $x(\varphi^*)$ is the coordinate of the bar in where $\varphi(x) = \varphi^*$.

The semi-analytical procedure for determining the non-homogeneous solution along the loading process consists of parameterizing the non-homogeneous equilibrium path with the stress σ. In successive discrete steps (N_{steps} is the number of steps), we define $\sigma_n \in [0, \sigma^{crit}]$, starting at step 1 with $\sigma_1 = \sigma^{crit}$ and decreasing the stress until reaching $\sigma_{N_{steps}} = 0$. Thus, given σ_n, we determine the corresponding terms $(\varphi_0)_n$, $(\varphi_\infty)_n$ for $(\sigma_\infty)_n = \sigma_n$, and numerically integrate the curve $\pi_r(\varphi(x), \sigma_n) = 0$ using expression (D.49). If the solution $\varphi(x) > \varphi_{n-1}(x)$, we take $\varphi_n(x) = \varphi(x)$, if not, we take $\varphi_n(x) = \varphi_{n-1}(x)$. This semi-analytical procedure is sketched in Figure D.1-b.

D.4.1.2. Finite element solution and the arc-length control strategy

The finite element solution of the 1D test is assessed with a unit length bar. The model parameters are Young modulus $E = 100MPa$, fracture energy $G_c = 0.001N/mm$, and characteristic length: $\ell = 0.02mm$. A perturbation of the bar area is established, as depicted in Figure D.1-a The region of the bar with coordinates $0 \leq x \leq \ell$ is modeled with 32 finite elements with sizes becoming smaller as $x \to 0$. A fine mesh in this region is necessary to assess the tendency of the localization zone thickness as the damage increases to 1.

Figure D.1-c. depicts plots of force f versus displacement δ. We compare the semi-analytical solution with two finite element solutions obtained with the arc-length procedure. The parameter $\Delta\hat{\varphi}^{opt}$ of the arc-length procedure are 10^{-4}, and 0.5×10^{-4}, respectively, enforcing very short step increments.

We identify the bar localization zone as the points satisfying $\dot{\varphi} > 0$. The localization zone size, L_{dam}, changes during the loading process. Figure D.1-d shows L_{dam} versus the maximum damage, $(\varphi_0)_n$, as the loading process progresses. This Figure plots the solutions of the finite element and semi-analytical models. Details are shown in the inset. Observe that the localization zone width tends to zero as the

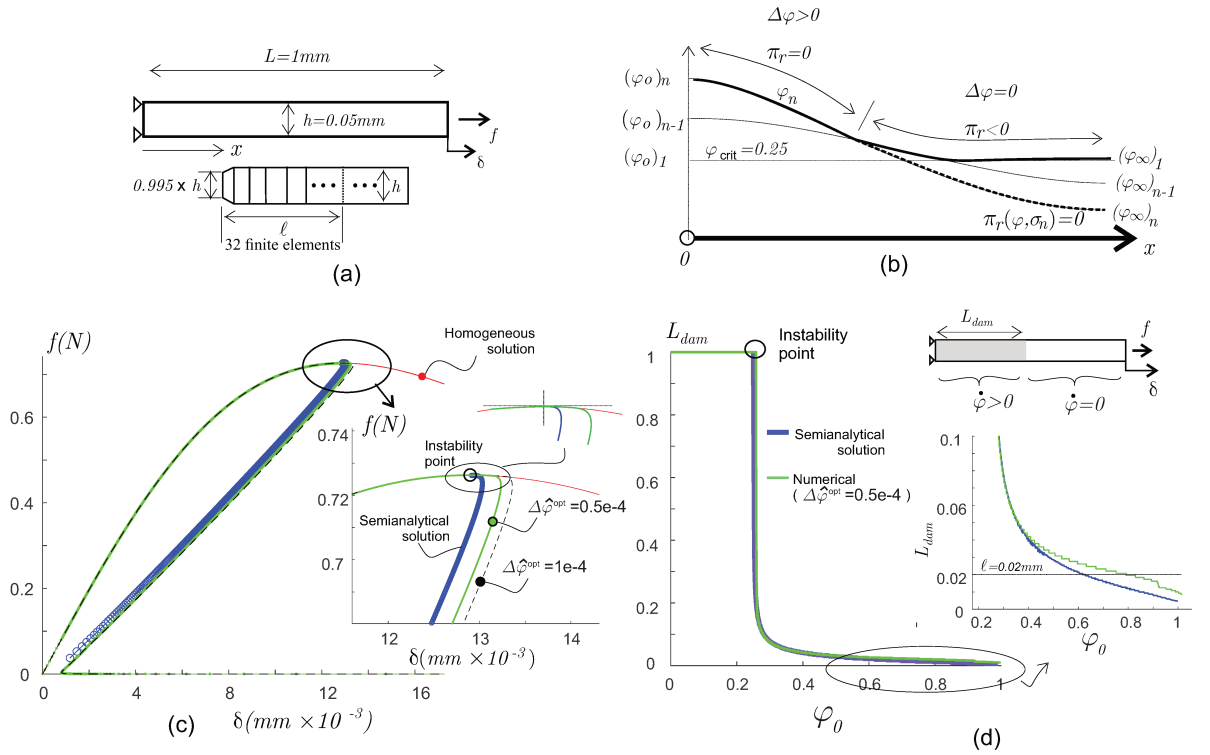

Figura D.1: Bar under tensile load. a) Geometrical perturbation and material properties. b) Semi-analytical procedure satisfying the complementarity conditions. c) Force versus displacement plot. Curves corresponding to the homogeneous and localized solutions have horizontal tangent lines at the limit point. See further details in the inset. d) Size of the localization zone, L_{dam}, in terms of the maximum damage, φ_0, in successive load steps.

damage grows to 1. This result means that all nodal displacements, except the ones closer to $x = 0$, display a backtrack behaviour, as shown in Figure D.2. This feature makes this problem particularly difficult to attain solutions with loading techniques based on displacement control.

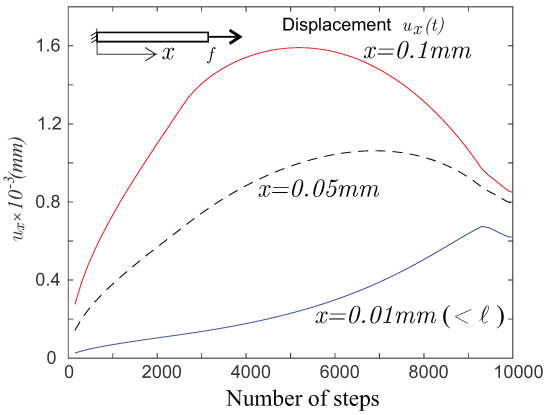

Figura D.2: Bar under tensile load. Displacements, u_x, of bar points at coordinates: $x = 0.1mm$, $x = 0.05mm$, and $x = 0.01mm$ versus number of load step. Solution with $\Delta\hat{\varphi}^{opt} = 0.5 \times 10^{-4}$.

D.4.2. DENT panel test under uniform displacement

A Double-edged notched test (DENT) whose specimen geometry is depicted in Figure D.3-a is assessed. The phase field problem (D.13) is solved using two procedures: a) the compact history function,

as proposed in equations (D.14)–(D.16), and b) the Bound-Constrained Optimization Problem (BCOP) methodology, as proposed in equation (D.18).

Uniform vertical displacements in the top and bottom edges of the specimen are prescribed. Assuming two symmetric cracks propagating from both notches, only one-fourth of the specimen is modeled. The model parameters are Young modulus $E = 2.5GPa$, Poisson's ratio $\nu = 0.25$, fracture energy $G_c = 5N/mm$, and characteristic length: $\ell = 1.8mm$.

A uniform finite element mesh, with element sizes $1.67h_e \times h_e$ ($h_e = 0.1mm$), is taken for modeling the crack propagation region.

The accuracy of solutions is estimated by computing the area, $W^{ext} = \int_0^\infty 2f(\delta)d\delta$, enclosed by the force-displacement curve once the specimen reaches the complete load capacity loss. Under linear elastic fracture conditions, the area should reproduce the energy release W^E (per unit thickness) ruled by the fracture energy G_c:

$$W^E = G_c \frac{b}{2} \,, \tag{D.50}$$

where the term $b/2$ is the crack path length at the end of the crack propagation process. Thus, the relative percent error of the energy release is:

$$e_W = \frac{W^{ext} - W^E}{W^E} \times 100 \,. \tag{D.51}$$

D.4.2.1. Results obtained with the compact history function methodology

Results of the numerical assessments, in terms of force $f/2$ versus displacement δ, are plotted in Figure D.3-b. We show three results run with phase field enrichment at the crack tip (PFTE) and different tolerances $\Delta\hat{\varphi}^{opt}$ (10^{-2}, 5×10^{-3}, and 2.5×10^{-3}, respectively). We also show the solution attained without phase field enrichment (without PFTE) and $\Delta\hat{\varphi}^{opt} = 10^{-2}$. The Figure inset depicts a zoom of the structural limit load region. The limit loads of solutions obtained with and without PFTE are notably different, a feature that agrees with the results reported in the literature ([145], [113]).

Though the results with PFTE look very similar in all three cases, the accuracy measured in terms of the error, e_W, depicted in Table D.1, gives a different insight.

The mechanical partition of the staggered scheme converges to the required tolerance in all steps, independently of the parameter $\Delta\hat{\varphi}^{opt}$. Convergence of the mechanical partition demanded between 3 to 7 iterations per step.

The plot in Figure D.3-c displays the evolution of the CTOD (Crack Tip Opening Displacement) measured at the original crack tip versus the step number. This variable shows a non-monotonous increase as the crack propagates. Therefore, due to the non-monotonic behaviour, the CTOD is not an adequate variable that can be taken as the arc-length parameter.

Identifying the crack tip as the point on the symmetry x-axis intersected by the phase field iso-level curve of value $\varphi = 0.92$, then, Figure D.3-d plots the crack length versus the step number. Notice that the arc-length control strategy strictly regulates the crack tip advance during the snap-back process.

D.4.2.2. Results obtained with the BCOP methodology.

The effectiveness of the arc-length control strategy is additionally examined by solving the damage stage of the staggered scheme through the BCOP methodology defined with equation (D.18). This BCOP methodology is implemented with the interior-point-convex algorithm of Matlab[5]. The mechanical stage is identical to that used with the compact history function approach, i.e., the equation (D.23) and the control equation (D.27) are solved together in this stage.

[5] Quadprog Matlab routine.

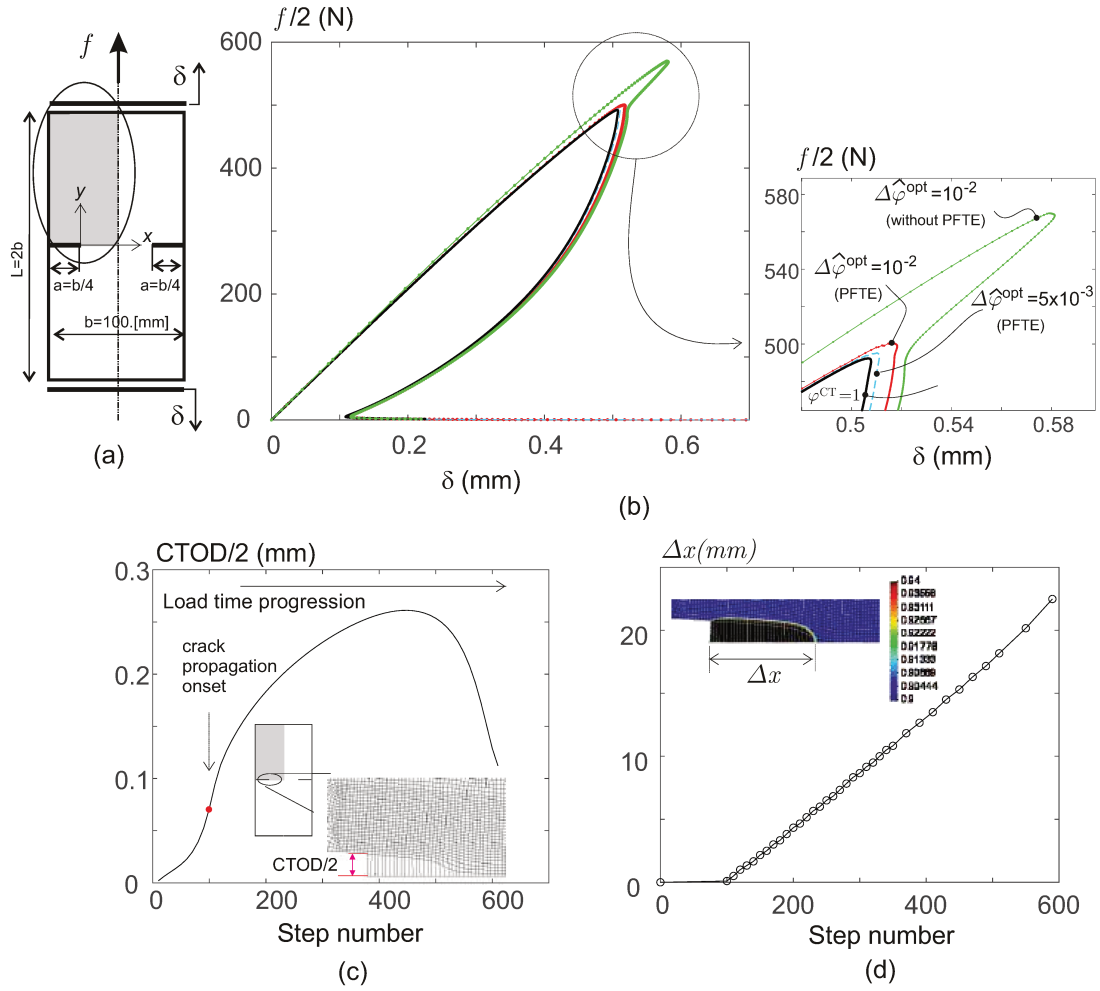

Figura D.3: Double-edged notched test (DENT). a) Specimen geometry. b) Half of the total force f versus displacement δ. Solutions obtained with $\Delta\hat{\varphi}^{opt}$: 10^{-2}, 5×10^{-3}, and 2.5×10^{-3} (with PFTE) and 10^{-2} (without PFTE). c) CTOD versus step number. d) Crack tip position versus step number.

Figure D.4-a compares the load versus displacement curves obtained with the BCOP methodology and the compact history function with tolerance $\Delta\hat{\varphi}^{opt} = 0.5\times10^{-2}$ and PFTE. Both solutions are almost indistinguishable. However, Figure D.4-b displays notable differences in phase field distributions along the crack path transverse direction. The phase field obtained with the compact history function shows a more dispersed solution than that obtained with the BCOP. This feature agrees with similar comparisons reported in the literature.

Table D.1 compares the errors, e_W, defined in equation (D.51) in different runs. It also reports the number of steps to attain the displacements $\delta = 0.2mm$ for the BCOP solution and $\delta = 0.7mm$ for the compact history function solution. In this sense, the performance is similar for both methodologies. However, the problem solved with the BCOP methodology demands a substantially higher CPU time than that required by the compact history function methodology.

Figure D.11 in Section D.5 examines additional outcomes of the numerical efficiency of the arc-length control strategy combined with the BCOP approach for solving this test.

D.4.3. Notched plate with hole (NPWH)

The notched plate with an eccentric hole (NPWH) depicted in Figure D.5-a is evaluated. The load consists of a prescribed displacement δ. This plate has been experimentally tested, numerically assessed,

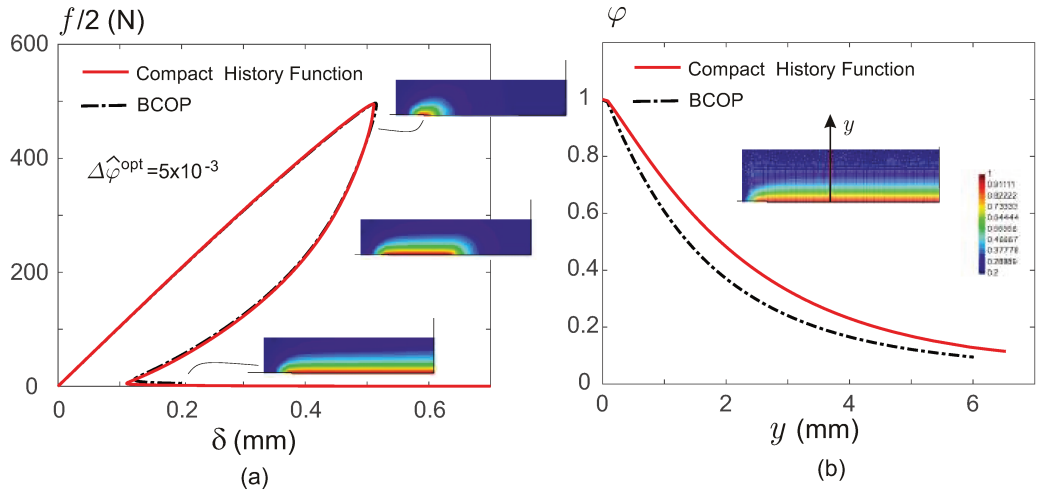

Figura D.4: Double-edged notched test (DENT). Comparison of results obtained with the compact history function and BCOP approaches. a) Half of the total force f versus displacement δ, tolerance $\Delta\hat{\varphi}^{opt}$: 0.5^{-2} (with PFTE). c) Phase field along a line orthogonal to the crack path, at the end of analysis.

and reported in the work of Ambati et al. [196].

The material used to perform the experimental test is concrete. However, in the present simulation, we adopt similar model parameters to those taken in the reference work, i.e., Young modulus $E = 5.98GPa$, Poisson's ratio $\nu = 0.221$ and $G_c = 2.28N/mm$. The phase field characteristic length is $\ell = 0.5mm$, which is five times higher than that adopted by Ambati et al. The value $\ell = 0.5mm$ allows us to use a coarse mesh with 8500 bilinear quadrilateral finite elements. In the region of the specimen where the crack is expected to propagate, the mesh is uniform with element sizes between $0.15mm$ and $0.25mm$. Tests are run without PFTE and $\Delta s^{max} = 0.6Nmm$.

Tabla D.1: Double-edged notched test (DENT). Relative percent errors and number of steps required for different runs. Solutions obtained with PFTE. Comparison between procedures using compact history function and BCOP methodologies.

$\Delta\hat{\varphi}^{opt}(\times 10^{-2})$	Compact history function		BCOP methodology	
	e_W	Number of steps	e_W	Number of steps
2.5	–	–	24 %	220
1.0	13 %	600	12.3 %	585
0.5	10 %	1150	8.5 %	1300
0.25	8 %	2340	6.7 %	2450

D.4.3.1. Results

The attained crack path at the end of the analysis, when $\delta = 2mm$, is shown in Figure D.5-b. It is similar to that observed in the experimental and numerical results of the reference work. The plots of load f versus displacement δ curves obtained with tolerance $\Delta\hat{\varphi}^{opt} = 10^{-2}, 2 \times 10^{-2}, 5 \times 10^{-2}$, and 10×10^{-2}, are shown in Figure D.5-c. The inset of this Figure depicts a zoom of these plots in the snap-back region, coinciding with the instant when the crack reaches the eccentric hole.

The errors of the solutions in different runs are assessed with expression (D.51). Here, W^E is the area enclosed by the curve with tolerance $\Delta\hat{\varphi^{opt}} = 10^{-2}$. This solution is taken as the reference one. These errors are shown in Table D.2.

The initial crack starts at the sharp notch root (Point I in Figure D.5-b) in coincidence with point A in the load-displacement curve. Then, it propagates until its intersection with the eccentric hole at point II in Figure D.5-b. The equilibrium curve displays a marked snap-back effect when the crack

Tabla D.2: NPWH specimen. Relative percent error for different runs and number of steps (staggered strategy).

$\Delta\hat{\varphi^{opt}}$ ($\times 10^{-2}$)	e_W	Number of steps
2	3 %	1730
5	16 %	665
10	45 %	280

is close to intersecting the hole boundary, coinciding with Point C in the Figure inset, details of the crack morphology are shown in Figure D.5-d. The unloading process continues until reaching Point D, details are shown in Figure D.5-e. As expected, the crack deviates its direction to intersect the hole boundary orthogonally, such as required by the boundary condition in equation (D.5)-b. A posterior reload, from Point D to F, is observed. The parameter Δs^{max} plays a role in this loading stage by limiting the maximum step length. During this reloading process, in the neighborhood of point II shown in Figure D.5-b, there is a stress state with positive principal stresses parallel to the crack. This effect induces a stable damage increase and a widening of the area with $\varphi = 1$, as shown in Figure D.5-g. The features observed in the sequence of pictures in Figure D.5-d, e, f, and g are captured with a precise crack advance control strategy supplied by the arc-length technique.

Also, the reloading process generates a second crack starting on the smooth boundary at the right part of the eccentric hole. This instant corresponds to Point F in Figure D.5-c. The propagation process of this second crack, from Point III to Point IV in Figure D.5-b, describes an equilibrium curve with a well-marked snap-back effect.

The characteristic equilibrium curve of this test displays a similar feature to that shown by the specimen with an eccentric hole in Figure D.8. Two limit points define the nucleation of both cracks, and two well-marked snap-backs determine the equilibrium curve at posterior loading regimes. However, in this test, the nucleation of both cracks has different natures. The material fracture energy governs the crack nucleation in the notch root. Instead, the material strength governs the crack nucleation on the right part of the eccentric hole; the lack of a pre-existing notch produces this effect. Hence, the first crack is not susceptible to the material strength, and consequently, it is not sensitive to the characteristic length parameter ℓ. By which, the limit load (Point A in Figure D.5-c) of our numerical result agrees well with the solution of Ambati et al. Alternatively, the second crack is sensitive to the material strength and governed by the parameter ℓ. So, the corresponding limit load, point F in Figure D.5-c, does not coincide with that reported by Ambati et al. Further details of the discussion about crack nucleation in both cases can be seen in the works of Kumar et al. [156].

D.4.4. Single edge notched shear test (SENST)

The (SENST) square specimen with size 1x1mm shown in Figure D.6-a is evaluated. This specimen undergoes prescribed displacements on its boundary compatible with a pure shear deformation mode. A phase field approach assesses the fracture path with model parameters $E = 210GPa$, $\nu = 0.3$, $G_c = 2.7N/mm$, and characteristic length $\ell = 0.015mm$. This test has been widely solved and reported in the literature using a phase field approach. In Section D.5, we compare the performance of these results with our assessments.

We evaluate the equilibrium curve using two finite element meshes: a) the coarse mesh with 13100 bilinear quadrilateral elements is homogeneous only in the region intersected by the crack, and the finite element size in this zone is $h^{ef} \approx \ell/4$, b) the finer mesh with 390990 bilinear quadrilateral elements is a homogeneous structured mesh in the complete domain, with finite element sizes $h^{ef} \approx 0.0016mm$. Phase field tip enrichment (PFTE) is modeled in all cases. Using the coarse mesh, we obtain four equilibrium curves with tolerances $\Delta\hat{\varphi}^{opt}$, 0.5×10^{-2}, 1×10^{-2}, 2×10^{-2}, and 4×10^{-2}. The force F versus displacement δ curves are shown in Figure D.6-b. The structural behaviour in these cases is stable under

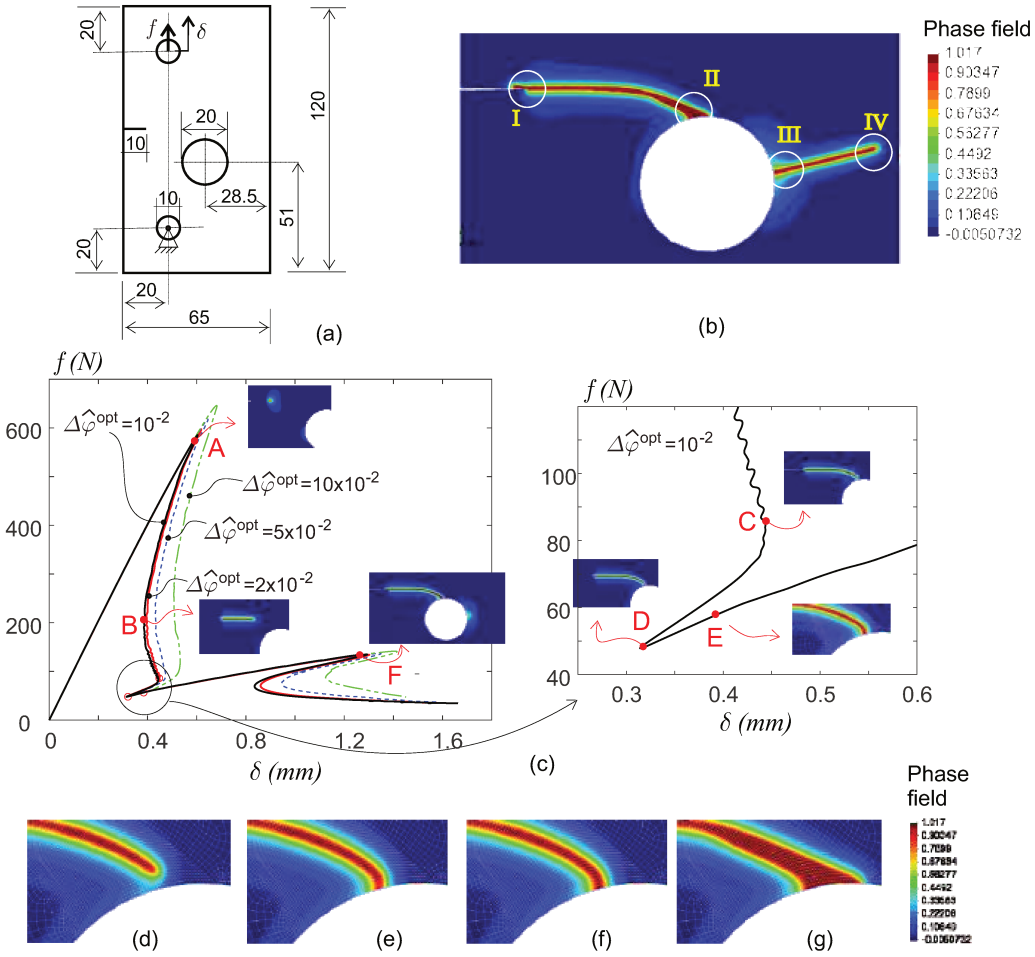

Figura D.5: Notched plate with a hole (NPWH). a) Specimen geometry. b) Crack path at the end of the analysis ($\delta = 2mm$). c) Force f versus displacement δ. d), e), f), and g) Sequence of crack advance images when the crack intersects the hole. Images: d), e), f), and g) correspond to Points C, D, E, and F in the equilibrium curve, respectively.

prescribed displacements, except when the crack reaches the bottom part of the specimen where snap-backs are captured. The subsequent structural responses, from Point A to B, display a spurious apparent strength increase attributed to the combined effect of compressive stresses in the lower right part of the specimen and the adopted type of free energy partition defined in Equation (D.8).

Figure D.6-c compares F versus δ solutions obtained with the fine and coarse meshes and $\Delta\hat{\varphi}^{opt} = 4 \times 10^{-2}$ in both cases.

Accuracy versus computational cost assessment. Table D.3 shows the errors of our coarse mesh numerical solutions assessed with the expression (D.51). W^E is the area enclosed by the solution with tolerance $\Delta\hat{\varphi}^{opt} = 0.5 \times 10^{-2}$ and coarse mesh taken as the reference one. The Table also describes the number of steps requeired for solving the staggered scheme until reaching the displacement $\delta = 0.014mm$. The computational cost, CPU time[6], demanded in every run is also reported in the last column.

Additional discussion on the performance of the staggered scheme combined with our arc-length strategy for solving this problem are analysed in Section D.5.

[6]Our results are obtained with a desktop computer, with an AMD Ryzen 9 5900X 12-Cores processor, and a home-made Matlab code using sparse matrices and "parfor" for assembling global matrices. Running the same problems in sequential mode, with only one core, the CPU times for the instances $\Delta\hat{\varphi}^{opt} = 1 \times 10^{-2}$ and $\Delta\hat{\varphi}^{opt} = 4 \times 10^{-2}$ have been $9975.sec$ and $2850.sec$, respectively.

Tabla D.3: SENST specimen. Relative percent error for different runs, number of steps (staggered strategy), and CPU times.

$\Delta\hat{\varphi}^{opt}$ $(\times 10^{-2})$	e_W	Number of steps	CPU time (sec)
0.5	–	3540	5907
1	1.4 %	1697	2249
2	4.2 %	826	990
4	9.2 %	394	451

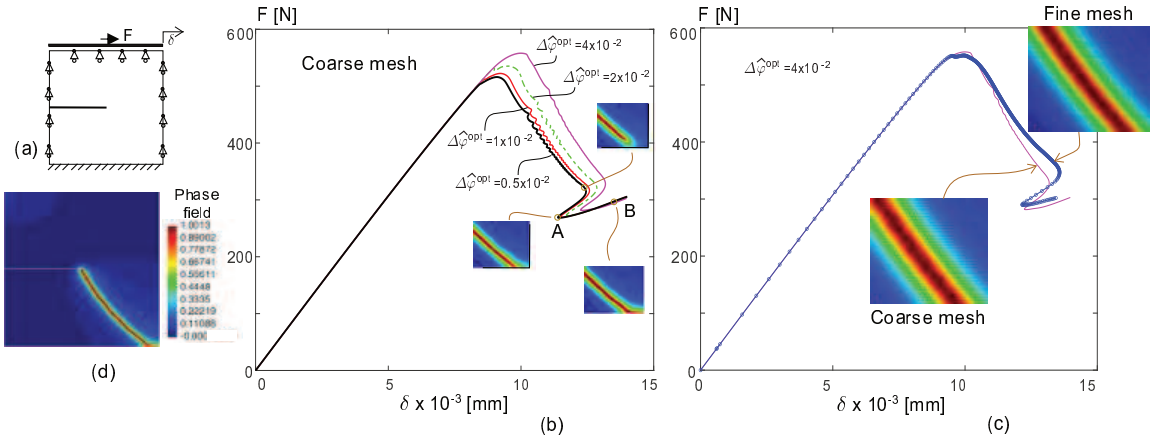

Figura D.6: Single edge notched shear test (SENST). a) Specimen geometry and boundary conditions. b) Coarse mesh: total shear force F on the top boundary versus displacement δ. The insets show the phase field variable evolution in three instants as the snap-back develops along the equilibrium curve. Phase field tip enrichment (PFTE) has been assumed. c) F versus δ curves, coarse and fine meshes with $\Delta\hat{\varphi}^{opt} = 4 \times 10^{-2}$. Points of the fine mesh result indicate load steps. d) Crack path at the end of the analysis ($\delta = 0.014mm$).

D.4.5. Fracture of an adhesively-bonded composite

The strength of a specimen composed of two plates bonded with an adhesive interface is evaluated. Figure D.7-a shows the specimen and the applied load. The expected fracture process in this problem results from two interacting mechanisms, interface delamination followed by a possible kinking out of the interface crack. The position d where the crack branches out the interface, see Figure D.7-k, results from complex interacting factors, some of which have been studied by Li et al. [197]. Interestingly, the crack branching out phenomenon depends not only on the relative plate/interface toughness, as explained from a Linear Elastic Fracture Mechanic perspective, but on the relative strengths of the plate and interface.

The mechanical model for simulating this problem is adopted from [198]. In this approach, the phase field model is combined with cohesive interfaces characterized by a conventional traction-separation law not influenced by the phase field variable. The phase field variable and the micro-stress component, which is normal to the interface, are constrained to be continuous across the interface. As mentioned above, the characteristic length of the phase field model in this test takes the role of a material parameter.

This test aims to evaluate the effectiveness of the arc-length control strategy in managing fracture problems undergoing distinct degradation mechanisms, such as interface decohesion and propagating cracks in the plate modeled with different techniques. Both of these mechanisms can trigger loading process instabilities. Therefore, the arc-length procedure needs to handle them both. Note that arc-length strategies controlling the phase field variable are not adequate in this case.

As mentioned before, the mechanical stage of the staggered procedure solves the displacements of a problem with fixed phase field variables. This stage takes into account the non-linearities associated with the interface degradation modeling. Therefore, the control equation (D.27) is here extended to manage the instabilities triggered by the interface decohesion. We define a control equation regulating the rate of the driving force term of the micro-force phase field equation as well as the power dissipation due to the

interface degradation, $\mathcal{D}_{CZM}$. A convex combination of both terms is taken as follows:

$$(1-\xi)\int_{\mathcal{B}} 2(1-\varphi)\dot{\mathcal{H}}\, d\mathcal{B} + \xi\mathcal{D}_{CZM} = \dot{s}\ , \qquad \xi \in [0,1]\ . \tag{D.52}$$

Following [13], the rate of dissipation $\mathcal{D}_{CZM}$ in the body $\mathcal{B}$ undergoing the degradation of the interface cohesive forces, and which are simulated with a damage model, can be evaluated through the expression:

$$\mathcal{D}_{CZM} = \frac{1}{2}\left(\lambda(\hat{\boldsymbol{f}}^{ext}\cdot\dot{\boldsymbol{u}}) - \dot{\lambda}(\hat{\boldsymbol{f}}^{ext}\cdot\boldsymbol{u})\right)\ . \tag{D.53}$$

Considering (D.52) and (D.53), the control equation expressed in increments is now rewritten as follows:

$$(1-\xi)\int_{\mathcal{B}} 2(1-\varphi)\Delta\mathcal{H}\, d\mathcal{B} + \frac{\xi}{2}\left(\lambda(\hat{\boldsymbol{f}}^{ext}\cdot\Delta\boldsymbol{u}) - \Delta\lambda(\hat{\boldsymbol{f}}^{ext}\cdot\boldsymbol{u})\right) - \Delta s = -res_s\ , \tag{D.54}$$

where λ and $\boldsymbol{u}$ take the values at the end of the previous step of the staggered scheme. Finally, after replacing equations (D.35) and (D.36) into (D.54) and operating on the algebraic expression, we determine the formulas for updating $\Delta\lambda$ and $\Delta\boldsymbol{u}$ that substitutes the equation (D.37) in the control strategy algorithm.

Geometric and material parameters. The plate thickness is $h = 2.5mm$, and its elastic modulus: $E_p = 100MPa$, fracture energy $G_p = 2.5\times10^{-4}N/mm$, and characteristic length $\ell_c = 0.06mm$. Thus, the plate critical stress is estimated through expression (D.46), $\sigma_p^{crit} = 2.1\times10^{-1}MPa$. The adhesive interface follows a damage law with exponential softening characterized by the fracture energy $G_i = 1.5\times10^{-4}N/mm$, an elastic modulus E_i assumed identical to that of the plate, $E_i = E_p$, and the interface strength σ_i is given in terms of the parameter Σ defined as the stress ratio: $\Sigma = \sigma_p^{crit}/\sigma_i$. Then, the shortest interface characteristic length corresponds to the case $\Sigma = 0.4$, and its value is estimated as $\ell_i = 0.53E_iG_i/(\sigma_i)^2 = 0.0289mm$.

Two uniform structured quadrilateral finite element meshes of sizes $h^{EF} = 0.0175mm$ and $h^{EF} = 0.00875mm$ are used for the numerical evaluations.

D.4.5.1. Parametric assessment of the composite fracture problem

Failure of the specimens is studied through a parametric analysis by varying Σ. Five cases with $\Sigma = 0.4$, 0.5, 0.6, 0.7, and 0.8 and using the arc-length control strategy are solved. Figure D.7-b displays the force versus displacement plots. Additionally, the fracture modes attained with this methodology are depicted in Figure D.7-c, d, e, f, and g, and the crack paths along the plate are shown in Figure D.7-h, i, j, k, and l, respectively. A deformed mesh detail of the case with $\Sigma = 0.4$ is also shown in the same Figure.

Considering that the test is undergoing a prescribed force, the arc-length strategy plays a role in tracing the equilibrium curves across the limit loads as well as in loading stages coinciding with the instant when the interface crack kinks out toward the plate. Responses displaying snap-backs are captured after the crack kinks out the interface. This feature is more pronounced as the parameter Σ is higher. In cases characterized with low values of Σ, i.e., 0.4 and 0.5, the control strategy responds adequately by assuming $\xi = 0.5$, meaning that a relatively similar weight is given to both, the phase field driving force term and the interface dissipation rate, in the control equation. Alternatively, in cases with high values of Σ, it is more convenient to adopt $\xi = 0.25$ that assigns a relatively high weight to the phase field driving force term in the control equation.

We evaluate the distance d at which the crack kinks out the interface using both finite element meshes. These results are displayed in Table D.4. Notice that slightly smaller distances d are estimated with the fine mesh.

Tabla D.4: Fracture of an adhesively-bonded composite. Distance d is assessed with two finite element meshes.

Σ	Fine mesh ($h^{EF} = 0.00875mm$)	Coarse mesh ($h^{EF} = 0.0175mm$)
	d/h	d/h
0.4	0.4	0.42
0.5	0.66	0.84
0.6	1.36	1.72
0.7	2.28	2.64
0.8	3.4	4.

D.4.6. Plate with an eccentric hole in tensile (EH)

The square plate with an eccentric hole (EH) undergoing vertical stretching, shown in Figure D.8-a, is evaluated. A uniform vertical displacement, δ, is prescribed on the top edge of the specimen. The specimen does not have pre-established notches. Therefore, localization of damage in the phase field model is governed by a strength criterion based on the characteristic critical stress σ^{crit} defined in (D.44) (for $\varphi^{crit} = 0.25$).

We adopt material properties similar to those reported by Bharali et al. [146] for solving the same problem. The Young modulus is $E = 210GPa$, Poisson's ratio $\nu = 0.3$, $G_c = 2.7N/mm$, and $\ell = 0.02mm$ ($\sigma^{crit} = 1.73GPa$). The mesh has 4652 quadrilateral elements.

The equilibrium solution in terms of the load f versus displacement δ displays a characteristic behaviour with two limit points followed by two snap-backs, as shown in Figure D.8-b. The first snap-back initiates when the crack propagation starts on the specimen at the right part of the eccentric hole. The second snap-back initiates when the second crack starts its propagation on the left part of the eccentric hole. Four solutions are plotted with the control parameters $\Delta\hat{\varphi}^{opt} = 0.5\times10^{-2}$, 1×10^{-2}, 2×10^{-2}, and 5×10^{-2}. The errors of these solutions, e_W, are assessed with equation (D.51), where the areas enclosed by the curves, W^{ext}, are compared with the area enclosed by the reference solution, W^E that is the curve obtained with $\Delta\hat{\varphi}^{opt} = 0.5\times10^{-2}$. Table D.5 show the errors and the number of steps required for the staggered strategy in every run.

Tabla D.5: EH specimen. Relative percent error for different runs and number of steps (staggered strategy).

$\Delta\hat{\varphi}^{opt}(\times10^{-2})$	e_W	Number of steps
1	3.7 %	1241
2	10.8 %	610
5	31.3 %	244

The maximum arc-length parameter is $\Delta s^{max} = 0.008\,Nmm$. Additional computational cost performances of this test are discussed in Section D.5.

D.4.7. Perforated plate

We simulate the perforated plate shown in Figure D.9, which is undergoing a loading process under the forces f. This test is reported in May et al. [193] from where we adopt the same elastic model parameters. The Young modulus is $E = 100MPa$ and Poisson's ratio $\nu = 0.3$. In the reference work, the material degradation is modeled with interface elements along the x-axis. The fracture energy of the interface model is $G_c = 2.5\times10^{-3}N/mm$, and the ultimate stress is $\sigma^{ult} = 1MPa$. In the present phase field model, we preserve the same G_c whereas ℓ is defined such that the critical stress, σ^{crit}, determined by expression (D.44), coincides with σ^{ult} of the interface model. The so-determined characteristic length is $\ell = 0.0812mm$. We use a mesh with 2396 quadrilateral elements.

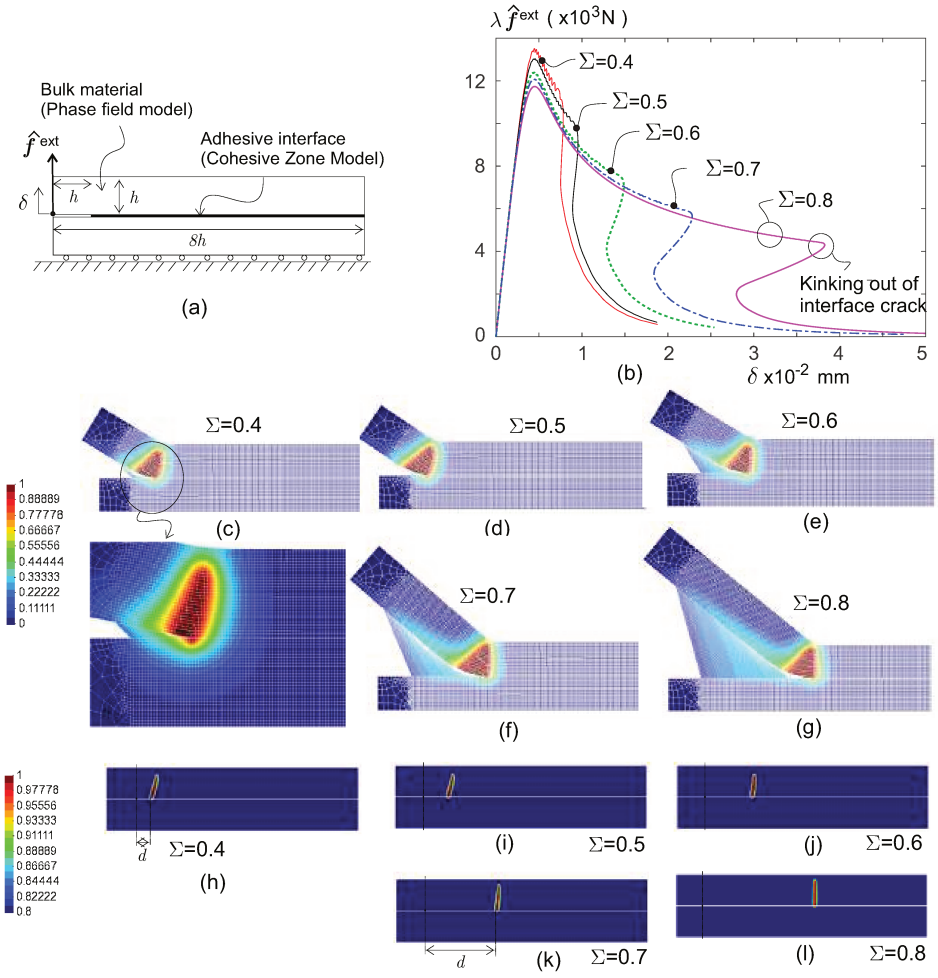

Figura D.7: Adhesively-bonded composite. a) Specimen geometry and load. b) Force $\lambda \hat{\boldsymbol{f}}^{ext}$ versus displacement δ. c) d), e), f), and g) deformed meshes and phase field distribution at the end of the analysis. h), i), j), k), and l) crack path in the plate at the end of the analysis.

Figure D.9-b plots the force f versus displacement δ. We show two solutions with $\Delta\hat{\varphi}^{opt} = 10^{-3}$ and 5×10^{-3}, respectively. Both solutions require approximately 600 and 1200 steps. All steps converge. The limit loads in this plot agree with those of the reference work.

The maximum arc-length parameter is $\Delta s^{max} = 6 \times 10^{-6} Nmm$, which dominates the control strategy during the unloading steps after crossing the peak loads.

D.5. Performance analysis of the staggered scheme combined with the arc-length strategy

Further performance on the computational costs for solving the EH, NPWH, and SENST tests discussed in sub-Sections D.4.6, D.4.3, and D.4.4 are analyzed. A summary of these analyses is described in Figures D.10. Additionally, Figure D.11 displays the performances of the DENT numerical test attained with the BCOP methodology in sub-Section D.4.2.

The plots on the left column of Figures D.10 and D.11 depict the computed phase field increment $\Delta\varphi = \|(\boldsymbol{\varphi}_n - \boldsymbol{\varphi}_{n-1})\|_\infty$ in every step of the staggered scheme using the arc-length strategy. Solutions for different values of $\Delta\hat{\varphi}^{opt}$ are shown. From Section D.3.2.1, equation (D.38), we recall that our strategy adjusts the arc-length parameter, s, to attain increments $\Delta\varphi$ as close as possible to an optimum desired

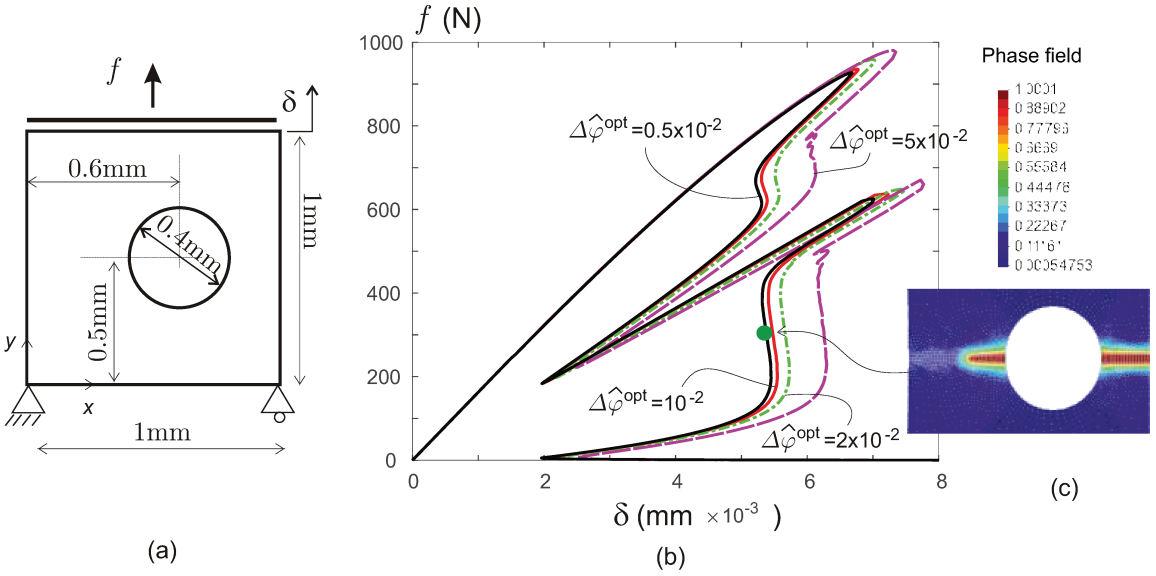

Figura D.8: Plate with an eccentric hole (EH). a) Specimen geometry. b) Total force f versus displacement δ.

phase field increment $\Delta\hat{\varphi}^{opt}$. Fulfillment of this condition means that the pseudo-time integration error holds bounded. In the four studied cases, we note that this characteristic feature of the algorithm is satisfied with a high degree of accuracy independently of the algorithm imposing the complementarity conditions in the micro-force balance equation.

The plots on the right column of both Figures display the number of Newton Raphson iterations ($niter$) necessary for solving the mechanical stage per each staggered scheme step ($nstep$). This information sheds light on the computational cost of every run. One staggered step of the present explicit approach requires one mechanical and one phase field stage evaluation per step. Also, one mechanical stage solution demands $niter$ Newton Raphson iterations. So, the total number of internal force vector and stiffness matrix evaluations is $niter + 1$. In the plots, we also depict for every run the average number of iterations per step (ANI). Therefore, the estimated number of times that the (mechanical) internal force vectors and stiffness matrices are computed in one run is $(ANI + 1) \times nstep$, while the estimated number of times that the phase field internal force vectors and the corresponding stiffness matrices are computed in one run is nstep. The number of steps required for solving different runs in these plots is indicated in color below the x-axis. This information, jointly with the equilibrium curves and accuracy analysis depicted in previous Sections, provides an insight into the expected accuracy in terms of the required computational cost for different runs.

Considering that the SENST problem is a widely used benchmark to assess the performance of various phase field algorithms, we compare the performance of our approach with that reported in the literature. Table D.6 compares several aspects of this analysis. Based on these results, we conclude that our methodology entails a moderate computational cost and provides solutions exhibiting snap-back behaviour even when using a large arc-length parameter, $\Delta\hat{\varphi}^{opt}$.

D.6. Conclusions

An arc-length procedure for controlling brittle fracture problems modeled with a phase field approach, whose balance equations are solved with a well-established staggered strategy, is proposed. The new contribution in this paper refers to the control equation governing the increment of displacements solved in the mechanical stage of the staggered strategy. This control equation determines, through an arc-length parameter, s, the driving force increase defining the phase field increase via the micro-force

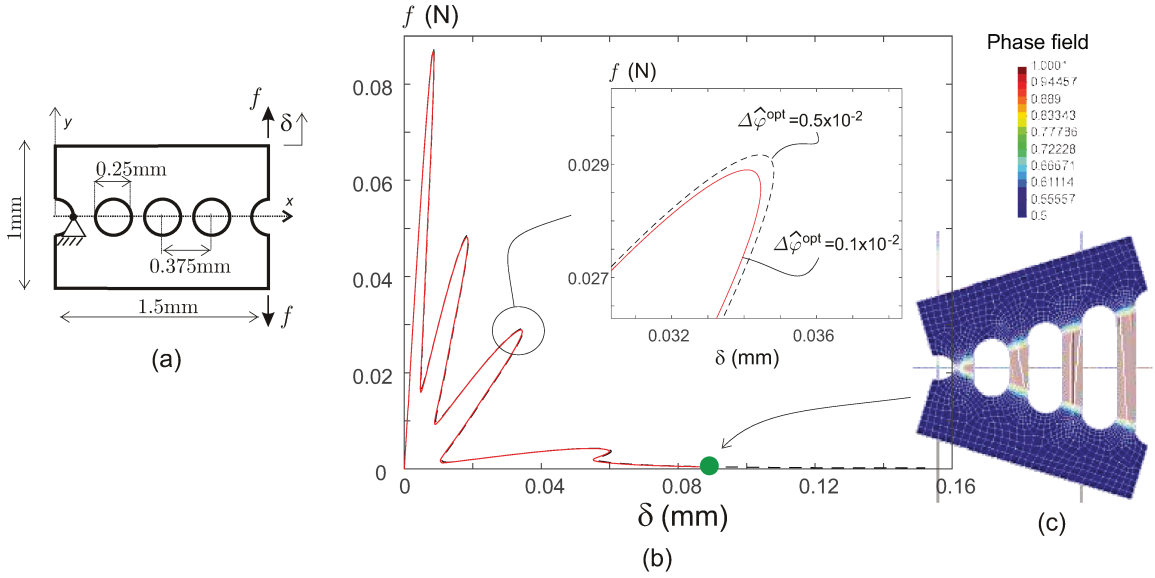

Figura D.9: Perforated plate. a) Specimen geometry. b) Force f versus displacement δ curves.

Tabla D.6: Performance comparative analysis using the SENST test. M: monolithic, STG: staggered; nstep: number of monolithic/staggered steps; niter AVG: average number of Newton-Raphson iterations required for solving one mechanical stage. NR: not reported, N: nodes, FE: finite elements. Notes: (1) the number of Newton-Raphson iterations required per each mechanical stage solution is not reported. (2) CPU-time for coarse tolerance (10^{-2}). (3) CPU-time for adjusted tolerance (10^{-4}). (4) the Maximum number of iterations for solving a staggered step is prescribed to 30. No information is reported on the number of Newton Raphson iterations required for solving the mechanical stage. The number of staggered steps is not specifically reported. (5) Solved steps: 66, Refined steps: 50, Failed steps: 11. (6) CPU time for run with coarse mesh and $\Delta\hat{\varphi}^{opt} = 0.04$ ($e_W = 9.2\,\%$). (7) CPU time for run with coarse mesh and $\Delta\hat{\varphi}^{opt} = 0.01$ ($e_W = 1.4\,\%$). (8) CPU time for run with fine mesh and $\Delta\hat{\varphi}^{opt} = 0.04$.

Reference paper	Methodology	Mesh (N - FE)	$nsteps$	$nsteps \times niterAVG$	Capture snap-backs?	CPU time (sec)
[199]	M (BFGS)	390000 FE	100	3131	NO	60780
[199]	STG	390000 FE	100	9374	NO	417600
[181]	STG	11200 N	46 staggered step	$\approx$ 100 (1) iter/ stagg step	NO	6840 (2) 59760 (3)
[181]	M (with lineasearch)	11200 N	46	$\approx$ 30 iter/ stagg. step	NO	10800
[188]	STG	16384 FE	135	30 (4)	NO	NR
[146]	M (arc-length + linesarch)	Adaptative	127 (5)	1966	YES	2097
Present	STG	13100FE	394	1319	YES	451 (6)
	STG	13100FE	1697	4480	YES	2249 (7)
	STG	390990FE	420	1596	YES	17760 (8)

balance equation.

Compared with previously reported arc-length strategies, the control equation presented in this work allows for solving a wide range of problems, including those with the micro-force balance equation evaluated through optimization techniques with inequality constraints or those with multiple instability mechanisms.

The arc-length procedure implementation demands the evaluation of an additional internal force vector during the mechanical stage that can be calculated in combination with the conventional internal force vector. Also, similar to traditional arc-length procedures, a double back substitution is needed to evaluate $\Delta\lambda$ and $\Delta\boldsymbol{u}$ in each iteration of the mechanical stage. According to our numerical experiments, these operations do not significantly increase the computational burden of the original staggered strategy.

Through the numerical assessments discussed in Section D.4, we show the robustness, accuracy, and ability of the proposed arc-length strategy to trace equilibrium curves displaying abrupt snap-back responses, and to control quasi-static crack advance problems that, under displacement or force control techniques, are unstable. The crack advance is strictly controlled in every step, regardless of the structural brittleness of the assessed problem.

Accuracies of the numerical solutions in Section D.4 have been assessed through the area enclosed by the equilibrium curves. Considering brittle fracture problems and fully degraded notched specimens, the enclosed area of the force versus displacement equilibrium curve identifies the energy release in the test, which should be identical to the specimen fracture energy times the crack length. This criterion can be used as a strict form of verifying the energetic consistency of numerical solutions. Numerical methodologies which cannot trace the complete equilibrium curves, including snap-backs, do not pass this verification test.

The arc-length parameter is adjusted to yield an approximate pre-established desired damage increment per step. This feature is implemented through the $\Delta\hat{\varphi}^{opt}$ parameter. Then, the damage increase in each step stays controlled, even using an explicit staggered strategy. According to results presented in Section D.5, this procedure entails moderate computational costs for tracing the complete equilibrium curve, with the subsidiary advantage that we have never detected lack of convergence in the tests presented in Section D.4, and it is not necessary to use line search techniques.

Acknowledgments

This research has been supported with grants provided by CONICET: PIP 112202101 00455CO (2022-2024), the National University of Litoral, and the fund from ANPCyT: PICT-2020-SERIEA-02793, Argentina.

F.P. Duda gratefully acknowledges the support provided by the Brazilian agency CNPq (309370/2019-1).

Appendix I: Solutions obtained with staggered strategies without using the arc length procedure

This appendix describes supplementary solutions for the DENT test subjected to uniform stretching studied in Section D.4.2. Two variants of the staggered strategy evaluate these solutions. The purpose is to demonstrate that both variants implemented without the arc-length procedure fail to follow the equilibrium curve throughout the fracturing process. Consequently, the estimation of the energy release is significantly overestimated.

Variant I is an implicit staggered strategy with sub-iterations of the mechanical and the damage stages. At the load step k, sub-iterations j are repeated until reaching, between two consecutive sub-iterations, $j-1$ and j, an increment of phase field satisfying: $\|\varphi_k^j - \varphi_k^{j-1}\|_\infty \leq 0.01$. If this criterion is not satisfied in 100 sub-iterations, the scheme continues with the next load step. Variant II is an explicit staggered strategy with no sub-iterations, and $j=1$. In all these cases, the loading process is defined by imposing fixed increments of vertical displacement $\Delta\delta$.

Figure D.12 plots the total force f versus vertical displacement δ curves. The plot B corresponds to solutions obtained with variant I and an imposed displacement increment $\Delta\delta/b = 25\times10^{-6}$. Plots C and D correspond to solutions obtained with variant II and imposed displacement increments $\Delta\delta/b =$

5×10^{-6} and $\Delta\delta/b = 2.5 \times 10^{-6}$, respectively. These plots are compared with the solution A presented in Section D.4.2 with the tolerance parameter $\Delta\hat{\varphi}^{opt} = 10^{-2}$.

After crossing the peak load, solution B with the maximum sub-iterations fixed at 100, is determined with only two points (1 and 2 in Figure D.12). This staggered scheme variant lacks parameters controlling the crack tip advance during this loading process stage. Therefore, the intermediate structural equilibrium points are unable to be reached. The numerical consequence of this effect is relevant when the energy balance condition is examined. The energy balance condition accuracy is assessed through the relative percent error of the energy release, e_W, defined in equation (D.51), and is compared for the solutions reported in this Section in the fourth column of Table D.7. Additionally, Table D.7 describes computational costs, in terms of the number of total iterations of the mechanical stage.

Tabla D.7: Computational cost for solving the DENT test defined in terms of $nstep \times n_{subiter} \times niter$, where $nsteps$ is the number of load steps, $n_{subiter}$ is the number of sub-iterations in variant I, or 1 in variant II, and $niter$ is the number of Newton-Raphson iterations required by the mechanical stage. Last column is the relative percent error of the energy release, e_W, defined in equation (D.51).

Staggered strategy	Step length	$nsteps \times n_{subiter} \times niter$	e_W
Variant I	$\Delta\delta/b = 25. \times 10^{-6}$	2403	116 %
Variant II	$\Delta\delta/b = 2.5 \times 10^{-6}$	3271	133 %
Variant II	$\Delta\delta/b = 5 \times 10^{-6}$	2265	147 %
with arc-length	$\Delta\hat{\varphi}^{opt} = 1. \times 10^{-2}$	1860	13 %

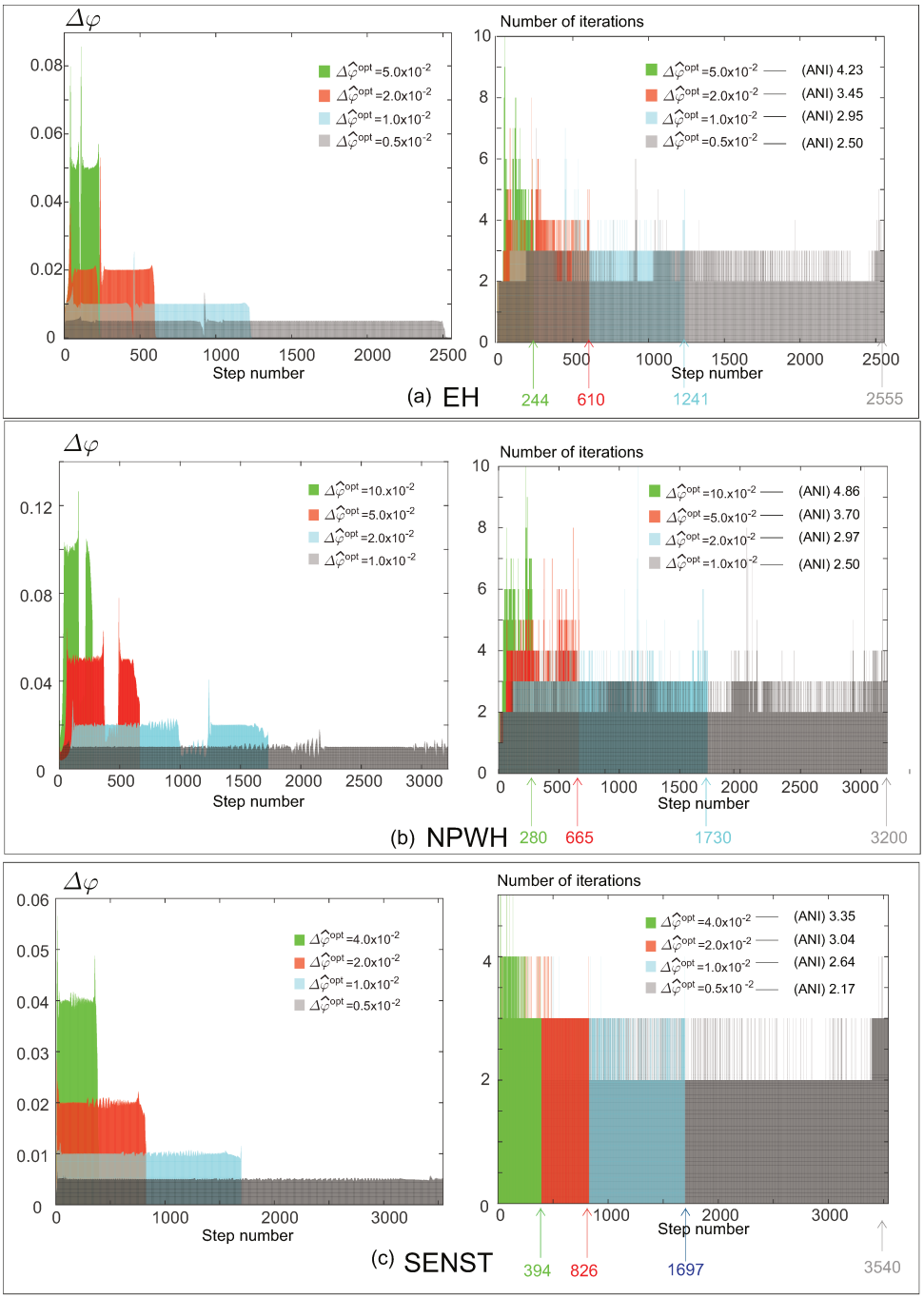

Figura D.10: Performance analysis. a) EH. b) NPWH, and c) SENST test. Left column: phase field increase ($\Delta\varphi = \|(\boldsymbol{\varphi}_n - \boldsymbol{\varphi}_{n-1})\|_\infty$) in each staggered scheme step (Step Number). Right column: number of iterations required by the mechanical stage solution in each staggered scheme step. Load versus displacement plots for the here reported tests, EH, NPWH, and SENST, are shown in Figures D.8-b, D.5-c, and D.6-b, respectively.

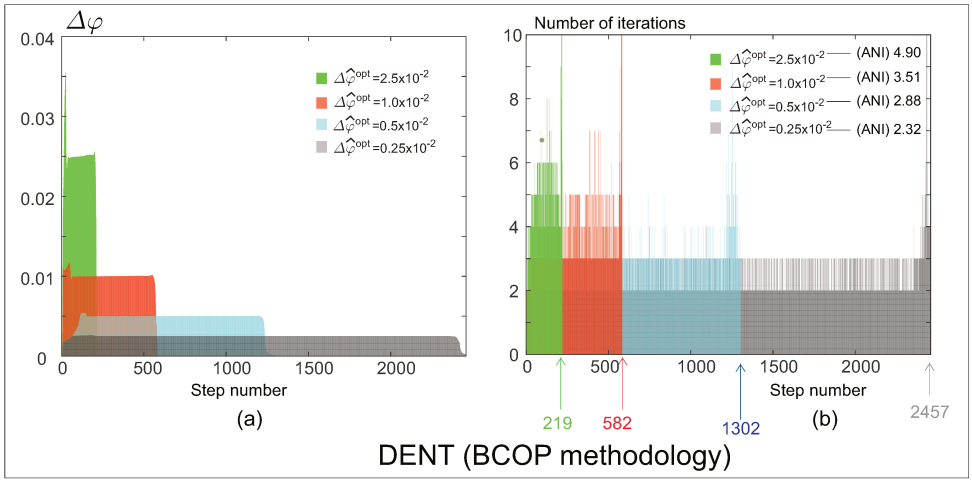

Figura D.11: Performance analysis. DENT test using the Bound-Constrained Optimization Problem (BCOP) methodology for solving the micro-force balance equation. Left column: phase field increase ($\Delta\varphi = \|(\varphi_n - \varphi_{n-1})\|_\infty$) in each staggered scheme step (Step Number). Right column: number of iterations required by the mechanical stage solution in each staggered scheme step.

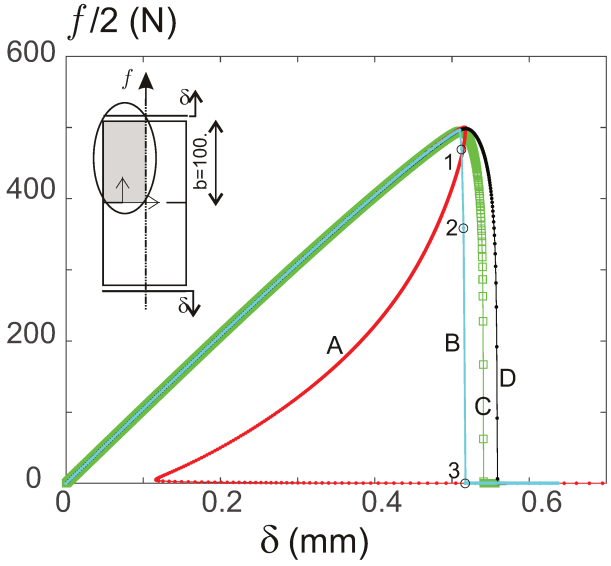

Figura D.12: Double-edged notched test (DENT). Solutions obtained with: arc-length procedure (curve A); variant I and $\Delta\delta/b = 25. \times 10{-}6$ (curve B); variant II and $\Delta\delta/b = 2.5 \times 10{-}6$ (curve C); variant II and $\Delta\delta/b = 5. \times 10{-}6$ (curve D).

Apéndice E

An overset improved element-free Galerkin-finite element method for the solution of transient heat conduction problems with concentrated moving heat sources

Juan C. Álvarez-Hostos, Zahur Ullah, Bruno A. Storti, Benjamín A. Tourn, Javier A. Zambrano-Carrillo (2024). “An overset improved element-free Galerkin-finite element method for the solution of transient heat conduction problems with concentrated moving heat sources”. *Computer Methods in Applied Mechanics and Engineering*, 418, 116574.

An overset improved element-free Galerkin-finite element method for the solution of transient heat conduction problems with concentrated moving heat sources

Juan C. Álvarez-Hostos[a,b,1], Zahur Ullah[c], Bruno A. Storti[d,e], Benjamín A. Tourn[a], Javier A. Zambrano-Carrillo[d]

[a]Centro de Investigación y Transferencia (CIT) Rafaela, Universidad Nacional de Rafaela (UNRaf)/Consejo Nacional de Investigación Científicas y Técnicas (CONICET), Rafaela, Argentina
[b]Department of Materials, Faculty of Chemical Engineering, Universidad Nacional del Litoral (UNL), Santa Fe, Argentina
[c]Advanced Composites Research Group (ACRG), School of Mechanical and Aerospace Engineering, Queen's University Belfast, Ashby Building, Belfast BT9 5AH, UK
[d]Centro de Investigación de Métodos Computacionales (CIMEC), Universidad Nacional del Litoral (UNL)/Consejo Nacional de Investigaciones Científicas y Técnicas (CONICET), Predio CCT-CONICET, Santa Fe, Argentina
[e]Université de Nantes, CNRS, Laboratoire de thermique et énergie de Nantes, LTeN, UMR 6607, Nantes F-44000, France

Keywords: Transient heat conduction; Moving heat sources; Overset; Chimera; Improved element-free Galerkin; Finite element method

Abstract. A novel Overset Improved Element-Free Galerkin-Finite Element Method (Ov-IEFG-FEM) for solving transient heat conduction problems with concentrated moving heat sources is introduced in this communication. The method is a mesh-less/mesh-based chimera-type approach that utilises a coarse finite element mesh to discretise the problem geometry, while a separate set of overlapping nodes (patch nodes) moves with the heat source to capture the marked thermal gradients with higher accuracy using the Improved Element-Free Galerkin (IEFG) technique. Outside of the heat source area, where accuracy requirements are significantly lower, the thermal problem is solved using the Finite Element Method (FEM). The approach involves solving the problem over these two overlapping computational domains and transferring numerical information between the approximations performed on both. Such transfer of information occurs through immersed boundaries that are properly defined, enabling straightforward achievement of accurate results. The proposed Ov-IEFG-FEM is conceived to provide an enriched solution by appropriately coupling the temperature fields computed on the patch nodes and the coarse background mesh using IEFG and FEM, respectively. A comprehensive explanation concerning the appropriate coupling between the temperature fields of both the coarse background finite element mesh and the fine arrangement of moving patch nodes for the IEFG computations, is also provided in this communication. Numerical experiments demonstrate the method effectiveness in accurately and efficiently solving transient heat conduction problems with concentrated moving heat sources.

E.1. Introduction

The numerical solution of transient heat conduction problems with moving heat sources is crucial in applied sciences and engineering, and especially useful in predicting the performance of various manufacturing processes. Some of these include grinding [200], spot welding [201], arc welding [202, 203], friction stir welding [204], additive manufacturing (e.g. selective laser melting [205–208] and fused deposition modelling [209]), laser [210] and plasma [211] cutting, among others. The finite element method

[1]Corresponding author. E-mail address: jchostos@cimec.unl.edu.ar (J.C. Álvarez-Hostos).

(FEM) is a thoroughly developed numerical technique, which is also commonly used to solve transient heat conduction problems with moving heat sources. However, the linear piecewise approximations commonly used in FEM-based solutions can introduce difficulties in accurately capturing high thermal gradients near the heat source, particularly due to the discontinuous derivatives at the element faces [212]. This is because linear approximations cannot accurately represent the markedly non-linear temperature distribution that occurs in the heat source vicinity. Consequently, significant mesh refinement along the heat source path [213, 214], adaptive re-meshing procedures [205, 207, 208] or higher-order approximation schemes [203, 206, 215] may be necessary to obtain accurate results in such cases. Implementing marked mesh refinement along the heat source path or adaptive re-meshing techniques can be challenging and sometimes even impossible in real-world applied problems, especially those involving moving heat sources following curved paths in complex 3-D geometries. Therefore, despite the potential of these techniques to address the issue of accurately capturing high thermal gradients near moving heat sources, their implementation is -to the authors' best knowledge- still limited to controlled numerical experiments of simpler geometries.

According to recent literature, marked mesh refinement along the heat source path or adaptive re-meshing techniques have been primarily demonstrated and validated in test problems related to laser cutting [210], additive manufacturing [205, 207, 208, 215, 216], arc welding [213, 214], and plasma cutting [211]. The choice to use higher order approximations in FEM requires adding more nodal temperatures to each element, which often leads to larger and more computationally demanding systems of equations. In addition, it should be noted that higher order approximations in standard FEM formulations for heat transfer analysis do not always guarantee continuity in thermal gradients, and hence, heat flux. The construction of approximations with continuous derivatives in these formulations is well-known to be challenging, and it often requires either the use of highly complex finite elements with a large number of nodal unknowns or the application of post-processing techniques to the discontinuous derivative fields that result from using simpler elements [217–219]. Mesh-less or mesh-free techniques have emerged as a promising alternative to overcome the challenges posed by traditional FEM and other mesh-based discretisation methods. This is based on two main features [212, 220, 221]:(i) the possibility of achieving higher order approximations with continuous derivatives more easily than FEM and other mesh-based techniques, and (ii) the greater flexibility in adding or removing nodes. Recent developments in these techniques have shown great potential in solving complex heat transfer problems, as demonstrated by several researchers. Some of these challenging problems include transient heat conduction in anisotropic media with phase change [222], inverse heat conduction analysis [223], natural [224] and forced [225] convection, heat transfer in multiphase flow [226], phase-change in advection-diffusion [227, 228] and moving boundary [225, 229–232] systems, thermo-mechanical analysis under both small [233, 234] and large strains [235], as well as topology optimisation [236].

The versatility of mesh-less methods has also enabled the implementation of such numerical techniques in the solution of both linear and non-linear problems involving concentrated moving heat sources, which are the main focus of this work. For instance, Xiao et al. [204] proposed an improved version of the symmetric smooth particle hydrodynamics (SSPH) method to accurately model the non-linear transient heat conduction in friction stir welding processes. Stubblefield et al. [237] developed a computational framework based on smooth particle hydrodynamics (SPH) to perform thermo-mechanical analysis of additive friction stir-deposition (AFS-D) processes, achieving good agreement between numerical and experimental results. Moarrefzadeh [202] applied the meshless local Petrov-Galerkin (MLPG) method to predict residual stress induced by welding, and showed its accuracy by comparing numerical results with experimental data obtained via the hole-drilling strain-gauge method. Saucedo-Zendejo and Cortés-Vargas [238] demonstrated the reliability of finite point set (FPS) methods for the thermo-elastic analysis of welding processes by comparing numerical results with those obtained using the FEM. Wessels et al.

[230] embedded a rigorous phase change model in a stabilised optimal transportation mesh-free (OTM) framework, allowing for detailed and realistic simulation of the moving heat source-powder bed interaction during melting and solidification in selective laser melting (SLM) processes. Finally, Wang et al. [232] introduced a hot optimal transportation mesh-free (HOTM) method that couples OTM to the variational thermo-mechanics constitutive updates for general dissipative solids, and successfully applied it to predict the interaction between the powder feeding beam and the laser radiation in a laser cladding process. Khosravifard et al. [201] coupled the radial point interpolation method to an adaptive nodes refinement procedure for the solution of transient heat conduction problems with moving point heat sources, including also thermo-elastic analyses and its validation with FEM-based solutions. Champagne and Pham [239] used the element-free Galerkin (EFG) method to predict the transient temperature distribution in arc welding processes with a composite moving heat source comprising a circular surface part and a volumetric truncated cone-shaped part, providing also a reliable validation with experimental results. Such study has also included a parametric analysis to predict the effects of size and shape of influence domains, weight functions used to construct the moving least squares (MLS) approximations, and background integration points/nodes ratio on the numerical accuracy. Chen and Duan [206] developed a second-order EFG model for SLM processes, demonstrating the potential of this approach to achieve accurate thermo-mechanical analysis near the moving heat source in complex geometries with a significantly lower number of nodes in comparison with FEM-based solutions. An Overset improved element-free Galerkin (Ov-IEFG) formulation was recently developed by Álvarez-Hostos et al. [203] to solve transient heat conduction problems with moving heat sources, providing an alternative easy-to-implement procedure to address problems with complex geometries and highly concentrated moving heat sources that follow curved paths. The Ov-IEFG approach involves a fine arrangement of nodes undergoing a rigid body motion consistent with the moving heat source path, superimposed on a coarse distribution of background nodes representing the problem domain. Such feature allows the search of support domain nodes at each integration point and the computation of improved moving least squares (IMLS) approximations to be performed only once and kept during the entire transient heat conduction analysis, while the smoothness and continuity of the IMLS approximations and their derivatives enable a straightforward coupling between the moving and background arrangements of nodes. This particular aspect leads to a significant reduction of computing time with respect to standard implementations of EFG methods, since both the search of support domain nodes at each integration point and the computation of shape functions are the most computationally demanding procedures in EFG frameworks [240, 241]. Accordingly, the Ov-IEFG technique has been introduced as a very good alternative to approaches based on adaptive nodes refinement.

The studies discussed so far offer a comprehensive outlook on the emergence of mesh-less techniques for solving transient heat conduction problems with moving heat sources. Particularly for EFG methods, several researchers have devoted special efforts to improve numerical stability and computational efficiency by adopting approaches originally developed for FEM. These include the implementation of dimension splitting methods (DSM) [242–245], proper orthogonal decomposition (POD) approaches [246, 247], variational multiscale techniques [246–249], reduced integration methods [250–252], extended approximations with cover functions based on linear combination of polynomials [245, 253], and streamline upwind stabilisation techniques [228, 251]. Furthermore, researchers have also introduced more efficient strategies for numerical integration [254], devised innovative approaches for constructing shape functions [203, 255, 256], and incorporated parallel computation algorithms [256, 257] into their methodologies.

The implementation of the techniques mentioned above in EFG methods is relatively straightforward due to the analogies with FEM, beyond the differences in the construction of shape functions and the assembling of the algebraic equations system. Such analogies have enabled the development of hybrid

approaches combining the strengths of both methods, which consist in using EFG and FEM to solve the problem in different regions. These techniques are mainly devoted to improve computational efficiency by using EFG methods only in those regions demanding higher numerical accuracy [255, 256, 258], whereas the less computationally expensive FEM is used in the remaining part of the problem domain. There are also other works where the hybrid EFG-FEM is used to enable the direct imposition of Dirichlet-type boundary conditions at the nodal positions, which is performed using a strip of finite elements for discretisation along the corresponding boundaries [105]. To couple regions discretised with FEM and represented by EFG nodes, most hybrid EFG-FEM procedures require interface elements that utilise ramp or blending functions for a seamless transition between the two approximations [105, 259]. Some authors have recently succeeded in performing a direct coupling between EFG and FEM regions, i.e. without the need for interface or coupling elements [255, 256, 260]. Ullah et al. [255, 256] achieved this by using a EFG formulation based on max-ent shape functions, whose weak Kronecker delta property provided a direct way to couple with the FEM-discretised regions. This approach was implemented in the solution of large deformation non-linear inelastic problems, demonstrating its potential for the efficient achievement of accurate results. Zhang et al.[260] used MLS approximations with support sizes that vary linearly and decrease towards the coupling interface, which enables them to match the nodal spacing and achieve the Kronecker delta property in the transition region. This approach was successfully implemented in solving classical topology optimisation problems, demonstrating its effectiveness in producing accurate solutions.

Although the positive features of hybrid EFG-FEM-based numerical solutions, these procedures still demand well-defined coupling boundaries where the EFG and FEM regions share common nodes. In order to overcome this need for a topological relationship between EFG and FEM regions, the current communication is devoted to developing a novel hybrid EFG-FEM procedure formulated within the framework of overset approaches. The literature concerning the development and improvement of overset techniques in the framework of mesh-based methods is extensive, with numerous successful applications ranging from simple potential problems [261, 262] to more complex scenarios involving fluid-structure interaction [261, 263, 264], moving heat sources [148, 265], shape optimisation[266], and even multi-physics transport phenomena in AM processes [265]. Recently, the possibility of utilising these approaches within mesh-less methods has been demonstrated through the Ov-IEFG procedure developed by Álvarez-Hostos et al.[203]. The IMLS used in such Ov-IEFG procedure have the potential to provide continuous and smooth high-order approximations within a moving local support domain, in a remarkably simple manner. This particular feature has enabled the seamless coupling of both temperature and heat flux distributions computed over two arrangements of overlapping nodes, allowing for a straightforward solution to transient heat conduction problems with moving heat sources.

The preceding literature review provides a comprehensive perspective on (i) potential of overset techniques to solve transient heat conduction problems with moving heat sources [148, 265], (ii) the simpler coupling between overlapping domains when using overset approaches in EFG frameworks [203], and (iii) the noteworthy improvement in computational efficiency achieved through hybrid EFG-FEM approaches that limit the use of EFG approximations only to regions requiring higher numerical accuracy [255, 256, 258]. Based on such features, the current work is devoted to developing a novel overset improved element-free Galerkin finite element method (Ov-IEFG-FEM) for the solution of transient heat conduction problems with moving heat sources. The method utilises a coarse finite element mesh to discretise the problem geometry, while a distinct set of overlapping nodes (patch nodes) moves with the heat source to capture the marked thermal gradients with higher accuracy using the Improved Element-Free Galerkin (IEFG) technique. This approach is devised as a modification to enhance the Ov-IEFG procedure developed in a previous work [203], as it relied on a coarse distribution of background nodes representing the problem geometry to perform an IEFG-based solution rather than using the less compu-

tationally expensive FEM. Despite the lack of topological relationship between the coarse mesh used to discretise the problem domain and the fine arrangement of patch nodes moving with the heat source, a seamless coupling between these overlapping domains can be achieved via a reciprocal transfer of information performed through suitably defined immersed boundaries. To the best of the authors' knowledge, the development of an overset approach that combines both FEM and EFG frameworks is unprecedented in the literature. A novel Ov-IEFG-FEM is proposed in this study, which will be specifically implemented for solving transient heat conduction problems with concentrated moving heat sources.

According to the aspects discussed earlier, the main contributions of this work can be summarised as follows:

- The introduction of an overset technique that combines FEM and IEFG frameworks, which will be particularly used in this work to provide an efficient and easy-to-implement approach for solving transient heat conduction problems with concentrated moving heat sources.

- A noteworthy improvement in computational efficiency with respect to the Ov-IEFG approach proposed in a previous communication [203], since the current Ov-IEFG-FEM makes use of the IEFG formulation only in the region demanding higher numerical accuracy (i.e., the moving heat sources vicinity.)

- An overset framework where the transfer of information between the coarse FEM-based solution in the problem domain and the IEFG-based computations in the moving patch nodes is straightforward, and the achievement of a seamless coupling is entirely based on IMLS approximations.

The FEM-based solution computed in the background mesh is kept for the region $\Omega_{\text{FEM}} - \Omega_{\text{IEFG}}$ of smooth temperature gradients, whereas the solution is enriched in Ω_{IEFG} using the patch nodes intended to implement the IEFG method. The transfer of information from Ω_{FEM} to Ω_{IEFG} and visceversa is performed according the boundary Γ_{IEFG} and the closed surface $\mathcal{S}_{\text{IEFG}\rightarrow\text{FEM}}$, respectively. The FEM-based solution of the thermal problem in Ω_{FEM} is used to determine the temperature that must be imposed on Γ_{IEFG} via the penalty method, so that the IEFG-based solution to be performed in Ω_{IEFG} is subjected to the results obtained in Ω_{FEM}.

E.2. Governing equations

The transient heat conduction problem in a domain Ω with boundary Γ will be solved via an Ov-IEFG-FEM, which is schematised in Fig. E.1. This method involves the definition of two overlapping computational domains: one consists in the discretisation of the entire problem geometry using a coarse mesh $\Omega_{\text{FEM}} \approxeq \Omega$ to perform a FEM-based solution, and the other is represented by a fine overlapping arrangement of patch nodes Ω_{IEFG} used to enrich the solution in regions of high temperatures and marked thermal gradients via the higher accuracy provided by the IEFG method.

The temperature distribution to be imposed on Γ_{IEFG} is determined from a high-order local reconstruction of the FEM-based solution, which is performed using IMLS approximations with the set $\mathcal{N}_{\text{rec}}$ of nodes belonging to those elements whose centres are enclosed by the surface $\mathcal{S}_{\text{rec}}$. Such elements are coloured in yellow, whereas $\mathcal{S}_{\text{rec}}$ is represented by the black dashed lines. The IEFG-based solution of the thermal problem in Ω_{IEFG} is used to determine the temperature that must be imposed in the set $\mathcal{N}_{\text{enc}}$ of those nodes h of the background mesh that are enclosed by the surface $\mathcal{S}_{\text{IEFG}\rightarrow\text{FEM}}$ (depicted by green circles in Fig. E.1), so that the FEM-based solution to be performed in the background mesh Ω_{FEM} is conversely subjected to the results obtained in Ω_{IEFG}.

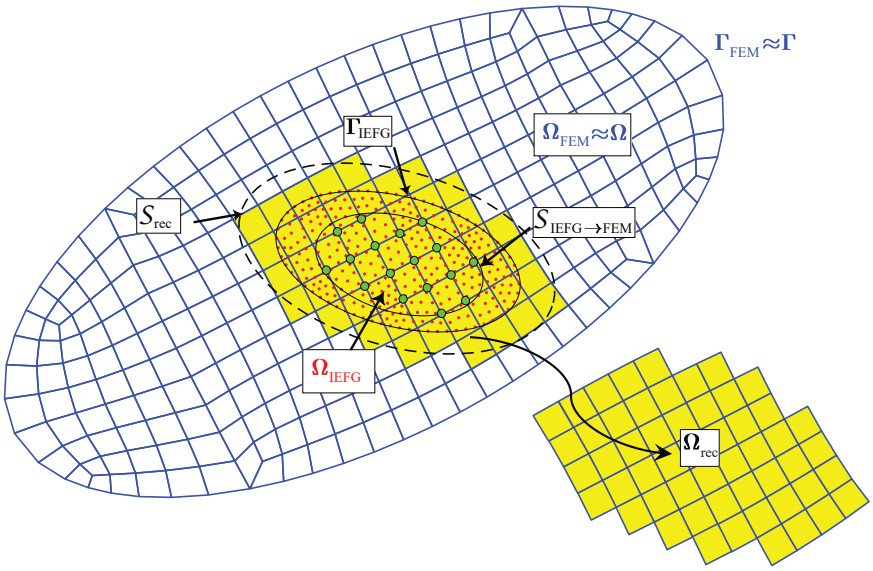

Figura E.1: Representation of the problem domain for a numerical solution performed via the proposed Ov-IEFG-FEM.

In this case, the Kronecker delta property of the shape functions used in FEM allows the imposition of temperature in the form of prescribed nodal values, eliminating the need for the penalty method required on Γ_{IEFG}.

E.2.1. Transient heat conduction equation in background mesh and patch nodes

The internal energy balance concerning the transient heat conduction with a moving heat source in a solid domain Ω with boundary Γ is governed by the following partial differential equation [203]:

$$\rho c_p \left(\frac{\partial T}{\partial t} - \vec{v} \cdot \nabla T \right) = \nabla \cdot (k \nabla T) + \dot{Q}, \quad \text{in} \quad \Omega, \tag{E.1}$$

where ρ, c_p and k are the density, specific heat and conductivity of the solid, whereas T is the temperature. The quantities $\dot{Q}$ and $\vec{v}$ denote the power density distribution and velocity of the moving heat source, respectively. The problem is subjected to the following initial and boundary conditions:

$$\begin{aligned} T &= T_0 \quad \text{at} \;\; t = 0, \quad \text{in} \; \Omega, \\ T &= \bar{T} \quad \text{on} \;\; \Gamma_T \times [0, t_f], \\ k \nabla T \cdot \hat{n} &= \bar{q} \quad \text{on} \;\; \Gamma_q \times [0, t_f], \end{aligned} \tag{E.2}$$

where the temperature $\bar{T}$ and heat flux $\bar{q}$ are imposed on the non overlapping boundaries Γ_T and Γ_q ($\Gamma = \Gamma_T \cup \Gamma_q$), respectively. Special care must be taken on the meaning of the advective term in Eq. (E.1), according to the approach adopted to handle the moving heat source. If the Rosenthal's approach is utilised [213, 267], the advective term is associated with a description of the transient heat conduction problem in a coordinates system attached to the moving heat source.

This approach assumes a spatially fixed heat source, while accounting for the effects of its motion via the advective term. To implement the proposed Ov-IEFG-FEM under this approach, the advective term is incorporated into both the background mesh $\Omega_{\text{FEM}} \approxeq \Omega$ and the arrangement of patch nodes representing the overlapping domain Ω_{IEFG}. In this case, the patch nodes remain fixed at the position assumed for the moving heat source. Rosenthal's simplification is only applicable to problems with regular geometries

and heat sources that follow simple paths, so that information concerning the current location of the heat source is not required to properly compute the temperature distribution around it [203, 213, 268]. Nevertheless, due to its controlled conditions and low computational cost, this technique will be utilised in this communication to perform an analysis on the convergence and accuracy of the proposed Ov-IEFG-FEM. It should be noted that while the Rosenthal's approach is suitable for this specific numerical analysis, the main focus of this work is to demonstrate the potential of the Ov-IEFG-FEM in handling applied problems with more complex geometries and moving heat source paths.

The Rosenthal's simplification is unfeasible under such conditions, whereby following the moving heat source path becomes mandatory. To implement the Ov-IEFG-FEM under this more realistic approach, it is necessary for the overlapping domain Ω_{IEFG} to undergo a rigid-body motion that follows the path of the moving heat source. In this case, the FEM-based solution to be performed in the coarse background mesh Ω_{FEM} that discretises the fixed solid domain Ω does not include the advective term.

Conversely, the advective term must still be included in the IEFG-based computations performed in the patch nodes representing the overlapping moving domain Ω_{IEFG}. This advective term is no longer related to a transient heat conduction problem described in a coordinate system attached to the moving heat source, but to an Arbitrary Lagrangian-Eulerian (ALE) description [269] concerning the relative motion between the solid domain Ω (whose velocity is null) and the moving patch nodes representing Ω_{IEFG}.

The appropriate coupling between the temperature distributions computed over the overlapping computational domains Ω_{FEM} and Ω_{IEFG} is performed via the recursive imposition of the following restrictions:

$$T = \bar{T}_{\text{IEFG}} \quad \text{at } \vec{x}^{(h)} \times [0, t_f], \ h \in \mathcal{N}_{\text{enc}}, \tag{E.3}$$

$$T = \bar{T}_{\text{FEM}} \quad \text{on } \Gamma_{\text{IEFG}} \times [0, t_f], \tag{E.4}$$

where $\bar{T}_{\text{IEFG}}$ in Eq. (E.3) are the temperatures computed at nodes $h \in \mathcal{N}_{\text{enc}}$ by using the IEFG-based solution performed in Ω_{IEFG}, whereas $\bar{T}_{\text{FEM}}$ in Eq. (E.4) is the temperature distribution computed on Γ_{IEFG} via the IMLS approximations achieved from the local reconstruction performed with the temperature of the nodes included in $\mathcal{N}_{\text{rec}}$.

These features put in clear perspective the strongly reciprocal dependence between the FEM-based solution performed in the coarse background mesh and the enriched approximations achieved via the IEFG formulation in the fine arrangement of patch nodes that moves with the heat source, according to the restrictions (E.3)-(E.4) imposed for the appropriate coupling of the temperature distributions computed in such overlapping domains.

The temperatures $\bar{T}_{\text{IEFG}}$ to be imposed at nodes $h \in \mathcal{N}_{\text{enc}}$ for the FEM-based solution in the coarse background mesh are computed from the IMLS approximations concerning the thermal problem solved via the IEFG technique in the fine arrangement of patch nodes, whereas the temperature distribution $\bar{T}_{\text{FEM}}$ to be imposed on Γ_{IEFG} via the penalty method is computed from an IMLS-based reconstruction of the thermal problem solved via FEM in the coarse background mesh.

E.2.2. Formulation and iterative algorithm concerning the Ov-IEFG-FEM

The Ov-IEFG-FEM is developed over the weak formulation framework of the transient heat conduction problem, which is developed for both Ω_{FEM} and Ω_{IEFG}.

In the coarse background mesh discretising Ω_{FEM} [148]:

$$\int_{\Omega_{\text{FEM}}} \delta T \rho C_p \frac{\partial T}{\partial t} \mathrm{d}\Omega + \int_{\Omega_{\text{FEM}}} \nabla \delta T . k \nabla T \mathrm{d}\Omega - \int_{\Omega_{\text{FEM}}} \delta T \rho C_p \vec{v} . \nabla T \mathrm{d}\Omega = \int_{\Omega_{\text{FEM}}} \delta T \dot{Q} \mathrm{d}\Omega + \int_{\Gamma_q} \delta T \, \bar{q} \, \mathrm{d}\Gamma. \tag{E.5}$$

In the fine arrangement of patch nodes representing Ω_{IEFG} [203]:

$$\int_{\Omega_{\text{IEFG}}} \delta T \rho C_p \frac{\partial T}{\partial t} \mathrm{d}\Omega + \int_{\Omega_{\text{IEFG}}} \nabla \delta T . k \nabla T \mathrm{d}\Omega - \int_{\Omega_{\text{IEFG}}} \delta T \rho C_p \vec{v} . \nabla T \mathrm{d}\Omega = \int_{\Omega_{\text{IEFG}}} \delta T \dot{Q} \mathrm{d}\Omega + \int_{\substack{\Gamma_q \\ (\text{IEFG})}} \delta T \, \bar{q} \, \mathrm{d}\Gamma + \int_{\Gamma_{\text{IEFG}}} \delta T h_p \left(\bar{T}_{\text{FEM}} - T \right) \mathrm{d}\Gamma. \tag{E.6}$$

In Eq. (E.6), h_p is the penalty parameter for the imposition of (E.4) on the boundary Γ_{IEFG}. The weak formulation (E.5) to be solved via FEM does not include penalty integrals for the imposition of temperature $\bar{T}$ on boundary Γ_T, since the Kronecker delta property of the shape functions used in such mesh-based method allows the imposition of Dirichlet conditions in the form of prescribed nodal values.

The solution of (E.5) via FEM is performed using the same interpolating approximations for both temperature $T(\vec{x})|_{\Omega_{\text{FEM}}} \approxeq T_{\text{FEM}}(\vec{x})$ and its virtual variation $\delta T(\vec{x})|_{\Omega_{\text{FEM}}} \approxeq \delta T_{\text{FEM}}(\vec{x})$ in Ω_{FEM}, which in this communication consists in standard linear interpolating finite element basis functions:

$$T_{\text{FEM}}(\vec{x}) = \sum_{I=1}^{n_{\text{FEM}}} \varphi_{\text{FEM}}^{(I)}(\vec{x}) \, \hat{T}_{\text{FEM}}^{(I)}, \qquad \delta T_{\text{FEM}}(\vec{x}) = \sum_{I=1}^{n_{\text{FEM}}} \varphi_{\text{FEM}}^{(I)}(\vec{x}) \, \delta \hat{T}_{\text{FEM}}^{(I)}, \qquad \text{for all} \quad \vec{x} \in \Omega_{\text{FEM}} \tag{E.7}$$

where n_{FEM} is the nodes number of the background mesh. Conversely, the IEFG formulation of (E.6) is obtained using the same IMLS approximations for both temperature $T(\vec{x})|_{\Omega_{\text{IEFG}}} \approxeq T_{\text{IEFG}}(\vec{x})$ and its virtual variation $\delta T(\vec{x})|_{\Omega_{\text{IEFG}}} \approxeq \delta T_{\text{IEFG}}(\vec{x})$ in Ω_{IEFG}:

$$T_{\text{IEFG}}(\vec{x}) = \sum_{I=1}^{n_{\text{IEFG}}} \varphi_{\text{IEFG}}^{(I)}(\vec{x}) \, \hat{T}_{\text{IEFG}}^{(I)}, \qquad \delta T_{\text{IEFG}}(\vec{x}) = \sum_{I=1}^{n_{\text{IEFG}}} \varphi_{\text{IEFG}}^{(I)}(\vec{x}) \, \delta \hat{T}_{\text{IEFG}}^{(I)}, \qquad \text{for all} \quad \vec{x} \in \Omega_{\text{IEFG}} \tag{E.8}$$

where n_{IEFG} is the number of patch nodes representing the overlapping domain Ω_{IEFG} intended to enrich the numerical solution near the moving heat source.

The IMLS approximations to be used in this work are constructed with cubic splines-based weight functions [203], whereas both the geometry of the nodal influence domains and the polynomial basis vector can be chosen appropriately according to the particular features of each problem.

Rectangular [203] and circular [225] influence domains are often used in bidimensional problems, whereas spherical [239], cylindrical [203] and right-angled hexahedral [228] influence domains are common choices in tridimensional problems.

The construction of IMLS can be about 30 % faster compared to standard MLS [242, 243, 251], and details on the implementation of IMLS can be found in previous communications concerning the IEFG-based solution of both bidimensional [203, 225, 251, 252] and tridimensional [203, 242, 243] problems.

The substitution of the linear interpolating finite element basis functions (E.7) in (E.5) leads to the FEM approximation in the background mesh, which holds for any $\delta \hat{T}_{\text{FEM}}^{(I)}$:

$$\sum_{J=1}^{n_{\text{FEM}}} \underbrace{\left[\int_{\Omega_{\text{FEM}}} \varphi^{(I)}_{\text{FEM}} \rho\, c_p \varphi^{(J)}_{\text{FEM}}\, \mathrm{d}\Omega\right]}_{C^{(IJ)}_{\text{FEM}}} \dot{\hat{T}}^{(J)}_{\text{FEM}} + \sum_{J=1}^{n_{\text{FEM}}} \underbrace{\left[\int_{\Omega_{\text{FEM}}} \nabla\varphi^{(I)}_{\text{FEM}} \cdot k \nabla\varphi^{(J)}_{\text{FEM}}\, \mathrm{d}\Omega\right]}_{K^{(IJ)}_{\text{FEM}}} \hat{T}^{(J)}_{\text{FEM}}$$
$$- \sum_{J=1}^{n_{\text{FEM}}} \underbrace{\left[\int_{\Omega_{\text{FEM}}} \varphi^{(I)}_{\text{FEM}} \rho\, c_p \vec{v} \cdot \nabla\varphi^{(J)}_{\text{FEM}}\, \mathrm{d}\Omega\right]}_{A^{(IJ)}_{\text{FEM}}} \hat{T}^{(J)}_{\text{FEM}} = \underbrace{\left[\int_{\Omega_{\text{FEM}}} \varphi^{(I)}_{\text{FEM}} \dot{Q}\, \mathrm{d}\Omega\right]}_{F^{(I)}_{\text{FEM}(\dot{Q})}} + \underbrace{\left[\int_{\Gamma_q} \varphi^{(I)}_{\text{FEM}} \bar{q}\, \mathrm{d}\Gamma\right]}_{F^{(I)}_{\text{FEM}(\bar{q})}}. \quad \text{(E.9)}$$

Similarly, the IEFG formulation in the fine arrangement of moving patch nodes that represents the overlapping domain Ω_{IEFG} is obtained after substituting the IMLS approximations (E.8) in (E.6):

$$\sum_{J=1}^{n_{\text{IEFG}}} \underbrace{\left[\int_{\Omega_{\text{IEFG}}} \varphi^{(I)}_{\text{IEFG}} \rho\, C_p \varphi^{(J)}_{\text{IEFG}}\, \mathrm{d}\Omega\right]}_{C^{(IJ)}_{\text{IEFG}}} \dot{\hat{T}}^{(J)}_{\text{IEFG}} + \sum_{J=1}^{n_{\text{IEFG}}} \underbrace{\left[\int_{\Omega_{\text{IEFG}}} \nabla\varphi^{(I)}_{\text{IEFG}} \cdot k \nabla\varphi^{(J)}_{\text{IEFG}}\, \mathrm{d}\Omega\right]}_{K^{(IJ)}_{\text{IEFG}}} \hat{T}^{(J)}_{\text{IEFG}}$$
$$- \sum_{J=1}^{n_{\text{IEFG}}} \underbrace{\left[\int_{\Omega_{\text{IEFG}}} \varphi^{(I)}_{\text{IEFG}} \rho\, C_p \vec{v}.\nabla\varphi^{(J)}_{\text{IEFG}}\, \mathrm{d}\Omega\right]}_{A^{(IJ)}_{\text{IEFG}}} \hat{T}^{(J)}_{\text{IEFG}} + \sum_{J=1}^{n_{\text{IEFG}}} \underbrace{\left[\int_{\Gamma_{\text{IEFG}}} \varphi^{(I)}_{\text{IEFG}} h_p \varphi^{(J)}_{\text{IEFG}}\, \mathrm{d}\Gamma\right]}_{P^{(IJ)}_{\text{IEFG}}} \hat{T}^{(J)}_{\text{IEFG}}$$
$$= \underbrace{\left[\int_{\Gamma_{\text{IEFG}}} \varphi^{(I)}_{\text{IEFG}} h_p \bar{T}_{\text{FEM}}\, \mathrm{d}\Gamma\right]}_{F^{(I)}_{\text{IEFG}(h_p)}} + \underbrace{\left[\int_{\Omega_{\text{IEFG}}} \varphi^{(I)}_{\text{IEFG}} \dot{Q}\, \mathrm{d}\Omega\right]}_{F^{(I)}_{\text{IEFG}(\dot{Q})}} + \underbrace{\left[\int_{\substack{\Gamma_q \\ (\text{IEFG})}} \varphi^{(I)}_{\text{IEFG}} \bar{q}\, \mathrm{d}\Gamma\right]}_{F^{(I)}_{\text{IEFG}(\bar{q})}}. \quad \text{(E.10)}$$

The FEM approximation in the background mesh (E.9) and the IEFG formulation in the moving patch nodes (E.10) are finally summarised as follows:

$$\sum_{J=1}^{n_{\text{FEM}}} C^{(IJ)}_{\text{FEM}} \dot{\hat{T}}^{(J)}_{\text{FEM}} + \sum_{J=1}^{n_{\text{FEM}}} \left(K^{(IJ)}_{\text{FEM}} - A^{(IJ)}_{\text{FEM}}\right) \hat{T}^{(J)}_{\text{FEM}} = F^{(I)}_{\text{FEM}(\dot{Q})} + F^{(I)}_{\text{FEM}(\bar{q})}, \quad \text{(E.11)}$$

$$\sum_{J=1}^{n_{\text{IEFG}}} C^{(IJ)}_{\text{IEFG}} \dot{\hat{T}}^{(J)}_{\text{IEFG}} + \sum_{J=1}^{n_{\text{IEFG}}} \left(K^{(IJ)}_{\text{IEFG}} - A^{(IJ)}_{\text{IEFG}} + P^{(IJ)}_{\text{IEFG}}\right) \hat{T}^{(J)}_{\text{IEFG}} = F^{(I)}_{\text{IEFG}(h_p)} + F^{(I)}_{\text{IEFG}(\dot{Q})} + F^{(I)}_{\text{IEFG}(\bar{q})}. \quad \text{(E.12)}$$

For implementation purposes, the semi-discrete problems (E.11) and (E.12) are properly re-written in the following arrangements of matrices and vectors:

$$\mathbf{C}_{\text{FEM}} \dot{\hat{\mathbf{T}}}_{\text{FEM}} + \left(\mathbf{K}_{\text{FEM}} - \mathbf{A}_{\text{FEM}}\right) \hat{\mathbf{T}}_{\text{FEM}} = \mathbf{F}_{\text{FEM}(\dot{Q})} + \mathbf{F}_{\text{FEM}(\bar{q})}, \quad \text{(E.13)}$$

$$\mathbf{C}_{\text{IEFG}} \dot{\hat{\mathbf{T}}}_{\text{IEFG}} + \left(\mathbf{K}_{\text{IEFG}} - \mathbf{A}_{\text{IEFG}} + \mathbf{P}_{\text{IEFG}}\right) \hat{\mathbf{T}}_{\text{IEFG}} = \mathbf{F}_{\text{IEFG}(h_p)} + \mathbf{F}_{\text{IEFG}(\dot{Q})} + \mathbf{F}_{\text{IEFG}(\bar{q})}. \quad \text{(E.14)}$$

The semi-discrete problems will be integrated in time using a fully implicit backward finite difference scheme, which results in the following set of algebraic equations:

$$\left(\frac{\mathbf{C}_{\text{FEM}}}{\Delta t} + \mathbf{K}_{\text{FEM}} - \mathbf{A}_{\text{FEM}}\right) \hat{\mathbf{T}}_{\text{FEM}}\Big|_{t+\Delta t} = \frac{\mathbf{C}_{\text{FEM}}}{\Delta t} \hat{\mathbf{T}}_{\text{FEM}}\Big|_{t} + \left(\mathbf{F}_{\text{FEM}(\dot{Q})} + \mathbf{F}_{\text{FEM}(\bar{q})}\right)\Big|_{t+\Delta t}, \quad \text{(E.15)}$$

$$\left(\frac{\mathbf{C}_{\text{IEFG}}}{\Delta t}+\mathbf{K}_{\text{IEFG}}-\mathbf{A}_{\text{IEFG}}+\mathbf{P}_{\text{IEFG}}\right)\hat{\mathbf{T}}_{\text{IEFG}}\Big|_{t+\Delta t}=\frac{\mathbf{C}_{\text{IEFG}}}{\Delta t}\hat{\mathbf{T}}_{\text{IEFG}}\Big|_{t}+\left(\mathbf{F}_{\text{IEFG}(h_p)}+\mathbf{F}_{\text{IEFG}(\dot{Q})}+\mathbf{F}_{\text{IEFG}(\bar{q})}\right)\Big|_{t+\Delta t}. \tag{E.16}$$

The reciprocal dependence of the thermal problems to be solved in the overlapping domains Ω_{FEM} and Ω_{IEFG} at each time step is addressed via the iterative solution of the algebraic systems of equations (E.15) and (E.16). The transfer of information from Ω_{FEM} to Ω_{IEFG} is performed via the penalty matrix $\mathbf{P}_{\text{IEFG}}$ and the penalty vector $\mathbf{F}_{\text{IEFG}(h_p)}$, whereas the transfer of information from Ω_{IEFG} to Ω_{FEM} is performed by using the IEFG-based solution of the thermal problem in Ω_{IEFG} to compute the temperatures at the positions $\vec{x}^{(h)}$ of nodes $h \in \mathcal{N}_{\text{enc}}$ and by prescribing these nodal values in the background mesh. The nodal parameters of vector $\hat{\mathbf{T}}_{\text{IEFG}}$ are used to compute the temperature $\bar{T}_{\text{IEFG}}$ of each node $h \in \mathcal{N}_{\text{enc}}$ as follows:

$$\bar{T}_{\text{IEFG}}=T_{\text{IEFG}}(\vec{x}^{(h)})=\sum_{I=1}^{n_{\text{IEFG}}}\varphi^{(I)}_{\text{IEFG}}(\vec{x}^{(h)})\,\hat{T}^{(I)}_{\text{IEFG}},\qquad \text{for all}\quad h\in\mathcal{N}_{\text{enc}}. \tag{E.17}$$

The temperature $\bar{T}_{\text{FEM}}$ on Γ_{IEFG} required to assemble the penalty vector $\mathbf{F}_{\text{IEFG}(h_p)}$ is also computed via IMLS approximations, but using the vector $\hat{\mathbf{T}}_{\text{rec}}$ of nodal parameters $\hat{T}^{(I)}_{\text{rec}}$ obtained from the local reconstruction of the FEM-based solution, i.e.:

$$\bar{T}_{\text{FEM}}=\sum_{I=1}^{n_{\text{rec}}}\varphi^{(I)}_{\text{rec}}(\vec{x})\,\hat{T}^{(I)}_{\text{rec}},\qquad \text{for all}\quad \vec{x}\in\Gamma_{\text{IEFG}}, \tag{E.18}$$

where n_{rec} is the number of nodes included in $\mathcal{N}_{\text{rec}}$. In this communication, a similar procedure to that proposed by Storti et al. [148, 262] for overlapping non-structured meshes in FEM frameworks is used to perform the current IMLS-based local reconstruction. The procedure of Storti et al. [148, 262] has been conceived to keep the convergence features of standard numerical solutions based on a single mesh, and involves a high order interpolation algorithm that uses a least-squares adjustment enforced to fit the nodal values via Lagrange multipliers. With the purpose of keeping the convergence features of a standard IEFG-based solution, this technique is extended to the current Ov-IEFG-FEM to enforce the following condition in the IMLS approximations of Eq. (E.18):

$$\sum_{J=1}^{n_{\text{rec}}}\varphi^{(J)}_{\text{rec}}(\vec{x}^{(I)})\,\hat{T}^{(J)}_{\text{rec}}=\hat{T}^{(I)}_{\text{FEM}}\qquad \text{for all}\quad I\in\mathcal{N}_{\text{rec}}, \tag{E.19}$$

to this end, the following Lagrangian functional must be minimised:

$$\mathcal{L}\left(\hat{\mathbf{T}}_{\text{rec}},\boldsymbol{\lambda}\right)=\frac{1}{2}\int_{\Omega\text{rec}}\left(\sum_{J=1}^{n_{\text{rec}}}\varphi^{(J)}_{\text{rec}}(\vec{x})\,\hat{T}^{(J)}_{\text{rec}}-T_{\text{FEM}}(\vec{x})\right)^2\mathrm{d}\Omega+\sum_{J=1}^{n_{\text{rec}}}\lambda^{(J)}\left(\sum_{I=1}^{n_{\text{rec}}}\varphi^{(I)}_{\text{rec}}(\vec{x}^{(J)})\,\hat{T}^{(I)}_{\text{rec}}-\hat{T}^{(J)}_{\text{FEM}}\right)\qquad \text{for all}\quad I,J\in\mathcal{N}_{\text{rec}}, \tag{E.20}$$

where each of the Lagrange multipliers, denoted as $\lambda^{(J)}$, is included in the vector $\boldsymbol{\lambda}$. The domain $\Omega_{\text{rec}}\subset\Omega_{\text{FEM}}$ is formed by the union of those elements whose centres are enclosed by $\mathcal{S}_{\text{rec}}$, as depicted in Fig. E.1. The minimisation of (E.20) leads to the following system of equations:

$$\begin{bmatrix}\mathbf{G} & \boldsymbol{\Lambda}\\ \boldsymbol{\Lambda}^{\text{T}} & \mathbf{0}\end{bmatrix}\begin{bmatrix}\hat{\mathbf{T}}_{\text{rec}}\\ \boldsymbol{\lambda}\end{bmatrix}=\begin{bmatrix}\mathbf{F}_{\text{rec}}\\ \hat{\mathbf{T}}^{(\Omega_{\text{rec}})}_{\text{FEM}}\end{bmatrix}, \tag{E.21}$$

where the components of $\mathbf{G}$, $\boldsymbol{\Lambda}$, and $\mathbf{F}_{\text{rec}}$ are

$$G^{(IJ)}=\int_{\Omega\text{rec}}\varphi^{(I)}_{\text{rec}}(\vec{x})\,\varphi^{(J)}_{\text{rec}}(\vec{x})\mathrm{d}\Omega,\qquad \Lambda^{(IJ)}=\varphi^{(I)}_{\text{rec}}(\vec{x}^{(J)}),\qquad \text{and}\quad F^{(I)}_{\text{rec}}=\int_{\Omega\text{rec}}\varphi^{(I)}_{\text{rec}}(\vec{x})\,T_{\text{FEM}}(\vec{x})\,\mathrm{d}\Omega, \tag{E.22}$$

respectively. It is worth to remark that the temperature $T_{\text{FEM}}(\vec{x})$ used in the assembling of $\mathbf{F}_{\text{rec}}$ is computed according to (E.7), and the components of $\hat{\mathbf{T}}^{(\Omega_{\text{rec}})}_{\text{FEM}}$ are the temperatures $\hat{T}^{(J)}_{\text{FEM}}$ of nodes $J\in\mathcal{N}_{\text{rec}}$.

Based on the procedures described above, the implementation of the proposed Ov-IEFG-FEM is summarised in the following algorithm given as a flowchart in pseudo code:

1. Initialisation of $\hat{\mathbf{T}}_{\text{FEM}}\Big|_t$ and $\hat{\mathbf{T}}_{\text{IEFG}}\Big|_t$ according to the initial condition $T = T_0$. Assembling of (E.15) and (E.16).
2. Iterative Ov-IEFG-FEM: set $\omega = 0$, $\hat{\mathbf{T}}^{(\omega)}_{\text{FEM}}\Big|_{t+\Delta t} = \hat{\mathbf{T}}_{\text{FEM}}\Big|_t$ and $\hat{\mathbf{T}}^{(\omega)}_{\text{IEFG}}\Big|_{t+\Delta t} = \hat{\mathbf{T}}_{\text{IEFG}}\Big|_t$.
   - *a)*
     - if $\omega \geq 1$, $\bar{T}^{(\omega+1)}_{\text{IEFG}} = \bar{T}^{(\omega)}_{\text{IEFG}}$.
     - Otherwise, no temperature is imposed at nodes $h \in \mathcal{N}_{\text{enc}}$
   - *b)* Solving (E.15): $\hat{\mathbf{T}}_{\text{FEM}}\Big|_t$, $\hat{\mathbf{T}}^{(\omega)}_{\text{FEM}}\Big|_{t+\Delta t} \rightarrow \hat{\mathbf{T}}^{(\omega+1)}_{\text{FEM}}\Big|_{t+\Delta t}$.
   - *c)* Solving (E.21) to obtain $\hat{\mathbf{T}}_{\text{rec}}$, and computing $\bar{T}^{(\omega+1)}_{\text{FEM}}$ using (E.18) on Γ_{IEFG}.
   - *d)* Solving (E.16): $\hat{\mathbf{T}}_{\text{IEFG}}\Big|_t$, $\hat{\mathbf{T}}^{(\omega)}_{\text{IEFG}}\Big|_{t+\Delta t} \rightarrow \hat{\mathbf{T}}^{(\omega+1)}_{\text{IEFG}}\Big|_{t+\Delta t}$.
   - *e)* Computing $\bar{T}^{(\omega+1)}_{\text{IEFG}}$ using (E.17) at nodes $h \in \mathcal{N}_{\text{enc}}$.
   - *f)* Stop criterion:
     - if $\omega = 0$, $\omega \leftarrow \omega + 1$, go back to (a).
     - Otherwise:
       - if $\frac{\|\bar{T}^{(\omega+1)}_{\text{FEM}} - \bar{T}^{(\omega)}_{\text{FEM}}\|_{\text{L}_2(\Gamma_{\text{IEFG}})}}{\|\bar{T}^{(\omega+1)}_{\text{FEM}}\|_{\text{L}_2(\Gamma_{\text{IEFG}})}} + \frac{\|\bar{T}^{(\omega+1)}_{\text{IEFG}} - \bar{T}^{(\omega)}_{\text{IEFG}}\|_{\text{L}_2(\mathcal{N}_{\text{enc}})}}{\|\bar{T}^{(\omega+1)}_{\text{IEFG}}\|_{\text{L}_2(\mathcal{N}_{\text{enc}})}} \geq \epsilon$, $\omega \leftarrow \omega + 1$, then go back to (a).
       - Otherwise, set $t \leftarrow t + \Delta t$, $\hat{\mathbf{T}}_{\text{FEM}}\Big|_t = \hat{\mathbf{T}}^{(\omega+1)}_{\text{FEM}}\Big|_{t+\Delta t}$, and $\hat{\mathbf{T}}_{\text{IEFG}}\Big|_t = \hat{\mathbf{T}}^{(\omega+1)}_{\text{IEFG}}\Big|_{t+\Delta t}$, and go to the next time step (g).
   - *g)* Next time step:
     - if $t < t_f$, Assemble (E.15) and (E.16), and then go back to (2).
     - Otherwise, got to (3).
3. Compute the temperature distributions T_{FEM} in $\Omega_{\text{FEM}} - \Omega_{\text{IEFG}}$ using (E.7), and T_{IEFG} in Ω_{IEFG} using (E.8). Obtain the effective solution of the heat transfer problem as $T = T_{\text{FEM}} \cup T_{\text{IEFG}}$.

It is important to note that the time denoted as t_f in the flowchart does not signify the duration needed to reach a steady state. Rather, it indicates the point up to which the transient analysis is intended to be carried out. In fact, the presence of a heat source in constant motion entails a transient problem for which steady conditions are generally not reached. This is only possible in the simplest cases where the problem can be solved under the Rosenthal's approximation [213, 268], where a steady solution with a seamless coupling along Γ_{IEFG} could be achieved via a simple time-marching scheme as it time-accuracy is not required [270]. Conversely, the iterative procedure explained in the flowchart is performed to obtain a seamless coupling along Γ_{IEFG} at each time step of the fully implicit backward finite difference scheme of Eqs. (E.15)-(E.16), aiming to time-accuracy as well. To achieve a seamless temperature transition at Γ_{IEFG}, a distance criterion between Γ_{IEFG} and $\mathcal{S}_{\text{IEFG}\rightarrow\text{FEM}}$ must be implemented. In this communication, such criterion consists of setting the Γ_{IEFG}-$\mathcal{S}_{\text{IEFG}\rightarrow\text{FEM}}$ distance to be 1.5 to 3 times the average element size of the background mesh. Importantly, this criterion remains valid whether the problem is addressed under the Rosenthal's approximation or when actually following the moving heat source scanning path. The choice of this distance criterion is based on the work of Storti et al. [148], where it was established that a distance of at least twice the average element size of the background mesh is necessary for an overset formulation fully developed in an FEM framework. Regarding the separation between $\mathcal{S}_{\text{rec}}$ and Γ_{IEFG}, a distance of at least one element size of the background mesh is sufficient to achieve a smooth and accurate IMLS-based reconstruction using the nodes $\mathcal{N}_{\text{rec}}$ of those elements whose centres are enclosed by $\mathcal{S}_{\text{rec}}$ defining the reconstruction subdomain Ω_{rec}. Extensive numerical tests were conducted to investigate the effect of further enlarging Ω_{rec}, even using the entire background mesh for the IMLS-based reconstruction. However, it was found that such enlargement did not result in any significant change in

terms of accuracy and smoothness of the results. Therefore, the decision was made to keep Ω_{rec} as small as possible for computational efficiency purposes. In order to ensure an accurate computation of high temperatures and marked thermal gradients near the moving heat source, it is crucial to configure the nodes spacing around the current centre position of Ω_{IEFG} to be smaller than the effective radius of the moving heat source. In this regard, the arrangement of patch nodes in all the problems to be addressed in this communication will be configured to substantially fulfil such requirement.

E.3. Numerical examples and results

To enable an appropriate analysis of convergence and accuracy, the Ov-IEFG-FEM method will initially be applied to a problem with controlled conditions and low computational cost. Specifically, a rectangular thin plate with a moving heat source that follows a horizontal straight path at a constant velocity will be considered. The Rosenthal's coordinate transformation will be used to allow for the assumptions of a spatially fixed heat source and Ω_{IEFG}, resulting in the introduction of the advective term in both Ω_{FEM} and Ω_{IEFG}. The potential of the Ov-IEFG-FEM will subsequently be demonstrated by solving problems with moving heat sources subjected to more complex paths that cannot be approximated by the Rosenthal's approach. In these cases, the assumptions of a spatially fixed heat source and Ω_{IEFG} will no longer hold. Instead, the path of the moving heat source must be followed by the overlapping domain Ω_{IEFG}, which, according to the ALE description concerning the relative motion between the fixed background mesh Ω_{FEM} and the moving patch nodes representing Ω_{IEFG}, is the only domain that includes the advective term. As a final example, the Ov-IEFG-FEM potential is also demonstrated in the solution of a more complex tridimensional non-linear problem with temperature dependent properties and phase change effects.

E.3.1. Convergence analysis under Rosenthal's formulation

The benchmark problem considered for the convergence analysis of the Ov-IEFG-FEM is depicted in Fig. E.2, which consists in a rectangular thin plate made of steel and subjected to a circular moving heat source with Gaussian distribution[203, 213, 268]:

$$\dot{Q} = \dot{Q}_0 e^{-r^2/r_0^2}, \tag{E.23}$$

where $\dot{Q}_0$ is the maximum energy density released by the heat source at its centre times the plate thickness, whereas r is the distance from heat source centre. The effective radius r_0 is defined to contain the whole heat source power $\dot{Q}_T$ within an uniform distribution $\dot{Q}_0$, i.e. $\dot{Q}_T$=$\dot{Q}_0 \pi r_0^2$. The problem symmetry allows the numerical solution considering only the upper half $y \geq 0$, and the moving heat source with velocity $\vec{v} = (u, 0)$ is assumed at the fixed location $(x, y) = (50, 0)$ (mm) for the Rosenthal's description. In this benchmark problem, all the boundaries have been considered to be adiabatic.

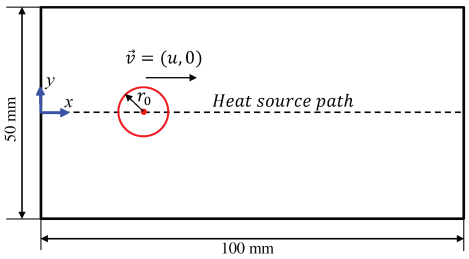

Figura E.2: Representation of the benchmark problem to be solved under the Rosenthal's formulation for accuracy and convergence analysis of the proposed Ov-IEFG-FEM.

Therefore, the convergence for each case has been assessed according to the following L_2 norm-based normalised errors:

$$\textbf{Ov-IEFG-FEM:} \quad E_{\mathrm{L}_2}^{\text{Ov-IEFG-FEM}} = \frac{\left(\|T_{\text{FEM}} - T_{\text{ref}}\|^2_{\mathrm{L}_2(\Omega_{\text{FEM}} - \Omega_{\text{IEFG}})} + \|T_{\text{IEFG}} - T_{\text{ref}}\|^2_{\mathrm{L}_2(\Omega_{\text{IEFG}})} \right)^{1/2}}{\|T_{\text{ref}}\|_{\mathrm{L}_2(\Omega)}},$$

$$\textbf{IEFG:} \quad E_{\mathrm{L}_2}^{\text{IEFG}} = \frac{\|T_{\text{IEFG}} - T_{\text{ref}}\|_{\mathrm{L}_2(\Omega)}}{\|T_{\text{ref}}\|_{\mathrm{L}_2(\Omega)}},$$

$$\textbf{FEM:} \quad E_{\mathrm{L}_2}^{\text{FEM}} = \frac{\|T_{\text{FEM}} - T_{\text{ref}}\|_{\mathrm{L}_2(\Omega)}}{\|T_{\text{ref}}\|_{\mathrm{L}_2(\Omega)}} \tag{E.24}$$

The accuracy and convergence of the Ov-IEFG-FEM will be performed by comparison with a very refined FEM-based solution referred as T_{ref}, where the domain has been discretised with the mesh of Fig. E.3 consisting of $1000 \times 250 = 25 \times 10^4$ quadrilateral elements exponentially clustered towards the heat source location. The problem has been solved considering the parameters and material properties of Table E.1, with the transient heat conduction analysis performed until $t_f = 50$ s. The convergence features of the proposed Ov-IEFG-FEM will also be compared to standard FEM and IEFG solutions based on a unique mesh and a single nodes distribution, respectively.

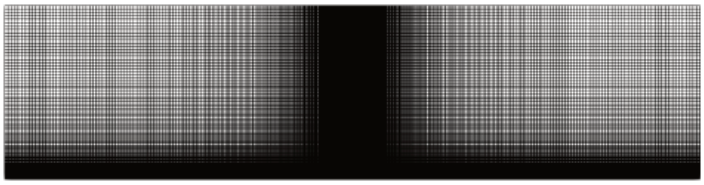

Figura E.3: Mesh for the refined FEM-based reference solution.

Tabla E.1: Parameters and material properties for transient heat conduction in steel thin plate with moving heat source along the horizontal axis of symmetry.

Geometry and problem parameters	Values
Plate length (mm)	100
Plate width (mm)	50
Total heat source power $\dot{Q}_T$ (W)	20π
Heat source effective radius r_o (mm)	0.2
Initial temperature T_0 (^{o}C)	25
Heat source speed u (mm/s)	2
Material properties	**Values**
Conductivity (W.mm^{-1}.K^{-1})	0.025
Specific heat capacity (J.kg^{-1}.K^{-1})	658
Density (kg.mm^{-3})	7.6×10^{-6}

The Ov-IEFG-FEM-based solutions have been performed using a uniform background mesh with an overlapping fine distribution of patch nodes at the moving heat source location, and exponentially clustered towards its centre. The meshes and nodes distributions for the standard solutions purely based on FEM and IEFG have also been clustered towards the heat source location. For visualisation purposes, the most refined meshes and nodes distribution used in the convergence analysis of FEM, IEFG and Ov-IEFG-FEM are shown in Fig. E.4(a)-(c). Since the convergence analysis is being performed with

non-uniform meshes and nodes distribution, it has been more meaningful to estimate the convergence rate in terms of the total number of nodes N rather than focusing on element sizes or nodal spacings Δl. Assuming a sufficiently regular solution where both temperature and its first derivative are continuous throughout Ω, and recognising the inverse proportionality between Δl and N, it is possible to stablish a relationship between convergence rates measures in terms of h and N.

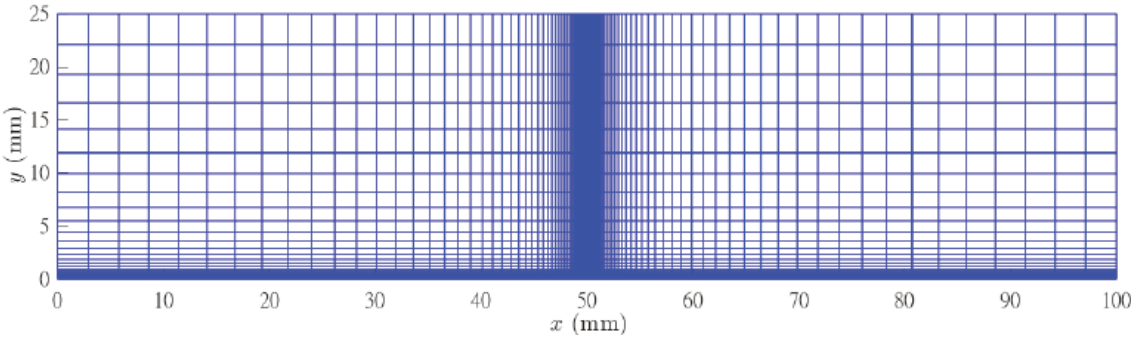

(a) FEM, $172 \times 43 = 7,396$ elements (7,612 nodes)

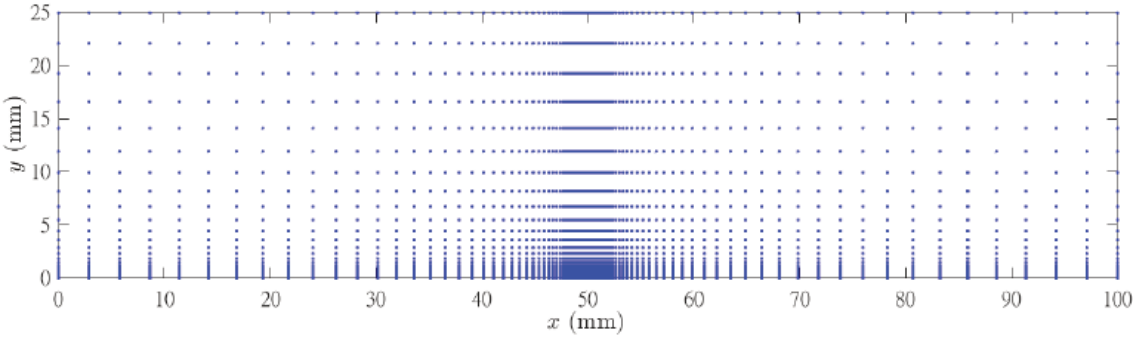

(b) IEFG, $173 \times 44 = 7,612$ nodes

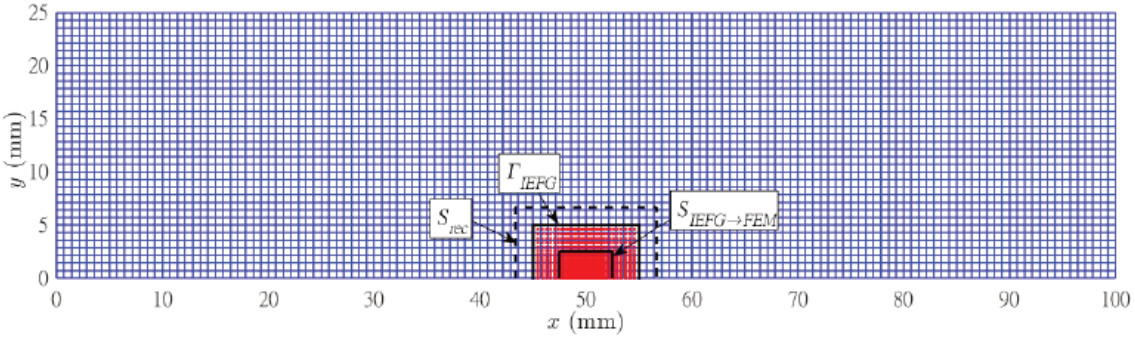

(c) Ov-IEFG-FEM, $141 \times 36 + 71 \times 36 = 7,632$ nodes

Figura E.4: Finest nodes distribution and meshes used in the convergence analysis of FEM, IEFG, and the proposed Ov-IEFG-FEM.

If the convergence rate in terms of h is $E \approx \mathcal{O}(\Delta l^p)$, the convergence rate in terms of N will be $E \approx \mathcal{O}(N^{-p/d})$, where d represents the spatial dimension of the problem [148, 262]. Time integration in the current benchmark problem has been performed under an implicit backward finite difference scheme with time step $\Delta t = 1 \times 10^{-4}$, and the convergence behaviour obtained at different times are depicted in Fig.E.5(a)-(c). The Ov-IEFG-FEM exhibits convergence rates of $E \approx \mathcal{O}(N^{-1.3}) \approx \mathcal{O}(\Delta l^{2.6})$, which are slightly higher for $t = 5$ s. These convergence rates match those corresponding to the solutions purely based on IEFG, with the Ov-IEFG-FEM also exhibiting higher accuracy. This highlights the remarkable

potential of the Ov-IEFG-FEM approach. It not only surpasses the quadratic convergence rate of standard FEM ($E \approx \mathcal{O}(\Delta l^2)$), but also recovers the IEFG accuracy by using this meshless approach only in the region governing the solution error, i.e. near the heat source. The thermal field and temperature profile along the horizontal axis $(x, 0)$ obtained for $t = 25$ s under the proposed Ov-IEFG-FEM are depicted in Fig. E.6(a)-(b) for visualisation purposes, which demonstrates both the seamless coupling along Γ_{IEFG} and the smooth capture of the high thermal gradients near the moving heat source. It is also worth to mention that the IMLS-based reconstruction using the set $\mathcal{N}_{\text{rec}}$ has exhibited a perfect fitting with the nodal values of the FEM-based solution performed in the coarse background mesh, according to the Lagrange multipliers-based restriction introduced in Eq. (E.20). This aspect is demonstrated via the computation of the following L_2 norm:

$$E_{L_2}^{\text{rec}} = \frac{\left\| \bar{T}_{\text{FEM}} - T_{\text{FEM}} \right\|_{\text{L}_2(\mathcal{N}_{\text{rec}})}}{\left\| T_{\text{FEM}} \right\|_{\text{L}_2(\mathcal{N}_{\text{rec}})}}, \tag{E.25}$$

and the corresponding results are summarised in Table E.2. It can be stated from these results that the IMLS-based reconstruction of the temperature field in $\Omega_{\text{rec}} \in \Omega_{\text{FEM}}$ does not introduce error at the positions of nodes belonging to $\mathcal{N}_{\text{rec}}$, with respect to the FEM-based solution performed in the coarse background mesh.

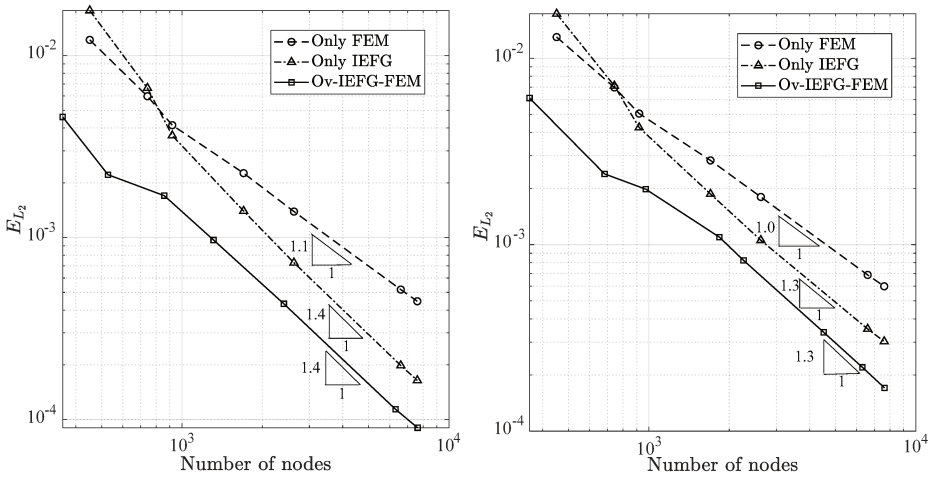

(a) $t = 5$ s (b) $t = 25$ s

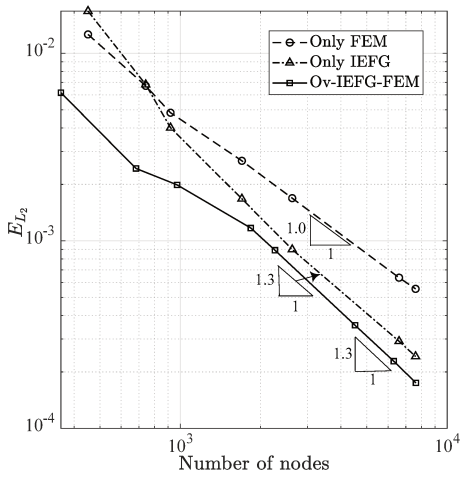

(c) $t = 50$ s

Figura E.5: Convergence behaviour of FEM, IEFG, and the proposed Ov-IEFG-FEM at different times.

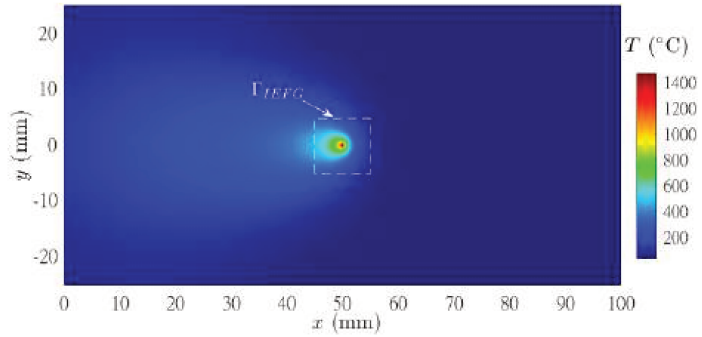

(a) Temperature distribution

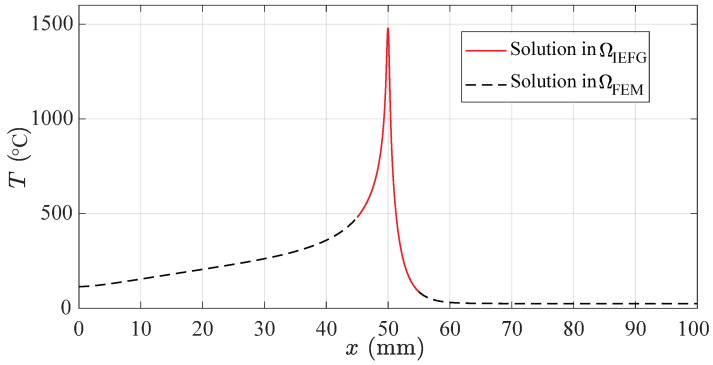

(b) Temperature profile along $(x, 0)$

Figura E.6: Solution obtained via the Ov-IEFG-FEM at $t = 25$ s under Rosenthal's coordinates transformation. Although the numerical solution has been performed at the upper half of the plate, the corresponding temperature distribution is plotted in (a) over the entire plate for better visualisation.

The virtually null errors reported in Table E.2 ($E^{\text{rec}}_{L_2} \sim 10^{-16}$) demonstrate the perfect fulfilment of the Lagrange multipliers-based restriction of Eq. (E.20). Such reconstruction perfectly fitting the background FEM-based solution at the nodes of set $\mathcal{N}_{\text{rec}}$ has also allowed the seamless coupling along Γ_{IEFG}. These results demonstrate the successful extension of both the immersed boundaries distance criterion and the nodal values fitting high order reconstruction technique introduced in the fully FEM-based overset procedure developed by Storti et. al [148], to the current Ov-IEFG-FEM framework.

Tabla E.2: Nodal error in the IMLS-based reconstruction of the FEM-based solution over the set of nodes set $\mathcal{N}_{\text{rec}}$.

Divisions in Ω_{FEM} and Ω_{IEFG}	Number of nodes	Error		
		$t = 5$s	$t = 25$s	$t = 50$s
$20 \times 5 - 20 \times 10$	357	2.63×10^{-16}	1.74×10^{-16}	2.72×10^{-16}
$32 \times 8 - 20 \times 10$	528	1.59×10^{-16}	2.08×10^{-16}	2.17×10^{-16}
$32 \times 8 - 32 \times 16$	858	1.84×10^{-16}	1.86×10^{-16}	1.81×10^{-16}
$40 \times 10 - 40 \times 20$	1312	1.77×10^{-16}	2.35×10^{-16}	2.33×10^{-16}
$60 \times 15 - 52 \times 26$	2407	2.30×10^{-16}	3.36×10^{-16}	2.88×10^{-16}
$120 \times 30 - 70 \times 35$	6307	2.28×10^{-16}	3.00×10^{-16}	2.84×10^{-16}
$140 \times 35 - 70 \times 35$	7632	2.42×10^{-16}	2.24×10^{-16}	2.63×10^{-16}

E.3.2. Ov-IEFG-FEM to actually follow the heat source scanning path

The Ov-IEFG-FEM will be initially applied to the same benchmark problem of the previous section, but now focusing on accurately tracking the scanning path of the moving heat source. Subsequently, the versatility and potential of the proposed formulation will be further explored by extending its application to more complex scanning paths, such as (i) sinusoidal path and (ii) S-type path commonly encountered in the analysis of metal additive manufacturing processes.

E.3.2.1. Simple straight horizontal scanning path

The scanning begins from $(x, y) = (0, 0)$ mm at $t = 0$ s. The background mesh and patch nodes configuration at different times for the first benchmark problem are depicted in Fig. E.7(a)-(c), and the corresponding temperature distributions are given in Fig. E.8(a)-(c). The patch domain Ω_{IEFG} is represented with $29 \times 15 = 435$ nodes clustered towards the heat source centre, whereas the domain has been discretised with an uniform background mesh of $48 \times 12 = 576$ elements (637 nodes). Accordingly, the smooth and stable capture of marked thermal gradients depicted in Fig. E.8(a)-(c) near the moving heat source has been achieved with only $435 + 637 = 1,072$ nodes.

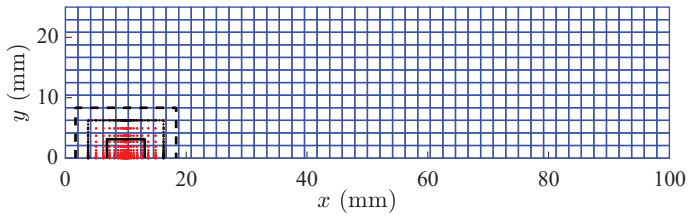

(a) $t = 5$ s

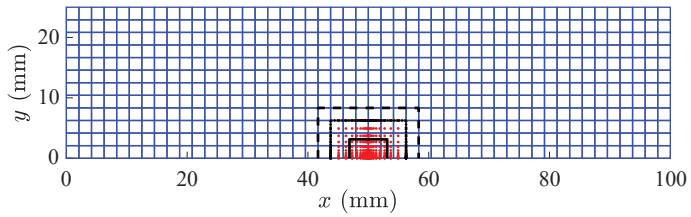

(b) $t = 25$ s

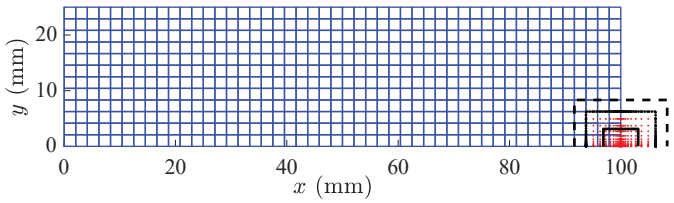

(c) $t = 50$ s

Figura E.7: Patch nodes (red) and background mesh used to solve the transient heat conduction problem over the rectangular thin plate, with the patch nodes actually following the simple horizontal scanning path of the moving heat source. The black dashed lines represent $\mathcal{S}_{\text{rec}}$. The temperature $\bar{T}_{\text{FEM}}$ is imposed (integrated) on Γ_{IEFG} using the Gauss points located on it (black points), whereas $\bar{T}_{\text{IEFG}}$ is reciprocally imposed at those nodes h of the background mesh that are enclosed by $\mathcal{S}_{\text{IEFG}\to\text{FEM}}$ (black solid line).

Achieving a similar stability via FEM has required the mesh of Fig. E.9 consisting of 4,302 elements (4,435 nodes) refined along the scanning path, and the results are compared to the proposed Ov-IEFG-FEM-based solution in Fig. E.10. The temperature distributions of Fig. E.8 exhibit a seamless coupling

at Γ_{IEFG}, highlighting the suitability and potential of the proposed Ov-IEFG-FEM in scenarios where tracking the scanning path of the moving heat source with the patch nodes is required. Additionally, the temperature profiles in Fig. E.10 exhibit excellent agreement between the Ov-IEFG-FEM and a standard FEM-based solution, confirming the accuracy of the proposed approach. The smooth and accurate results presented in Figs. E.8 and E.10 correspond to a Γ_{IEFG}-$\mathcal{S}_{\text{IEFG}\to\text{FEM}}$ distance of 1.5 times the element size of the background mesh. This finding indicates that the distance criterion for immersed boundaries can be less restrictive within the context of the proposed Ov-IEFG-FEM framework, in comparison with that required in the fully FEM-based overset framework developed by Storti et al. [148].

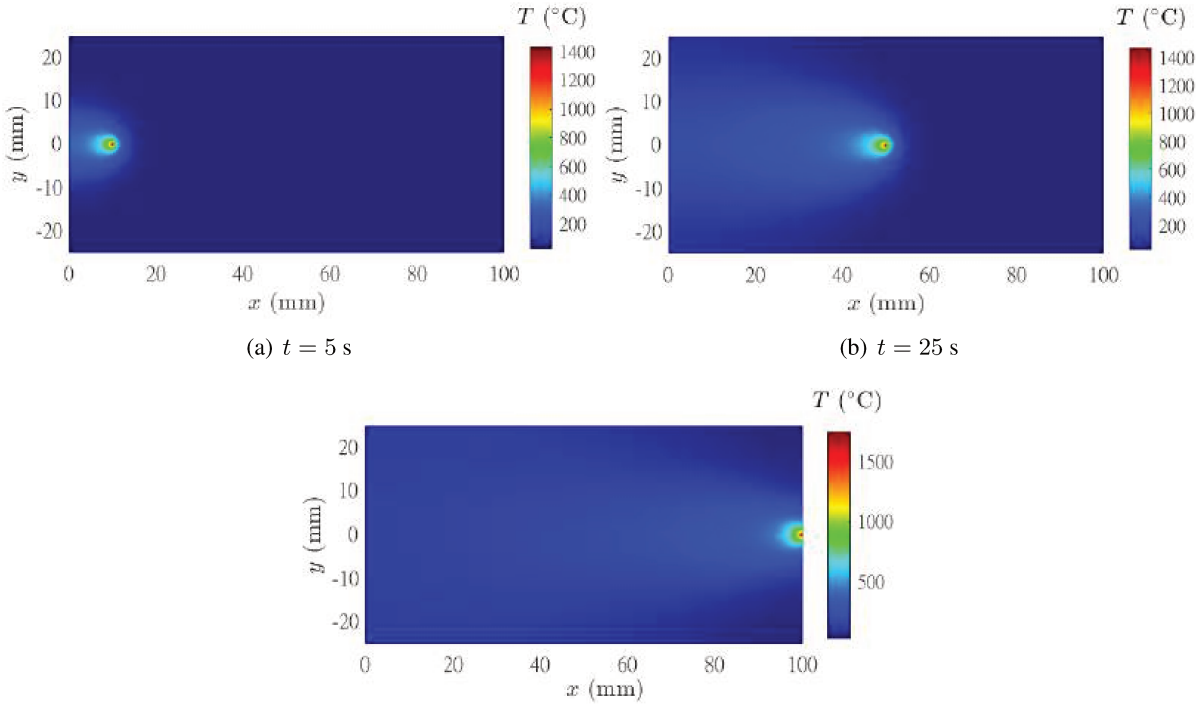

Figura E.8: Temperature distributions computed via the proposed Ov-IEFG-FEM, with the patch nodes actually following the horizontal scanning path of the moving heat source.

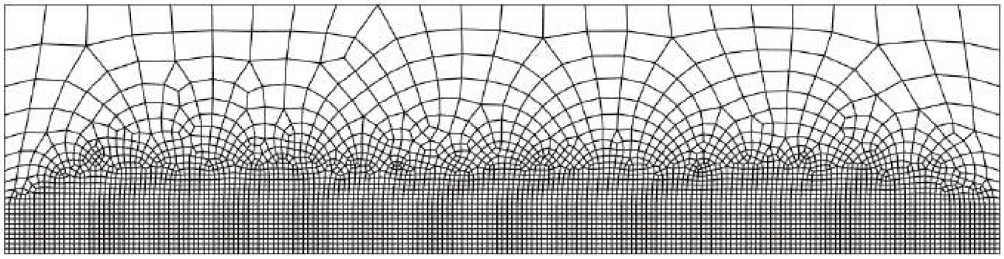

Figura E.9: Mesh refined along the scanning path for the FEM-based solution of the transient heat conduction problem over the rectangular thin plate with a moving heat source following a horizontal straight path.

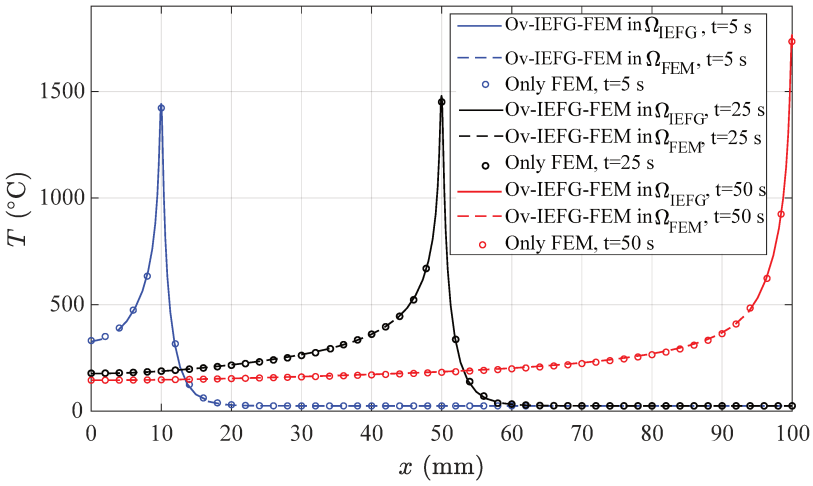

Figura E.10: Temperature profiles computed along the horizontal scanning path via the proposed Ov-IEFG-FEM with moving patch nodes, compared to the standard FEM-based solution.

E.3.2.2. Sinusoidal path

This problem involves the same parameters and material properties of Table E.1, but with the moving heat source now following the scanning path depicted in Fig. E.11.

The background mesh and patch nodes configuration at different times for the sinusoidal scanning path are depicted in Fig. E.12(a)-(c), and the corresponding temperature distributions are given in Fig. E.13(a)-(c). The results are depicted for the heat source at positions $P_1 = (x_1, y_1) = (31.25, 37.5)$, $P_2 = (x_2, y_2) = (50, 25)$, $P_3 = (x_3, y_3) = (68.75, 12.5)$, which correspond to times $t_1 = 11.571$ s, $t_2 = 23.142$ s and $t_3 = 34.713$ s, respectively.

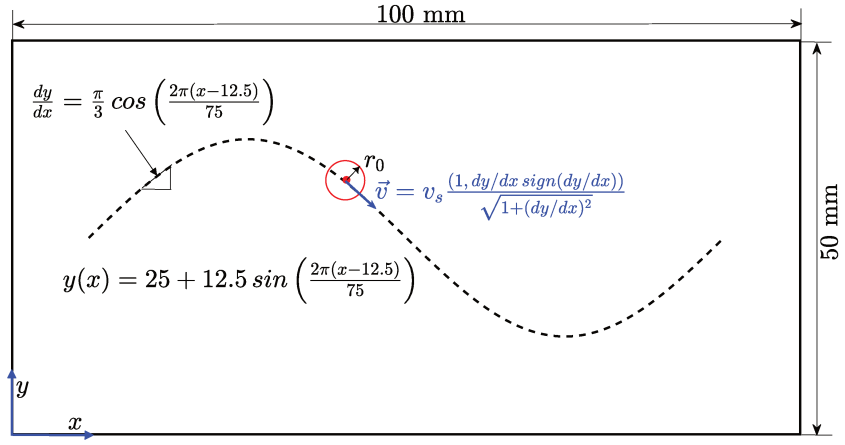

Figura E.11: Representation of the transient heat conduction problem over the rectangular thin plate with a moving heat source following a sinusoidal scanning path.

The patch domain Ω_{IEFG} is represented with $29 \times 29 = 841$ nodes clustered towards the heat source centre, whereas the domain has been discretised with an uniform background mesh of $48 \times 24 = 1152$ elements (1,225 nodes).

Accordingly, the smooth and stable capture of marked thermal gradients depicted in Fig. E.13(a)-(c) near the moving heat source have been achieved with only 841+1,225 = 2,066 nodes. These results also demonstrate that the Ov-IEFG-FEM potential to provide seamless coupling between the IEFG and FEM-based solutions is not limited to simple straight paths. Achieving a similar stability via FEM has required the mesh of Fig. E.14 consisting 167,296 elements (167,537 nodes) refined along the scanning path.

In Fig. E.15, the very refined FEM-based solution is compared to the results achieved via the proposed Ov-IEFG-FEM. This comparison has been performed considering the temperature profiles along both horizontal and vertical axes passing over the moving heat source, and the results exhibit an excellent agreement between the Ov-IEFG-FEM and the FEM-based solution.

This outcome confirms that the achievement of accurate results via the Ov-IEFG-FEM is not limited to simple straight scanning paths, providing also an appropriate capture of high temperature and marked thermal gradients in the vicinity of moving heat sources following curved paths. The $\Gamma_{\text{IEFG}} - \mathcal{S}_{\text{IEFG}\rightarrow\text{FEM}}$ distance in this example has also been of 1.5 times the element size of the background mesh, and $\Gamma_{\text{IEFG}} - \mathcal{S}_{\text{rec}}$ separation was of one element size. Therefore, the distances criteria established in this work also hold for curved scanning paths.

E.3.2.3. S-type scanning path

The thin steel plate is now subjected to a moving heat source following the S-type path depicted in Fig. E.16, and the materials properties and process parameters are still the same of Table E.1. Additionally heat losses due to convection and radiation are considered over the entire plate surface, also depicted in Fig. E.16.

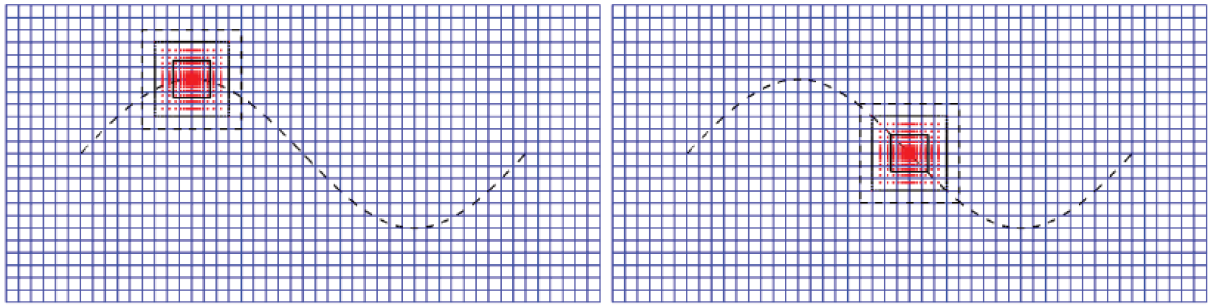

(a) P_1 (b) P_2

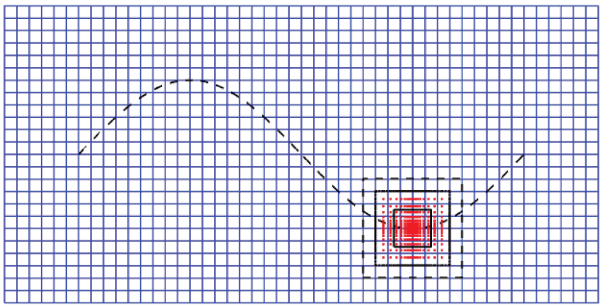

(c) P_3

Figura E.12: Patch nodes (red) and background mesh used to solve the transient heat conduction problem over the rectangular thin plate with the moving heat source following a sinusoidal scanning path.

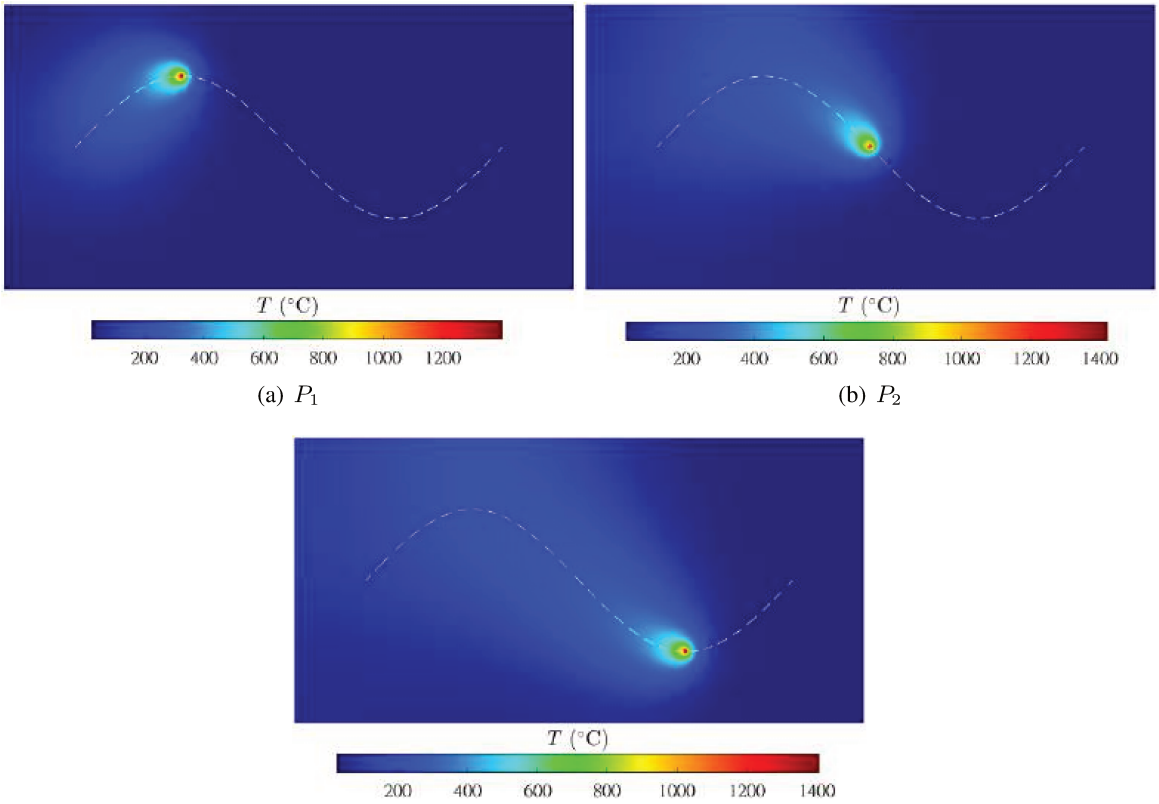

(a) P_1 (b) P_2

(c) P_3

Figura E.13: Temperature distributions computed via the proposed Ov-IEFG-FEM, with the patch nodes following the sinusoidal scanning path of the moving heat source.

The convective heat transfer coefficient is set to $h_{\text{conv}} = 10^{-5}$ W.mm^{-2}K^{-1}, the Stefan-Boltzmann constant is $\sigma = 5.67 \times 10^{-14}$ W.mm^{-2}K^{-4}, and the steel emissivity is $\varepsilon = 0.8$. The background mesh and patch nodes configuration at different times for the S-Type scanning path are depicted in Fig. E.17(a)-(c), and the corresponding temperature distributions are given in Fig. E.18(a)-(c).

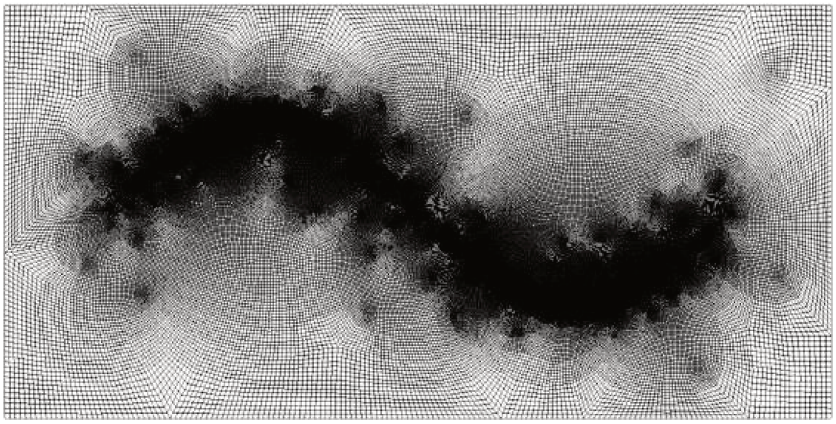

Figura E.14: Fine mesh for the FEM-based solution of the transient heat conduction problem over the rectangular thin plate with a moving heat source following a sinusoidal path. The mesh is very refined along the scanning path.

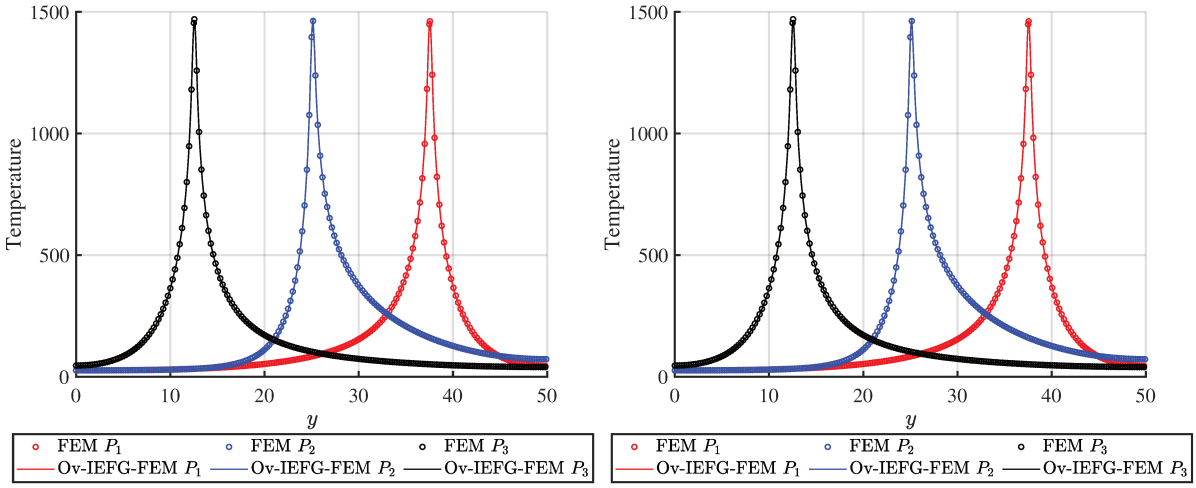

(a) Horizontal temperature profiles

(b) Vertical temperature profiles

Figura E.15: Temperature profiles computed along the horizontal and vertical axes passing over the current heat source position, comparison between the results computed via the proposed Ov-IEFG-FEM and a very fine FEM-based solution.

The results are depicted for the heat source at positions $P_1 = (x_1, y_1) = (0, 25)$, $P_2 = (x_2, y_2) = (50, 25)$, $P_3 = (x_3, y_3) = (100, 25)$, which correspond to times $t_1 = 12.5$ s, $t_2 = 1262.5$ s and $t_3 = 2512.5$ s, respectively.

The patch domain Ω_{IEFG} is represented with $29 \times 29 = 841$ nodes clustered towards the heat source centre, whereas the domain has been discretised with an uniform background mesh of $48 \times 24 = 1152$ elements (1,225 nodes). Accordingly, the smooth and stable capture of marked thermal gradients depicted in Fig. E.18(a)-(c) near the moving heat source has been achieved with only $841 + 1,225 = 2,066$ nodes. These results demonstrate the feasibility of using the Ov-IEFG-FEM to accurately capture the re-heating effects induced by re-scanning with moving heat sources along S-type paths, also considering the influence of convective and radiative heat loss. These aspects are commonly encountered in processes like metal additive manufacturing.

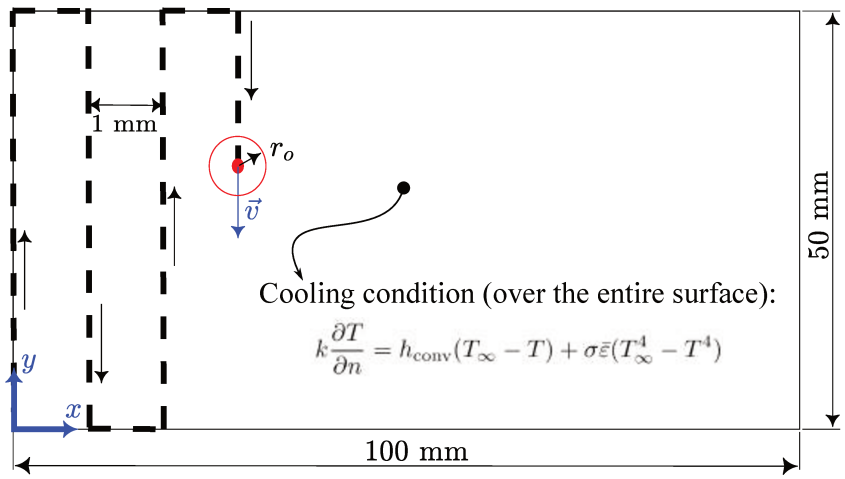

Figura E.16: Representation of the transient heat conduction problem over the rectangular thin plate with a moving heat source following a S-type path.

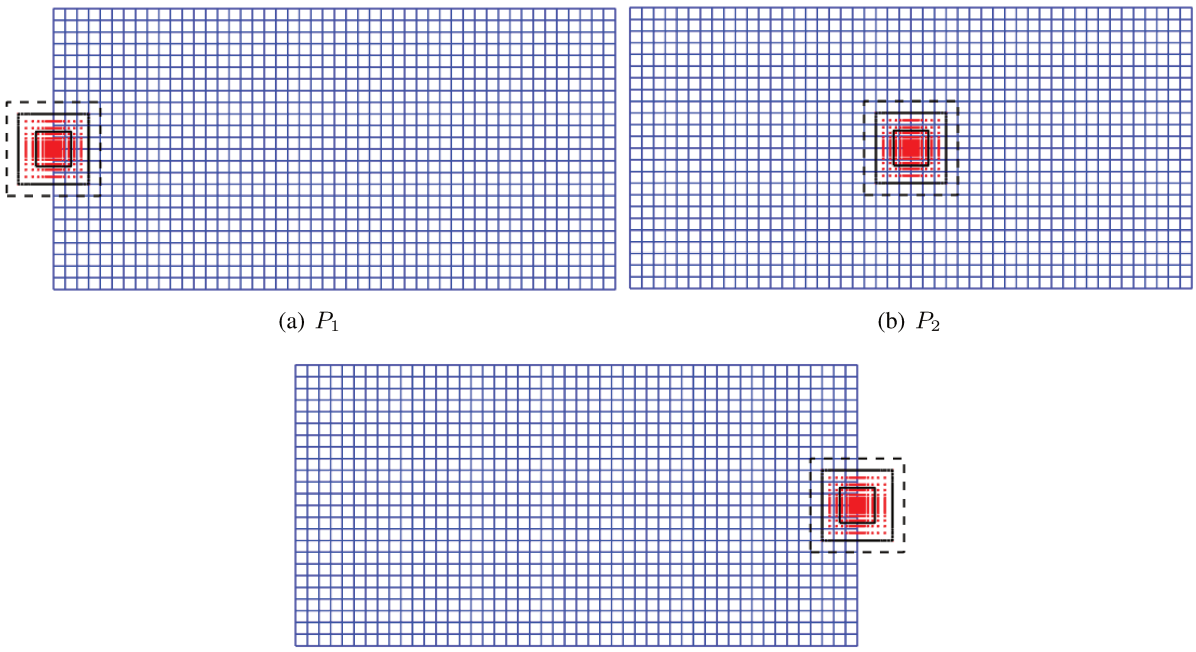

(a) P_1 (b) P_2

(c) P_3

Figura E.17: Patch nodes (red) and background mesh used to solve the transient heat conduction problem over the rectangular thin plate with the moving heat source following a S-type scanning path.

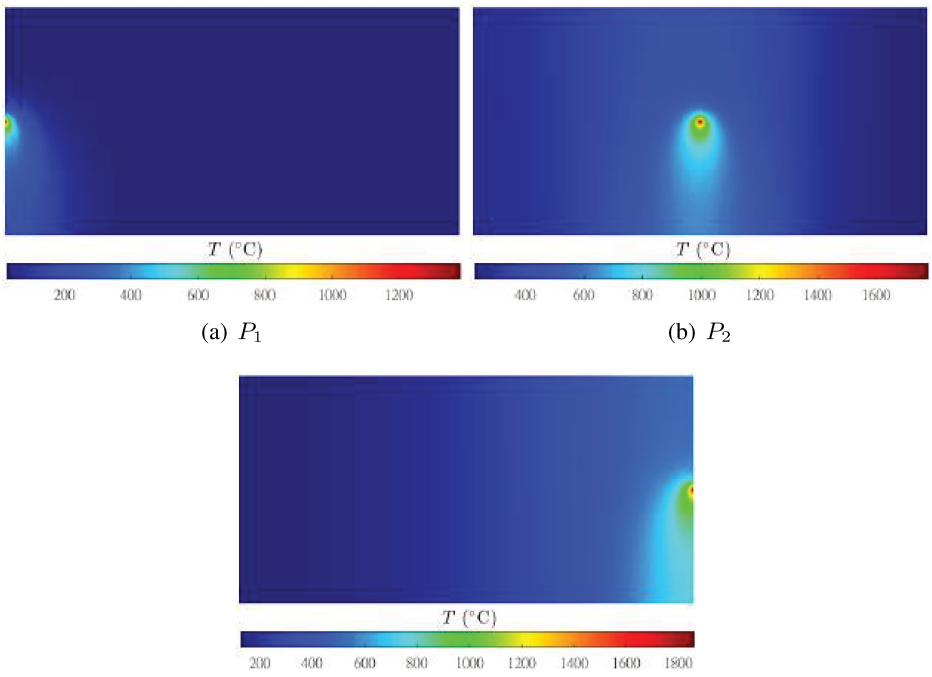

(a) P_1 (b) P_2

(c) P_3

Figura E.18: Temperature distributions computed via the proposed Ov-IEFG-FEM, with the patch nodes following the S-type scanning path of the moving heat source.

Since the scanning path virtually covers the entire plate, the stable solution of this problem via the FEM has required a uniform mesh of $300 \times 150 = 45,000$ elements (45,451 nodes). The results are compared to the proposed Ov-IEFG-FEM-based solution in Fig. E.19(a)-(c), exhibiting an excellent matching between both approaches.

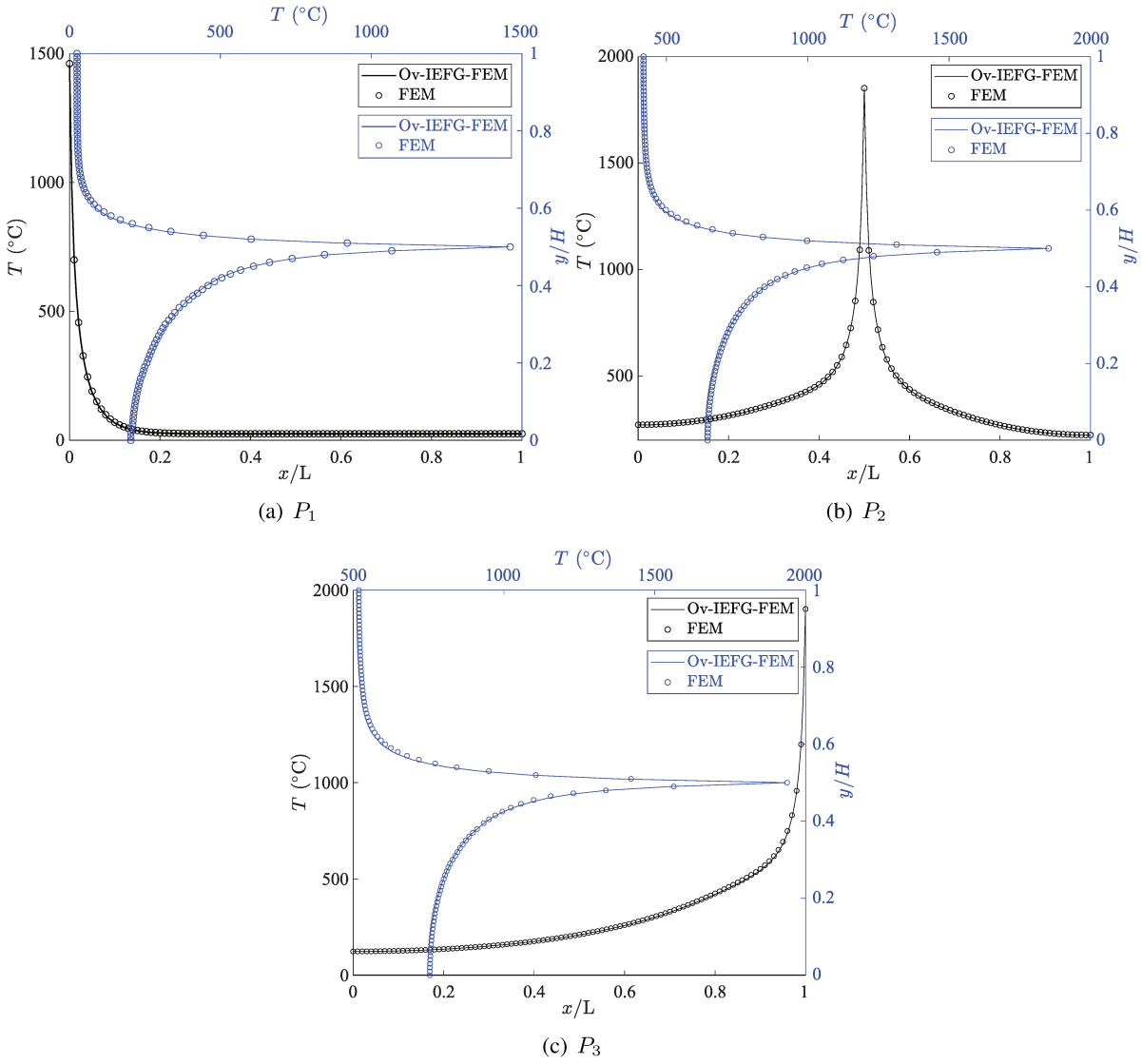

(a) P_1 (b) P_2

(c) P_3

Figura E.19: Temperature profiles computed along the horizontal (black) and vertical (blue) axes passing over the current heat source position, comparison between the results computed via the proposed Ov-IEFG-FEM and a very fine FEM-based solution.

E.3.2.4. Applied three-dimensional problem with curved geometries, phase change effects and temperature dependent properties

The proposed Ov-IEFG-FEM will be now used in the thermal modelling a moving heat source following a curved path over a circumferential arc-shaped part made of AlSi10Mg alloy, with the geometric features depicted in Fig. E.20(a).

This thermal problem also includes non-linear aspects concerning temperature-dependent material properties and phase change effects, aligned with the parameters and material properties given in Table

E.3.

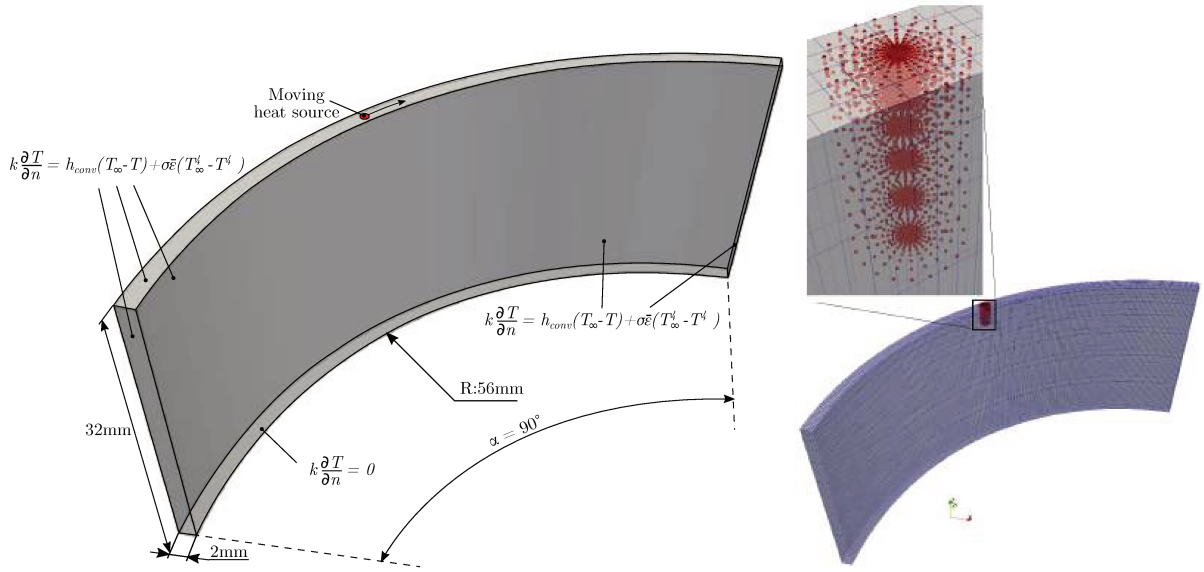

(a) Part geometry and boundary conditions

(b) Detail on the discretisation of Ω_{FEM} and representation of Ω_{IEFG}

Figura E.20: Configuration and boundary conditions of the three-dimensional problem with curved geometry and temperature-dependent material properties, and detail of the arc-shaped part discretisation via FEM and representation of the region near the moving heat source with the overlapping patch nodes for IEFG computations.

The problem has been solved using the background mesh and patch nodes depicted in Fig. E.20(b), with the patch nodes performing a purely translational rigid body motion aligned with the moving heat source. The background mesh discretising the arc-shaped part consists of 8,800 trilinear hexahedral elements (11,934 nodes), whereas the patch domain Ω_{IEFG} is represented with only 1,755 nodes clustered towards the vertical axis passing through the moving heat source centre. The process parameters listed in Table E.3 align with those commonly used in direct metal laser sintering (DMLS) with AlSi10Mg alloys [271], which provides a valuable context to assess the Ov-IEFG-FEM potential in the thermal modelling of metal additive manufacturing processes.

The time step Δt to solve the transient problem has been setted considering a laser spot radius of 0.1 mm, i.e. $\Delta t = (0.1\text{ mm})/(v_s) = (0.1\text{ mm})/(200\text{ mm/s}) = 5 \times 10^{-4}$ s. The nodes representing Ω_{IEFG} have an average spacing near the heat source of approximately 0.036 mm, which is three times smaller than the heat source effective radius to ensure its proper capture. The time step is also small enough to solve the transient problem in Ω_{FEM} under a fully explicit forward difference scheme, significantly saving computing times. Assessing the thermal properties at an average temperature of 900 K (based on the results reported in Figs. E.21-E.22), the Fourier number in Ω_{FEM} is $Fo = k\Delta t \times (2\rho\, Cp \Delta l^2)^{-1} \approxeq 0.1$ ensuring stability under the explicit time integration scheme. The value of $\Delta l = 0.4$ mm is the effective length of the smallest element discretising Ω_{FEM}. The time integration in Ω_{IEFG} is performed under a fully implicit backward finite difference scheme, and now the iterative process is performed until convergence is reached in both the restrictions (E.3)-(E.4) and the temperature-dependent non-linearities.

During phase change, the material properties in the mushy zone are computed via a linear mixing rule based on the solid phase fraction $f_s(T)$:

Tabla E.3: Parameters and material properties for transient heat conduction in AlSi10Mg alloy arc-shaped part with a moving heat source following a curved path.

Problem parameters	Values
Initial Temperature T_0 (K)	300
Velocity magnitude of the moving heat source (mm/s)	200
Heat source total power $\dot{Q}_T$ (W)	70
Heat source effective radius r_o (mm)	0.1
Material properties	**Values**
Conductivity of solid phase k_s (W.mm^{-1}.K^{-1})	$\left[\frac{(138-150)(T(\mathrm{K})-830)}{830-300}+138\right]\times 10^{-3}$
Conductivity of liquid phase k_l (W.mm^{-1}.K^{-1})	$\left[\frac{(84-79)(T(\mathrm{K})-870)}{1122-870}+79\right]\times 10^{-3}$
Specific heat capacity of solid phase C_{ps} (J.kg^{-1}.K^{-1})	$\frac{(1123-870)(T(\mathrm{K})-830)}{830-300}+870$
Specific heat capacity of liquid phase C_{pl} (J.kg^{-1}.K^{-1})	$\frac{(1737-1186)(T(\mathrm{K})-870)}{1114-870}+1186$
Density of solid phase ρ_s (kg.mm^{-3})	$\left[\frac{(2620-2720)(T(\mathrm{K})-830)}{830-300}+2620\right]\times 10^{-9}$
Density of liquid phase ρ_l (kg.mm^{-3})	$\left[\frac{(2420-2500)(T(\mathrm{K})-870)}{1114-870}+2420\right]\times 10^{-9}$
Solidus temperature T_{sol} (K)	830
Liquidus temperature T_{liq} (K)	870
Fusion specific latent heat ΔH_f (J.kg^{-1})	423000
Laser power absorptivity η	0.95
Thermal emissivity ε	0.8

$$
\begin{aligned}
k &= k_s(T)f_s(T) + [1 - f_s(T)]k_l(T),\\
Cp &= Cp_s(T)f_s(T) + [1 - f_s(T)]Cp_l(T),\\
\rho &= \rho_s(T)f_s(T) + [1 - f_s(T)]\rho_l(T),
\end{aligned}
\tag{E.26}
$$

and the solid phase fraction is given by the following simple piecewise function:

$$
f_s(T) = \begin{cases} 1 & T < T_{sol} \\ \frac{T_{liq}-T}{T_{liq}-T_{sol}} & T_{sol} \le T \le T_{liq} \\ 0 & T > T_{liq}. \end{cases}
\tag{E.27}
$$

The effect of latent heat releasing during phase change is included via the effective specific heat technique[227, 229, 272]:

$$
Cp_{eff} = Cp - \Delta H_f \frac{df_s}{dT}.
\tag{E.28}
$$

The moving heat source is given by a surface heat flux with the following Gaussian distribution:

$$
k\frac{\partial T}{\partial n} = \frac{2\eta\dot{Q}_T}{\pi r_0^2} e^{-2r^2/r_0^2}
\tag{E.29}
$$

The temperature distributions obtained at different time steps are presented in Fig. E.21(a)-(c) for the outer surface of the part and in Fig. E.22 for axial slices passing through the heat source position. These results demonstrate the ability of the proposed Ov-IEFG-FEM to accurately compute temperature distri-

butions, even in the vicinity of the heat source. The smooth and stable temperature profiles near the heat source indicate a seamless coupling at Γ_{IEFG}. These findings highlight the robustness of the Ov-IEFG-FEM, which remains effective in handling complex problems involving material non-linearities, curved three-dimensional geometries, and realistic process parameters typically encountered in laser powder bed fusion processes like DMLS. Furthermore, it is noteworthy that the smooth and stable temperature distributions presented in Figs. E.21-E.22 were obtained using a relatively small number of nodes, specifically 11,934 for the entire part and 1,755 for the thermally affected zone near the moving heat source. This demonstrates the computational efficiency of the Ov-IEFG-FEM, even when dealing with significant differences in scales between the entire part and the localised region influenced by the moving heat source.

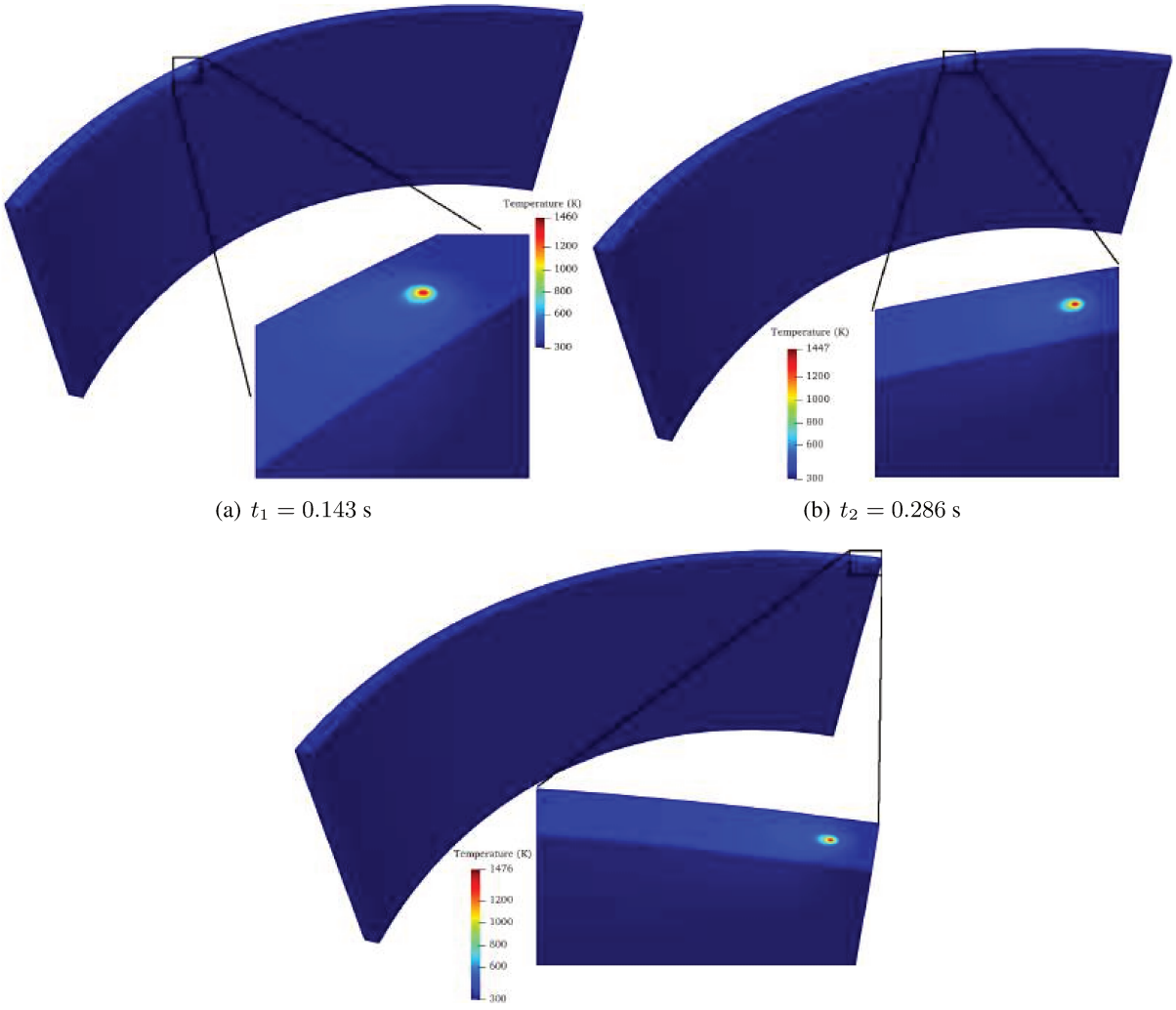

(a) $t_1 = 0.143$ s

(b) $t_2 = 0.286$ s

(c) $t_3 = 0.429$ s

Figura E.21: Temperature distributions computed via the proposed Ov-IEFG-FEM, in the non-linear applied three-dimensional problem with curved geometry.

The smooth temperature profiles and solidus-liquidus isotherms contours depicted in Fig. E.22 also demonstrate the suitability of the proposed Ov-IEFG-FEM approach to provide an accurate and stable capture of the phase change region (mushy zone) in the domain bulk, below the current position of the moving heat source. The temperature profiles computed along the arc length s covered by the moving heat source path are depicted in Fig. E.23, exhibiting a stable capture of very high temperatures and

marked thermal gradients near a very concentrated heat source moving with high speed. These results also exhibit a seamless temperature coupling on Γ_{IEFG}, demonstrating the noteworthy potential of the Ov-IEFG-FEM to address problems involving more complex and realistic geometries and temperature-dependent non-linearities. It is important to note that these results were computed using a single i7-7500U 2.90 GHz processor (i7 is a trademark of Intel Corporation, Santa Clara, C. A., USA) running on the WINDOWS10 Home Basic operating system (WINDOWS is a trademark of Microsoft Corporation, Redmond, C. A., USA) with 12 GB of RAM.

Despite the modest computational resources, the proposed Ov-IEFG-FEM proved to be computationally efficient in solving this complex large-scale problem. The solution of the heat conduction problem at each time step using the proposed Ov-IEFG-FEM has taken approximately 0.6 seconds on average, as a consequence of both restricting the higher-order approximations of the IEFG formulation to the non-linearities induced in the zone thermally affected by the moving heat source and using an explicit time integration scheme in Ω_{FEM} to overcome the need for solving the equation systems of the FEM discretisation. In contrast, a standard FEM approach would require a highly refined mesh to accurately capture the behaviour of the moving heat source, making it impractical with the available computational capabilities. In fact, solving similar large-scale problems with the FEM often necessitates non-conforming octree-mesh refinements for efficient numerical results [273], but this technique is beyond the scopes of this communication.

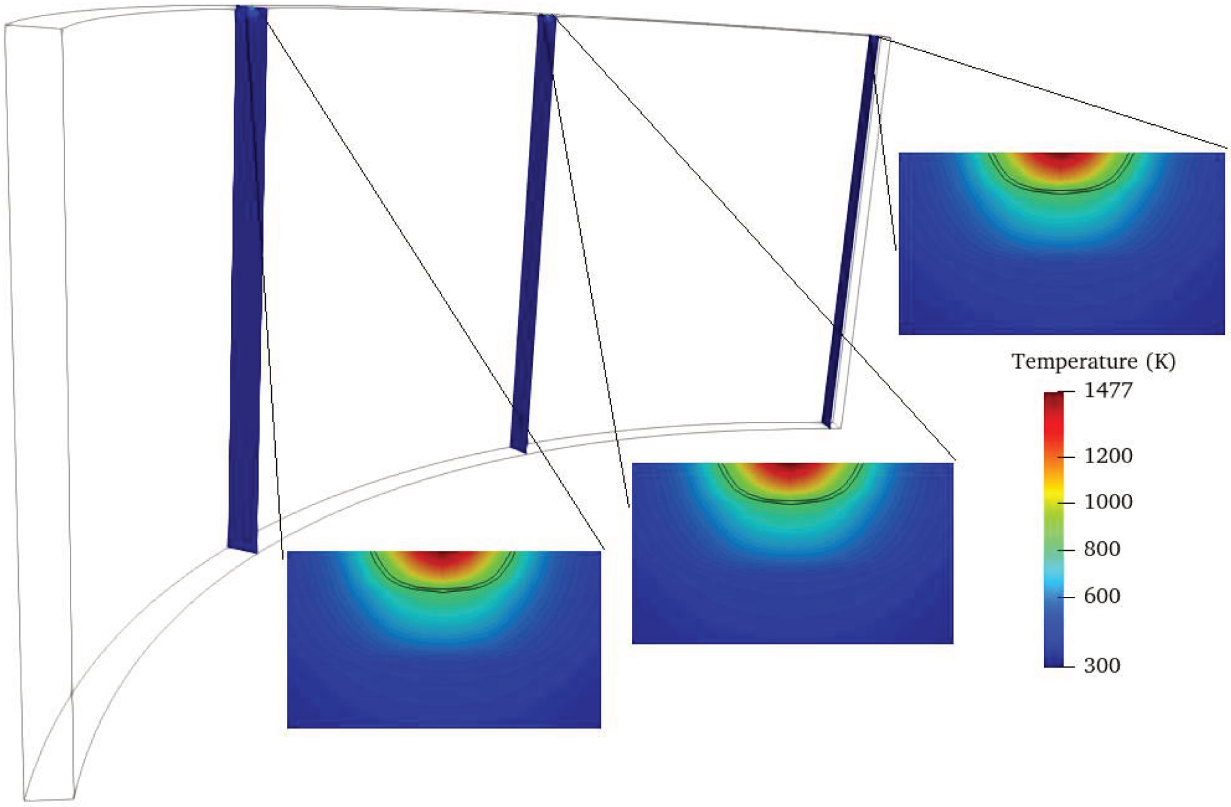

Figura E.22: Temperature distributions in axial slices located at the position occupied by the moving heat source at different times.

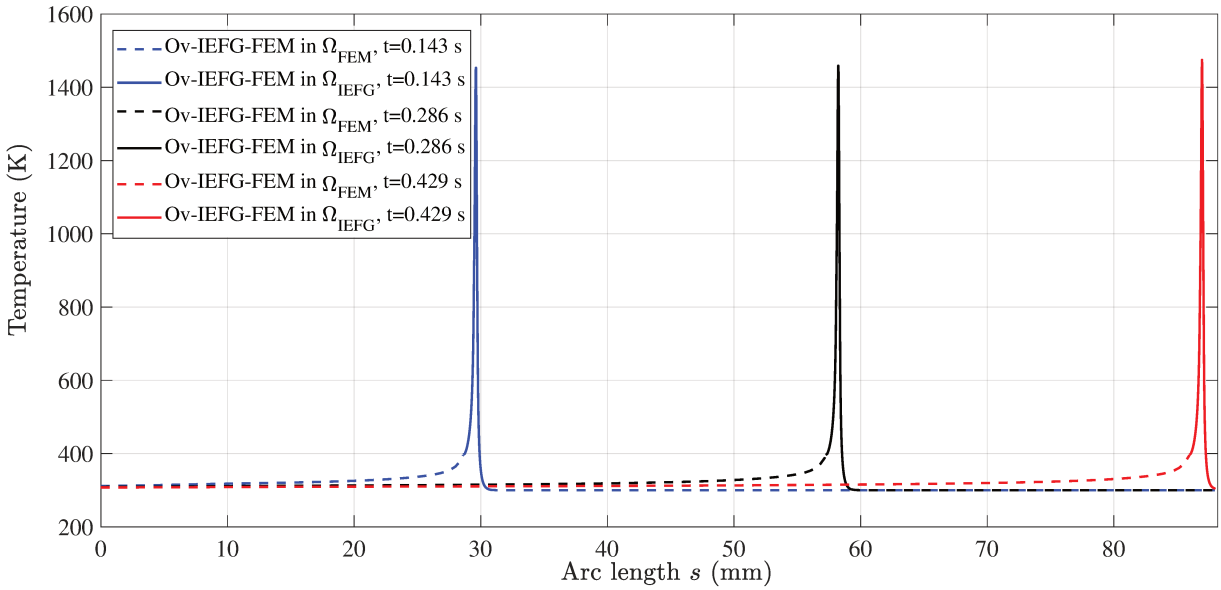

Figura E.23: Temperature profiles along the arc length s covered by the heat source path in the non-linear applied three-dimensional problem with curved geometry.

Thus, a direct comparison with a conventional FEM-based solution was not conducted for this specific large-scale problem, in contrast to the previous two-dimensional benchmark cases. However, it remains imperative to evaluate the Ov-IEFG-FEM accuracy in addressing the intricate challenges of 3-D non-linear heat conduction problems with moving heat sources. In order to facilitate a fair and meaningful comparison between the proposed Ov-IEFG-FEM and FEM-based solution, it is advisable to explore a similar 3-D problem of smaller dimensions while retaining the complexities associated with curved geometry, phase change effects, and temperature-dependent properties. The dimensions selected for the numerical validation are half of those depicted in the arc-shaped part of Fig. E.20(a), specifically reducing the height from 32 mm to 16 mm and the revolution angle from 90° to 45°. The process parameters and material properties remain the same as in Table E.3, with the only changes being made to the power and effective radius of the moving heat source. These parameters have been changed to $\dot{Q}_T = 60$ W and $r_0 = 0.1$ mm, such that the mesh depicted in Fig. E.24 suffices to provide an appropriate capture of the moving heat source effects in the FEM-based solution.

This mesh consists of 140,800 elements and 157,437 nodes, which are exponentially clustered towards the upper surface to provide an appropriate capture of the moving heat source effects. The background mesh discretising Ω_{FEM} in the Ov-IEFG-FEM-based computations has consisted of only 4,400 elements and 5,994 nodes, whereas Ω_{IEFG} is still represented with the distribution of 1,755 nodes depicted in Fig. E.20 (b). The solution of the non-linear problem under the standard FEM-based computations has taken approximately 100 seconds on average at each time step, whereas it has taken only 0.55 seconds under the Ov-IEFG-FEM. The computation time using the Ov-IEFG-FEM for this smaller-sized problem is only slightly less than that corresponding to the geometry in Fig. E.20, as the computation time is predominantly dominated by higher-order approximations of the IEFG-based solution of the thermal problem near the moving heat source.

The computation times of the Ov-IEFG-FEM have been dramatically lower compared to those of the standard FEM-based solution, mainly due to the reduced number of nodes (degrees of freedom) required under the proposed mesh-less/mesh-based hybrid approach. The temperature profiles computed under

both the Ov-IEFG-FEM and the FEM along the arc length s covered by the moving heat source are compared in Fig. E.25, and the results obtained exhibit an excellent agreement between both numerical solutions at different times.

This demonstrates that the proposed Ov-IEFG-FEM is also able to provide accuracy in addressing the intricate challenges of 3-D problems involving curved geometries and non-linearities concerning phase-change and temperature-dependent properties, in a computationally efficient manner.

E.4. Discussion

The results obtained using the proposed Ov-IEFG-FEM demonstrate its effectiveness in accurately solving transient heat conduction problems with moving heat sources. This novel approach combines the high-order approximations of the IEFG method within the region of interest, specifically near the heat source, with less computational expensive FEM-based computations using a coarse mesh outside this region for computational efficiency. This combination allows for a simplified and efficient solution, while maintaining numerical accuracy. The convergence analysis conducted in section E.3.1 under Rosenthal's formulation provides clear evidence of the effectiveness of the Ov-IEFG-FEM approach.

It outperforms both IEFG-based solutions and traditional FEM-based solutions in terms of convergence features. The Ov-IEFG-FEM achieves comparable convergence rates to pure IEFG-based solutions and offers higher accuracy compared to solutions based on both FEM and IEFG. This can be attributed to the fact that errors in the numerical solution of these problems are mainly governed by the high thermal gradients developed in the region affected by the moving heat source.

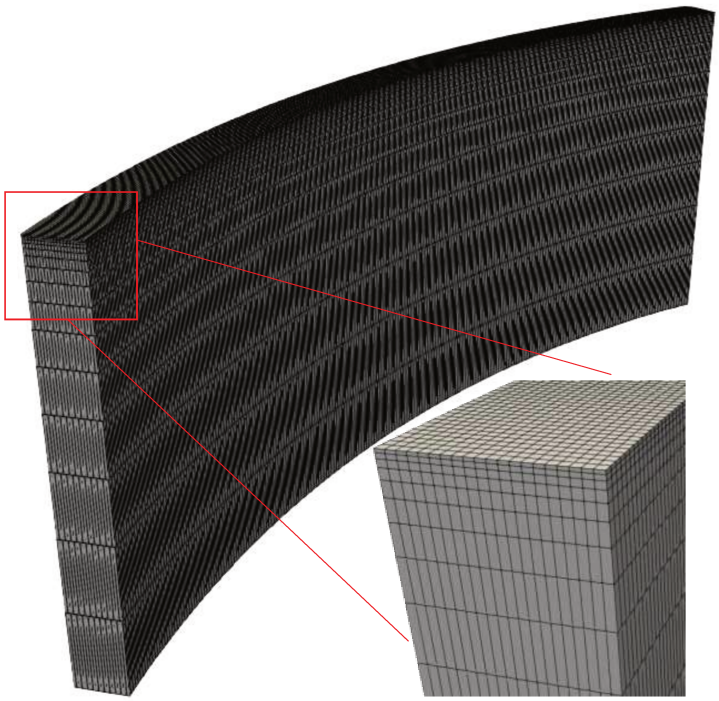

Figura E.24: Mesh used in the standard FEM-based solution of the 3-D problem of smaller dimensions, to be performed for numerical validation of the Ov-IEFG-FEM.

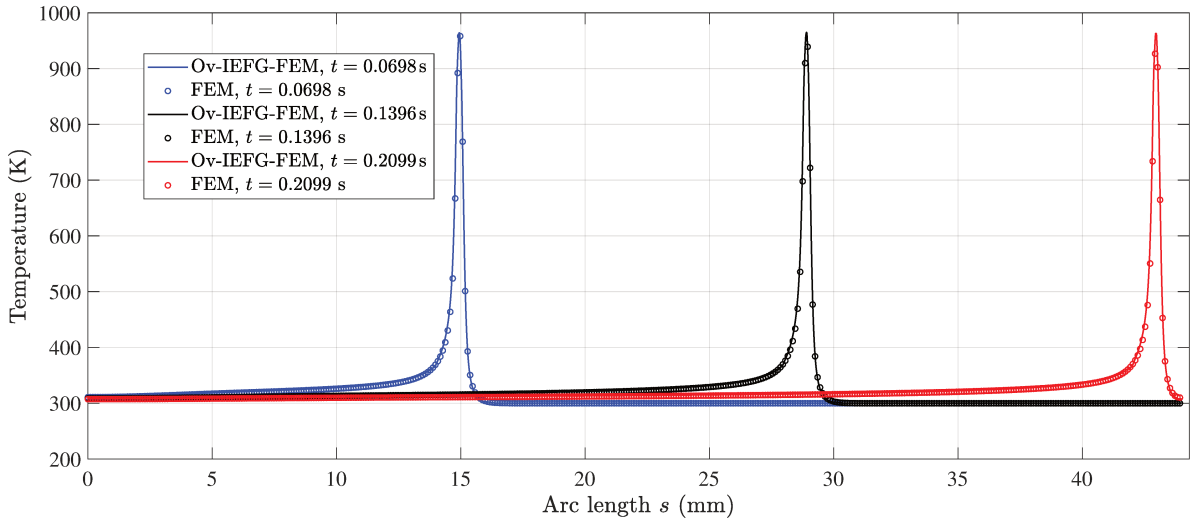

Figura E.25: Comparison of the temperature profile computed via the Ov-IEFG-FEM along the arc length s covered by the moving heat source, with those obtained from a standard FEM-based solution.

The Ov-IEFG-FEM approach allows for the implementation of the IEFG method and offers more flexibility in node refinement within this specific region. As a result, the Ov-IEFG-FEM exhibits convergence rates similar to solutions based solely on IEFG, even when the thermal problem throughout most of the computational domain is solved via FEM. The seamless coupling along Γ_{IEFG} is kept when the Ov-IEFG-FEM is used to actually track the moving heat source with the patch nodes representing the overlapping domain Ω_{IEFG}, resulting in excellent numerical accuracy and computational efficiency. The Ov-IEFG-FEM has successfully captured high temperatures and significant thermal gradients near the moving heat source, using significantly fewer nodal unknowns compared to FEM-based solutions, in all the 2-D benchmark cases involving straight, sinusoidal, and S-type scanning paths.

This aspect has been especially evident in the case of the moving heat source following a sinusoidal path, where the difference between the nodal unknowns required with the Ov-IEFG-FEM and the pure FEM-based solution has been remarkably significant. Fig. E.26 provides a better perspective on this, comparing the evolution in time of the temperature computed at the heat source position using the Ov-IEFG-FEM with the results achieved via the FEM. The plots clearly demonstrate that the solutions purely based on FEM required mesh refinement up to 167,537 nodes (results reported in section E.3.2.2) to achieve stability and accuracy levels comparable to the Ov-IEFG-FEM with only 2,066 nodes. On the other hand, FEM-based solutions with coarser meshes exhibited significant temperature fluctuations and lacked accuracy. The Ov-IEFG-FEM demonstrates remarkable stability, thanks to the rigid body motion of the patch nodes representing Ω_{IEFG}, which guarantees that the heat source remains centred at all times. This ensures a consistent capture of the energy released by the source at each time step.

Additionally, the higher order approximation provided by the IEFG formulation further enhances the accuracy within Ω_{IEFG}. In contrast, solutions purely based on FEM demand a highly refined mesh along the heat source path to achieve stability in capturing the released energy. The approach of aligning element faces in the refined region with the source path could potentially improve stability.

However, this becomes challenging for heat sources following complex trajectories, limiting the applicability of this method to cases with simple heat source paths and domain geometries. It is also worth to remark that the proposed Ov-IEFG-FEM is not only able to provide a seamless coupling in

temperature along Γ_{IEFG}, but also in heat flux. A seamless and continuous heat flux distribution can be computed for the entire domain as:

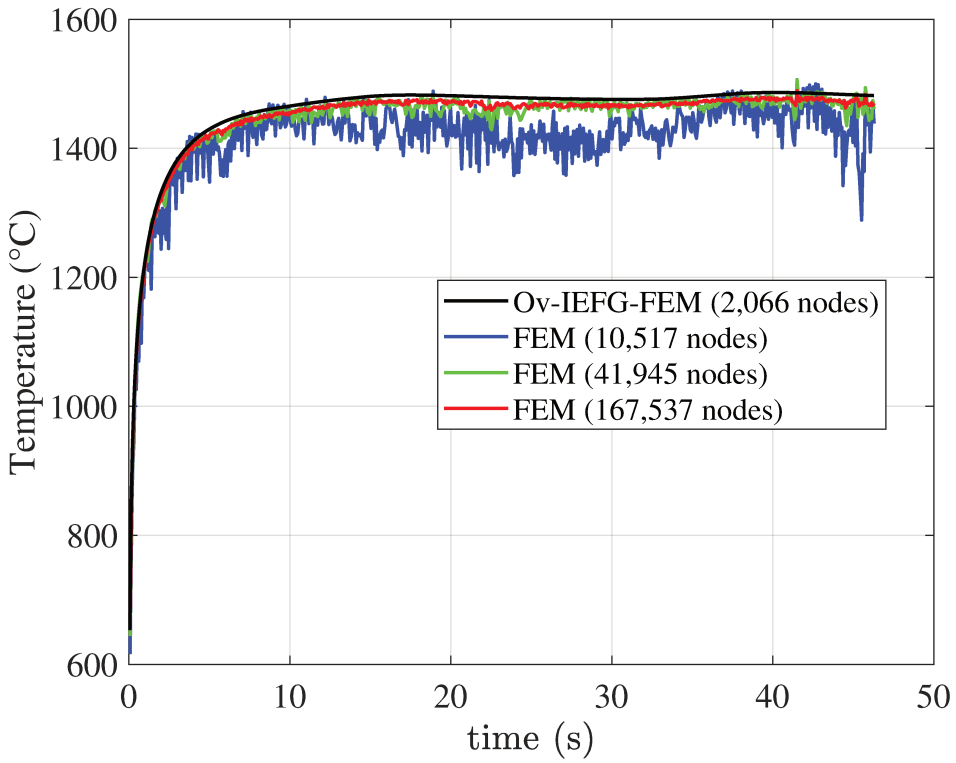

Figura E.26: Temperature at the position occupied by the moving heat source at different times for the 2-D benchmark problem of the moving heat source following a sinusoidal path.

$$\vec{q} = -k\nabla T = \begin{cases} -k \sum_{I=1}^{n_{\text{rec}}} \nabla \varphi_{\text{rec}}^{(I)}(\vec{x}) \hat{T}_{\text{rec}}^{(I)} & \text{in } \Omega_{\text{FEM}} - \Omega_{\text{IEFG}} \\ \\ -k \sum_{I=1}^{n_{\text{IEFG}}} \nabla \varphi_{\text{IEFG}}^{(I)}(\vec{x}) \hat{T}_{\text{IEFG}}^{(I)} & \text{in } \Omega_{\text{IEFG}} \end{cases} , . \tag{E.30}$$

For such a heat flux computation, the IMLS approximations $\varphi_{\text{rec}}^{(I)}$ and nodal parameters $\hat{T}_{\text{rec}}^{(I)}$ are now computed from a global reconstruction of the FEM-based solution in the coarse background mesh, i.e. $\Omega_{\text{rec}} = \Omega_{\text{FEM}}$ and $n_{\text{rec}} = n_{\text{FEM}}$. For the moving heat source following the sinusoidal path, the implementation of (E.30) allows the achievement of the smooth heatlines depicted in Fig. E.27. These results demonstrate the Ov-IEFG-FEM noteworthy potential for straightforwardly constructing enriched temperature and heat flux distributions through a simple IMLS-based coupling between the solutions computed in Ω_{FEM} and Ω_{IEFG}, in a remarkably simple manner. This sets it apart from overset techniques developed within the context of mesh-based methods, where the discontinuous element-wise or cell-wise approximations of spatial derivatives hinder a continuous coupling between the heat fluxes computed in the patch and background meshes or grids. Typically, this issue is addressed by creating a final global enriched solution over a single mesh or grid reconstructed from the patch and background meshes or grids, involving the substitution of overlapping regions with non-structured grids. The reconstructed mesh or grid retains the nodal values of the non-substituted elements or cells, and the enriched heat flux field is computed by performing temperature derivatives over this single mesh [148, 203, 262].

The rigid body motion of the overlapping nodes representing Ω_{IEFG} in the proposed Ov-IEFG-FEM allows them to precisely track the path of the moving heat source. This innovative approach serves two crucial purposes. Firstly, it eliminates the need for time-consuming procedures involved in searching for neighbouring nodes and constructing IMLS approximations, as these tasks are performed just once. Secondly, it optimises the use of more accurate and computationally expensive IEFG approximations, limiting their application to the immediate vicinity of the moving heat source.

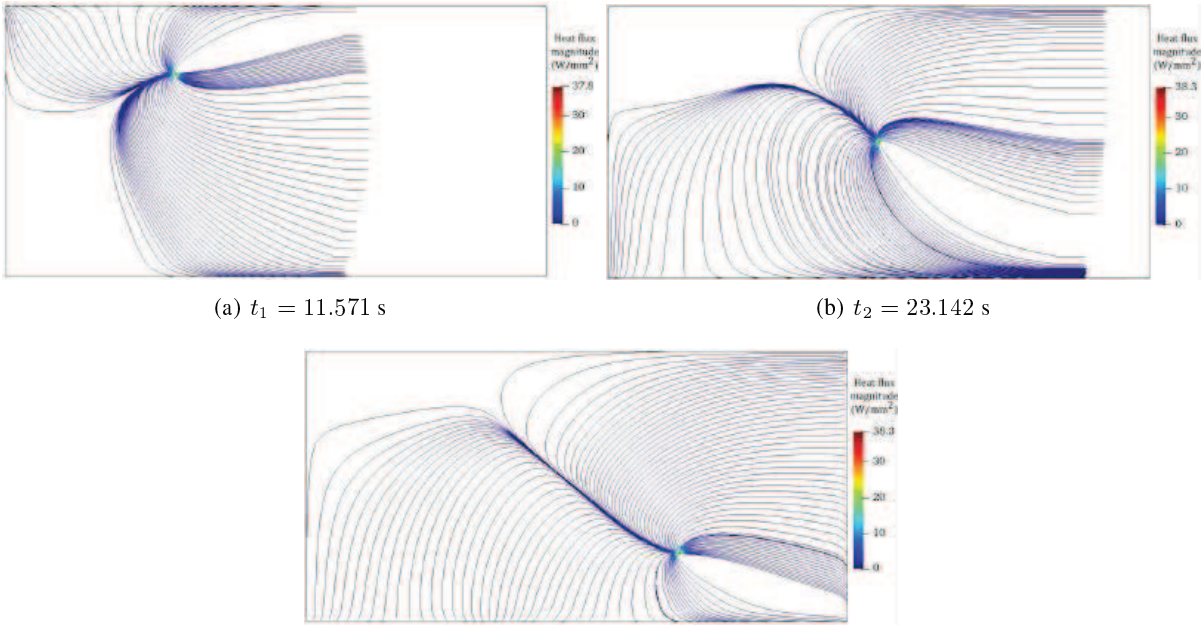

(a) $t_1 = 11.571$ s (b) $t_2 = 23.142$ s

(c) $t_3 = 34.713$ s

Figura E.27: Heatlines achieved via the computation of a continuous heat flux field under the proposed Ov-IEFG-FEM.

Consequently, this method efficiently achieves an enriched numerical solution by combining accuracy with computational efficiency. The significance of such features for real applications has been demonstrated in the computing times involved in the three-dimensional non-linear problem solved in section 3.2.4, where the process parameters and domain size align with those commonly involved in the DMLS of AlSi10Mg alloys. This approach enables higher-order approximations in the region of interest, specifically in the vicinity of the moving heat source, represented by only 1,755 nodes defining Ω_{IEFG}. Meanwhile, the explicit time integration used in the coarse mesh Ω_{FEM} is enough to fulfil the low accuracy requirements away from the thermally affected zone.

E.4.1. Stabilisation of the advection-diffusion problem within the Ov-IEFG-FEM framework

The specific features of the Ov-IEFG-FEM procedure proposed in this communication always demand the computation of an advective transport term over the fine arrangement of patch nodes, and additionally over the background mesh if the heat transfer problem is addressed using the Rosenthal's approach. It is well-known that solving advection-diffusion problems under a standard Bunov-Galerkin formulation is prone to stability issues for computational Péclet numbers ($Pe = 1/2\,\rho\, c_p u \Delta l/k$) greater than one, which is an aspect that can be addressed using stabilisation techniques [274]. While the problems solved in this communication have not yet encountered heat sources moving at velocities high

enough to result in $Pe > 1$, it can be demonstrated that the proposed Ov-IEFG-FEM framework allows for the use of streamline upwind techniques to ensure stability in scenarios where advection dominates the internal energy balance given by (E.1). For this purpose, the transient heat conduction in the rectangular plate subjected to a moving heat source following a horizontal straight path will be re-explored, with the moving heat source now being set at a velocity of magnitude $u = 100$ mm/s and total power $\dot{Q}_T = 80\pi$ W. The background mesh and arrangement of moving patch nodes are the same of Fig. E.7, and the thermal properties are still those reported in Table E.1. The computational Péclet number is computed considering the largest spacing between neighbouring nodes in the moving patch arrangement $\Delta l_{max} = 1.077$ mm, whereby $Pe = 9.365$ for the IEFG computations in Ω_{IEFG}. This value of Péclet notably exceeds the unit limit, which explains the spurious oscillations of the results reported depicted in Fig. E.28 for the solution performed under a standard Bunov-Galerkin formulation.

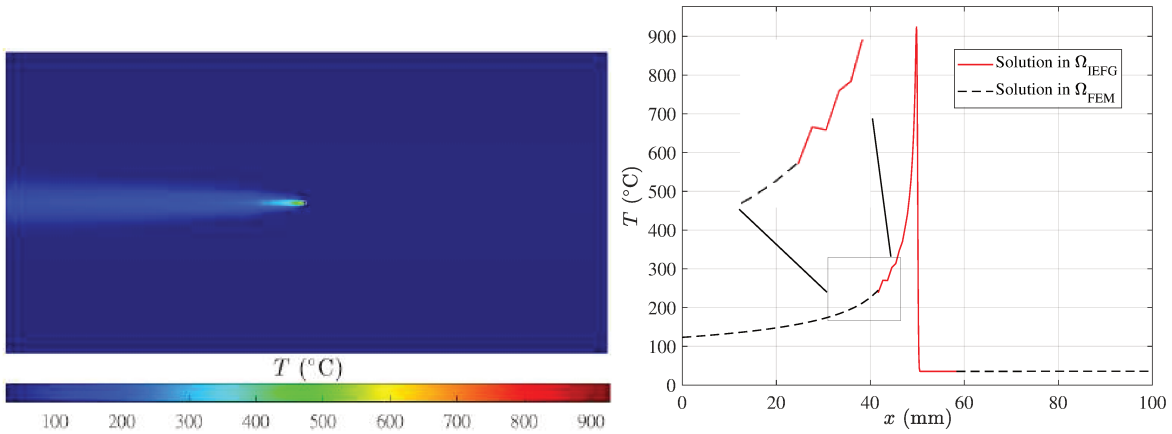

(a) Temperature distribution

(b) Temperature profile along the horizontal scanning path

Figura E.28: Unstable results obtained via the Ov-IEFG-FEM with advection dominating the heat transfer problem in the moving domain Ω_{IEFG}, when it is solved under a standard Bunov-Galerkin formulation. These results correspond to $t = 0.5$ s.

This issue can be overcome using a streamline-upwind Petrov-Galerkin (SUPG) stabilised formulation to solve the heat transfer problem over the moving arrangement of patch nodes representing Ω_{IEFG}, which implies the following modifications in $C^{(IJ)}_{\text{IEFG}}$, $A^{(IJ)}_{\text{IEFG}}$ and $F^{(I)}_{\text{IEFG}(\dot{Q})}$:

$$\begin{aligned} C^{(IJ)}_{\text{IEFG}} &= \int \left(\varphi^{(I)}_{\text{IEFG}} + \tau_{\text{SUPG}}\, \vec{v}\cdot\nabla\varphi^{(I)}_{\text{IEFG}}\right) \rho\, C_p \varphi^{(J)}_{\text{IEFG}}\, \mathrm{d}\Omega, \\ A^{(IJ)}_{\text{IEFG}} &= \int \left(\varphi^{(I)}_{\text{IEFG}} + \tau_{\text{SUPG}}\, \vec{v}\cdot\nabla\varphi^{(I)}_{\text{IEFG}}\right) \rho\, C_p \vec{v}\cdot\nabla\varphi^{(J)}_{\text{IEFG}}\, \mathrm{d}\Omega, \\ F^{(I)}_{\text{IEFG}(\dot{Q})} &= \int \left(\varphi^{(I)}_{\text{IEFG}} + \tau_{\text{SUPG}}\, \vec{v}\cdot\nabla\varphi^{(I)}_{\text{IEFG}}\right) \dot{Q}\, \mathrm{d}\Omega, \end{aligned} \tag{E.31}$$

where the stabilisation parameter τ_{SUPG} is computed according to[251]:

$$\tau_{\text{SUPG}} = \left(\frac{1}{\tau_1^2} + \frac{1}{\tau_2^2} + \frac{1}{\tau_3^2}\right)^{-1/2}, \tag{E.32}$$

with:

$$\tau_1 = \frac{h_{\text{loc}}}{2||\vec{v}||}, \qquad \tau_2 = \mathrm{d}t, \qquad \tau_3 = \frac{\rho c_p h_{\text{loc}}^2}{12\, k}, \tag{E.33}$$

and the local length scale h_{loc} defined as:

$$h_{\text{loc}} = 2||\vec{v}|| \left(\sum_{I=1}^{n} \left| \vec{v} \cdot \nabla \varphi_{\text{IEFG}}^{(I)} \right| \right)^{-1} \tag{E.34}$$

The possibility of extending the SUPG stabilised formulation to the IEFG framework has already been demonstrated in previous communications [228, 251]. It has also been proven that the utilisation of IMLS approximations resembling the piecewise linear behaviour of shape functions used in standard FEM-based solutions allows the suppression of terms involving second-order derivatives that would otherwise manifest in a full SUPG weak formulation [228, 251, 252]. This can be achieved using nodal influence domains with support sizes $d_m = d_{\text{max}} \times \Delta l$ resembling the spacing between neighbouring nodes, where d_{max} is the support multiplier. Setting the support multiplier to $d_{\text{max}} = 1.15$ is enough for such a purpose [228, 251], and solving the current problem under these stabilising guidelines has given rise to the smooth and stable results depicted in Fig. E.29.

These outcomes demonstrate the possibility of using the proposed Ov-IEFG-FEM in a SUPG framework, in problems markedly dominated by advection that demand stabilisation techniques.

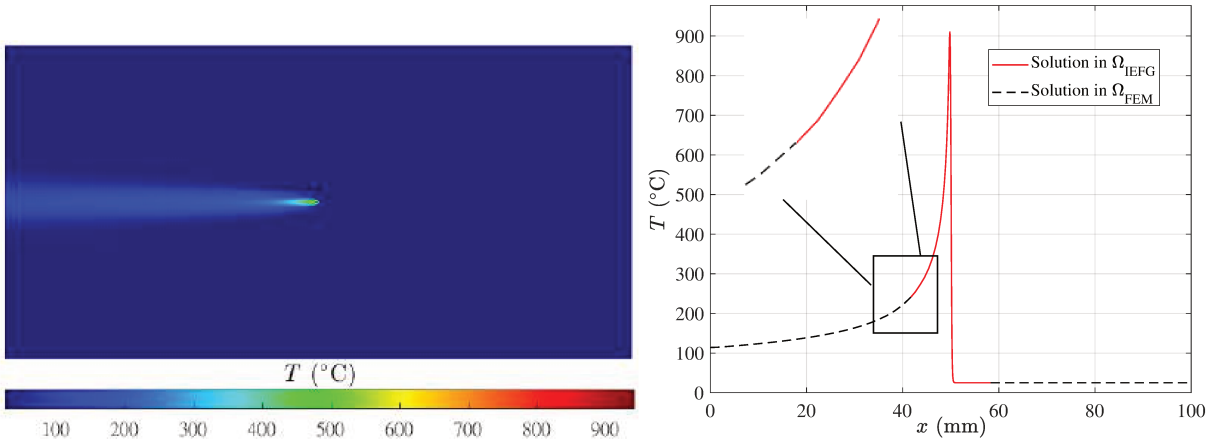

(a) Temperature distribution

(b) Temperature profile along the horizontal scanning path

Figura E.29: Stable results obtained via the Ov-IEFG-FEM with advection dominating the heat transfer problem in the moving domain Ω_{IEFG}, when it is solved under the SUPG stabilised formulation.

E.4.2. Relaxed coupling to improve computational efficiency

An additional approach to enhance the computational efficiency of the proposed Ov-IEFG-FEM is introduced in this section. It is based on the observation that the temperature distribution computed in Ω_{IEFG} shows negligible variations between successive time steps. This characteristic is evident in the results depicted in Fig. E.23, where the temperature profile computed in Ω_{IEFG} virtually retains its shape while occupying different positions corresponding to the motion of the heat source. The relaxed coupling approach to be introduced in this communication makes use of such a feature to relax the full solution of the temperature profile in Ω_{IEFG} at every time step, which is instead moved with the heat source and used to solve the thermal problem only in Ω_{FEM}.

On the other hand, the full coupling described in the pseudo code of Section E.2.2 is performed to update the solution in Ω_{IEFG} only every m_r relaxed time steps. The finite number m_r of relaxed time steps is prescribed to achieve computational efficiency without significantly compromising accuracy. A comparison between the computing times achieved under the fully coupled Ov-IEFG-FEM and the relaxed Ov-IEFG-FEM with $m_r = 10$ is given in Fig. E.30(a), whereas a comparison between the solutions achieved under both approaches is depicted in Fig. E.30(b). These results demonstrate that performing the relaxed coupling has allowed to reduce the computing times by a factor of almost 30 ($546.2/19.31 = 28.28$) for the entire transient analysis, which is expected considering that the transfer of information and solution of the thermal problem only in Ω_{FEM} have taken about only 0.01 s at

each relaxed time step.

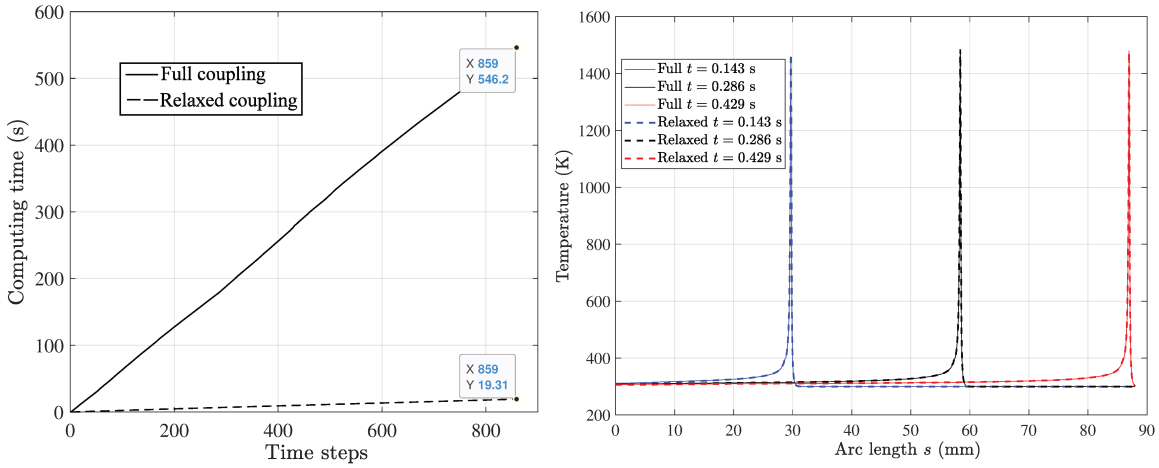

(a) Part geometry and boundary conditions

(b) Detail on the discretisation of Ω_{FEM} and representation of Ω_{IEFG}

Figura E.30: Comparison between the computing times and temperature profiles achieved under the fully coupled and relaxed Ov-IEFG-FEM.

Furthermore, the temperature profiles achieved under both the fully and relaxed coupled approaches are virtually indistinguishable each other, and the quantitative mismatching is below 1 %. This outcome demonstrate the noteworthy potential of the relaxed coupling approach to enhance computational efficiency without compromising numerical accuracy. Another significant aspect depicted in Fig. E.30(a) is that the factor of computing times reduction increases with the time scale of the problem, which is a very positive feature for the very large time scales usually involved in applied transient heat transfer problems with moving heat sources (welding, additive manufacturing, grinding).

E.5. Conclusions

An overset improved element-free Galerkin–finite element method has been developed to efficiently and accurately solve transient heat conduction problems involving moving heat sources. The iterative procedure proposed for coupling the temperature fields computed in both the background finite element mesh and the patch nodes facilitates seamless coupling in both 2-D and 3-D complex problems, even with marked non-linearities common in real applications. Comparisons have shown that the proposed technique outperforms solutions solely based on either the finite element method or the improved element-free Galerkin method. One of the notable advantages of this approach is the significant reduction of nodal unknowns, leading to reduced computing times compared to standard numerical techniques using fixed meshes or nodes. The fine distribution of patch nodes performing a rigid body motion, eliminates the need to define nodal influence domains, conform integration points, and search for support domain nodes at each integration point between successive node configurations, which are cumbersome and computationally demanding procedures often required in mesh-less solutions that use adaptive node refinement techniques. The successful implementation of the overset improved element-free Galerkin–finite element method in a 3-D non-linear problem with curved geometry and process parameters typically used in direct metal laser sintering of AlSi10Mg alloys demonstrates its potential for further applications.

Future work could involve coupling the proposed technique with active/inactive elements approaches commonly used to model domain growth in the numerical simulation of metal additive manufacturing processes. This would open up possibilities for full thermal simulation of metal additive manufacturing processes using the proposed method.

Apéndice F

Solving linear elasticity benchmark problems via the overset improved element-free Galerkin-finite element method

Javier A. Zambrano-Carrillo, Álvarez-Hostos Juan C., Serebrinsky Santiago, A.E. Huespe "Solving linear elasticity benchmark problems via the overset improved element-free Galerkin-finite element method". *Finite Elements in Analysis and Design*, 241, 104247

Solving linear elasticity benchmark problems via the overset improved element-free Galerkin-finite element method

Javier A. Zambrano-Carrillo[a], Álvarez-Hostos Juan C.[b,c,1], Serebrinsky Santiago[d], A.E. Huespe[a,e]

[a]Centro de Investigación de Métodos Computacionales (CIMEC), Universidad Nacional del Litoral (UNL)/Consejo Nacional de Investigaciones Científicas y Técnicas (CONICET), Predio CCT-CONICET Santa Fe, Argentina.
[b]Centro de Investigación y Transferencia (CIT) Rafaela, Universidad Nacional de Rafaela (UNRaf) / Consejo Nacional de Investigación Científicas y Técnicas (CONICET), Rafaela, Argentina.
[c] Departamento de Materiales, Facultad de Ingeniería Química, Universidad Nacional del Litoral (UNL), Santa Fe, Argentina.
[d]YPF Tecnología S.A. (Y-TEC - CONICET), Av. del Petróleo s/n, e/129 y 143 (1923), Berisso, Argentina.
[e]Programa de Engenharía Mecânica, COPPE, Universidade Federal do Rio de Janeiro, Cidade Universitária, Rio de Janeiro, CEP 21941-972, RJ, Brazil.

Keywords: Overset; Improved element-free Galerkin; Finite element method; Linear elasticity; Convergence analysis

Abstract. A novel approach for the solution of linear elasticity problems is introduced in this communication, which uses a hybrid chimera-type technique based on both finite element and improved element-free Galerkin methods. The proposed overset improved element-free Galerkin-finite element method (Ov-IEFG-FEM) for linear elasticity uses the finite element method (FEM) throughout the entire problem geometry, whereas a fine distribution of overlapping nodes is used to perform higher order approximations via the improved element-free Galerkin (IEFG) technique in regions demanding more computational accuracy. The method relies on keeping the FEM-based results in those regions where low order of approximation is enough to provide the required accuracy, i.e. outside the region where the solution will be enriched via the IEFG technique. The overlapping domains perform an iterative transfer of kinematics information through well-defined immersed boundaries, and a detailed explanation on this regard is also presented in this communication. The Ov-IEFG-FEM is used in a set of increasingly complex linear elasticity problems, and the outcomes demonstrate the suitability and reliability of this technique to solve such problems in an accurate and remarkably simple manner.

F.1. Introduction

Mesh-free methods rise interest in the area of computational mechanics being widely used in many engineering applications, since these methods require only a set of nodes to represent the problem domain thus making them ideal for modeling problems related to large deformations [275, 276], material damage [277, 278], moving boundaries [230, 279, 280], dissimilar or layered materials [281], initiation, nucleation and crack growth [282–284] and topology optimization [205, 236, 285]. Among the mesh-free methods developed so far, element-free Galerkin methods (EFGM) have gained popularity due to their successful applicability in different areas within computational mechanics such as fluid-dynamics [226, 286–288], non-linear solid-mechanics [289–294], heat transfer problems with phase change [295–297] and moving boundaries [230, 245, 279, 280], among others. These methods have the following features [212]: (i) the possibility of achieving more easily higher order approximations with continuous derivatives than FEM and other mesh-based techniques, and (ii) the greater flexibility in adding or removing nodes. The first feature allows a straightforward implementation of intrinsic shape functions enrichment to improve accuracy near singularities such as crack tips [298] or very localized heat sources [149], whereas the second feature makes the method suitable to address problems with variable domain [206, 280, 299] and moving boundaries [291, 300, 301] in a straightforward manner. Some of these include: heat transfer modelling of the start-up stage of direct chill casting [280, 299], thermo-mechanical analysis of additive manufacturing processes [206], metal forming computational plasticity [291], free surface flow fluid dynamics [300] and crack propagation analysis [300]. Other notable advantages of EFGM lie on their convergence rate, which often excels that of the finite element method (FEM) [15, 149, 212, 279]. Additionally, EFGM can achieve high precision in capturing marked local gradients [15, 279, 281, 298]. Furthermore, EFGM eliminate the need for post-processing to achieve

[1]Corresponding author. E-mail address: jchostos@cimec.unl.edu.ar (J.C. Álvarez-Hostos).

continuous strains, stresses, or other field variables due to its inherent continuity in shape functions and their spatial derivatives [212]. In contrast, achieving this continuity in FEM is challenging and typically requires either the use of highly complex finite elements with numerous nodal unknowns or post-processing to manage the discontinuous derivative fields produced by simpler elements [217, 218, 302]. These particular features have strongly promoted the implementation of EFGM in the solution of increasingly complex solid mechanics problems.

The positive features of EFGM for solving solid mechanics problems have already been widely demonstrated in the context of linear elasticity [212], and several approaches aimed at streamlining their implementation and enhancing their accuracy in solving such problems have been introduced in the last years. Ren et al [303] addressed 2D elastic problems via an interpolating EFG method, by using shape functions constructed with moving least squares (MLS) constrained to satisfy the Kronecker delta identity. This approach enabled the imposition of Dirichlet conditions in the form of prescribed nodal values, eliminating the need for additional techniques like Lagrange multipliers or Penalty methods often required in EFGM based on standard MLS approximations [212]. Sun et al. [304] introduced the dimension-splitting moving least squares (DS-MLS) in the EFG-based solution of 2D linear elasticity problems, allowing the solution of the weak-form of the momentum balance equation with a set of MLS approximations along a series of 1D subdomains or slices. This improves computational efficiency since the solution of the 2D problem is obtained by linear interpolation of the 1D MLS approximations series, eliminating the need for 2D MLS approximations across the entire problem domain. Peng et al [305] used complex variable MLS (CVMLS) for the solution of 2-D linear elasticity problems via the complex variable EFGM (CVEFGM), which improves computational efficiency by allowing the construction of 2D approximations with only 1D polynomial basis functions. A further implementation of this approach in the context of elastodynamics problems was made by Cheng et al. [306], also enhancing computational efficiency with respect to standard EFGM. Cheng et al. [307] achieved high efficiency in solving 3D elasticity problems by leveraging the potential of improved complex variable MLS (ICVMLS) approximations to allow for the construction of shape function for 2D domains only using 1D basis polynomials, and decomposing the 3D elasticity problem into a series of 2D problems where such shape functions are used to obtain solutions via the improved complex variable EFGM (ICVEFGM) technique. The improvement of computational performance via dimension splitting techniques is not only restricted to EFG methods, but has also gained popularity in the framework of other mesh-less methods such as the hybrid reproducing kernel particle method developed by Peng et al. [308] for 3D linear elasticity problems or the space splitting idea introduced by Dehghan and Abbaszadeh [309] in the framework of the local radial basis functions (LRBF) method for the solution of transport phenomena problems. This coupling of the 2D solution series yields results for the entire 3D elasticity problem, resulting in a hybrid ICVEFG (HICVEFG) solution. Gao et al [310] developed a stable and efficient scheme for the EFG-based solution of 3D linear elasticity problems, via a quadratically consistent one-point integration scheme developed over the Hu-Washizu three-field variational principle [212]. The proposed approach was demonstrated to be superior with respect to other integration schemes and standard EFGM in terms of accuracy, convergence, efficiency and stability. EFGM are also attractive for the solution of linear fracture mechanics problems, allowing accurate computation of stress intensity factors at the crack tips in a remarkably simple manner. Some recent examples include the ICVEFG with enriched basis functions formulated and successfully implemented by Pan et al. [311] to solve linear elastic fracture mechanics (LEFM) problems in orthotropic media, the optimized EFG technique developed by Garg and Pant [312] for linear thermo-elastic fracture mechanics analysis in functionally graded materials, and subsequently enhanced by Awasthi and Pant [313] via parametric optimization to improve computational efficiency in the framework of linear thermo-elastic fracture analysis of orthotropic media.

The efforts to enhance both efficiency and accuracy in solutions based on EFGM have been extended to large deformation elasticity problems as well. For instance, Qiang et al. [276] addressed two-dimensional large deformation elasticity problems using the interpolating EFG method. Such approach was successfully extended to three-dimensional cases and further improved by Bourantas et al. [294], via the introduction of stabilizing restrictions. It is also worth mentioning that the potential of EFGM has not been only limited to linear or non-linear elasticity problems, but it has also been showcased in path-dependent solid-mechanics problems with inelastic strains under both small [289, 290, 293] and large deformations [110, 256, 291, 292]. Some examples include the solution of elasto-plasticity problems performed by Peng et al. [314] via the CVEFGM, and the implementation of non-singular weight functions performed by Sun et al. [315] in order to allow the achievement of accurate of stable solutions for elasto-plasticity problems via the improved interpolating EFGM (IIEFGM). The potential of EFG techniques to solve increasingly complex solid mechanics problems has also enabled their implementation in structural topology optimization [205, 285, 316] and solid bodies contact modelling [317].

The works discussed so far put in an appropriate perspective the potential of EFG techniques to solve both linear and nonlinear solid mechanics problems in a straightforward manner, also providing improved accuracy. However, it is well known that EFGM tend to be computationally more expensive than FEM to perform a given task [15, 149, 286]. This drawback of EFGM remains despite the analogies with FEM, beyond the differences regarding the construction of shape functions and assembling of the algebraic equations systems. This specific limitation has led to the development of hybrid EFGM-FEM techniques aimed at enhancing computational efficiency, since these approaches are primarily conceived to confine implementation of EFGM to specific regions demanding higher order approximations to provide a good accuracy. The first coupled EFGM-FEM technique was introduced by Belytschko et al. [103], using interface elements in the coupling region with shape functions comprised of a linear interpolation between the MLS of EFGM and the standard interpolation of FEM. This procedure was demonstrated to fulfill consistency in the framework of elastostatics, elastodynamics and dynamic fracture problems. There are also other works where the hybrid EFG-FEM is used to enable the direct imposition of Dirichlet-type boundary conditions at the nodal positions, which is performed using a strip of finite elements for discretization along the corresponding boundaries [104, 105].

Most of the FEM-EFGM coupling procedures reported in the recent literature involve previously well-specified regions to be discretized via the FEM and EFGM, with a prescribed topological relationship to be properly coupled. Rohit et al. [106] presented a review on the implementation in the last decades of the coupled procedures between mesh-free and FEM methods that have appeared as a new alternative in computational methods with important achievements. In addition, the remarkable progress in the resolution of the main deficiencies of conventional methods and mesh-free methods in premature phases was analyzed. Such communication also included a comprehensive review of the various coupling techniques used for the interface elements of the meshless and FEM methods. The shape function formulation in FEM and EFGM was discussed in general, showing the key contribution of FEM-EFGM coupling techniques in the numerical solution of solid and structural mechanics problems. Particularly, hybrid FEM-EFGM have been found to be useful in linear elastic fracture mechanics [107] and crack-growth modelling in both ductile [108] and brittle [109] materials. Most hybrid EFG-FEM procedures require interface elements that use ramp or blending functions for a seamless transition between the FEM and EFGM regions, whereby the implementation of these approaches in scenarios involving geometries of complex topology can be very challenging. Nevertheless, some authors have recently succeeded in performing such coupling without the need of transition elements. Zhang et al [253, 318] proposed the construction of MLS approximations with support domains decreasing linearly towards the coupling interface, such that these match the nodal spacing to approximate the Krocneker delta property in the transition region. Such an approach enabled the development of topology optimization procedures based on hybrid FEM-EFGM for both hypo-elastic [253] and hyper-elastic [318] structures, also reducing computational cost via an adaptive multi-level quadrature scheme for numerical integration. A novel procedure of automatic error-based adaptive coupling for EFGM-FEM has been developed by Ullah et al. [110] for linear, nonlinear, and also path-dependent solid-mechanics problems. The shape functions for the EFG approximations were constructed via the max-entropy formulation, allowing a weak fulfillment of Kronecker delta property. This particular feature has not only enabled the imposition of Dirichlet boundary conditions in the form of prescribed nodal values, but also eliminated the need for interface elements in the coupling between EFG and FEM regions. This approach was also successfully implemented in a parallel computational framework [256], and Nguyen et al. [316] proposed further enhancements for better scalability.

Despite the advantages presented by hybrid numerical solutions based on EFG-FEM, these coupling methods still require well-defined transition boundaries in areas where EFGM and FEM share common nodes. To address this kind of needs for topological relationship in domain coupling-based procedures, chimera-type overlapping domains methods have been developed in the context of both mesh-less and mesh-free methods. Several works corresponding to overset procedures developed in the framework of mesh-based methods [148, 262] have been successfully applied in problems such as fluid-structure interaction [261, 263, 264], moving heat sources [148], and multiphysical transport phenomena in manufacturing processes [265]. A recent study conducted by Álvarez-Hostos et al. [149] has introduced one of the first overset approaches based on mesh-less methods, which is the Overset Improved EFG (Ov-IEFG) technique. This technique conceived in principle to address transient heat conduction problems with moving heat sources, performs with a fine arrangement of nodes that follows the heat source path over a coarse distribution of nodes distribution representing the entire problem domain. This enables the search for support domain nodes at each integration point and the corresponding calculation of improved MLS (IMLS) approximations to be performed only once and preserved throughout the transient heat conduction analysis, which

is highly advantageous as it results in a significant reduction in computation times compared to EFG-based procedures subjected to adaptive redistribution of nodes. The smoothness and continuity of the IMLS approximations and their derivatives allow for direct coupling between the moving nodes distribution and the background coarse nodes distribution via an iterative procedure conceived to perform a reciprocal transfer of information between the moving and background overlapping domains, through properly defined immersed boundaries.

Although the Ov-IEFG has the potential for easy coupling between the overlapping domains, it is still challenging in terms of computational cost because it uses EFG in both domains. In this sense, an overset procedure that uses EFG approximations only in regions demanding high numerical accuracy would be very useful. In order to address this aspect, Álvarez-Hostos et al. [15] introduced the overset IEFG-FEM (Ov-IEFG-FEM). Such hybrid mesh-less/mesh-based technique has been firstly developed and implemented in the context of transient heat conduction problems with moving heat sources, by using a fine distribution of nodes moving with the heat source and overlapping with a coarse mesh discretizing the entire domain geometry. The method performs higher order IEFG approximations with the overlapping nodes following the moving heat source according to the accuracy requirements, whereas less computationally expensive FEM-based calculations are performed in the rest of the problem domain. Based on the potential of the Ov-IEFG-FEM to solve problems with marked moving gradients in small regions, the focus of this work is on performing an appropriate extension of the positive features of this technique to the solution of linear elasticity problems exhibiting such issues. The paper is structured with Section 2 presenting the formulation of the Ov-IEFG-FEM in the context of linear elasticity problems, along with the iterative algorithm regarding the overlapping domains coupling. Section 3 showcases numerical examples of the benchmark problems worked on, along with their respective outcomes. Subsequently, Section 4 explores discussions regarding the outcomes of Section 3, and finally, conclusions are presented in Section 5.

F.2. Methodological framework

Linear elasticity benchmark problems will be solved via the Ov-IEFG-FEM, whose schematic representation can be seen in Fig. F.1 for an arbitrary domain Ω with boundary Γ. The entire problem domain is discretized with a coarse background mesh to perform FEM-based computations, whereas an overlapping domain represented by a fine distribution of nodes is used to enrich the solution in a specific area by using the IEFG method to achieve higher order mesh-less approximations.

F.2.1. Governing equations

The domain Ω of Fig. F.1 is occupied by an isotropic linear elastic solid subjected to a set of Dirichlet and Neumann conditions on the non-overlapping boundaries $\Gamma_{\mathbf{u}}$ and $\Gamma_{\mathbf{t}}$ ($\Gamma_{\mathbf{u}} \cup \Gamma_{\mathbf{t}} = \Gamma$), respectively. The solid deformation is governed by the quasi-static form of the linear momentum balance equation:

$$\nabla \cdot \boldsymbol{\sigma} + \mathbf{f} = 0 \qquad \forall \mathbf{x} \in \Omega, \tag{F.1}$$

where $\mathbf{f}$ is the body force density and $\boldsymbol{\sigma}$ is the Cauchy stress tensor, which for an isotropic linear elastic solid under small strains is given by:

$$\boldsymbol{\sigma} = \mu \left(\nabla \mathbf{u} + \nabla \mathbf{u}^T \right) + \lambda \nabla \cdot \mathbf{u} \mathbf{I}, \tag{F.2}$$

where $\mu = E/[2(1+\nu)]$ and $\lambda = E\nu/[(1+\nu)(1-2\nu)]$ are the Lamé's constants, whereas $\mathbf{I}$ is the second order identity tensor and $\mathbf{u}$ is the displacement field. The Lamé's constants are given in terms of the Young's modulus E and the Poisson's ratio ν. The solution of (F.1) is subjected to the following boundary conditions:

$$\begin{aligned} \mathbf{u} &= \mathbf{u}_D \quad \text{on} \quad \Gamma_{\mathbf{u}}, \quad \text{and} \\ \mathbf{m}\sigma \cdot \hat{\mathbf{n}} &= \mathbf{t} \quad \text{on} \quad \Gamma_{\mathbf{t}}, \end{aligned} \tag{F.3}$$

where $\mathbf{u}_D$ is the displacement to be imposed on $\Gamma_{\mathbf{u}}$, and $\mathbf{t}$ is the surface traction vector on $\Gamma_{\mathbf{t}}$.

F.2.2. Conceptual description of the Ov-IEFG-FEM

The Ov-IEFG-FEM is conceived to solve the governing equations of the linear elasticity problem described in Section 2.1, by constructing an unique enriched solution via an appropriate coupling of the overlapped domains

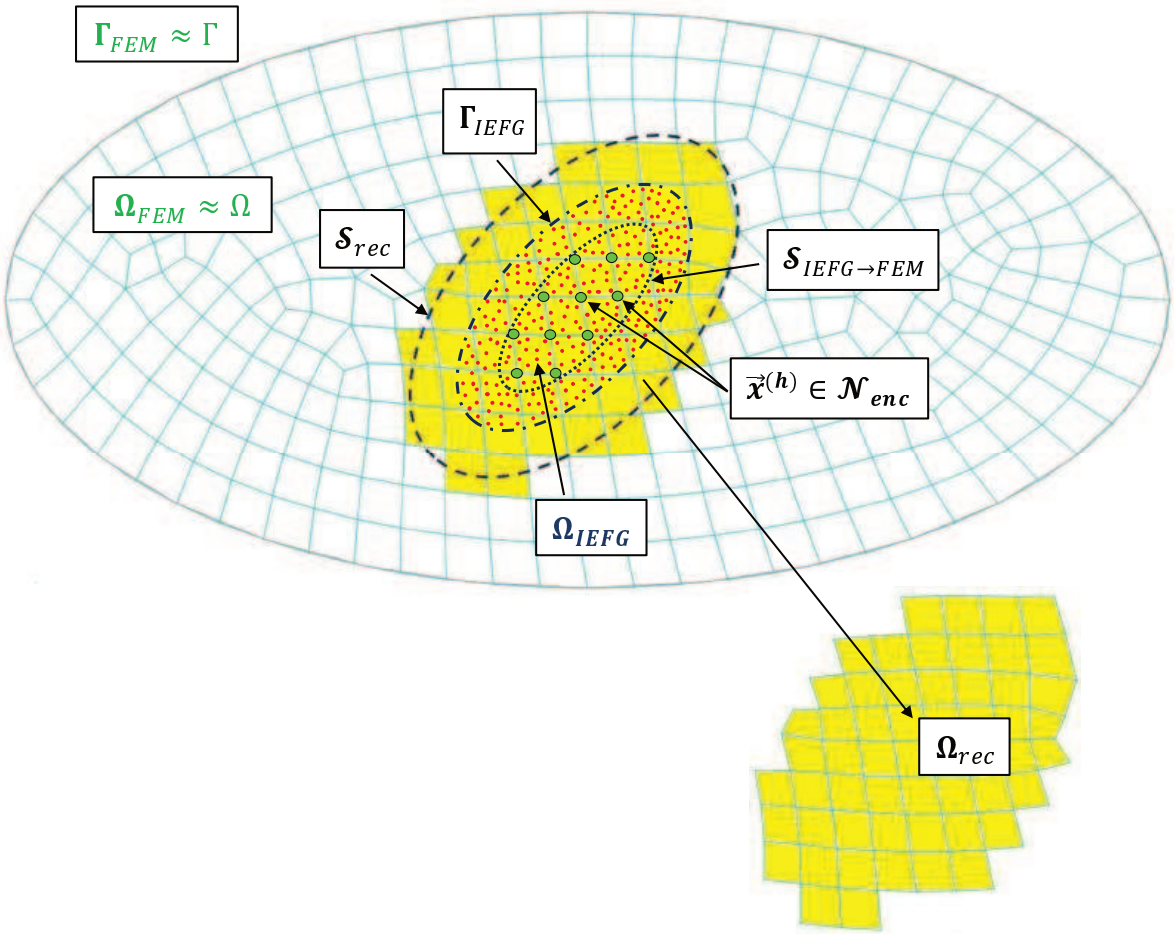

Figura F.1: Representation of the problem domain for a numerical solution performed via the proposed Ov-IEFG-FEM

Ω_{FEM} and Ω_{IEFG} depicted in Fig. F.1. The results concerning the FEM-based solution performed in the background mesh discretizing Ω_{FEM} are kept in the regions outside the patch domain Ω_{IEFG} represented by a fine distribution of nodes (depicted in red) to enrich the solution via the IEFG technique, whereas the boundary Γ_{IEFG} and the closed surface $\mathcal{S}_{\text{IEFG}\to\text{FEM}}$ are intended to perform the reciprocal transfer of information between the overlapping domains Ω_{FEM} and Ω_{IEFG}. The boundary Γ_{IEFG} and the closed surface $\mathcal{S}_{\text{IEFG}\to\text{FEM}}$ are depicted by dashed and dotted black lines, respectively. The FEM-based solution is used to compute the displacements to be imposed on Γ_{IEFG} via the penalty method, whereby the solution performed in Ω_{IEFG} via the IEFG method depends on the results obtained in the background mesh. Conversely, the solution obtained via the IEFG technique in the patch domain Ω_{IEFG} is used to determine the displacements to be prescribed at the set of nodes $\mathcal{N}_{\text{enc}}$ (depicted in green) of the background mesh enclosed by the surface $\mathcal{S}_{\text{IEFG}\to\text{FEM}}$. It is important to highlight that the displacements to be imposed on Γ_{IEFG} are calculated through a high-order local reconstruction of the FEM-based solution, which is performed in the domain $\Omega_{\text{rec}} \subset \Omega_{\text{FEM}}$ constructed with those finite elements whose centers are enclosed by $\mathcal{S}_{\text{rec}}$. These elements are depicted in yellow color in Fig. F.1, whereas $\mathcal{S}_{\text{rec}}$ is represented by the black dashed line in the same figure. The coupling between the solutions obtained in the overlapping domains Ω_{FEM} and Ω_{IEFG}, consists on a staggered/recursive imposition of the following kinematic constraints:

$$\begin{aligned} \mathbf{u} = \bar{\mathbf{u}}_{\text{IEFG}} \quad \text{at} \quad \mathbf{x}^{(h)}, \quad h \in \mathcal{N}_{\text{enc}}, \quad \text{and} \\ \mathbf{u} = \bar{\mathbf{u}}_{\text{FEM}} \quad \text{on} \quad \Gamma_{\text{IEFG}}, \end{aligned} \tag{F.4}$$

where $\bar{\mathbf{u}}_{\text{IEFG}}$ corresponds to the displacements computed at nodes $h \in \mathcal{N}_{\text{enc}}$ using the solution peformed in Ω_{IEFG} via the IEFG technique, whereas $\bar{\mathbf{u}}_{\text{FEM}}$ are the displacements computed on Γ_{IEFG} by using the IMLS approximations obtained from the local reconstruction performed with the set $\mathcal{N}_{\text{enc}}$ of nodes belonging to the elements

included in Ω_{rec}.

This procedure establishes the reciprocal dependence between the solutions obtained in both the FEM background mesh Ω_{FEM} and the fine distribution of nodes representing the patch domain Ω_{IEFG}. The displacements $\bar{\mathbf{u}}_{\text{IEFG}}$ to be imposed at nodes $h \in \mathcal{N}_{\text{enc}}$ are calculated by means of the IMLS approximations concerning the solution performed via the IEFG technique in the fine distribution of nodes representing the overlapping domain Ω_{IEFG}, whereas the displacements $\bar{\mathbf{u}}_{\text{FEM}}$ that are imposed on Γ_{IEFG} are computed from the IMLS-based local reconstruction of the mechanical problem solved in the background mesh Ω_{FEM} via the FEM.

F.2.3. Formulation and iterative algorithm for the Ov-IEFG-FEM in linear elastic problems

The Ov-IEFG-FEM is implemented following the weak formulation of the mechanical problem in both domains, Ω_{FEM} and Ω_{IEFG}. It is written using matrix notation. The weak formulation in Ω_{FEM} is [212]

$$\int_{\Omega_{\text{FEM}}} \delta\mathbf{u}^T \mathbf{L}^T \mathbf{C}\, \mathbf{L}\mathbf{u}\, \mathrm{d}\Omega = \int_{\Omega_{\text{FEM}}} \delta\mathbf{u}^T \mathbf{f}\, \mathrm{d}\Omega + \int_{\Gamma_t} \delta\mathbf{u}^T \mathbf{t}\, \mathrm{d}\Gamma, \quad \forall \delta\mathbf{u} \in \mathcal{V}_{\text{FEM}}, \tag{F.5}$$

whereas for the fine distribution of nodes in Ω_{IEFG} is given by [212]

$$\int_{\Omega_{\text{IEFG}}} \delta\mathbf{u}^T \mathbf{L}^T \mathbf{C}\, \mathbf{L}\mathbf{u}\, \mathrm{d}\Omega = \int_{\Omega_{\text{IEFG}}} \delta\mathbf{u}^T \mathbf{f}\, \mathrm{d}\Omega + \int_{\Gamma_{\text{IEFG}} \cap \Gamma_t} \delta\mathbf{u}^T \mathbf{t}\, \mathrm{d}\Gamma + \int_{\Gamma_{\text{IEFG}}} \delta\mathbf{u}^T \alpha \left(\bar{\mathbf{u}}_{\text{FEM}} - \mathbf{u}\right) \mathrm{d}\Gamma, \quad \forall \delta\mathbf{u} \in \mathcal{V}_{\text{IEFG}}, \tag{F.6}$$

where α is the penalty parameter for the imposition of the displacements of $\bar{\mathbf{u}}_{\text{FEM}}$ on Γ_{IEFG}, $\mathbf{C}$ is the elasticity tensor in matrix notation, and $\mathbf{L}$ is the differential operator for the computation of small strains in matrix notation $\mathbf{m}\varepsilon = \mathbf{L}\mathbf{u}$[212]. As can be noticed in the weak formulation of the problem to be solved in Ω_{FEM} (F.5), no penalty integrals are included for the imposition of the Dirichlet conditions because the Kronecker delta property of the shape functions used in FEM allows the imposition of displacements in the form of prescribed nodal values.

The solution of (F.5) via FEM is carried out using the same approximations for both displacement $\mathbf{u}(\mathbf{x})|_{\Omega_{\text{FEM}}} \cong \mathbf{u}_{\text{FEM}}(\mathbf{x})$ and its virtual variation $\delta\mathbf{u}(\mathbf{x})|_{\Omega_{\text{FEM}}} \cong \delta\mathbf{u}_{\text{FEM}}(\mathbf{x})$ in Ω_{FEM}, which consist of standard linear interpolating finite element basis functions

$$\mathbf{u}_{\text{FEM}}(\mathbf{x}) = \sum_{I=1}^{n_{\text{FEM}}} \mathbf{N}_{\text{FEM}}^{(I)}(\mathbf{x})\, \tilde{\mathbf{u}}_{\text{FEM}}^{(I)}, \qquad \delta\mathbf{u}_{\text{FEM}}(\mathbf{x}) = \sum_{I=1}^{n_{\text{FEM}}} \mathbf{N}_{\text{FEM}}^{(I)}(\mathbf{x})\, \delta\tilde{\mathbf{u}}_{\text{FEM}}^{(I)}, \qquad \mathbf{x} \in \Omega_{\text{FEM}}, \tag{F.7}$$

where n_{FEM} is the number of nodes belonging to the background mesh. On the other hand, the solution of (F.6) via the IEFG is obtained using the same IMLS approximations for both displacement $\mathbf{u}(\mathbf{x})|_{\Omega_{\text{IEFG}}} \cong \mathbf{u}_{\text{IEFG}}(\mathbf{x})$ and its virtual variation $\delta\mathbf{u}(\mathbf{x})|_{\Omega_{\text{IEFG}}} \cong \delta\mathbf{u}_{\text{IEFG}}(\mathbf{x})$ in the Ω_{IEFG} domain:

$$\mathbf{u}_{\text{IEFG}}(\mathbf{x}) = \sum_{I=1}^{n_{\text{IEFG}}} \mathbf{N}_{\text{IEFG}}^{(I)}(\mathbf{x})\, \tilde{\mathbf{u}}_{\text{IEFG}}^{(I)}, \qquad \delta\mathbf{u}_{\text{IEFG}}(\mathbf{x}) = \sum_{I=1}^{n_{\text{IEFG}}} \mathbf{N}_{\text{IEFG}}^{(I)}(\mathbf{x})\, \delta\tilde{\mathbf{u}}_{\text{IEFG}}^{(I)}, \qquad \mathbf{x} \in \Omega_{\text{IEFG}}, \tag{F.8}$$

where n_{IEFG} represents the number of nodes representing to the overlapping domain Ω_{IEFG} used to enrich the numerical solution in the zone of interest via the IEFG technique. In Eqs. (F.7) and (F.8), $\mathbf{N}_{\text{FEM}}^{(I)}(\mathbf{x})$ and $\mathbf{N}_{\text{IEFG}}^{(I)}(\mathbf{x})$ are the matrix operators of shape functions at the I^{th} node, i.e.

$$\mathbf{N}_{\text{FEM}}^{(I)}(\mathbf{x}) = N_{\text{FEM}}^{(I)}(\mathbf{x})\, \mathbf{I}, \qquad \mathbf{N}_{\text{IEFG}}^{(I)}(\mathbf{x}) = N_{\text{IEFG}}^{(I)}(\mathbf{x})\, \mathbf{I}. \tag{F.9}$$

In Eq. (F.9), $N_{\text{FEM}}^{(I)}(\mathbf{x})$ and $N_{\text{IEFG}}^{(I)}(\mathbf{x})$ are the basis functions for the FEM and IEFG computations, respectively. In this work, $N_{\text{FEM}}^{(I)}(\mathbf{x})$ consists in a set of standard bilinear interpolating polynomials used to construct the standard element-wise approximating shape functions[15, 302]. The IMLS approximations implemented in this work for $N_{\text{IEFG}}^{(I)}(\mathbf{x})$ are based on cubic splines weight functions [15, 149, 212], whereas the geometry of the nodal influence domains are appropriately chosen according to the particular characteristics of each problem. The IMLS $N_{\text{IEFG}}^{(I)}(\mathbf{x})$

for each I-th node is computed as

$$N_{\text{IEFG}}^{(I)}(\mathbf{x}) = \hat{W}(\mathbf{x}-\mathbf{x}^{(I)})\frac{\sum_{i=1}^{4} P_i(\mathbf{x})P_i(\mathbf{x}^{(I)})}{(P_i,P_i)}, \tag{F.10}$$

where $\hat{W}(\mathbf{x}-\mathbf{x}^{(I)})$ is the weight function given by

$$\hat{W}(r) = \begin{cases} \frac{2}{3} - 4r^2 - 4r^3 & \text{if } r \leq \frac{1}{2}, \\ \frac{4}{3} - 4r + 4r^2 - \frac{4}{3}r^3 & \text{if } \frac{1}{2} < r \leq 1, \\ 0 & \text{if } r > 1, \end{cases} \tag{F.11}$$

and r is the distance from the sample point $\mathbf{x}$ to the node $\mathbf{x}^{(I)}$, normalized by size of the nodal influence domain. Also, (P_i, P_i) are the components of the diagonal moment matrix constructed with the weighted orthogonal polynomial basis vector of components P_i, which in this particular work is obtained from a standard bilinear basis function $\mathbf{q}(\mathbf{x})^T = [1, x, y, xy]$. Within the IEFG method both rectangular [149] and circular [279] domains of influence are frequently used in two-dimensional problems. On the other hand, spherical [239], cylindrical [149], and right-angled hexahedral [296] domains of influence are frequently used in three-dimensional problems. It should be noted that the construction of IMLS can be 30 % faster compared to the standard MLS procedure [242, 243, 286], more details concerning the implementation of IMLS can be found in the literature related to solutions using the IEFG method for both two-dimensional [149, 279, 286, 287], and three-dimensional [149, 242, 243] problems. For purposes of simplicity, the notation $(\mathbf{x})$ indicating the dependence of the IMLS with position is omitted hereinafter.

By performing the substitution of the interpolating linear basis functions of FEM (F.7) into expression (F.5) so that it holds for any $\delta\tilde{\mathbf{u}}_{\text{FEM}}^{(I)}$, the FEM approximation in the background mesh is obtained:

$$\sum_{J=1}^{n_{\text{FEM}}} \underbrace{\int_{\Omega_{\text{FEM}}} \mathbf{B}_{\text{FEM}}^{(I)\,T}\mathbf{C}\,\mathbf{B}_{\text{FEM}}^{(J)}\,\mathrm{d}\Omega}_{\mathbf{K}_{\text{FEM}}^{(IJ)}}\tilde{\mathbf{u}}_{\text{FEM}}^{(J)} = \underbrace{\int_{\Omega_{\text{FEM}}} \mathbf{N}_{\text{FEM}}^{(I)}\mathbf{f}\,\mathrm{d}\Omega}_{\mathbf{F}_{\text{FEM(f)}}^{(I)}} + \underbrace{\int_{\Gamma_t} \mathbf{N}_{\text{FEM}}^{(I)}\mathbf{t}\,\mathrm{d}\Gamma}_{\mathbf{F}_{\text{FEM(t)}}^{(I)}}, \tag{F.12}$$

where $\mathbf{B}_{\text{FEM}}^{(I)} = \mathbf{L}\,\mathbf{N}_{\text{FEM}}^{(I)}$. Similarly, the IEFG formulation in the fine distribution of nodes representing the overlapping domain Ω_{IEFG} is obtained through the substitution of approximations (F.8) in (F.6):

$$\sum_{J=1}^{n_{\text{IEFG}}} \underbrace{\int_{\Omega_{\text{IEFG}}} \mathbf{B}_{\text{IEFG}}^{(I)\,T}\mathbf{C}\,\mathbf{B}_{\text{IEFG}}^{(J)}\,\mathrm{d}\Omega}_{\mathbf{K}_{\text{IEFG}}^{(IJ)}}\tilde{\mathbf{u}}_{\text{IEFG}}^{(J)} + \sum_{J=1}^{n_{\text{IEFG}}} \underbrace{\int_{\Gamma_{\text{IEFG}}} \mathbf{N}_{\text{IEFG}}^{(I)}\alpha\mathbf{N}_{\text{IEFG}}^{(J)}\,\mathrm{d}\Gamma}_{\mathbf{P}_{\text{IEFG}}^{(IJ)}}\tilde{\mathbf{u}}_{\text{IEFG}}^{(J)} =$$
$$\underbrace{\int_{\Omega_{\text{IEFG}}} \mathbf{N}_{\text{IEFG}}^{(I)}\mathbf{f}\,\mathrm{d}\Omega}_{\mathbf{F}_{\text{IEFG(f)}}^{(I)}} + \underbrace{\int_{\Gamma_t} \mathbf{N}_{\text{IEFG}}^{(I)}\mathbf{t}\,\mathrm{d}\Gamma}_{\mathbf{F}_{\text{IEFG(t)}}^{(I)}} + \underbrace{\int_{\Gamma_{\text{IEFG}}} \mathbf{N}_{\text{IEFG}}^{(I)}\alpha\bar{\mathbf{u}}_{\text{FEM}}\,\mathrm{d}\Gamma}_{\mathbf{F}_{\text{IEFG}(\alpha)}}, \tag{F.13}$$

where $\mathbf{B}_{\text{IEFG}}^{(I)} = \mathbf{L}\,\mathbf{N}_{\text{IEFG}}^{(I)}$. Rewriting expressions (F.12) and (F.13) in matrix and vector arrangements, leads to the following system of equations:

$$\mathbf{K}_{\text{FEM}}\tilde{\mathbf{U}}_{\text{FEM}} = \mathbf{F}_{\text{FEM(f)}} + \mathbf{F}_{\text{FEM(t)}} \tag{F.14}$$

$$(\mathbf{K}_{\text{IEFG}} + \mathbf{P}_{\text{IEFG}})\,\tilde{\mathbf{U}}_{\text{IEFG}} = \mathbf{F}_{\text{IEFG(f)}} + \mathbf{F}_{\text{IEFG(t)}} + \mathbf{F}_{\text{IEFG}(\alpha)}. \tag{F.15}$$

The coupling between the formulations inherent in each overlapping domain Ω_{FEM} and Ω_{IEFG} is performed through the iterative solution of the algebraic systems (F.14) and (F.15). The transfer of information from Ω_{FEM} to Ω_{IEFG} is done by means of the penalty matrix $\mathbf{P}_{\text{IEFG}}$ and the penalty vector $\mathbf{F}_{\text{IEFG}(\alpha)}$, whereas the transfer of information from Ω_{IEFG} to Ω_{FEM} is done by using the solution obtained via the IEFG method in Ω_{IEFG} to calculate the displacements at positions $\mathbf{x}^{(h)}$ of the nodes $h \in \mathcal{N}_{\text{enc}}$ and then prescribing these nodal values in the

FEM background mesh. The nodal parameters $\tilde{\mathbf{u}}_{\text{IEFG}}^{(I)}$ are used to calculate the displacements $\bar{\mathbf{u}}_{\text{IEFG}}$ of each node $h \in \mathcal{N}_{\text{enc}}$, as defined below:

$$\bar{\mathbf{u}}_{\text{IEFG}} = \mathbf{u}_{\text{IEFG}}\left(\mathbf{x}^{(h)}\right) = \sum_{I=1}^{n_{\text{IEFG}}} \mathbf{N}_{\text{IEFG}}^{(I)}\left(\mathbf{x}^{(h)}\right) \tilde{\mathbf{u}}_{\text{IEFG}}^{(I)}, \qquad h \in \mathcal{N}_{enc}. \tag{F.16}$$

The displacements $\bar{\mathbf{u}}_{\text{FEM}}$ at the boundary Γ_{IEFG} needed to assemble the penalty vector $\mathbf{F}_{\text{IEFG}(\alpha)}$ are also calculated by IMLS approximations, but using a vector $\tilde{\mathbf{U}}_{\text{rec}}$ of nodal parameters $\tilde{\mathbf{u}}_{\text{rec}}^{(I)}$ obtained from the local reconstruction of the solution in FEM, i.e:

$$\bar{\mathbf{u}}_{\text{FEM}} = \sum_{I=1}^{n_{\text{rec}}} \mathbf{N}_{rec}^{(I)}(\mathbf{x})\, \tilde{\mathbf{u}}_{\text{rec}}^{(I)}, \qquad \mathbf{x} \in \Gamma_{\text{IEFG}}, \tag{F.17}$$

where n_{rec} is the number of nodes included in $\mathcal{N}_{enc}$. In this work, a procedure similar to that proposed by Storti et al. [148, 266] for the superposition of unstructured meshes in FEM-based chimera-type techniques is used to carry out the current local reconstruction based on IMLS. The procedure of Storti et al [148, 266] is designed to maintain the convergence features of standard numerical solutions based on a single mesh, and involves a high-order interpolation algorithm that uses a least-squares adjustment to the nodal values via Lagrange multipliers. In order to maintain the convergence features of a standard IEFG-based solution, this technique is extended to the current Ov-IEFG-FEM to enforce the following condition on the IMLS approximations:

$$\sum_{J=1}^{n_{\text{rec}}} \mathbf{N}_{\text{rec}}^{(J)}\left(\mathbf{x}^{(I)}\right) \tilde{\mathbf{u}}_{\text{rec}}^{(J)} = \tilde{\mathbf{u}}_{\text{FEM}}^{(I)}, \qquad I \in \mathcal{N}_{\text{rec}}. \tag{F.18}$$

To attain this objective, the following augmented Lagrangian functional must be minimized:

$$\mathcal{L}\left(\tilde{\mathbf{U}}_{\text{rec}}, \boldsymbol{\gamma}\right) = \frac{1}{2}\int_{\Omega_{\text{rec}}} \left(\sum_{J=1}^{n_{\text{rec}}} \mathbf{N}_{\text{rec}}^{(J)}(\mathbf{x})\, \tilde{\mathbf{u}}_{\text{rec}}^{(J)} - \mathbf{u}_{\text{FEM}}(\mathbf{x})\right)^2 \mathrm{d}\Omega + \sum_{J=1}^{n_{\text{rec}}} \gamma^{(J)} \left(\sum_{I=1}^{n_{rec}} \mathbf{N}_{\text{rec}}^{(I)}\left(\mathbf{x}^{(J)}\right) \tilde{\mathbf{u}}_{\text{rec}}^{(I)} - \tilde{\mathbf{u}}_{\text{FEM}}^{(J)}\right) \qquad I, J \in \mathcal{N}_{\text{rec}}, \tag{F.19}$$

where each of the Lagrange multipliers $\gamma^{(J)}$ are included in the vector $\boldsymbol{\gamma}$. The domain $\Omega_{\text{rec}} \subset \Omega_{\text{FEM}}$ is formed by the union of the elements whose centers are enclosed by S_{rec}, as shown in Fig. F.1. Minimization of expression (F.19) leads to the following system of equations:

$$\begin{bmatrix} \mathbf{G} & \boldsymbol{\Lambda} \\ \boldsymbol{\Lambda}^T & \mathbf{0} \end{bmatrix} \begin{bmatrix} \tilde{\mathbf{U}}_{\text{rec}} \\ \boldsymbol{\gamma} \end{bmatrix} = \begin{bmatrix} \mathbf{F}_{\text{rec}} \\ \tilde{\mathbf{U}}_{\text{FEM}}^{(\Omega_{\text{rec}})} \end{bmatrix}, \tag{F.20}$$

where the components of $\mathbf{G}$,$\boldsymbol{\Lambda}$ and $\mathbf{F}_{\text{rec}}$ are:

$$\mathbf{G}^{(IJ)} = \int_{\Omega_{\text{rec}}} \mathbf{N}_{\text{rec}}^{(I)}(\vec{x})\mathbf{N}_{\text{rec}}^{(J)}(\mathbf{x})\, \mathrm{d}\Omega, \quad \boldsymbol{\Lambda}^{(IJ)} = \mathbf{N}_{\text{rec}}^{(I)}\left(\mathbf{x}^{(J)}\right), \quad \text{and} \quad \mathbf{F}_{\text{rec}}^{(I)} = \int_{\Omega_{\text{rec}}} \mathbf{N}_{\text{rec}}^{(I)}(\mathbf{x})\mathbf{u}_{\text{FEM}}(\mathbf{x})\, \mathrm{d}\Omega \tag{F.21}$$

It should be noted that the displacement $\mathbf{u}_{FEM}(\mathbf{x})$ used in the assembly of $\mathbf{F}_{\text{rec}}$ is calculated according to the expression (F.7), and the components of $\tilde{\mathbf{U}}_{\text{FEM}}^{(\Omega_{\text{rec}})}$ are the displacements $\tilde{\mathbf{u}}_{\text{FEM}}^{(J)}$ of nodes $J \in \mathcal{N}_{\text{rec}}$.

Based on the procedures described above, the application of the proposed Ov-IEFG-FEM method can be summarized in the following algorithm developed in the form of pseudocode:

1. Assembly of (F.14) and solving to obtain $\tilde{\mathbf{U}}_{\text{FEM}}$.
2. Iterative Ov-IEFG-FEM: set iter $= 1$, $\tilde{\mathbf{U}}_{\text{FEM}}^{\text{iter}} = \tilde{\mathbf{U}}_{\text{FEM}}$.
   a) Solving (F.20) to obtain $\tilde{\mathbf{U}}_{\text{rec}}$ and calculate $\bar{\mathbf{u}}_{\text{FEM}}^{\text{iter}}$ using (F.17) on Γ_{IEFG}.

b) Solving (F.15) to obtain $\tilde{\mathbf{U}}^{\text{iter}}_{\text{IEFG}}$.

c) Computing $\bar{\mathbf{u}}^{\text{iter+1}}_{\text{IEFG}}$ using (F.16) at nodes $h \in \mathcal{N}_{\text{enc}}$.

d) Stop criterion:

- If iter $= 1$, iter $\leftarrow$ iter $+ 1$, return to (a).
- Otherwise:
  - if $\frac{\|\bar{\mathbf{u}}^{\text{iter}}_{\text{FEM}} - \bar{\mathbf{u}}^{\text{iter}-1}_{\text{FEM}}\|_{L_2(\Gamma_{\text{IEFG}})}}{\|\bar{\mathbf{u}}^{\text{iter}}_{\text{FEM}}\|_{L_2(\Gamma_{\text{IEFG}})}} + \frac{\|\bar{\mathbf{u}}^{\text{iter}}_{\text{IEFG}} - \bar{\mathbf{u}}^{\text{iter}-1}_{\text{IEFG}}\|_{L_2(\mathcal{N}_{\text{enc}})}}{\|\bar{\mathbf{u}}^{\text{iter}}_{\text{IEFG}}\|_{L_2(\mathcal{N}_{\text{enc}})}} \geq \epsilon$, iter $\leftarrow$ iter $+ 1$, then return to (a)
  - Otherwise go to (3).

3. Computing the displacements $\mathbf{u}_{\text{FEM}}$ in $\Omega_{\text{FEM}} - \Omega_{\text{IEFG}}$ using (F.7) and $\mathbf{u}_{\text{IEFG}}$ in Ω_{IEFG} using (F.8). Obtain the enriched solution of the linear elastic problem as $\mathbf{u} = \mathbf{u}_{\text{FEM}} \cup \mathbf{u}_{\text{IEFG}}$.

In order to obtain a seamless displacement transition along the Γ_{IEFG} boundary, a distance criterion between Γ_{IEFG} and $\mathcal{S}_{\text{IEFG}\rightarrow\text{FEM}}$ has to be implemented. In this work, this criterion consists of setting the distance $\Gamma_{\text{IEFG}} - \mathcal{S}_{\text{IEFG}\rightarrow\text{FEM}}$ from 1.5 to 3 times the average size of the background mesh elements. This distance criterion is based on the work of Storti et al. [148] in the context of FEM-based chimera-type techniques, which was successfully implemented by AÍvarez-Hostos et al [15, 149] in the formulation of both the mesh-less Ov-IEFG [149] technique and the hybrid mesh-less/mesh-based Ov-IEFG-FEM [15] in the framework of heat transfer problems with moving heat sources. In this criterion, it was also established to use a separation distance between $\mathcal{S}_{\text{rec}}$ and Γ_{IEFG} of at least one element size of the background mesh, which is sufficient to achieve a smooth and accurate reconstruction based on the IMLS procedure using the $\mathcal{N}_{\text{rec}}$ nodes of those elements included in Ω_{rec}.

F.3. Numerical examples and results

To conduct a thorough analysis of convergence and accuracy, the Ov-IEFG-FEM method is applied to a series of increasingly complex elasticity benchmark problems. The Ov-IEFG-FEM will be used in the numerical solution of (i) Timoshenko cantilever beam [212], (ii) the infinite plate with a centered hole [212], and (iii) the linear elastic fracture mechanics (LEFM) benchmark problem of a Single Edge Notched Tension (SENT) specimen [319]. For the 2D examples evaluated in this section, both the elasticity matrix $\mathbf{C}$ for an isotropic material and the differential operator matrix $\mathbf{L}$ are defined as follows for 2D problems:

$$\mathbf{C}_{(\text{plane stress})} = \frac{E}{(1-\nu^2)}\begin{bmatrix} 1 & \nu & 0 \\ \nu & 1 & 0 \\ 0 & 0 & \frac{1-\nu}{2} \end{bmatrix}, \qquad \mathbf{C}_{(\text{plane strain})} = \frac{E}{(1+\nu)(1-2\nu)}\begin{bmatrix} 1-\nu & \nu & 0 \\ \nu & 1-\nu & 0 \\ 0 & 0 & \frac{1-2\nu}{2} \end{bmatrix}, \tag{F.22}$$

$$\mathbf{L} = \begin{bmatrix} \frac{\partial}{\partial x} & 0 \\ 0 & \frac{\partial}{\partial y} \\ \frac{\partial}{\partial y} & \frac{\partial}{\partial x} \end{bmatrix}, \tag{F.23}$$

The Timoshenko cantilever beam and the infinite plate with a centered hole benchmark problems were solved under plane stress conditions, whereas the Single Edge Notched Tension (SENT) problem was solved assuming plane strain. The Ov-IEFG-FEM performance will be compared to that of solutions entirely based on IEFG or FEM, and accuracy and convergence analyses will be properly conducted by comparison with the corresponding analytical solutions. Convergence for each problem is assessed using a normalized energy norm-based error:

$$E_{\text{norm}} = \sqrt{\frac{\int_\Omega \left(\boldsymbol{\varepsilon}^{\text{Num}} - \boldsymbol{\varepsilon}^{\text{Exact}}\right)^T \mathbf{C}\left(\boldsymbol{\varepsilon}^{\text{Num}} - \boldsymbol{\varepsilon}^{\text{Exact}}\right) \mathrm{d}\Omega}{\int_\Omega \left(\boldsymbol{\varepsilon}^{\text{Exact}}\right)^T \mathbf{C}\,\boldsymbol{\varepsilon}^{\text{Exact}} \mathrm{d}\Omega}}. \tag{F.24}$$

Convergence analyses are conducted using uniform meshes and node distributions for the Timoshenko cantilever beam, whereas non uniform meshes and node distributions are used in the problem concerning the infinite plate with a hole. Regarding the SENT model problem, an analysis on both the stress estimation near the crack tip and determination of the mode-I stress intensity factor K_I will be performed. The convergence rate estimation is

performed in terms of the total number of nodes n, which in the case of the Ov-IEFG-FEM is $n = n_{\text{IEFG}} + n_{\text{FEM}}$. Such a measure is used since it is more convenient to perform an appropriate convergence analysis in the cases of non uniform meshes and nodes distribution, where it is not possible to properly define a unique value for element size or nodal spacing Δl.

Assuming a sufficiently regular solution for the displacements and their first spatial derivatives across Ω, the inverse proportionality between Δl and n allows a straightforward determination of a relationship between the measures of the convergence rates as a function of Δl and n. If the convergence rate as a function of Δl is $E \approx \mathcal{O}(\Delta l^p)$, the convergence rate as a function of N will $E \approx \mathcal{O}\left(N^{-p/d}\right)$ [15, 148, 266]. The parameter d represents the spatial dimension of the problem, so it will be $d = 2$ for the two-dimensional benchmark problems addressed in this communication.

F.3.1. Timoshenko cantilever beam

The Timoshenko cantilever beam will be solved using the dimensions and material properties of the example considered by Liu and Gu [212]. The cantilever beam has a length of $L = 4.8$ m by a width of $D = L/4 = 1.2$ m, the Young's modulus is $E = 3 \times 10^7$ Pa and the Poisson's ratio $\nu = 0.3$. The displacements at the left edge of the beam are restricted to be

$$u_x = -\frac{P(2+\nu)y}{6EI}\left[y^2 - \frac{D^2}{4}\right], \qquad u_y = \frac{P\nu L}{2EI}y^2,$$

whereas the right side is subjected to a parabolic shear load given by

$$t_{xy} = \frac{P}{2I}\left[\frac{D^2}{4} - y^2\right],$$

in order to be aligned with the analytical solution [212]. The total applied load is $P = 100$ N, and the cross-sectional rectangular inertia moment of the beam is $I = D^3/12$ considering unit thickness. The geometry and boundary conditions can be visualized in Fig. F.2. Solutions based on the Ov-IEFG-FEM are computed over structured background meshes and uniform fine distribution of patch nodes located at the left side of the beam, where displacement gradients are expected to be high due to the kinematic restrictions.

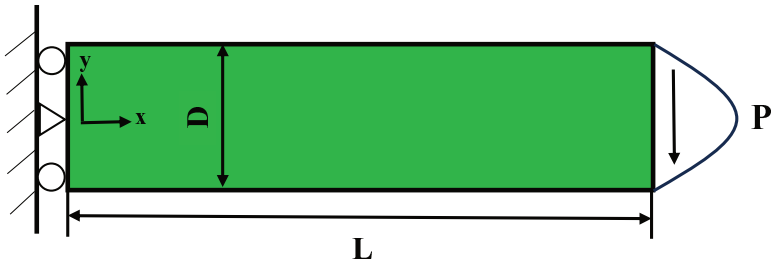

Figura F.2: Representation of geometry and boundary conditions for a cantilever beam.

The solutions performed via the Ov-IEFG-FEM will also be compared to numerical results entirely obtained via standard FEM and IEFG formulations. The problem is solved for increasingly refined meshes for FEM and node distributions for IEFG computations, and some intermediate meshes and node distributions used during such convergence analysis are presented in Fig. F.3 for the solutions performed via FEM, IEFG, and Ov-IEFG-FEM. Solutions obtained through the Ov-IEFG-FEM regarding the distributions of displacement magnitude and σ_{xx} stress component are presented in Figs. F.4 and F.5, respectively.

Fig.F.4 demonstrates that the coupling procedure concerning the Ov-IEFG-FEM allows the nodes representing the patch domain Ω_{IEFG} to deform in unison with the entire problem domain, which is discretized using the FEM mesh. This hybrid mesh-less/mesh-based chimera-type technique has provided a seamless coupling along the transition boundary Γ_{IEFG} not only for the displacement distributions (Fig. F.4), but also for the stress distributions (Fig. F.5) linked to the displacement derivatives according to Eq. (F.2).

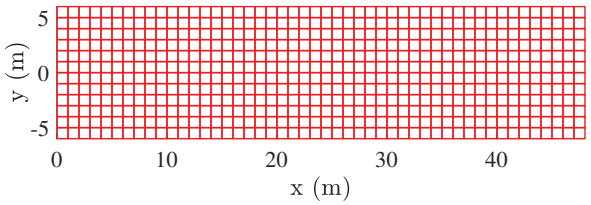

(a) Mesh for FEM-based solution only.

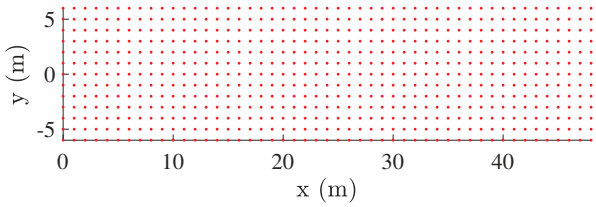

(b) Node distribution for IEFG-based solution only.

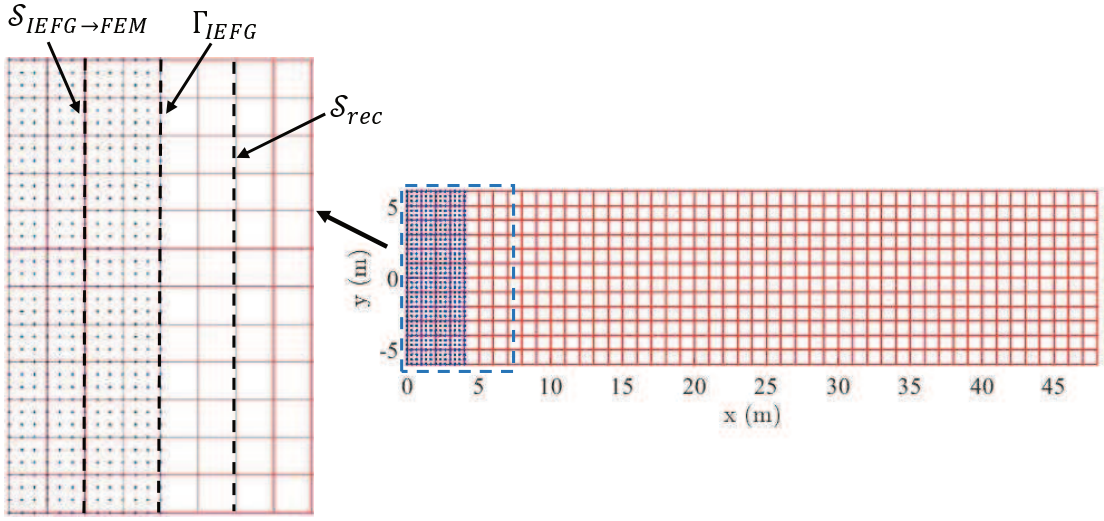

(c) Patch nodes distribution and backgroun mesh for the Ov-IEFG-FEM-based solutions.

Figura F.3: Intermediate meshes and node distributions used in the cantilever beam analysis via (a) FEM, (b) IEFG, and (c) Ov-IEFG-FEM. For the Ov-IEFG-FEM, the patch of nodes and background mesh are depicted in blue and red, respectively. Black dashed lines are used to indicate the immersed contours $\mathcal{S}_{\text{IEFG}\to\text{FEM}}$, $\mathcal{S}_{\text{rec}}$, and also the bounday Γ_{IEFG} of the patch domain Ω_{IEFG}. The displacements $\tilde{\mathbf{U}}_{\text{FEM}}$ are imposed on Γ_{IEFG} by integration via the penalty method, whereas $\tilde{\mathbf{U}}_{\text{FEM}}$ are imposed at nodes $h \in \mathcal{N}_{\text{enc}}$ enclosed by $\mathcal{S}_{\text{IEFG}\to\text{FEM}}$.

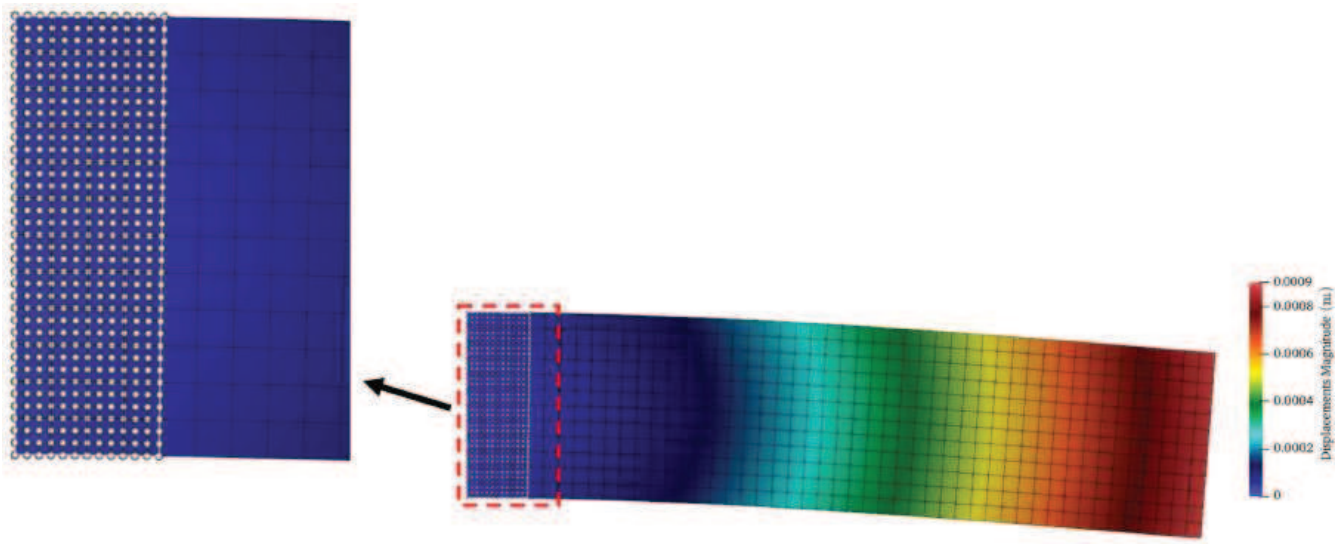

Figura F.4: Displacement magnitude by the proposed Ov-IEFG-FEM method for the cantilever beam.

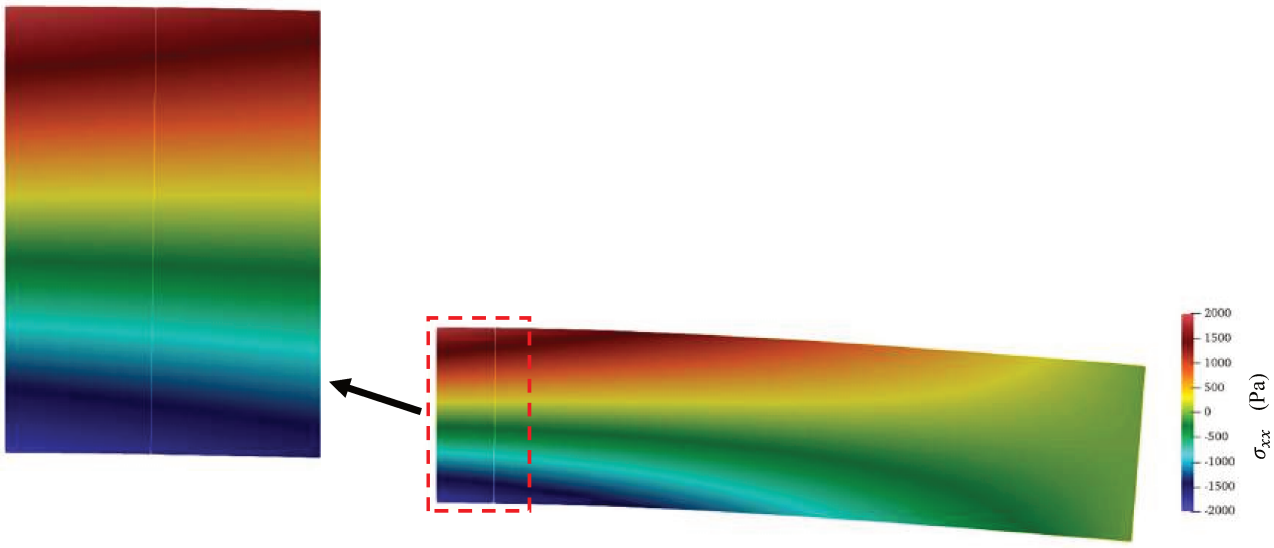

Figura F.5: Stress distribution σ_{xx} by the proposed Ov-IEFG-FEM method for the cantilever beam in its deformed condition.

The convergence attained with Ov-IEFG-FEM for this benchmark problem is depicted in Fig. F.6, and compared to that of solutions obtained solely through standard FEM and IEFG techniques. The Ov-IEFG-FEM with the patch domain Ω_{IEFG} placed in the region near the clamped boundary has allowed the achievement of a convergence rate of $E_{\text{norm}} \approx \mathcal{O}(N^{-0.69}) \approx \mathcal{O}(\Delta l^{1.38})$, which falls between those of the solutions purely based on FEM ($E_{\text{norm}} \approx \mathcal{O}(\Delta l^{1.04})$) and IEFG ($E_{\text{norm}} \approx \mathcal{O}(\Delta l^{1.54})$).

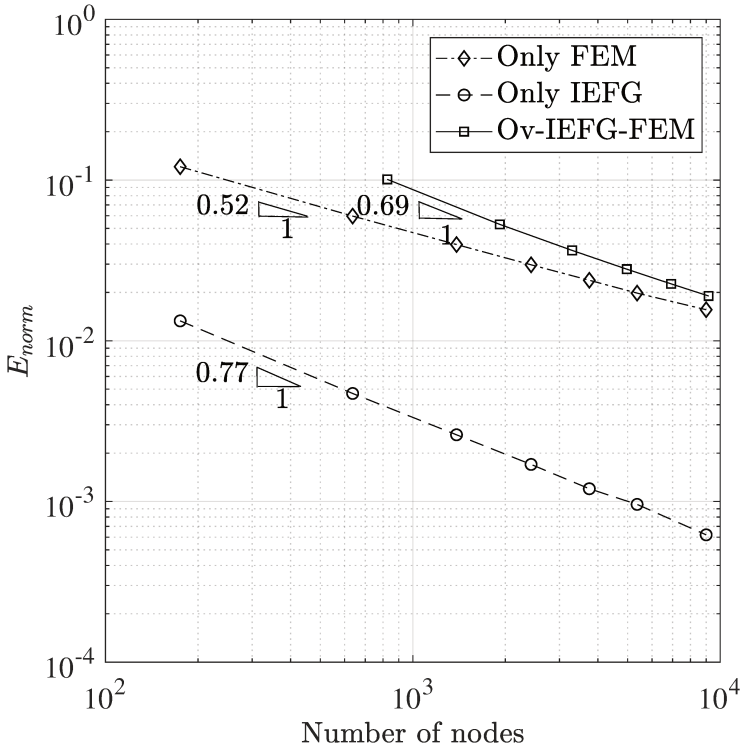

Figura F.6: Convergence behavior of FEM, IEFG, and the proposed Ov-IEFG-FEM for the cantilever beam.

F.3.2. Infinite plate with a centered hole.

This problem involves an infinite plate with a centered hole of radius R, as schematized in Fig. F.7 (a). The plate is subjected to a uniformly distributed horizontal surface traction $\sigma_{xx}|_{\infty} = T = 1000$ Pa at $x = \infty$. The mechanical properties used are: Young's modulus is $E = 210$ GPa and the Poisson's ratio $\nu = 0.3$. The exact solutions for the stress field in this problem is given by as follows[320]:

$$\sigma_{xx} = T\left\{1 - \frac{R^2}{r^2}\left[\frac{3}{2}\cos(2\theta) + \cos(4\theta)\right] + \frac{3a^4}{2r^4}\cos(4\theta)\right\} \tag{F.25}$$

$$\sigma_{yy} = -T\left\{\frac{R^2}{r^2}\left[\frac{1}{2}\cos(2\theta) - \cos(4\theta)\right] + \frac{3a^4}{2r^4}\cos(4\theta)\right\} \tag{F.26}$$

$$\tau_{xy} = -T\left\{\frac{R^2}{r^2}\left[\frac{1}{2}\sin(2\theta) + \sin(4\theta)\right] - \frac{3a^4}{2r^4}\sin(4\theta)\right\}, \tag{F.27}$$

where the cartesian stress components have been expressed in terms of the polar coordinates for the purpose of mathematical conciseness in which: $r = \sqrt{x^2 + y^2}$, $\theta = \tan^{-1}\left(\frac{y}{x}\right)$.

Due to the symmetry of this benchmark problem, the solutions were carried out using only the top-right quarter of the plate. This quarter has finite dimensions of 10×10 m×m with a hole radius of $R = 1$ m. It is constrained with displacements $u_x = 0$ along the $x = 0$ axis and $u_y = 0$ along the $y = 0$ axis. As depicted in Fig. F.7 (b), the surface loads for the numerical solution have been prescribed according to $(21) - (23)$ to properly reproduce the behavior of the infinite plate subjected to the uniform remote surface traction.

Contrary to the numerical solutions performed for the Timoshenko cantilever beam benchmark problem via the Ov-IEFG-FEM, both the background meshes used to discretize Ω_{FEM} and the node distributions used to represent the patch domain Ω_{IEFG} are non-uniform in the current benchmark problem. Since marked stress concentrations are expected to arise near the plate hole, the patch domain Ω_{IEFG} has been allocated to enrich the numerical solutions in such region.

Solutions purely based on standard FEM and IEFG techniques are also compared to the numerical results obtained via the Ov-IEFG-FEM. Also in this case, the convergence analysis has been performed using increasingly refined meshes for FEM and nodes distributions for IEFG computations. Some of the intermediate meshes and node distributions used in the convergence analysis of the FEM, IEFG, and Ov-IEFG-FEM in the current benchmark problem are shown in Fig. F.8. The distributions of displacement magnitude and the σ_{xx} stress component in the plate are depicted in Figs. F.9 and F.10, respectively.

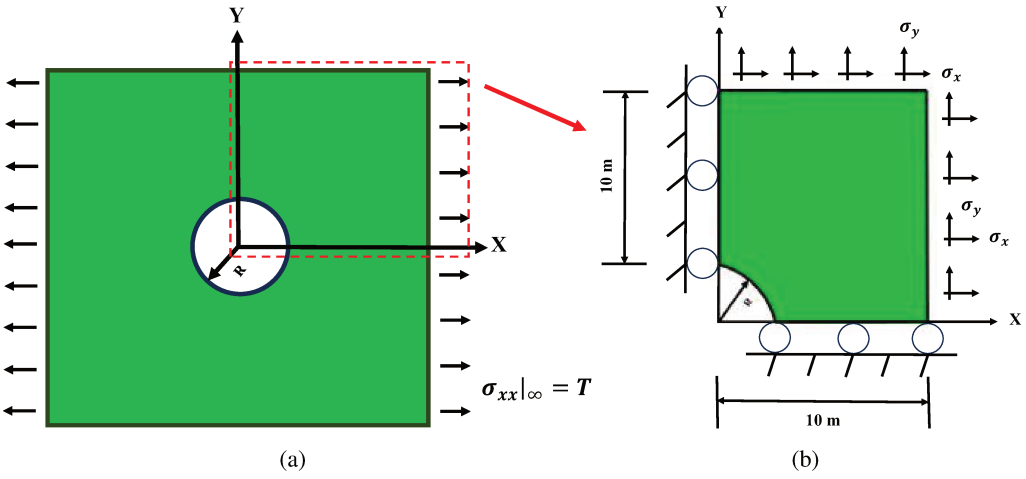

Figura F.7: Representation of geometry and boundary conditions for an infinite plate with a centered hole.

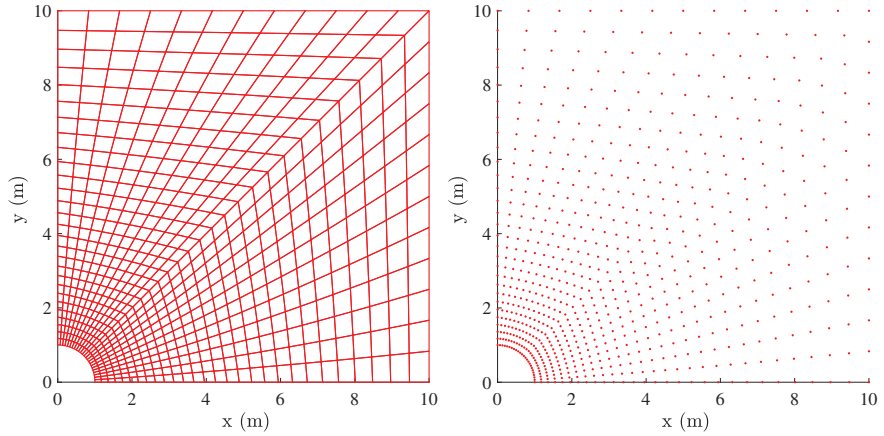

(a) FEM mesh.

(b) IEFG nodes distribution.

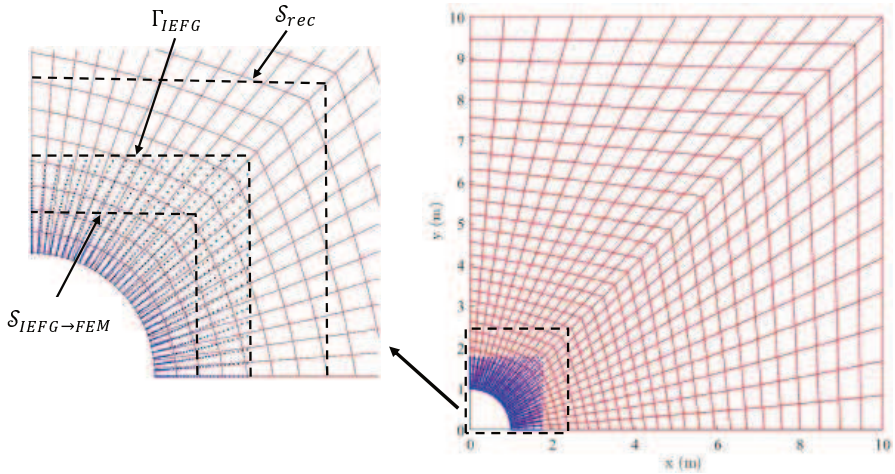

(c) Patch of nodes (blue) and background mesh used in Ov-IEFG-FEM.

Figura F.8: Intermediate meshes and node distributions used in the convergence analysis for an infinite plate with a hole in the center.

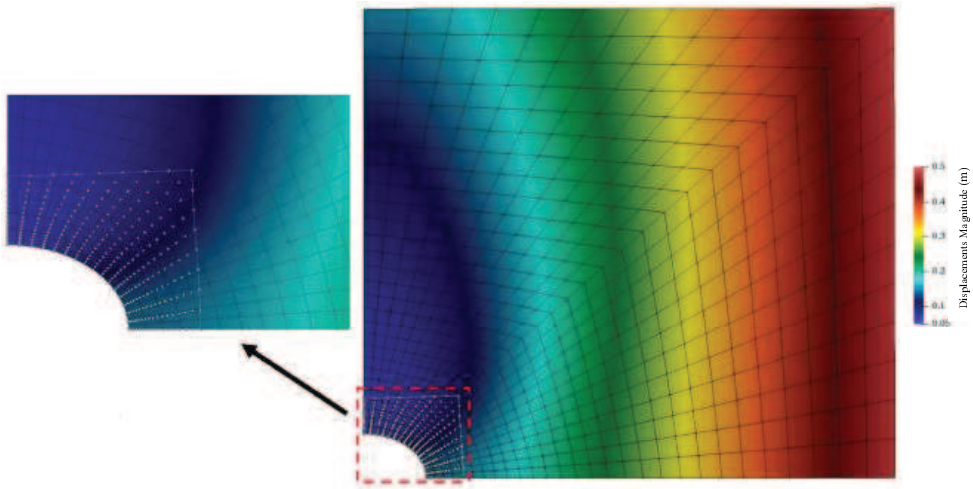

Figura F.9: Displacement magnitude using the proposed Ov-IEFG-FEM method for an infinite plate with a hole at the center in its deformed condition.

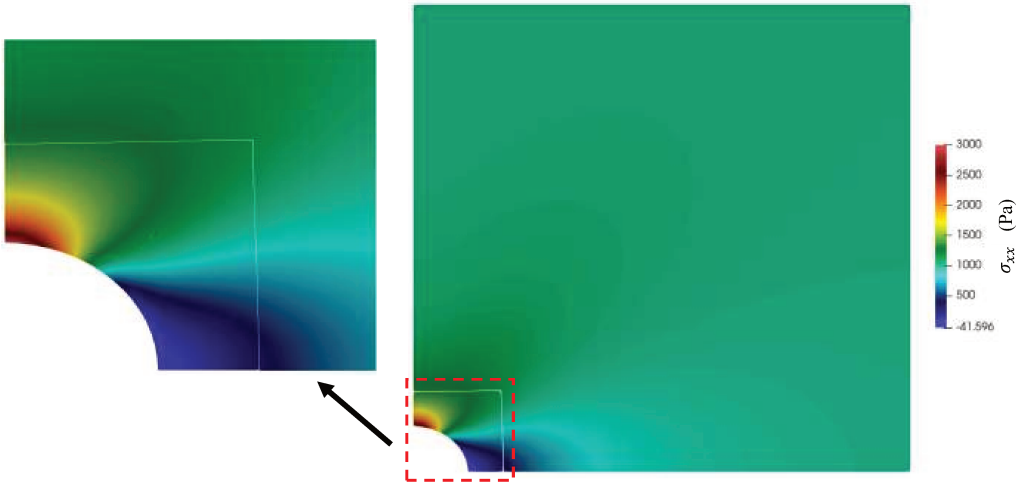

Figura F.10: Distribution of the σ_{xx} stress component achieved via the proposed Ov-IEFG-FEM for the infinite plate with a centered hole benchmark problem.

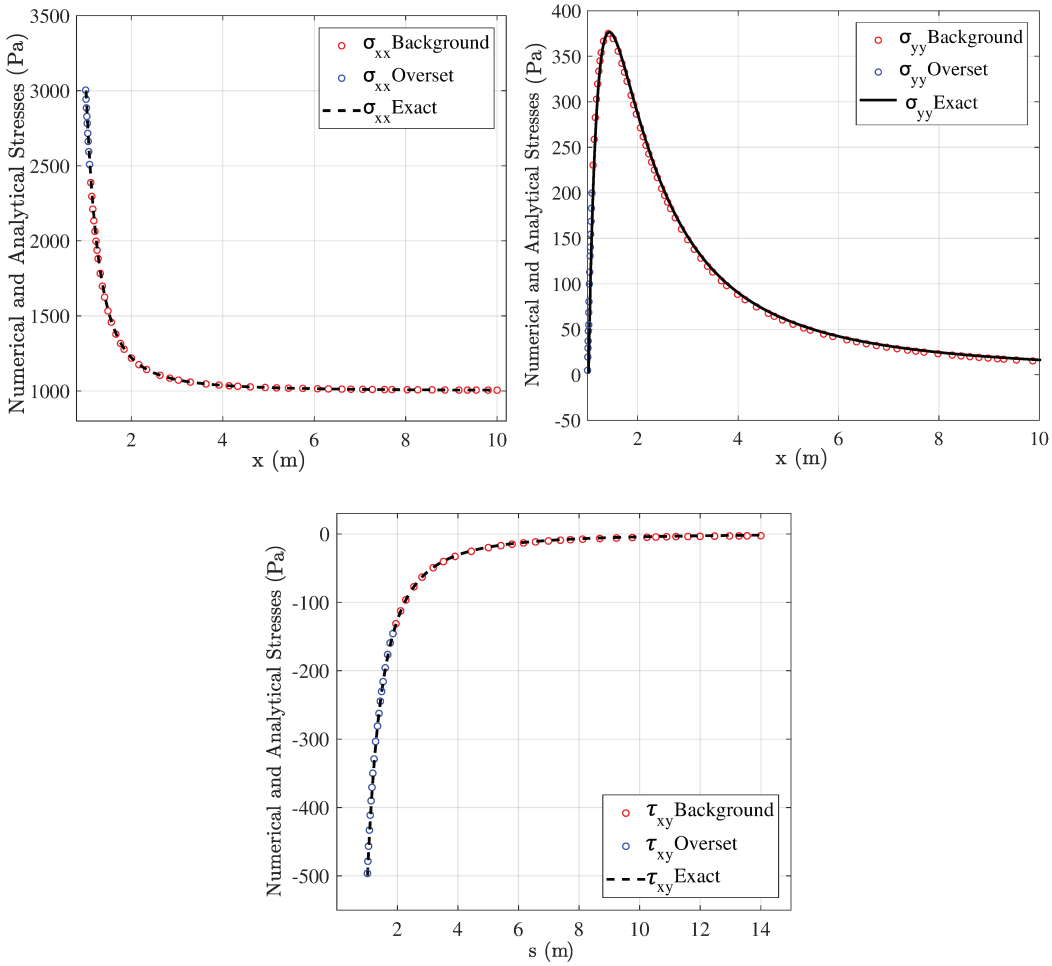

Figura F.11: σ_{xx} and σ_{yy} stress components computed via the Ov-IEFG-FEM along the horizontal line $(x, 0)$, and τ_{xy} stress component computed along the arc length s of a diagonal 45º line. For comparison, the numerical results have been plotted over the analytical solution.

Also in this case, it is evident that the Ov-IEFG-FEM has allowed a unison deformation between the FEM background mesh extended over the entire plate and the nodes representing the patch domain Ω_{IEFG}. Moreover, it allowed a straightforward achievement of a seamless coupling between the FEM and IEFG regions along the transition boundary Γ_{IEFG} for both displacements (Fig. F.9) and stresses (Fig. F.10). The numerical results obtained via the Ov-IEFG-FEM also exhibit an excellent agreement with the exact solution, as visualized in the plots given in Fig.F.11 for the σ_{xx} and σ_{yy} stress components computed along the horizontal line $(x, 0)$ and τ_{xy} stress component computed along the 45º line. Such outcome now further confirms the significant potential of the proposed approach to achieve accurate results in a remarkably simple manner, via the enrichment provided by the higher-order IEFG computations performed in Ω_{IEFG}. The convergence behavior obtained using the Ov-IEFG-FEM in this problem is observed in Fig. F.12, which is compared with those corresponding to standard FEM and IEFG technique. It is evident that the IEFG-based enrichment in the patch domain Ω_{IEFG} positioned near the hole at the plate center has allowed the Ov-IEFG-FEM to achieve a convergence rate of $E_{\text{norm}} \approx \mathcal{O}(N^{-0.64}) \approx \mathcal{O}(\Delta l^{1.28})$, which clearly exceeds that of the standard FEM ($E_{\text{norm}} \approx \mathcal{O}(\Delta l^{0.98})$) and closely matches that of IEFG technique ($E_{\text{norm}} \approx \mathcal{O}(\Delta l^{1.32})$).

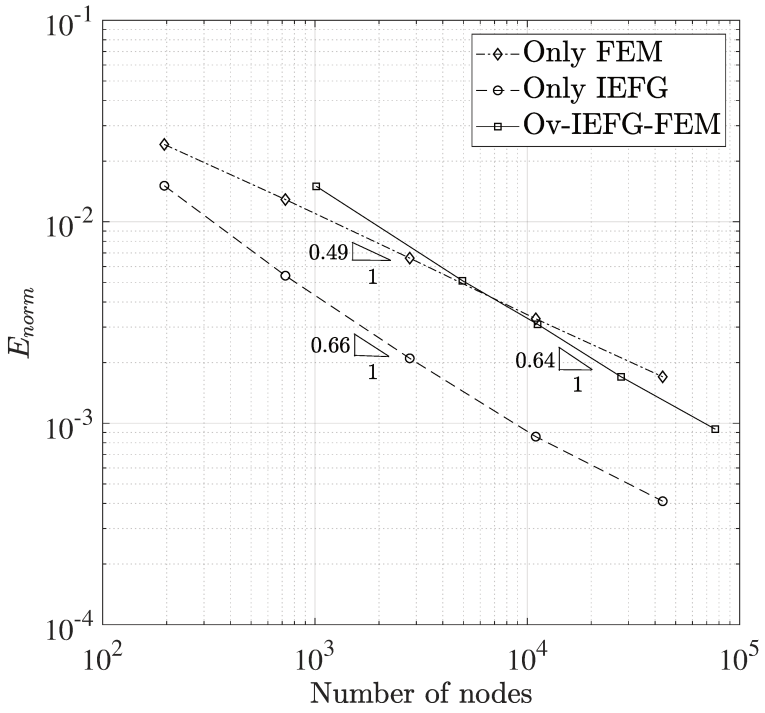

Figura F.12: Convergence behavior of FEM, IEFG, and the proposed Ov-IEFG-FEM for an infinite plate with a hole at the center.

F.3.3. Single Edge Notched Tension (SENT) Specimen.

The geometry of this problem is a SENT type specimen of dimensions $L = 0.2$ m height by $b = 0.05$ m width, with a predefined horizontal crack of 0.025 m. The Young's modulus and Poisson's ratio are $E = 5.5$ GPa and $\nu = 0.25$, respectively. The specimen is subjected to a remote uniform surface traction $P = 100$ MPa at the top edge of the geometry, as shown in Fig.F.13.

Due to the test symmetry, the problem is modeled considering only half of the specimen. Therefore, the computational domain used in the numerical tests has finite dimensions of 0.05×0.1 m$\times$m. Half of the bottom edge is constrained vertically to emulate a crack length and in the lower right corner is kinematically constrained to avoid rigid body motions. Similar to the numerical solutions performed for the infinite plate with a centered hole benchmark problem, both meshes concerning the FEM-based computations and the node distributions used to implement the IEFG technique are non-uniform. The solutions based on the Ov-IEFG-FEM have been performed using a mixed background mesh consisting in a coarse unstructured discretization that gradually transitions into a structured and moderately refined mesh towards the lower boundary of the domain, whereas the patch domain Ω_{IEFG} is repre-

sented with a fine distribution of nodes properly located and exponentially clustered towards the crack tip.

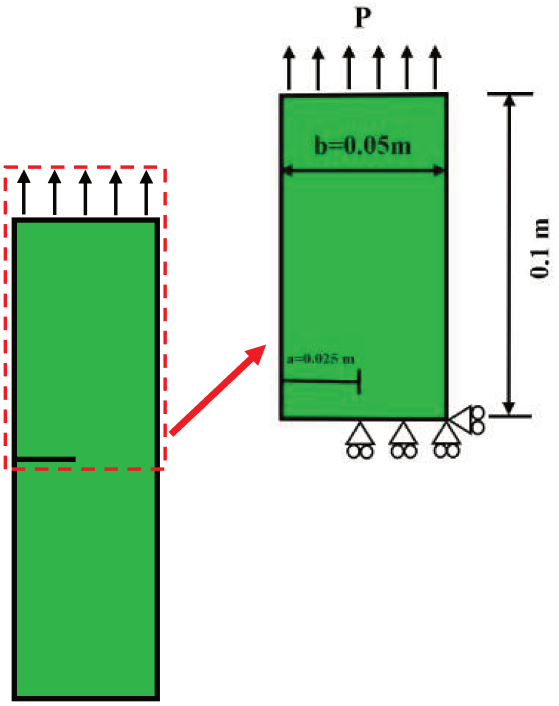

Figura F.13: Representation of geometry and boundary conditions for a Single Edge Notched Tension (SENT) specimen.

These settings for the mesh discretizing Ω_{FEM} and the patch nodes representing Ω_{IEFG} have been used to fulfill the immersed boundaries distance criteria explained at the end of section 2 without resulting in an excessively large size of Ω_{IEFG}, which would hinder the effective use of the potential inherent in the higher order approximations of the IEFG technique to capture the unbounded stresses towards the crack tip. Also in this case, numerical solutions purely based on standard FEM and IEFG procedures are compared to the results obtained via Ov-IEFG-FEM. As depicted in Fig.F.14 (a)-(b), the meshes and node distributions used in the solutions performed via the standard FEM and IEFG techniques are mostly unstructured with a gradual transition to a structured small rectangle enclosing the crack tip.

This particularly small region is subjected to the same refinement of the patch domain Ω_{IEFG} used in the solutions obtained via the Ov-IEFG-FEM, in order to achieve a fair comparison. This is because it allows the standard FEM and IEFG techniques to maintain the same average mesh size and nodal spacing near the crack tip as in the Ov-IEFG-FEM solutions, with a similar number of nodes across the entire problem domain. Some intermediate meshes and node distributions used in the numerical solutions obtained via FEM, IEFG and Ov-IEFG-FEM for this problem are shown in Fig.F.14. The distributions of displacement magnitude and σ_{yy} stress component for this problem are illustrated in Figs. F.15 and F.16, respectively.

Also in this singular problem, the Ov-IEFG-FEM has allowed a unison deformation of the FEM background mesh extended throughout the entire geometry with the nodes representing the patch domain Ω_{IEFG} in the crack tip region. Consistently, a smooth coupling between the FEM and IEFG regions along the transition boundary Γ_{IEFG} has also been achieved. The numerical results obtained via the Ov-IEFG-FEM show a good agreement with the reference solution developed by Tada [1], as illustrated in the plot of Fig. F.17 for the different stress components near the crack tip.

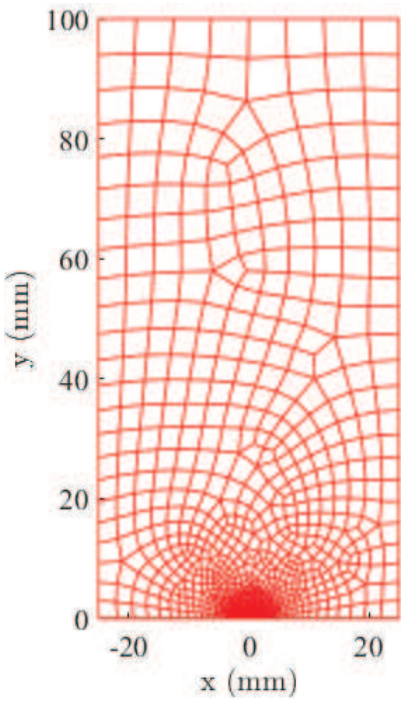

(a) FEM mesh.

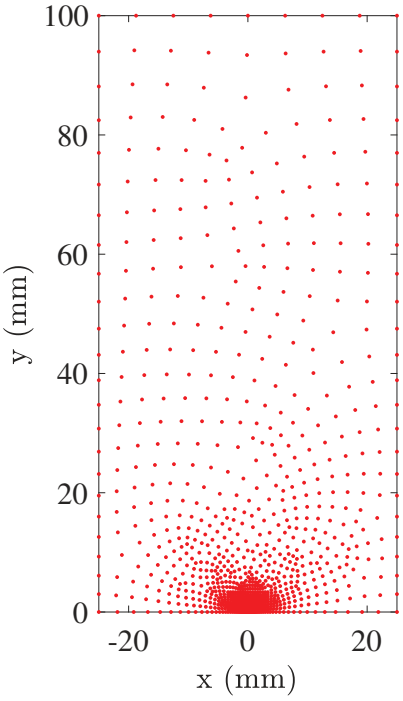

(b) IEFG nodes distribution.

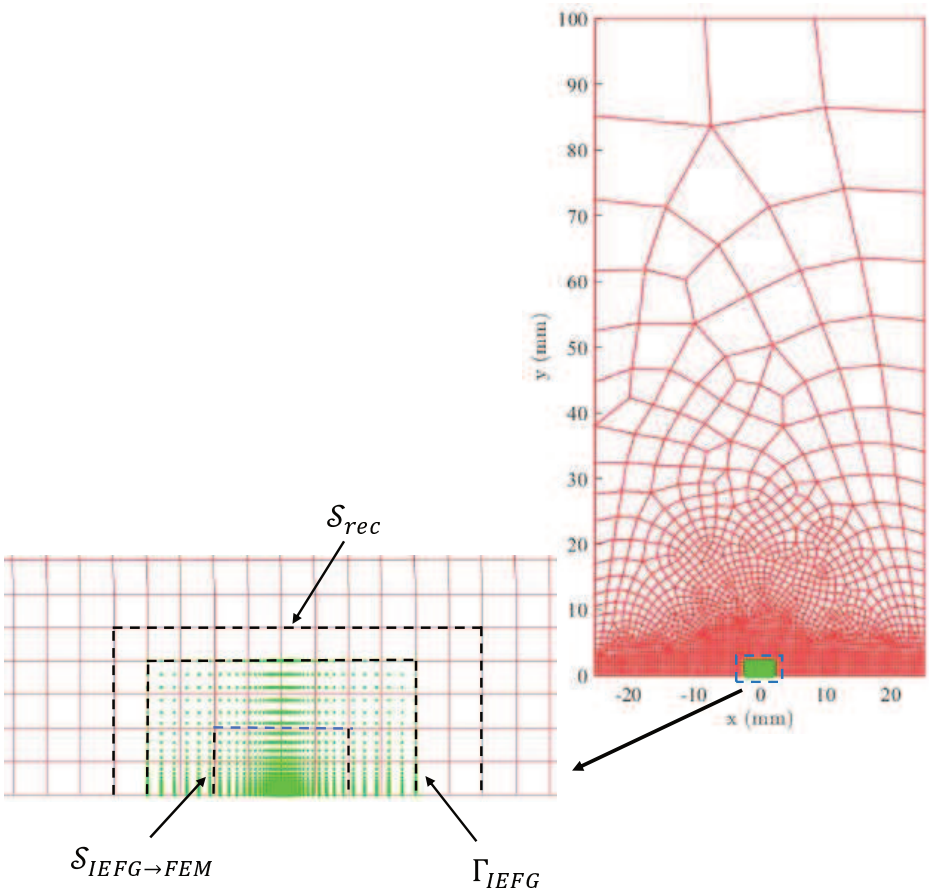

(c) Patch of nodes (green) and background mesh used in Ov-IEFG-FEM.

Figura F.14: Meshes and node distributions used in the analysis of the SENT specimen.

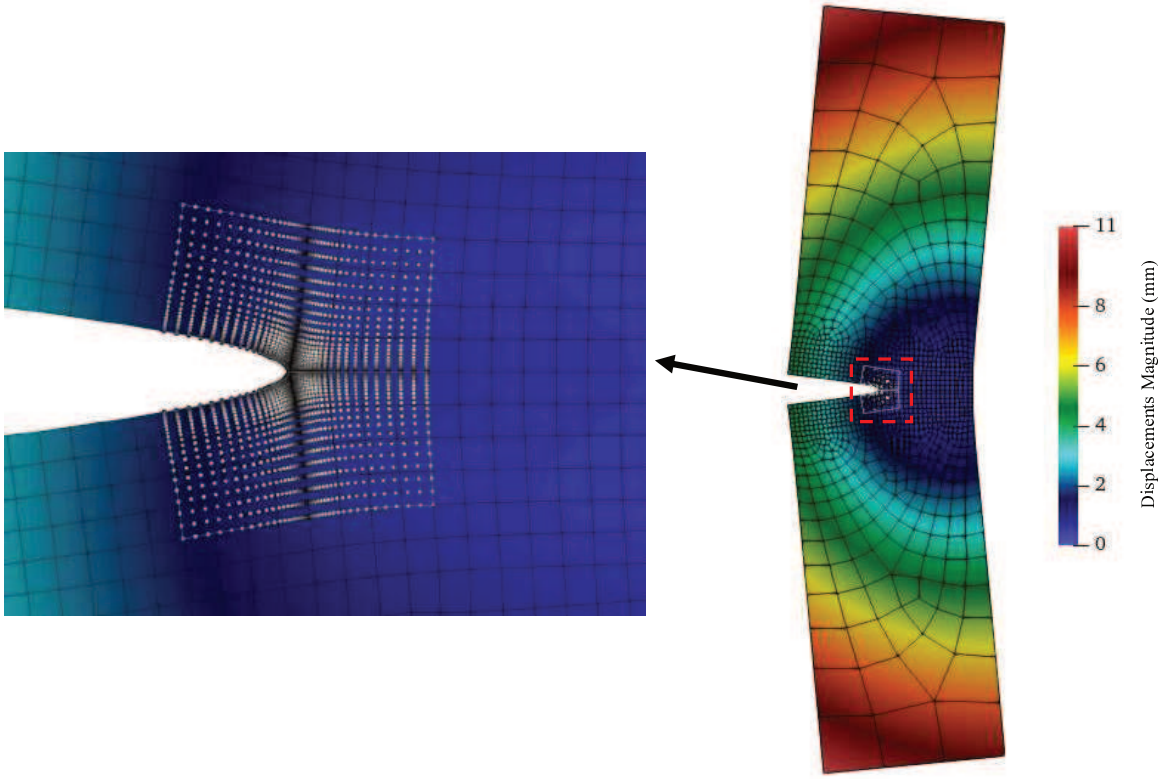

Figura F.15: Displacement magnitude using the proposed Ov-IEFG-FEM method for a SENT specimen.

These results demonstrate the Ov-IEFG-FEM potential to achieve accurate results in a straightforward manner, via properly allocated IEFG computations performed in the patch domain Ω_{IEFG} encompassing the crack tip. Numerical computations of the mode-I stress intensity factor K_I were also performed via the proposed Ov-IEFG-FEM, and compared to those achieved using standard FEM and IEFG techniques. The numerical computation of K_I was performed via the area J-integral of Moran and Shih [321], which is a common practice to ensure an accurate computation of stress intensity factors in the framework of numerical solutions based on both FEM and IEFG [107, 281]. The K_I reference formula developed by Tada [1] is:

$$K_I^{\text{ref}} = P\sqrt{b}\,F(a/b), \quad \text{and} \quad F(a/b) = \sqrt{\frac{2b}{\pi a}\tan\left(\frac{\pi a}{2b}\right)}\,\frac{0.752 + 2.02(a/b) + 0.37\left[1 - \sin\left(\frac{\pi a}{2b}\right)\right]^3}{\cos\left(\frac{\pi a}{2b}\right)}. \tag{F.28}$$

Further discussion about this formula can be found in [322] and references therein. The results obtained along with the CPU times required for each simulation are summarized in Table F.1. In this communication, the entire set of numerical solutions have been performed using a desktop computer with an AMD Ryzen 9 5900X 12-Cores processor. The standard IEFG-based solutions markedly surpass the accuracy of the FEM, which is an aspect thoroughly reported and demonstrated in the literature [15, 212, 279]. The Ov-IEFG-FEM exhibits a great potential on confining the higher-order computations of the IEFG technique to the region of interest Ω_{IEFG} encompassing the crack tip, thereby providing improved accuracy without the resorting to unnecessary and computationally expensive IMLS approximations throughout the entire problem domain.

A complementary study was conducted by varying the crack depth of the SENT specimen, with K_I computed for each change in crack length. The numerical solutions for K_I were obtained using an intermediate-level discretization, consisting of a coarse FEM background mesh with 581 nodes discretizing Ω_{FEM} and a radial node distribution concentrated towards the crack tip with 124 nodes representing the patch domain Ω_{IEFG}. Simulations were performed in two cases: the first using a structured coarse mesh background, and the second using a distorted coarse mesh background to observe potential perturbations in K_I computation.

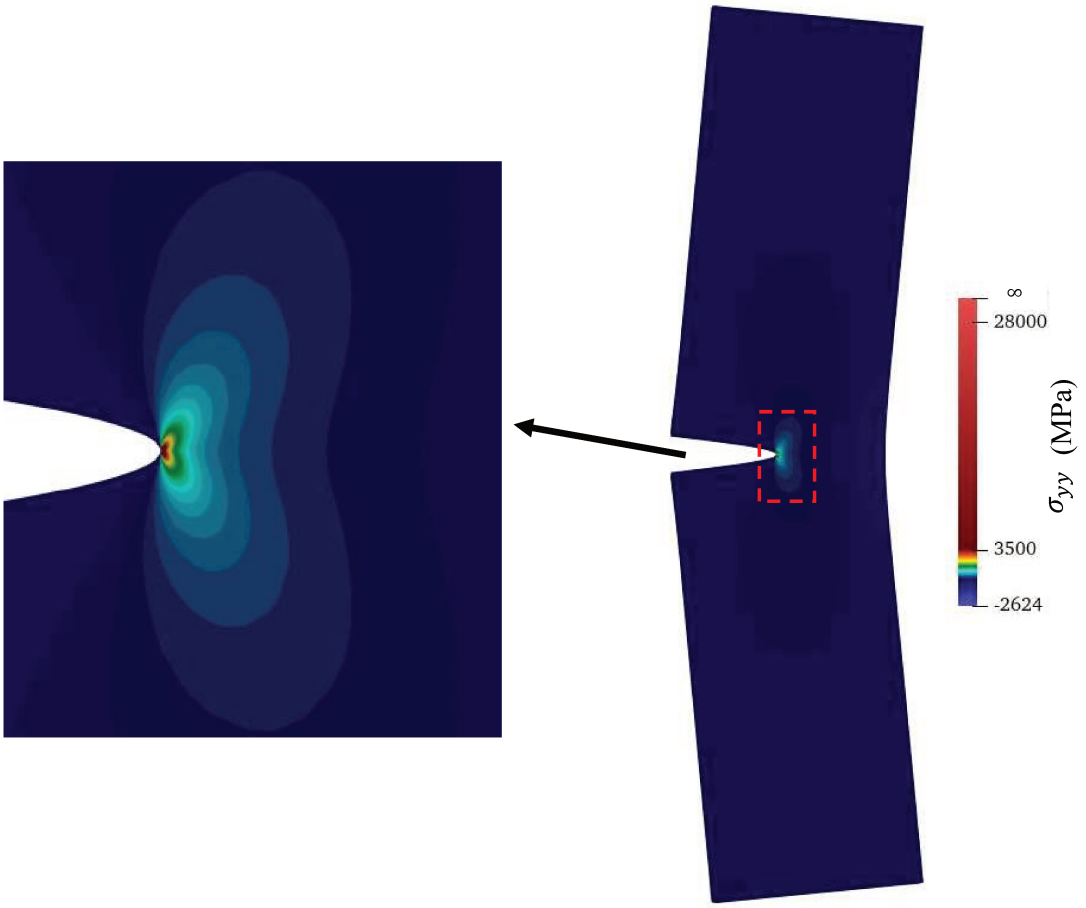

Figura F.16: σ_{yy} stress distribution using the proposed Ov-IEFG-FEM method for a SENT specimen in its deformed condition.

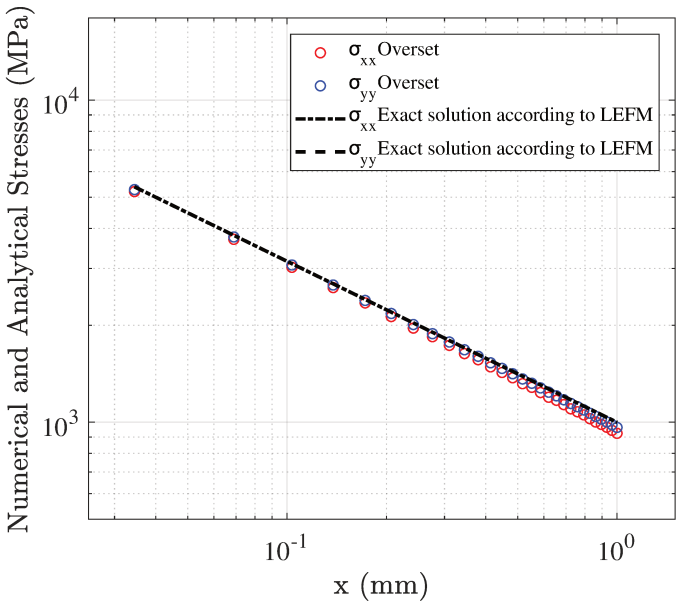

Figura F.17: Comparison of the numerical solutions obtained via the Ov-IEFG-FEM with the reference solution developed by Tada[1]

Tabla F.1: Normalized comparison of K_I values for each of the implemented methods (FEM, IEFG and Ov-IEFG-FEM) and demanded CPU times.

FEM			IEFG			Ov-IEFG-FEM		
Nodes	${K_I}^{num}/{K_I}^{ref}$	CPU time (sec)	Nodes	${K_I}^{num}/{K_I}^{ref}$	CPU time (sec)	Nodes $n_{\text{FEM}}+n_{\text{IEFG}}$	${K_I}^{num}/{K_I}^{ref}$	CPU time (sec)
749	0.994	0.015	749	0.997	2.499	$\underset{581+213}{812}$	0.993	1.090
1166	0.995	0.022	1166	0.997	2.643	$\underset{581+496}{1077}$	0.995	1.221
1425	0.995	0.024	1425	0.998	3.222	$\underset{907+496}{1403}$	0.999	1.412
1798	0.995	0.027	1798	0.999	3.357	$\underset{293+1326}{1619}$	0.999	1.864
1922	0.996	0.030	1922	1.000	3.628	$\underset{907+861}{1768}$	1.000	1.992
6252	0.996	0.091	-	-	-	-	-	-
17553	0.996	0.191	-	-	-	-	-	-
35102	0.996	0.438	-	-	-	-	-	-
89334	0.997	1.245	-	-	-	-	-	-
209174	0.998	3.201	-	-	-	-	-	-

The calculation of K_I was performed by varying the crack depth on the horizontal axis, starting from a distance of 0.005 m up to a final distance of 0.045 m. The stress distribution σ_{yy} for both cases and two crack lengths are shown in Figs. F.18 and F.19. The results for K_I obtained from both the reference solution [1] and the numerical solutions via the Ov-IEFG-FEM for the two studied cases, can be observed in Fig. F.20. The results obtained in this complementary test have also exhibited the achievement of a seamless $\Omega_{\text{FEM}} - \Omega_{\text{IEFG}}$ coupling, together with an accurate computation of K_I for different crack lengths. The positive features of accuracy and seamless coupling between overlapping domains have been kept also in the case of the distorted background mesh.

F.4. Discussion

The results obtained using the Ov-IEFG-FEM proposed in this work demonstrate effectiveness in solving linear elastic problems, allowing for a seamless coupling between the FEM computations in Ω_{FEM} and the IEFG higher order approximations performed in the patch domain Ω_{IEFG} for accuracy enrichment purposes. The noteworthy potential of the Ov-IEFG-FEM has been demonstrated in the context of increasingly complex benchmark problems, demonstrating the versatility to adequately solve problems in different geometries without the need for a prescribed topological relationship between the overlapping domains. Although the Ω_{FEM}-Ω_{IEFG} coupling is performed in terms of displacements, the solutions achieved via the Ov-IEFG-FEM have also exhibited a seamless coupling in the stress distributions linked to the displacement spatial derivatives by (F.2). Since the spatial derivatives of the FEM-based computations are inherently discontinuous, the seamless and continuous stress distributions throughout the entire problem domain has been computed in all the benchmark problems as

$$\bar{\boldsymbol{\sigma}} = \mathbf{CLu} = \begin{cases} \mathbf{C}\displaystyle\sum_{I=1}^{n_{\text{rec}}} \mathbf{B}_{\text{rec}}^{(I)} \tilde{\mathbf{u}}_{\text{rec}}^{(I)} & \text{in} \quad \Omega_{\text{FEM}} - \Omega_{\text{IEFG}} \\ \mathbf{C}\displaystyle\sum_{I=1}^{n_{\text{IEFG}}} \mathbf{B}_{\text{IEFG}}^{(I)} \tilde{\mathbf{u}}_{\text{IEFG}}^{(I)} & \text{in} \quad \Omega_{\text{IEFG}}, \end{cases} \tag{F.29}$$

This distinguishes it from overset techniques developed over mesh-based methods, since the discontinuous approximations of the spatial derivatives at the element level hinder a continuous coupling between stresses and strains computed in both the background and patch meshes. This problem is often addressed by creating a final global enriched solution on a single mesh reconstructed from the background and overlapping meshes, which involves replacing the overlapping regions with unstructured meshes.

The reconstructed mesh retains the nodal values of the original elements outside the reconstruction, and the

enriched study variables are computed by performing the spatial derivatives of these variables on this single mesh [148, 149, 266].

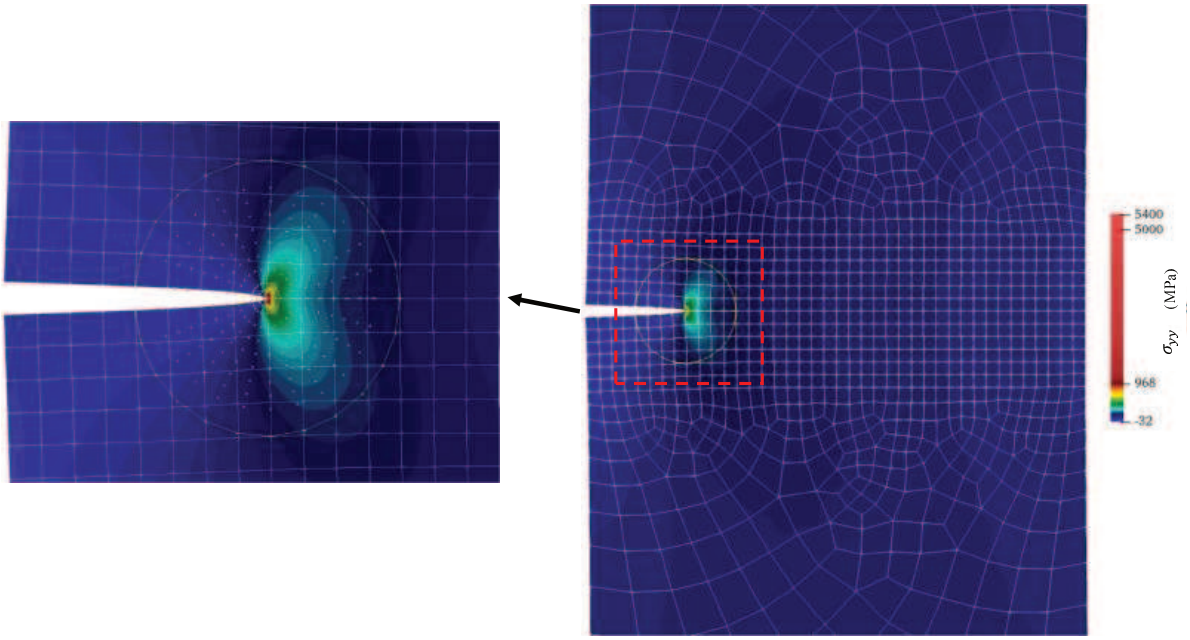

(a) 10 mm

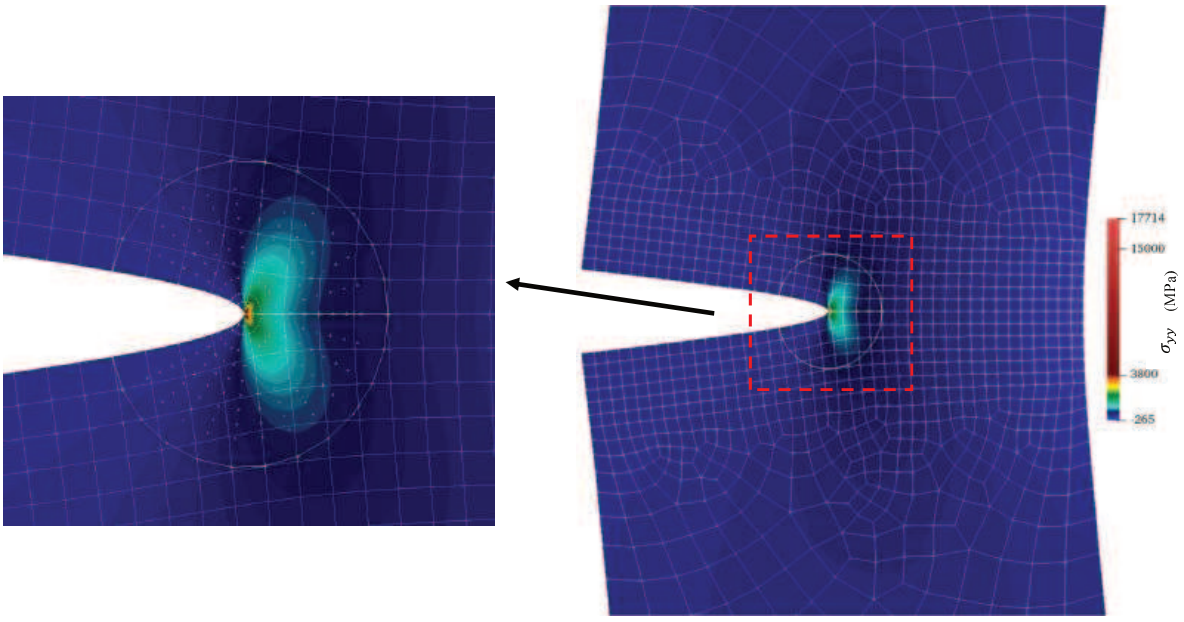

(b) 25 mm

Figura F.18: σ_{yy} stress distribution for SENT specimen with structured background mesh for different crack lengths.

In the benchmark problems concerning the Timoshenko cantilever beam and infinite plate with a centered hole, the convergence rate of the proposed Ov-IEFG-FEM has exceeded that corresponding to the solutions performed via standard FEM computations. Moreover, such convergence rates clearly exhibited a trend to approach that corresponding to the solutions entirely based on the IEFG technique.

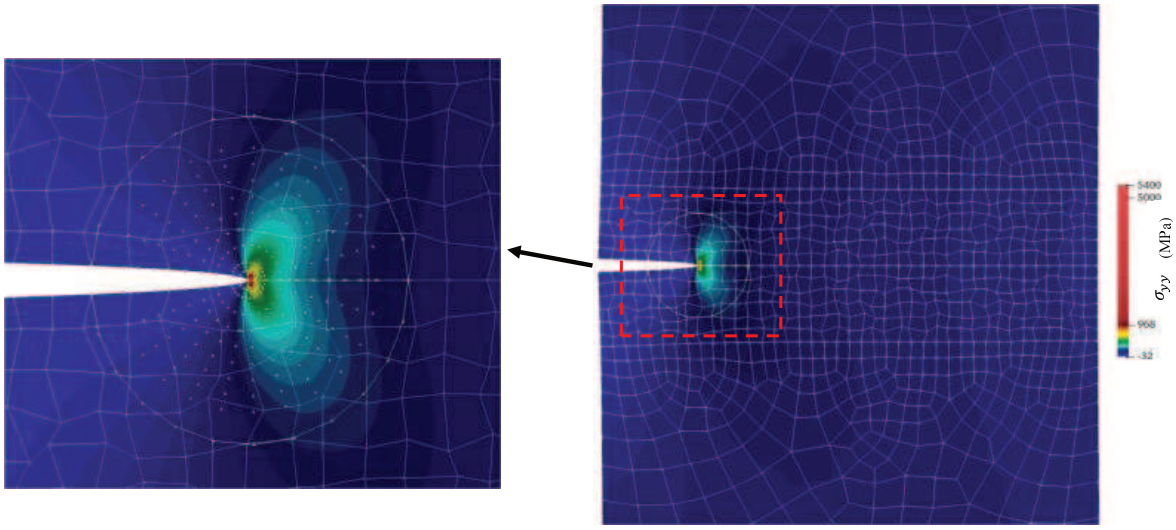

(a) 10 mm

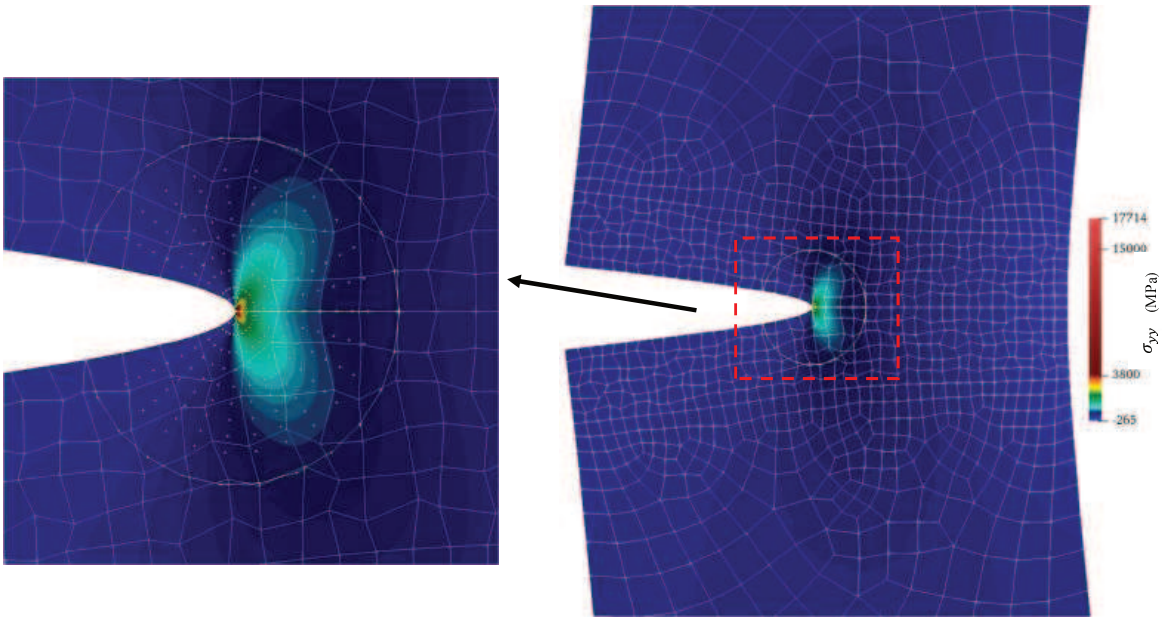

(b) 25 mm

Figura F.19: σ_{yy} stress distribution for SENT specimen with distorted background mesh for different crack lengths.

Although the convergence rate achieved via the Ov-IEFG-FEM in the Timoshenko cantilever beam benchmark problem has surpassed that of the standard FEM-based solutions, it has not come close enough to that of the IEFG. Locating the patch domain Ω_{IEFG} in the region where high displacement gradients were expected (near the clamped boundary) has improved the convergence rate compared to the FEM, but it did not provide an improvement in the overall accuracy compared to the standard numerical solutions entirely based on either FEM or IEFG. This aspect is outlined in Fig. F.6, where the convergence line corresponding to the Ov-IEFG-FEM entails a larger error compared with the solutions purely based on FEM or IEFG. Even though the displacement gradients in the rest of the domain are less pronounced compared to the region near the clamped boundary, they are still significant so that their effect on the accuracy of the numerical solutions remains relevant. There is no region within the domain that contributes significantly more to the numerical error compared to the rest of the domain. When using a solution based solely on IEFG throughout the entire domain, its high-order interpolation is utilized effectively, resulting in a convergence line that is notably lower than those of pure FEM and Ov-IEFG-FEM in Fig. F.6. On the other hand, because there

is no specific region that significantly dominates the error, employing IEFG only in the clamped region under the Ov-IEFG-FEM scheme causes the numerical accuracy in most of the domain to be influenced by the interpolation characteristics of FEM. Consequently, the overall error of the Ov-IEFG-FEM remains at the same order as the solution entirely based on FEM, with a slight increase due to the additional error introduced in the coupling region (see error norm in the pseudocode of the iterative coupling algorithm explained in Section 2.3.). This also explains the convergence rate of the Ov-IEFG-FEM falling between that of standard solutions completely based on FEM and IEFG. There is a small region of marked gradients governed by the IEFG solution, which is coupled to a larger region with less pronounced but still significant gradients, where the approximations are instead governed by the FEM.

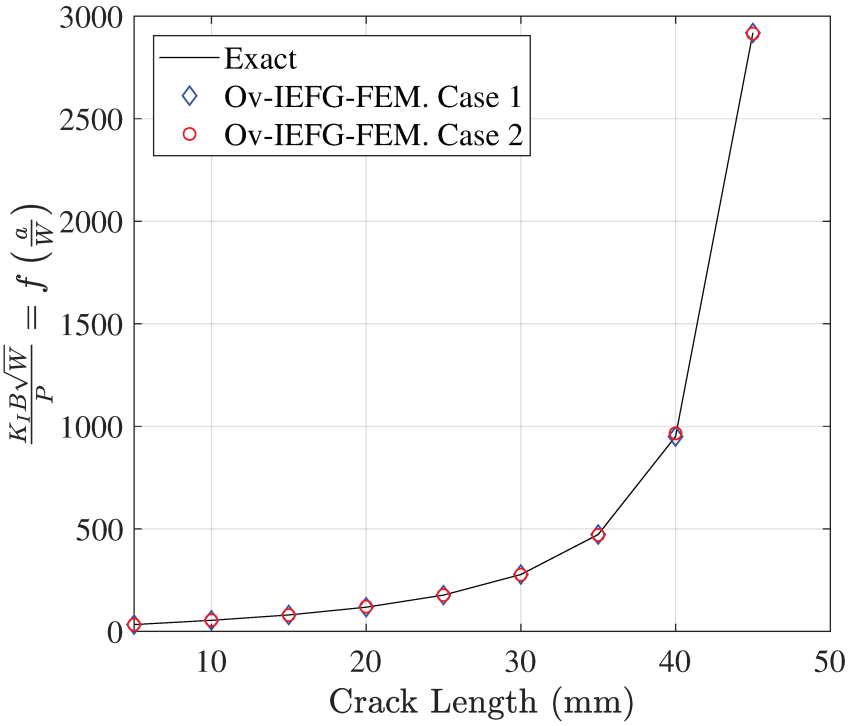

Figura F.20: Comparison of K_I values between reference solution [1] and the proposed Ov-IEFG-FEM for case 1: Structured FEM background mesh and case 2: Distorted FEM background mesh.

For the problem concerning the infinite plate with a centered hole, the situation is different and more favorable for implementing the Ov-IEFG-FEM. The error in this particular case is mainly governed by the marked stress gradients near the plate hole, exhibiting a clear trend towards a virtually uniform stress distribution far from the hole region. This allows the achievement of a convergence rate under the Ov-IEFG-FEM not only clearly surpassing that of the purely FEM-based solution, but also virtually matching that of the computations entirely performed via the IEFG technique. This outcome highlights that the specific features of this problem allowed the Ov-IEFG-FEM to effectively leverage the node refinement flexibility and higher order approximations of the IEFG technique only within the region of interest Ω_{IEFG}. As a result, despite a significant portion of the computational domain being solved by FEM, convergence rates are comparable to those of purely IEFG-based solutions. The discussed aspects indicate that the implementation of Ov-IEFG-FEM is advantageous in problems with regions of particularly pronounced or elevated stress gradients, such as the infinite plate with a centered hole, whereas it may not be beneficial in problems lacking these characteristics, such as the cantilever beam.

The features of the SENT problem make it ideal for the implementation of the Ov-IEFG-FEM, and the results achieved under such a chimera-type meshless/mesh-based technique exhibit better accuracy than the solutions entirely based on FEM and IEFG techniques. The stress singularity at the crack tip leads to marked gradients around it, whereas the stress field is virtually uniform in the rest of the problem domain. The patch domain Ω_{IEFG} has been strategically allocated in a very small region encompassing the crack tip with a rectangular distribution of nodes exponentially clustered towards it, as depicted in Fig. F.14. The SENT configuration is even more extreme than

that of the infinite plate with the centered circular hole, to the point where it can be determined that the region near the crack tip almost completely dominates the error inherent in the numerical solution of this problem. Unlike the previous cases concerning the Timoshenko cantilever beam and the infinite plate with a centered circular hole, the SENT problem does not have bounded stress values due to the singularity at the crack tip. Therefore, the accuracy of the numerical solutions was not evaluated in terms of the energy-based error norm (F.24), but rather in terms of the calculation of the stress intensity factor K_I. The suitability of confining the IEFG computations only to the region encompassing the crack tip is demonstrated by inspection of the results of Table F.1, which show that the Ov-IEFG-FEM provides similar accuracy compared to the standard solutions based entirely on the IEFG technique. For instance, the Ov-IEFG-FEM has provided a $K_I^{\text{num}}/K_I^{\text{ref}}$ ratio of 0.999 with a total of 1619 nodes (293 in Ω_{FEM}+1326 in Ω_{IEFG}), and the IEFG technique applied to the entire problem domain with 1798 nodes yielded the same $K_I^{\text{num}}/K_I^{\text{ref}}$ ratio. The Ov-IEFG-FEM has also overall allowed calculation times to be halved compared to those of solutions entirely based on the IEFG technique, despite using a similar total number of nodes for the numerical computations. The reason for this lies in the fact that the Ov-IEFG-FEM utilizes a considerably smaller number of nodes for IEFG calculations within Ω_{IEFG} compared to the standard solutions that have relied solely on the IEFG technique across the entire problem domain. The computing times of the Ov-IEFG-FEM are predominantly influenced by IEFG computations in Ω_{IEFG}, given that this meshless technique is well-known for incurring significantly higher computational times compared to FEM [15, 149, 212]. Another important aspect is that this superior performance of Ov-IEFG-FEM with respect to the standard IEFG technique has been achieved despite the iterative solution of linear equation systems required for the $\Omega_{\text{FEM}} - \Omega_{\text{IEFG}}$ coupling, which is consistent with the widely-known fact that determining the support domain nodes and computation of shape functions in EFG techniques is significantly more time-consuming than solving the resulting system of equations [15, 149, 240, 241, 323]. Particularly in this SENT problem, the Ω_{FEM}-Ω_{IEFG} coupling has taken around 10 iterations for the different meshes and node distributions reported in Table F.1. This particular outcome further emphasizes that determining support domain nodes and computing shape functions at each integration point in IEFG is so time-consuming that performing an Ov-IEFG-FEM iterative procedure involving 10 recursive solutions of the linear system of equations concerning the approximations in Ω_{FEM} and Ω_{IEFG} is still preferred. Although the iterative solution in the Ov-IEFG-FEM context might be expected to increase computation times, restricting IEFG calculations to the region near the crack tip significantly reduces the costly tasks of determining support domain nodes and computing shape functions at each integration point. This has the overall effect of reducing computation times compared to the IEFG-based solution, even though the latter involves solving only a single linear system of equations. It must be emphasized that the current analysis has been focused so far on cases where similar numbers of nodes (degrees of freedom) are present in FEM, IEFG, and Ov-IEFG-FEM, allowing for a more equitable comparison between the methods. In this sense, a further discussion in this regard will also be provided.

Despite the much lower computational times exhibited by FEM compared to Ov-IEFG-FEM, even after significant reduction in calculation times by the latter technique compared to the solutions entirely based on IEFG, it is important to note that for similar numbers of nodes, the accuracy achieved by neither Ov-IEFG-FEM nor IEFG is matched by FEM-based results. This can be determined by simple inspection of the FEM-based results reported in Table F.1, where it is observed that the $K_I^{\text{num}}/K_I^{\text{ref}}$ ratio of 0.998 obtained with the standard FEM-based computations with a total of 209174 nodes still does not approach the level of accuracy achieved by Ov-IEFG-FEM and IEFG. Additionally, for these highly refined FEM-based solutions, the computation times begin to approach those of Ov-IEFG-FEM, indicating a diminishing advantage of FEM in terms of computational efficiency when striving for similar levels of accuracy in K_I calculation. This aspect is better illustrated in Fig. F.21, which plots the relationship between K_I^{num} accuracy and computational times for the numerical solutions performed using Ov-IEFG-FEM, IEFG, and FEM. First, it is evident that Ov-IEFG-FEM exhibits lower computation times compared to solutions solely based on IEFG. Additionally, although both techniques initially have higher computation times than FEM, they can improve their accuracy without a significant increase in computation times. This is due to the well-known fact that IEFG-based calculations can significantly enhance the capture of stress intensification near singularities without requiring a substantial increase in the number of degrees of freedom near the crack tip [282, 324]. Conversely, a clear trend is observed where FEM significantly exceeds the computation times of both IEFG and Ov-IEFG-FEM when attempting to achieve their levels of accuracy. This occurs because, although FEM initially shows lower computation times for a similar number of nodes, achieving comparable accuracy requires significantly more refinement. This increased refinement results in higher computation times, causing FEM to lose its initial computational efficiency advantage over IEFG and Ov-IEFG-FEM.

It is recognized that advanced FEM-based techniques exist to better capture the stress intensity factor, such as

high-order quadrilateral elements with modified nodal positions for enriched approximations in radially distributed and refined meshes towards the crack tip [107]. The approach proposed in this communication does not aim to surpass the performance of these well-established techniques but rather to efficiently utilize the positive characteristics of IEFG, particularly its smoothness and non-local interpolation to capture stress intensification in a simpler manner. The results discussed so far regarding the capture of the stress intensity factor have been obtained using uniform and structured meshes and node distributions near the crack tip, which are typically not ideal for linear fracture mechanics problems. Additionally, the IMLS used in the IEFG formulation have been constructed with bilinear basis polynomials without any enrichment, similar to those used in FEM-based solutions. This approach highlights the potential of IEFG to achieve accurate results without the need for cumbersome modifications to its standard formulation. However, the high computational cost of using IEFG across the entire domain is significant. Therefore, the proposed Ov-IEFG-FEM aims to retain the positive aspects of IEFG concerning the achievement of accuracy via a very simple and straightforward implementation, while reducing computational costs. This has been achieved by restricting Ω_{IEFG} to the vicinity of the crack, and using less computationally expensive FEM-based computations for the rest of the domain.

Additionally, it should be emphasized that the improvements introduced by the Ov-IEFG-FEM are achieved without the need for prescribing complex topological relationships between the background mesh discretizing Ω_{FEM} and the fine distribution of nodes representing Ω_{IEFG}. This feature enables its easy implementation in problems involving marked moving gradients, which is achieved by merely performing an appropriate positioning of Ω_{IEFG} according to the changes in the problem domain configuration. This has been put in a better perspective in the complementary study previously conducted to calculate K_I for different crack depths, where it was only necessary to shift Ω_{IEFG} according to the position of the crack tip. Additionally, it was performed without modifying either the nodes distribution of Ω_{IEFG} or the configuration of the background mesh Ω_{FEM} that discretizes the problem domain. This complementary analysis was performed using a patch domain Ω_{IEFG} with a radial node distribution refined towards the crack tip, thereby further enhancing the accuracy of the IEFG technique. The successful implementation of this procedure has demonstrated two significant aspects:

1. The IEFG computations in Ω_{IEFG} can also be performed by using more suitable node distributions, similar to those used in FEM-based procedures properly adapted to LEFM. Although IEFG computations have already shown to achieve very accurate results with a uniform node distribution near the crack tip—which is not ideally suited for linear fracture mechanics problems—using a refined radial node distribution towards the crack tip can significantly improve accuracy.

2. Seamless $\Omega_{\text{FEM}} - \Omega_{\text{IEFG}}$ stress coupling can be achieved regardless of the geometry of Γ_{IEFG}, demonstrating the potential of the current Ov-IEFG-FEM to handle overlapping domains with very different topologies.

These positive features have enabled a significant reduction in the total number of nodes required to solve the SENT problem via the Ov-IEFG-FEM. Actually, the results shown in Figs. F.18 to F.20 were achieved using only 705 nodes (581 in Ω_{FEM} and 124 in Ω_{IEFG}). This reduction has led to decreased computing times up to $t_c \approx 0.85$ s, while keeping the highly accurate capture of the stress intensity factor ($K_I^{\text{num}}/K_I^{\text{ref}} = 1.000$). This global computing time has comprised 0.4 seconds for the support domain nodes determination and computation of shape functions at each integration point, and 0.45 seconds for the iterative $\Omega_{\text{FEM}} - \Omega_{\text{IEFG}}$ coupling. This clearly demonstrates that the assembly stage of the IEFG formulation is the dominant factor in the overall computation time for the Ov-IEFG-FEM, as this stage still accounts for nearly half of the total computation time even when the number of nodes in Ω_{IEFG} has been significantly reduced to just 124. The stress distributions of Figs. F.18-F.19 and the accurate stress intensity factors plotted in Fig. F.20 for different crack lengths were obtained keeping both the background mesh Ω_{FEM} and the nodes configuration in Ω_{IEFG}, and merely performing a uniform rigid body translation of the 124 nodes representing Ω_{IEFG} so that its center is precisely located at the crack tip. Such a particular feature of the Ov-IEFG-FEM allows the information concerning the support domain nodes at each integration point and the IMLS approximations can be processed only once and kept throughout the entire analysis for different crack lengths. As a result, computing times for subsequent positions of the crack tip will solely encompass the computational costs associated with the stage of iterative $\Omega_{\text{FEM}} - \Omega_{\text{IEFG}}$ coupling ($t_c \approx 0.45$ s). Reminding that the results depicted in Figs. F.18 to F.20 were achieved using 705 nodes, it is noteworthy that the computation time reported in Table F.1 for a solution purely based on IEFG with a similar number of nodes (749) was approximately 2.5 seconds. While the potential of EFG methods to eliminate and add degrees of freedom more freely in a region of interest has positioned them as an attractive alternative for improving accuracy without the need for high-quality mesh generation required by mesh-based techniques such as FEM [107, 108, 325], their

notable computational cost related to support domain nodes determination and shape function computation at each integration point remains a significant drawback [15, 110, 149, 212, 286].

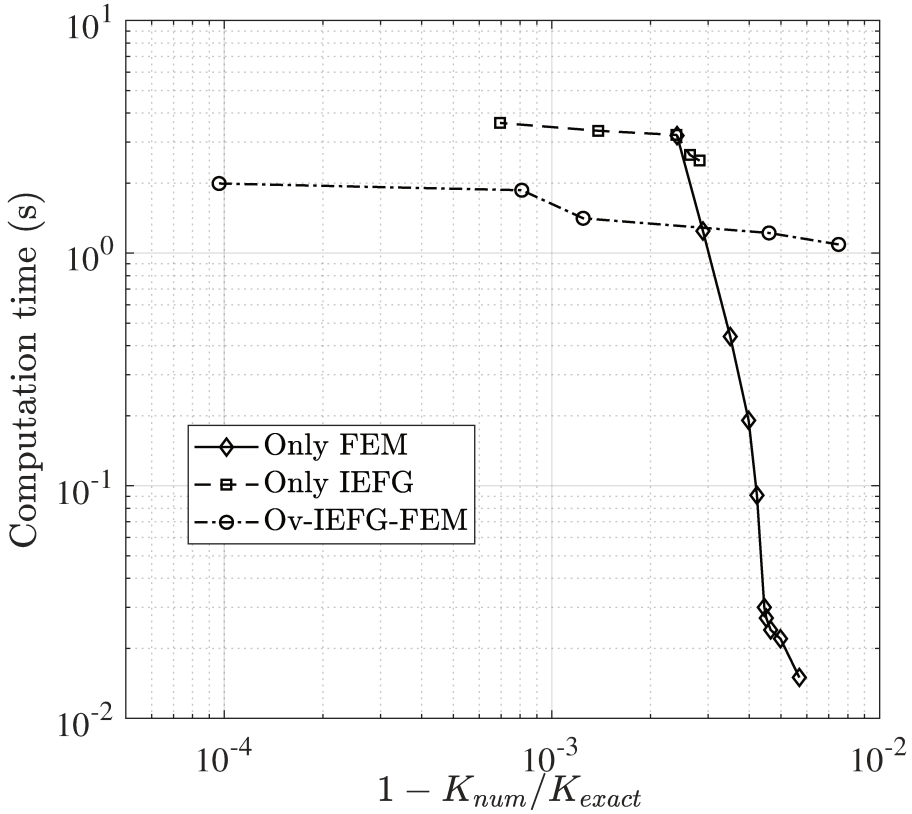

Figura F.21: Comparison of CPU times as a function of K_I normalization for each of the implemented techniques.

The proposition of using the Ov-IEFG-FEM in linear elasticity problems offers a solution to address this particular drawback of computational costs in EFG methods, which often significantly exceed those of standard mesh-based approaches when using the same number of nodes [149, 212]. This approach represents an easily implementable solution for making more efficient use of the high accuracy provided by IEFG computations, eliminating the need for cumbersome adaptive node reconfiguration procedures to capture marked gradients effectively. In this regard, the fact that the Ov-IEFG-FEM has reduced the computing times to surpass five-fold the IEFG-based solution in this particular analysis of the SENT problem is attributed to the following factors: (i) A significant reduction of the number of nodes used for IEFG computations in the region of interest, while using less computationally expensive FEM approximations in the rest of the problem domain, (ii) The potential of performing the time-consuming procedures involved in searching for neighboring nodes and constructing IMLS approximations only once, and keeping this information and the nodes configuration in Ω_{IEFG} during the entire analysis by merely translating such patch domain according to the crack tip position. Recognizing that computation times of EFG methods are still notably higher than those of mesh-based techniques such as FEM and FVM, the main idea of this communication has been to propose an alternative approach that is easy to implement and allows for more efficient utilization of the high-order approximations achievable simply with these meshless techniques. This is achieved by significantly reducing the number of required nodes for IEFG-based computations, in such a way that the use of this technique to enhance the accuracy of numerical solutions does not incur in a significant increase in computation times compared to standard mesh-based formulations. It is worth noting that adaptive remeshing procedures and variable mapping between successive meshes in FEM are also cumbersome [107, 256], alongside the previously discussed requirement for special elements to handle asymptotic stress fields near the crack tip [107]. Therefore, the proposed Ov-IEFG-FEM represents a viable alternative to address these challenges in a remarkably simple manner.

F.4.1. Comparison with non-overlapping EFG-FEM coupling techniques

Unlike the Ov-IEFG-FEM used in this communication, there are other EFG-FEM coupling approaches where EFG and FEM regions do not overlap, but only interact along a shared boundary. These non-overlapping techniques consist in handling the interactions between the EFG and FEM approximations, in order to ensure consistency and accuracy across the shared boundary. The first EFG-FEM non-overlapping coupling technique was developed by Belytshcko [103], succeeding in coupling by introducing interface elements along the boundary communicating the regions approximated by EFG and FEM. This was required to ensure an appropriate coupling of the displacement fields, given the lack of Kronecker delta property of the MLS approximations. Although this technique does not succeed in providing a smooth coupling in the shape functions derivatives for stress and strain computations, this feature does not adversely affect the overall results since the coupling is only affecting a small number of nodes throughout the entire problem domain [103]. Further efforts were made to eliminate the need for interface elements along the EFG-FEM coupling boundary such as the hierarchical IEFG-FEM blending formulations proposed by Huerta et al. [105], the Lagrange multipliers-based coupling proposed by Hegen et al [326], and the integration constraints implemented by Wang et al [258]. Later, Ullah et al.[110, 255, 256] used the weak Kronecker delta property of max-ent shape functions to provide a very straightforward coupling between the EFG and FEM regions. These works put in an appropriate perspective that shape functions fulfilling the Kronecker delta property allow for a simple EFG-FEM coupling without interface elements. Given the Kronecker delta property of Moving Kriging (MK) shape functions, EFG with MK (EFGMK) is a mesh-less approach that can also be used for such a purpose.

The performance of the proposed Ov-IEFG-FEM for linear elasticity problems is compared in this section to a non-overlapping EFGMK-FEM coupling technique belonging to the family of shared boundary-type coupling methods originally proposed in the pioneer work of Belytshcko [103]. It is performed in the framework of the infinite plate with a centered hole benchmark problem. The features of this problem are appropriate to demonstrate the potential of EFG-FEM hybrid methods, which are conceived to enhance solutions by using EFG methods only in localized regions where using higher-order approximations is actually favorable [110, 256]. The comparison is carried out using the node distributions and meshes shown in Fig. F.22. In Fig. F.22(a), the non-overlapping EFGMK-FEM technique is illustrated. This arrangement clearly separates the domains for EFGMK and FEM approximations, with nodes shared only along the common boundary connecting these regions. Conversely, Figs. F.22(b) and (c) show the computational domains for the Ov-IEFG-FEM. In this approach, the mesh-less region for IEFG computations overlaps rather than replaces the FEM mesh. In order to remark the key feature of the Ov-IEFG-FEM concerning its independence from a predefined topological relationship between overlapping domains, two scenarios are examined. The first scenario, shown in Fig. F.22(b), features IEFG nodes aligned with the FEM background mesh. The second scenario, depicted in Fig. F.22(c), demonstrates independent node refinement for IEFG, resulting in overlapping nodes that do not align with the FEM background mesh.

The results concerning the displacement components u_x along $(x, 0)$ and u_y along $(0, y)$ are depicted in Fig.F.23(a)-(b), whereas the stress components σ_{xx} and σ_{yy} along $(0, x)$ are depicted in Fig.F.24(a)-(b). The displacement components exhibit a perfectly seamless coupling across all three scenarios: the non-overlapping EFGMK-FEM, the Ov-IEFM-FEM with overlapping nodes aligned to the background mesh, and the Ov-IEFG-FEM with overlapping nodes not aligned with the background mesh. This outcome demonstrates that the Kronecker delta property of the MK in the EFGMK-FEM provides a seamless displacements coupling without the need for transition/interface elements at the coupling boundary region, and also that the proposed Ov-IEFG-FEM allows the achievement of such a seamless coupling without being subjected to a prescribed topological relationship between the overlapping domains. This potential of the Ov-IEFG-FEM to achieve a seamless coupling regardless the background mesh and overlapping nodes distribution being performed independently is also exhibited in the stress distributions, as depicted in F.24(a)-(b).

This has not been possible in the framework of the EFGMK-FEM, as demonstrated by the slightly unstable behavior exhibited by the stress components computed near the fitted coupling boundary where the EFGMK and FEM regions share common nodes. Although the non-overlapping EFGMK-FEM eliminates the need for interface elements, it still does not resolve the irregular stress transitions that were also present in the coupling method originally proposed by Belytschko [103], which used interface elements.

The outcomes of this brief analysis put in an appropriate perspective two remarkably positive features of the Ov-IEFG-FEM in the solution of linear elasticity problems, despite its reliance on an iterative procedure. The

features are: (i) The method allows a straightforward achievement of smooth coupling not only in displacement, but also in stress field; and (ii) This is achieved without requiring a predefined topological relationship between the IEFG and FEM regions, meaning that neither node sharing nor a carefully defined strip of interface/transition elements at a common boundary is required.

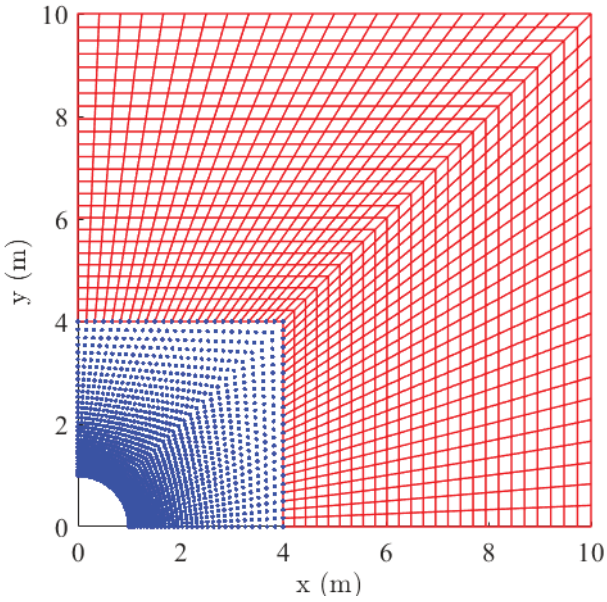

(a) EFGMK-FEM

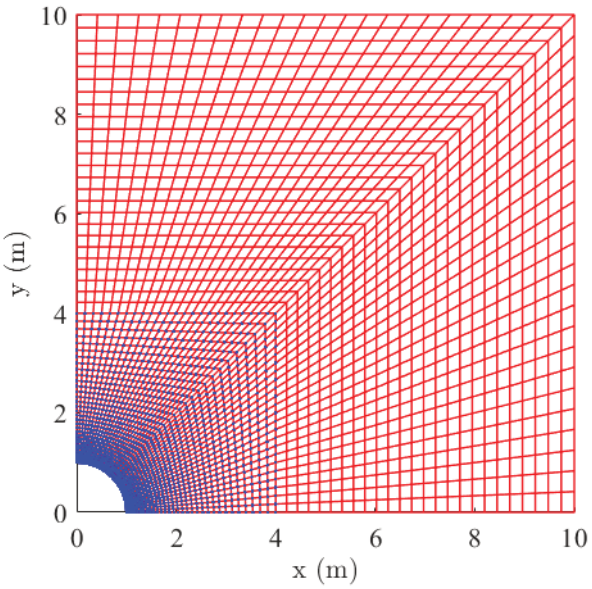

(b) Ov-IEFG-FEM fitted

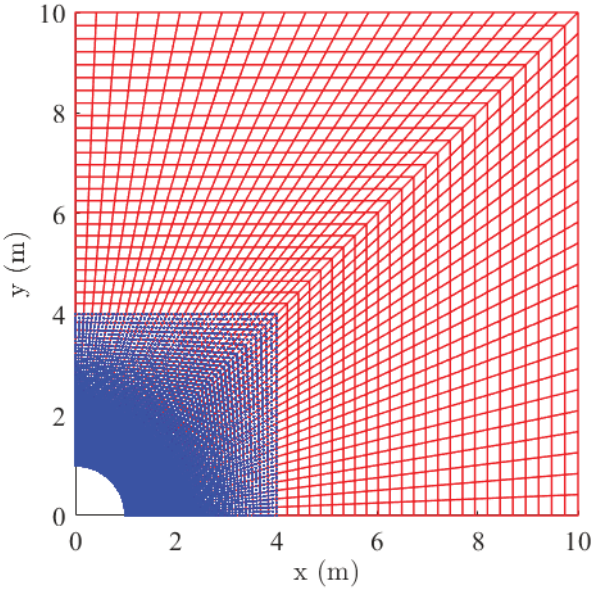

(c) Ov-IEFG-FEM unfitted

Figura F.22: Discretizations used for comparison of the Ov-IEFG-FEM with the non-overlapping EFGMK-FEM technique, in the framework of the infinite plate with a centered hole benchmark problem.

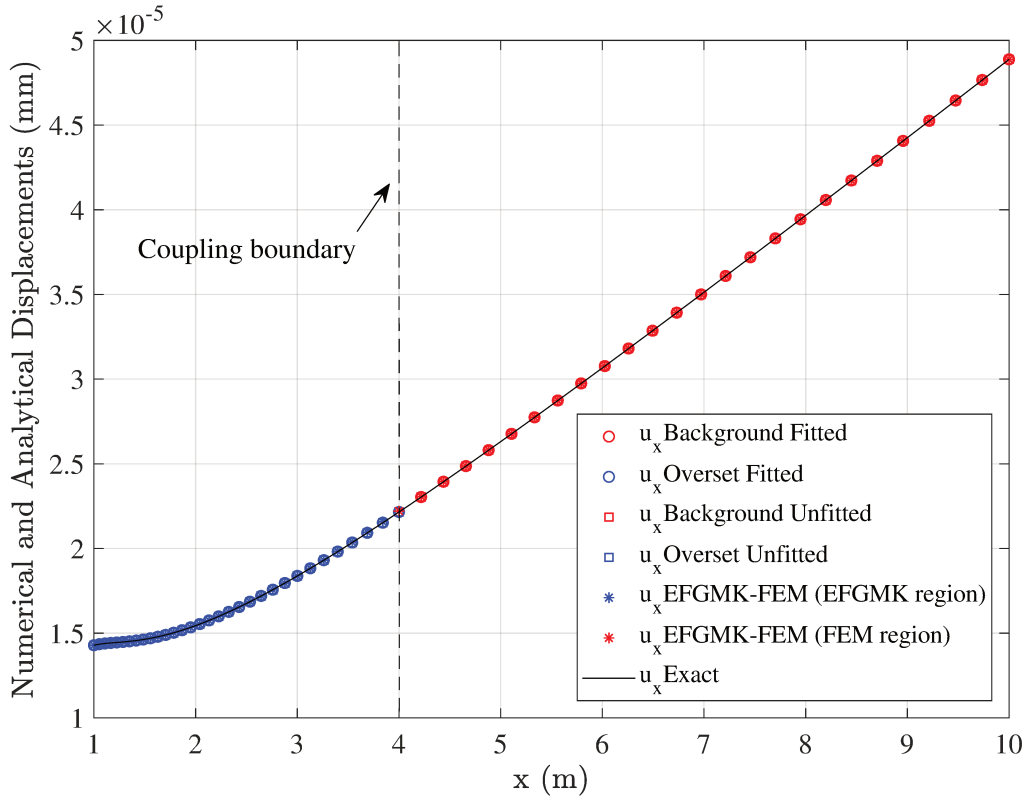

(a) u_x

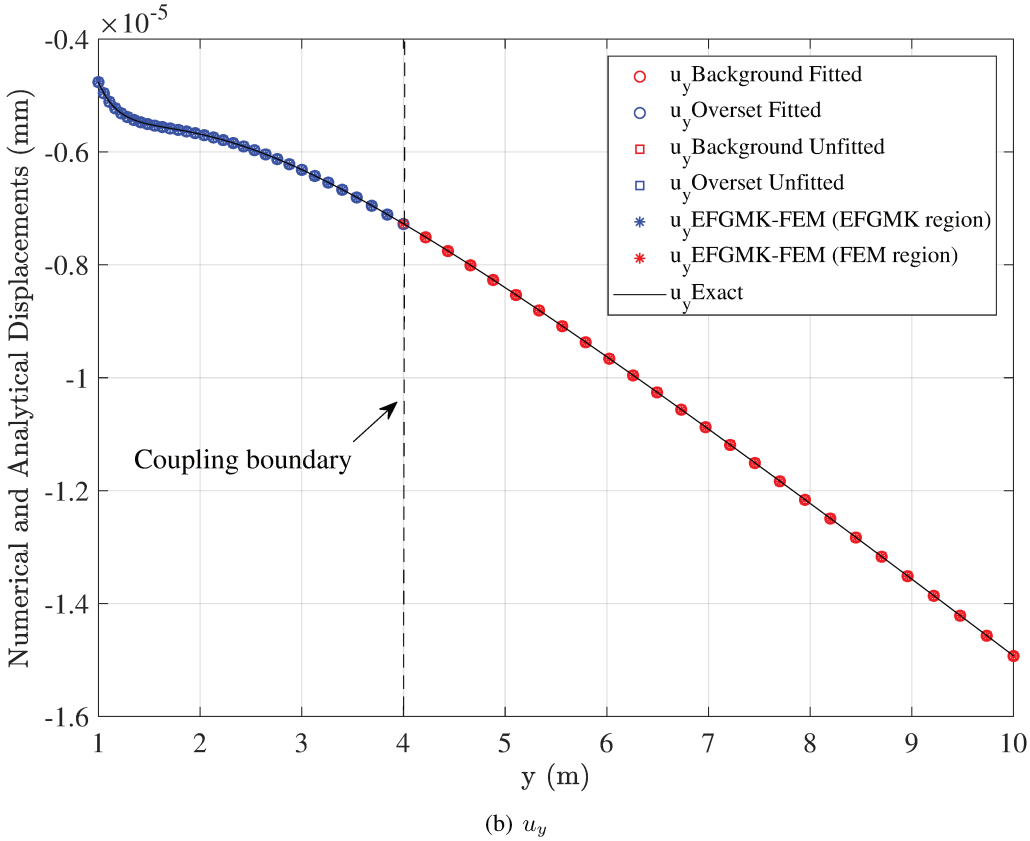

(b) u_y

Figura F.23: Comparison on the displacement components u_x along $(x, 0)$ and u_y along $(0, y)$.

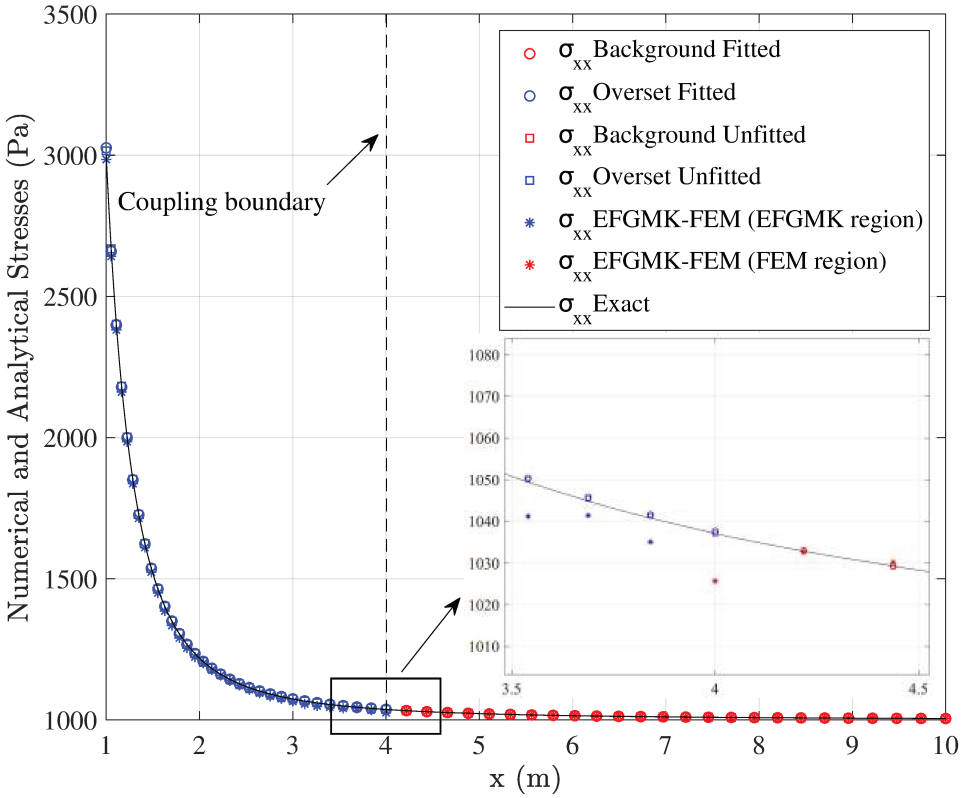

(a) σ_{xx}

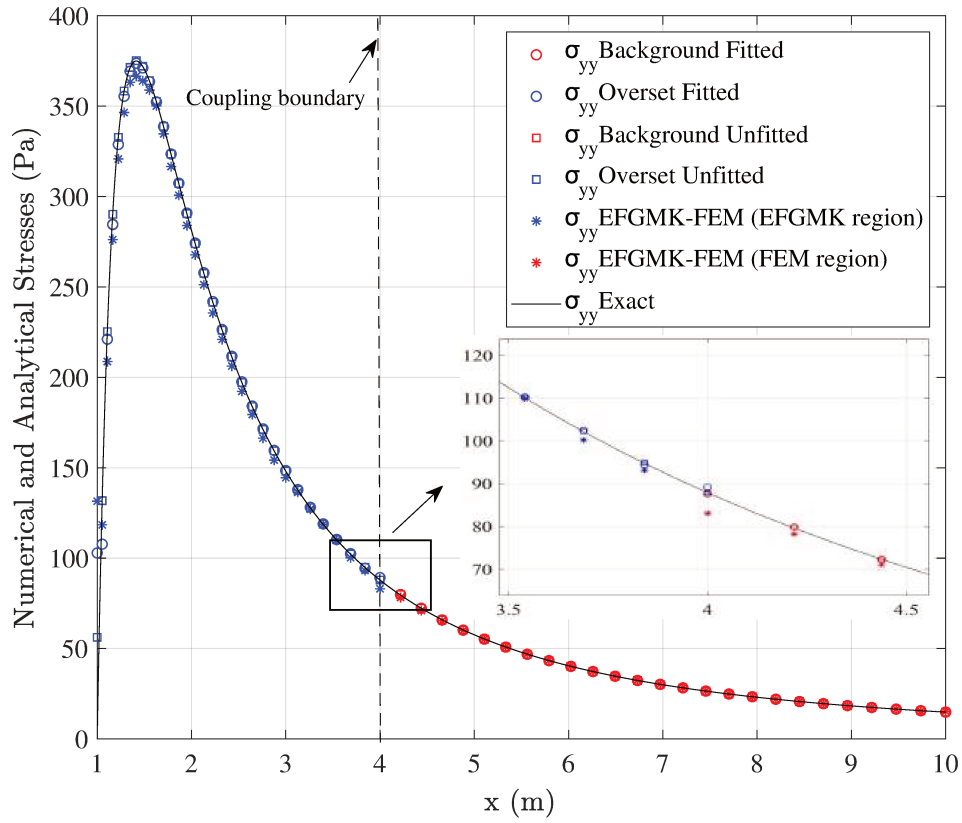

(b) σ_{yy}

Figura F.24: Comparison on the stress components σ_{xx} and σ_{yy} along $(0, x)$.

F.5. Conclusions

The overset improved Element-Free Galerkin-Finite Element Method (Ov-IEFG-FEM) has been implemented to solve linear elastic benchmark problems, demonstrating its efficacy in seamlessly coupling a background domain discretized via coarse mesh for Finite Element Method (FEM) computations with a patch domain represented by a fine node arrangement to perform higher-order approximations using the improved Element-Free Galerkin (IEFG) method in regions requiring enhanced accuracy. This approach particularly leverages the IEFG potential to capture significant stress concentrations in a remarkably simple manner, while mitigating the computational overhead associated with using EFG methods over the entire problem domain. The outcomes of this communication illustrate that the Ov-IEFG-FEM achieves convergence rates comparable to purely IEFG-based solutions, while significantly reducing computation times. By strategically positioning the mesh-less patch domain near regions of high gradients, numerical solution accuracy is enhanced without the need for extensive node re-configurations or complex mesh adaptations required by single-domain methods.

Across the benchmark problems—Timoshenko cantilever beam, infinite plate with a centered hole, and the single-edge notched tension (SENT) specimen—Ov-IEFG-FEM consistently demonstrates improved accuracy compared to purely FEM-based solutions, particularly in scenarios with pronounced stress gradients. Notably, the approach maintains computational efficiency, achieving over five-fold reductions in computing times compared to standard IEFG-based solutions with a similar number of nodes. Moreover, the straightforward implementation of this method that allows the patch domain nodes to be adapted with minimal adjustments via simple rigid translations, underscores its practicality for effectively handling evolving geometries and moving gradients. This can be particularly advantageous in fracture mechanics scenarios where adaptability and precision are critical.

In conclusion, Ov-IEFG-FEM offers a compelling alternative to address the computational challenges of traditional IEFG methods, providing a robust framework for enhancing numerical accuracy in linear elasticity without compromising computational efficiency. Future research could explore enhancements and applications across broader problem classes, such as solving more complex fracture mechanics problems using constitutive damage models.

Acknowledgments

- This research has been supported by grants from CONICET and the Universidad Nacional del Litoral (UNL).
- S.A. Serebrinsky wishes to thank YPF S.A. and YPF Tecnología S.A. for granting permission to publish this paper.
- This work is dedicated to the memory of Msc. Aristides Gonzalez, a beloved friend, respected academic, and outstanding professional. May he rest in eternal peace.

Bibliografía

[1] Hiroshi Tada, Paul C. Paris, y George R. Irwin. *The stress analysis of cracks*, volumen 34. Handbook, Del Research Corporation, 1973.

[2] D. Leguillon. Strength or toughness? a criterion for crack onset at a notch. *European Journal of Mechanics-A/Solids*, 21(1):61–72, 2002.

[3] R.O. Ritchie. The conflicts between strength and toughness. *Nature materials*, 10(11):817–822, 2011.

[4] G. Noselli, V.S. Deshpande, y N.A. Fleck. An analysis of competing toughening mechanisms in layered and particulate solids. *International Journal of Fracture*, 183(2):241–258, 2013.

[5] D. Chuprakov, O. Melchaeva, y R. Prioul. Injection-sensitive mechanics of hydraulic fracture interaction with discontinuities. *Rock mechanics and rock engineering*, 47(5):1625–1640, 2014.

[6] D.I. Garagash. Cohesive-zone effects in hydraulic fracture propagation. *Journal of the Mechanics and Physics of Solids*, 133:103727, 2019.

[7] B. Giovanardi, S. Serebrinsky, y R. Radovitzky. A fully-coupled computational framework for large-scale simulation of fluid-driven fracture propagation on parallel computers. *Computer Methods in Applied Mechanics and Engineering*, 372:113365, 2020.

[8] Julieta Gutiérrez. Multi-scale modeling of hydraulic stimulation in reservoirs with natural fractures. *Y-TEC, CONICET*, 2023.

[9] J.W. Foulk III, G.C. Johnson, P.A. Klein, y R.O. Ritchie. On the toughening of brittle materials by grain bridging: Promoting intergranular fracture through grain angle, strength, and toughness. *Journal of the Mechanics and Physics of Solids*, 56(6):2381–2400, 2008.

[10] H. Chen, C.i Zhang, Q. Lu, H. Chen, Z. Yang, Y. Wen, S. Hu, y L. Chen. A two-set order parameters phase-field modeling of crack deflection/penetration in a heterogeneous microstructure. *Computer Methods in Applied Mechanics and Engineering*, 347:1085–1104, 2019.

[11] B. Ji y H. Gao. Mechanical properties of nanostructure of biological materials. *J. Mech. Phys. Solids*, 52: 1963–1990, 2004.

[12] M.A. Gutiérrez. Energy release control for numerical simulations of failure in quasi-brittle solids. *Communications in Numerical Methods in Engineering*, 20(1):19–29, 2004.

[13] C.V. Verhoosel, J.J.C. Remmers, y M.A. Gutiérrez. A dissipation-based arc-length method for robust simulation of brittle and ductile failure. *International journal for numerical methods in engineering*, 77(9): 1290–1321, 2009.

[14] J Zambrano, S Toro, PJ Sánchez, FP Duda, CG Méndez, y AE Huespe. An arc-length control technique for solving quasi-static fracture problems with phase field models and a staggered scheme. *Computational Mechanics*, 73(4):751–772, 2024.

[15] Juan C. Álvarez Hostos, Zahur Ullah, Bruno A. Storti, Benjamín A. Tourn, y Javier A. Zambrano-Carrillo. An overset improved element-free Galerkin-finite element method for the solution of transient heat conduction problems with concentrated moving heat sources. *Computer Methods in Applied Mechanics and Engineering*, 418:116574, 2024. doi: 10.1016/j.cma.2023.116574.

[16] Javier A Zambrano-Carrillo, Juan C Álvarez-Hostos, Santiago Serebrinsky, y Alfredo E Huespe. Solving linear elasticity benchmark problems via the overset improved element-free galerkin-finite element method. *Finite Elements in Analysis and Design*, 241:104247, 2024.

[17] G.A. Francfort y J.-J. Marigo. Revisiting brittle fracture as an energy minimization problem. *Journal of the Mechanics and Physics of Solids*, 46(8):1319–1342, 1998.

[18] Blaise Bourdin y Antonin Chambolle. Implementation of an adaptive finite-element approximation of the mumford-shah functional. *Numerische Mathematik*, 85:609–646, 2000.

[19] Matteo Negri y M Paolini. Numerical minimization¶ of the mumford–shah functional. *Calcolo*, 38:67–84, 2001.

[20] Fernando Fraternali. Free discontinuity finite element models in two-dimensions for in-plane crack problems. *Theoretical and Applied Fracture Mechanics*, 47(3):274–282, 2007.

[21] Bernd Schmidt, Fernando Fraternali, y Michael Ortiz. Eigenfracture: an eigendeformation approach to variational fracture. *Multiscale Modeling & Simulation*, 7(3):1237–1266, 2009.

[22] Luigi Ambrosio y Vincenzo Maria Tortorelli. Approximation of functional depending on jumps by elliptic functional via t-convergence. *Communications on Pure and Applied Mathematics*, 43(8):999–1036, 1990.

[23] Luigi Ambrosio. On the approximation of free discontinuity problems. *Boll. Un. Mat. Ital., B*, (7):105–123, 1992.

[24] Blaise Bourdin. Image segmentation with a finite element method. *ESAIM: Mathematical modelling and numerical analysis*, 33(2):229–244, 1999.

[25] Morton E Gurtin y Paolo Podio-Guidugli. Configurational forces and the basic laws for crack propagation. *Journal of the Mechanics and Physics of Solids*, 44(6):905–927, 1996.

[26] Morton E Gurtin, Eliot Fried, y Lallit Anand. *The mechanics and thermodynamics of continua*. Cambridge university press, 2010.

[27] Eliot Fried, Milton N da Silva Jr, Fernando P Duda, y Angela C Souza. Phase-field model for the corrosion and cracking of metals in aqueous environments. En *ISOPE International Ocean and Polar Engineering Conference*, páginas ISOPE–I. ISOPE, 2011.

[28] Gianfranco Capriz. *Continua with microstructure*, volumen 35. Springer Science & Business Media, 1989.

[29] Amir Abdollahi y Irene Arias. Phase-field modeling of crack propagation in piezoelectric and ferroelectric materials with different electromechanical crack conditions. *Journal of the Mechanics and Physics of Solids*, 60(12):2100–2126, 2012.

[30] Zachary A Wilson, Michael J Borden, y Chad M Landis. A phase-field model for fracture in piezoelectric ceramics. *International Journal of Fracture*, 183:135–153, 2013.

[31] Corrado Maurini, B Bourdin, G Gauthier, y Veronique Lazarus. Crack patterns obtained by unidirectional drying of a colloidal suspension in a capillary tube: experiments and numerical simulations using a two-dimensional variational approach. En *Fracture Phenomena in Nature and Technology: Proceedings of the IUTAM Symposium on Fracture Phenomena in Nature and Technology held in Brescia, Italy, 1-5 July 2012*, páginas 75–91. Springer, 2014.

[32] Blaise Bourdin, Jean-Jacques Marigo, Corrado Maurini, y Paul Sicsic. Morphogenesis and propagation of complex cracks induced by thermal shocks. *Physical review letters*, 112(1):014301, 2014.

[33] Blaise Bourdin, Chukwudi Chukwudozie, y Keita Yoshioka. A variational approach to the numerical simulation of hydraulic fracturing. En *SPE Annual Technical Conference and Exhibition?*, páginas SPE–159154. SPE, 2012.

[34] Mary F Wheeler, Thomas Wick, y Winnifried Wollner. An augmented-lagrangian method for the phase-field approach for pressurized fractures. *Computer Methods in Applied Mechanics and Engineering*, 271:69–85, 2014.

[35] Chukwudi P Chukwudozie. *Application of the variational fracture model to hydraulic fracturing in poroelastic media*. Louisiana State University and Agricultural & Mechanical College, 2016.

[36] Zachary A Wilson y Chad M Landis. Phase-field modeling of hydraulic fracture. *Journal of the Mechanics and Physics of Solids*, 96:264–290, 2016.

[37] Christopher J Larsen, Christoph Ortner, y Endre Süli. Existence of solutions to a regularized model of dynamic fracture. *Mathematical Models and Methods in Applied Sciences*, 20(07):1021–1048, 2010.

[38] Blaise Bourdin, Christopher J Larsen, y Casey L Richardson. A time-discrete model for dynamic fracture based on crack regularization. *International journal of fracture*, 168:133–143, 2011.

[39] M Hofacker y C30082661352 Miehe. A phase field model of dynamic fracture: Robust field updates for the analysis of complex crack patterns. *International Journal for Numerical Methods in Engineering*, 93(3): 276–301, 2013.

[40] Roberto Alessi, Jean-Jacques Marigo, y Stefano Vidoli. Gradient damage models coupled with plasticity and nucleation of cohesive cracks. *Archive for Rational Mechanics and Analysis*, 214:575–615, 2014.

[41] Marreddy Ambati, Tymofiy Gerasimov, y Laura De Lorenzis. Phase-field modeling of ductile fracture. *Computational Mechanics*, 55:1017–1040, 2015.

[42] C. Miehe, F. Aldakheel, y A. Raina. Phase field modeling of ductile fracture at finite strains: A variational gradient-extended plasticity-damage theory. *International Journal of Plasticity*, 84:1–32, 2016.

[43] Sergio Conti, Matteo Focardi, y Flaviana Iurlano. Phase field approximation of cohesive fracture models. En *Annales de l'Institut Henri Poincaré C, Analyse non linéaire*, volumen 33, páginas 1033–1067. Elsevier, 2016.

[44] Vito Crismale y Giuliano Lazzaroni. Viscous approximation of quasistatic evolutions for a coupled elastoplastic-damage model. *Calculus of Variations and Partial Differential Equations*, 55:1–54, 2016.

[45] Francesco Freddi y Flaviana Iurlano. Numerical insight of a variational smeared approach to cohesive fracture. *Journal of the Mechanics and Physics of Solids*, 98:156–171, 2017.

[46] Marreddy Ambati, Roland Kruse, y Laura De Lorenzis. A phase-field model for ductile fracture at finite strains and its experimental verification. *Computational Mechanics*, 57:149–167, 2016.

[47] Michael J Borden, Thomas JR Hughes, Chad M Landis, Amin Anvari, y Isaac J Lee. A phase-field formulation for fracture in ductile materials: Finite deformation balance law derivation, plastic degradation, and stress triaxiality effects. *Computer Methods in Applied Mechanics and Engineering*, 312:130–166, 2016.

[48] Michel Frémond y Boumediene Nedjar. Damage, gradient of damage and principle of virtual power. *International journal of solids and structures*, 33(8):1083–1103, 1996.

[49] Eric Lorentz y Stéphane Andrieux. Analysis of non-local models through energetic formulations. *International Journal of Solids and Structures*, 40(12):2905–2936, 2003.

[50] Kim Pham y Jean-Jacques Marigo. The variational approach to damage: I. the foundations. *Academie des Sciences. Comptes Rendus. Mecanique*, 338(4):191–198, 2010.

[51] Kim Pham y Jean-Jacques Marigo. The variational approach to damage: Ii. the gradient damage models. *Academie des Sciences. Comptes Rendus. Mecanique*, 338(4):199–206, 2010.

[52] Kim Pham, Hanen Amor, Jean-Jacques Marigo, y Corrado Maurini. Gradient damage models and their use to approximate brittle fracture. *International Journal of Damage Mechanics*, 20(4):618–652, 2011.

[53] Thanh Tung Nguyen, Julien Yvonnet, Michel Bornert, Camille Chateau, Karam Sab, R Romani, y Robert Le Roy. On the choice of parameters in the phase field method for simulating crack initiation with experimental validation. *International Journal of Fracture*, 197:213–226, 2016.

[54] F.P. Duda, A. Ciarbonetti, P.J. Sánchez, y A.E Huespe. A phase-field/gradient damage model for brittle fracture in elastic-plastic solids. *International Journal of Plasticity*, 65:269–296, 2015.

[55] B.D. Coleman y W. Noll. The thermodynamics of elastic materials with heat conduction and viscosity. *Archive for Rational Mechanics and Analysis*, 13:167–178, 1963.

[56] Wikipedia. Macaulay brackets. https://en.wikipedia.org/wiki/Macaulay_brackets.

[57] C. Miehe, F. Welschinger, y M. Hofacker. Thermodynamically consistent phase-field models of fracture: Variational principles and multi-field finite element implementations. *International journal for numerical methods in engineering*, 83(10):1273–1311, 2010.

[58] Geoffrey H Campbell, Manfred Rühle, Brian J Dalgleish, y Anthony G Evans. Whisker toughening: a comparison between aluminum oxide and silicon nitride toughened with silicon carbide. *Journal of the American Ceramic Society*, 73(3):521–530, 1990.

[59] Anthony G Evans y David B Marshall. Overview no. 85 the mechanical behavior of ceramic matrix composites. *Acta metallurgica*, 37(10):2567–2583, 1989.

[60] J Aveston. The properties of fiber composites. En *Conference Proceedings, National Physical Laboratory, 1971*. IPC Science and Technology Press, 1971.

[61] J Aveston y A Kelly. Theory of multiple fracture of fibrous composites. *Journal of Materials Science*, 8: 352–362, 1973.

[62] J.P. Parmigiani y M.D. Thouless. The roles of toughness and cohesive strength on crack deflection at interfaces. *Journal of the Mechanics and Physics of Solids*, 54(2):266–287, 2006.

[63] Donald S Dugdale. Yielding of steel sheets containing slits. *Journal of the Mechanics and Physics of Solids*, 8(2):100–104, 1960.

[64] Grigory Isaakovich Barenblatt. The mathematical theory of equilibrium cracks in brittle fracture. *Advances in applied mechanics*, 7:55–129, 1962.

[65] Arne Hillerborg, Mats Modéer, y P-E Petersson. Analysis of crack formation and crack growth in concrete by means of fracture mechanics and finite elements. *Cement and concrete research*, 6(6):773–781, 1976.

[66] Alan Needleman. A continuum model for void nucleation by inclusion debonding. 1987.

[67] A Needleman. An analysis of decohesion along an imperfect interface. *International Journal of Fracture*, 42:21–40, 1990.

[68] Viggo Tvergaard y John W Hutchinson. The relation between crack growth resistance and fracture process parameters in elastic-plastic solids. *Journal of the Mechanics and Physics of Solids*, 40(6):1377–1397, 1992.

[69] T Ungsuwarungsri y WG Knauss. The role of damage-softened material behavior in the fracture of composites and adhesives. *International Journal of Fracture*, 35:221–241, 1987.

[70] Clemens V Verhoosel y René de Borst. A phase-field model for cohesive fracture. *International Journal for numerical methods in Engineering*, 96(1):43–62, 2013.

[71] Thanh-Tung Nguyen, Julien Yvonnet, Q-Z Zhu, Michel Bornert, y Camille Chateau. A phase-field method for computational modeling of interfacial damage interacting with crack propagation in realistic microstructures obtained by microtomography. *Computer Methods in Applied Mechanics and Engineering*, 312: 567–595, 2016.

[72] Thanh Tung Nguyen, Julien Yvonnet, Michel Bornert, y Camille Chateau. Initiation and propagation of complex 3d networks of cracks in heterogeneous quasi-brittle materials: Direct comparison between in situ testing-microct experiments and phase field simulations. *Journal of the Mechanics and Physics of Solids*, 95:320–350, 2016.

[73] M. Paggi y J. Reinoso. Revisiting the problem of a crack impinging on an interface: a modeling framework for the interaction between the phase field approach for brittle fracture and the interface cohesive zone model. *Computer Methods in Applied Mechanics and Engineering*, 321:145–172, 2017.

[74] Marco Paggi y Peter Wriggers. A nonlocal cohesive zone model for finite thickness interfaces–part i: mathematical formulation and validation with molecular dynamics. *Computational Materials Science*, 50 (5):1625–1633, 2011.

[75] Marco Paggi y Peter Wriggers. A nonlocal cohesive zone model for finite thickness interfaces–part ii: Fe implementation and application to polycrystalline materials. *Computational Materials Science*, 50(5): 1634–1643, 2011.

[76] Marco Paggi y Peter Wriggers. Stiffness and strength of hierarchical polycrystalline materials with imperfect interfaces. *Journal of the Mechanics and Physics of Solids*, 60(4):557–572, 2012.

[77] MT Aranda, IG García, A Quintanas-Corominas, y J Reinoso. Crack impinging on a curved weak interface: Penetration or deflection? *Journal of the Mechanics and Physics of Solids*, 178:105326, 2023.

[78] J. Zambrano, S. Toro, P.J. Sánchez, F.P. Duda, C.G. Méndez, y A.E Huespe. Interaction analysis between a propagating crack and an interface: Phase field and cohesive surface models. *International Journal of Plasticity*, 156:103341, 2022.

[79] Steve Weiner y H Daniel Wagner. The material bone: structure-mechanical function relations. *Annual review of materials science*, 28(1):271–298, 1998.

[80] John Donald Currey. Mechanical properties of mother of pearl in tension. *Proceedings of the Royal society of London. Series B. Biological sciences*, 196(1125):443–463, 1977.

[81] R. Menig, M.H. Meyers, M.A. Meyers, y K.S Vecchio. Quasi-static and dynamic mechanical response of haliotis rufescens (abalone) shells. *Acta mater*, 48:2383–2398, 2000.

[82] John D Currey. *The mechanical adaptations of bones*, volumen 870. Princeton University Press, 2014.

[83] Huajian Gao, Baohua Ji, Ingomar L Jäger, Eduard Arzt, y Peter Fratzl. Materials become insensitive to flaws at nanoscale: lessons from nature. *Proceedings of the national Academy of Sciences*, 100(10):5597–5600, 2003.

[84] Steve Weiner, Arthur Veis, Elia Beniash, Talmon Arad, Jerry W Dillon, Boris Sabsay, y Farida Siddiqui. Peritubular dentin formation: crystal organization and the macromolecular constituents in human teeth. *Journal of structural biology*, 126(1):27–41, 1999.

[85] W Tesch, Naomi Eidelman, P Roschger, F Goldenberg, K Klaushofer, y P Fratzl. Graded microstructure and mechanical properties of human crown dentin. *Calcified Tissue International*, 69(3), 2001.

[86] Baohua Ji y Huajian Gao. Mechanical properties of nanostructure of biological materials. *Journal of the Mechanics and Physics of Solids*, 52(9):1963–1990, 2004.

[87] Qunfeng Cheng, Mengxi Wu, Mingzhu Li, Lei Jiang, y Zhiyong Tang. Ultratough artificial nacre based on conjugated cross-linked graphene oxide. *Angewandte Chemie*, 125(13):3838–3843, 2013.

[88] Zhiyong Tang, Nicholas A Kotov, Sergei Magonov, y Birol Ozturk. Nanostructured artificial nacre. *Nature materials*, 2(6):413–418, 2003.

[89] Seyed Mohammad Mirkhalaf Valashani y Francois Barthelat. A laser-engraved glass duplicating the structure, mechanics and performance of natural nacre. *Bioinspiration & biomimetics*, 10(2):026005, 2015.

[90] Eduard Riks. An incremental approach to the solution of snapping and buckling problems. *International journal of solids and structures*, 15(7):529–551, 1979.

[91] MA Crisfield. Accelerated solution techniques and concrete cracking. *Computer methods in applied mechanics and engineering*, 33(1-3):585–607, 1982.

[92] E Ramm. Strategies for tracing the non-linear response near limit points. *Nonlinear. finite element analysis in structural mechanic/Springer-Verlag*, 1981.

[93] M.G.D. Geers. Enhanced solution control for physically and geometrically non-linear problems. part i—the subplane control approach. *International Journal for Numerical Methods in Engineering*, 46(2):177–204, 1999.

[94] M.G.D. Geers. Enhanced solution control for physically and geometrically non-linear problems. part ii—comparative performance analysis. *International Journal for Numerical Methods in Engineering*, 46 (2):205–230, 1999.

[95] R De Borst. Computation of post-bifurcation and post-failure behavior of strain-softening solids. *Computers & Structures*, 25(2):211–224, 1987.

[96] Julien Vignollet, Stefan May, René De Borst, y Clemens V Verhoosel. Phase-field models for brittle and cohesive fracture. *Meccanica*, 49:2587–2601, 2014.

[97] Thomas Wick. Modified newton methods for solving fully monolithic phase-field quasi-static brittle fracture propagation. *Computer Methods in Applied Mechanics and Engineering*, 325:577–611, 2017.

[98] C. Miehe, M. Hofacker, y F. Welschinger. A phase field model for rate-independent crack propagation: Robust algorithmic implementation based on operator splits. *Computer Methods in Applied Mechanics and Engineering*, 199(45-48):2765–2778, 2010.

[99] H. Amor, J.J. Marigo, y C. Maurini. Regularized formulation of the variational brittle fracture with unilateral contact: Numerical experiments. *Journal of the Mechanics and Physics of Solids*, 57(8):1209–1229, 2009.

[100] Thomas Helfer, Benoît Bary, Tran Thang Dang, Olivier Fandeur, y Bruno Michel. Modélisation par champ de phase des matériaux fragiles: aspects numériques et applications au combustible nucléaire oxyde. En *13e colloque national en calcul des structures*, 2017.

[101] Patrick Farrell y Corrado Maurini. Linear and nonlinear solvers for variational phase-field models of brittle fracture. *International Journal for Numerical Methods in Engineering*, 109(5):648–667, 2017.

[102] Ye Lu, Thomas Helfer, Benoît Bary, y Olivier Fandeur. An efficient and robust staggered algorithm applied to the quasi-static description of brittle fracture by a phase-field approach. *Computer methods in applied mechanics and engineering*, 370:113218, 2020.

[103] T. Belytschko, D. Organ, y Y. Krongauz. A coupled finite element-element-free Galerkin method. *Computational Mechanics*, 17(3):186–195, 1995. doi: 10.1007/bf00364080.

[104] Y. Krongauz y T. Belytschko. Enforcement of essential boundary conditions in meshless approximations using finite elements. *Computer Methods in Applied Mechanics and Engineering*, 131(1–2):133–145, 1996. doi: 10.1016/0045-7825(95)00954-x.

[105] Antonio Huerta, Sonia Fernández-Méndez, y Wing Kam Liu. A comparison of two formulations to blend finite elements and mesh-free methods. *Computer Methods in Applied Mechanics and Engineering*, 193 (12-14):1105–1117, 2004. doi: 10.1016/j.cma.2003.12.009.

[106] Gaurang R. Rohit, Jagdish M. Prajapati, y Vikram B. Patel. Coupling of Finite Element and Meshfree Method for Structure Mechanics Application: A Review. *International Journal of Computational Methods*, 17(04):1850151, 2019. doi: 10.1142/s0219876218501517.

[107] Himanshu Pathak, Akhilendra Singh, y Indra Vir Singh. Fatigue crack growth simulations of homogeneous and bi-material interfacial cracks using element free Galerkin method. *Applied Mathematical Modelling*, 38(13):3093–3123, 2014. doi: 10.1016/j.apm.2013.11.030.

[108] Sachin Kumar, I. V. Singh, y B. K. Mishra. A coupled finite element and element-free Galerkin approach for the simulation of stable crack growth in ductile materials. *Theoretical and Applied Fracture Mechanics*, 70:49–58, 2014. doi: 10.1016/j.tafmec.2014.02.006.

[109] Apiwish Thongraksa, Pornkasem Jongpradist, Pruettha Nanakorn, y Jukkrawut Tunsakul. Shear fracture propagation in quasi-brittle materials by an element-free Galerkin method. *Theoretical and Applied Fracture Mechanics*, 123:103713, 2023. doi: 10.1016/j.tafmec.2022.103713.

[110] Z. Ullah, W. M. Coombs, y C. E. Augarde. An adaptive finite element/meshless coupled method based on local maximum entropy shape functions for linear and nonlinear problems. *Computer Methods in Applied Mechanics and Engineering*, 267:111–132, 2013. doi: 10.1016/j.cma.2013.07.018.

[111] J. Zambrano, J. Gutierrez, S. Toro, P.J. Sánchez, F.P. Duda, S. Serebrinsky, y A.E. Huespe. Toughening effect analysis in problems of propagating cracks interacting with interfaces. *The Seventh International Conference on Computational Modeling of Fracture and Failure of Materials and Structures. Prague, Czech Republic*, página 172, 2023.

[112] Michael J Borden, Clemens V Verhoosel, Michael A Scott, Thomas JR Hughes, y Chad M Landis. A phase-field description of dynamic brittle fracture. *Computer Methods in Applied Mechanics and Engineering*, 217:77–95, 2012.

[113] E. Tanné, T. Li, B. Bourdin, J.J. Marigo, y C. Maurini. Crack nucleation in variational phase-field models of brittle fracture. *Journal of the Mechanics and Physics of Solids*, 110:80–99, 2018.

[114] A.E. Huespe, J. Oliver, M.D.G. Pulido, S. Blanco, y D. Linero. On the fracture models determined by the continuum-strong discontinuity approach. *International journal of fracture*, 137(1-4):211–229, 2006.

[115] A. Needleman. Some issues in cohesive surface modeling. *Procedia IUTAM*, 10:221–246, 2013.
[116] M. Alam, J.P. Parmigiani, y J.J. Kruzic. An experimental assessment of methods to predict crack deflection at an interface. *Engineering Fracture Mechanics*, 181:116–129, 2017.
[117] Javier A. Zambrano, Alfredo E. Huespe, Santiago Serebrinsky, Sebastian Toro, y Pablo J. Sánchez. Diseño de materiales compuestos para aumento de tenacidad bajo el enfoque de diseños bio-inspirados. *Asociación Argentina de Mecánica Computacional*, XL:787–796, 2023.
[118] Vincent C Nardone y Karl M Prewo. Tensile performance of carbon-fibre-reinforced glass. *Journal of materials science*, 23:168–180, 1988.
[119] Craig A Folsom, Frank W Zok, Fred F Lange, y David B Marshall. Mechanical behavior of a laminar ceramic/fiber-reinforced epoxy composite. *Journal of the American Ceramic Society*, 75(11):2969–2975, 1992.
[120] MY He, FE Heredia, DJ Wissuchek, MC Shaw, y AG Evans. The mechanics of crack growth in layered materials. *Acta metallurgica et materialia*, 41(4):1223–1228, 1993.
[121] Wen-Chiang Tu, Fred F Lange, y Anthony G Evans. Concept for a damage-tolerant ceramic composite with "strong" interfaces. *Journal of the American Ceramic Society*, 79(2):417–424, 1996.
[122] W Kreher y W Pompe. Increased fracture toughness of ceramics by energy-dissipative mechanisms. *Journal of Materials Science*, 16:694–706, 1981.
[123] AG Evans y KT Faber. Crack-growth resistance of microcracking brittle materials. *Journal of the American ceramic society*, 67(4):255–260, 1984.
[124] LRF Rose. Microcrack interaction with a main crack. *International Journal of Fracture*, 31:233–242, 1986.
[125] John W Hutchinson. Crack tip shielding by micro-cracking in brittle solids. *Acta metallurgica*, 35(7): 1605–1619, 1987.
[126] David KM Shum y John W Hutchinson. On toughening by microcracks. *Mechanics of Materials*, 9(2): 83–91, 1990.
[127] Manfred Ruehle, Anthony G Evans, Robert M McMeeking, PG Charalambides, y JW Hutchinson. Microcrack toughening in alumina/zirconia. *Acta Metallurgica*, 35(11):2701–2710, 1987.
[128] Albert Lin y Marc André Meyers. Growth and structure in abalone shell. *Materials Science and Engineering: A*, 390(1-2):27–41, 2005.
[129] Katia Bertoldi, Davide Bigoni, y WJ Drugan. Nacre: an orthotropic and bimodular elastic material. *Composites Science and Technology*, 68(6):1363–1375, 2008.
[130] F. Song, X. Zhang, y Y. Bai. Microstructure and characteristics in the organic matrix layers of nacre. *J. Mater*, 17 (7):1567–1570., 2002.
[131] R.Z. Wang, Z. Suo, A.G. Evans, N. Yao, y I.A Aksay. Deformation mechanisms in nacre. *J. Mater. Res*, 16: 2485–2493, 2001.
[132] Z. Huang y X. Li. Origin of flaw-tolerance in nacre. *Sci. Rep*, 3:1693, 2013.
[133] H. Li, Y. Yue, X. Han, y X. Li. Plastic deformation enabled energy dissipation in a bionano wire structured armor. *Nano Lett*, 14 (5):2578–2583, 2014.
[134] B.L. Smith, T.E. Schaer, M. Viani, J.B. Thompson, N.A. Frederick, J. Kindt, A. Belcher, G.D. Stucky, D.E. Morse, y P.K. Hansma. Molecular mechanistic origin of the toughness of natural adhesive mbres and composites. *Nature*, 399:761–763, 1999.
[135] Palla Murali, Tanmay K. Bhandakkar, Wei Li Cheah, Mark H. Jhon, Huajian Gao, y Rajeev Ahluwalia. Role of modulus mismatch on crack propagation and toughness enhancement in bioinspired composites. *Physical Review*, 84:015102, 2011.
[136] AP Jackson, Julian FV Vincent, y RM Turner. The mechanical design of nacre. *Proceedings of the Royal society of London. Series B. Biological sciences*, 234(1277):415–440, 1988.
[137] Andrew P Jackson, Julian FV Vincent, y RM Turner. Comparison of nacre with other ceramic composites. *Journal of Materials Science*, 25:3173–3178, 1990.
[138] Horacio D Espinosa, Allison L Juster, Felix J Latourte, Owen Y Loh, David Gregoire, y Pablo D Zavattieri. Tablet-level origin of toughening in abalone shells and translation to synthetic composite materials. *Nature communications*, 2(1):173, 2011.
[139] Fan Liu, Tiantian Li, Zian Jia, y Lifeng Wang. Combination of stiffness, strength, and toughness in 3d printed interlocking nacre-like composites. *Extreme Mechanics Letters*, 35:100621, 2020.
[140] M.Y. He y J.W. Hutchinson. Crack deflection at an interface between dissimilar elastic materials. *International journal of solids and structures*, 25(9):1053–1067, 1989.
[141] D. Martinez y V. Gupta. Energy criterion for crack deflection at an interface between two orthotropic media. *Journal of the Mechanics and Physics of Solids*, 42(8):1247–1271, 1994.

[142] Avtar Singh, Taranjeet Singh Sandhu, y Siladitya Pal. Interplay of various fracture mechanisms in bio-inspired staggered structure. *Mechanics of Materials*, 139:103215, 2019.

[143] B. Bourdin, G. A Francfort, y J.J. Marigo. Numerical experiments in revisited brittle fracture. *Journal of the Mechanics and Physics of Solids*, 48(4):797–826, 2000.

[144] J.Y. Wu. Robust numerical implementation of non-standard phase-field damage models for failure in solids. *Computer Methods in Applied Mechanics and Engineering*, 340:767–797, 2018.

[145] N. Singh, C.V. Verhoosel, R. De Borst, y E.H. Van Brummelen. A fracture-controlled path-following technique for phase-field modeling of brittle fracture. *Finite Elements in Analysis and Design*, 113:14–29, 2016.

[146] R. Bharali, S. Goswami, C. Anitescu, y T. Rabczuk. A robust monolithic solver for phase-field fracture integrated with fracture energy based arc-length method and under-relaxation. *Computer Methods in Applied Mechanics and Engineering*, 394:114927, 2022.

[147] E. Börjesson, J.J.C. Remmers, y M. Fagerström. A generalised path-following solver for robust analysis of material failure. *Computational Mechanics*, 70(2):437–450, 2022.

[148] Bruno A. Storti, Alejandro E. Albanesi, Ignacio Peralta, Mario A. Storti, y Víctor D. Fachinotti. On the performance of a Chimera-FEM implementation to treat moving heat sources and moving boundaries in time-dependent problems. *Finite Elements in Analysis and Design*, 208:103789, 2022. doi: 10.1016/j.finel.2022.103789.

[149] Juan C. Álvarez Hostos, Bruno Storti, Benjamín A. Tourn, y Víctor D. Fachinotti. Solving heat conduction problems with a moving heat source in arc welding processes via an overlapping nodes scheme based on the improved element-free Galerkin method. *International Journal of Heat and Mass Transfer*, 192:122940, 2022. doi: 10.1016/j.ijheatmasstransfer.2022.122940.

[150] Kaitlynn M Conway, Cody Kunka, Benjamin C White, Garrett J Pataky, y Brad L Boyce. Increasing fracture toughness via architected porosity. *Materials & Design*, 205:109696, 2021.

[151] J.L. Strom y J.P. Parmigiani. Transition of crack path at bi-material interfaces. *Engineering Fracture Mechanics*, 115:13–21, 2014.

[152] Tao You, Qi-Zhi Zhu, Peng-Fei Li, y Jian-Fu Shao. Incorporation of tension-compression asymmetry into plastic damage phase-field modeling of quasi brittle geomaterials. *International Journal of Plasticity*, 124: 71–95, 2020.

[153] M. Arriaga y H. Waisman. Combined stability analysis of phase-field dynamic fracture and shear band localization. *International Journal of Plasticity*, 96:81–119, 2017.

[154] Mehrdad Isfandbod y Emilio Martínez-Pañeda. A mechanism-based multi-trap phase field model for hydrogen assisted fracture. *International Journal of Plasticity*, página 103044, 2021.

[155] F.P. Duda, A. Ciarbonetti, S. Toro, y A.E. Huespe. A phase-field model for solute-assisted brittle fracture in elastic-plastic solids. *International Journal of Plasticity*, 102:16–40, 2018.

[156] A. Kumar, B. Bourdin, G.A. Francfort, y O. Lopez-Pamies. Revisiting nucleation in the phase-field approach to brittle fracture. *Journal of the Mechanics and Physics of Solids*, 142:104027, 2020.

[157] J.Y. Wu y V.P. Nguyen. A length scale insensitive phase-field damage model for brittle fracture. *Journal of the Mechanics and Physics of Solids*, 119:20–42.

[158] A.C. Hansen-Dörr, R. de Borst, P. Hennig, y M. Kästner. Phase-field modelling of interface failure in brittle materials. *Computer Methods in Applied Mechanics and Engineering*, 346:25–42, 2019.

[159] T.T. Nguyen, J. Yvonnet, D. Waldmann, y Q.C. He. Phase field modeling of interfacial damage in heterogeneous media with stiff and soft interphases. *Engineering Fracture Mechanics*, 218:106574, 2019.

[160] A. Needleman. Some issues in cohesive surface modeling. *Procedia IUTAM*, 10:221–246, 2014.

[161] V.I. Levitas. Phase transformations, fracture, and other structural changes in inelastic materials. *International Journal of Plasticity*, 140:102914, 2021.

[162] F.P Duda, A.F. Sarmiento, y E. Fried. Coupled diffusion and phase transition: Phase fields, constraints, and the cahn–hilliard equation. *Meccanica*, páginas 1–19, 2021.

[163] L. De Lorenzis y T. Gerasimov. Numerical implementation of phase-field models of brittle fracture. En *Modeling in Engineering Using Innovative Numerical Methods for Solids and Fluids*, páginas 75–101. Springer, 2020.

[164] A.E. Huespe y J. Oliver. Crack models with embedded discontinuities. En G. Hofstetter y G. Meshke, editores, *Numerical modeling of concrete cracking*, páginas 99–159. Springer, 2011.

[165] M. Ortiz y A. Pandolfi. Finite-deformation irreversible cohesive elements for three-dimensional crack-propagation analysis. *International journal for numerical methods in engineering*, 44(9):1267–1282, 1999.

[166] M. N. da Silva Jr, F.P. Duda, y E. Fried. Sharp-crack limit of a phase-field model for brittle fracture. *Journal of the Mechanics and Physics of Solids*, 61(11):2178–2195, 2013.

[167] Ted L Anderson. *Fracture mechanics: fundamentals and applications*. CRC press, 2017.
[168] J Dundurs. Edge-bonded dissimilar orthogonal elastic wedge. *J Appl Mech*, 36:650–652, 1969.
[169] W. Lee, Y.H. Yoo, y H. Shin. Reconsideration of crack deflection at planar interfaces in layered systems. *Composites science and technology*, 64(15):2415–2423, 2004.
[170] M.Y. He y J.W. Hutchinson. Kinking of a crack out of an interface. *J. Appl. Mech.*, 56(2):270–278, 1989.
[171] H.C. Tankasala, V.S. Deshpande, y N.A. Fleck. Crack kinking at the tip of a mode i crack in an orthotropic solid. *International journal of fracture*, 207(2):181–191, 2017.
[172] J.W. Pro, S. Sehr, R.K. Lim, L.R. Petzold, y M.R. Begley. Conditions controlling kink crack nucleation out of, and delamination along, a mixed-mode interface crack. *Journal of the Mechanics and Physics of Solids*, 121:480–495, 2018.
[173] M. Shah, C. Mabru, F. Rezai-Aria, I. Souki, y R.A. Pasha. An estimation of stress intensity factor in a clamped se (t) specimen through numerical simulation and experimental verification: case of fcgr of aisi h11 tool steel. *ACTA METALLURGICA SINICA-ENGLISH LETTERS*, 25(4):307–319, 2012.
[174] O.L. Manzoli, A.L. Gamino, E.A. Rodrigues, y G.K.S. Claro. Modeling of interfaces in two-dimensional problems using solid finite elements with high aspect ratio. *Computers & Structures*, 94:70–82, 2012.
[175] Julieta Gutierrez, Alfredo E Huespe, y Santiago A Serebrinsky. Efecto combinado de la tenacidad y la tensión crítica en la deflexión de fracturas hidráulicas. *Mecánica Computacional*, 39(20):707–716, 2022.
[176] F. Barthelat, H. Tang, P. Zavattieri, C.-M. Li, y H. Espinosa. On the mechanics of mother-of-pearl: a key feature in the material hierarchical structure. *Mech. Phys. Solids*, 55 (2):306–337., 2007.
[177] K.S. Katti, D.R. Katti, S.M. Pradhan, y A. Bhosle. Platelet interlocks are the key to toughness and strength in nacre. *J. Mater. Res*, 20 (5:1097–1100, 2005.
[178] L.S. Dimas y M.J. Buehler. Modeling and additive manufacturing of bioinspired composites with tunable fracture mechanical properties. *SoftMatter*, 10 (25):4436–4442, 2014.
[179] S. Kamat, X. Su, R. Ballarini, y A.H Heuer. Structural basis for the fracture toughness of the shell of the conch strombus gigas. *Nature*, 405:1036–1040, 2000.
[180] K. Okumura y P.-G de Gennes. Why is nacre strong? elastic theory and fracture mechanics for biocomposites with stratimed structures. *Eur.Phys.J.E*, 4:121–127., 2001.
[181] T. Gerasimov y L. De Lorenzis. A line search assisted monolithic approach for phase-field computing of brittle fracture. *Computer Methods in Applied Mechanics and Engineering*, 312:276–303, 2016.
[182] P.K. Kristensen y E. Martínez-Pañeda. Phase field fracture modelling using quasi-newton methods and a new adaptive step scheme. *Theoretical and Applied Fracture Mechanics*, 107:102446, 2020.
[183] T. Heister, M.F. Wheeler, y T. Wick. A primal-dual active set method and predictor-corrector mesh adaptivity for computing fracture propagation using a phase-field approach. *Computer Methods in Applied Mechanics and Engineering*, 290:466–495, 2015.
[184] O. Lampron, D. Therriault, y M. Lévesque. An efficient and robust monolithic approach to phase-field quasi-static brittle fracture using a modified newton method. *Computer Methods in Applied Mechanics and Engineering*, 386:114091, 2021.
[185] A. Kopaničáková, H. Kothari, y R. Krause. Nonlinear field-split preconditioners for solving monolithic phase-field models of brittle fracture. *Computer Methods in Applied Mechanics and Engineering*, 403: 115733, 2023.
[186] B. Bourdin. Numerical implementation of the variational formulation for quasi-static brittle fracture. *Interfaces and free boundaries*, 9(3):411–430, 2007.
[187] S. Burke, Ch. Ortner, y E. Süli. An adaptive finite element approximation of a variational model of brittle fracture. *SIAM J. Numer. Anal.*, 48(3):980–1012, 2010.
[188] M.K. Brun, T. Wick, I. Berre, J.M. Nordbotten, y F.A. Radu. An iterative staggered scheme for phase field brittle fracture propagation with stabilizing parameters. *Computer Methods in Applied Mechanics and Engineering*, 361:112752, 2020.
[189] F.P. Duda, J.M. Barbosa, L.J. Guimarães, y A.C. Souza. Modeling of coupled deformation-diffusion-damage in elastic solids. *International Journal of Modeling and Simulation for the Petroleum Industry*, 1(1):85–93, 2007.
[190] J.J. Brust y C.G. Marcia, R.F.and Petra. Large-scale quasi-newton trust-region methods with low-dimensional linear equality constraints. *Computational Optimization and Applications*, 74(3):669–701, 2019.
[191] E. Martínez-Pañeda, S.D Busto, y C. Betegón. Non-local plasticity effects on notch fracture mechanics. *Theor. Appl. Fract. Mech.*, 92:276–287, 2017.
[192] T. Gerasimov y L. De Lorenzis. On penalization in variational phase-field models of brittle fracture. *Com-*

puter Methods in Applied Mechanics and Engineering, 354:990–1026, 2019.

[193] S. May, J. Vignollet, y R. de Borst. A new arc-length control method based on the rates of the internal and the dissipated energy. *Engineering Computations*, 33(1):100–115, 2016.

[194] M. A. Crisfield. *Non-linear Finite Element Analysis of Solids and Structures, Essential, Volume 1*. John Wiley & Sons, 2000.

[195] K. Pham y J.J. Marigo. Construction and analysis of localized responses for gradient damage models in a 1d setting. *Vietnam Journal of Mechanics*, 31(3-4):233–246, 2009.

[196] M. Ambati, T. Gerasimov, y L. De Lorenzis. A review on phase-field models of brittle fracture and a new fast hybrid formulation. *Computational Mechanics*, 55(2):383–405, 2015.

[197] S. Li, M.D. Thouless, A.M. Waas, J.A. Schroeder, y P.D. Zavattieri. Use of mode-i cohesive-zone models to describe the fracture of an adhesively-bonded polymer-matrix composite. *Composites Science and Technology*, 65(2):281–293, 2005.

[198] J. Zambrano, S. Toro, P.J. Sánchez, F.P. Duda, C.G. Méndez, y A.E. Huespe. Interaction analysis between a propagating crack and an interface: Phase field and cohesive surface models. *International Journal of Plasticity*, página 103341, 2022.

[199] J.Y. Wu, Y. Huang, y V.P. Nguyen. On the bfgs monolithic algorithm for the unified phase field damage theory. *Computer Methods in Applied Mechanics and Engineering*, 360:112704, 2020.

[200] Shuailing Lan y Feng Jiao. Modeling of heat source in grinding zone and numerical simulation for grinding temperature field. *The International Journal of Advanced Manufacturing Technology*, 103(5-8):3077–3086, 2019. doi: 10.1007/s00170-019-03662-w.

[201] A. Khosravifard, M. R. Hematiyan, y N. Ghiasi. A meshfree method with dynamic node reconfiguration for analysis of thermo-elastic problems with moving concentrated heat sources. *Applied Mathematical Modelling*, 79:624–638, 2020. doi: 10.1016/j.apm.2019.10.055.

[202] Ali Moarrefzadeh, Shahram Shahrooi, y Mahdi Jalali Azizpour. The application of the meshless local Petrov-Galerkin method for the analysis of heat conduction and residual stress due to welding. *The International Journal of Advanced Manufacturing Technology*, 104(1-4):723–742, 2019. doi: 10.1007/s00170-019-03830-y.

[203] Juan C. Álvarez-Hostos, Bruno Storti, Benjamín A. Tourn, y Víctor D. Fachinotti. Solving heat conduction problems with a moving heat source in arc welding processes via an overlapping nodes scheme based on the improved element-free Galerkin method. *International Journal of Heat and Mass Transfer*, 192:122940, 2022. doi: 10.1016/j.ijheatmasstransfer.2022.122940.

[204] Yihua Xiao, Haifei Zhan, Yuantong Gu, y Qinghua Li. Modeling heat transfer during friction stir welding using a meshless particle method. *International Journal of Heat and Mass Transfer*, 104:288–300, 2017. doi: 10.1016/j.ijheatmasstransfer.2016.08.047.

[205] Wajid Khan, Siraj ul Islam, y Baseer Ullah. Structural optimization based on meshless element free Galerkin and level set methods. *Computer Methods in Applied Mechanics and Engineering*, 344:144–163, 2019. ISSN 0045-7825. doi: 10.1016/j.cma.2018.09.024.

[206] Songtao Chen y Qinglin Duan. An adaptive second-order element-free Galerkin method for additive manufacturing process. *Computational Materials Science*, 183:109911, 2020. doi: 10.1016/j.commatsci.2020.109911.

[207] Kajal Khan, Gunther Mohr, Kai Hilgenberg, y A. De. Probing a novel heat source model and adaptive remeshing technique to simulate laser powder bed fusion with experimental validation. *Computational Materials Science*, 181:109752, 2020. doi: 10.1016/j.commatsci.2020.109752.

[208] Alaa Olleak y Zhimin Xi. Simulation of Layer-by-Layer Selective Laser Melting Process with an Efficient Remeshing Technique. *Procedia Manufacturing*, 34:613–618, 2019. doi: 10.1016/j.promfg.2019.06.167.

[209] Qing Xia, Gangming Sun, Junseok Kim, y Yibao Li. Multi-scale modeling and simulation of additive manufacturing based on fused deposition technique. *Physics of Fluids*, 35(3):034116, 2023. doi: 10.1063/5.0141316.

[210] S. Peirovi, M. Pourasghar, A. Farokhi Nejad, y M. A. Hassan. A study on the different finite element approaches for laser cutting of aluminum alloy sheet. *The International Journal of Advanced Manufacturing Technology*, 93(1-4):1399–1413, 2017. doi: 10.1007/s00170-017-0599-0.

[211] Mohd Shahar Sulaiman, Yupiter H. P. Manurung, Baohua Chang, Mohd Shahriman Adenan, Qairul Najmi Enseri, Norasiah Muhammad, Hui Leng Choo, Muhd Faiz Mat, Birgit Awiszus, Andre Haelsig, Salina Saidin, y Yusuf Olanrewaju Busari. Analysis on grain growth of SS316L induced by plasma cutting process using probabilistic FEM with experimental verification. *The International Journal of Advanced Manufacturing Technology*, 122(7-8):2987–3005, 2022. doi: 10.1007/s00170-022-10082-w.

[212] G. R. Liu. *Mesh Free Methods*. CRC Press, second edition, 2009. doi: 10.1201/9781420040586.

[213] Edgar O. Reséndiz-Flores y Félix R. Saucedo-Zendejo. Two-dimensional numerical simulation of heat transfer with moving heat source in welding using the Finite Pointset Method. *International Journal of Heat and Mass Transfer*, 90:239–245, 2015. doi: 10.1016/j.ijheatmasstransfer.2015.06.023.

[214] Fatemeh Hejripour, Brian T. Helenbrook, Daniel T. Valentine, y Daryush K. Aidun. Mass transport and solidification phenomenon in dissimilar metals arc welding. *International Journal of Heat and Mass Transfer*, 144:118703, 2019. doi: 10.1016/j.ijheatmasstransfer.2019.118703.

[215] Christian Burkhardt, Paul Steinmann, y Julia Mergheim. Thermo-mechanical simulations of powder bed fusion processes: accuracy and efficiency. *Advanced Modeling and Simulation in Engineering Sciences*, 9 (1), 2022. doi: 10.1186/s40323-022-00230-y.

[216] Lin Cheng y Gregory J. Wagner. An optimally-coupled multi-time stepping method for transient heat conduction simulation for additive manufacturing. *Computer Methods in Applied Mechanics and Engineering*, 381:113825, 2021. doi: 10.1016/j.cma.2021.113825.

[217] Huerta Donea. *Finite Element Methods for Flow Problems*. John Wiley & Sons, 2003. ISBN 0471496669. URL https://www.ebook.de/de/product/3664971/donea_huerta_finite_element_methods_for_flow_problems.html.

[218] Pavel Solin, Karel Segeth, y Ivo Dolezel. *Higher-Order Finite Element Methods*. Chapman and Hall-CRC, 2003. doi: 10.1201/9780203488041.

[219] J. Bathe. *Finite Element Procedures (Second Edition)*. Prentice Hall, second edition, 2014.

[220] Sahil Garg y Mohit Pant. Meshfree Methods: A Comprehensive Review of Applications. *International Journal of Computational Methods*, 15(04):1830001, 2018. doi: 10.1142/s0219876218300015.

[221] Manish Kumar, Aditya Kumar Jha, Yash Bhagoria, y Pankaj Gupta. A review to explore different meshless methods in various Structural problems. *IOP Conference Series: Materials Science and Engineering*, 1116 (1):012119, 2021. doi: 10.1088/1757-899x/1116/1/012119.

[222] Jianping Zhang, Yang Shen, Huiyao Hu, Shuguang Gong, Shuying Wu, Zhiqi Wang, y Jian Huang. Transient heat transfer analysis of orthotropic materials considering phase change process based on element-free Galerkin method. *International Communications in Heat and Mass Transfer*, 125:105295, 2021. doi: 10.1016/j.icheatmasstransfer.2021.105295.

[223] Cheng-Yu Ku, Chih-Yu Liu, Weichung Yeih, Chein-Shan Liu, y Chia-Ming Fan. A novel space–time meshless method for solving the backward heat conduction problem. *International Journal of Heat and Mass Transfer*, 130:109–122, 2019. doi: 10.1016/j.ijheatmasstransfer.2018.10.083.

[224] Yu Yang y Sy-bor Wen. A new high accuracy meshfree method to directly simulate fluid dynamics and heat transfer of weakly compressible fluids. *International Journal of Heat and Mass Transfer*, 123:25–39, 2018. doi: 10.1016/j.ijheatmasstransfer.2018.02.081.

[225] Juan C. Álvarez Hostos, Benjamín Tourn, Javier A. Zambrano-Carrillo, Alirio J. Sarache-Piña, Luis A. Rondón-Silva, Alfonso D. Bencomo, y Eli S. Puchi-Cabrera. A simple staggered approach for comprehensive analysis of forced convection heat transfer using the improved element-free Galerkin–reduced integration penalty method to solve the fluid dynamics problem. *Engineering Analysis with Boundary Elements*, 150:672–696, 2023. doi: 10.1016/j.enganabound.2023.02.047.

[226] M. Afrasiabi, M. Roethlin, y K. Wegener. Thermal simulation in multiphase incompressible flows using coupled meshfree and particle level set methods. *Computer Methods in Applied Mechanics and Engineering*, 336:667–694, 2018. doi: 10.1016/j.cma.2018.03.021.

[227] Juan C. Álvarez Hostos, Eli S. Puchi Cabrera, y Alfonso D. Bencomo. Element-Free Galerkin Formulation by Moving Least Squares for Internal Energy Balance in a Continuous Casting Process. *steel research international*, 86(11):1403–1418, 2015. doi: 10.1002/srin.201400352.

[228] Juan C. Álvarez-Hostos, Alfonso D. Bencomo, Eli S. Puchi-Cabrera, Víctor D. Fachinotti, Benjamín Tourn, y Joselynne C. Salazar-Bove. Implementation of a standard stream-upwind stabilization scheme in the element-free Galerkin based solution of advection-dominated heat transfer problems during solidification in direct chill casting processes. *Engineering Analysis with Boundary Elements*, 106:170–181, sep 2019. doi: 10.1016/j.enganabound.2019.05.008.

[229] J. C. Álvarez-Hostos, A. D. Bencomo, y E. S. Puchi Cabrera. Element-free Galerkin formulation for solving transient heat transfer problems of direct chill casting processes. *Canadian Metallurgical Quarterly*, 56(2): 156–167, 2017. doi: 10.1080/00084433.2017.1288882.

[230] H. Wessels, C. Weißenfels, y P. Wriggers. Metal particle fusion analysis for additive manufacturing using the stabilized optimal transportation meshfree method. *Computer Methods in Applied Mechanics and Engineering*, 339:91–114, 2018. doi: 10.1016/j.cma.2018.04.042.

[231] Juan C. Álvarez-Hostos, Erick A. Gutierrez-Zambrano, Joselynne C. Salazar Bove, Eli S. Puchi-Cabrera, y Alfonso D. Bencomo. Solving heat conduction problems with phase-change under the heat source term approach and the element-free Galerkin formulation. *International Communications in Heat and Mass Transfer*, 2019.

[232] Hao Wang, Huming Liao, Zongyue Fan, Jiang Fan, Laurent Stainier, Xiaobai Li, y Bo Li. The Hot Optimal Transportation Meshfree (HOTM) method for materials under extreme dynamic thermomechanical conditions. *Computer Methods in Applied Mechanics and Engineering*, 364:112958, 2020. doi: 10.1016/j.cma.2020.112958.

[233] Juan C. Álvarez-Hostos, Eli S. Puchi-Cabrera, y Alfonso D. Bencomo. Stress Analysis of a Continuous Casting Process, on the Basis of the Element-Free Galerkin Formulation. *steel research international*, 88 (2):1600019, 2016. doi: 10.1002/srin.201600019.

[234] Juan Carlos Álvarez-Hostos, A. D. Bencomo, y E. S. Puchi Cabrera. Simple iterative procedure for the thermal-mechanical analysis of continuous casting processes, using the element-free Galerkin method. *Journal of Thermal Stresses*, 41(2):160–181, 2018. doi: 10.1080/01495739.2017.1389325.

[235] J. C. Álvarez-Hostos, A. D. Bencomo, E. S. Puchi Cabrera, J.-D. Guérin, y L. Dubar. Modeling the viscoplastic flow behavior of a 20MnCr5 steel grade deformed under hot-working conditions, employing a meshless technique. *International Journal of Plasticity*, 103:119–142, 2018. doi: 10.1016/j.ijplas.2018.01.005.

[236] Qiyin Lin, Jihong Wang, Jun Hong, Zheng Liu, y Zhihua Wang. A biomimetic generative optimization design for conductive heat transfer based on element-free Galerkin method. *International Communications in Heat and Mass Transfer*, 100:67–72, 2019. doi: 10.1016/j.icheatmasstransfer.2018.12.001.

[237] G. G. Stubblefield, K. Fraser, B. J. Phillips, J. B. Jordon, y P. G. Allison. A meshfree computational framework for the numerical simulation of the solid-state additive manufacturing process, additive friction stir-deposition (AFS-D). *Materials and Design*, 202:109514, 2021. doi: 10.1016/j.matdes.2021.109514.

[238] F. R. Saucedo-Zendejo y A. C. Cortes-Vargas. A meshfree method for analysis of thermo-elastic problems with moving heat sources in welding. *Journal of Physics: Conference Series*, 2275(1):012009, 2022. doi: 10.1088/1742-6596/2275/1/012009.

[239] Olivier Champagne y Xuan-Tan Pham. Numerical simulation of moving heat source in arc welding using the Element-free Galerkin method with experimental validation and numerical study. *International Journal of Heat and Mass Transfer*, 154:119633, 2020. doi: 10.1016/j.ijheatmasstransfer.2020.119633.

[240] S. H. Ju y H. H. Hsu. Solving numerical difficulties for element-free Galerkin analyses. *Computational Mechanics*, 53(2):273–281, 2013. doi: 10.1007/s00466-013-0906-z.

[241] James Olliff, Brad Alford, y Daniel C. Simkins. Efficient searching in meshfree methods. *Computational Mechanics*, 62(6):1461–1483, 2018. doi: 10.1007/s00466-018-1574-9.

[242] Z. J. Meng, H. Cheng, L. D. Ma, y Y. M. Cheng. The hybrid element-free Galerkin method for three-dimensional wave propagation problems. *International Journal for Numerical Methods in Engineering*, 117(1):15–37, 2018. doi: 10.1002/nme.5944.

[243] H. Cheng, M. J. Peng, y Y. M. Cheng. A hybrid improved complex variable element-free Galerkin method for three-dimensional advection-diffusion problems. *Engineering Analysis with Boundary Elements*, 97: 39–54, 2018. doi: 10.1016/j.enganabound.2018.09.007.

[244] H. Cheng, M. J. Peng, y Y. M. Cheng. The dimension splitting and improved complex variable element-free Galerkin method for 3-dimensional transient heat conduction problems. *International Journal for Numerical Methods in Engineering*, 114(3):321–345, feb 2018. doi: 10.1002/nme.5745.

[245] Jufeng Wang y Fengxin Sun. A hybrid generalized interpolated element-free Galerkin method for Stokes problems. *Engineering Analysis with Boundary Elements*, 111:88–100, 2020. doi: 10.1016/j.enganabound.2019.11.002.

[246] Mehdi Dehghan y Mostafa Abbaszadeh. Proper orthogonal decomposition variational multiscale element free Galerkin (POD-VMEFG) meshless method for solving incompressible Navier-Stokes equation. *Computer Methods in Applied Mechanics and Engineering*, 311:856–888, 2016. doi: 10.1016/j.cma.2016.09.008.

[247] Mostafa Abbaszadeh, Mehdi Dehghan, Amirreza Khodadadian, Nima Noii, Clemens Heitzinger, y Thomas Wick. A reduced-order variational multiscale interpolating element free Galerkin technique based on proper orthogonal decomposition for solving Navier–Stokes equations coupled with a heat transfer equation: Nonstationary incompressible Boussinesq equations. *Journal of Computational Physics*, 426:109875, 2021. doi: 10.1016/j.jcp.2020.109875.

[248] Jianghong Chen, Xiaohua Zhang, Ping Zhang, y Jiheng Deng. Variational multiscale element free Galerkin method for natural convection with porous medium flow problems. *International Journal of Heat and Mass*

Transfer, 107:1014–1027, 2017. doi: 10.1016/j.ijheatmasstransfer.2016.11.008.

[249] Tao Zhang y Xiaolin Li. Variational multiscale interpolating element-free Galerkin method for the nonlinear Darcy-Forchheimer model. *Computers & Mathematics with Applications*, 2019. doi: 10.1016/j.camwa.2019.07.003.

[250] Juan C. Álvarez-Hostos, Victor D. Fachinotti, Alirio J. Sarache Piña, Alfonso D. Bencomo, y Eli S. Puchi-Cabrera. Implementation of standard penalty procedures for the solution of incompressible Navier-Stokes equations, employing the element-free Galerkin method. *Engineering Analysis with Boundary Elements*, 96:36–54, 2018. doi: 10.1016/j.enganabound.2018.08.008.

[251] Juan C. Álvarez-Hostos, Marcela A. Cruchaga, Víctor D. Fachinotti, Javier A. Zambrano Carrillo, y Esteban Zamora. A plausible extension of standard penalty, streamline upwind and immersed boundary techniques to the improved element-free Galerkin-based solution of incompressible Navier–Stokes equations. *Computer Methods in Applied Mechanics and Engineering*, 372:113380, 2020. doi: 10.1016/j.cma.2020.113380.

[252] Juan C. Álvarez-Hostos, Joselynne C. Salazar-Bove, Marcela A. Cruchaga, Víctor D. Fachinotti, y Rafael A. Mujica-Agelvis. Solving steady-state lid-driven square cavity flows at high Reynolds numbers via a coupled improved element-free Galerkin–reduced integration penalty method. *Computers and Mathematics with Applications*, 99:211–228, 2021. doi: 10.1016/j.camwa.2021.08.013.

[253] Tao Zhang y Xiaolin Li. A generalized element-free Galerkin method for Stokes problem. *Computers & Mathematics with Applications*, 75(9):3127–3138, 2018. doi: 10.1016/j.camwa.2018.01.035.

[254] Bingbing Wang, Qinglin Duan, y Minghao Zhao. Improved integration scheme for the second-order consistent element-free Galerkin method. *Engineering Analysis with Boundary Elements*, 98:157–171, 2019. doi: 10.1016/j.enganabound.2018.10.020.

[255] Z. Ullah, W. M. Coombs, y C. E. Augarde. An adaptive finite element/meshless coupled method based on local maximum entropy shape functions for linear and nonlinear problems. *Computer Methods in Applied Mechanics and Engineering*, 267:111–132, 2013. doi: 10.1016/j.cma.2013.07.018.

[256] Zahur Ullah, Will Coombs, y C. Augarde. Parallel computations in nonlinear solid mechanics using adaptive finite element and meshless methods. *Engineering Computations*, 33(4):1161–1191, 2016. doi: 10.1108/ec-06-2015-0166.

[257] P. Metsis y M. Papadrakakis. Overlapping and non-overlapping domain decomposition methods for large-scale meshless EFG simulations. *Computer Methods in Applied Mechanics and Engineering*, 229-232: 128–141, 2012. doi: 10.1016/j.cma.2012.03.012.

[258] Hui-Ping Wang, Cheng-Tang Wu, Yong Guo, y Mark E. Botkin. A coupled meshfree/finite element method for automotive crashworthiness simulations. *International Journal of Impact Engineering*, 36(10-11):1210–1222, 2009. doi: 10.1016/j.ijimpeng.2009.03.004.

[259] T. Rabczuk, S. P. Xiao, y M. Sauer. Coupling of mesh-free methods with finite elements: basic concepts and test results. *Communications in Numerical Methods in Engineering*, 22(10):1031–1065, 2006. doi: 10.1002/cnm.871.

[260] Yaqing Zhang, Wenjie Ge, Yonghong Zhang, y Zhenfei Zhao. Topology optimization method with direct coupled finite element–element-free Galerkin method. *Advances in Engineering Software*, 115:217–229, 2018. doi: 10.1016/j.advengsoft.2017.09.012.

[261] August Johansson, Benjamin Kehlet, Mats G. Larson, y Anders Logg. Multimesh finite element methods: Solving PDEs on multiple intersecting meshes. *Computer Methods in Applied Mechanics and Engineering*, 343:672–689, jan 2019. doi: 10.1016/j.cma.2018.09.009.

[262] Bruno Storti, Luciano Garelli, Mario Storti, y Jorge D'Elía. A matrix-free Chimera approach based on Dirichlet–Dirichlet coupling for domain composition purposes. *Computers and Mathematics with Applications*, 79(12):3310–3330, 2020. doi: 10.1016/j.camwa.2020.01.021.

[263] Michael J. Brazell, Jayanarayanan Sitaraman, y Dimitri J. Mavriplis. An overset mesh approach for 3D mixed element high-order discretizations. *Journal of Computational Physics*, 322:33–51, 2016. doi: 10.1016/j.jcp.2016.06.031.

[264] F. Meng, J. W. Banks, W. D. Henshaw, y D. W. Schwendeman. Fourth-order accurate fractional-step IMEX schemes for the incompressible Navier–Stokes equations on moving overlapping grids. *Computer Methods in Applied Mechanics and Engineering*, 366:113040, 2020. doi: 10.1016/j.cma.2020.113040.

[265] Ming-Jian Li, Jiawei Chen, Yanping Lian, Feiyu Xiong, y Daining Fang. An efficient and high-fidelity local multi-mesh finite volume method for heat transfer and fluid flow problems in metal additive manufacturing. *Computer Methods in Applied Mechanics and Engineering*, 404:115828, 2023. doi: 10.1016/j.cma.2022.115828.

[266] Bruno Storti, Luciano Garelli, Mario Storti, y Jorge D'Elía. Optimization of an internal blade cooling

passage configuration using a Chimera approach and parallel computing. *Finite Elements in Analysis and Design*, 177:103423, 2020. doi: 10.1016/j.finel.2020.103423.

[267] D. Rosenthal. The Theory of Moving Sources of Heat and Its Application to Metal Treatments. *Transactions Asme*, (43):849–866, 1946.

[268] Xuan-Tan Pham. Two-Dimensional Rosenthal Moving Heat Source Analysis Using the Meshless Element Free Galerkin Method. *Numerical Heat Trasnfer, Part A: Applications*, 63(11):807–823, jun 2013. doi: 10.1080/10407782.2013.757089.

[269] Jean Donea, Antonio Huerta, Jean-Philippe Ponthot, y Antonio Rodríguez-Ferran. Arbitrary Lagrangian-Eulerian Methods, 2017.

[270] H. Lomax, Thomas H. Pulliam, y David W. Zingg. *Fundamentals of Computational Fluid Dynamics*. Springer Berlin Heidelberg, 2001. doi: 10.1007/978-3-662-04654-8.

[271] Mihir Samantaray, Seshadev Sahoo, y Direndranath Thatoi. Computational modeling of heat transfer and sintering behavior during direct metal laser sintering of AlSi10Mg alloy powder. *Comptes Rendus Mécanique*, 346(11):1043–1054, 2018. doi: 10.1016/j.crme.2018.08.006.

[272] J. C. Álvarez-Hostos, A. D. Bencomo, E. S. Puchi Cabrera, y I. M. Figueroa Poleo. A pseudo-transient heat transfer simulation of a continuous casting process, employing the element-free Galerkin method. *International Journal of Cast Metals Research*, 31(1):47–55, 2017. doi: 10.1080/13640461.2017.1366002.

[273] Joan Baiges, Michele Chiumenti, Carlos A. Moreira, Miguel Cervera, y Ramon Codina. An adaptive Finite Element strategy for the numerical simulation of additive manufacturing processes. *Additive Manufacturing*, 37:101650, 2021. doi: 10.1016/j.addma.2020.101650.

[274] Wing Kam Liu Belytschko y Khalil Elkhodary Brian Moran. *Nonlinear Finite Elements for Continua and Structures*. John Wiley & Sons, 2013. ISBN 1118632702.

[275] T. Rabczuk y T. Belytschko. A three-dimensional large deformation meshfree method for arbitrary evolving cracks. *Computer Methods in Applied Mechanics and Engineering*, 196(29–30):2777–2799, 2007. doi: 10.1016/j.cma.2006.06.020.

[276] Qiang Wu, PiaoPiao Peng, y YuMin Cheng. The interpolating element-free Galerkin method for elastic large deformation problems. *Science China Technological Sciences*, 64(2):364–374, 2020. doi: 10.1007/s11431-019-1583-y.

[277] I. Guiamatsia, B. G. Falzon, G. A. O. Davies, y L. Iannucci. Element-Free Galerkin modelling of composite damage. *Composites Science and Technology*, 69(15–16):2640–2648, 2009. doi: 10.1016/j.compscitech.2009.08.005.

[278] Haitian Yang y Yiqian He. Solving heat transfer problems with phase change via smoothed effective heat capacity and element-free Galerkin methods. *International Communications in Heat and Mass Transfer*, 37 (4):385–392, 2010. doi: 10.1016/j.icheatmasstransfer.2009.12.002.

[279] Juan C. Álvarez Hostos, Benjamín Tourn, Javier A. Zambrano-Carrillo, Alirio J. Sarache-Piña, Luis A. Rondón-Silva, Alfonso D. Bencomo, y Eli S. Puchi-Cabrera. A simple staggered approach for comprehensive analysis of forced convection heat transfer using the improved element-free Galerkin–reduced integration penalty method to solve the fluid dynamics problem. *Engineering Analysis with Boundary Elements*, 150:672–696, 2023. doi: 10.1016/j.enganabound.2023.02.047.

[280] J. C. Álvarez Hostos, A. D. Bencomo, y E. S. Puchi Cabrera. Element-free Galerkin formulation for solving transient heat transfer problems of direct chill casting processes. *Canadian Metallurgical Quarterly*, 56(2):156–167, 2017. doi: 10.1080/00084433.2017.1288882.

[281] Himanshu Pathak, Akhilendra Singh, y Indra Vir Singh. Numerical simulation of bi-material interfacial cracks using EFGM and XFEM. *International Journal of Mechanics and Materials in Design*, 8(1):9–36, 2011. doi: 10.1007/s10999-011-9173-3.

[282] Stéphane Bordas, Timon Rabczuk, y Goangseup Zi. Three-dimensional crack initiation, propagation, branching and junction in non-linear materials by an extended meshfree method without asymptotic enrichment. *Engineering Fracture Mechanics*, 75(5):943–960, 2008. doi: 10.1016/j.engfracmech.2007.05.010.

[283] Timon Rabczuk, Stéphane Bordas, y Goangseup Zi. A three-dimensional meshfree method for continuous multiple-crack initiation, propagation and junction in statics and dynamics. *Computational Mechanics*, 40 (3):473–495, 2007. doi: 10.1007/s00466-006-0122-1.

[284] T. Rabczuk y T. Belytschko. Cracking particles: a simplified meshfree method for arbitrary evolving cracks. *International Journal for Numerical Methods in Engineering*, 61(13):2316–2343, 2004. doi: 10.1002/nme.1151.

[285] Ming Wu, Lijun Liu, y Junling Ding. An enthalpy method based on fixed-grid for quasi-steady modeling of solidification/melting processes of pure materials. *International Journal of Heat and Mass Transfer*, 108:

1383–1392, 2017. doi: 10.1016/j.ijheatmasstransfer.2017.01.018.

[286] Juan C. Álvarez Hostos, Marcela A. Cruchaga, Víctor D. Fachinotti, Javier A. Zambrano Carrillo, y Esteban Zamora. A plausible extension of standard penalty, streamline upwind and immersed boundary techniques to the improved element-free Galerkin-based solution of incompressible Navier–Stokes equations. *Computer Methods in Applied Mechanics and Engineering*, 372:113380, 2020. doi: 10.1016/j.cma.2020.113380.

[287] Juan C. Álvarez Hostos, Joselynne C. Salazar Bove, Marcela A. Cruchaga, Víctor D. Fachinotti, y Rafael A. Mujica Agelvis. Solving steady-state lid-driven square cavity flows at high Reynolds numbers via a coupled improved element-free Galerkin–reduced integration penalty method. *Computers amp; Mathematics with Applications*, 99:211–228, 2021. doi: 10.1016/j.camwa.2021.08.013.

[288] Juan C. Álvarez Hostos, Victor D. Fachinotti, Alirio J. Sarache Piña, Alfonso D. Bencomo, y Eli S. Puchi Cabrera. Implementation of standard penalty procedures for the solution of incompressible Navier–Stokes equations, employing the element-free Galerkin method. *Engineering Analysis with Boundary Elements*, 96:36–54, 2018. doi: 10.1016/j.enganabound.2018.08.008.

[289] Juan C. Álvarez Hostos, Eli S. Puchi Cabrera, y Alfonso D. Bencomo. Stress Analysis of a Continuous Casting Process, on the Basis of the Element-Free Galerkin Formulation. *steel research international*, 88 (2), 2016. doi: 10.1002/srin.201600019.

[290] Juan Carlos Álvarez Hostos, A. D. Bencomo, y E. S. Puchi Cabrera. Simple iterative procedure for the thermal–mechanical analysis of continuous casting processes, using the element-free Galerkin method. *Journal of Thermal Stresses*, 41(2):160–181, 2017. doi: 10.1080/01495739.2017.1389325.

[291] J. C. Álvarez Hostos, A. D. Bencomo, E. S. Puchi Cabrera, J.-D. Guérin, y L. Dubar. Modeling the viscoplastic flow behavior of a 20MnCr5 steel grade deformed under hot-working conditions, employing a meshless technique. *International Journal of Plasticity*, 103:119–142, 2018. doi: 10.1016/j.ijplas.2018.01.005.

[292] E. S. Puchi-Cabrera, J.-D. Guérin, J. G. La Barbera-Sosa, J. C. Álvarez Hostos, P. Moreau, M. Dubar, y L. Dubar. Friction Correction of Austenite Flow Stress Curves Determined under Axisymmetric Compression Conditions. *Experimental Mechanics*, 60(4):445–458, 2019. doi: 10.1007/s11340-019-00492-5.

[293] S. Y. Yu, M. J. Peng, H. Cheng, y Y. M. Cheng. The improved element-free Galerkin method for three-dimensional elastoplasticity problems. *Engineering Analysis with Boundary Elements*, 104:215–224, 2019. doi: 10.1016/j.enganabound.2019.03.040.

[294] George Bourantas, Benjamin F. Zwick, Grand R. Joldes, Adam Wittek, y Karol Miller. Simple and robust element-free Galerkin method with almost interpolating shape functions for finite deformation elasticity. *Applied Mathematical Modelling*, 96:284–303, 2021. doi: 10.1016/j.apm.2021.03.007.

[295] Juan C. Álvarez Hostos, Erick A. Gutierrez-Zambrano, Joselynne C. Salazar-Bove, Eli S. Puchi-Cabrera, y Alfonso D. Bencomo. Solving heat conduction problems with phase-change under the heat source term approach and the element-free Galerkin formulation. *International Communications in Heat and Mass Transfer*, 108:104321, 2019. doi: 10.1016/j.icheatmasstransfer.2019.104321.

[296] Juan C. Álvarez Hostos, Alfonso D. Bencomo, Eli S. Puchi-Cabrera, Víctor D. Fachinotti, Benjamín Tourn, y Joselynne C. Salazar-Bove. Implementation of a standard stream-upwind stabilization scheme in the element-free Galerkin based solution of advection-dominated heat transfer problems during solidification in direct chill casting processes. *Engineering Analysis with Boundary Elements*, 106:170–181, 2019. doi: 10.1016/j.enganabound.2019.05.008.

[297] Juan C. Álvarez Hostos, Eli S. Puchi Cabrera, y Alfonso D. Bencomo. Element-Free Galerkin Formulation by Moving Least Squares for Internal Energy Balance in a Continuous Casting Process. *steel research international*, 86(11):1403–1418, 2015. doi: 10.1002/srin.201400352.

[298] Mohit Pant, I. V. Singh, y B. K. Mishra. Numerical simulation of thermo-elastic fracture problems using element free Galerkin method. *International Journal of Mechanical Sciences*, 52(12):1745–1755, 2010. doi: 10.1016/j.ijmecsci.2010.09.008.

[299] Juan C. Álvarez Hostos, Benjamín A. Tourn, Javier A. Zambrano-Carrillo, Alirio J. Sarache-Piña, y Víctor D. Fachinotti. Solving heat conduction problems in the start-up stage of direct chill casting processes via a temperature-enthalpy mixed formulation based on the improved element-free Galerkin method. *International Journal of Heat and Mass Transfer*, 212:124231, 2023. doi: 10.1016/j.ijheatmasstransfer.2023.124231.

[300] Xiaodong Wang, Jie Ouyang, Jin Su, y Binxin Yang. On the superiority of the mixed element free Galerkin method for solving the steady incompressible flow problems. *Engineering Analysis with Boundary Elements*, 36(11):1618–1630, 2012. doi: 10.1016/j.enganabound.2012.05.006.

[301] Yulong Shao, Qinglin Duan, y Shasha Qiu. Consistent element-free Galerkin method for three-dimensional crack propagation based on a phase-field model. *Computational Materials Science*, 179:109694, 2020. doi:

10.1016/j.commatsci.2020.109694.

[302] Klaus-Jürgen Bathe. *Finite element procedures*. [Boston, Mass.], 2006. ISBN 9780979004902.

[303] Ren Hongping y Yumin Cheng. The interpolating element-free Galerkin (IEFG) method for two-dimensional elasticity problems. *International Journal of Applied Mechanics*, 03(04):735–758, 2011. doi: 10.1142/s1758825111001214.

[304] Fengxin Sun, Jufeng Wang, Qi Wei, y Yong Wu. An improved meshless method based on the dimension splitting moving least-squares method for elasticity problems. *Engineering Analysis with Boundary Elements*, 150:374–384, 2023. doi: 10.1016/j.enganabound.2023.02.025.

[305] Peng. Miaojuan, Liu. Pei, y Yumin. Cheng. The complex variable element-free galerkin (CVEFG) method for two-dimensional elasticity problems. *International Journal of Applied Mechanics*, 01(02):367–385, 2009. doi: 10.1142/s1758825109000162.

[306] Cheng Yumin, Jianfei Wang, y Li Rongxin. The complex variable element-free galerkin (CVEFG) method for two-dimensional elastodynamics problems. *International Journal of Applied Mechanics*, 04(04): 1250042, 2012. doi: 10.1142/s1758825112500421.

[307] Heng Cheng, Miaojuan Peng, Yumin Cheng, y Zhijuan Meng. The hybrid complex variable element-free Galerkin method for 3D elasticity problems. *Engineering Structures*, 219:110835, 2020. doi: 10.1016/j.engstruct.2020.110835.

[308] Piaopiao Peng, Heng Cheng, y Yumin Cheng. A Hybrid Reproducing Kernel Particle Method for Three-Dimensional Elasticity Problems. *International Journal of Applied Mechanics*, 15(09), 2023. doi: 10.1142/s1758825123500801.

[309] Mehdi Dehghan y Niusha Narimani. An element-free Galerkin meshless method for simulating the behavior of cancer cell invasion of surrounding tissue. *Applied Mathematical Modelling*, 59:500–513, 2018. doi: 10.1016/j.apm.2018.01.034.

[310] Xin Gao, Qinglin Duan, Yulong Shao, Xikui Li, Biaosong Chen, y Hongwu Zhang. Quadratically consistent one-point (QC1) integration for three-dimensional element-free Galerkin method. *Finite Elements in Analysis and Design*, 114:22–38, 2016. doi: 10.1016/j.finel.2016.01.003.

[311] Jin-Hu Pan, D. M. Li, Xu-Bao Luo, y Wei Zhu. An enriched improved complex variable element-free Galerkin method for efficient fracture analysis of orthotropic materials. *Theoretical and Applied Fracture Mechanics*, 121:103488, 2022. doi: 10.1016/j.tafmec.2022.103488.

[312] Sahil Garg y Mohit Pant. Numerical simulation of adiabatic and isothermal cracks in functionally graded materials using optimized element-free Galerkin method. *Journal of Thermal Stresses*, 40(7):846–865, 2017. doi: 10.1080/01495739.2017.1287534.

[313] Ayush Awasthi y Mohit Pant. Thermoelastic fracture analysis in orthotropic media using optimized element free Galerkin algorithm. *Mechanics of Advanced Materials and Structures*, 31(2):271–296, 2022. doi: 10.1080/15376494.2022.2114039.

[314] Miaojuan Peng, Dongming Li, y Yumin Cheng. The complex variable element-free Galerkin (CVEFG) method for elasto-plasticity problems. *Engineering Structures*, 33(1):127–135, 2011. doi: 10.1016/j.engstruct.2010.09.025.

[315] Jie Sun, Hong-Liang Yi, Ming Xie, y He-Ping Tan. New implementation of local RBF meshless scheme for radiative heat transfer in participating media. *International Journal of Heat and Mass Transfer*, 95:440–452, apr 2016. doi: 10.1016/j.ijheatmasstransfer.2015.12.002.

[316] Van Dung Nguyen, Charlotte Kirchhelle, Amir Abdollahi, Julián Andrés García Grajales, Dongli Li, Kamel Benatia, Khariton Gorbunov, Sylvin Bielle, Alain Goriely, y Antoine Jérusalem. A numerical framework coupling finite element and meshless methods in sequential and parallel simulations. *Finite Elements in Analysis and Design*, 219:103927, 2023. doi: 10.1016/j.finel.2023.103927.

[317] Aazim Shafi Lone, G. A. Harmain, y Azher Jameel. Enriched element free Galerkin method for solving frictional contact between solid bodies. *Mechanics of Advanced Materials and Structures*, 30(20):4227–4245, 2022. doi: 10.1080/15376494.2022.2092791.

[318] Z. L. Zhang y M. B. Liu. A decoupled finite particle method for modeling incompressible flows with free surfaces. *Applied Mathematical Modelling*, 60:606–633, aug 2018. doi: 10.1016/j.apm.2018.03.043.

[319] Ted L. Anderson. *Fracture mechanics: fundamentals and applications*. CRC press, 1995.

[320] Qinglin Duan, Bingbing Wang, Xin Gao, y Xikui Li. Quadratically consistent nodal integration for second order meshfree Galerkin methods. *Computational Mechanics*, 54(2):353–368, 2014. doi: 10.1007/s00466-014-0989-1.

[321] B. Moran y C. F. Shih. A general treatment of crack tip contour integrals. *International Journal of Fracture*, 35(4):295–310, 1987. doi: 10.1007/bf00276359.

[322] X.-K. Zhu. Corrected stress intensity factor solution for a British standard single edge notched tension (SENT) specimen. *Fatigue amp; Fracture of Engineering Materials amp; Structures*, 39(1):120–131, 2015. doi: 10.1111/ffe.12351.

[323] C. A. D. Fraga Filho, L. L. Schuina, y B. S. Porto. An Investigation into Neighbouring Search Techniques in Meshfree Particle Methods: An Evaluation of the Neighbour Lists and the Direct Search. *Archives of Computational Methods in Engineering*, 27(4):1093–1107, 2019. doi: 10.1007/s11831-019-09345-9.

[324] T. Belytschko, Y. Y. Lu, y L. Gu. Element-free Galerkin methods. *International Journal for Numerical Methods in Engineering*, 37(2):229–256, 1994. doi: 10.1002/nme.1620370205.

[325] B. N. Rao y S. Rahman. A coupled meshless-finite element method for fracture analysis of cracks. *International Journal of Pressure Vessels and Piping*, 78(9):647–657, 2001. doi: 10.1016/s0308-0161(01)00076-x.

[326] D. Hegen. Element-free Galerkin methods in combination with finite element approaches. *Computer Methods in Applied Mechanics and Engineering*, 135(1–2):143–166, 1996. doi: 10.1016/0045-7825(96)00994-2.

Doctorado en Ingeniería
Mención mecánica computacional

Título de la obra:

Contribuciones al modelado computacional de fractura frágil: nuevas estrategias y métodos híbridos

Autor: Javier Alexander Zambrano Carrillo

Lugar: Santa Fe, Argentina

Palabras Claves:

Mecánica computacional, mecánica de fractura,
modelo de campo de fase, fractura frágil, propagación de grietas,
mecanismos de interacción grieta-interface, tenacidad y resistencia a la fractura,
materiales compuestos, diseños bioinspirados,
metodología escalonada, estrategia de control de longitud de arco,
método de elemento finito, método de Galerkin libre de elementos mejorado,
métodos híbridos.